JOURNAL
OF
APPLIED PHYSICS

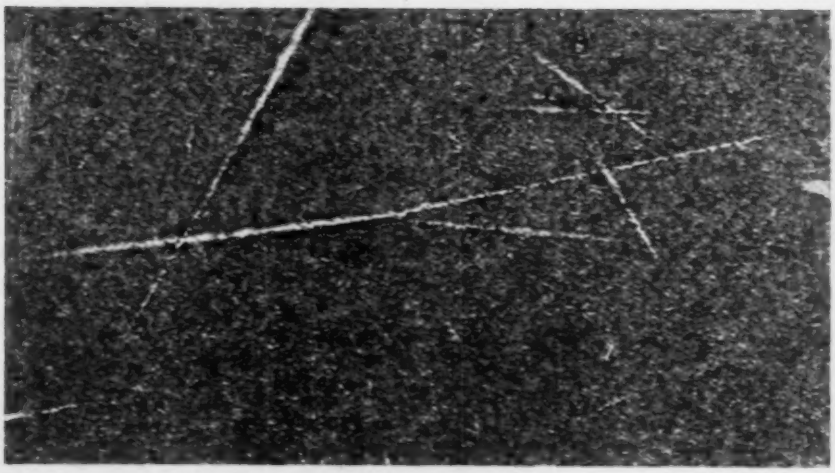

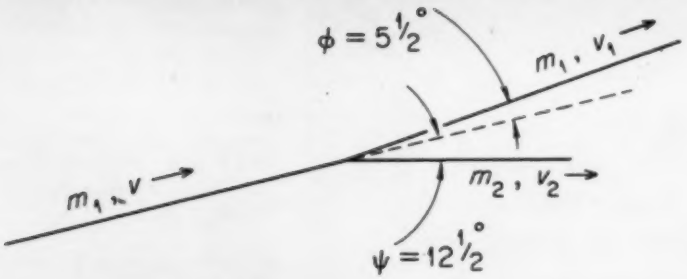

$$\tan\phi = \frac{m_2 \sin\theta}{m_1 + m_2 \cos\theta}$$

$$\theta = \pi - 2\psi$$

IF $\phi = 5\frac{1}{2}°$ AND $\theta = 155°$, $\frac{m_1}{m_2} = 5.3$

IF $m_2 = 16$, $m_1 = 85$

December
1960
Vol. 31 No. 12

Scattering of a Fission Fragment by an Oxygen Lattice Atom.

See Page 2199.

Special Issue on Electron Physics

NEW FRAMING

CAMERA

for the research group that has everything

This is the production model of the new Beckman & Whitley Model 192 Continuous-Writing Framing Camera.

Delivered to Avco Research and Advanced Development Division, outside Boston, the instrument will be used in experimental studies with high-temperature electric arcs or plasma jets, hypervelocity instrumentation, aeroballistics, and aerothermodynamics.

Shown focusing the objective lens of the newly installed camera is Glenn Hanson, head of the physics photography section of the division.

Chiefly, the advantage of the Model 192 is that it is capable of making 80 35-mm photographs of an ultra-high-speed event without the necessity of synchronizing the camera and the event. Its top operating speed is 1,400,000 exposures per second.

May we send you further details or discuss with you the problems you may have which the Model 192 or one of our other cameras might solve?

Beckman & Whitley

SAN CARLOS 8, CALIF. · U.S.A.

JOURNAL OF APPLIED PHYSICS

Vol. 31, No. 12 DECEMBER, 1960

In This Issue

Special Issue on Electron Physics

Recent Appearance Potential Measurements Using an Electrostatic Electron Selector . . . Larkin Kerwin and Paul Marmet 2071

Photoemission and Related Properties of the Alkali-Antimonides . . . William E. Spicer 2077

Oxygen on Nickel . . . L. H. Germer and C. D. Hartman 2085

Potential Distributions in a Low-Pressure Thermionic Converter . . . Peter L. Auer 2096

Bounds on Low-Energy Scattering Parameters . . . Larry Spruch and Leonard Rosenberg 2104

Regular Articles

New Complex Phase in the Copper-Gold System . . . R. E. Scott 2112

Experimental Investigation in Lead of the Whipple "Meteor Bumper" . . . Arnold E. Olshaker 2118

Magnetic Viscosity Due to Solute Atom Pairs. Part I. Theory of the Effect . . . G. Biorci, A. Ferro, and G. Montalenti 2121

Electron Optical Study of Basal Dislocations in Graphite . . . S. Amelinckx and P. Delavignette 2126

Mechanical Properties of Thin Single-Crystal Gold Films . . . Avery Catlin and Walter P. Walker 2135

Experimental Investigations of the Cesium Plasma Cell . W. A. Ranken, G. M. Grover, and E. W. Salmi 2140

Correlation of Low-Temperature Caloric and Magnetic Effects in TiFe . . K. Schröder and C. H. Cheng 2154

Effects of Irradiation on the Thermal Conductivity of Synthetic Sapphire . . . R. Berman, E. L. Foster, B. Schneidmesser, and S. M. A. Tirmizi 2156

Measurement of Thermal Conductivity by Utilization of the Peltier Effect. II. Correction for Wire Radiation and Determination of Specimen Radiation Emissivity . R. Simon, R. T. Bate, and E. H. Lougher 2160

Determination of Electrode Shapes for Axially Symmetric Electron Guns . . . Kenneth J. Harker 2165

Multiple Tube Collimator for Gas Beams . . . G. R. Hanes 2171

Corbino Disk . . . D. A. Kleinman and A. L. Schawlow 2176

Study of Initial Conditions in Constant Velocity Impact . . . James F. Bell 2188

Prediction of Fatigue Life . . . A. M. Freudenthal 2196

Electron Microscope Observations of Fission Fragment Tracks in Thin Films of UO_2 . . . T. S. Noggle and J. O. Stiegler 2199

Direct Measurements of the Surface Energies of Crystals . . . John J. Gilman 2208

Production of Dislocation Loops by a Combined Climb and Glide Mechanism . . . J. T. Fourie and H. G. F. Wilsdorf 2219

Electron Microscope Studies of Colloids in KCl . . . R. E. Simon and R. L. Sproull 2224

Some Effects Occurring in Dislocated Tellurium . . . J. S. Blakemore, J. W. Schultz, and K. C. Nomura 2226

Filled and Empty Dangling Bonds in III–V Compounds . . . D. B. Holt 2231

Velocity Behavior of a Growing Crack . . . E. N. Dulaney and W. F. Brace 2233

X-Ray Measurement of Grain Size . . . B. E. Warren 2237

Mechanism of Photoconductivity in Microcrystalline Powders . . . Richard H. Bube 2239

Field-Effect Modulation of Photoconductance in a Quasi-Intrinsic Semiconductor . . R. R. Bockemuehl 2255

Uniform Avalanche Effect in Silicon Three-Layer Diodes . . . A. Goetzberger 2260

Theoretical and Experimental Study of the Backscattering Cross Section of an Infinite Ribbon . . . Michael S. Macrakis 2261

Observation of Domains in Iron Whiskers Under High Fields . . . C. A. Fowler, Jr., E. M. Fryer, and David Treves 2267

Subsidiary Resonance in the Coincidence Region in Yttrium Iron Garnet . . . F. C. Rossol 2273

Gold-Induced Climb of Dislocations in Silicon . . . W. C. Dash 2275

Changes in Macroscopic Shape, Lattice Parameter, and Density in Crystals Due to Point Defects . . . R. W. Balluffi and R. O. Simmons 2284

Angular Distribution and Polarization of the Radiation Emitted by Electrons Accelerated in a Synchrotron . . . D. E. Bedo, D. H. Tomboulian, and J. A. Rigert 2289

High-Temperature Discharges in Ferroelectric Ceramics . . . John W. Northrip 2293

Experimental Study of Arc Stability. I . . . J. D. Cobine and G. A. Farrall 2296

Atom Ejection Patterns in Single-Crystal Sputtering . . . G. S. Anderson and G. K. Wehner 2305

Letters to the Editor:

Damage in UO_2 Films and Particles During Reactor Irradiation . . . T. K. Bierlein and B. Mastel 2314

Fission Fragment Damage in Nonfissionable Thin Films . . . T. K. Bierlein and B. Mastel 2315

Noise Figure and Gain of Parametric Converters . . . H. Heffner and G. Wade 2316

Ferromagnetic-Antiferromagnetic Interaction in Fe-FeS . . . J. H. Greiner, I. M. Croll, and M. Sulich 2316

Effect of Aging Time After Cleavage on the Plasticity of MgO Single Crystals . . . Carl A. Stearns 2317

Books Reviewed . . . 2318

Announcement . . . 2319

Author Index to Volume 31 . . . 2320

Subject Index to Volume 31 . . . 2335

Index to Advertisers . . . xxix

JOURNAL OF APPLIED PHYSICS

A journal of general physics and its applications to other sciences and to industry

Published by the

American Institute of Physics

GOVERNING BOARD

Members

Ralph A. Sawyer, *Chairman*
James G. Baker
R. H. Bolt
W. R. Brode
Harvey Brooks
Dirk Brouwer
J. W. Buchta
Vernet E. Eaton
J. H. Elliott
Herbert A. Erf
S. A. Goudsmit
W. W. Havens, Jr.
Winston E. Kock
R. Bruce Lindsay
H. V. Neher
C. J. Overbeck
G. E. Pake
Ray Pepinsky
F. W. Sears
Frederick Seitz
John Strong
George E. Uhlenbeck
M. E. Warga
Victor F. Weisskopf
W. R. Willets

ADMINISTRATION

Elmer Hutchisson
Director

Wallace Waterfall
Secretary and Treasurer

Henry A. Barton
Administrative Consultant

W. C. Kelly
Director of Education

Eugene H. Kone
Director of Public Relations

Hugh C. Wolfe
Director of Publications

Kathryn Setze
Assistant Treasurer

Norma Frankel
Publications Editor

Sistina Greco
Circulation Manager

Edward Tober
Manager, Production and Distribution

Theodore Vorburger
Advertising Manager

Emily Wolf
Manager, Special Services

Editor
J. H. Crawford, Jr.

Assistant Editor
Ethel McMillan

Editorial Board

Arthur Kantrowitz
A. A. Kip
James A. Krumhansl
J. E. Goldman
J. L. Tuck
C. A. Wert
Herman A. Haus
C. Lester Hogan
R. S. Rivlin

THE JOURNAL OF APPLIED PHYSICS is devoted to general physics and its applications to other sciences, to engineering, and to industry. Previous to 1937, this journal was called PHYSICS.

The JOURNAL OF APPLIED PHYSICS welcomes articles of two distinct kinds: (1) Descriptions of new results in experimental or theoretical physics which are of general interest to physicists. The author should explain his contribution in such a way that a physicist or engineer in another field of specialization can appreciate its objectives and essential features. (2) Critical reviews of particular areas of physics or surveys of extensive investigations at a single laboratory. Authors contemplating writing such should correspond with the Editor before they begin writing.

The JOURNAL OF APPLIED PHYSICS welcomes Letters to the Editor which are short [approximately four (4) typewritten pages] communications without abstracts. Timeliness, briefness, and degree of current importance of the subject matter will be of primary concern in the publication of Letters. Letters should not be looked upon as partial publication or announcement of more comprehensive work, but rather self-contained presentations in themselves.

Manuscripts should be submitted to the Editor, J. H. Crawford, Jr., Solid State Division, Oak Ridge National Laboratory, Oak Ridge, Tennessee. Authors should read the "Information for Contributors," facing page 1 of the January issue, before writing articles or letters. The *Style Manual* of the American Institute of Physics is also helpful to writers preparing manuscripts for journals published by the American Institute of Physics. It can be obtained for $1.00 from the American Institute of Physics, 335 East 45 Street, New York 17, New York.

Corrected proofs and all correspondence concerning papers in the process of publication should be addressed to the Publication Manager, American Institute of Physics, 335 East 45 Street, New York 17, New York.

Subscriptions, renewals, and orders for back numbers should be addressed to the American Institute of Physics, 335 East 45 Street, New York 17, New York.

Subscription Price	U.S. and Canada	Elsewhere
To members of member organizations of the American Institute of Physics and Affiliated Societies ..	$12.00	$13.00
To all others	14.00	16.00

Back Number Prices

Yearly back number rate when complete year is available: $17.00.
Single copies: $1.75 each (exception: March, 1958—$3.00 each).

Changes of address should be sent to the American Institute of Physics.

Advertising rates supplied on request. Orders, advertising copy, and cuts should be sent to the American Institute of Physics.

The Journal of Applied Physics is published monthly at Prince and Lemon Streets, Lancaster, Pennsylvania.
Second-class postage paid at Lancaster, Pa.

SILICON NEWS from Dow Corning

(PART 2)

The Untouchables

Single Crystal Silicon... the "Pinnacle of Purity"

Dow Corning single crystal silicon is produced by vacuum zone refining hyper-pure polycrystalline rod. Result: The purest silicon produced! Typically, impurity content is only 0.15 part per billion of boron for crystals that are consistently above 1000-ohms centimeter resistivity. Boron content is even lower for crystals of 2000-ohms centimeter and above . . . available on a selective basis.

This highest purity P-type silicon is the result of a completely integrated processing facility that starts with the production of trichlorosilane and ends with the crystals heat-sealed in airtight polyethylene envelopes. Purity and quality control dominate every step — in producing the basic chemicals . . . in growing polycrystalline rod . . . in vacuum zone refining . . . in product evaluation and in packaging.

Purity pays off . . . in rectifiers and diodes having higher peak inverse voltage ratings — in maximum utilization because of uniform lateral and radial profiles over the entire length of the rod. With Dow Corning single crystal rod, you're assured of maximum yield and minimum waste per rod. Rod diameter variation is controlled to less than 1.4 mm (0.055 inches)— simplifying mechanical preparation for either the diffusion or alloying process.

Hyper-pure silicon for every need is now available from Dow Corning. If you grow your own crystals from polycrystalline chunk using the Czochralski method . . . if you zone refine polycrystalline rod . . . if you need 1000-ohm centimeter or better resistivity in single crystal P-type — Dow Corning should be on your preferred source list.

Each Dow Corning single crystal rod is checked for resistivity over its entire length. Resistivity and lifetime profiles, like those shown below, are supplied with each crystal.

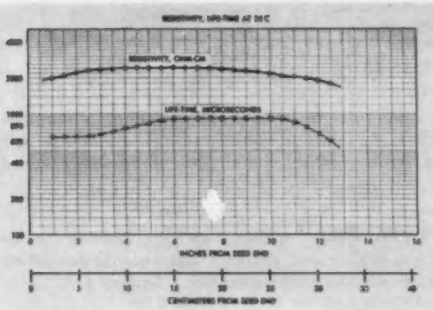

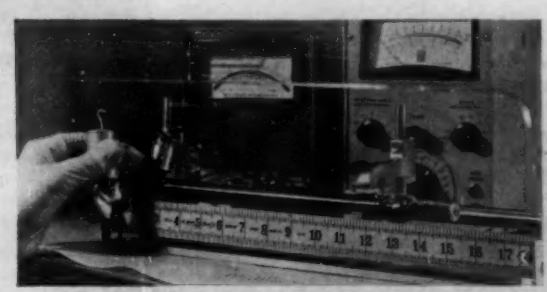

Write for "Hyper-Pure Silicon for Semiconductor Devices." Address Dept. 4712.

HYPER-PURE SILICON DIVISION
Address: HEMLOCK, MICHIGAN

Dow Corning CORPORATION
MIDLAND, MICHIGAN
ATLANTA BOSTON CHICAGO CLEVELAND DALLAS LOS ANGELES NEW YORK WASHINGTON, D.C.

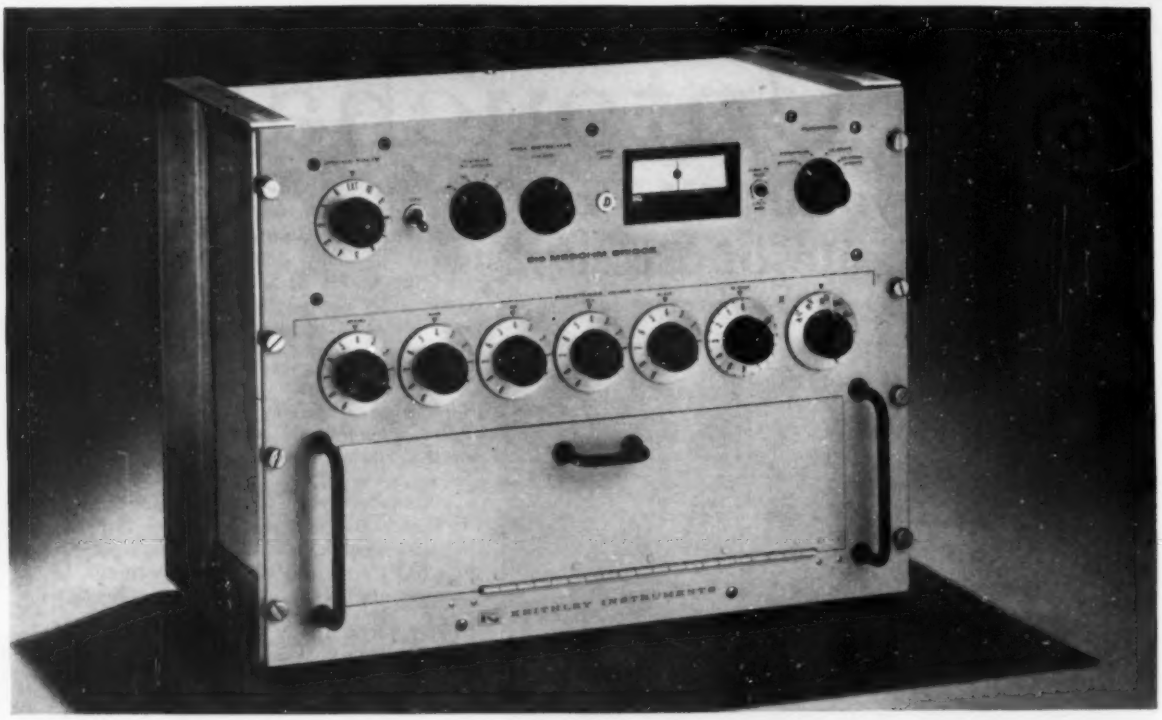

new self-contained, line-operated high megohm bridge

KEITHLEY MODEL 515 *measures 10^5 to 10^{15} ohms with accuracy of 0.5 to 1%*

The new 515 Megohm Bridge answers the need for a highly accurate, guarded Wheatstone Bridge for the standardization and calibration of resistors in the range of 10^5 to 10^{15} ohms. It also is ideal for measurement of resistor voltage coefficient, leakage and insulation resistances.

ACCURACY of the 515 is 0.05% up to 10^8 ohms, decreasing to 0.25% at 10^{12} ohms and to 1.0% from 10^{14} to 10^{15} ohms.

SPEED OF STANDARDIZATION AND CALIBRATION is greatly increased over previously available bridges through a semi-automatic calibration feature, which minimizes the user's time and effort. Resistance standards of 10^5 and 10^6 ohms are wire-wound, accurate to 0.02%. Standards of 10^7, 10^8, 10^9, 10^{10}, 10^{11}, and 10^{12} ohms are deposited carbon or carbon-graphite of only moderate stability. It is, therefore, necessary to establish values of higher standards by "laddering", an operation in which each resistor is compared to another one-tenth its value. Errors in the standard are compensated by adjusting an auxiliary "memory" potentiometer. This need be adjusted only once for each carbon resistor standard, after which the bridge is direct reading. Rechecking of standards every few days is sufficient to maintain rated accuracy.

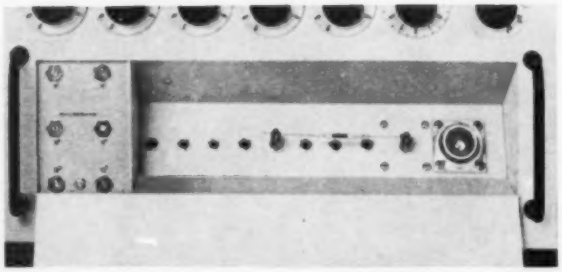

A shielded measuring compartment, easily accessible in the 515 front panel, permits the making of critical measurements without stray pickup. The rigid setup eliminates the need for cables and any noise caused by cable flexure. Provision is also made for external measurements using the Remote Test Chamber.

SELF-CONTAINED, no auxiliary equipment is necessary with the 515 for bridge potentials up to 10 volts. If a range up to 1000 volts is desired, the Keithley Model 240 or 241 power supply is recommended. Both the bridge and power supply are available in a single cabinet, as a coordinated, wide-range measuring system.

OTHER FEATURES include shielded measuring compartment; a sensitive null detector with non-linear off-null indication; bench or rack operation; remote test chamber.

Model 515 Megohm Bridge $1500.00

For complete details write:

KEITHLEY INSTRUMENTS, INC.
12415 EUCLID AVENUE
CLEVELAND 6, OHIO

A HISTORIC TELEPHONE EXPERIMENT BEGINS IN AN ILLINOIS TOWN

New technology brings the dream of an electronic central office to reality... foreshadows new kinds of telephone service.

Today, the science of communications reaches dramatically into space, bouncing messages off satellites. But an equally exciting frontier lies closer to home. Bell Telephone Laboratories engineers have created a revolutionary new central office. At Morris, Illinois, an experimental model of it has been linked to the Bell System communications network and is being tried out in actual service with a small group of customers.

This is a special electronic central office which does not depend on mechanical relays or electromagnets. A photographic plate is its permanent memory. Its "scratch pad," or temporary memory, is a barrier grid storage tube. Gas-filled tubes make all connections. Transistor circuits provide the logic.

The new central office is versatile, fast and compact. Because it can store and use enormous amounts of information, it makes possible new kinds of services that will be explored in Morris. For example, some day it may be feasible for you to ring other extensions in your home . . . to dial people you frequently call merely by dialing two digits . . . to have your calls transferred to a friend's house where you are spending the evening . . . to have other numbers called in sequence when a particular phone is busy.

The idea behind the new central office was understood 20 years ago, but first Bell Laboratories engineers had to create new technology and devices to bring it into being. A Bell Laboratories invention, the transistor, is indispensable to its economy and reliability.

This new experiment in switching technology is another example of how Bell Telephone Laboratories works to improve your Bell communications services.

BELL TELEPHONE LABORATORIES

World center of communications research and development

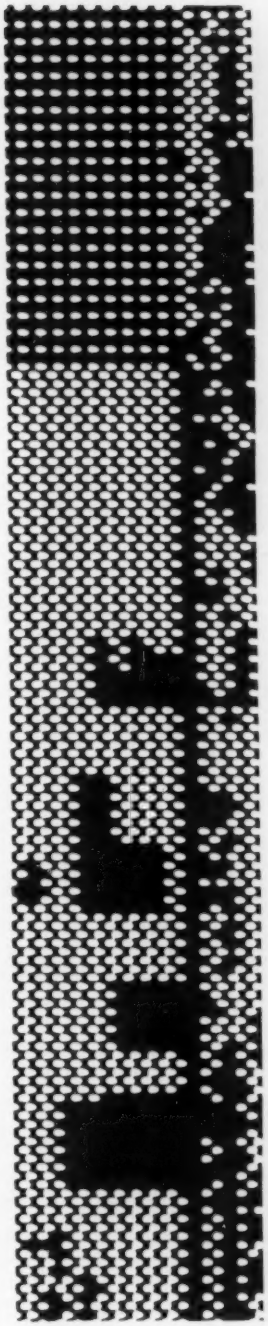

Part of a memory plate of the new electronic central office is shown at right (enlarged 8 times). Spots are coded instructions which guide the system in handling calls and keeping itself in top operating form. Over two million spots are required. Logic and memory are physically separated in the machine, so new functions can be easily added. The experiment is being conducted in co-operation with the Illinois Bell Telephone Company and the Western Electric Company.

AEROSPACE CORPORATION

are creating a climate conducive to significant scientific achievement

"Essentially, this corporation will be people—people of the highest quality. The United States Air Force recognizes that men of great scientific and technical competence can perform at their best only when they can exercise their initiative to the full under leadership which creates the climate for creativity. We expect Aerospace Corporation to provide that kind of environment."

SECRETARY OF THE AIR FORCE

Among those providing their leadership to this new non-profit public service corporation are: Dr. Ivan A. Getting, president; Allen F. Donovan, senior vice president, technical; Jack H. Irving, vice president and general manager, systems research and planning; Edward J. Barlow, vice president and general manager, engineering division; and Dr. Chalmers W. Sherwin, vice president and general manager, laboratories division.

These scientist/administrators are now selecting the scientists and engineers who will achieve the mission of Aerospaee Corporation: concentrating the full resources of modern science and technology on rapidly achieving those advances in missile/space systems indispensable to the national security.

The functions of Aerospace Corporation include responsibility for: advanced systems analysis; research and experimentation; initial systems engineering; and general technical supervision of new systems through their critical phases, on behalf of the United States Air Force.

Aerospace Corporation is already engaged in a wide variety of specific systems projects and research programs—offering scientists and engineers the opportunity to exercise their full capabilities, on assignments of unusual scope, within a stimulating environment.

Immediate opportunities exist for:

- WEAPONS SYSTEM PROJECT DIRECTOR
- SENIOR SCIENTISTS/SUPERVISORS:
  Propulsion Systems
  Guidance Systems
  Spacecraft Design
  Telecommunications
- SENIOR PHYSICISTS:
  Nuclear Propulsion
  Energy Conversion
  Solid State

Those capable of contributing in these and other areas are invited to direct their resumes to:

Mr. James M. Benning, Room 123,
P.O. Box 95081, Los Angeles 45, Calif.

AEROSPACE CORPORATION

A new and vital force engaged in accelerating the advancement of space science and technology

Project Vela's

[illegible] IN THE SKY

is designed to detect nuclear explosions in space. Opportunities to work on this, and other advanced research programs at Los Alamos, exist for Ph.D. physicists in atomic and molecular physics, ionic collision processes, and upper atmosphere physics. Also available are challenging positions for chemists and engineers.

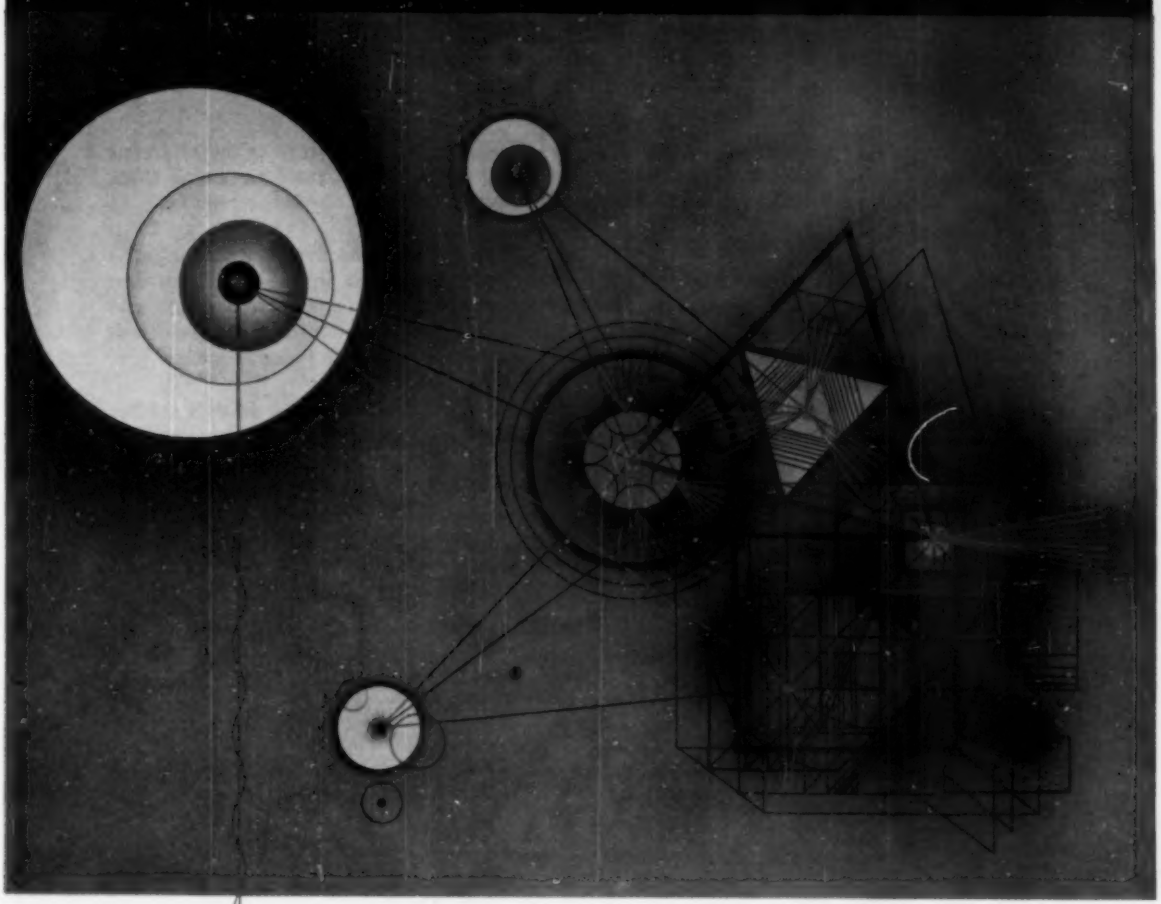

For employment write to: Personnel Director, Division 60-118

los alamos
scientific laboratory
OF THE UNIVERSITY OF CALIFORNIA
LOS ALAMOS, NEW MEXICO

Experimental Physicists – MS & PhD

COLLISION STUDIES IN PLASMA PHYSICS

...Part of a broad program in radio physics attracting scientists to SYLVANIA

ARL
Applied Research Laboratory

New effectiveness for communication and detection systems in natural and man-made environments may result from current Sylvania efforts in the field of plasma physics.

In the Radio Physics Department of the Applied Research Laboratory, investigators are studying a variety of wave propagation and scattering techniques in ionized gases and conducting fluids. Of particular promise are experimental developments in microwave diagnostics of ionized gas flow.

Through microwave heating, inelastic collisions are being induced between free electrons in ionized air. To measure collision frequency, the fractional energy loss G per collision must be known. New experiments will measure the temperature dependence of G in the afterglow of a DC discharge in ionized air. Small shock tube environments are also being explored.

Additional programs involve electromagnetic phenomena associated with solar flares and aurora, propagation in non-uniform media, and formulation of a new microscopic electrodynamics theory of the ionosphere.

The Applied Research Laboratory's studies in radio physics offer important opportunities to advance your professional reputation in a genuine scientific environment. Qualified physicists will be invited to meet the manager of the Radio Physics Department to discuss programs in progress and the opportunities for initiating original studies.

Please write in confidence to Dr. Leonard Sheingold, Director, Applied Research Laboratory

Waltham Laboratories / **SYLVANIA ELECTRONIC SYSTEMS**
A Division of

SYLVANIA
Subsidiary of GENERAL TELEPHONE & ELECTRONICS

100 First Avenue—Room 12-B—Waltham 54, Massachusetts

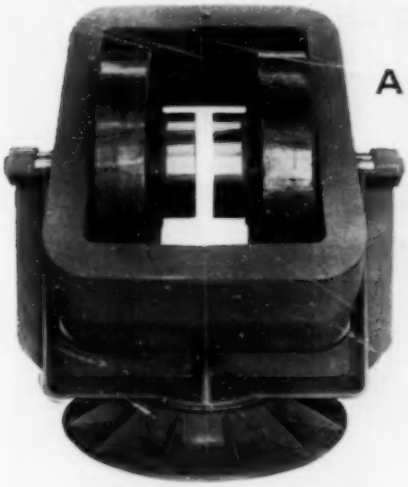

A NEW STANDARD OF EXCELLENCE

An exacting investigation into optimum methods for the design and fabrication of precision laboratory electromagnets has produced definite proof that the casting of magnet yokes affords positive advantages in performance. Many laboratories now benefit from this "new standard of excellence" made possible in part by these new design concepts.

FIGURE A. BOLTED AND MACHINED MAGNET YOKE
FIGURE B. HARVEY-WELLS CAST MAGNET YOKE
FIGURE C. YOKE CROSS SECTION CAST MAGNET
FIGURE D. YOKE CROSS SECTION MACHINED AND BOLTED MAGNET

FIGURE A

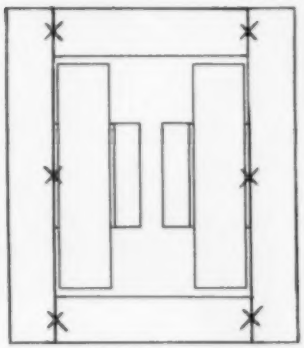

FIGURE B

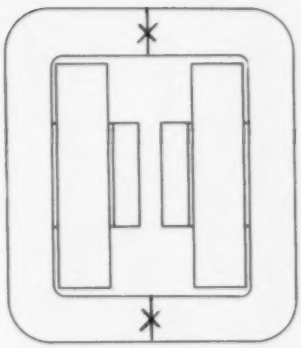

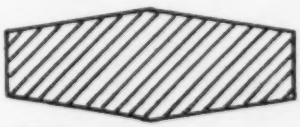

FIGURE C

FIGURE D

Figure A illustrates the older method of constructing a magnet yoke by machining and bolting a number of pieces of metal. This allows a number of joints, shown by the X's, which cumulatively allow a build-up of machine tolerances, with subsequent variations in parallelism at the pole faces and a tendency to stress at high field strengths. Figure B shows the Harvey-Wells cast magnet yoke. Casting requires fewer such joints permitting far greater rigidity and stability. This in turn allows improved homogeneity through changing fields and greater homogeneous volumes at fixed fields.

The greater strength of the hexagonal cross section of the cast magnet yoke, shown in Figure C as compared to the rectangular cross section of the older method shown in Figure D is a further example of the increased inherent rigidity of cast magnets, with the attendant virtues as described above.

By casting the entire magnet yoke from the same batch of metal at the same time, there is no possibility of any variation in characteristics between different sections of the same magnet. In fact, the magnetization curve for a low carbon cast yoke as compared to a curve for 10-10 steel shows a superior resistance to saturation at lower levels.

Additional features of the Harvey-Wells electromagnet system include wafer coils for increased power and cooling efficiencies and continuously regulated solid state power supplies. Please write for complete information and technical specifications.

HW

HARVEY-WELLS CORPORATION P.O. BOX 189 FRAMINGHAM, MASS. TR 2-4365 CE 5-7370

Pioneering Achievements at JPL

Following an impressive period, beginning in 1938, in the pioneering and development of all forms of rocketry—JPL's jump into outer space began with the successful flight of America's first satellite, Explorer I. When the moon probes Pioneer III and IV proved equally successful, the Jet Propulsion Laboratory's position as an outstanding center of research and development was again confirmed.

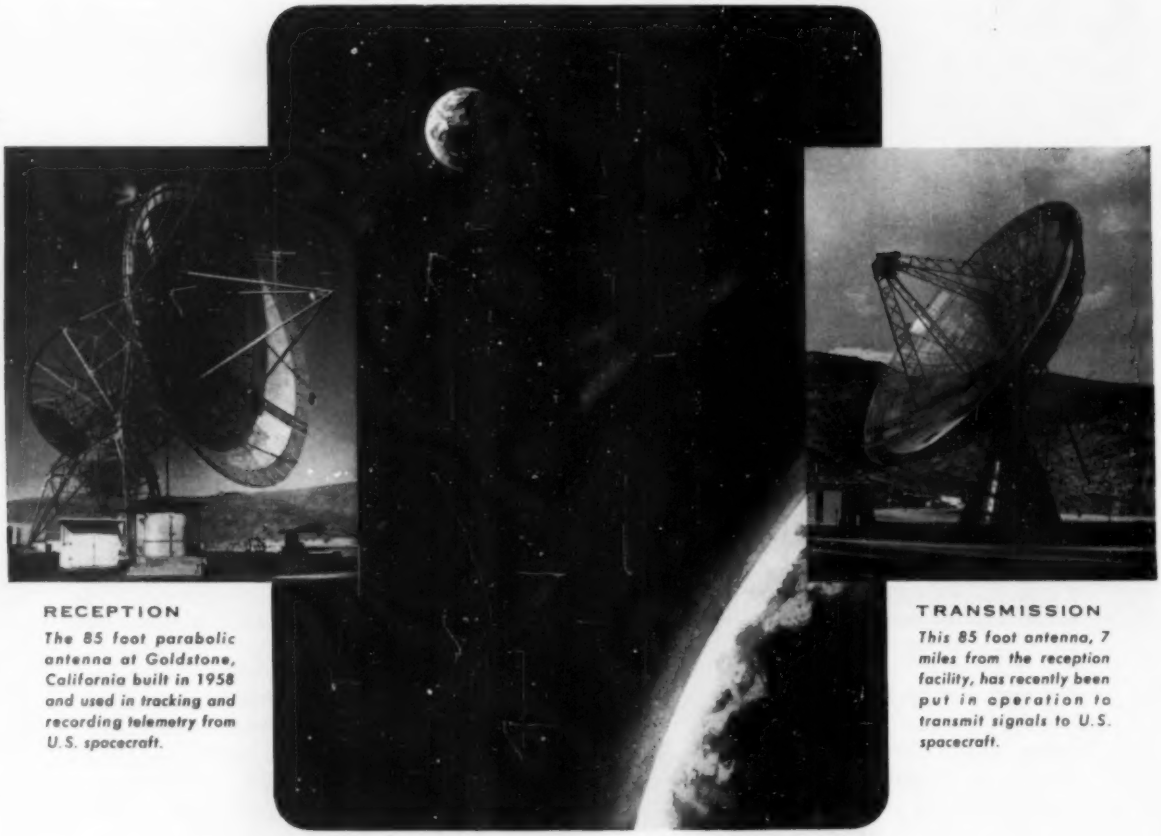

RECEPTION

The 85 foot parabolic antenna at Goldstone, California built in 1958 and used in tracking and recording telemetry from U.S. spacecraft.

TRANSMISSION

This 85 foot antenna, 7 miles from the reception facility, has recently been put in operation to transmit signals to U.S. spacecraft.

PIONEERING IN SPACECRAFT COMMUNICATIONS

With the completion of the new transmitting antenna installation at the Goldstone Deep Space Instrumentation Facility in California, a unique space communications research and operations laboratory now exists which makes possible still further communications achievements in space research. The facility is being used in various ways. Two-way communications with space probes permits precision tracking, precision radio guidance, and wideband data reception. Working as a bistatic, CW Doppler radar, the facility permits accurate tracking of dark satellites whose orbits are only imperfectly known, as well as accurate tracking of the moon and, later, the planets.

The purely scientific data produced by such a facility ranges from propagation data and lunar reflectivity characteristics to the wideband data communicated to the station from the scientific instruments aboard the space probes. This is but one of the many space exploration activities pioneered by the Jet Propulsion Laboratory.

jpl

CALIFORNIA INSTITUTE OF TECHNOLOGY

JET PROPULSION LABORATORY

A Research Facility operated for the National Aeronautics and Space Administration

PASADENA, CALIFORNIA

Employment opportunities for Engineers and Scientists interested in basic and applied research in these fields:

COMMUNICATIONS • INSTRUMENTATION • INFRARED • ASTROPHYSICS • GEOPHYSICS • GEOCHEMISTRY • ASTRONOMY • PROPULSION • MASER • STRUCTURES • PHYSICS •

Send professional resume, with full qualifications and experience, for our immediate consideration

500-TIMES MAGNIFICATION–VERTICALLY

...for detailed waveform analysis

Waveform Details of a 100-v Staircase

Vertical Expansion 500 Times

Horizontal Expansion 500 Times

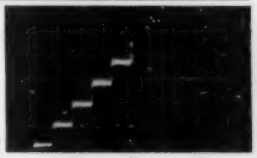

Vertical	Horizontal
50 mv/cm	10 μsec/cm
V_C = +92.5	

Vertical	Horizontal
25 v/cm	5 ms/cm
V_C = 0	

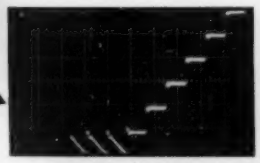

Vertical	Horizontal
50 mv/cm	10 μsec/cm
V_C = −5.5	

TYPICAL APPLICATIONS

FAST-RECOVERY AMPLIFIER—observe small signals riding with large gates.

MODULATION MONITOR—measure amplitude modulation on a digital train pulse.

HIGH-AMPLITUDE HUM REJECTION—reject up to 200 volts peak-to-peak common-mode hum.

SEMICONDUCTOR CHARACTERISTICS—measure Zener diode ac impedance and Zener voltage together, measure transistor output impedance.

PULSE-HEIGHT ANALYSIS—select any pulse above a preset dc level.

COMPONENT MATCHING—check components to easily-interpreted tolerances.

MAIN CHARACTERISTICS

3 Modes of Operation—as a conventional preamplifier, as a differential-input preamplifier, or as a calibrated differential comparator.

50-mv/cm Sensitivity—nine calibrated attenuation steps to 25 v/cm.

Wide Passband—dc to 13 mc with Tektronix fast-rise scopes.

±100-volt Dynamic Range—permits common-mode signals up to 100 volts to be applied to the unit without attenuation.

40,000 to 1 Common-mode Rejection Ratio—allows measurement of differential signals less than 50 millivolts.

Comparison Voltage Accuracy—within 0.25% on the ±1-volt scale; within 0.20% on the ±10-volt scale; within 0.15% on the ±100-volt scale.

Safety Feature—the Type Z eliminates "floating oscilloscope" operation.

AC and DC VTVM—extends oscilloscope accuracy in both ac and dc voltage measurements to 0.2%.

Price, Type Z Plug-in Unit, f.o.b. factory **$525**

New differential plug-in preamplifier rejects up to 100 v of an input signal . . . accepts 100-v waveforms for oscilloscope display at 50-mv/cm sensitivity . . . provides an equivalent vertical scale length of ±2000 centimeters.

You can now display small segments of large waveforms at maximum oscilloscope sensitivity, with vertical expansion equivalent to as much as 500 times. You can select magnified "window" displays of all portions of a waveform, and make amplitude measurements with a degree of accuracy that closely approaches the possibilities of digital techniques. The flexibility and simplicity of the analog (oscilloscope) presentation is retained for accurate analyses of complex waveforms.

The new Type Z Plug-In Unit is a triple-purpose device, acting also as a conventional preamplifier and a differential-input preamplifier. It can be used in all Tektronix Type 530, 540, 550, and *580 Series Oscilloscopes. Ask your Tektronix Field Engineer to demonstrate the dynamic range, waveform resolution, and amplitude accuracy of the Type Z in your application.

**with Type 81 Adapter.*

Tektronix, Inc.

P. O. Box 500 • Beaverton, Oregon

Phone Mitchell 4-0161 • TWX—BEAV 311 • Cable: TEKTRONIX

TEKTRONIX FIELD OFFICES: Albuquerque, N. Mex. • Atlanta, Ga. • Baltimore (Towson, Md.) • Boston (Lexington, Mass.) • Buffalo, N.Y. • Chicago (Park Ridge, Ill.) • Cleveland, Ohio • Dallas, Texas • Dayton, Ohio Denver, Colo. • Detroit (Lathrup Village, Mich.) • Endicott (Endwell, N.Y.) • Greensboro, N.C. • Houston, Texas • Indianapolis, Ind. • Kansas City (Mission, Kan.) • Los Angeles Area (East Los Angeles, Calif., Encino, Calif. • West Los Angeles, Calif.) • Minneapolis, Minn. • New York City Area (Albertson, L.I., N.Y. • Stamford, Conn. • Union, N.J.) • Orlando, Fla. • Philadelphia, Pa. • Phoenix (Scottsdale, Ariz.) Poughkeepsie, N.Y. • San Diego, Calif. • San Francisco (Palo Alto, Calif.) • St. Petersburg, Fla. • Syracuse, N.Y. • Toronto (Willowdale, Ont.), Canada • Washington, D.C. (Annandale, Va.).

TEKTRONIX ENGINEERING REPRESENTATIVES: Hawthorne Electronics, Portland, Oregon • Seattle, Washington. Tektronix is represented in twenty overseas countries by qualified engineering organizations.

In Europe please write Tektronix Inc., Victoria Ave., St. Sampsons, Guernsey C.I., for the address of the Tektronix Representative in your country.

Physicists • Electronic Engineers

for assignments on APL's satellite program

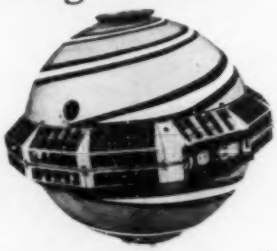

Research • Development • Systems Engineering

You will find association with APL particularly rewarding if you appreciate an atmosphere conducive to original thinking, and if you are capable of making contributions to advance the state-of-the-art.

Satellite Development Group

The group is concerned with research and development of satellite-borne equipment, which will be capable of performing highly complex functions. The instruments have to operate in a space environment on exceedingly low power sources, and they have to work for five to ten years without malfunction.

Emphasis is on conceptual design rather than hardware fabrication. Engineers will work without close supervision, will enjoy freedom to create and investigate, and do not have to spend much time writing proposals. BS or more in physics or electronic engineering required. Two or more years of experience in transistor switching circuits and familiarity with utilization of memory and/or logical devices desired.

Satellite Ground Systems Group

This group is responsible for the design of data handling systems for use in shipboard and airborne navigational equipment, and for ground tracking equipment. Assignments involve development of novel and highly sophisticated data processing systems, systems coordination, and technical supervision of contractors.

BS or more in physics or electronic engineering plus four to five years of experience in data processing systems required.

For details about these career opportunities, address your inquiry to:
Professional Staff Appointments

The Applied Physics Laboratory
The Johns Hopkins University

8653 Georgia Avenue, Silver Spring, Md.
(Suburb of Washington, D. C.)

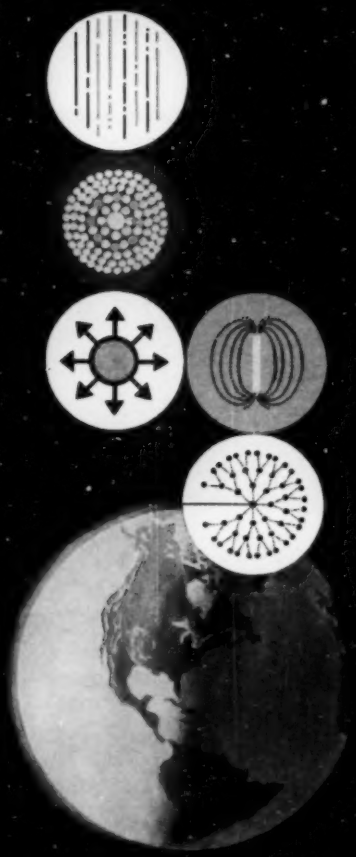

Expanding the Frontiers of Space Technology in

PHYSICS

Lockheed Missiles and Space Division is engaged in a broad, long-range program of basic scientific research at its laboratories adjacent to Stanford University in Palo Alto, California. Equipment is modern and includes extensive facilities for plasma and spectroscopic research; a variety of shock tubes; a 3.5 mev Van De Graaf accelerator; complete laboratory test facilities; and one of the largest and most modern computing centers in the world.

A group of more than fifty physicists is engaged in research and the fundamental investigation of problems in the following areas:

Nuclear Physics: The measurement and theory of nuclear cross sections; beta, gamma and X-ray spectroscopy; theory of nuclear structure; radiation physics.

Theoretical Physics: The phenomenology and effects of atomic explosions and radiative properties in air under conditions of very high temperatures.

Space Physics: Basic research on the physics of the earth's upper atmosphere and beyond, including: measurement of atmospheric composition and density at orbital altitudes; laboratory experiments on upper atmospheric atomic and molecular reactions; hydro magnetic interactions with the earth's magnetic fields; simulation and study of meteor impacts; and particle radiation.

Plasma Physics: Energy transfer between a plasma and external electromagnetic fields; the transport of microwave and optical radiation through plasmas.

Atomic Physics: Mass spectroscopy; theory and measurements of low energy interactions.

Such programs reach far into the future and deal with unknown and challenging environments. If you are experienced in one of the above areas, or in related work such as astrophysics or chemical physics, you are invited to share in the efforts of a company that has an outstanding record of achievement, and make an important individual contribution to your country's scientific progress. Write Research and Development Staff, Dept. F-32, 962 W. El Camino Real, Sunnyvale, California. U.S. citizenship or existing Department of Defense industrial security clearance required.

Lockheed

MISSILES AND SPACE DIVISION

Systems Manager for the Navy POLARIS FBM; the Air Force AGENA Satellite in the DISCOVERER, MIDAS and SAMOS Programs; Air Force X-7; and Army KINGFISHER

SUNNYVALE, PALO ALTO, VAN NUYS, SANTA CRUZ, SANTA MARIA, CALIFORNIA
CAPE CANAVERAL, FLORIDA • ALAMOGORDO, NEW MEXICO • HAWAII

N-371

AVAILABLE FROM **HAMNER**... A COMPLETE LINE OF

NUCLEAR AMPLIFIERS

To fill any counting or budgetary requirement, Hamner now offers a complete line of three basic nuclear amplifiers, each available with a choice of discriminators on the same basic chassis. These three circuit types are:

- The N-328, based on the ORNL double delay line A-8 circuit, for unexcelled overload protection and minimum baseline shift, at high counting rates. (Ask about Hamner's exclusive fast coincidence pick-off circuit, optional on the same chassis.)
- The N-302, Chase-Higinbotham design, for outstanding linearity, low noise and non-overload properties.
- The Hamner N-371, double RC circuit for low cost, routine counting or analysis applications.

Each amplifier is available with either integral discriminator or single channel pulse height analyzer on the same chassis. All units offer research quality specifications which will be demonstrated on request.

Hamner also markets a wide variety of other advanced type nuclear counting equipments which are tailored to operate with these amplifiers in forming various counting systems.

For full specifications on these instruments, contact Hamner or your area representative.

N-328

N-302

Hamner

HAMNER ELECTRONICS CO., INC.

Department 12AP, P.O. Box 531, Princeton, New Jersey, PEnnington 7-1320

sparks advanced electronic R&D at Amherst Laboratories

Creativity can assume infinite form and direction. The ideal formula for creativity has yet to be determined. However, at Amherst Laboratories, progressive leadership in advanced electronic R&D can be attributed to the dynamic stimulus of the Fifth Freedom... Freedom of the mind, an essential ingredient in keeping the world free. To some, it is "freedom of thought"..."freedom of investigation"...whatever the title...it is successful at Amherst Laboratories. Results are evidenced in the conclusion of numerous projects and the ever increasing backlog of prime assignments in advanced Ground, Air and Space Communications.

PROFESSIONAL STAFF AND MANAGEMENT OPPORTUNITIES *are unlimited for Physicists, Mathematicians and Electronics Engineers with advanced degrees and creative desire.*

You are invited to direct inquiries in confidence to Dr. R. L. San Soucie, Amherst Laboratories... or call NF 3-8313 for information. All inquiries will be acknowledged promptly.

SYLVANIA ELECTRONIC SYSTEMS
A Division of SYLVANIA
Subsidiary of GENERAL TELEPHONE & ELECTRONICS
1183 Wehrle Drive, Williamsville, New York

AMHERST LABORATORIES

Shrinking the Universe... through Communications

How Do You Meet a Challenge?

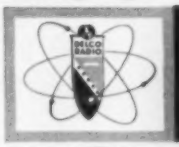

Delco Radio is doing it with TALENT and RESOURCES

We feel the challenge of new concepts in electronics and Solid State Physics can only be met by an intelligent application of outstanding abilities and resources.

To meet this challenge, Delco—over the years—has built up over one million square feet of modern manufacturing, laboratory and office facilities. Newest in the Delco complex is a 125,000 sq. ft. engineering and research facility now under construction in Kokomo, Ind., and scheduled for completion in 1961. In addition, Delco has available the extensive services of the General Motors Technical Center and field test facilities.

But physical resources are only half the answer. It took bold, imaginative talent to lead Delco to its present respected position in the electronics industry. Likewise, the challenge of the future requires a constant infusion of new ideas and new talent.

To maintain and further expand leadership in these areas, we are conducting aggressive programs in semiconductor device development and new materials research. This activity has created unusual opportunities for those who qualify. Specifically, we are vitally interested in ambitious men with experience and TALENT in the following areas:

SEMICONDUCTOR DEVICE DEVELOPMENT

We need men with experience in the techniques of semiconductor device development including alloying and diffusion.

We need a man with experience in the chemistry of semiconductor devices.

We need a man with experience in semiconductor materials to lead a program on metallurgical research of new semiconductor materials.

We need a man with experience in semiconductor device encapsulation.

PROCESS ENGINEERING

We need several men for production set-up and trouble shooting.

EQUIPMENT DEVELOPMENT

We need men to develop automatic and semi-automatic fabrication equipment.

We're eager to find experienced personnel with a desire for a stimulating challenge and the abilities to fulfill this challenge. Responsible positions are available for those who qualify.

If you're interested in becoming a member of our Delco—GM team of outstanding scientists and engineers, send your resume today to the attention of Mr. Carl Longshore, Supervisor Salaried Employment.

DELCO RADIO
DEPENDABILITY
RELIABILITY

Division of General Motors · Kokomo, Indiana

The new Hughes MOBOT* Mark 2 System offers new versatility for every remote handling requirement

Around, over and under, the Mark 2 Arm reaches the hard to get at places. Superior to any other remote controlled arm, the Mark 2 will move 180 degrees in any direction at each of three joints; the wrist will rotate continuously in either direction. Hand telescopes 3-1/2 inches. The Mark 2 Arm is five feet long and will lift 25 lbs. while the arm is in any position. It can be mounted on a wall, pole, boom or remote controlled vehicle.

The modules making up the electro-mechanical MOBOT Mark 2 System—Mark 2 Arm (or Arms), Television System, Command System—can be custom combined to meet your exact requirements. Buy only the capabilities you need.

The versatility of the system, the flexibility of the arm, and the ability to perform reliably in almost any environment, make the MOBOT Mark 2 System ideal for use in "hot" cells, reactor maintenance and repair, underwater construction or salvage, fire fighting or automating any dangerous or tedious manufacturing operation. *Trademark of H.A.C.

For firm prices and delivery dates, or for engineering assistance with your remote handling requirement, contact: HUGHES NUCLEAR ELECTRONICS LABORATORY, P.O. Box 90915, Los Angeles 45, Calif., TWX INGL 4076 ORchard 0-1515, Ext. 5355.

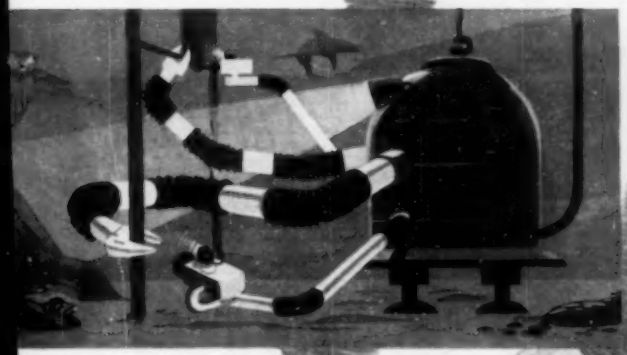

NOW...more freedom of movement than the human arm

CREATING A NEW WORLD WITH ELECTRONICS

HUGHES

HUGHES AIRCRAFT COMPANY
NUCLEAR ELECTRONICS LABORATORY

SEE THE MOBOT MARK 2 SYSTEM IN OPERATION AT THE ATOMFAIR-WEST IN SAN FRANCISCO, DECEMBER 12-15, BOOTH 419-21

DUBROVIN VACUUM GAUGES

Made expressly by WELCH
For Moderately Reduced Pressures

No. 1451 C.
Table Mounting

• Sensitive
• Compact
• Practical

Far More Sensitive Than
Mercury Manometer

• Range: 0.2 mm To 20 mm of Hg. • Two Sensitivities Available
• Pyrex-Brand or Soft-Glass Construction

EASY TO INSTALL - CONVENIENT TO USE

No. 1451 H.
Wall Mounting

The Welch-Dubrovin Gauges are made in two gasic types. One 9 times and the other 6 times as sensitive as a mercury manometer. Because of this "magnifying factor," the gauge is as sensitive as a manometer which uses a liquid of low density, but has the advantage of using mercury which dissolves very few organic or inorganic vapors and which requires no conversion factor. Unlike mechanical or optical magnifying devices, any small errors due to capillarity, adhesion, etc., are not magnified. The smallest division on the 9-to-1 type is 0.2 mm and on the 6-to-1 type is 0.5 mm of Hg. Fractions of these values may be estimated. Both types are available with Pyrex-brand or soft glass in either table or wall mounting.

PRICED AT $47.50 AND $55.00

WRITE FOR COMPLETE LITERATURE. IF YOU DO NOT HAVE OUR VACUUM PUMP CATALOG WRITE FOR IT.

W. M. WELCH SCIENTIFIC COMPANY
DIVISION OF W. M. WELCH MANUFACTURING COMPANY
ESTABLISHED 1880
1515 Sedgwick Street, Dept. C-1 Chicago 10, Illinois U. S. A.
Manufacturers of Scientific Instruments and Laboratory Apparatus

Journal
of
Applied Physics

Volume 31, Number 12 December, 1960

Special Issue on Electron Physics

Invited papers presented at the APS Division of the Electron Physics Symposium, Montreal, Quebec, June 15–17, 1960.

Recent Appearance Potential Measurements Using an Electrostatic Electron Selector*

LARKIN KERWIN AND PAUL MARMET
Centre de Recherches en Physique, Université Laval, Québec, Canada
(Received August 4, 1960)

The general principles of measuring appearance potentials by the electron bombardment method are reviewed. Recent improvements in the design of an electrostatic electron selector so as to improve the electron bombardment technique are described. The new instrument provides an electron beam with an energy spread of less than 50 mv. By means of it, measurements have been made on the vibrational levels N_2^+ and H_2^+.

1. WHY ONE MAKES ELECTRON SELECTORS

THESE days science is able, if requested, to present a very detailed description of the electronic structure composing the exterior of atoms and molecules. The great bulk of this information has been obtained by spectroscopists. Their observation of a photon emitted by a molecule leads directly to a knowledge of the energy interval between two levels which an electron can occupy. From a series of such observations comes the beautiful description of the molecule: the numbers and states of the electrons, their energetic levels, the relative positions and motions of the nuclei, the modes of bending and rotation of the whole structure, and so on. Such elegant descriptions of fundamental structures are one of the major accomplishments of physics.

From some forty years, mass spectrometrists have been playing a minor role in this activity. Their techniques have not been applied to nearly as many species as those of the spectroscopists, and the precision of their measurements is usually several orders of magnitude less than those of their optical colleagues. However, two facts enable them to be occasionally of some use: a few species which defy the best efforts of the spectroscopists have proven amenable to mass spectrometry, and their measurements can give the value of an energy level directly rather than the difference between two levels.

One method of the mass spectrometrist is as follows: a beam of electrons whose energy is known and can be varied is directed onto some molecules about which information is sought. As the energy of the electron beam is increased, it will reach a value sufficient to remove an electron from a molecule by collision. At this instant the molecule becomes an ion, and if the process takes place in the source of a mass spectrometer, the latter instantly announces the fact of the ion's formation by detecting it. The energy of the electron beam at this instant is thus the ionization potential of the molecule, or to put it another way, the depth of the potential well of the valence electron. In Fig. 1 this threshold of ionization is shown at T.

If the energy of the electron beam is further increased, the probability of ion formation among the molecules is enhanced, and the ion current detected in the spectrometer increases. This is indicated by section A of

* Invited paper presented to the annual meeting of the Division of Electron Physics of the American Physical Society, Montréal, Canada, June 15th, 1960.

Copyright © 1960 by the American Institute of Physics.

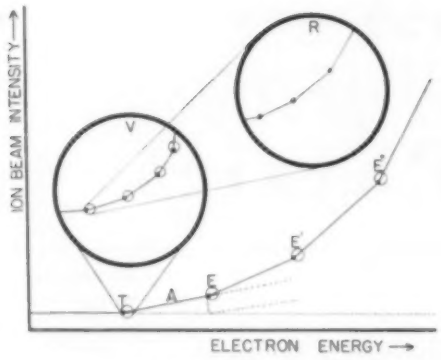

FIG. 1. Ionization curve.

the "ionization curve." The precise nature of section A is presently a matter of dispute. In the case of atoms, where the process is simple, it is generally agreed that it is a straight line to a fair approximation.

As the energy of the electron beam is still further increased, it may become sufficient not only to ionize the atom but to excite it as well, i.e., knock one of its remaining electrons to a higher energy level. At this point, the electron beam can produce two effects, each with its own probability. The first, production of the ion, continues in an approximately straight line (shown as a dotted line), following section A. The second, excitation of the ion, is initiated at point E, and also goes along in approximately linear fashion. The total ion current is the sum of these, as indicated by the continuous line. Other excited states may be initiated at points E' and E''. The energy interval between such breaks corresponds to the energy interval between the excited states of the ion, just as the position of the first break gave the value of the ionization potential. The relative slopes of the segments between breaks may be processed to give the relative probabilities of ion formation to the various states.

In the case of molecules, the segments such as A are usually slightly curved, and if examined in detail might be found to consist of a number of subsegments of approximately equal spacing. For simple gases these would be about 0.25 ev long. These are indicated in Fig. 1 at detail V, and correspond to another phenomenon: the setting in of vibrations of the nuclei in the molecule as a result of the electron collision. The vibrational energy which a molecule may possess is quantized, and so various modes of vibration are excited as the electron energy increases. In practice, the vertical scale of the ionization curve is enormously amplified in looking for such detail, as seen in the qualitative drawing.

One further example of information which might be obtained from an ionization curve is shown in detail R. Here the segment corresponding to a given vibrational state is shown to be further subdivided into levels corresponding to the various modes by which the entire molecule can rotate, an activity for which the energy required is also quantized. In the present state of the art, the realization of such detail (segments about 0.001 ev long) is quite utopian.

This brings us to the reason why the observation of even electronic excited states is a delicate matter. The difficulty lies in the fact that the bombarding electron beam is not monoenergetic, but contains electrons of various energies making up an energy spread ΔE. As the mean energy of the beam attains the value required to initiate a new process, some of the electrons with higher than average energy are already contributing to it, while others are not. As a result, the process is initiated by an electron beam which effectively increases in intensity over an energy interval ΔE. This results in a rounded section of the ionization curve instead of a clean break. It may be taken as a convenient rule of thumb that it is difficult to observe details which are separated by an energy interval equal to or less than ΔE. The energy spread in an electron beam obtained by thermal emission may be four ev, with the result that most ionization curves of molecular ions are curved throughout, and no detail can be identified. The picture is almost as bad for atomic ions. In a few cases, careful analysis of such curved lines can yield some data, as has been shown by Clarke.[1]

In the early days of the art, much work was done on interpreting the one detail that is always available in spite of energy spread—the threshold. Many important contributions were made in this way by people such as Bleakney, Hogness, Lunn, Lozier, Tate, Smith, Hipple, Honig, Hagstrum, and others.

More recently, considerable attention has been paid to the problem of reducing the energy spread of the electron beam. Some of the more noticeable advances have been:

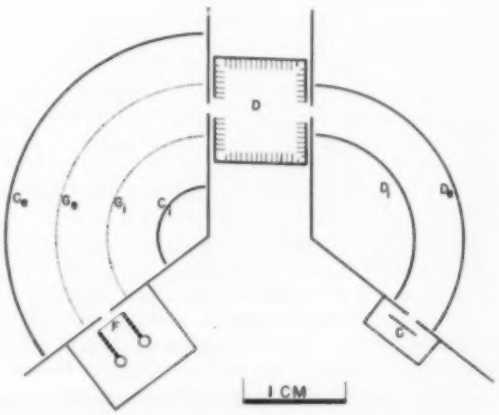

FIG. 2. Plan of selector and analyzer.

[1] E. M. Clarke, Can. J. Phys. 32, 764 (1954).

Retarding Potential Difference (RPD) Method: Developed by Fox,[2] this consists essentially in measuring the difference in ion current produced by an electron beam when its maximum energy is determined by two different settings of a control grid. This increment of ion current is caused by electrons whose energy spread is equal to the difference in voltage settings of the grid. In this way, a beam of effective ΔE equal to 0.1 ev has been obtained. Mostly in the hands of Fox and his colleagues, but also when used by Frost, McDowell, Schiff, Cloutier, Schultz, and others, this method has yielded much information about excited electron states.

Electrostatic Selector: Developed by Clarke at Laval, this method consists in sending the electron beam through an electrostatic energy filter. The first selector produced an effective energy spread of about 0.3 ev and several notable contributions were made through its use. It is also the method described at length in this paper.

Differential Method: If an ionization curve consisting of several straight segments (see Fig. 1) is differentiated once, a stepped line will result. If differentiated twice, a series of delta functions or spikes will result. The appearance of the latter obviously lends itself better to the detection of discontinuities than does the initial segmented curve. Morrison[3] had exploited this method, and in a valuable series of papers has made many contributions to the knowledge of excited states.

2. HOW ONE MAY BUILD A BETTER SELECTOR

The remainder of this paper is devoted to our efforts at Laval University to improve the performance of the electrostatic selector. The performance of the first selector was limited by space charge built up by reflected electrons. Studies of the manner in which the space charge was created and maintained were made on several models using pulse techniques, and several improvements were suggested. These are indicated in Fig. 2.

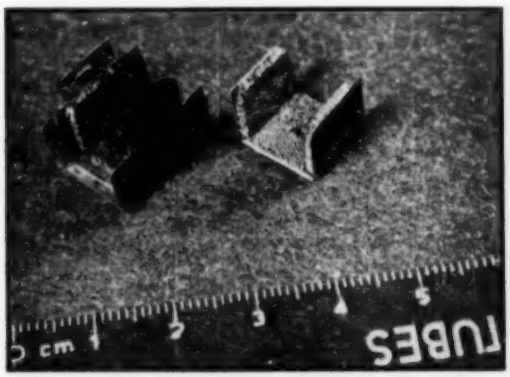

FIG. 3. Electron velvet ionization chamber.

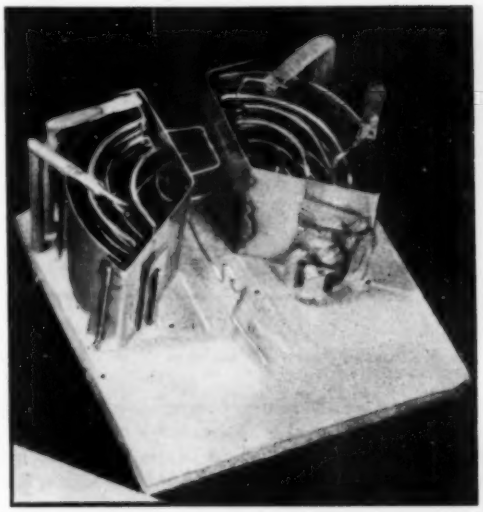

FIG. 4. Complete selector and energy analyzer.

Mesh Electrodes: The main selector electrodes G_e and G_i were made of 90% transparent tungsten mesh instead of solid plates. Electrons which struck these electrodes passed through for the main part, and were prevented from returning by being captured on collectors C_e and C_i maintained at a positive potential. The formation of space charge was prevented, even at beam energies as low as 0.5 ev, with a consequent reduction in energy spread.

Electron Velvet: When the beam of electrons was directed into the ionization chamber D, reflection from its walls caused a new space charge problem which could not be solved by mesh walls. This is because the electrons escaping from the walls and accelerated to capturing plates could produce ions at unknown energies. A nonreflecting surface was therefore sought. Experiments with various kinds of surfaces resulted in the development of electron velvet. An ionization chamber made of it is seen in Fig. 3. It consists of many thousands of 0.5-mm diameter gold-plated copper tubes one mm long attached to a plated base. This material reflects slow electrons to the extent of only about 20%, sufficiently low for the purpose.

Vertical Focusing: The cylindrical electrostatic lens provides direction focusing in the planes normal to the cylindrical walls. A certain focusing and beam adjustment normal to these planes was achieved by adding electrodes at the top and bottom of the selector. These

[2] R. E. Fox, W. M. Hickam, and T. Kjeldaas, Jr., Phys. Rev. **89**, 555 (1953).
[3] J. D. Morrison, J. Chem. Phys. **21**, 1767 (1953).

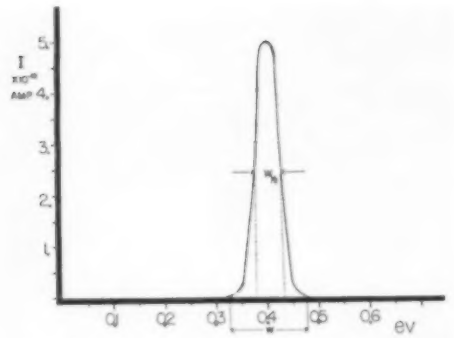

FIG. 5. Measured energy distribution of the selector-analyzer.

were of tungsten mesh and were provided with exterior plates for the removal of space charge as in the case of the selector electrodes. The use of this vertical focusing always increased the beam intensity by at least a factor of three.

Further details concerning the construction, dimensions, and potentials used with this selector have been published.[4] Figure 4 shows a photograph of the complete selector, together with an analyzer used to measure the energy distribution.

The result of these improvements may be judged from the comparison in Table I. The energy spread of the selector was measured by constructing a second selector ("analyzer") to investigate the performance of the first. Experiments with retardation potential methods of measuring the energy spread give erroneous results because of the space charge which is built up at the retarding plate. The energy distribution resulting from the combination is shown in Fig. 5. The width at half-height is seen to be about 50 mv. This means that the selector alone had a corresponding energy spread of about 25 mv. In some cases, total width was certainly less than 50 mv.

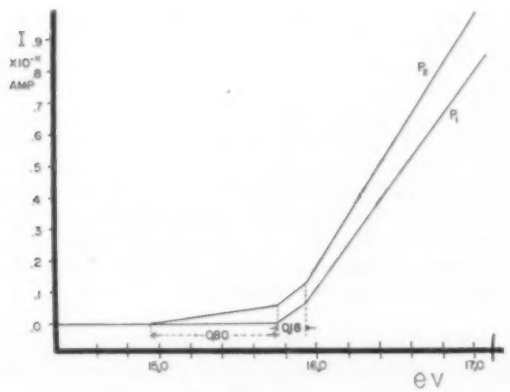

FIG. 6. Ionization curves for argon.

[4] P. Marmet and L. Kerwin, Can. J. Phys. **38**, 787 (1960).

3. SOME RECENT MEASUREMENTS

The first test of the new selector was made using argon. The instrument was mounted in a bell jar so that no mass discrimination was made. The ionization curves obtained are shown in Fig. 6, which is a composite of many runs. The curve shown at P_1 is obtained at relatively low pressure (5×10^{-4} mm Hg). Following the appearance potential, a break is seen at $0.18_1\pm0.01$ ev (average of 50 runs). This interval agrees well with the 0.178-ev difference between the $^2P_{\frac{1}{2}}$ and the $^2P_{\frac{3}{2}}$ states of argon known from spectroscopy.[5] The breaks associated with these levels are quite sharp, and confirm the expected performance of the selector.

At relatively higher pressures (5×10^{-3} mm Hg), the curve appears as at P_2. The process appearing at 0.8 ± 0.1 ev below the threshold for A^+ (12 runs) is ascribed to the formation of A_2^+. Hornbeck and Molnar[6] have reported the formation of this ion at these pressures in considerable abundance, and give its appearance potential as being $0.7_{-0.2}{}^{+0.7}$ ev below the threshold for A^+. Our measurements thus fix the appearance potential for A_2^+ at 14.95 ± 0.1 ev.

TABLE I. Comparison of old and new selectors.

Selector	Current	ΔE	Energy range
First	10^{-8} amp	300 mv	6–50 v
Second	10^{-7} amp	50 mv	0–100 v

TABLE II. Values for three vibrational levels of the N_2 molecule compared with spectroscopic values.

Transition	Selector	Spectroscopy
1–2	0.275 ± 0.01 ev	0.2696 ev
2–3	0.267 ± 0.01 ev	0.2655 ev
3–4	0.262 ± 0.01 ev	0.2616 ev

Measurements were next made on nitrogen. In this case the appearance potential was followed by a series of breaks separated by about $\frac{1}{4}$ ev, which are ascribed to the vibrational states of the nitrogen molecule. This is the first time that such states have been reported by the electron impact method. Values for the first three vibrational levels are compared with spectroscopic values in Table II. The agreement is quite satisfactory.

Measurements made on the hydrogen ion are of particular interest because no spectroscopic data exists for this, the simplest molecular structure (as Professor Paul Giguère says, it is composed of one and one-half atoms).

The lower curve in Fig. 7 represents the potential energy diagram of the neutral hydrogen molecule. Using a Morse function for the potential, the levels of the various vibrational states may be calculated by

[5] C. Moore, Natl. Bur. Standards (U. S.) Circ. **No. 467** (1949).
[6] J. A. Hornbeck and J. P. Molnar, Phys. Rev. **84**, 621 (1951).

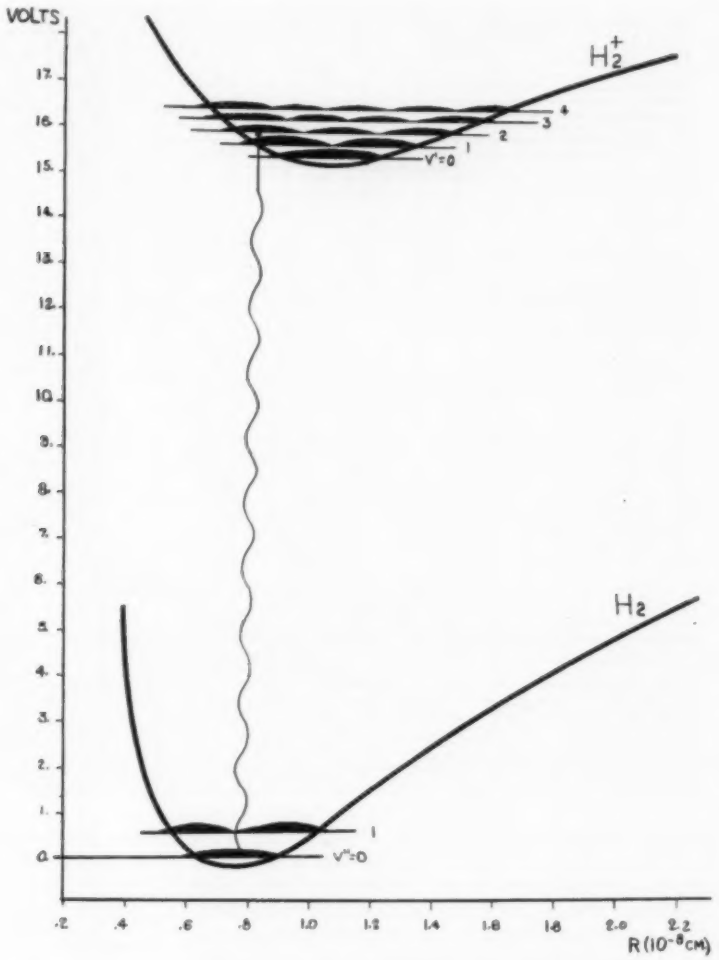

FIG. 7. Potential curve for neutral and ionized hydrogen molecules.

quantum mechanical methods.[7] These theoretical values have been verified by spectroscopic observations.[8] The waves on the various levels represent qualitatively the probability of nuclear separation. At ordinary mass spectrometer source temperatures, the population of the first excited level in neutral hydrogen is negligible, the molecules being in the ground state ($v''=0$).

The upper curve in Fig. 7 represents the potential energy diagram of H_2^+. This has been calculated theoretically for a Morse function,[9] and the vibrational levels established. These values agree with those calculated by extrapolation of the observed vibrational levels for various excited states of the neutral hydrogen molecule (e.g., Richardson). However, no direct experimental measurements have been made of these levels. The probable values of nuclear separation are indicated qualitatively for several levels by wavy lines.

When the ionization curves for H_2^+ are obtained with the new electron selector, they appear as in Fig. 8, where several individual curves are reproduced.[10] A

TABLE III. Comparison of average increments of energies producing successive breaks in electron-selector ionization curves for H_2^+ and spacing of vibrational levels derived from Richardson's constants.

Selector		References	
A	0.27±0.02 ev	1–2	0.2693±0.0016 ev
B	0.25 ev	2–3	0.2540±0.0023 ev
C	0.23 ev	3–4	0.2386±0.0030 ev
D	0.21 ev	4–5	0.2232±0.0039 ev

[7] G. Herzberg, *Molecular Spectra and Molecular Structure* (D. Van Nostrand Company, Inc., Princeton, New Jersey, 1950).
[8] O. W. Richardson, *Molecular Hydrogen and Its Spectrum*, (Yale University Press, New Haven, Connecticut, 1934).
[9] E. A. Hylleraas, Z. Physik **71**, 739 (1931).
[10] P. Marmet and L. Kerwin, Can. J. Phys. **38**, 972 (1960).

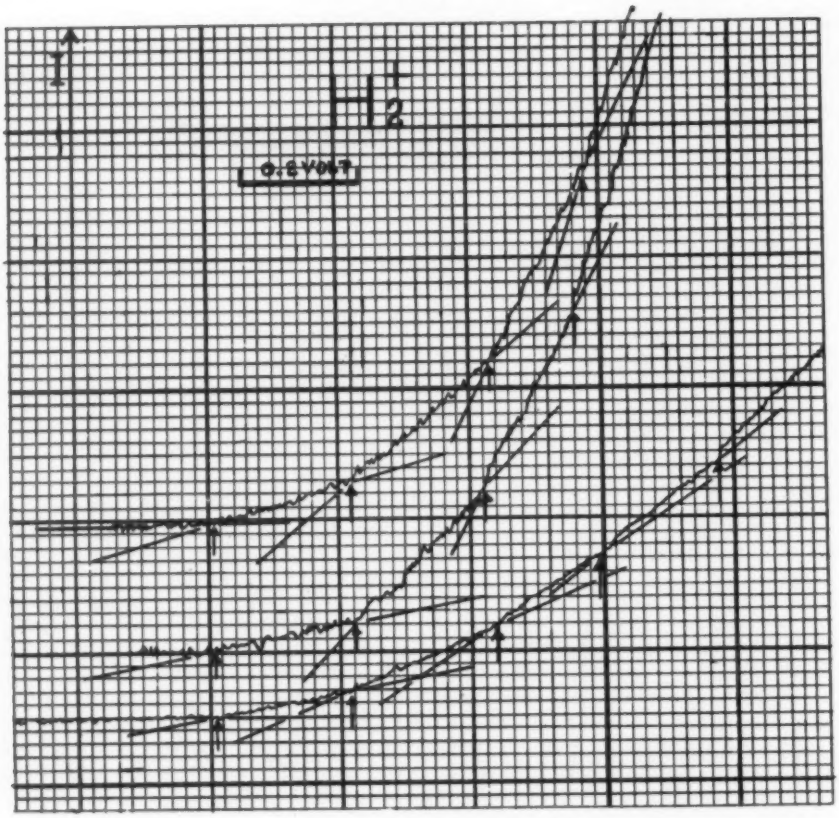

FIG. 8. Ionization curves for hydrogen.

number of breaks are seen to be separated by about 0.25 ev. Average values of the differences in energy required to produce successive breaks were taken from 20 runs. They are compared in Table III with differences between the first four vibrational levels as calculated from Richardson's constants (Herzberg). Our selector values clearly show the narrowing vibrational levels.

As may be noted in Fig. 7, the most probable transition from the ground state of the molecule to the ion is not to the first vibrational level but to one such that a probable nuclear separation is equal to that of the molecule (Franck-Condon principle). There is a certain probability for transitions to nearby levels. Experimentally, the probabilities may be calculated from the slopes of the appearance potential curve segments. In our case, the relative probabilities were:

		Reference value
to A:	0.4	0.4
B:	0.6	0.8
C:	1.0	1.0
D:	0.7	0.9

The reference values are those published by Krauss,[11] who calculated the probabilities theoretically. The agreement is good, and the wider nuclear separation in the ion is established experimentally.

It is a pleasure to acknowledge the assistance of the National Research Council of Canada in this project.

[11] M. Krauss, J. Chem. Phys. **26**, 1776 (1957).

JOURNAL OF APPLIED PHYSICS VOLUME 31, NUMBER 12 DECEMBER, 1960

Photoemission and Related Properties of the Alkali-Antimonides

WILLIAM E. SPICER
RCA Laboratories, Princeton, New Jersey
(Received August 4, 1960)

The photoemissive process in the semiconducting alkali-antimonides is examined and values are given for the band gaps and electron affinities. The high photoelectric efficiencies of these materials are attributed to the ability of the excited electrons to traverse relatively large distances (250 A) without overwhelming energy losses, rather than to negligibly small electron affinities. The efficiency is found to be strongly dependent on the percentage of the electrons which are excited into states above the vacuum level. The properties of these materials depend to a large extent on the crystal structure. Cs_3Sb and Na_2KSb have a cubic structure, are *p* type, and seem to have a relatively simple valence band structure. K_3Sb and Na_3Sb have hexagonal crystal structures, are *n* type, and seem to have a relatively complex valence band structure. The evidence for an effect of band bending on the photoemission is considered.

I. INTRODUCTION

THE alkali metals form semiconducting compounds with antimony which have a three to one ratio.[1,2] Because they are very efficient photoemitters, these semiconductors have been studied over the last 25 years with the aim of gaining an understanding of this emission. However, it has long been evident that such an understanding could only follow more general knowledge of the materials as solid state systems. As a result, many properties other than photoemission have been investigated.

A large number of papers concerning the alkali-antimonides has appeared since Görlich first discovered the high photoelectric efficiency of Cs_3Sb in 1936.[3] Only those papers will be mentioned which bear most directly on the points under discussion. Other references may be found in the papers cited here and in the recent review article of Görlich.[4]

The materials which will be discussed here are Na_3Sb, K_3Sb, Rb_3Sb, Cs_3Sb, and the multi-alkali materials[5] Na_2KSb, [Cs]Na_2KSb, and [Rb]Na_2KSb. The symbols [Cs] and [Rb] used in the last two expressions indicate a surface layer of cesium or rubidium on the Na_2KSb. The alkali-antimonides are usually formed in films about 100 to 5000 A thick by reacting an evaporated antimony layer with alkali vapor.[6] In this form, they seem to be made up of small crystallites. For x-ray studies, the alkali metal is usually reacted with antimony powder.

[1] For the pruposes of this paper, these particular compounds will be termed the "alkali-antimonides" although compounds are formed of these materials in different ratios.

[2] The chemical composition Cs_3Sb was established independently by N. S. Zaitsev [J. Tech. Phys. (U.S.S.R.) **9**, 661 (1939)] and by A. H. Sommer [Nature **148**, 468 (1941); Proc. Phys. Soc. (London) **55**, 145 (1943)].

[3] P. Görlich, Z. Physik **101**, 335 (1936); Phil. Mag. [7] **25**, 256 (1938).

[4] P. Görlich, Advances in Electronics and Electron Phys. **11**, 1 (1959).

[5] A. H. Sommer, Rev. Sci. Instr. **26**, 725 (1955).

[6] A. H. Sommer and W. E. Spicer, *Methods of Experimental Physics*, edited by K. Lark-Horovitz and V. A. Johnson (Academic Press, Inc., New York, 1959), Vol. 6B, Chap. 12.4, p. 376.

II. THE PHYSICS OF PHOTOELECTRIC EMISSION

Before discussing in detail the photoemission from the alkali-antimonides, some general remarks about photoemission from semiconductors are appropriate. In the spectral regions of high yield, the photoemission must be due to electrons which are generated in the bulk of the material and diffuse to the surface.[7] Clearly, only the electrons which are excited into states above the vacuum level can possibly escape; however, due to energy loss process, some of these will arrive at the surface with less than escape velocities. The best-identified energy loss process in photoemitters is that in which a sufficiently energetic electron excites a valence band electron into the conduction band forming a hole-electron pair. This was first observed by Apker and Taft.[8,9] It is this process which gives rise to avalanche breakdown in semiconductors and, as such, it has been studied in detail in silicon.[10] The experimental[11] and theoretical work[12] has indicated that, for a sufficiently energetic electron, the mean free path for this type of collision is between 15 and 100 A. Since both energy and momentum must be conserved, the threshold energy for this event is greater than the band gap

[7] Since the maximum escape depth of photoelectrons is about 250 A, absorption coefficients greater than 10^4/cm are necessary to provide the high yields obtained in good emitters. Such high absorption coefficients are associated only with excitation from one fundamental band to another.

[8] L. Apker and E. Taft, J. Opt. Soc. Am. **43**, 78 (1953).

[9] H. Miyazawa [J. Phys. Soc. Japan **8**, 169 (1953)] has suggested that Apker and Taft's data could be attributed to structure in the valence band of Cs_3Sb. If this were so, the structure which appears at low energies for photons of about 4 ev should move to higher energies with increasing photon energy. This is not the case. The mechanism suggested by Apker and Taft has been so well established in a large variety of semiconductors (see, for example, footnotes 10 and 14) that one must assume that it occurs in photoemitters. Taft and Philipp [E. A. Taft and H. R. Philipp, Phys. Rev. **115**, 1583 (1959)] have shown that valence band structure can be identified in the velocity distribution of photoelectrons from Cs_3Sb, but this is not the structure referred to by Miyazawa.

[10] K. G. McKay, Phys. Rev. **94**, 877 (1954); A. G. Chynoweth and K. G. McKay, *ibid.* **102**, 369 (1956); **106**, 418 (1957); J. Appl. Phys. **30**, 1811 (1959), and the references given in these papers.

[11] B. Senitzky, Phys. Rev. **116**, 874 (1959); A. G. Chynoweth, J. Appl. Phys. **31**, 1161 (1960).

[12] P. A. Wolff, Phys. Rev. **95**, 1415 (1954).

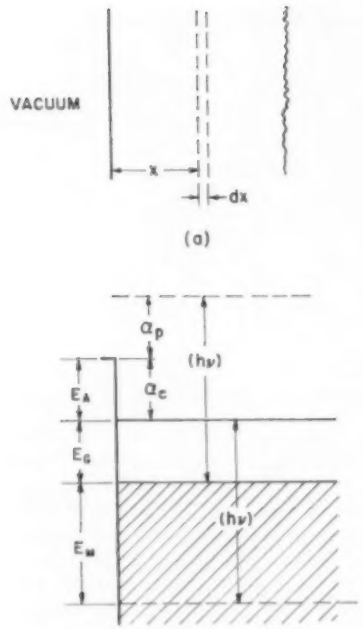

FIG. 1. (a) Here a semi-infinite photoemitter is represented. The photoemission from a section of material of thickness dx parallel to and a distance x from the surface is being considered for light incident from the vacuum. (b). The energy band diagram for a photoemitter. E_A is the electron affinity, E_G is the band gap, and $h\nu$ is the energy of an incident photon. The optical transitions can be divided into two groups: those to states above the vacuum level (associated with the absorption coefficient α_p) and those to states below the vacuum level (associated with the absorption coefficient α_c). E_M is the lowest energy level in the valence band from which an electron can be excited into the conduction band by a photon of energy $h\nu$.

energy.[12] For germanium and silicon, it is about twice the band gap.[13,14] Thus it appears that we have a very effective energy loss mechanism with a relatively small mean free path (15 to 100 A), a very large energy loss per collision (greater than band gap), and a minimum energy below which the scattering event cannot take place (roughly, twice the band gap).

For electrons with energies less than that necessary for pair production, the dominating energy loss mechanism is not so well identified; however, it seems most probable that it is the process of phonon production, i.e., lattice scattering.[15] This process is probably accentuated by scattering of the electrons by crystal defects which would increase the scattering between phonon producing collisions, and thus decrease the actual distance between these collisions. In this process, the energy loss per collision is only about 0.02 ev, and the mean free path between collisions should be greater than for pair production. Burton,[16] in studying photoemission from Cs_3Sb, and Dekker,[17] in analyzing data on the secondary emission from MgO, arrived at about 250 A as the depth from which electrons could escape. Since the electron affinities of these two materials are considerably less than their band gaps, this gives a measure of the escape depth which can be expected when pair production does not limit the escape depth.[18]

It is useful to examine the photoemissive process more formally. Let us consider a slab of material of thickness dx which is located a distance x from the emitting surface [see Fig. 1(a)]. It is then possible to write the expression

$$di(x,h\nu)d(h\nu)=\alpha_p(h\nu)I(x,h\nu)P(x,h\nu)dxd(h\nu) \quad (1)$$

for the photoemission from the slab.[19] Here, $di(x,h\nu)$ is the emission from the slab of material which has a thickness dx. $I(x,h\nu)$ is the light intensity at x in photons/sec. $P(x,h\nu)$ is the probability of an electron excited at x by a photon of energy $h\nu$ escaping from the material. $\alpha_p(h\nu)$ is the absorption coefficient for excitation into states above the vacuum level. As is shown by Fig. 1(b), the optical absorption can be divided into two types of events: the transitions into states above the vacuum level, α_p, and those into states below the vacuum level, α_c. Clearly, photoemission is only possible from the transitions of type α_p. The total absorption coefficient, α_t, is the sum of α_p and α_c. $I(x,h\nu)$ is given by:

$$I(x,h\nu)=I_0(x,h\nu)e^{-\alpha_t(h\nu)x}, \quad (2)$$

where $I_0(x,h\nu)$ is the intensity of the incident light in photons/sec. It appears that

$$P(x,h\nu)=B(h\nu)e^{-\beta(h\nu)x} \quad (3)$$

is a good approximation for the probability of escape. Burton[16] has studied the escape probability in Cs_3Sb, and found that the experimental data could be fitted best by an expression of this form. Similarly, it has been successfully used in the theory of secondary emission[17] (dropping, of course, the $h\nu$ dependence of B and β). The theoretical validity of this approximation has been examined elsewhere.[20]

[12] A. G. Chynoweth and K. G. McKay, Phys. Rev. **108**, 29 (1957).

[13] J. Tau, J. Phys. Chem. Solids **8**, 219 (1959); V. Vavilov, *ibid.* **8**, 223 (1959).

[15] This is supported by the temperature dependence of photoemission for photon energies greater than those at the threshold. See the reference to Miyazawa's article in footnote 9.

[16] J. A. Burton, Phys. Rev. **72**, 531(A) (1947) and private communication. Some of Burton's data are given by V. K. Zworykin and E. G. Ramberg in *Photoelectricity* (John Wiley & Sons, Inc., New York, 1949), p. 59.

[17] A. J. Dekker, *Solid State Physics*, edited by F. Seitz and D. Turnbull (Academic Press, Inc., New York, 1958), Vol. 6, p. 251.

[18] Assuming a mean free path between lattice collisions of about 30 A, this is the sort of escape depth which would be expected for energy loss due to phonon production.

[19] W. E. Spicer, Phys. Rev. **112**, 114 (1958).

[20] As Dekker has shown [A. J. Dekker, *Solid State Physics* (Prentice-Hall, Inc., Englewood Cliffs, New Jersey, 1957), p. 432], Eq. (4) is given by diffusion with loss. Hebb [M. H. Hebb, Phys. Rev. **81**, 702 (1951)] has pointed out that a more exact approach to the actual physical situation is given by the "age theory," developed for use in neutron diffusion. Using this, Hebb derived

By placing Eqs. (2) and (3) in (1) and integrating from zero to infinity, an expression can be obtained for the photoelectric yield[13]:

$$V(h\nu)d(h\nu)=\frac{\alpha_p(h\nu)}{\alpha_t(h\nu)+\beta(h\nu)}B(h\nu)d(h\nu). \qquad (4)$$

Here, $V(h\nu)$ is the photoelectric yield in electrons per incident photon. Although Eq. (4) is obviously not an exact expression for the photoemissive yield, it does indicate the principal features of the photoemissive process. As will be shown later, it is also possible to apply it directly to certain materials.

It is useful to examine Eq. (4) with the two types of energy loss mechanism mentioned previously, and note the various classifications into which photoemitters fall[21] according to the relative values of their band gaps and the threshold for pair production. The first group would be those materials in which the electron affinity is larger than the threshold for pair production. For these materials, the escape depth will be something like 30 A. Thus, β would dominate the denominator of Eq. (4) and, provided that $B(h\nu)$ did not depend strongly on $h\nu$,[22] the photoelectric yield should be proportional to α_p. Since to the first approximation only those electrons escape which do not suffer collisions, one would expect the energy distribution of the emitted electrons to be similar to that which the electrons had immediately after excitation, provided correction is made for the effect mentioned in footnote 22. Since the escape depth in this type of emitter is small compared to the distance for optical absorption, small photoelectric yields are to be expected. Germanium, boron, and tellurium,[23] which have electron affinities much larger than their band gaps, fall into this category.

In contrast to the type of materials discussed previously are those materials whose electron affinities are sufficiently small, compared to the threshold for pair production, so that there is a high probability for escape even after pair production has taken place. From the data of Apker and Taft[8] and that of Burton,[16] it is clear that Cs_2Sb falls into this class. For such materials, the escape depth is comparable with the optical absorption depth, i.e., α_t and β are comparable. Since, in the threshold region, α_p will be small and increasing with photon energy much faster than α_t or β, the yield should be proportional to α_p in this spectral region. However, as the photon energy is increased, α_p will increase and eventually become comparable to $\alpha_t+\beta$, and the yield will no longer be proportional to α_p. Because of the large escape depths for electrons, high photoelectric yields should be expected for this class of materials. Materials such as Cs_3Sb and the alkali halides belong to this class.

There is a third class of materials which falls between the two discussed above. In these materials, the electron affinity is smaller than the threshold for pair production, but large enough so that the electrons have a small probability for escape when pair production takes place. This could lead to an actual decrease in yield for increasing photon energy. AgBr may fall in this class.[24] In the formalization of Eq. (4), β will be highly dependent on photon energy.[25]

III. PHOTOEMISSION FROM THE ALKALI-ANTIMONIDES

A. Cs_3Sb, Rb_3Sb, Na_2KSb, $[Cs]Na_2KSb$, and $[Rb]Na_2KSb$

In order to attempt to understand the photoemission from a semiconductor, one must first know the band gap and electron affinity. The band gap may be obtained from optical absorption and photoconductivity data. The optical absorption measurements of a number of workers[16,26–28] indicate a band gap of 1.6 ev for Cs_3Sb.[29] Spicer,[19] combining optical absorption and photoconductivity measurements, has arrived at values of the band gap for the other alkali-antimonide materials under discussion here (see Table I).[30]

a more exact expression for the escape probability. However, he found that the experimental photoemission data he was treating could be fitted equally well by Eq. (3). A similar conclusion was reached by Lye and Dekker [R. G. Lye and A. J. Dekker, Phys. Rev. **107**, 977 (1957)] in considering the secondary emission from semiconductors.

[21] For a prior discussion of these classifications, see E. A. Taft, H. R. Philipp, and L. Apker, Phys. Rev. **110**, 876 (1958).

[22] The principal dependence of $B(h\nu)$ on $h\nu$ would be expected to arise from the fact that only that part of the velocity which is directed perpendicular to the surface is effective in overcoming the surface barrier.

[23] L. Apker, E. A. Taft, and J. Dickey, Phys. Rev. **74**, 1462 (1948).

[24] E. A. Taft, H. R. Philipp, and L. Apker, Phys. Rev. **110**, 876 (1958).

[25] To be more exact, β will be a function of the initial energy of the excited electron and the integration in Eq. (1) should be carried out for each value of initial energy.

[26] N. D. Morgulis, P. G. Borzyak, and B. I. Djatlowizkaja, Izvest. Akad. Nauk S.S.S.R., Ser Fiz. **12**, 126 (1948).

[27] P. G. Borzyak, J. Tech. Phys. (U.S.S.R.) **20**, 923 (1950).

[28] G. Wallis, Ann. Physik [6] **17**, 401 (1956).

[29] Since data indicate appreciable absorption as well as photoconductivity below 1.6 ev [see footnotes 19, 27, 28, and S. Imamura, J. Phys. Soc. Japan **14**, 1497 (1959)], there may be an indirect transition a few tenths of an electron volt below 1.6 ev; however, since there are alternative explanations for this absorption and photoconductivity, additional work must be done before a definitive statement can be made. In any case, it appears that the suggestion of Miyazawa (see article cited in footnote 9), that there is an indirect band to band transition at about 0.5 ev, can be ruled out. The study of the indirect optical transition in silicon and SiC [see W. C. Dash and R. Newman, Phys. Rev. **99**, 1151 (1955); H. R. Philipp, *ibid.* **111**, 440 (1958)] suggests strongly that such a transition should have been seen in the photoconductivity measurements if it lay so far below the direct gand gap.

[30] Imamura (see reference in footnote 29) obtained values of between 1.6 and 2.2 ev for the "absorption edge" in these materials. This edge may be analogous to that found at 2.1 ev in germanium [see H. R. Philipp and E. A. Taft, Phys. Rev. **113**, 1002 (1959) and J. C. Phillips, J. Phys. Chem. Solids **12**, 208 (1960)]. However, such an absorption edge should not be confused with the band gap. The band gap values obtained by Imamura from his photoconductivity measurements are in fairly good agreement with those of Spicer. Imamura derives a complicated model for the band structure of these materials. As in the case of Miyazawa, the validity of this is very doubtful, since he has to assume that an indirect optical transition is very improbable com-

If no photoemission occurred from defect levels, the threshold of photoemission should give the sum of the band gap and electron affinity. However, in the alkali-antimonides, the threshold of response is determined by defect photoemission because of the large concentration of defect levels. By use of the formulation put forth in Sec. II, Spicer[19] has found it possible to separate the defect and intrinsic photoemissive processes for some of the alkali-antimonides. Since the available data indicate that these materials belong to the class of materials, discussed in Sec. II, which have an electron affinity that is small compared to the threshold for pair production, the photoelectric yield from the valence band should be proportional to α_p near the threshold of response. For Cs_3Sb, Rb_3Sb, and all of the multi-alkali materials, Spicer found that near the threshold the photoemissive yield had the form

$$Y(h\nu)=G(h\nu-E_0)^{\frac{1}{2}}$$

over a spectral range of about one electron volt. In this expression, G and E_0 are constants. Since one would expect the yield to be proportional to α_p in this region, it was assumed that α_p had the form[31]

$$\alpha_p=C(h\nu-E_0)^{\frac{1}{2}}, \tag{5}$$

where C is a constant and E_0 is the sum of band gap and electron affinity. Substituting this into Eq. (4), Spicer obtained

$$Y(h\nu)=\frac{(h\nu-E_0)^{\frac{1}{2}}B}{(h\nu-E_0)^{\frac{1}{2}}+\gamma}, \tag{6}$$

where $\gamma=(\alpha_c+\beta)/C$. By assuming α_c and β to be constant, γ can be treated as a constant fitting parameter. The value of γ is a measure of the photon energy at which α_p becomes comparable to $\alpha_c+\beta$. At this point the photoemission is no longer proportional to α_p but increases more slowly than α_p. In fitting the calculated to the experimental curves, it was found that the parameter B could be treated as being independent of photon energy.[32]

Using this development, it was found possible to obtain a fit to the experimental data from Cs_3Sb, Rb_3Sb, Na_2KSb, [Cs]Na_2KSb and [Rb] Na_2Ksb.[19] A typical curve is shown in Fig. 2.[19] Here the calculated curve fits the experimental data up to the region of the threshold but, in that region, falls off more swiftly with decreasing photon energy than the experimental data. This is as would be expected if the photoemission at the threshold is from defect levels. Note also that the defect photoemission is greatly decreased at liquid nitrogen temperature. This is the behavior to be expected from a p-type material due to the freezing of electrons out of the acceptor states. The values obtained for the electron affinities of the various materials are given in Table I.

For Cs_3Sb, Taft and Philipp (see reference in footnote 9) have been able to place a lower limit on the electron affinity by correlating structure which appears in both the optical absorption and the velocity distribution of photoemission. They find that the electron affinity is greater than 0.4 ev, in good agreement with Spicer's value of 0.45 for this material.

B. K_3Sb and Na_3Sb

A typical response curve for K_3Sb is presented in Fig. 3.[19] The general behavior of the Na_3Sb curves are similar. Spicer[19] did not find it possible to fit the simple theory discussed above to the response curves of these two materials. Reasons for this will be discussed in Sec. VI. Because of this inability to fit calculated curves to the response curves for K_3Sb and Na_3Sb, he was only able to place limits on the possible values for their electron

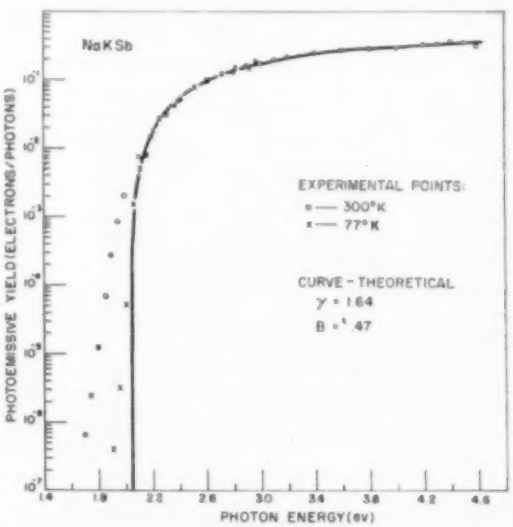

FIG. 2. Photoemission from Na_2KSb [from Spicer (footnote 19)]. A value of 2.0 ev is obtained for the sum of the band gap and electron affinity. To obtain the fit, values of 1.64 and 0.47, respectively, were taken for the parameters γ and B in Eq. (6).

pared to a direct transition. In the case of Imamura, it is necessary to assume the indirect transition to be about 10^4 less probable than the direct transition when both are energetically possible.

[31] This should just be considered to give, to a good approximation, the general envelope of the α_p vs $h\nu$ curve in the threshold region, and not as evidence that structure does not exist in the actual α_p vs $h\nu$ curve. It is worth noting the analogy with the optical absorption data on Cs_3Sb; Wallis (footnote 28) found that the room temperature optical absorption coefficient could be well fitted by a curve of the form $(h\nu-E_G)^{\frac{1}{2}}$, but Taft and Philipp (see work cited in footnote 9) found that the structure appeared when the Cs_3Sb was cooled to about 90°K. Similarly, Eq. (5) should just be expected to hold in the threshold region; otherwise, the absorption coefficient would increase without limit as $h\nu$ increases. Fortunately, the yield is not strongly dependent on α_p where α_p is comparable to $(\alpha_c+\beta)$, i.e., away from the threshold.

[32] One might expect B to have at least a photon energy dependence due to the fact that only the velocity directed perpendicular to the surface barrier is available to overcome that barrier (see footnote 22); however, since the electrons which arrive at the surface will be losing energy principally through phonon production, an electron which has greater than the minimum escape energy strikes the surface several times before its energy is reduced below that of the surface barrier.

TABLE I. Summary of the results from the alkali-antimonides. E_G is the band gap and E_A is the electron affinity.

Material	Crystal structure	Conductivity type	E_G(ev)[a]	E_A(ev)[a]	Limit on E_A(ev)[b]	Peak quantum efficiency (electron/photon)
Na_3Sb	hexagonal	n	1.1	2.0–2.4	···	0.02[a]
K_3Sb	hexagonal	n	1.1	1.1–1.8	>0.6	0.07[a]
Rb_3Sb	hexagonal(?)	n or p	1.0	1.2	···	0.10[a]
Cs_3Sb	cubic	p	1.6	0.45	>0.4	0.30[b]
Na_2KSb	cubic	p	1.0	1.0	···	0.30[a]
$[Rb]Na_2KSb$	cubic	p	1.0	0.7	···	···
$[Cs]Na_2KSb$	cubic	p	1.0	0.55	···	0.40[a]

[a] From the reference given in footnote 19.
[b] From the work of Taft and Philipp cited in footnote 9.

affinities. These are given in Table I. By the method mentioned in the last section, Taft and Philipp deduced that the lower limit for the electron affinity of K_3Sb is 0.6 ev (see work cited in footnote 9). This is in agreement with the value of Spicer.

As can be seen from Fig. 3, the threshold of response could be increased by about 0.5 ev by the addition of potassium. In this spectral region, an increased response was observed on cooling the material to 77°K. This behavior suggests that these materials are n type due to a potassium or, in the case of Na_3Sb, sodium excess.

IV. CRYSTAL STRUCTURE OF THE ALKALI-ANTIMONIDES

Since a correlation has been found between the properties of the alkali-antimonides and their crystal structures, a brief section will be devoted to this. Brauer and Zintl found that Na_3Sb and K_3Sb have a hexagonal structure ($D0^{18}$ type).[33] Solomon[34] and Gnutzmann[35] have found the crystal structure of Rb_3Sb to be also of this type. However, on the basis of changes in the physical characteristics of this material, Imamura[29] has suggested that it may exist in either the hexagonal or the cubic form. Through his own observations, the author has come to the same conclusion. Jack and Wachtel[36] have reported that Cs_3Sb has a face-centered cubic lattice with a structure similar to that of NaTl, in which cesium atoms occupy the sodium positions and equal numbers of cesium and antimony atoms randomly occupy the thallium positions. However, Gnutzmann[35] and Scheer and Zalm[36] did not find any evidence for the random occupancy; rather, the lattice seemed to have an ordered BiF_3-type structure. As Scheer and Zalm[36] pointed out, this may have been due to high background which could obscure the super lattice lines, but it also may be possible that Cs_3Sb exists in both forms, i.e., with and without ordering.

Scheer and Zalm[36] and McCarroll[37] found that Na_2KSb has an ordered cubic lattice. McCarroll[37] has also studied the complete system $Na_{3-x}K_xSb(0 \leq x \leq 3)$ and found that the only deviation from stoichiometry for the cubic Na_2KSb was in a substitution of potassium up to 2.5% on sodium sites.

The cubic and hexagonal structures differ significantly in density and manner of coordination. The spacings in the hexagonal lattices are such that interstitial atoms may well fit into the lattices; whereas, for the cubic structures, interstitials may be prohibited.[37,38]

There is one defect common to all of this x-ray work. The structure of the material studied by x rays may not be exactly the same as that of the photosensitive samples. This is probably not important except when

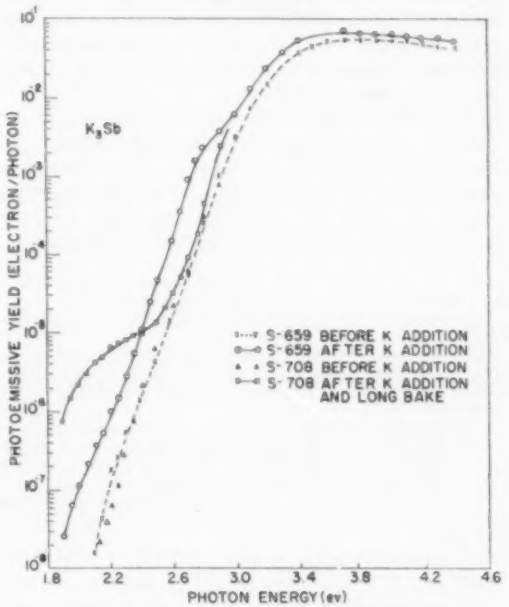

FIG. 3. Photoemission from K_3Sb [from Spicer (footnote 19)]. The addition of excess potassium produces photoemission centered at about 2.1 ev and perhaps 2.8 ev. The value for E_A+E_G is probably between 2.2 and 2.9 ev. S-659 and S-708 refer to individual tubes.

[33] G. Brauer and E. Zintl, Z. physik Chem. **37B**, 323 (1937).
[34] A. Solomon (private communication).
[35] G. Gnutzmann, Ph.D. dissertation, University of Münster (1953).
[36] K. H. Jack and M. M. Wachtel, Proc. Roy. Soc. (London) **239A**, 46 (1957); J. J. Scheer and P. Zalm, Philips Research Repts. **14**, 143 (1959).
[37] W. H. McCarroll, J. Phys. Chem. Solids (to be published).
[38] S. Imamura, J. Phys. Soc. Japan **14**, 1491 (1959).

ambiguity appears in the x-ray work (as in the case of Cs_3Sb), or in an attempt to correlate physical measurements with the crystal structure (as in the case of Rb_2Sb). Where such ambiguity occurs, it is quite important that the physical measurements and lattice determinations be made on the same sample. Certainly this would be more satisfying in all cases.[39]

V. DEFECT LEVELS IN THE ALKALI-ANTIMONIDES

Despite the size of its band gap, Cs_3Sb has a relatively high room temperature conductivity (about 10^{-2}/ohm-cm).[40] Sakata's Hall data[40] indicate mobilities of about 10 cm²/v-sec and free carrier densities as high as 5×10^{16}/cm³ at 345°K. The actual concentration of defect levels[41] is probably much larger.[42] From the experimental data, it seems apparent that the conductivity is due to a departure from stoichiometry. Attempts to detect such departures by chemical analysis have indicated an excess of cesium.[36,43,44] This is probably due to excess cesium which has been adsorbed on the walls and other parts of the vacuum tube, rather than excess cesium in the Cs_3Sb.

From the work of Borzyak,[27] Sakata,[40] Sommer,[45] and Imamura,[38] it is clear that Cs_3Sb is normally *p* type, and that within certain limits the conductivity decreases with cesium addition and increases with antimony addition. If a sufficiently high partial pressure of cesium is maintained above the Cs_3Sb, it can be driven through a conductivity minimum and become *n* type. However, when the cesium pressure is removed, the excess cesium leaves the cathode and the material returns to *p*-type conductivity.

Jack and Wachtel[36] have suggested that Cs_3Sb is *p* type due to cesium atoms in antimony sites. They found this model attractive because of the random distribution of cesium and antimony on one of the sublattices,[46] and because of an analogy which they drew between Cs_3Sb and intermetallic semiconductors such as Mg_2Sn.[47] The model of Jack and Wachtel can only be reconciled with the data of Borzyak, Sommer, and Imamura if one assumes the presence of interstitial atoms forming donor states as well as the substitutional cesium atoms. It would be surprising if a lattice so closely packed as is that of Cs_3Sb could accommodate the 10^{17}/cm³ or more cesium interstitials necessary to explain the data. A more satisfying picture is obtained if one assumes that the Cs_3Sb contains cesium vacancies which give rise to *p*-type levels; this viewpoint will be taken throughout this paper.

Sommer[45] studied not only the resistance of Cs_3Sb as a function of the relative alkali content, but extended this type of measurement to all of the other alkali-antimonide compounds under discussion here. Imamura[38] has done similar work on Na_3Sb, K_3Sb, and Rb_3Sb, making Hall and thermoelectric as well as conductivity measurements. This work indicates that the multi-alkali materials which have a cubic lattice (as does Cs_3Sb) are *p*-type conductors, whereas the materials with hexagonal symmetry (Na_3Sb, K_3Sb, and Rb_3Sb) are *n* type.[48] However, Rb_3Sb has shown *p*-type behavior on occasion. As mentioned in Sec. III, Spicer[19] believes that the photoemission in the threshold region is due to photoexcitation from defect levels. He has studied the emission near the threshold as a function of temperature and (when possible) alkali excess, and has found general agreement with the workers mentioned here as to the conductivity type of these materials. He found Rb_3Sb to be *p* type.

The finding that the materials with hexagonal lattice are *n* type due to an excess of alkali may be related to the fact that their lattices are packed loosely enough to allow the inclusion of interstitial alkali atoms. Since the multi-alkali materials have a cubic lattice, it is not surprising that they, like Cs_3Sb, are *p* type. It seems most likely that this is due to vacant alkali sites acting as acceptors.[49]

VI. THE EFFECT OF BAND BENDING ON PHOTOEMISSION

Since most of the photoelectrons in efficient photoemitters originate in the valence band, their photoemissive properties are principally determined by the intrinsic properties of the semiconductor. This is in contrast to the thermionic emission from semiconductors such as BaO, where the thermionic emission is determined by the defect level scheme. However, the defect level scheme will affect the photoemission from the valence band through the process of band bending.[50] As can be seen from Fig. 4, the effective surface barrier

[39] W. H. McCarroll is now studying the crystal structures of samples taken from sensitive cathodes.

[40] T. Sakata, J. Phys. Soc. Japan **8**, 125, 272 (1953); **9**, 1030, 1031 (1954).

[41] In this paper, the term "defect level" will be used for any energy level introduced into a semiconductor by a lattice imperfection whether by a foreign atom, vacancy, or any other type of defect.

[42] By assuming the conductivity to be due to a single level with no compensation, Sakata obtained values for his defect concentrations between 10^{20} and 10^{21}/cm³.[40] However, the scheme of defect levels may be much more complicated.

[43] It should be noted that in the paper of Jack and Wachtel (footnote 36), no experimental evidence is given for an excess of cesium.

[44] N. S. Khlebnikov, J. Tech. Phys. (U.S.S.R.) **17**, 333 (1947); K. Miyake, J. Appl. Phys. **31**, 76 (1960).

[45] A. H. Sommer, J. Appl. Phys. **29**, 1568 (1958).

[46] At present, it is not certain that the photosensitive cathode has this type of structure. See discussion in Sec. V.

[47] Such an analogy may be misleading, since the difference in electronegativity of the components is considerably smaller for compounds such as Mg_2Sn than it is for Cs_3Sb. See, for example, F. A. Kroger and H. J. Vink, in *Solid State Physics*, edited by F. Seitz and D. Turnbull (Academic Press, Inc., New York, 1956), Vol. 3, p. 366.

[48] In agreement with the previous work on K_3Sb [P. G. Borzyak, Izvest. Akad. Nauk S.S.S.R., Ser. Fiz. **9**, 173 (1941); Proc. Conf. on Cathode Electronics, Acad. Sci. UkSSR (1952), p. 18; R. Suhrman and C. Kangro, Naturwissenschaften **40**, 137 (1953)].

[49] There is no evidence for the random distribution of alkali and antimony atoms in the multi-alkali lattices.

[50] For a more complete discussion of the influence of defect levels on photoemission see W. E. Spicer, RCA Rev. **19**, 555 (1958).

to photoelectric emission can be changed by bending of the bands. The bands will bend in such a direction as to make the Fermi level at the surface coincide with that in the interior. The types of bending which can be expected for various dopings are shown in Fig. 4. It should be noted that bending tends to be beneficial for photoemission when the bulk is p type.[50]

The bending of the bands is, of course, due to the dipole layer set up by transfer of charge from the surface. For a given potential difference between the surface and bulk, the thickness of the dipole layer is determined by the distribution of energy levels into which the surface charge can go. The thickness of this dipole layer is quite important for photoemission. If it is large compared to the depth of photoemission,[51] the effect on the photoemission will be small. If the dipole layer is small compared to the depth of photoemission, it will have the maximum effect. In the latter case, however, it is very difficult to separate the effect of band bending from that of the electron affinity, which is defined as the energy difference between the bottom of the conduction band and the vacuum level at the surface.[52] A rough calculation indicates that band bending would occur only over approximately 10 A for a density of defect states of $10^{20}/cm^3$, and over 100 A for a density of $10^{18}/cm^3$. It is also possible that a substance could be added to the surface which would form its own dipole layer without changing the occupancy of the defect levels in the host material at all, e.g., polar molecules.

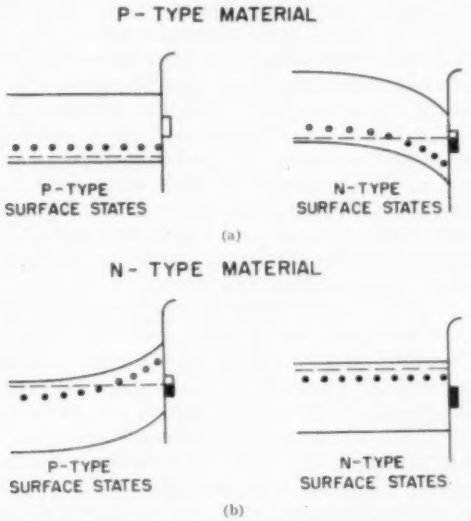

FIG. 4. The type of band bending which may be expected for surface states near the center of the forbidden gap. The Fermi level is indicated by the dashed line.

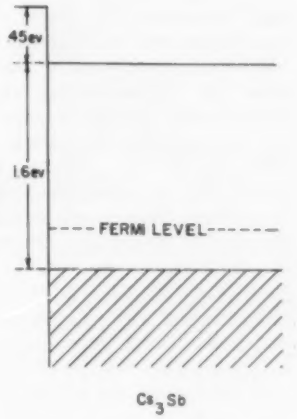

FIG. 5. Energy diagram for Cs_3Sb. The electron affinity is 0.45 ev and the band gap is 1.6 ev.

VI. CONCLUSIONS

A. Introduction

From the data presented here, it seems possible to obtain a general picture of the photoemissive processes in the alkali-antimonides; however, there are many questions still to be answered, and assumptions which need further verification. Many of the conclusions drawn here should also apply to the photoemission from other materials.

B. Electron Affinity and Depth of Escape of Photoelectrons

As a result of his work, Burton thought that the electron affinity of Cs_3Sb was very small (at most a few tenths of an electron volt) or even negative.[16] Until recently, this value has been accepted by most workers in the field. However, Spicer has obtained the value of 0.45 ev for the electron affinity,[19] and Taft and Philipp (see work cited in footnote 9) have come to the conclusion that it is greater than 0.4 ev. It is unlikely that the high photoelectric yields obtained above 2.05 ev could be due to photoemission from defect levels, because of the relatively small absorption coefficients which must be associated with such transitions; therefore, Spicer's value seems to be well confirmed by the results of Taft and Philipp. An energy level diagram for Cs_2Sb, based on his values, is given in Fig. 5.

One reason why it has been attractive to assume a very small or negative electron affinity for Cs_3Sb is the relatively long escape depth which was found by Bur-

[51] The depth of photoemission is here taken to be the maximum depth from which appreciable emission is obtained for radiation incident from the vacuum. This will be determined by either the thickness of the semiconductor necessary to absorb most of the light, or by the depth from which an excited electron can escape. The depth of escape will be given by the smaller of the above parameters.

[52] The values of electron affinity which will be reported here and which have been reported previously should be understood as "apparent electron affinities" because of the difficulty in separating electron affinity effects from that of band bending. However, we will continue to term our values "electron affinities" until the separation is possible. Since there is good agreement on the threshold of photoemissive response in these materials, it is clear that the electron affinity is reproducible.

ton,[16] and which is necessary to explain the high quantum efficiency of that material. The data from the multialkali material with and without Cs or Rb on the surface show that this assumption is not necessary. Adding Cs to the surface of Na_2KSb reduces the electron affinity by 0.45 ev; however, the yield is only increased by about 30%.[19] This is not consistent with any theory that assumes that the surface barrier must be quite small or nonexistent for electrons to escape from large depths. Rather, it is consistent with a model which assumes that the electrons can diffuse to the surface and still retain energies of the order of an electron volt. Thus, it appears that electrons with energies less than that required for pair production can move through large distances (probably total path lengths of a few hundred angstroms) with an energy loss of only a fraction of an electron volt. It also appears that, with the most efficient photoemitters, the primary parameter determining the yield in regions of high optical absorption is simply the fraction of the absorbed radiation which excites electrons into states above the vacuum level. The increase of the yield from Na_2KSb with the addition of Cs, as well as the similarity of the peak yields for Cs_3Sb and Na_2KSb, can be explained on this basis.[19]

C. Bending of the Bands

No definitive evidence of band bending has been found for the antimonides. It is unlikely that the fit between the calculated curves and the experimental data found by Spicer[19] for a number of the alkali-antimonides would have been possible if there were considerable band bending over more than about 50 A. Similarly, it is doubtful if Taft and Philipp (see reference in footnote 9) could have seen valence band structure in the velocity distribution of photoemission if there were a significant amount of band bending over an appreciable distance. Since they found this structure in K_3Sb as well as in Cs_3Sb, it is not likely that Spicer's inability to fit his calculated curves to the experimental data for K_3Sb was due to band bending in that material. On the other hand, the measured electron affinities are certainly larger for the *n*-type than for the *p*-type materials. This is the trend which would be expected if band bending were taking place. Since there is no way of detecting bending of the bands which takes place over distances short compared to the depth of photoemission, such band bending is not excluded.

D. Conductivity Type and Defect Centers

It is certain that the materials with cubic lattice structure are *p* type, and those with hexagonal lattice are *n* type. The case of Rb_3Sb is still not quite clear. It is also certain that the conductivity is mainly due to departure from stoichiometry. For the *n*-type materials, there seems to be agreement that the departure is associated with an alkali excess. For the cubic materials, the author strongly believes that the conductivity is due to an antimony excess; however, there seems to be no agreement on this point at present. In any case, there is insufficient experimental evidence to support the assumption, made in the past, that Cs_3Sb contains excess alkali.

The author would also like to propose that the cubic materials are *p* type due to vacant alkali sites, and that the hexagonal materials are *n* type due to interstitial alkali atoms.[53] This seems to be the most reasonable way to explain the difference in the conductivity types of the two materials. However, here again definitive work must ge done before there can be any certainty about the types of defect centers.

E. Band Structure and Photoemission

The work of Taft and Philipp suggests that the structure in the valence band of K_3Sb, which has a hexagonal lattice, is more prominent than it is in the case of Cs_3Sb, which has a cubic structure. Similarly, Spicer[19] has found that the spectral dependence of the absorption coefficient for transitions into energy levels above the vacuum level, α_p, can be approximated by a simple three-halves power law for the cubic materials, whereas no such simple approximation holds for the hexagonal materials. Although other explanations may be possible for this result of Spicer, it suggests again that the valence band of the hexagonal materials has stronger structure than that of the cubic materials, producing a more complicated α_p. This is in agreement with theory, since the 5*p* states of antimony which should form the valence band would experience more splitting in the asymmetrical crystal field of the hexagonal lattice than in the symmetrical crystal field of the cubic lattice.

It has long been apparent that the energy band structure of semiconductors is closely associated with their photoelectric properties because it determines the band gap and the electron affinity. It is becoming increasingly clear that it also plays an important role through its determination of more subtle parameters, such as the energy distribution of the excited photoelectrons and the threshold energy for pair production. Because of this dependence on energy band structure, photoemission should prove to be an increasingly important tool in the investigation of energy band structure.

ACKNOWLEDGMENTS

The author is grateful for the many stimulating conversations which he has had with members of the staff of the RCA Laboratories. In particular, he is indebted to W. H. McCarroll, D. S. McClure, and especially A. H. Sommer. He is also grateful to J. A. Burton for additional information on his Cs_3Sb work.

[53] This last proposal has been made previously by Imamura; see footnote 38.

JOURNAL OF APPLIED PHYSICS VOLUME 31, NUMBER 12 DECEMBER, 1960

Oxygen on Nickel

L. H. GERMER AND C. D. HARTMAN
Bell Telephone Laboratories, Murray Hill, New Jersey

(Received August 4, 1960)

Low-energy electron diffraction, with the diffracted electrons post-accelerated and observed on a fluorescent screen, has been used to study the adsorption of oxygen on a (100) face of a nickel crystal. Upon admitting oxygen to a clean face at room temperature, or at elevated temperatures up to 350°C, the first adsorbed atoms are arranged in narrow bands parallel to [110] directions on the crystal surface. Within one of these bands, atoms lie on lines at right angles to the band; these lines have a uniform separation of 4.98 A, but the atoms along each line are somewhat randomly spaced in multiples of the nickel spacing of 2.49 A. With further oxygen exposure (30×10^{-6} mm Hg sec) sufficient to produce half of a monolayer (one oxygen atom for every four surface nickel atoms), the arrangement is very chaotic unless the crystal has been heated, but after heating the arrangement is a simple square array with edge of 4.98 A. Further exposure to oxygen (100×10^{-6} mm sec) will produce a full monolayer consisting of this same square array with an additional oxygen atom at the center of each square. With still further exposure, oxygen, at least in part as physisorbed molecules, is piled on top of this first monolayer of atoms, the added molecules forming an array with square symmetry and edges parallel to the edges of the square array of surface nickel atoms. At least several layers of oxygen molecules can be adsorbed and are not removed by pumping at room temperature. Heating at 350°C removes a great deal of the adsorbed oxygen, and the structure of the remainder agrees with that of NiO having the orientation of the nickel crystal. This oxide is removed at 830°C, and the first layer of oxygen atoms at 880°C.

INTRODUCTION

THE arrangement of oxygen atoms and molecules upon a cube face of a crystal of nickel has been investigated by the diffraction of low energy electrons. The electron beam, of energy corresponding to potential differences of the order of 100 volts, strikes the crystal face at normal incidence, and the electrons of the resulting diffraction pattern are post-accelerated so that the pattern in back reflection directions can be seen on a fluorescent screen.[1–3] Various complex diffraction patterns appear, and changes in them can be observed continuously while more oxygen is being deposited or after some has been removed by heating the crystal.

Two basic experiments have been carried out. In the first of these, initially the crystal is completely clean; in the second, initially it is covered by a thick layer of oxygen.

In an experiment of the first type the diffraction pattern from the crystal is observed continuously while oxygen is being deposited upon it at a constant low controlled pressure. The crystal has sometimes been annealed at various low temperatures during the course of the experiment. The experiment ends with the attainment of a steady state in which the crystal is covered by many layers of oxygen molecules which produce a diffraction pattern of their own, but shield the underlying crystal so completely that there is no diffraction pattern whatsoever from it.

In the second type of experiment, one starts at this final stage in which the crystal is completely shielded from the impinging electrons by a thick layer of oxygen. The crystal is heated progressively to higher temperatures, and the diffraction pattern is observed after each heating. The final steady state at the end of this experiment is reached when diffraction patterns at all electron beam voltages consist of the normal Laue beams from the nickel crystal without any other diffraction features.

Many of the observations reported here are not new. They have been made previously by Professor H. E. Farnsworth and his collaborators.[4–8] In particular, they have found oxygen atoms deposited upon an initially clean nickel surface with the arrangement which we describe as "half a monolayer" and with the arrangement which we describe as a "full monolayer." Here, their experimental conditions were very similar to those under which we have found these structures. They have found NiO also. However, the facility with which we can make observations has enabled us to discover some details in the development of these structures which were not found by Farnsworth *et al.* Because of differences in experimental procedures, chiefly annealing of the crystal with its adsorbed oxygen, it has not seemed feasible to make detailed comparisons of results obtained in the two sets of investigations.

DIFFRACTION FROM A CLEAN CRYSTAL

Under favorable conditions, which are, unfortunately, by no means always obtained, the crystal is easily cleaned by heating. For these cases, it will appear from evidence to be presented later that, after the crystal has

[1] E. J. Scheibner, L. H. Germer, and C. D. Hartman, Rev. Sci. Instr. **31**, 112 (1960).
[2] L. H. Germer, E. J. Scheibner, and C. D. Hartman, Phil. Mag. **5**, 222 (1960).
[3] L. H. Germer and C. D. Hartman, Rev. Sci. Instr. **31**, 784 (1960).
[4] R. E. Schlier and H. E. Farnsworth, Advances in Catalysis **9**, 434 (1957).
[5] H. E. Farnsworth, R. E. Schlier, T. H. George, and R. Burger, J. Appl. Phys. **29**, 1150 (1958).
[6] H. E. Farnsworth and J. Tuul, J. Phys. Chem. Solids **9**, 48 (1959).
[7] H. E. Farnsworth, R. E. Schlier, and J. Tuul, J. Phys. Chem. Solids **9**, 57 (1959).
[8] H. E. Farnsworth and H. H. Madden, *International Conference on Structure and Properties of Thin Films* at Lake George, New York, September 9–11, 1959.

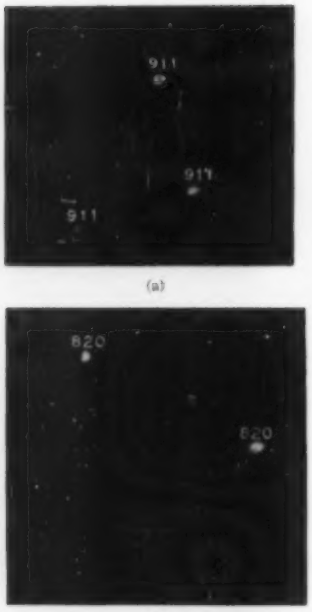

FIG. 1. Laue diffraction beams from a clean cube face of a nickel crystal. Deviations from fourfold symmetry are due to imperfect crystal alignment. (a) Pattern at 234 volts. Strong diffraction beams having Miller indices (911) in the A azimuth of the crystal, with much weaker diffraction beams in the B azimuth. (b) Pattern at 198 volts. Strong diffraction beams having Miller indices (820) in the B azimuth, with much weaker beams in the A azimuth. Azimuth designations are given in Fig. 2.

been heated to 975°C (as determined by a Pt−PtRh (10%) thermocouple welded to the crystal) and allowed to cool, its surface is completely clean.

Typical diffraction patterns from the crystal in this clean condition are reproduced in Fig. 1. Both patterns should show fourfold symmetry, but in the first place the orientation of the crystal with its face normal to the electron beam is a little imperfect, and in the second place reflections are sometimes obscured by the electron gun. As a result, in Fig. 1(a) one sees only three of the four strong diffraction spots from the crystal, and in Fig. 1(b) only two of them. These spots are respectively in the A and B azimuths, according to the designation of azimuths in the sketch of Fig. 2.

All sets of diffraction beams from the clean crystal appear in one or the other of these principal azimuths. Beams appear at maximum intensities at voltages which are quite well defined from the upper experimental limit of about 450 down to below 150. Below this lower voltage, beams show less voltage discrimination because of slight penetration of electrons into the crystal. The relationships between the electron wavelengths at which sets of diffraction beams reach maximum intensities, and the sines of the angles between the primary beam and one of the diffraction beams of the set, are plotted as crosses in Fig. 3. This angle is measured on the photographed patterns and is averaged to take account of the imperfect crystal alignment. The sloping lines on the figure represent, for the A and B azimuths respectively, $\lambda=(a_0/2^{\frac{1}{2}})\sin\theta=2.49\sin\theta$ Angstrom units, and $\lambda=(a_0/2)\sin\theta=1.76\sin\theta$, where a_0 is the unit cell edge of the nickel lattice. The open circles are calculated positions for all possible Laue beams within the wavelength and angle range of the experiments. The (511) and (620) reflections, which are not marked down on the figure, are observed also, but at the low voltages of these beams the voltage discrimination is so broad that good values cannot be determined.

These diffraction patterns, appearing in one or the other of the two principal azimuths and satisfying the relationships represented by the straight lines of Fig. 3, are the only diffraction features which can be found immediately after the crystal has been cleaned by heating to 975°C. This fact, together with the other observations to be reported in this paper, constitute the evidence that the crystal is completely clean.[9]

PROOF THAT THE ABSORBED GAS IS OXYGEN

The most sensitive test for the presence of adsorbed gas is perhaps the appearance of the fluorescent screen for a primary electron beam corresponding to 50 volts. At this low potential difference, no diffraction features from the nickel crystal can appear (as one can see from Fig. 3), and on the other hand, any adsorbed gas with which we have experimented (except hydrogen) produces an observable diffraction pattern at this voltage.

With our usual vacuum conditions, no diffraction features can be seen at 50 volts immediately after the

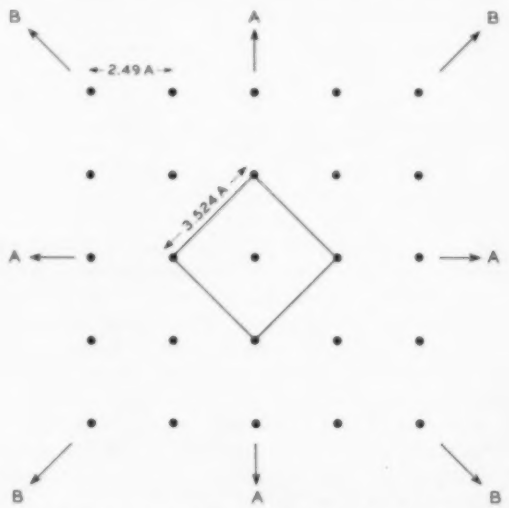

FIG. 2. Designation of the principal azimuths of the crystal. The dots represent centers of nickel atoms in the surface layer. Nickel has a fcc structure with $a_0=3.524$ A. To make the orientation agree with that of all the diffraction patterns reproduced in this paper, this figure must be rotated by about 30° in a clockwise direction (or by about 60° in a counter-clockwise direction).

[9] In some experiments the crystal has not been cleaned by this simple treatment, and sometimes no successful cleaning treatment has been found. For these recalcitrant crystals, the cure has been the heroic procedure of removing the crystal and replacing it by another. It is hoped that a better method will be developed.

crystal has been heated to 975°C and allowed to cool. On three different occasions the crystal has been left in this condition, and the screen examined at 50 volts after a number of hours. In two of these tests no diffraction pattern could be seen after 16 hours and 18 hours, respectively. In the third test, after 65 hours a pattern was seen which corresponds, according to observations to be reported, to accumulated oxygen on the surface amounting to about one-tenth of a monolayer. In many other experiments the crystal was left with a small amount of gas, less than a monolayer, on its surface; in some cases no change was observed after many hours, and in other cases a change corresponding to some additional gas was seen, but with the total amount still less than a monolayer.

The observed pressures under which these tests were made were in some cases as low as 2×10^{-10} mm Hg. Even at such a pressure many monolayers could accumulate in 20 hours, and the observation that the accumulated surface gas was less than one-tenth of a monolayer must be interpreted to mean that the pressure was really lower than the gauge indicated, or the sticking probability of the residual gas no greater than 0.007.

Under these satisfactory vacuum conditions, the time required for the first diffraction features to appear after opening a Granville-Phillips valve to admit oxygen has been found to vary inversely with the measured oxygen pressure, without, however, a very strict inverse proportionality. Experiments have been carried out in the pressure range from 3×10^{-9} to 1×10^{-7} mm Hg. Failure to find accurate inverse proportionality with pressure can perhaps be attributed to the adsorption of oxygen on some parts of the apparatus which were not saturated before the experiments. In some of the best controlled experiments the pressure was almost unchanged for a long period of time at about 2×10^{-8} mm Hg. In these best tests the pressure-time product required for the first diffraction features to appear was about 4×10^{-6} mm Hg sec. The first observable features represent, as described later, about 0.1 monolayer. What we have interpreted as a complete monolayer is deposited on the surface, in times greater than those just indicated, by a factor larger than 10—at about 100×10^{-6} mm Hg sec.

These tests prove conclusively that the new diffraction patterns appearing after the Granville-Phillips valve is opened are produced by the gas admitted by this valve. Analyses of the oxygen furnished by AIRCO indicate impurities too low to have any significant effect.

In a later section it is reported that the first layer of adsorbed oxygen is not removed by heating at temperatures below about 880°C, but that much of the oxygen which can be adsorbed in thicker layers is removed at 350°C. We believe that these observations offer evidence that the first layer of oxygen is atomic, but layers on top of the first (unless they are combined to form NiO) are molecular.

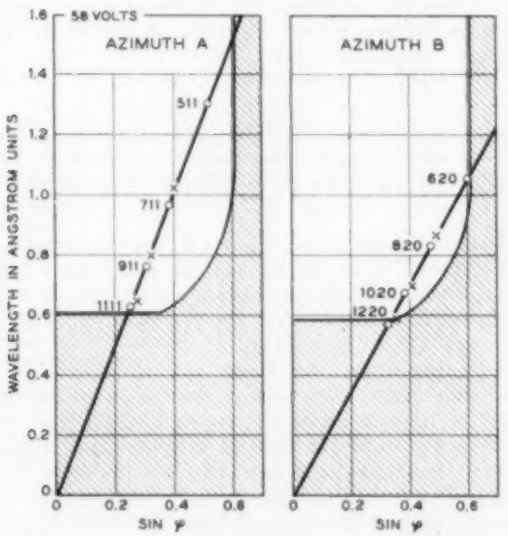

FIG. 3. Diffraction beams from the nickel crystal. Observed diffraction beams at maximum intensity are plotted as crosses. [Weak diffraction beams at potentials far from the values at which they reach their maximum intensities fall, of course, also on these lines. For example, the weak but sharp beams in the *B* azimuth in Fig. 1(a), and the weak but sharp beams in the *A* azimuth in Fig. 1(b)]. Calculated diffraction beams for zero inner potential are plotted as open circles. Within the error of the measurements the experimental points are brought into agreement with theory by an assumed inner potential of 16 volts.

THE FIRST MONOLAYER

This section describes experiments in which oxygen is admitted to a clean nickel surface, with observation and interpretation of the diffraction patterns which are found until the time when the surface is covered by a monolayer. A monolayer is considered to be completed when additional gas molecules are adsorbed on top of those already there, or at least in a plane farther removed from the nickel atoms than are those already on the surface. Diffraction from oxygen lying on top of the first monolayer will be taken up in a later section.

The Basic Two-Dimensional Unit Cell

The diffraction patterns which appear before a monolayer is completed can be related to a square two-dimensional unit cell parallel to the simple square cell of Fig. 2, but with twice the cell edge, $a=2^{\frac{1}{2}}\,a_0=4.98$ A (where $a_0=3.524$ A, the edge of the unit cell of fcc nickel). It is convenient to use this large two-dimensional cell to give two-dimensional Miller indices to the beams of the new diffraction patterns.

The calculated crystal spacings and azimuths of possible diffraction beams from this two-dimensional square array are written down in the first three columns of Table I. [Two of these beams, the (20) and (22), are produced by the nickel crystal. They are, respectively, the beams of the *A* and *B* azimuths represented by the

TABLE I. Diffraction beams from structure of Fig. 5(b). The four-structure.

Miller indices	Calculated Spacing in a.u.	Calculated Azimuth	Measured Spacing in a.u.	Measured Azimuth
10	4.98	*A*	5.20	*A*
11	3.52	*B*	3.36	*B*
20	2.49	*A*	2.46	*A*, from Ni lattice
21	2.24	26.5° to *A* azi	2.22	25.5° to *A* azi
22	1.76	*B*	1.76	*B*, from Ni lattice
30	1.66	*A*	1.67	*A*
31	1.58	18.5° to *A* azi	1.59	18.5° to *A* azi

straight lines of Fig. 3.] All of the diffraction beams of this list have been observed at an electron beam voltage of 200. Although 50-volt electrons at times offer a more sensitive way of detecting adsorbed gas, the diffraction pattern is more restricted at lower voltages. At 50 volts, for example, only the (10) and (11) reflections are within the limits of the fluorescent screen. For this reason, diffraction patterns for 200-volt electrons will be considered before taking up those obtained at 50 volts. Some examples of patterns at 50 volts from a monolayer of oxygen atoms, and less than a monolayer, will be reproduced in a later section. These patterns can now be dispensed with for the presentation given here, although many of them were essential in unraveling the results.

A diffraction pattern showing all of the possible reflections from the oxygen structure of the square array with cell edge 4.98 A is reproduced in Fig. 4, with the diffraction spots identified by their two-dimensional Miller indices. Data from a pattern similar to that of Fig. 4 are given in columns four and five of Table I. It is clear that oxygen giving rise to this pattern is arranged as shown in Fig. 5(b). This we have called the four-structure because four is the ratio of the number of surface nickel atoms to the number of oxygen atoms.

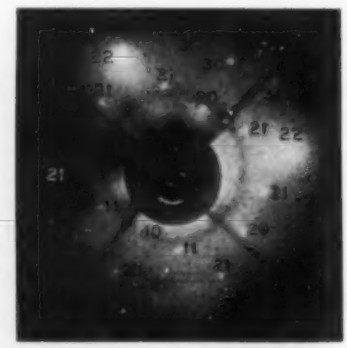

FIG. 4. Diffraction pattern at 200 volts from nickel crystal covered by half a monolayer of oxygen atoms. The arrangement of atoms is that of Fig. 5(b). All possible reflections are found from the square cell of edge 4.98 A (Table I). The diffraction spots are identified on the photograph by their two-dimensional Miller indices.

Arrangement of the Atoms

When oxygen is admitted to a clean crystal surface, the diffraction pattern of Fig. 4 is not the first pattern which is seen. It has been reproduced here first because the unit cell basic to other patterns is most simply shown by it. The diffraction features in the order of their appearance are described below.

Observing the diffraction pattern at 200 volts for an initially clean crystal surface when oxygen is admitted at a low controlled pressure, one sees first the clean crystal pattern of Fig. 6(a). This is identical with that of Fig. 1(b), except for longer exposure time giving stronger spots. Only the crystallographic notation has been changed.

Additional diffraction features can be seen first at an oxygen exposure of about 4×10^{-6} mm Hg sec. These first features are diffuse (30) reflections, and (21) reflections streaked out as shown in the photograph of Fig. 6(b). The (10) reflections are sometimes found, also, with some patterns appearing much sharper than Fig. 6(b), like the sketch of Fig. 6(c).[10] No trace can be seen of (11) or (31) reflections.

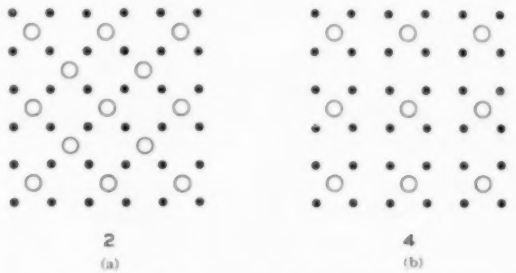

FIG. 5. Sketches of arrangements of adsorbed oxygen atoms on cube face of nickel. Solid dots are centers of nickel atoms in the surface layer, and open circles adsorbed oxygen atoms. (a) The two-structure, which is a full monolayer by our definition. (b) The four-structure, which is half a monolayer.

The patterns show a number of progressive changes with continued exposure to oxygen. These are influenced by the temperature of the crystal. The course of the changes is recorded in Table II, in column three for the crystal maintained at about 350°C, and in column four for the crystal never heated above room temperature. In the case of the warm crystal, the temperature is attained by electron bombardment, but the bombarding tungsten ribbon is turned off from time to time and the crystal allowed to cool in order to observe the diffraction pattern. The data of this table represent the results of 13 different series of tests, in each of which an attempt

[10] No photographs are available because of progressive tarnishing of the mirror in the experimental tube, which finally made photographing of patterns impossible.

was made to maintain the oxygen pressure constant. The highest pressure in any of these tests was 1×10^{-7} mm Hg, and the lowest about 3×10^{-9}. The values of the pressure-time product of column one are rough averages. The considerable observed variations from these averages may have been due to recording pressures different from those in the immediate neighborhood of the crystal, due to adsorption characteristics of the various tube parts.

Thinking first of the data of column three, one notes that for an exposure of about 30×10^{-6} mm sec, a crystal which has been heated from time to time gives all of the possible diffraction beams characteristic of what we call the four-structure. (Fig. 4 and Table I.) A crystal which has had this amount of oxygen exposure, but has not been heated during the exposure time, gives no clear diffraction pattern at all. Heating such an exposed crystal to 350°C results, however, after cooling, in a sharp pattern with all of the possible diffraction beams of the four-structure (see column four for 30×10^{-6} mm sec oxygen exposure). It is clear that oxygen corresponding to 30×10^{-6} mm sec exposure arranges itself on a warm crystal surface with the four-structure configuration, but on a cold surface it remains highly disorganized until the crystal has been heated.

When oxygen exposure has been increased to several times that necessary to give a diffraction pattern representing the four-structure, one observes a diffraction pattern made up of the (11) and (31) reflections only [paying no attention, of course to (20) and (22) reflections due to the underlying crystal which are always present]. Such a pattern is reproduced as Fig. 7. The structure corresponding to it, represented by the sketch of Fig. 5(a), has been named the two-structure from the ratio of the number of surface nickel atoms to the number of adsorbed oxygen atoms. In the case of the warm crystal, the development of the two-structure is made

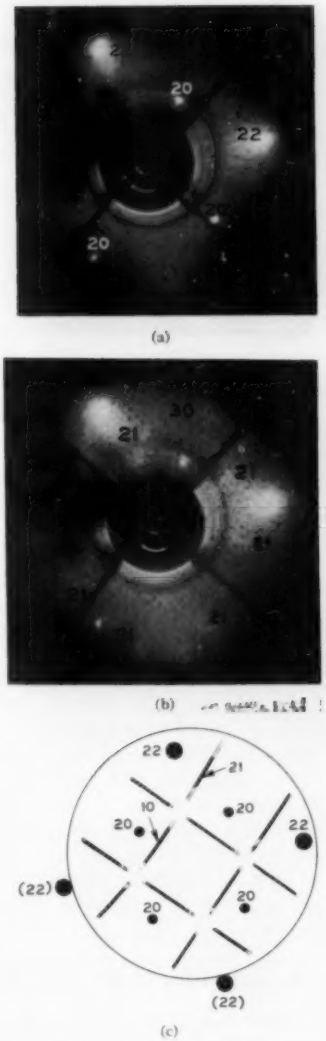

FIG. 6. Diffraction patterns at 200 volts representing the *beginning* of the deposition of oxygen on a (100) surface. (a) Pattern from the clean crystal, with diffraction spots identified by their two-dimensional Miller indices. (b) Pattern from crystal with 0.1 monolayer of oxygen atoms. (c) Sketch of some patterns from 0.1 monolayer, unfortunately not photographed.

TABLE II. Development of diffraction pattern with oxygen exposure.

(1) Oxygen pressure-time product in mm Hg sec	(2) Estimated fraction of a monolayer	(3) Crystal annealed frequently	(4) Crystal not heated
		[Figs. 6(b), 6(c), 8]	
4×10^{-6}	0.1	(21) streaked	(21) streaked
		(30) diffuse	(30) diffuse
20×10^{-6}	0.3	(21) sharp	unchanged
		(30) sharp	
30×10^{-6}	0.5	four-structure	No clear pattern,
		[Figs. 4, 5(a)]	but will give 4-
		(10) sharp	structure pat-
		(11) sharp	tern promptly
		(21) sharp	after slight
		(30) sharp	warming.
		(31) sharp	
100×10^{-6}	1.	two-structure	two-structure
		[Figs. 7, 5(b)]	
		(11) sharp	(11)
		(31) sharp	(31)

evident by the gradual weakening and final complete disappearance of the (10), (21), and (30), reflections. In the case of a crystal which has not been heated, one sees (11) and (31) reflections emerge from a very diffuse background.

The arrangement of oxygen atoms in the two-structure [Fig. 5(a)] is appropriately called a monolayer, and the arrangement in the four-structure Fig. [5(b)] half a monolayer.[11] The first diffraction pattern when

[11] The observed oxygen exposure of $pt=100\times10^{-6}$ mm sec required to complete a monolayer can be used to calculate mean sticking probability. On the assumption that each oxygen molecule striking the surface has the probability ϵ of dissociating into atoms with each of them then occupying one site of the two-structure, this yields $\epsilon=n(MT)^{\frac{1}{2}}/3.4\times10^{22}pt=0.01$ (M is molecular weight of oxygen, T its absolute temperature, and $n=4\times10^{14}$ the number of molecules of oxygen per square cm required for a two-structure

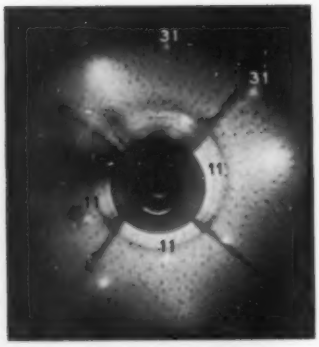

FIG. 7. Diffraction pattern at 200 volts from a *complete* monolayer of oxygen. The two-structure, Fig. 5(b).

oxygen is admitted to a clean surface appears at an oxygen exposure about one-fifth or one-tenth as great as that required to produce half a monolayer. This is the reason for stating, in column two of Table II, that the first diffraction pattern is observed at a coverage of 0.1 monolayer.

Various patterns of intermediate character have been observed from the warmed crystal. At an oxygen exposure three or four times that required to produce the first observable pattern, the (21) and (30) reflections become sharp, still without the appearance of (11) and (31) reflections. With further exposure these missing reflections, together with the (10), appear weakly. The (11), (31), and (10) reflections grow relatively stronger with continued oxygen exposure. When their strength seems equal to that of the (21) and (30), we consider that the four-structure is complete. More oxygen results in weakening of the (21) and (30), and also the (10), until these three reflections entirely disappear with completion of the two-structure. The interpretation of many of these intermediate patterns, as representing less than half a monolayer, or more than half a monolayer, is obvious.

Interpretation of the Early Diffraction Patterns

More thought is required for interpretation of the early diffraction patterns in which the (11) and (31) reflections are missing. A key to the interpretation of these early patterns is the fact that the (21) reflections are streaked. The direction of these streaks is not toward the center of the pattern, but rather apparently parallel to the edges of the square array of surface nickel atoms. The sense of the streaks can be described by saying that the four reflections of the type (12) are parallel to [10] lines of nickel atoms, and the four reflections of the type (21) are parallel to [01] lines of nickel atoms. This is as they are shown in the sketch of Fig. 6(c).

These streaks must arise from two different sets of bands of oxygen atoms parallel, respectively, to the two edges of the basic square. Most of the features of the diffraction pattern are accounted for by assuming atoms arranged in one of these bands as shown in Fig. 8. This is intended to represent atoms of oxygen on lines normal to the length of the band of atoms, with a constant spacing of $a=4.98$ A between lines. On each line atoms are placed at random, but always fitting in between four surface nickel atoms.

It is easy to see that this band of atoms, with atoms at random positions as just described, will give no reflections of the types (11) and (31). With the directions of axes as shown in Fig. 8, reflections (01) and (03) will appear, but not (10) and (30). The (21) reflection [and the equivalent $(\bar{2}1)$ reflection] will be present, represented by the inclined lines drawn in the figure, but there will be no (12) reflection [or the equivalent $(1\bar{2})$]. The reflections (21), $(\bar{2}1)$, $(\bar{2}\bar{1})$ and $(2\bar{1})$ will be drawn out into streaks parallel to the indicated x axis because of the narrowness of the atom band in this direction. This band of atoms, together with a symmetrical band at right angles to it, will give all of the reflections of the form {21} streaked as they are shown in Figs. 6(b) and 6(c).

From the dimensions of the (21) reflections, one readily works out values of the average length and width of a band of atoms. These can be calculated independently from observed dimensions of the diffuse (30) reflections. The values obtained in either way are about nine atom spacings for the lengths of the bands of atoms, and about three atom spacings for their widths.

There is one important feature of the diffraction patterns from approximately 0.1 monolayer of oxygen atoms which remains unaccounted for. This is the occasional, but not invariable, absence of the (10) reflections. One notes in Fig. 4 that this reflection can be

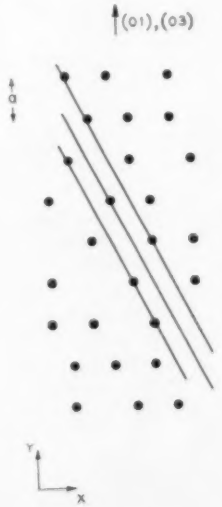

FIG. 8. Proposed arrangement of the first adsorbed oxygen atoms on cube face of nickel. The spacing a is 4.98 A, which is double the edge of the square array of surface nickel atoms.

made up of atoms). Schlier and Farnsworth[4] report an estimated sticking probability of oxygen on a (100) nickel face of 0.005, and oxygen exposure of 120×10^{-6} mm sec to give what they first thought to be a monolayer (the four-structure), later corrected to half a monolayer.[6]

found at only one location because of misalignment of the crystal, and it may there be obscured by a wire which supports the drift tube. Furthermore, the expected (10) reflections will be quite diffuse, with the same angular spreads which the (30) reflections have. These reasons seem to be not quite adequate to account for the fact that we do not always find a (10) reflection before the patches of atoms become sufficiently regular in both dimensions to produce also observable (11) and (31) reflections. This anomaly is not understood.

Other anomalies lack explanation also. One of these is the apparent lack of coherence between different bands of oxygen atoms. Since all of these are simply related to the nickel lattice, they are related to each other, and one might expect resolving power appropriate to total areas very much larger than those of individual bands of atoms. The evidence that different bands scatter incoherently has led to the suggestion (from Professor David P. Shoemaker of MIT) that these first oxygen atoms are adsorbed at disturbed portions of the surface where the surface nickel atoms are themselves not very regularly arranged. Another observation, which still lacks clear explanation, is the fact that good patterns from two-dimensional arrays of surface atoms appear at certain electron wavelengths only. This we are tempted to relate to steps on the surface of the crystal or to oxygen penetration. That steps alone cannot be an entirely adequate explanation is indicated by the fact that such steps do *not* result in sharp voltage discrimination for diffraction beams from the nickel lattice itself at the lowest voltages. The situation is still quite unclear in several particulars.

An intermediate pattern obtained from the annealed crystal at a coverage of about 0.3 monolayer still requires interpretation. In this pattern the (21) reflection is no longer streaked and the (30) reflection is no longer very diffuse, but the (11) and the (31) reflections have not yet appeared. It seems clear that to produce this type of diffraction pattern, the original bands of atoms must have increased considerably in size in both dimensions, but chiefly in width, without losing the peculiar type of randomness of atomic positions which divides the patches into distinct classes. When the crystal is not heated, this type of structure does not develop, presumably because, without the added atomic mobility, additional atoms produce new bands of atoms rather than adding themselves to increase the size of those already formed.

Summary

When a clean (100) face of a nickel crystal is exposed to oxygen, the first diffraction pattern is observed when the surface coverage is about 0.1 monolayer. This pattern corresponds to oxygen atoms arranged in bands lying parallel to the edges of the square array of surface nickel atoms, that is, parallel to [110] directions lying on the surface of the crystal. In one of these bands the atoms are arranged in lines normal to the band, with a separation (4.98 A) between lines equal to twice the separation of surface nickel atoms. In each line the atoms have random spacings of multiples of half this distance (2.49 A), with presumably a minimum spacing of 4.98 A. In a typical experiment the mean lengths and widths of these bands, calculated from the diffuseness of diffraction features, were respectively nine atom spacings and three atom spacings. This arrangement of adsorbed atoms is not altered by annealing at 300°C.

With oxygen exposure giving a coverage of about 0.3 monolayer, the arrangement of surface atoms in isolated narrow bands of atoms is about the same as it is for the smaller coverage unless the crystal is heated. Surface mobility conferred by heat causes bands of atoms to be consolidated into patches which are no longer particularly narrow, but in which the random character of the spacings in one dimension is still present. The patches of surface atoms are then still of two distinct types, although the observations do not suggest any difference between the length and breadth of a typical patch.

When the surface coverage is further increased to about half a monolayer, the arrangement of surface atoms becomes very chaotic if the crystal has not been heated. Heating to 200 or 300°C results in the very sharp diffraction patterns characteristic of the four-structure.

With still more oxygen added to the surface, the arrangement described as the two-structure is finally reached. In the case of a crystal which has not been heated, the reflections characteristic of this structure develop gradually from a very diffuse background. In the case of a warm crystal, one observes the gradual weakening, and final disappearance, of those reflections from the four-structure which are excluded by the centering atom in the two-structure. There is some slight evidence that the sticking probability is higher until the time when the surface is half covered than it is while the centering atom is being adsorbed to change the four-structure into the two-structure.

MORE THAN A MONOLAYER

Deposition of Multilayers of Oxygen

After the first monolayer of oxygen atoms is completed at an oxygen exposure of the order of 100×10^{-6} mm sec, more oxygen produces no observed change in the diffraction pattern until the total exposure has been doubled, an observed exposure of 225×10^{-6} mm sec. At this time, diffuse new diffraction spots can be seen without any detected change of patterns from the nickel crystal or from the two-structure of oxygen atoms, even at 50 volts. When the oxygen exposure has reached 300×10^{-6} mm sec, the patterns from the two-structure and the nickel lattice are observably weaker without decrease in sharpness. By the time the exposure has reached 400×10^{-6} mm sec, patterns from the two-structure can no longer be seen at 50 volts, although

TABLE III. More than a monolayer of oxygen.

Oxygen pressure-time product in mm Hg sec	Observed patterns from Ni crystal	Observed patterns from two-structure	New diffuse pattern
100×10^{-6}	Sharp, strong at all appropriate voltages	Sharp, strong at all appropriate voltages	None
225×10^{-6}	Sharp, strong at all appropriate voltages	Sharp, strong at all appropriate voltages	Just detected
300×10^{-6}	Sharp, but less strong at all appropriate voltages	Sharp, but less strong at all appropriate voltages	Weak
400×10^{-6}	Patterns weak but sharp	No pattern at 50 volts. Weak at higher voltages but still sharp	Stronger
600×10^{-6}	No pattern at any voltage	No pattern at any voltage	Strong

two-structure patterns and patterns from the nickel lattice are observed weakly at higher voltages. With exposure of 600×10^{-6} mm sec no trace can be seen of any patterns arising from the two-structure, nor can Laue beams from the nickel be found at any voltages up to 500. The new diffuse diffraction spots, which obviously come from oxygen lying on top of the first monolayer, have become progressively stronger, while the patterns from the two-structure and the nickel lattice were growing weaker. These observations are summarized in Table III, which can be thought of as an extension of Table II.

The three diffraction patterns of Fig. 9 for 50 volt electrons illustrate the development, with increasing oxygen exposure, of the four-structure [Fig. 9(a)] into the two-structure with a superincumbent layer of oxygen or oxide [Fig. 9(c)]. These patterns illustrate also the effect of annealing in producing sharper diffraction patterns.[12]

The first of these patterns was obtained from an annealed crystal after an oxygen exposure of 50×10^{-6} mm sec. It shows (10) and (11) reflections corresponding to the four-structure; this structure would not have developed without anneal (see Table II). The second pattern [Fig. 9(b)], after an oxygen exposure of 200×10^{-6} mm sec, shows only the (11) reflections, characteristic of the two-structure. The diffuseness of the diffraction spots is due to the fact that the crystal was not annealed after its original cleaning. The final pattern [Fig. 9(c)], showing the (11) reflections of the two-structure and a new diffraction spot from superposed NiO, was obtained after a very heavy oxygen exposure and a subsequent high temperature anneal at 700°C. The effect of this anneal was to cause the reappearance of the initially completely obscured two-structure pattern, and to sharpen very greatly the diffraction spot in the *A* azimuth, which can now be identified as probably due to NiO.

Patterns obtained after 600×10^{-6} mm sec of oxygen exposure are reproduced in Fig. 10. These very diffuse patterns appear in the principal azimuths of the crystal,

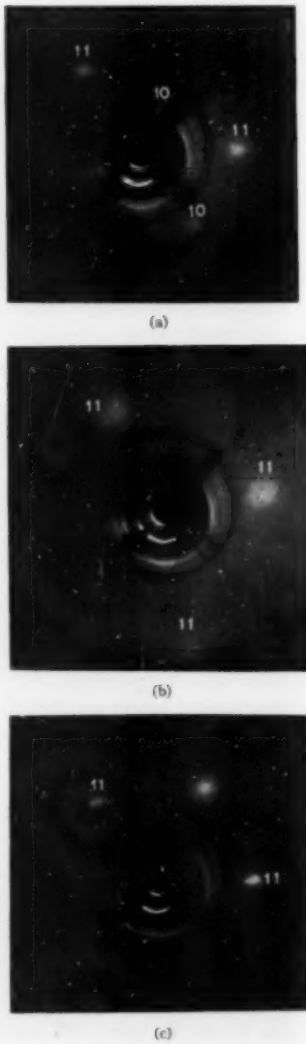

FIG. 9. Diffraction patterns at 50 volts for progressively higher oxygen exposures. (a) Showing (10) and (11) reflections representing the four-structure, from a crystal annealed at 350°C after oxygen exposure of about 50×10^{-6} mm sec. (b) Showing only (11) reflections representing the two-structure, from a crystal after oxygen exposure of 200×10^{-6} mm sec. The diffuseness of the pattern is evidence that the crystal was *not* annealed. (c) Showing (11) reflections representing the two-structure, with an additional rather sharp diffraction beam in the *A* azimuth attributed to NiO. The crystal had been annealed at 700°C after oxygen exposure of 600×10^{-6} mm sec; before anneal there was only the *A* azimuth beam, which was very diffuse [like Fig. 10(a)].

[12] In the patterns of Fig. 9 the unsymmetrical adjustment of the crystal is more serious than at higher voltages, but the reflections can nevertheless be readily identified. The two most prominent spots, appearing in all three photographs at 11 o'clock and 3 o'clock, are (11) reflections in the *B* azimuth—the other two reflections to complete the pattern of fourfold symmetry are off the screen at the lower left. In addition to these two spots, the photograph of Fig. 9(a) shows two (10) reflections very close to the center at 1 o'clock, and farther out at 5 o'clock. In Fig. 9(c) appears a new diffraction spot in the *A* azimuth at 1 o'clock.

but only at voltages in the neighborhood of 48, 85, and 135. The diffuse beams at 48 volts are in the *A* azimuth, those at 135 volts in the *B* azimuth, and those at 85 volts in both azimuths.

Removal by Heat

No detectable change in these patterns is produced by pumping out the oxygen and maintaining the crystal for long periods of time in very high vacuum. Warming the crystal to temperatures below 300°C causes very little gas evolution and not very much change of the patterns, but perhaps some slight increase in sharpness attributable to some crystal growth.

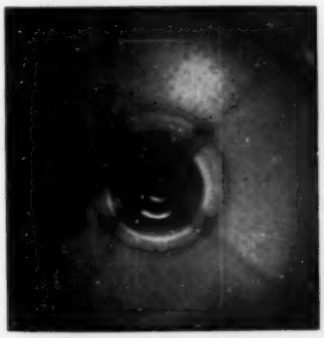

(a)

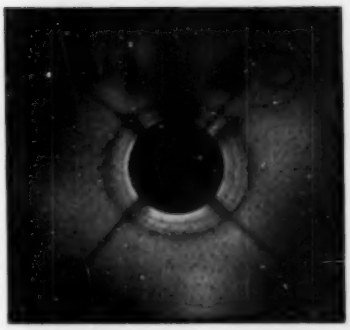

(b)

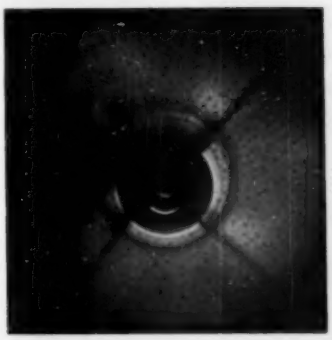

(c)

FIG. 10. Patterns obtained after oxygen exposure of 600 $\times 10^{-6}$ mm sec, and subsequent anneal at 275°C. (a) 48 volts, showing diffraction beams in the *A* azimuth at maximum intensity. (b) 135 volts, showing beams in the *B* azimuth at at maximum intensity. (c) 84 volts, showing beams in both azimuths.

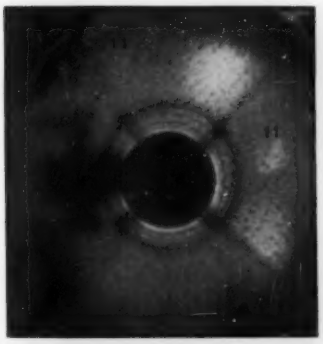

(a)

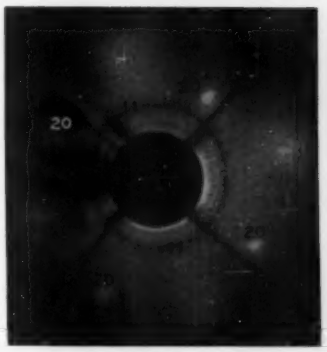

(b)

FIG. 11. Patterns after anneal at 350°C. (a) 48 volts. The *A* azimuth diffraction beams of Fig. 10(a) are now much less diffuse. The (11) reflections of the two-structure now appear also. (b) 135 volts. The *B* azimuth beams of Fig. 10(b) are now less diffuse. Also shows the (20) reflections from the nickel lattice and (11) reflections from the two-structure.

A marked change of the diffraction patterns is observed after heating to 350°C; this change is accompanied by considerable gas evolution. After such heating the beams at 85 volts are no longer found, but the beams at 48 volts in the *A* azimuth, and at 135 volts in the *B* azimuth are sharpened. Patterns can now be seen also from the underlying two-structure and the nickel crystal. Such patterns from crystals which have had a few seconds anneal at 350°C are reproduced in Fig. 11. The patterns of Figs. 10(a) and 11(a) were obtained at 48 volts, before and after, respectively, anneal at 350°C, and the patterns of 10(b) and 11(b) at 135 volts before and after anneal.

Further increase in sharpness of the new and originally diffuse diffraction spots is produced by anneal at still higher temperatures. Examples of this further gain in sharpness are shown in Figs. 9(c) and 12, which were obtained after anneal at 700°C. Figs. 10(a), 11(a), and 9(c) represent a sequence at 48 volts after anneal treatment at 275°C, 350°C, and 700°C, respectively. A corresponding sequence at 135 volts after these same heat treatments is shown in Figs. 10(b), 11(b), and 12(b).

Observations upon these diffraction patterns are collected in Table IV, together with calculated data for a crystal of NiO with its axes arranged parallel to those of the nickel crystal. One sees that the two sets of

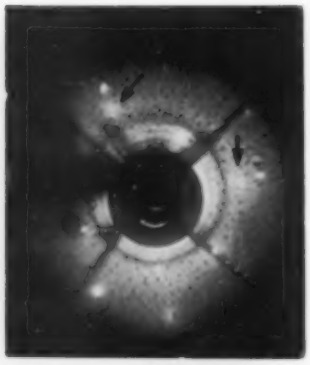

(a)

(b)

FIG. 12. Patterns after anneal at 700°C, oxide beams still more sharp. (a) 220 volts. *B* azimuth beams attributed to NiO. Also (22) beams from the nickel lattice, and (11) and (31) beams of the two-structure. (b) 135 volts. Like Fig. 11(b), but still less diffuse.

diffraction beams obtained after anneal at 350°C (columns five, six and seven) agree quite well with the lowest voltage set of beams calculated for NiO in the *A* azimuth, and the lowest voltage set in the *B* azimuth. The voltages at which the beams are strongest (48 and 135) correspond to the calculated voltages of 63 and 156, with indicated inner potentials of 15 and 21 volts, respectively. The surface grating spacing of the *B* azimuth beam calculated from the positions of the beams is 2.10 A, agreeing very well with that of NiO, 2.09 A. The *A* azimuth beam corresponds, as well as we can measure it, to 3.45 A, which differs from the NiO spacing of 2.95 A by 17 percent. This seems more than the probable error of the measurement which, however, is very large.

A tentative explanation for this large discrepancy is that the surface of the NiO is different from its bulk in some unknown way, and this difference shows up only in the 48 volt diffraction beam because electrons of this voltage penetrate so slightly. Perhaps there is a single layer of oxygen molecules on the oxide surface. Such an explanation gets support from the fact that the 350° anneal promptly causes a large evolution of gas not quickly evolved at 300°C, and after this gas removal the layers of foreign material on the crystal surface are more transparent to electrons and therefore thinner. The 350°C anneal has two effects: it removes gas adsorbed on top of the oxide, and it causes crystal growth in the oxide so that the patterns arising from it are sharper. The two original sets of diffraction beams at 84 volts correspond to a spacing of 3.20 A in the *A* azimuth, and to 2.67 A in the *B* azimuth. We assume that these have their origin in this gas layer, but we have had no success in finding a possible structure for the layer.

It seems to be quite possible that the anneal at 350°C causes sufficient growth of crystals to leave much of the nickel surface clean. The composite patterns of Fig. 11 are then due to NiO crystals' lying upon the nickel crystal, but not covering it completely. (The nickel surface is, however, covered everywhere by a firmly

TABLE IV. Patterns from thick layers.

NiO		Observed diffraction beams						
Miller indices	Calculated voltage	After 275°C anneal		After 350°C anneal			After 700°C anneal	
		Voltage	Spacing (*A*)	Voltage	Spacing (*A*)	Inner potential (volts)	Voltage	Inner potential (volts)
(1)	(2)	(3)	(4)	(5)	(6)	(7)	(8)	(9)
				A azimuth				
	(2.95 A)							
5 1 1	63	48		48	3.45	15	48	15
		84	3.20					
7 1 1	114							
9 1 1	183						(166)	
11 1 1	269						(237)	
13 1 1	372						(330)	
				B Azimuth				
	(2.09 A)							
		84	2.67					
8 2 0	156	135		135	2.10	21	135	21
							(175)	
10 2 0	233						220	13
12 2 0	328						315	13

held single layer of oxygen atoms in the two-structure.) There are two reasons for believing that this agglomeration of NiO into relatively large crystals is not the entire effect of the anneal treatment. These reasons are the considerable evolution of gas at 350°C, and the accompanying disappearance of the two sets of 84 volt diffraction beams, which presumably had their origin in this gas.

Although some further changes are brought about by anneal at 700°C, the beams at 48 and 135 volts still persist, and are the strongest features which can be seen in addition to those of the nickel crystal and of the two-structure. These features are further sharpened by this anneal, which is shown in Figs. 9(c) and 12(b). New diffraction beams appear also in the *B* azimuth at 220 volts [Fig. 12(a)] and at 315 volts. Both of these agree well with calculated diffraction beams from NiO, as indicated in Table IV, columns one, two, eight and nine. There are, however, other weak beams at 166, 237, and 330 volts in the *A* azimuth, and at 175 volts in the *B* azimuth, which do not fit the pattern calculated for NiO. These beams, indicated in parentheses in column eight of Table III, have not been found in all experiments. Their origin is unknown.

The NiO is promptly and completely removed at 830°C leaving, however, the monolayer of oxygen (two-structure) unchanged on the surface. Part of this last layer is removed at 860°C, and all of it is sometimes removed at 880°C. The temperature commonly used to clean the surface in these experiments has been about 100 degrees above this, 975°C. This is effective in cleaning the surface quite quickly. It seems probable that the lower temperature of 880°C would also clean the surface completely if the crystal were maintained at this temperature for a considerable time. These observations are collected in Table V.

TABLE V. Removal of oxygen by heat (after initial exposure of 600×10^{-6} mm sec or more).

Temperature (C°)	Gas evaluation	Observed change	Diffraction pattern
300	Only slight		NiO pattern, uninterpreted diffraction beams from physisorbed molecular oxygen
350	Considerable	First appearance of patterns from two-structure and from Ni crystal	NiO pattern, two-structur pattern, Ni Laue beams
700		NiO pattern somewhat sharper	NiO pattern sharper, otherwise unchanged
830		NiO removed	Two-structure pattern, Ni Laue beams
860		Part of first layer removed	Ni Laue beams, four-structure pattern from some areas, two-structure pattern also
880		More of first layer removed	Ni Laue beams, patterns sometimes seen from small fraction of a monolayer
975		First layer entirely removed	Ni Laue beams only

ACKNOWLEDGMENTS

A number of people have taken an interest in these experiments, and we have profited greatly by discussions with them. Those who have been most helpful have been Drs. P. Kisliuk, R. D. Heidenreich, H. D. Hagstrum, E. A. Wood, and S. Geller.

Potential Distributions in a Low-Pressure Thermionic Converter

PETER L. AUER
General Electric Research Laboratory, Schenectady, New York
(Received August 2, 1960)

A plane diode model of a low-pressure cesium-filled thermionic converter is treated. It is assumed that all ions and electrons are created at the surface of the hot cathode with a Maxwellian distribution corresponding to the cathode temperature. The charged species are then assumed to move through the plasma, consisting of electrons, ions, and neutral cesium atoms, as free particles under the influence of their mutual space charge field. A method is outlined by which the potential distributions corresponding to different operating conditions may be calculated completely. In this fashion the operating characteristics of the converter may be related to the self-consistent space charge potentials. Instabilities as possible sources of tube oscillations are briefly discussed.

I. INTRODUCTION

IN order to discuss the operating characteristics of low pressure cesium-filled thermionic converters, a simple model amenable to rigorous analysis is chosen. This model consists of a plane diode containing a hot cathode which acts as an emitter, and a cold anode which serves as the collector. The intervening space is filled with cesium gas which, on contact with the hot cathode, becomes partially ionized, furnishing a plasma consisting of neutral cesium, cesium ions, and electrons. It will be assumed that all ions and electrons are born at the hot cathode, their rates of production being given by quasi-thermodynamic arguments. The ions and electrons are treated as free particles moving under the influence of their mutually generated space charge field. All collisional interactions between the charged species themselves, and between charged species and neutrals, are neglected. These assumptions allow for the exact calculation of the self-consistent space charge potential by a method to be sketched in some detail.

It follows readily from the above description that the model under consideration is best suited to describe converters in which the electrode spacing is small compared to a collision mean free path. In this respect the model is diametrically opposite to the plasma thermocouple description of a thermionic converter.[1] The latter approach is conventionally justified by transport theoretic arguments wherein it is assumed that departure from local thermodynamic equilibrium is small. Linear relations between local temperature gradients and potential differences then may be obtained. The requirement that particle probability distributions depart but slightly from the Maxwell-Boltzmann distribution, however, in turn demands that characteristic dimensions be large compared to the square root of the cesium atom to electron mass ratio—a number here taken to be 500.

Since the large majority of present day converter experiments operate under conditions more favorable to the no-collision approximation, this model will be taken as the starting point. Before embarking on a detailed description of the theoretical analysis, a brief review will be given of potential sheath distributions expected to develop in thermodynamic equilibrium. A more complete discussion of this subject will be found in Langmuir's original treatment.[2] In view of the fact that results of thermodynamic analyses are independent of the details of microscopic mechanisms, the following section bears some import for any converter model.

II. EQUILIBRIUM THEORY

Thermodynamic equilibrium may be visualized as follows. A container with metal walls of given work function and containing cesium is placed in a thermal bath. The cesium plays two roles, in that it reacts actively with the metal walls to furnish a surface with a work function which may differ from the inherent work function of the metal,[3,4] while it also produces a plasma gas in container by thermal ionization. In regions sufficiently removed from the metal walls, the plasma will be neutral; in the vicinity of the walls, however, a potential sheath will develop. This is due to the fact that the chemical potential, or Fermi level, of a free electron must be the same everywhere in thermodynamic equilibrium. The neutral density, of course, is constant throughout space and the local relation between electrons and ions is specified by the Saha equation. This relation furnishes a description of the potential sheath in terms of equilibrium quantities.

The following notation will be used. Boltzmann's constant times temperature, denoted θ, is measured in electron volts. In terms of the thermal wavelength

$$\Lambda = h/(2\pi m\theta)^{\frac{1}{2}}, \tag{1}$$

the basic unit of density becomes

$$2\Lambda^{-3} = 6.25\times 10^{21}\times\theta^{\frac{3}{2}}\ \text{cm}^{-3}. \tag{2}$$

The local density of electrons, ions, and neutrals may be

[1] H. W. Lewis and J. R. Reitz, J. Appl. Phys. **30**, 1439 (1959); **30**, 1838 (1959); **31**, 723 (1960).

[2] I. Langmuir, Phys. Rev. **43**, 224 (1933).
[3] J. B. Taylor and I. Langmuir, Phys. Rev. **44**, 423 (1933).
[4] I. Langmuir and K. H. Kingdon, Science **57**, 58 (1923).

written in the form

$$N_e(x)=2\Lambda^{-3}\exp(-E_g/\theta)\exp[e(V(x)-V_p)/\theta]$$
$$N_i(x)=2\Lambda^{-3}\exp(-E_g/\theta)\exp[-e(V(x)-V_p)/\theta] \quad (3)$$
$$N_a(x)=P_t/\theta-4\Lambda^{-3}\exp(-E_g/\theta)=\text{const},$$

where x measures distance from the wall in cm, E_g is the chemical potential of free electron in electron volts in the bulk gas, $V(x)$ is the local potential in volts, and V_p is the constant neutral plasma value of the potential in the bulk gas, with e the electronic charge; the total pressure of the gas is denoted P_t. If p_μ is the total vapor pressure measured in microns (10^{-3} mm) of mercury, the units of P_t become

$$P_t/\theta=8.40\times10^{11}(p_\mu/\theta)\ \text{cm}^{-3}. \quad (4)$$

The chemical potential E_g may be obtained by substituting the expressions of Eq. (3) into the Saha equation:

$$\frac{N_e(x)N_i(x)}{N_a}=\frac{\omega_e\omega_i}{\omega_a}\Lambda^{-3}\exp(-E_i/\theta)$$
$$\frac{\omega_e\omega_i}{\omega_a}\approx1, \quad (5)$$

where the ω denote statistical weights and the ratio is taken as unity for cesium at temperatures of interest to converter experiments. The ionization potential of cesium, E_i, is taken to be 3.89 ev. The final expression becomes

$$E_g=E_i-\theta\ln\tfrac{1}{2}\{[1+2.68\times10^{-10}p_\mu\theta^{-\frac{5}{2}}\exp(E_i/\theta)]^{\frac{1}{2}}-1\}. \quad (6)$$

From the value of E_g and the effective work function of the metal wall, it is possible to determine the nature of the potential sheath at the metal to gas interface. If W is the work function in electron volts, the electron density at the wall surface becomes

$$N_e(0)=2\Lambda^{-3}\exp(-W/\theta), \quad (7)$$

and by comparison with Eq. (3)

$$e[V_p-V(0)]=W-E_g, \quad (8)$$

TABLE I. Debye length in microns, and chemical potential in electron volts, for several temperature and cesium pressure values.

$\frac{L_D}{E_g}$ / kT in ev	$p=0.1\ \mu$	$p=1.0\ \mu$	$p=10\ \mu$
0.10	*188*	*166*	*91.2*
	2.95	2.84	2.72
0.20	*3.38*	*2.68*	*0.99*
	4.39	4.01	3.70
0.25	*6.86*	*2.14*	*0.69*
	5.62	5.04	4.47

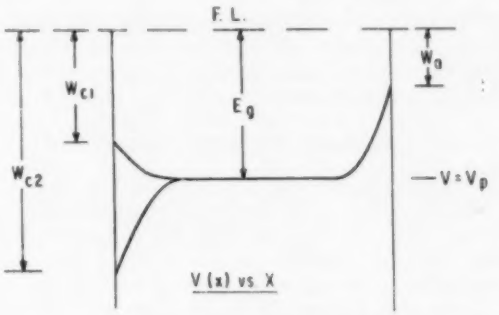

FIG. 1. Potential sheath distributions at thermodynamic equilibrium.

where $V(0)$ is the potential at the surface. Thus, the potential sheath is ion rich if W is greater than E_g, and electron rich if W is less than E_g. It may be noted that in general E_i does not determine the equilibrium sheath structure, since the entropylike logarithmic term in Eq. (6) always plays a comparable role.

The sheath potential distribution is readily obtained from Poisson's equation. Integration leads to a statement of stress balance:

$$N_a+N_e(x)+N_i(x)-[V'(x)]^2/8\pi\theta=P_t/\theta$$
$$[V'(x)]^2=32\pi\theta\Lambda^{-3}\exp(-E_g/\theta)\times\{\cosh[e(V_p-V(x))/\theta]-1\}, \quad (9)$$

where the prime denotes differentiation with respect to argument. Further integration yields the potential distribution in the form

$$\tanh[e|V_p-V(x)|/4\theta]=\exp(-x/L_D)\tanh[e|V_p-V(0)|/4\theta], \quad (10)$$

where the Debye length, L_D,

$$L_D^2=\theta\exp(E_g/\theta)/16\pi e^2\Lambda^{-3}$$
$$L_D=6.36\times10^{-9}\theta^{-\frac{1}{2}}\exp(E_g/2\theta)\ \text{cm}, \quad (11)$$

is the characteristic distance of the sheath.

It may be noted that the Debye length does not have monotone variation with temperature. Starting from low temperatures, the Debye length decreases with increasing temperature as the fractional degree of ionization increases. Once the fractional ionization approaches unity, continued increase in temperature will then increase the Debye length linearly at constant pressure. Thermionic converters may often operate at the vicinity of the minimum point, where a shift in temperature in one direction may cause a change in the Debye length in the same or opposite direction.

Table I contains both the Debye length in microns as the first entry (italics), and the chemical potential in electron volts as the second entry, for three different pressure and temperature values. A schematic representation of sheath structure is depicted in Fig. 1 where, for the sake of illustration, the work function of the

metal wall on the left is chosen to have two possible values, one greater and one less than the bulk gas chemical potential, while the work function of the metal wall on the right is chosen to be less than either of these.

III. NONEQUILIBRIUM MODEL

Conceptually, the transition from the previously described equilibrium situation to the nonequilibrium one is straightforward. It is only necessary to keep the high work function metal on the left of Fig. 1 hot, while cooling the low work function metal on the right until all emission from it ceases. The electrical circuit consisting of hot cathode and cold anode may be completed by connecting the two through a resistanceless external conductor. This guarantees that the Fermi level remains the same at both electrodes and produces a converter operating at short circuit. It may be asked how these steps affect the equilibrium value of the potential distribution.

In order to answer this question, it is first necessary to determine the rate at which ions and electrons are supplied to the tube. Since collision processes in the bulk gas are to be neglected, all ions and electrons are assumed to be born at the surface of the hot cathode. The electron emission flux at the cathode is given by the Richardson equation

$$J_e^+(0)=\Lambda^{-3}\exp(-W_c/\theta)\mu_e$$
$$u_e^2=2\theta/\pi m, \tag{12}$$

where the plus sign denotes forward direction, and m is the electronic mass. By comparison of Eqs. (12) and (7) it will be noted that the electron density due to the forward emission flux is one half of the equilibrium value.

The ion forward emission rate may be obtained by the following quasi-equilibrium arguments. In general, the forward and reverse flux of ions and neutral atoms at the surface of the cathode can be related through the "reaction matrix"

$$J_i^+=(1-A)J_i^-+BJ_a^-$$
$$J_a^+=AJ_i^-+(1-B)J_a^-, \tag{13}$$

where the minus sign refers to the incoming, reverse flux. Since in equilibrium the forward and reverse flux of any given species must be equal, the rate parameters must satisfy the relation

$$A/B=[J_a^-/J_i^-]_{eq}=[J_a^+/J_i^+]_{eq}=\left[\frac{N_a}{N_i(0)}\right]_{eq}, \tag{14}$$

and the last identity above follows from the assumption that ions and atoms are of the same mass. The arbitrariness of A and B can be removed by making a "strong binding" approximation. In this it is assumed that the probability of formation of an outgoing ion from the metal surface does not depend on whether the incoming species was an ion or neutral atom; consequently,

$$J_i^+/J_a^+=[J_i^+/J_a^+]_{eq}. \tag{15}$$

In general, Eqs. (14) and (15) allow nontrivial solutions of Eq. (13), providing

$$1=A+B. \tag{16}$$

The above constitute a completely determined set of relations. In particular, the forward ion flux may be related to the incoming neutral flux

$$J_i^+/J_a^-=\frac{B}{1-Bf}$$
$$B=\left(\frac{N_i(0)}{N_i(0)+N_a}\right)_{eq}$$
$$=\{1+2\exp[-(W_c-E_i)/\theta]\}^{-1} \tag{17}$$
$$f=\begin{cases}1-\exp(-eV_{max}/\theta); & V\geq 0\\ 0; & V<0,\end{cases}$$

where f measures the fraction of the forward flux reflected by a positive potential barrier of magnitude V_{max} with respect to the surface potential at the cathode. If it is further assumed that the neutral gas is in thermal equilibrium with the hot cathode, and pressure balance exists in the converter, the neutral flux J_a^- may be specified in terms of the cesium vapor pressure at some known point

$$J_a^-=P_a/(2\pi M\theta)^{\frac{1}{2}}, \tag{18}$$

where P_a is the neutral pressure at the cathode, θ corresponds to the cathode temperature, and M is the cesium mass.

A parameter α, which will be useful in subsequent discussions, can be defined in terms of the forward ion emission flux

$$J_i^+(0)=\alpha\Lambda^{-3}\exp(-W_c/\theta)(2\theta/\pi M_a)^{\frac{1}{2}}$$
$$\alpha=\left(\frac{B}{1-Bf}\right)\left(\frac{\Lambda^3P_a}{2\theta}\right)\exp(W_c/\theta), \tag{19}$$

where use has been made of Eq. (17). It will be noted that α measures the ratio of ion to electron density due to their respective forward emission fluxes. At equilibrium

$$\alpha_{eq}=[\exp 2(W_c-E_g)/\theta], \tag{20}$$

it may be verified by explicit calculation that if P_t is substituted for P_a, and f is set equal to unity, Eq. (19) yields the same result. This illustrates the fact that at low fractional ionization, large retarding potentials for ions produce ion distributions in the vicinity of the cathode which closely resemble the situation at equilibrium.

The required nonequilibrium potential distributions may be obtained once the local density of ions and

electrons are known. These may be obtained, in turn, from the probability distribution functions which satisfy the Vlasov equation

$$\begin{aligned} u\frac{\partial f_e}{\partial x}+\frac{e}{m}V'(x)\frac{\partial f_e}{\partial u}&=0\\ u\frac{\partial f_i}{\partial x}-\frac{e}{M}V'(x)\frac{\partial f_i}{\partial u}&=0\\ V''(x)=4\pi e\int_{-\infty}^{\infty}(f_e-f_i)du.& \end{aligned} \tag{21}$$

Solutions are obtained in the form

$$\begin{aligned} f_e&=f_e[\tfrac{1}{2}mu^2-eV(x)]\\ f_i&=f_i[\tfrac{1}{2}Mu^2+eV(x)], \end{aligned} \tag{22}$$

and are subject to boundary conditions at the cathode

$$f_e(0,u)=J_e^+(0)\left(\frac{m}{\theta}\right)\exp(-mu^2/2\theta);\quad 0\leqslant u\leqslant\infty$$

$$f_i(0,u)=J_i^+(0)\left(\frac{M}{\theta}\right)\exp(-mu^2/2\theta);\quad 0\leqslant u\leqslant\infty \tag{23}$$

$$V(0)=0.$$

Equation (23) describes only the outgoing part of the distribution and conforms to the assumption that both ions and electrons issue with a Maxwellian velocity distribution corresponding to the cathode temperature. The complete distribution, in general, will differ considerably from the equilibrium Maxwell-Boltzmann distribution on account of the presence of accelerating and retarding fields in the plasma. References to more complete discussion of this matter may be found elsewhere.[5] The distributions are always normalized so that the net flux of a given species is constant throughout the tube.

IV. POTENTIAL DISTRIBUTIONS

It will be convenient to introduce the following reduced potentials, densities, and distances:

$$\begin{aligned} \eta(\xi)&=eV(\xi)/\theta\\ n_e(\xi)&=N_e(\xi)\Lambda^3\exp(W_c/\theta)\\ \alpha n_i(\xi)&=N_i(\xi)\Lambda^3\exp(W_c/\theta)\\ \xi&=x/L_c, \end{aligned} \tag{24}$$

where the characteristic length L_c is of the form

$$\begin{aligned} L_c^2&=(\theta\Lambda^3/8\pi e^2)\exp(W_c/\theta)\\ &=2(\alpha_{eq})^{\frac{1}{2}}L_D^2, \end{aligned} \tag{25}$$

and use has been made of Eqs. (11) and (20).

[5] H. Poritsky, IRE Trans. PGED **1**, 60 (1953).

With these definitions Poisson's equation takes the form

$$\eta''(\xi)=\tfrac{1}{2}[n_e(\eta)-\alpha n_i(\eta)]. \tag{26}$$

In the foregoing, note has been taken of the fact that the form of the velocity distributions previously described assure that the reduced densities are explicit functions of the reduced potential. It is convenient to introduce a quantity $F(\eta)$ which is a measure of the magnitude of the local electric field

$$F(\eta)=[\eta'(\xi)]^2. \tag{27}$$

The Poisson equation may now be rewritten in the form

$$F'(\eta)=n_e(\eta)-\alpha n_i(\eta), \tag{28}$$

and the potential distribution follows from

$$\begin{aligned} \xi&=\int_0^{\eta}d\eta_0/[F(\eta_0)]^{\frac{1}{2}}\\ \xi_a&=L/L_c=\int_0^{\eta_a}d\eta/[F(\eta)]^{\frac{1}{2}}, \end{aligned} \tag{29}$$

where L is the distance of separation between cathode and anode and η_a is the anode potential with respect to the cathode.

Analytic representations are readily obtained for $F(\eta)$, reducing the problem of computing actual potential distributions to numerical quadrature. In general, $F(\eta)$ is a multivalued function of η and the integration of Eq. (29) proceeds sectionally. The numerical evaluation of potential distributions will not be given at this time; however, qualitative aspects of three classes of potential distributions of interest to converter experiments will be discussed in what follows. It will be shown that a number of inferences concerning operating characteristics may be drawn from such an analysis.

A. Class One Distributions

Class one distributions contain all monotone distributions with an ion-rich cathode sheath, as well as distributions in which the entire tube is ion rich. Examples of both cases are depicted schematically in curves 1 and 2 of Fig. 2. In the event the distributions are monotone, as in curve 1, it may be shown that

$$\begin{aligned} n_e(\eta)&=[1-E(\eta)]\exp(\eta)\\ n_i(\eta)&=[1+E(\eta_a-\eta)]\exp(-\eta)\\ E(\eta)&=2/(\pi)^{\frac{1}{2}}\int_0^{(\eta)^{\frac{1}{2}}}\exp(-l^2)dl, \end{aligned} \tag{30}$$

where the above reflects the fact that electrons are accelerated away from the cathode, while ions are reflected back by the potential maximum η_a at the

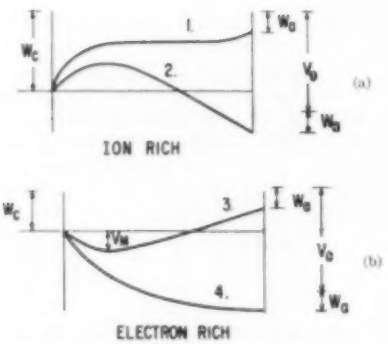

FIG. 2. (a) Class one ion-rich potential distributions; (b) Class two electron-rich potential distributions.

anode. The actual distribution follows from

$$\begin{aligned} F(\eta) &= F(0)+G(\eta) \\ &\quad -\alpha \exp(-\eta_a)[H(\eta_a)-H(\eta_a-\eta)] \\ G(\eta) &= \exp(\eta)[1-E(\eta)]+2(\eta/\pi)^{\frac{1}{2}}-1 \\ H(\eta) &= \exp(\eta)[1+E(\eta)]-2(\eta/\pi)^{\frac{1}{2}}-1. \end{aligned} \tag{31}$$

The magnitude of the field at the cathode as given by $F(0)$ is a function of α and the tube width ξ_a. From the above, the ion to electron density ratio at the cathode becomes

$$N_i(0)/N_e(0)=\alpha[1+E(\eta_a)]\geq 1, \tag{32}$$

where the inequality arises from the requirement that the cathode be ion rich. Since the asymptotic value of $E(\eta)$ is unity for large argument, this in turn requires that α be at least greater than $\frac{1}{2}$.

The situation is somewhat more complicated in the case of parabolic types of distributions such as given by curve 2. In this case a potential maximum of magnitude η_{max}, say, has developed in the plasma. Ions are partially reflected back to the left of the peak, while those which pass through are accelerated on the right; consequently, the ion density becomes

$$\begin{aligned} n_i(\eta) &= [1+E(\eta_{max}-\eta)]\exp(-\eta); \quad \xi\leq\xi_{max} \\ &= [1-E(\eta_{max}-\eta)]\exp(-\eta); \quad \xi\geq\xi_{max} \end{aligned} \tag{33}$$

where ξ_{max} marks the position of the potential maximum. The potential minimum at the anode, $-\eta_a$, serves to reflect electrons back to the cathode

$$\begin{aligned} n_e(\eta) &= [1+E(\eta-\eta_a)]\exp(\eta); \qquad \eta<0 \\ &= [1+E(\eta-\eta_a)-2E(\eta)]\exp(\eta); \quad \eta\geq 0. \end{aligned} \tag{34}$$

The quantity $F(\eta)$ corresponding to curve 2 may be found by methods described above and subject to the condition $F(\eta_{max})=0$.

If it is considered that curve 1 depicts the nonequilibrium situation at short circuit, it may be imagined that curve 2 will ultimately result as the output voltage is increased. As long as no barriers develop to electron flow, the electron current flowing to the anode equals the saturation limited value

$$I=I_s=eJ_e^+(0); \quad \eta_a\geq 0. \tag{35}$$

As soon as the anode voltage drops below the cathode value, a barrier develops and the electron current will decrease exponentially:

$$\begin{aligned} I &= I_s\exp(\eta_a) \\ &= I_s\exp[-(eV_a-\Delta W)/\theta]; \quad \eta_a<0, \end{aligned} \tag{36}$$

where V_a is the magnitude of the output voltage and ΔW is the difference in work function between cathode and anode. The simple law of Eq. (36) is always valid whenever the maximum barrier to electron flow resides at the anode.

B. Class Two Distributions

In complete analogy with the previous case, class two contains all monotone distributions with electron-rich cathode sheaths, as well as those in which the entire tube is electron rich. Examples of these are depicted schematically as curves 4 and 3 of Fig. 2. Class two distributions constitute a sort of mirror image of class one distributions. For example, if the distribution is monotone, as in curve 4, the reduced densities become

$$\begin{aligned} n_e(\eta) &= [1+E(\eta-\eta_a)]\exp(\eta) \\ n_i(\eta) &= [1-E(-\eta)]\exp(-\eta), \end{aligned} \tag{37}$$

and these are to be compared with Eq. (30). A similar analogy exists between quantities corresponding to curves 3 and 2.

The electron current corresponding to curve 4 is still given correctly by Eq. (36). However, in the case of curve 3 a potential minimum of magnitude η_{min}, say, has developed between the cathode and anode. The corresponding electron current becomes

$$I=I_s\exp(-\eta_{min}). \tag{38}$$

Detailed calculations indicate that the variation of η_{min} with output voltage is in general less rapid than linear until η_a approaches $-\eta_{min}$. Thus, it is expected that the electron current varies less rapidly than exponential with output voltage as long as the maximum barrier to electron flow resides in the plasma.

On account of the disparity in masses, the ionic current is in general negligible in comparison with the electronic current until considerable electron retarding potentials are obtained. It may be argued that when the two currents are comparable, the distribution may in most respects resemble that of curve 4 or 2 with the maximum absent. If this is indeed the case, the open circuit voltage may be readily related to other quantities. The open circuit voltage is defined as that value of the output voltage where the net current to the anode is zero. This in turn requires the electron and ion currents to be the same, providing it is assumed that

back emission from the anode and other sources of leakage currents are completely absent. In this way one finds from Eq. (36) that

$$J_e^+(0)\exp(\eta_a)=J_i^+(0)$$
$$\exp[-(eV_{0c}-\Delta W)/\theta]=\alpha(m/M)^{\frac{1}{2}}, \tag{39}$$

where V_{0c} is the magnitude of the output voltage at open circuit. In the event E_i exceeds considerably W_c, the above simplifies with the use of Eq. (19):

$$eV_{0c}\approx E_i-W_c=W_a+\theta\ln[10^{12}\theta^{\frac{1}{2}}/p_\mu], \tag{40a}$$

where p_μ is the neutral pressure in microns at the cathode and $(M/m)^{\frac{1}{2}}$ is taken to be 500. If W_c considerably exceeds E_i,

$$eV_0\approx -W_a+\theta\ln[5\times10^{12}\theta^{\frac{1}{2}}/p_\mu]. \tag{40b}$$

According to Eq. (40a) a tube with cathode work function of three volts and anode work function of 1.5 volts, operating near 3000°K and 10 μ of cesium pressure, will develop at open circuit approximately 5.5 volts. Of course, in actual practice back emission from the anode will cause the observed voltage to be lower. The relations of Eqs. (39) and (40) may be used, however, to estimate ideal values of the open circuit voltage. Alternatively, if the back emission current I_b is known, the corresponding value of α may be obtained experimentally from

$$eV_{0c}=\Delta W+\theta\ln[I_e/(eJ_i^+(0)+I_b)], \tag{41}$$

where once more a potential distribution of the type depicted by curve 4 or 2 without the maximum has been assumed.

C. Class Three Distributions

In the foregoing, the tacit assumption has been made that in general it is possible to go continuously from curve 1 of Fig. 2 to curve 2 by increasing the output voltage, or from curve 4 to 3 by decreasing the output voltage. That this is not true may be seen from the following argument: Starting with curve 1 of Fig. 2, for example, as the output voltage increases a potential maximum eventually develops in the plasma. In order to go continuously to curve 2, the entire tube must remain ion rich. However, to the anode side of the maximum, ions are accelerated and electrons decelerated. This serves to make the anode side relatively less ion rich than in the absence of the maximum. The enhanced electron enrichment will continue this way, if allowed, until the anode voltage drops below the cathode value; this causes electrons to be reflected back towards the cathode, further enhancing the electron enrichment of the tube.

Eventually a situation will be reached where it is no longer possible to maintain the entire tube ion rich, and the distribution passes over to a member of the third class. Class three contains all oscillatory distributions which may be either ion rich or electron rich at the cathode, as illustrated in Fig. 3. The mode of transition from class one to three has its strict analogue for transition from class two to three, as may be observed by starting with curve 4 of Fig. 2 and decreasing the output voltage gradually. The onset of transition to class three will always take place at the anode whenever the ion and electron densities become equal; in terms of the reduced densities the requirement is

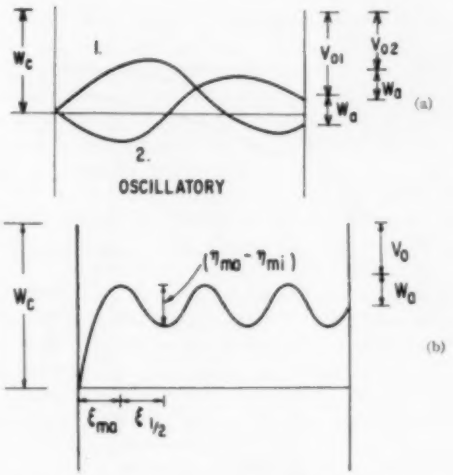

FIG. 3. Class three oscillatory potential distributions.

$$n_e(\eta_a)/n_i(\eta_a)=\alpha. \tag{42}$$

Since η_a may be considered a function of α and the tube spacing ξ_a, the actual transition point is a function of these quantities also.

In general, other variables being held constant, the greater ξ_a, the more prevalent class three distributions become over a range of operating conditions. This may be appreciated more readily when it is recognized that class three distributions are periodic except for sheath structure at the cathode. The periodicity is illustrated in Fig. 3(b) for a simple situation in which retarding barriers to electron flow are absent; the extension of the following discussion to more complicated situations will be straightforward.

It will be noted that to the anode side of the first potential maximum all ions which have passed over the barrier will continue on to the anode. Consequently, outside the cathode sheath

$$n_e(\eta)=[1-E(\eta)]\exp(\eta)$$
$$n_i(\eta)=[1-E(\eta_{\max}-\eta)]\exp(-\eta) \tag{43}$$
$$F(\eta)=\alpha\exp(-\eta_{\max})G(\eta_{\max}-\eta)-[G(\eta_{\max})-G(\eta)].$$

Since the field at the potential minimum must also be zero,

$$F(\eta_{\min})=0$$
$$\alpha\exp(-\eta_{\max})G(\eta_{\max}-\eta_{\min})=G(\eta_{\max})-G(\eta_{\min}). \tag{44}$$

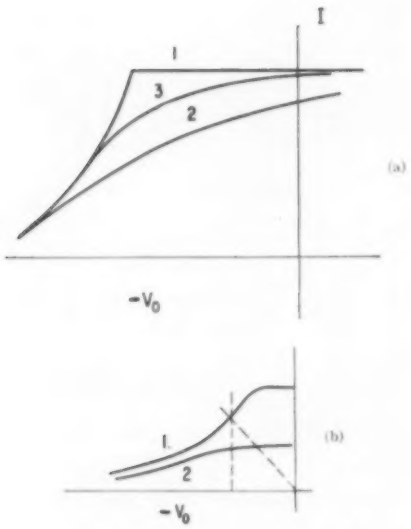

FIG. 4. (a) Current voltage plots corresponding to three classes of potential distributions; (b) Possible bistable mode.

The above relates the amplitude $(\eta_{max}-\eta_{min})$ to other tube parameters. The half-wavelength corresponding to Eq. (43) is

$$\xi_{\frac{1}{2}}=\int_{\eta_{min}}^{\eta_{max}} d\eta/[F(\eta)]^{\frac{1}{2}}, \tag{45}$$

and it will be noted that $\xi_{\frac{1}{2}}$ is an increasing function of the amplitude. Some further insight may be gained by assuming the amplitude sufficiently small to permit expansion of quantities in Eqs. (43) to (45), and retention of only lowest significant terms in the amplitude. In this manner the following are obtained:

$$\begin{aligned}(\eta_{max}-\eta_{min})&\approx(9\pi/16\alpha^2)\exp(2\eta_{max})[F'(\eta_{max})]^2\\ \xi_{\frac{1}{2}}&\approx 2(\eta_{max}-\eta_{min})^{\frac{1}{2}}|F'(\eta_{max})|^{-\frac{1}{2}}.\end{aligned} \tag{46a}$$

Alternatively it may be assumed that the amplitude is large and the asymptotic value of G in Eq. (44) can be used for an estimate to yield

$$(\eta_{max}-\eta_{min})\approx(\eta_{max}/\alpha^2)\exp(2\eta_{max}). \tag{46b}$$

The periodic portion of class three distributions may extend to arbitrary distances and are of special significance for tubes with large ξ_a operating under conditions where, on the average, the plasma tries to remain neutral. Within the scope of the present model, these oscillatory distributions play the role in the case of the converter of the neutral plasma column in the instance of thermodynamic equlibrium. As indicated by Eq. (46), the amplitude of fluctuations varies strongly with the extent of over and under neutralization at the maxima and minima. It is to be expected that the current voltage characteristics of class three distributions fall in between that of classes one and two. This point is illustrated schematically in Fig. 4(a), where the curves are labeled according to the class they represent. It may be imagined that the change from curve 2 to 3 to 1 can be effected by gradual increase in the cesium pressure, while at the same time the electrode work functions and cathode temperature are maintained constant.

In closing this section it may be mentioned that direct transitions between classes one and two may take place at the cathode whenever retarding potentials for either species is large enough to reflect an amount sufficient for space charge neutralization at the cathode. On the basis of the previous discussion it will be noted that such transitions are restricted to the range $\frac{1}{2}<\alpha<2$.

V. INSTABILITIES

There is reason to believe that some of the stationary distributions described in the previous section have associated instabilities which may be responsible for the current voltage oscillations observed in low pressure thermionic converters. In this connection three plausible examples will be cited.

It has been pointed out[6] that in the presence of large electron accelerating potentials, as depicted in curve 1 of Fig. 2, the relative directed velocity between electrons and ions can exceed appreciably the thermal spread and give rise to the familiar two-stream instability.[7] Unfortunately, the rigorous theoretical confirmation of this hypothesis is difficult, since it involves extension of the usual two-stream analysis to nonuniform distributions with spatial variations not necessarily small compared with the instability wavelength.

Another possibility, first proposed in connection with noise in lamp discharges,[8] is that ions trapped in potential wells of the type depicted by curve 3 of Fig. 2 are set into oscillation by the electronic current flowing in the tube.[9] These oscillations serve to modulate the magnitude of the electron barrier and, in turn, the current. If it is assumed that the electrons are in thermal equilibrium with the oscillating potential, a completely linear analysis yields the following dispersion relation:

$$\begin{aligned}\omega^2&=\omega_{pi}^2[1+(k\lambda_D)^{-2}]^{-1}\\ \omega_{pi}^2&=4\pi N_i e^2/M\\ \lambda_D^2&=\theta/4\pi N_e e^2,\end{aligned} \tag{47}$$

where ω, k are the frequency and wave number of the oscillation, and the densities refer to the unperturbed values in the wall. The effect of spatial variations and nonlinearity is difficult to estimate.

The present author has proposed that instabilities inherent in class three distributions may in part account for oscillations observed experimentally. The instability

[6] Marshall Rosenbluth (private communication).
[7] O. Penrose, Phys. Fluids **3**, 258 (1960).
[8] J. F. Waymouth, Sylvania Technologist **13**, 1 (1960).
[9] M. Gottlieb and R. J. Zollweg, Bull. Am. Phys. Soc. Ser. II, **5**, 383 (1960).

of class three distributions may be inferred from a previous analysis[10] which showed that, if electrons are emitted into a plasma with fully trapped ions or vice versa, the maximum amplitude of the spatially oscillatory potentials is approximately $\theta/3$. Consequently, any class three distribution with $(\eta_{max}-\eta_{min})\gtrsim\frac{1}{3}$ should be unstable against chance collisions tending to populate the trapping sites in the potential wells. It may be argued that even if the electrode spacing is small compared to a collision mean free path, the probability of collisions has finite statistical weight, and instabilities induced in this manner must be probable.

On this basis it may be argued that potential distributions corresponding to curves 1 and 2 of Fig. 3(a) represent bistable states which may be connected along either constant load or constant voltage lines as indicated in Fig. 4(b). The existence of these bistable distributions has been pointed out previously [p. 164 of the work cited in footnote 10(a)]. It is to be expected that under voltage and zero external impedance conditions, the oscillations inherent in bistable mode operation will have frequencies characteristic of the order of ion thermal velocities divided by ξ_1; consequently, the period of the oscillation should increase as $(\eta_{max}-\eta_{min})$ increases. These ion oscillations are closely related to the ones discussed by Waymouth, the principal difference arising from the fact that the ones considered here are intimately related to the quasi-neutral modes of tube operation.

In order to understand completely self-excited ion oscillations it becomes necessary to find a mechanism leading to self-excitation. A possible agency may be two stream interaction between current bearing electrons and trapped ions. An alternative suggestion[11] is that the oscillations are sustained because, for a certain class of ion space charge distributions which occur in the course of a cycle of the oscillation, there may be more than one self-consistent electron distribution. The actual electron distribution which occurs may then be different as the region of nonuniqueness is traversed in opposite directions in alternate half-cycle of the ion oscillation. For example, if in the course of the oscillation a secondary potential minimum develops in the region between the electrodes, the reflection of electrons will cause a sudden increase in local electron space charge, and hence a sudden fall in the electrical potential. The transition is initiated when the secondary minimum falls to the cathode potential, and will take place in a time of order of magnitude of the reciprocal of the electron plasma frequency. In the next half-cycle, the transition is initiated when the secondary minimum rises to cathode potential so that the electrons are no longer reflected. It can be shown that the hysteresis associated with the nonadiabation transitions in electron space charge introduces a phase shift in the electrical potential which results in the transfer of part of the electron energy into ion oscillations.[12]

The preceding discussion is not meant to present an exhaustive list of possible explanations of converter tube oscillations. Indeed, it would be extremely illuminating to have more experimental information on this matter as well as on other characteristics of tube performance which may be used to guide further theoretical analyses.

ACKNOWLEDGMENTS

It is a pleasure to acknowledge numerous illuminating conversations with Drs. H. Hurwitz, Jr., and J. M. Houston in the course of this work. Their comments have been of considerable value in clarifying certain points contained in the present paper.

[10] P. L. Auer and H. Hurwitz (a) J. Appl. Phys. **30**, 161 (1959); (b) **31**, 1007 (1960).

[11] H. Hurwitz (private communication).

[12] *Note added in proof*. The hysteresis referred to above is closely related to the hysteresis associated with the Kipp point in current limited vacuum tubes. See, for example, R. Salzberg and A. V. Haeff, RCA Rev. **2**, 336 (1938); C. E. Fay, A. L. Samuel, and W. Shockley, Bell System Tech. J. **17**, 49 (1938); J. R. Pierce, J. Appl. Phys. **15**, 721 (1944). In our present situation, the secondary potential minima associated with class three distributions are analogous to those produced by vacuum tube grids. The ion motion in the course of slow oscillations plays the role of slowly varying grid potential. I wish to thank Professor C. K. Birdsall for bringing these references to my attention.

Bounds on Low-Energy Scattering Parameters*

LARRY SPRUCH AND LEONARD ROSENBERG
Physics Department, Washington Square College, and Institute of Mathematical Sciences, New York University, New York, New York
(Received August 4, 1960)

Some recent results that determine an upper bound on the scattering length, whether or not composite bound states exist, are reviewed. The extension to the determination of an upper bound on $(-k\cot\eta)^{-1}$, where only one channel is open, is presented; the method used requires that the potential vanish identically beyond some given point. The results are applicable to the scattering of one compound system by another. Possible extensions and improvements of the method are discussed.

1. INTRODUCTION

FOR some time, the authors have been studying the possibility of replacing the variational or stationary principles of scattering theory by a much more powerful principle, a minimum principle. We were originally able to find minimum principles only for rather restricted cases, but it has proved possible to eliminate many of these restrictions. It will, unfortunately, be necessary to discuss some of the earlier work in order to arrive at some more recent results.[1] We would like to note that at one stage we received some very valuable assistance from Thomas F. O'Malley.

The virtues of minimum principles are very well known. In the determination of the ground-state energy of a quantum mechanical system, for example, where such a principle exists, we know that if additional parameters are introduced the answer obtained can only be improved. If two different forms of trial functions are used, the decision as to which of the two results obtained is more accurate is based on a criterion which is simple and final. The lower number is the better one.

Compare this with the stationary principles of scattering theory. As useful as they are, it remains true that a trial function with additional free parameters can give a *worse* result. The decision as to which of two results obtained from two different forms of trial functions must contain some metaphysical element.

Minimum principles for scattering theory have been discussed previously, but they refer to scattering of a particle by a center of force, and do not seem to be capable of generalization in a useful way to scattering of a particle by a compound system, let alone to scattering of compound systems by compound systems. Let us discuss the scattering of a particle by a center of force, using a method which has the virtue that it *is* capable of extension to more interesting cases.

* Research sponsored by the Geophysics Research Directorate of the Air Force Cambridge Research Center, Air Research and Development Command, the Office of Ordnance Research, U. S. Army, and the Office of Naval Research.

[1] Since much of the material of the first three sections has been published, these sections have been cut considerably. They were not eliminated entirely because it seemed that a collection of some of the results that have been obtained, which omitted details and proofs of mathematical theorems, might be useful.

2. UPPER BOUND ON SCATTERING LENGTH WHEN COMPOSITE BOUND STATES DO NOT EXIST

Starting with the simplest possible case, zero energy scattering by a short range potential $V(r)$, we assume that it cannot bind the particle.[2] The Schrödinger equation to be solved is

$$Hu(r)\equiv\left[-\frac{\hbar^2}{2\mu}\frac{d^2}{dr^2}+V(r)\right]u(r)=0, \tag{2.1}$$

where

$$u(o)=0, \quad u(r)\to -r+A \quad \text{for} \quad r\to\infty. \tag{2.2a}$$

A is the scattering length, and we would like to obtain a bound on it. To do so, we introduce a trial function $u_t(r)$ which satisfies the boundary conditions

$$u_t(o)=0, \quad u_t(r)\to -r+A_t \quad \text{for} \quad r\to\infty, \tag{2.2b}$$

where A_t is the trial scattering length. We then introduce the quantity

$$(2\mu/\hbar^2)\int(uHu_t-u_tHu)dr,$$

and evaluate it, on the one hand through the use of Green's theorem, and on the other, through the use of $Hu=0$. We find that

$$A-A_t=(2\mu/\hbar^2)\int uHu_t dr. \tag{2.3}$$

We now introduce the difference function, $w(r)$, defined by

$$w(r)=u_t(r)-u(r). \tag{2.4}$$

It follows that

$$w(o)=0, \quad w(r)\to(A_t-A)=\text{constant}, \quad Hw=Hu_t. \tag{2.5}$$

We can then rewrite our equation as

$$A=A_t+(2\mu/\hbar^2)\int u_tHu_t dr-(2\mu/\hbar^2)\int wHw dr. \tag{2.6}$$

[2] L. Spruch and L. Rosenberg, Phys. Rev. **116**, 1034 (1959); **117**, 1095 (1960).

This is the zero-energy form of an identity introduced by Kato.[3] Since w is supposedly a small quantity, the last term is a term of second order, and if we drop it we remain with a variational expression for A.

Now the point of our discussion is that we are not satisfied with a stationary principle but seek a minimum principle. We cannot then simply drop the term $\int wHwd\boldsymbol{r}$, but we must bound it. It is not, in general, a trivial matter to do so. We have assumed, however, that the particle cannot be bound to the center of force. It follows that the lowest energy of the system is 0, so that for any quadratically integrable trial function, Ψ_t,

$$\int \Psi_t H \Psi_t d\boldsymbol{r} > 0. \tag{2.7}$$

The conditions on Ψ_t can actually be relaxed somewhat to include functions which approach a constant asymptotically. But then we can choose $\Psi_t = w$, and we have

$$\int wHwd\boldsymbol{r} \geq 0,$$

and we have finally the desired bound

$$A \leq A_t + (2\mu/\hbar^2) \int u_t H u_t d\boldsymbol{r}. \tag{2.8}$$

Let us return to the question of normalization. In ordinary variational calculations, this is simply a matter of convenience, but for the purposes of obtaining a bound, the choice of normalization is of critical importance. If, for example, we had chosen

$$u(\boldsymbol{r}) \to (-\boldsymbol{r}/A)+1 \quad \text{and} \quad u_t(\boldsymbol{r}) \to (-\boldsymbol{r}/A_t)+1, \tag{2.9}$$

then $w(\boldsymbol{r}) \to \text{const} \times \boldsymbol{r}$, and the knowledge that no bound state existed would not in general suffice to give a bound on (w,Hw). A schematic representation of results obtained with different normalizations and different methods of determining the variational parameters is given in Fig. 1. (See also Appendix B.)

Somewhat after we had obtained a rigorous bound on the scattering length, but quite independently, Ohmura looked into the same question.[4] He did not, however, recognize the significance of the choice of normalization, and he unfortunately made the wrong choice so that, as he notes, the results do not in general provide a rigorous minimum. Further, he did not obtain any but purely formal results for the case where composite bound states exist; this is the problem discussed in Sec. 3.

[3] T. Kato, Progr. Theoret. Phys. (Kyoto) **6**, 394 (1951).

[4] T. Ohmura, J. Math. Phys. **1**, 27 (1960). Second-order terms are not always handled consistently, so that some of the conclusions are incorrect. The condition given by Eq. (25) is a case in point.

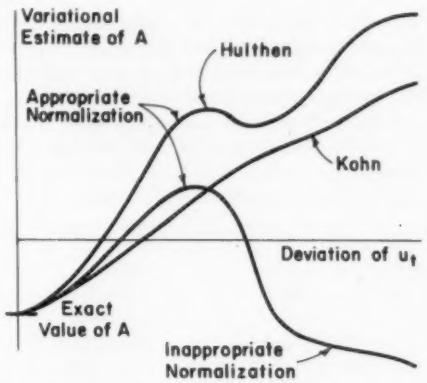

FIG. 1. A schematic representation of the estimate of A for the no bound-state case. The horizontal axis represents a measure of the deviation of the *form* of the trial function from that of the exact function. No matter how the variational parameters are chosen, the appropriate normalization $u(r) \to -r+A$ always leads to an estimate of A which lies above the exact value. The Kohn prescription for choosing the variational parameters leads to the lowest, and therefore the best, estimate of A for a given choice of the form of u_t; the Hulthen prescription gives an upper bound, but a trial function with additional parameters may lead to a worse estimate of A, indicated by the nonmonotonicity of the curve. The inappropriate normalization $u(r) \to (-r/A)+1$ will in general not give a rigorous bound on A. *Note added in proof.* The arrows denoting appropriate normalization should be drawn to the Hulthen and to the Kohn curves.

3. UPPER BOUND ON SCATTERING LENGTH WHEN BOUND STATES DO EXIST

We now consider this rather more complicated case. We still take the incident energy to be zero, but now we assume[5] that there are N and only N bound states of the particle in the center of force. For the moment, we choose $N=1$. ϕ_1 will represent the normalized wave function of this one state. It is a solution of the equation $H\phi_1 = E_1\phi_1$, where $E_1 < 0$. Formally, we can proceed as follows: The eigenfunctions of the Hamiltonian, ϕ_1, and the continuum states form a complete set in terms of which we can expand w. Let us define a new function, w', through

$$w' = w - (w,\phi_1)\phi_1.$$

Since we have subtracted off the negative energy component of w, it follows that

$$(w',Hw') \geq 0.$$

Substitution for w' gives

$$(w,Hw) \geq (w,H,\phi_1)(w,\phi_1).$$

To get this into a more useful form, we write

$$(w,\phi_1) = (w,H\phi_1)/E_1,$$

and then let H operate on w. We remain with

$$(w,Hw) \geq (\phi_1,Hu_t)^2/E_1.$$

[5] L. Rosenberg, L. Spruch, and T. F. O'Malley, Phys. Rev. **118**, 184 (1960).

The above result is not yet useful since it involves the unknown bound-state function ϕ_1. It is, however, possible to prove the very nice result that the inequality remains rigorous if one simply replaces ϕ_1 by a trial function ϕ_{1t} and E_1 by $E_{1t}\equiv(\phi_{1t},H\phi_{1t})$. The only requirement on ϕ_{1t} is that it be sufficiently accurate to give binding, i.e., that $E_{1t}<0$. A bound on (w,Hw) immediately gives a bound on A. We have

$$A\leq A_t+(2\mu/\hbar^2)(u_t,Hu_t)-(2\mu/\hbar^2)(\phi_{1t},Hu_t)^2/E_{1t}$$

if $E_{1t}<0$.

This result can be generalized. If there are N bound states, the last term is replaced by a sum of N terms, each of which involves a trial bound-state function. If we are dealing with compound systems, the trial functions must be appropriately symmetrized and all energies must be measured with respect to E_g, the sum of the ground-state energies of the isolated systems; H and E_{1t} are to be replaced by $H-E_g$ and $E_{1t}-E_g$. We are, however, still restricted to zero energy, and to cases for which only uncoupled channels are open.

4. SCATTERING OF ELECTRONS BY HYDROGEN ATOMS

A. Zero Energy Scattering

Before going on to the problem of nonzero energies, it might help to make the preceding discussion more concrete by considering the scattering of zero energy electrons by hydrogen atoms. An electron and a hydrogen atom can be in a triplet or in a singlet state, but there is no coupling between these states, so the scattering problem reduces to two uncoupled scattering problems. We want therefore to obtain bounds on A_T and on A_S, the triplet and the singlet scattering lengths, respectively.

There is known to be one bound singlet state of H^- of about $\frac{3}{4}$ ev. On theoretical and experimental grounds, the evidence is that there are no other bound states. We will assume this to be the case. We then have,[6] for the triplet case,

$$A_T\leq A_{Tt}+(2m/\hbar^2)\int\Psi_{Tt}(\mathrm{H}+13.6)\Psi_{Tt}d\tau,$$

where, for r_1 or $r_2\rightarrow\infty$,

$$\Psi_{Tt}\rightarrow(1-P_{12})R_{\mathrm{H}}(r_2)(-1+A_{Tt}/r_1).$$

P_{12} is the space exchange operator and $R_{\mathrm{H}}(r)$ is the hydrogen ground-state function with a binding energy of 13.6 ev. For singlet scattering, we must account for the bound state. We have

$$A_S\leq A_{St}+(2m/\hbar^2)\int\Psi_{St}(\mathrm{H}+13.6)\Psi_{St}d\tau$$

$$-(2m/\hbar^2)\left(\int\phi_{1t}(\mathrm{H}+13.6)\Psi_{St}d\tau\right)^2\Big/(E_{1t}+13.6).$$

[6] L. Rosenberg, L. Spruch, and T. F. O'Malley, Phys. Rev. **119**, 164 (1960).

The trial scattering function Ψ_{St} satisfies the same asymptotic boundary condition as does Ψ_{Tt}, but with $(1-P_{12})$ replaced by $(1+P_{12})$. ϕ_{1t} must be sufficiently accurate so that

$$E_{1t}\equiv(\phi_{1t},\mathrm{H}\phi_{1t})<-13.6.$$

Our results for a moderately complicated trial function were[6] $A_T>1.91a_0$ and $A_S>6.23a_0$. These results are rather lower and therefore somewhat better than the results that had been obtained previously by variational methods.

B. Dispersion Theory

A very interesting development in electron hydrogen scattering theory is the recent introduction of dispersion theoretic techniques to this problem by Gerjuoy and Krall.[7] They find that

$$\tfrac{3}{4}(A_{TB}-A_T)+\tfrac{1}{4}(A_{SB}-A_S)+\tfrac{1}{2}\ \mathrm{Res.}$$

$$=\tfrac{1}{2}\pi^{-2}\int_0^\infty\sigma_{\mathrm{tot}}(k)dk. \quad (4.1)$$

A_{TB} and A_{SB} are the triplet and singlet scattering lengths in the Born approximation. They are known to be $A_{TB}=5a_0$ and $A_{SB}=-7a_0$. The residue, Res., is determined in terms of the bound-state function (or functions) of H^-, while $\sigma_{\mathrm{tot}}(k)$ is the total cross section at the wave number k. It is remarkable that the integral over $\sigma_{\mathrm{tot}}(k)$, which includes elastic, inelastic, and ionization processes, can be expressed in such a simple way.

Gerjuoy and Krall evaluate the residue by using some quite crude H^- function, but it is possible to show that the value they obtained is not far from the correct value (see Appendix A). Putting in theoretical values for the various quantities, they find that lhs of Eq. (4.1) $\gtrsim 4.5a_0$ (theoretically).

On the other hand, putting in the presumably well-known high-energy values of $\sigma_{\mathrm{tot}}(k)$ and the low-energy experimental data of Brackmann, Fite, and Neynaber,[8] they find that rhs of Eq. (4.1) $=(5.1\pm0.5)a_0$.

There are three probable consequences of this quite good agreement:

(1) The experimental results just quoted[8] are correct. There were indications from some unpublished data that this might not be so.

(2) The upper bounds on A_T and on A_S that we quoted are close to the correct values.

(3) There really is only one bound state of H^-.

Gerjuoy and Krall made no attempt to extract any further information from their result, for it would not be very useful for the problem they were concerned

[7] E. Gerjuoy and N. A. Krall, Phys. Rev. **119**, 705 (1960); N. A. Krall and E. Gerjuoy, *ibid.* **120**, 143 (1960).

[8] R. T. Brackmann, W. L. Fite, and R. H. Neynaber, Phys. Rev. **112**, 1157 (1958).

with. Since their method is quite general, it is interesting to see what else can be learned. We will look into this for a moment. For convenience, we use the notation of the e^-H problem.

Equation (4.1) is really the sum of two separate results,[7]

$$\tfrac{3}{4}(A_{TB}-A_T)=(\tfrac{1}{2}\pi^{-2})\tfrac{3}{4}\int_0^\infty \sigma_{\mathrm{tot},T}(k)dk \quad (4.2a)$$

and

$$\tfrac{1}{4}(A_{SB}-A_S)+\tfrac{1}{2}\ \mathrm{Res}=(\tfrac{1}{2}\pi^{-2})\tfrac{1}{4}\int_0^\infty \sigma_{\mathrm{tot},S}(k)dk. \quad (4.2b)$$

It is therefore clear that one can obtain information about $\sigma_{\mathrm{tot},T}(k)$ and $\sigma_{\mathrm{tot},S}(k)$; the meaning of the notation should be obvious. Further, since

$$\sigma_{\mathrm{tot}}(k)=\tfrac{3}{4}\sigma_{\mathrm{tot},T}(k)+\tfrac{1}{4}\sigma_{\mathrm{tot},S}(k),$$

it follows that

$$0\leq\sigma_{\mathrm{tot},T}(k)\leq\tfrac{4}{3}\sigma_{\mathrm{tot}}(k)$$

and that

$$0\leq\sigma_{\mathrm{tot},S}(k)\leq 4\sigma_{\mathrm{tot}}(k).$$

One can therefore obtain *both* bounds on the scattering lengths from a knowledge of $\sigma_{\mathrm{tot}}(k)$ (for the singlet case, the residue would have to be considered as known). The bounds might of course be quite crude. The bounds would be useful if $\sigma(k)$ were not well known in the neighborhood of $k\approx 0$ (otherwise A could be obtained directly), if $\sigma(k)$ for other regions of k were known, and if one could be sure that $\sigma(k)$ for $k\approx 0$ were small compared to $\sigma(k)$ for some other region of k.

5. LOWER BOUND ON $k\tan\eta$ FOR STATIC POTENTIALS

Let us now discuss the case of a nonzero scattering energy, which we will denote by E. We return temporarily to the scattering of a particle by a center of force.[9]

We now impose as boundary conditions

$$u(o)=0, \quad u(r)\to \sin kr+\tan\eta\cos kr \quad \text{for} \quad r\to\infty.$$

$u_t(r)$ satisfies the same boundary conditions, but with the phase shift η replaced by the trial phase shift, η_t. The difference function $w(r)$, defined as before as $w(r)=u_t(r)-u(r)$, then satisfies

$$w(o)=0, \quad w(r)\to \text{const}\cos kr, \quad \mathrm{H}w=\mathrm{H}u_t.$$

The identity that corresponds to that previously derived at zero energy, first given by Kato,[2] is

$$k\tan\eta=k\tan\eta_t-(2\mu/\hbar^2)\int u_t(\mathrm{H}-E)u_t dr + (2\mu/\hbar^2)\int w(\mathrm{H}-E)w dr.$$

Once again, since w is of first order, one obtains a variational principle by dropping the last term. It will be recognized as the Kohn-Hulthen variational principle. As at zero energy, however, we want to do better; we want to obtain a bound on the last term. But there is now a serious obstacle. At zero scattering energy, there were a finite number of solutions of the Hamiltonian with energies below the energy of scattering. These were of course the negative energy bound-state solutions. It was then possible to introduce a function w' which was equal to the positive energy portion of w, the negative energy portion having been subtracted off. Now, however, for a nonzero scattering energy E, the solutions of the Hamiltonian which lie below E include the negative energy bound-state solutions *and* the continuum solutions from zero up to E. If we were to attempt to proceed as before, we would have to attempt to subtract off the effect of an infinite number of solutions. The resultant integral has a singular integrand, however, and we have therefore used an alternate approach.

This latter approach was to restrict ourselves to potentials which vanish identically beyond $r=R$. The form of $u(r)$ is then known to be a linear combination of sines and of cosines for $r>R$, and if we restrict $u_t(r)$ to that form for $r>R$, we have $\mathrm{H}w(r)=\mathrm{H}u_t(r)=0$ for $r>R$. If we now choose R for a given k so that $w(R)=0$, which we can do by the choice $kR=\frac{1}{2}\pi, \frac{3}{2}\pi, \cdots$ then the quantity to be bounded is

$$\int_0^R w(\mathrm{H}-E)w dr, \quad \text{where} \quad w(0)=W(R)=0.$$

While this quantity arose from a scattering problem, it is perfectly legal to think of it as having arisen from the bound-state problem of a particle confined to the region o to R, within which the potential $V(r)$ exists. (There is now an infinite barrier at $r=R$.) There will of course be an infinity of bound states, but the useful feature of the cutoff procedure is that the energies of these states are *discrete* even in the positive energy domain and there will be only a finite number M of states which have an energy less than the scattering energy E. We can therefore introduce a function w', which is w with its energy components less than E subtracted off, so that $(w', [\mathrm{H}-E]w')\geq 0$. This in turn leads to a bound on $(w,\mathrm{H}w)$ and finally on $k\tan\eta$. Replacing the exact bound state functions ϕ_i by sufficiently accurate trial functions ϕ_{it}, we have

$$k\tan\eta\geq k\tan\eta_t-2\mu/\hbar^2(u_t,[\mathrm{H}-E]u_t) + 2\mu/\hbar^2\sum_{i=1}^{M}(u_t,[\mathrm{H}-E]\phi_{it})^2/(E_{it}-E),$$

$$\phi_{it}(0)=\phi_{it}(R)=0, \quad (\phi_{it},\phi_{st})=\delta_{is}$$

$$(\phi_{it},\mathrm{H}\phi_{st})=E_{it}\delta_{is}, \quad E_{it}<E.$$

The indices i and s each run from 1 through M.

[9] A much more detailed report of this work may be found in L. Rosenberg and L. Spruch, Phys. Rev. **120**, 474 (1960).

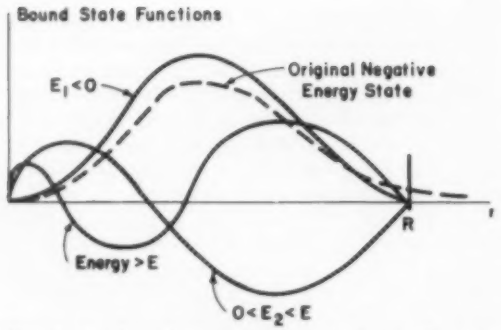

FIG. 2. A schematic representation of the negative-energy bound state and of the two lowest positive-energy bound states for a particle confined to the region 0 to R, within which there exists the potential $V(r)$. It is assumed that the original potential, where $V(r)$ was not cut off, was capable of supporting only one state.

The question of the appropriate choice of R is one of considerable practical importance. Figure 2 is a schematic representation of the case of a potential which can support one and only one (negative-energy) bound state. For the given choice of R, the state with energy $E_1<0$ is clearly not very much different from the original negative-energy state. Furthermore, there is only one other energy eigenvalue, E_2, for this R which lies below E, so that the subtraction procedure will involve two bound states. If R had been chosen much smaller, the new problem would be a very poor approximation to the real one of interest, while if R had been chosen much larger, the subtraction procedure would become very cumbersome because of the large number of states involved.

6. LOWER BOUND ON $k\tan\eta$ FOR SCATTERING BY COMPOUND SYSTEMS

At zero energy, the extension of the bound (on A) for scattering by a static potential to scattering by a compound system was a trivial matter. At nonzero energies, this extension of the bound (on $k\tan\eta$) is not only not trivial, but for the method just described is not even possible. The method breaks down even for nonidentical particles, so let us temporarily restrict ourselves to that case.

Assume that particle 1 is scattered by a system which is confined to a region of radius R. Assume further that this particle has zero interaction with the system when $r_1>R$. (This represents the cutoff procedure.) The form of the exact solution for $r_1>R$ will then be, with $\mathbf{r}$ representing the coordinates of all of the other particles,

$$u(\mathbf{r},r_1)=\psi_g(\mathbf{r})(\sin kr_1+\tan\eta\cos kr_1)+\sum C_n\psi_n(\mathbf{r})e^{-\gamma_n r_1}.$$

ψ_g represents the ground state and ψ_n an excited state of the scattering system. By conservation of energy, we have[4]

$$E_g+E=E_n-\hbar^2\gamma_n^2/(2m).$$

By assumption, there is only one open channel.

The form of $u_t(r,r_1)$ for $r_1>R$ is the same, with η replaced by η_t and C_n by C_{nt}. We therefore have

$$w(\mathbf{r},r_1=R)=\psi_g(\mathbf{r})(\tan\eta_t-\tan\eta)\cos kR+\sum(C_{nt}-C_n)\psi_n(\mathbf{r})e^{-\gamma_n R}.$$

There is now no choice of R which will cause $w(\mathbf{r},R)$ to vanish, because of the presence of the virtually excited states, so that one cannot now find a connection between the scattering problem and a bound-state problem, and the method of Sec. 5 breaks down for scattering by a compound system. It is of course true that, if R is chosen "large enough," the effect of the virtually excited states will be negligible. On the one hand, though, "large enough" is an exceedingly ambiguous phrase, and on the other we just saw that there are practical limitations as to how big an R can be chosen, so that this is not a very satisfying approach. We therefore consider an alternate approach.

Returning for a moment to scattering by a center of force, we consider the solutions of

$$(\mathrm{H}-E)\varphi=\mu\rho\varphi, \qquad \varphi(o)=0,$$
$$\varphi(r)=\text{const}\sin[kr+\delta(\mu)], \qquad r>R,$$

where $\rho(r)$ is non-negative and vanishes identically for $r>R$ [as does $V(r)$], but is otherwise arbitrary. In particular, we are interested in the eigenvalues μ_n defined as the values of μ for which the phase shift is given by $\delta(\mu_n)=\theta+n\pi$, where n is an integer, positive or negative, and where $0\leq\theta<\pi$. The corresponding eigenfunctions are denoted by $\varphi_n(r)$ and are normalized through

$$\int\varphi_n(r)\rho(r)\varphi_m(r)dr=\delta_{nm}.$$

Because of the cutoff character of $V(r)$, $\delta(\mu)\geq-kR$ for all μ, where $-kR$ is the phase shift due to an infinitely repulsive potential of range R. There are therefore only a finite number of eigenvalues μ_n which are negative. See Fig. 3 for a typical case.

Now the $\varphi_n(r)$ form a complete set in terms of which we can expand $w(r)$. If we define

$$w'(r)=w(r)-\sum_n{}'(w,\rho\varphi_n)\varphi_n,$$

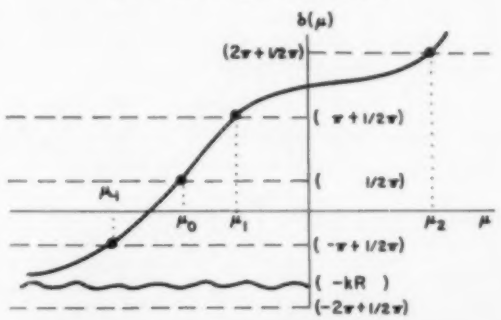

FIG. 3. Determination of the negative eigenvalues μ_n. θ has been chosen to be $\frac{1}{2}\pi$.

where the sum is restricted to those values of n for which the eigenvalues of $H-E$ are negative, then

$$(w', [H-E]w') \geq 0.$$

This in turn gives us the formal bound

$$(w, Hw) \geq \sum_n{}' (\varphi_n, [H-E]u_t)^2/\mu_n.$$

Once again the formal bound can be made a useful and still rigorous bound if the φ_n are replaced by sufficiently accurate trial functions φ_{nt}, and the μ_n by

$$\mu_{nt} \equiv \int \varphi_{nt}(H-E)\varphi_{nt}dr.$$

The virtue of this last approach is that it *can* be generalized to scattering by compound systems; the case in which identical particles are involved is included. One finds

$$k\tan\eta \geq k\tan\eta_t - 2\mu/\hbar^2 \int_0^R u_t(H-E)u_t dr + 2\mu/\hbar^2 \sum_n{}' \left(\int_0^R \varphi_{nt}(H-E)u_t dr\right)^2 \Big/ \mu_{nt},$$

$$\varphi_{nt}(0)=0, \qquad \varphi_{nt}(R)=\text{const}\sin(kR+\theta),$$

$$(\varphi_{nt}, \varphi\varphi_{mt}) = \delta_{nm}, \quad (\varphi_{nt}[H-E]\varphi_{mt}) = \mu_{nt}\delta_{mn}, \ \mu_{nt} < 0.$$

It must be assumed that we have found the correct number of negative eigenvalues.

7. POSSIBLE EXTENSIONS AND IMPROVEMENTS OF THE METHOD

In conclusion, we consider a number of ways in which the methods discussed thus far might possibly be extended or improved.

(1) Necessary conditions for existence of bound states. The success of the method described depends to some extent upon the use of a stratagem. The evaluation of the bound on (w, Hw) for the $E=0$ no bound-state case, for example, was *not* obtained by a mathematical analysis of the differential operator H. Rather, we depended upon an appeal to our experimental friends to tell us, if true, that there are no composite bound states. For the case in which there are bound states, the bound on the scattering length is rigorous only if the number of composite bound states accounted for is the exact number. Once again, we had to depend upon the experimentalists to tell us the exact number of such states. Unfortunately, the experimentalist cannot always tell us with any assurance the number of composite bound states; the case of H^- is an example. Furthermore, at positive energies the number of relevant bound states is determined by an artificial problem, and so can surely not be measured. This is also the case with regard to the number of negative eigenvalues μ_n.

The state of the art at present is that if we can find a given number of trial functions which give binding, then we know that there are *at least* that many bound states. What is required is a theory which would be able to specify conditions under which we could say that there are *at most* a given number of bound states. No such theory exists today for many body systems, though there are isolated instances where some results can be obtained. What is needed, in other words, is a theory which gives *necessary* as well as *sufficient* conditions for the existence of a specified number of bound states.

(2) Lower bound on $(-k\cot\eta)^{-1}$. Our entire discussion so far has centered on obtaining an upper bound on $(-k\cot\eta)^{-1}$ or, equivalently, a lower bound on $k\tan\eta$. It would be extremely useful to obtain a practical form for the other bound. We are not too sanguine about this possibility, however, except for the simplest systems. The reason is that even for the supposedly simpler bound state problem, the usual method for the determination of the lower bound on the energy of the ground state is an extremely difficult task, requiring the evaluation of a matrix element of H^2, and requiring further some information about other eigenvalues. There does not seem to be any reason to expect the situation to be any simpler for the scattering problem.

In this connection, incidentally, it might be noted that the rather crude information about the energy eigenvalues of excited states that is required for the determination of a bound on the ground-state energy is generally obtained not from fundamental principles, but from the experimental data. The only exception to this seems to be the recent determination[10] of a lower bound on the ground-state energy of He, and the method used there cannot readily be applied to many other systems.

It should be emphasized that points (1) and (2) are by no means independent. As one connection, for example, it is easy to show that if one knew how to obtain necessary conditions for the existence of bound states, one could obtain, in the Kato formalism, the eigenvalue α required for the determination of the other bound on $k\tan\eta$.

(3) Multichannel scattering. An important generalization would be to multichannel scattering, including the case of inelastic scattering. While we strongly believe that this should be possible, we have so far only examined two simple cases. These are two-channel processes which do *not* involve inelastic scattering. They are the one-dimensional scattering by a potential $V(x)$ which vanishes at $x \to \pm\infty$ but which is *not* an even function of x, and neutron-proton scattering with tensor forces.[11] There are three quantities of interest for a two-channel process, two phase shifts, and a

[10] N. W. Bazley, Proc. Natl. Acad. Sci. U. S. 45, 850 (1959).
[11] L. Spruch and R. Bartram (to be published).

mixing parameter. It does not seem possible to obtain in an independent way separate bounds on each of these three quantities. Rather, one obtains bounds on the elements of a matrix connected with the scattering matrix, and one then obtains bounds on each of the three quantities. The method used is an extension of the method of Kato, and therefore requires the evaluation of matrix elements of H^2, but it may be possible to eliminate that requirement for the determination of *one* of the bounds by the methods that we have described.

(4) Elimination of cutoff. The introduction of a cutoff point R, beyond which the potential must vanish, is a rather artificial technique with the not generally insurmountable but unpleasant consequence that one must make an estimate of the error introduced by the neglect of the potential tail. One should be able to obtain bounds without having to introduce R. We know of one way of doing this, at least for some simple problems,[12] but it involves the introduction of a Green's function, and this makes the integrations terribly tedious even for the simple cases. Some other way should be sought.

(5) Bound on the scattering amplitude $f(\theta)$. There are many occasions when one would prefer not to do a partial wave analysis, but would prefer to work with $f(\theta)$ itself. We have been able[12] to obtain a bound on $f(\theta)$ for scattering by a center of force, but the result involves a Green's function and is probably not generalizable in any simple and practical way to scattering by a compound system.

(6) Use of trial ground-state wave functions for isolated scattering components. The bounds that we have obtained do not, of course, require that we know the scattering function exactly. More significantly, they do not require that we know the composite bound-state wave functions exactly. Unfortunately, however, they *do* require that the ground-state wave functions of the isolated systems be known exactly. In electron hydrogen scattering, for example, we do not have to know the ground-state wave function of H^- exactly, but we do have to know the exact ground-state wave function of the hydrogen atom itself. Strictly speaking, then, the method is restricted to scattering processes involving only elementary particles, and a few two-particle Coulombic systems, such as the hydrogen atom and positronium. From a practical point of view, the method can be used profitably for scattering involving systems for which the ground-state wave function is known with reasonable accuracy, such as helium atoms and deuterons. It would be useful to obtain a minimum principle which allowed the use of trial ground-state functions for the isolated scattering components. On the other hand, it would probably not often be practical anyhow to attempt to obtain rigorous bounds, except perhaps at zero energy, for scattering involving complicated systems. Such problems would seem to call more for imaginative approximations than for rigor. The rigorous minimum principles for scattering should nevertheless be useful, even in their present form, for the interpretation of more complicated problems such as the scattering of electrons by O and N molecules, in that many of the various approximations that are often considered can be put to the test in an unambiguous way for some simple cases.

[12] L. Spruch and M. Kelly (unpublished).

APPENDIX A. EVALUATION OF RESIDUE

The residue that appears in the connection between the scattering lengths and $\sigma_{\text{tot}}(k)$ is defined by[7]

$$\text{Res.}=(-1/E_1)(m/2\pi\hbar^2)|I|^2,$$

where

$$I=\int d\tau w(\mathbf{r}_1,\mathbf{r}_2)V_i(\mathbf{r}_1,\mathbf{r}_2)e^{-\alpha_1\mathbf{n}_i\cdot\mathbf{r}_1}R_{\text{H}}(r_2).$$

$d\tau$ is the full volume element, $w(\mathbf{r}_1,\mathbf{r}_2)$ is the normalized spatially symmetric ground state of H^- with a binding energy of E_1 relative to the binding energy of a H atom, $R_{\text{H}}(r_2)$ is the normalized ground state of the H atom,

$$V_i(\mathbf{r}_1,\mathbf{r}_2)=-e^2/r_1+e^2/|\mathbf{r}_1-\mathbf{r}_2|,$$
$$\alpha_1=(2m/\hbar^2)|E_1|^{\frac{1}{2}},$$

and $\mathbf{n}_i$ is a unit vector in the direction of the incident beam. Since

$$(T_1-E_1)e^{-\alpha_1\mathbf{n}_i\cdot\mathbf{r}_1}=0,$$

where T_1 is the kinetic energy operator, and since

$$(T_2-e^2/r_2+13.6)R_{\text{H}}(r_2)=0,$$

we can rewrite I as

$$I=\int d\tau w(\mathbf{r}_1,\mathbf{r}_2)(\text{H}-E_1+13.6)e^{-\alpha_1\mathbf{n}_i\cdot\mathbf{r}_1}R_{\text{H}}(r_2).$$

Since

$$(\text{H}-E_1+13.6)w(\mathbf{r}_1,\mathbf{r}_2)=0,$$

upon integration by parts only the surface terms survive. For $r_1\rightarrow\infty$, we have

$$w(\mathbf{r}_1,\mathbf{r}_2)\rightarrow(\pi/a_0)^{\frac{1}{2}}C(\infty)R_{\text{H}}(r_2)e^{-\alpha_1 r_1}/r_1,$$

and we find

$$I=-(\hbar^2/2m)4\pi^{\frac{1}{2}}a_0^{-\frac{1}{2}}C(\infty).$$

The point in getting I into this form is that $C(\infty)$ is known quite accurately[13] from an analysis of various quite accurate H^- ground state functions. We find that $\text{Res.}=11.3a_0$.

[13] T. Ohmura, Y. Hara, and T. Yamanouchi, Progr. Theoret. Phys. (Kyoto) **22**, 152 (1959); T. Ohmura and H. Ohmura, Phys. Rev. **118**, 154 (1960).

APPENDIX B. APPROPRIATE VS INAPPROPRIATE NORMALIZATION

It is possible to make some definitive statements regarding the results that are obtained through the use of appropriate vs inappropriate normalization, that is, functions normalized according to Eqs. (2.2) and (2.9), respectively. For the purposes of the present appendix, we distinguish inappropriate normalization by the use of the subscript 2.

The analogue of Eq. (2.6) is

$$-\frac{1}{A}=-\frac{1}{A_t}+\frac{2\mu}{\hbar^2}\int u_{2t}Hu_{2t}d\boldsymbol{r}-\frac{2\mu}{\hbar^2}\int w_2Hw_2d\boldsymbol{r}, \quad \text{(B.1)}$$

where

$$w_2(\boldsymbol{r})\rightarrow(A^{-1}-A_t^{-1})r \quad \text{for} \quad r\rightarrow\infty.$$

To obtain a bound on $\int w_2Hw_2d\boldsymbol{r}$, we consider the inequality Eq. (2.8) with the particular choice $A_t=0$; the corresponding trial function will be denoted by $\tilde{u}_t$. We then have

$$A\leq(2\mu/\hbar^2)\int\tilde{u}_tH\tilde{u}_td\boldsymbol{r},$$

where the only requirements on $\tilde{u}_t$ are the boundary conditions

$$\tilde{u}_t(0)=0, \quad \tilde{u}_t(r)\rightarrow -r \quad \text{for} \quad r\rightarrow\infty.$$

Since $w_2(\boldsymbol{r})/(A_t^{-1}-A^{-1})$ satisfies precisely these boundary conditions, we immediately determine a bound on $\int w_2Hw_2d\boldsymbol{r}$. Upon substituting into Eq. (B.1), we find that

$$-\frac{1}{A}\leq-\frac{1}{A_t}+\frac{2\mu}{\hbar^2}\int u_{2t}Hu_{2t}d\boldsymbol{r}-\left(\frac{1}{A_t}-\frac{1}{A}\right)A. \quad \text{(B.2)}$$

As one immediate consequence, it follows that

$$-(1/A)\leq-(1/A_t)+(2\mu/\hbar^2)\int u_{2t}Hu_{2t}d\boldsymbol{r}$$

$$\text{for} \quad A>0. \quad \text{(B.3)}$$

Furthermore, recognizing that A_tu_{2t} is a permissible choice for u_t, it is trivial to check that Eq. (B.2) is entirely equivalent to Eq. (2.8). It is then clear that the bound obtained from Eq. (B.3), valid when A is positive, will be less accurate than that obtained from Eq. (2.8), since the former is obtained from the latter by dropping a term of well defined sign.

A similar situation holds in the case where N bound states exist, where, for $A>0$, the inequality

$$-\frac{1}{A}\leq-\frac{1}{A_t}+\frac{2\mu}{\hbar^2}\int u_{2t}Hu_{2t}d\boldsymbol{r}$$

$$-\frac{2\mu}{\hbar^2}\sum_{i=1}^{N}\frac{1}{E_{it}}\left(\int\phi_{it}Hu_{2t}d\boldsymbol{r}\right)^2$$

can be shown to be valid.

A variational calculation of the neutron-deuteron doublet scattering length, A_D, was recently performed by Efimov,[14] who used the inappropriate normalization. It was previously stated[15] that Efimov's calculation would have to be converted to that corresponding to the appropriate normalization in order to derive a bound on A_D. However, A_D is known to be positive experimentally, so that on the basis of the present discussion the Efimov calculation *does* give a bound on A_D. The conversion to appropriate normalization, while not necessary to validate the bound, will give an improved estimate of A_D.

[14] Y. N. Efimov, J. Exptl. Theoret. Phys. (U.S.S.R.) **35**, 137 (1958) [English transl.: Soviet Phys.—JETP **35**(8), 98 (1959)].
[15] L. Spruch and L. Rosenberg, Nuclear Phys. **17**, 30 (1960).

Regular Articles

New Complex Phase in the Copper-Gold System*

R. E. Scott†
Massachusetts Institute of Technology, Cambridge, Massachusetts
(Received May 23, 1960; and in final form, July 22, 1960)

At the composition 31.6 at. % gold, the equilibrium diagram shows a two-phase mixture of ordered and disordered material extending from 320°C to 350°C. However, a long anneal in this interval results in an x-ray pattern showing superstructure reflections with strong satellites. The satellite pattern is obtained both by lowering and raising the temperature, and hence is believed to represent an equilibrium structure. The satellite pattern is interpreted in terms of a Cu_3Au II type structure, which is derived from the ordered Cu_3Au I by introducing antiphase domain displacements $(\mathbf{a}_2+\mathbf{a}_3)/2$ at regular intervals along the a_1 axis, exactly analogous to the development of CuAu II from CuAu I. At 31.6 at. % gold, the period is $18a_1$ ($9\,a_1$ between consecutive domain boundaries). Between 320°C and 335°C, there is a two-phase mixture of Cu_3Au I and Cu_3Au II. From 335°C to about 345°C the structure is that of Cu_3Au II. From about 345°C to 350°C there is probably a two-phase mixture of Cu_3Au II and disordered material, but this has not been established. The satellite pattern is also obtained at the composition 29.2 at. % gold, and it is likely that the Cu_3Au II type structure exists over a range of compositions on the gold rich side of Cu_3Au.

I. INTRODUCTION

THE phase diagram of the copper-gold system reported by Hansen and Anderko[1] is largely based upon the electrical resistivity studies of Rhines, Bond and Rummel.[2] A small part of the diagram is shown in Fig. 1. At high temperatures, the material is disordered and statistically face-centered cubic at all compositions. At the composition CuAu, the critical temperature is $T_c=410$°C. Below 385°C the material has an ordered tetragonal structure called CuAu I. Between 385°C and 410°C there is the Johansson and Linde[3] ordered orthorhombic structure called CuAu II. This structure is obtained from CuAu I by reversing the copper and gold positions after every five unit cells along the a_1 direction. Between CuAu I and CuAu II, and again between CuAu II and disordered CuAu, there are two-phase regions. These regions exist over an appreciable composition range on either side of the CuAu composition, and they are indicated on the phase diagram.

At the Cu_3Au composition there is a critical temperature $T_c=390$°C, below which the material is ordered with a long-range order which is unity at low temperature, decreasing to $S=0.8$ just below T_c. On either side of the Cu_3Au composition, the diagram indicates a region which is considered to be a classical two-phase region consisting of a mixture of disordered and ordered material, the ordered material having a Cu_3Au type of long-range order.

However, if a composition around 32 at. % gold is heated to equilibrium at temperatures in the order-disorder transformation region, strong satellites appear around certain superstructure reflections. These satellites appear to represent an equilibrium structure which is quite different from the expected two-phase mixture of ordered and disordered material. Satellites from a sample of 32 at. % gold given a long heat treatment in the transformation region were first observed by Rudman.[4] Guinier and Griffoul[5] observed satellites on a quenched sample of approximately the Cu_3Au composition. Many other x-ray and electron diffraction studies[6–9] of the Cu-Au system have shown satellites about the superstructure reflections. In some of these

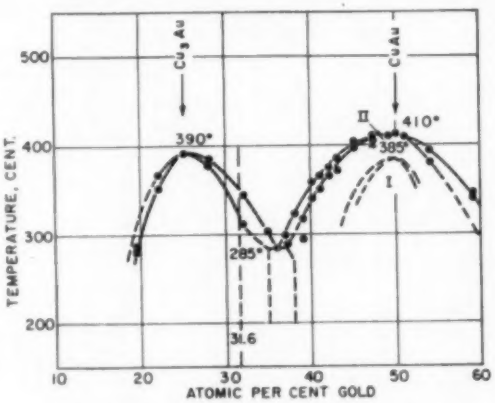

FIG. 1. Part of the Cu-Au equilibrium diagram, taken from Hansen and Anderko.

* Research sponsored by the U. S. Office of Naval Research.
† Present address: Space Technology Laboratories, Inc., Los Angeles, California.
[1] M. Hansen and K. Anderko, *Constitution of Binary Alloys* (McGraw-Hill Book Company, Inc., New York, 1958), p. 199.
[2] F. N. Rhines, W. E. Bond, and R. A. Rummel, Trans. Am. Soc. Metals **47**, 578 (1955).
[3] C. H. Johansson and J. O. Linde, Ann. Physik **25**, 1 (1936).
[4] P. S. Rudman, S.B. thesis, Massachusetts Institute of Technology (1951).
[5] A. Guinier and R. Griffoul, Rev. mét. **45**, 387 (1948).
[6] H. Raether, Z. angew. Phys. **4**, 53 (1952).
[7] S. Ogawa and D. Watanabe, J. Phys. Soc. Japan **9**, 475 (1954); Acta Cryst. **7**, 377 (1954).
[8] K. Fujiwara, J. Phys. Soc. Japan **12**, 7 (1957).
[9] M. Hirabayashi, J. Phys. Soc. Japan **14**, 262 (1959).

investigations it is not possible to decide to what extent the satellite pattern represents a true equilibrium state. A recent detailed treatment of the origin of satellites in the Cu-Au system has been given by Perio, Tournarie, and Okuzumi.[10]

This paper presents a detailed investigation of the single composition 31.6 at. % gold. The sample was held at various temperatures in the transformation range for times which were believed to be long enough to approximate equilibrium. The observed satellite pattern indicates that an ordered structure with periodic antiphase domains exists as an equilibrium phase in this region.

II. EXPERIMENTAL

Single crystals were prepared from 99.96 copper and 99.97 gold, so as to be approximately 32 at. % gold. The crystals were grown in a graphite crucible with a tapered nucleation end, in a furnace similar to that described by Lazarus and Chipman.[11] Immediately after growth they were homogenized just below the melting point. Sample slices with either 100 or 110 faces were cut, ground, and diamond polished. Back reflection Laue patterns showed the crystals to be single, although mosaic. The compositions were not precisely determined.

A single crystal with a 100 face was heated 10 days at 333°C and quenched in air. It was then mounted on an automatic diffractometer using Cu$K\alpha$ radiation with a single-crystal LiF monochromator. Intensity scans were made in the h_1h_2O plane of reciprocal space in the vicinity of the 110 superstructure reflection. The intensity contour plot is shown by Fig. 2. The pattern is seen to consist of a strong central peak, two strong satellites at the $h_1h_2h_3$ reciprocal space coordinates $(1\pm1/M)$, 1, 0 and two very faint satellites at $(1\pm3/M)$, 1,0, where M is approximately 18. The line h_1 1 0, along which the satellites lie, is normal to the 100 face of the crystal. No satellites of 110 were found in the h_3 direction (normal to the plane of Fig. 2).

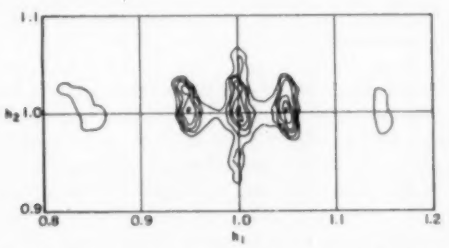

FIG. 2. Intensity contour plot in reciprocal space in the vicinity of the 110 reflection. Single crystal of copper-gold with 100 face, approximately 32 at. % gold, quenched from 333°C. Relative contour levels: 5, 10, 20, 40, 80, and 100, except faint satellites, which are barely detectable.

[10] P. Perio and M. Tournarie, Acta Cryst. **12**, 1032, 1044 (1959); H. Okuzumi, P. Perio, and M. Tournarie, Acta Cryst. **12**, 1039 (1959).

[11] D. Lazarus and D. R. Chipman, Rev. Sci. Instr. **22**, 211 (1951).

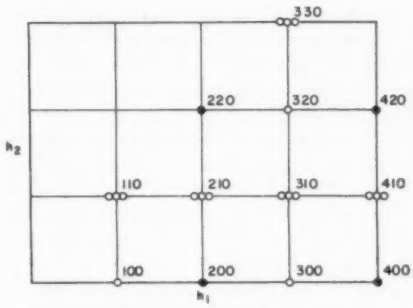

FIG. 3. Schematic representation of satellites observed from a single crystal of approximately 32 at. % gold quenched from 333°C. The satellites are on lines parallel to $h_1$00, which is normal to the 100 face of the crystal. Filled circles are fundamentals, open circles are central peaks or satellites of superstructure reflections.

When the crystal was similarly heated at 340°C, air-quenched and examined on the diffractometer, essentially the same pattern was obtained, except that the intensity of the central peak was much weaker in proportion to the primary satellites.

A number of reflections in the $h_1h_2$0 plane were similarly scanned, and the diffraction pattern is shown schematically in Fig. 3. The fundamental reflections are normal with no satellites. Of the superstructure reflections, there are satellites for $k+\ell=$odd, and no satellites for $k+\ell=$even. The satellites are in pairs approximately equidistant from the central spot. They are arranged along the h_1 direction, which is the direction normal to the 100 face of the crystal.

From this crystal with a 100 face, several thousandths of a centimeter were now removed by grinding, polishing, and etching. The new surface without further heat treatment gave a 110 reflection, with two satellite patterns which were equally intense and arranged in the h_1 and h_2 directions of Fig. 2. A crystal with a 110 face was ordered after cutting and polishing. About the 110 reflection there were satellites in both the h_1 and h_2 directions, rather than the one-dimensional satellite pattern that was obtained from the crystal with a 100 face. Thus, a crystal with a 100 face apparently takes the normal to this face for the preferred direction of the satellites within a thin surface layer. Below this layer there is no preference among the three orthogonal directions. If the crystal face is not 100, there is no preference even in the surface layer.

Powder briquets were used for studies of the growth and stability of the satellite pattern, and for measurements of lattice parameter and integrated intensities. The measurements were made with a Norelco diffractometer using filtered Cu$K\alpha$ radiation. Two powder briquets, approximately 32 at. % gold, obtained from B. W. Batterman, were used to study the growth of the satellite pattern at 325°C and 340°C, after being initially air-quenched from the disordered state. The 325°C specimen was air-quenched after three hours, 12

hours, two days, eight days, 16 days, and 32 days, and the (110) powder peak was observed. The growth of the satellite pattern proceeded by a diffuse gathering of the background after a few hours, a gradual increase in intensity and resolution into central peak and two satellites after two days, and subsequent sharpening to approximately the instrumental limitations by the end of 32 days. The specimen heated at 340°C proceeded similarly, but gave very sharp peaks after only two days. The positions of the satellites changed very little if at all during the growth.

One briquet was used to test whether the satellite pattern represents an equilibrium structure. The specimen was disordered one day at 375°C, quenched in air, then ordered two weeks at 330°C. The typical (110) satellite pattern was observed. It was again disordered, air-quenched, then ordered eight weeks at 270°C well below the transformation region, and air quenched. The normal (110) superstructure peak without satellites was observed. The briquet was then held for two weeks at 330°C and air-quenched, after which the satellite pattern was again observed. The specimen was again disordered, and the temperature lowered to 330°C without intermediate air quench. After 13 days at 330°C, it was air-quenched. The satellite pattern was again observed. Since the satellite pattern was obtained both by raising the temperature of a normally ordered material and by lowering the temperature of a disordered material, we conclude that the satellite pattern represents an equilibrium condition.

In all air quenches, the specimens were cool enough to handle after several minutes, and so had cooled to a temperature at which the atoms were immobile in the structure in a fraction of a minute. The justification for believing that the results are unaffected by quenching is found in the facts that the continuity of growth of the satellite pattern was not disturbed by intermediate quenching, and that the satellite pattern was obtained from the disordered form both with and without intermediate quench.

For the measurements of the lattice parameter and superstructure integrated intensity, four identical powder briquets were prepared in the standard way. They were sealed in evacuated tubes flushed several times with prepurified nitrogen, and subsequent diffraction patterns showed no lines from an oxide of copper. The composition was determined to be 31.6 at. % gold, by referring the lattice parameter in the disordered state to a chemically analyzed standard. The disordered briquets were then heat treated at various temperatures spanning the order-disorder transformation region. The times were believed to be sufficiently long so that no appreciable further change was taking place: 53 days at 304°C, 45 days at 319°C, 43 days at 330°C, and 35 days at 339°C. Measurements were also made at a later time on the 339°C specimen heated a further 24 days at 335°C, the 330°C specimen heated 24 days at 325°C, and the 304°C specimen heated seven days at 352°C, and again disordered and heated 21 days at 344°C. All specimens were heated in electric furnaces, regulated to about one or two degrees centigrade, and then were air-quenched. Regulation was checked by measuring the temperatures at various hours during the day and night. The furnace room was kept closed, and slow changes in ambient temperature were compensated for by small adjustments in furnace current. Regulation was found to be adequate using either Sola regulators or a West controller operating "high-low."

Diffractometer tracings for the (110) powder pattern peak for the 319°C, 325°C, 330°C, 335°C, 344°C, and 352°C samples are shown by Fig. 4. To be comparable, the peak heights should be doubled for the 319°C and 325°C tracings. Below 319°C there is a central peak only. Between 319°C and 325°C, satellites appear. With increase in temperature, the satellites increase and the central peak diminishes. Through a range including 335°C and 344°C the ratio of satellite to central peak intensity remains constant. At the temperature 352°C, both satellites and central peak have disappeared and long-range order no longer exists.

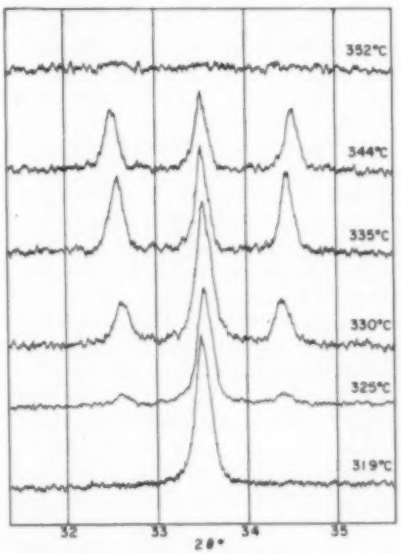

FIG. 4. Powder pattern recordings of the central peak and satellites for the (110) reflection from a sample of 31.6 at. % gold, air-quenched from the indicated temperatures. Filtered CuKα radiation. To be comparable, the peak heights should be doubled for the 319°C and 325°C samples.

To explore more fully the variation of the satellite and total superstructure integrated intensity, powder pattern tracings were made of the fundamental and superstructure reflections (100), (110), (111), (200), (210), (211), (220), and (311). Corrected areas $A(hkl)$ were obtained by correcting the measured areas for scale factor, multiplicity, the Lorentz polarization

factor, and the angular dependence of the structure factor. Additional experimental factors are about equally weighted in the sums $A(S)=A(100)+A(110)+A(210)+(A211)$ for the superstructures, and $A(F)=A(111)+A(200)+A(220)+A(311)$ for the fundamentals. The ratio $A(S)/A(F)$ may then be taken as a measure of the average square of the long-range order in the crystal. The ratio $A(S)/A(F)$ in arbitrary units is shown as a function of the quenching temperature in Fig. 5. The fraction of the total area of a superstructure peak which comes from the satellites alone was evaluated from the (110) and (210) powder reflections, where allowance was made for the fact that on a (210) powder pattern half of the satellites occur at the same 2θ as the central peak. This fraction multiplied by $A(S)/A(F)$ is also shown in Fig. 5.

The lattice parameter was determined from the (400), (331), and (420) powder reflections for each specimen by extrapolating to $\cos\theta=0$, the values of a calculated

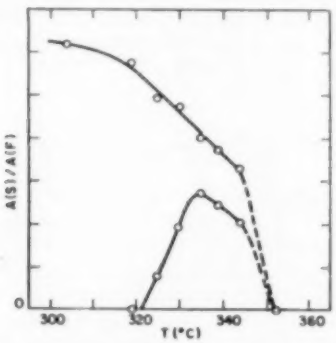

FIG. 5. Ratio of superstructure to fundamental corrected peak areas $A(S)/A(F)$ against the temperature of quenching, for a powder sample 31.6 at. % gold. Top curve includes central peaks and satellites; lower curve satellites only.

from the position of each α_1 peak maximum. The lattice parameter values are shown in Fig. 6. The large increase in going from 320°C to 350°C is of course due to the disappearance of long-range order. For these high order fundamentals, the α_1 and α_2 peaks were well resolved. Although there was no splitting of the α_1 and α_2 peaks, there was a noticeable variation in peak breadth. The $\Delta(2\theta)$ breadth of the (331) reflection is shown in Fig. 6. There is a marked increase between 320°C and 335°C, which can be interpreted as due to the existence of two phases in this temperature interval.

To determine whether the satellite pattern exists in equilibrium at compositions other than 31.6 at. % gold, a powder briquet of composition 29.2 at. % gold was prepared. It was heated at a temperature of 372°C, air-quenched, and the satellite pattern was obtained. Although the examination of this composition was preliminary and incomplete, it appeared that the temperature interval in which satellites existed was narrower than that for the 31.6 at. % gold sample.

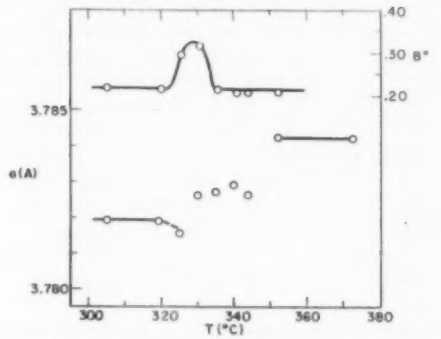

FIG. 6. Sample 31.6 at. % gold, quenched from various temperatures. Upper curve: breadth in degrees 2θ of the $(331)_{\alpha_1}$ fundamental reflection. Lower set of points: the lattice parameter determined from high order fundamentals.

III. INTERPRETATION

The diffraction patterns show satellites only on certain superstructure reflections, and the effect is not to be confused with cases arising from periodic lattice parameter or composition variations which give satellites also on the fundamental reflections. Let $\mathbf{a}_1\mathbf{a}_2\mathbf{a}_3$ be the axes defining a cubic cell containing four atoms. The simplest interpretation is in terms of antiphase domains which are nearly periodic in one dimension. We shall assume antiphase domain boundaries perpendicular to the $\mathbf{a}_1$ axis and occurring at intervals $\mathbf{a}_1M/2$. This produces a super cell with axes $\mathbf{A}_1\mathbf{a}_2\mathbf{a}_3$ where $\mathbf{A}_1=M\mathbf{a}_1$. The displacement which differentiates the structures on either side of an antiphase domain boundary is taken to be $\mathbf{\delta}=(\mathbf{a}_2+\mathbf{a}_3)/2$. This defines a system of antiphasing which is exactly analogous to that in the well known CuAu II.

In each cubic cell we assume that one position is occupied predominantly by Au and the other three positions by an average composition made up of the copper and the remaining gold. For the fully ordered state, this average composition is given by

$$G=\tfrac{1}{4}m_{\mathrm{Cu}}(\mathrm{Cu})+\tfrac{1}{3}(m_{\mathrm{Au}}-\tfrac{1}{4})(\mathrm{Au}),$$

where $m_{\mathrm{Au}}=0.316$ and $m_{\mathrm{Cu}}=0.684$. The distribution within the cubic cells is then given in Table I.

For the cubic cell $\mathbf{a}_1\mathbf{a}_2\mathbf{a}_3$ we use indices hkl, and for the supercell $\mathbf{A}_1\mathbf{a}_2\mathbf{a}_3$ indices Hkl. For the supercell, the contribution to the structure factor by the first cubic cell is given by

$$F_0=f_{\mathrm{Au}}+f_G\{\exp[\pi i(H/M+k)]+\exp[\pi i(k+l)]+\exp[\pi i(l+H/M)]\}. \quad (1)$$

For the complete supercell,

$$F(Hkl)=F_0\sum_{m=0}^{M/2-1}\exp[2\pi imH/M]+F_0\exp[\pi i(k+l)]\sum_{m=M/2}^{M-1}\exp[2\pi imH/M],$$

TABLE I. Distribution within the cubic cells.

Position	Normal domain	Antiphase domain
000	Au	G
$\frac{1}{2}$, $\frac{1}{2}$, 0	G	G
$\frac{1}{2}$, 0, $\frac{1}{2}$	G	G
0, $\frac{1}{2}$, $\frac{1}{2}$	G	Au

which reduces to

$$|F(Hkl)| = 2|F_0|\cos\frac{\pi}{2}(H+k+l)\frac{\sin\pi H/2}{\sin\pi H/M}. \quad (2)$$

It is convenient to express the structure factor of the supercell in terms of the indices hkl of the four-atom cell. Let $H/M = h \pm n/M$ where n is an integer.

$$|F(h,n,k,l)| = 2|F_0|\cos\frac{\pi}{2}(k+l\pm n)\frac{\sin\pi n/2}{\sin\pi n/M} \quad (3)$$

$$F_0 = f_{Au} + f_G\{\exp[\pi i(h+k\pm n/M)] + \exp[\pi i(k+l)] + \exp[\pi i(h+l\pm n/M)]\}. \quad (4)$$

The three types of reflections allowed by Eq. (3) are as follows:

hkl unmixed, $n=0$, fundamentals

$$F(hkl) = M(f_{Au}+3f_G), \text{ no satellites;}$$

hkl mixed, superstructure reflections

$(k+l)$ = even, $n=0$, central peak (5)

$$F(hkl) = M(f_{Au}-f_G), \text{ no satellites;}$$

$(k+l)$ = odd, n = odd, satellites

$$F(h\pm n/M,k,l) = (f_{Au}-f_G)2(\sin\pi n/M)^{-1}, \text{ no central peak.}$$

This simple model involving unidirectional antiphasing seems to be capable of explaining the observations. The satellites observed by single crystal measurements are shown by Figs. 2 and 3. They are completely explained by the model. However, central peaks on superstructure reflections such as 110, 210, 310, etc., are also recorded on Figs. 2 and 3, and these are not predicted by the model. The 110 reflection of Fig. 2 was obtained from a sample with a 100 face, and the satellites indicate that the antiphase boundaries are mainly parallel to the crystal surface. However, there is no reason to expect a perfect orientation of the antiphase boundaries parallel to the 100 crystal face; there can be some contribution from material in which the antiphase boundaries take the other two orthogonal orientations. If we call $\mathbf{a}_1$ the axis perpendicular to the antiphase boundaries regardless of their orientation in the crystal, Fig. 2 could be described as mainly a 110 reflection with some 101 and 011 contributions. The 101 contribution gives satellites represented by the weak wings in the h_2 direction of Fig. 2, and the 011 contribution gives the weak central peak observed even at 340°C. From the powder pattern data it will be concluded that in the temperature range 320°C–335°C there is a two-phase mixture of normal ordered material and material with the antiphased structure of our model. Hence at 333°C a central peak would be expected from the normal material and also from the part of the antiphased material with boundaries not parallel to the crystal face. At 340°C the material should be all in the antiphased form, and the central peak is due only to the antiphased material with boundaries not parallel to the crystal face.

For a powder sample the direction normal to the antiphase boundaries takes, with equal probability, the three directions $\mathbf{a}_1\mathbf{a}_2\mathbf{a}_3$. Equations (5) apply if for each powder pattern reflection (hkl) we average over all appropriate interchanges of hkl. For the (110) powder pattern reflection it is enough to average the contributions from 110, 101, and 011. Of the first two, each contribute a pair of satellites, while the third one has only a central peak. The peak areas are proportional to the square of the structure factors given by Eqs. (5). Since there are four primary satellites with $n=1$ and one central peak, the ratio of the satellite area to the combined satellite and central peak should be

$$\frac{4[2/(\sin\pi/M)]^2}{4[2/(\sin\pi/M)]^2+M^2}.$$

From the observed satellite separations $M=18$, approximately, and hence the above ratio is very nearly independent of M and equal to $16/(16+\pi^2)=0.62$. From Fig. 5 it is seen that, in the temperature interval 335°C to 344°C, the measured ratio of satellite to satellite plus central peak intensity is nearly constant and equal to about 0.64. The agreement is quite satisfactory, and we conclude that in this temperature interval the material is all in the form covered by the model, involving antiphase domain boundaries at intervals $M\mathbf{a}_1/2$.

Referring again to Fig. 5, it is seen that in the temperature interval 320°C–335°C the ratio of satellite intensity to total superstructure intensity increases from zero to the value 0.64. Our simple model does not explain this change in the ratio. The two most obvious interpretations are as follows:

(a) A more complex model which in the 320°C–335°C range corresponds to a continuous change from an ordered structure without antiphase domains to the fully antiphased structure represented by our model.

(b) A two-phase region containing varying proportions of ordered material without antiphase domains and the fully antiphased material of our model.

The second interpretation is the simpler and the more probable, and in addition there is experimental evidence to support it. The strongest support for a two-phase region would be given by a splitting of the high angle fundamental reflections. No appreciable change in lattice constants would be expected from antiphasing

alone. However, for a two-phase region there should be a separation into normal material with a lower gold content and antiphased material with a higher gold content. A difference in composition produces a difference in lattice parameter. Even if this difference is too small to produce two separate reflections, it can show up by a broadening of high order fundamental reflections. From Fig. 6 it is seen that in the 320°C–335°C range there is a very noticeable broadening of the (331) fundamental reflection, and this is exactly the temperature interval under discussion. Exactly the same variation is shown by the (420) reflection. Although the evidence is not as definite as would be desirable, the simplest interpretation is to conclude that in the temperature interval 320°C–335°C, there is a two-phase mixture of normal and antiphased material.

In analogy to the common notation CuAu I and CuAu II, it is convenient to use the notation Cu_3Au I and Cu_3Au II. In this notation we would say that below 320°C the material has a Cu_3Au I-type structure, ordered but without antiphase domains. Between 320°C and 335°C it is a two-phase mixture of Cu_3Au I and Cu_3Au II type structures. From 335°C to about 345°C it is the Cu_3Au II type structure with unidirectional periodic antiphase domains.

Between Cu_3Au II and the disordered phase there is presumably another two-phase region extending from about 345°C to 350°C. Unfortunately, this investigation did not include any samples annealed in this rather narrow temperature range, and hence no definite statement can be made for this upper part of the transformation range. If this narrow temperature range is indeed a two-phase mixture there should be a very noticeable broadening of the high order fundamentals.

IV. DISCUSSION AND CONCLUSIONS

At the composition 31.6 at. % gold, it has been shown that a complex phase Cu_3Au II exists in the temperature interval which has been thought previously to be just a two-phase mixture of ordered and disordered material. The complex phase represents an equilibrium structure. It is formed from the ordered cubic phase Cu_3Au I by introducing antiphase domains with displacements $(\mathbf{a}_2+\mathbf{a}_3)/2$ at regular intervals along the $\mathbf{a}_1$ axis, quite analogous to the formation of CuAu II from CuAu I. Between 320°C and 335°C there is a two-phase mixture of Cu_3Au I and Cu_3Au II. Between 335°C and about 345°C, Cu_3Au II is the equilibrium structure. Between about 345°C and 350°C there is presumably a two-phase mixture of Cu_3Au II and disordered material. Although this has not yet been established, it is probable by analogy to Newkirk's[12] finding of a two-phase mixture of CuAu II and disordered material near the CuAu composition. At the composition 31.6 at. % gold, the period of antiphasing is about $M=18$.

A preliminary examination indicated that the Cu_3Au II type structure also existed at the composition 29.2 at. % gold. Presumably the Cu_3Au II type structure exists over a range of composition on the gold rich side of Cu_3Au, similar to the existence of CuAu II over a range of composition about CuAu. For Cu_3Au II, however, the temperature interval is much narrower than that for CuAu II. It would appear that the boundary lines could be determined rather readily on the gold rich side of Cu_3Au by careful measurements of the width of high angle fundamental reflections.

The period of antiphasing was found to be $M=10$ at CuAu and about $M=11$ at 40 and 60 at. % gold.[3] At 31.6 at. % gold, $M=18$, approximately. A survey of the variation of M with composition would be extremely interesting, and it might be very helpful in trying to understand the reason for antiphasing in this system. The model on which Eqs. (5) are based predicts satellites for $n=1$, 3, 5, etc. Powder patterns show only the primary satellites for $n=1$. On the single crystal pattern of Fig. 2, there were faint $n=3$ satellites, much weaker than predicted by Eqs. (5). This could be explained by assuming that the antiphasing is not strictly periodic, and that M varies a little about the most probable value $M=18$.

A rather extensive x-ray study of the gold rich side of the Cu_3Au composition by Jaumot and Sutcliffe[13] completely missed the Cu_3Au II type structure. Presumably this was because they worked with the 300 superstructure reflection. On a powder pattern this reflection shows no satellites, and even with a single crystal, satellites can be observed only with suitable orientation of antiphasing and appropriate scanning in reciprocal space.

ACKNOWLEDGMENT

The author wishes to express his gratitude to Professor B. E. Warren, who suggested this topic, for his discussions and advice during the course of the investigation and during the preparation of the manuscript. He is also deeply indebted to Dr. B. S. Borie, whose comments and suggestions have been extremely valuable throughout the course of this investigation.

[12] J. B. Newkirk, J. Metals **5**, 823 (1953).
[13] F. E. Jaumot and C. H. Sutcliffe, Acta Met. **2**, 63 (1954).

Experimental Investigation in Lead of the Whipple "Meteor Bumper"*†

ARNOLD E. OLSHAKER
Massachusetts Institute of Technology, Cambridge, Massachusetts

(Received June 8, 1960)

Experimental results are presented to indicate the effects of a thin protective shield on reducing the penetration of simulated meteoroids. The study is mainly of lead impacting lead at 2.5 km/sec. The effects of thickness and separation of the shield are investigated. It is shown that a shield of thickness slightly less than half the projectile diameter at a separation of about five projectile diameters reduces the penetration of shield plus target to approximately one-third the depth of the unshielded crater. This shield is also effective against hardened steel ball bearings. Based on the assumption that the "fluid impact" penetration mechanism of lead at this velocity is qualitatively similar to that of structural materials at meteor velocities, it is concluded that the weight saving potential of "bumper" construction will make its use mandatory for space structures designed by the penetration condition.

INTRODUCTION

THIS study was carried out in the Aeroelastic and Structures Research Laboratory of MIT's Department of Aeronautics and Astronautics. The motivation behind the work is the author's belief that the increasing sizes and exposure times of thin-skinned space vehicles are hastening the time when meteoroid protection will become a major design condition.[1]

As early as 1946, Dr. F. L. Whipple, Director of the Smithsonian Astrophysical Observatory, postulated that a very thin "shield" surrounding a body would efficiently reduce meteoroid impact penetration.[2] Willig and Semon verified this concept by firing several exploratory shots at aluminum shields at 15 000 ft per sec.[3] It was felt that this order of velocity is an absolute minimum for investigating hypervelocity impact effects in aluminum or steel targets. This conclusion may be inferred from the theoretical solutions of similar material impact in aluminum and steel at meteor velocities by Dr. R. L. Bjork.[4] Especially for investigations of penetration reduction which involve deceleration of particles by shields, it becomes mandatory for initial projectile velocities to be well within the so-called hypervelocity region if results are to apply to meteoritic impact. The lower limits of this region are by no means clearly defined, but most noticeable in Bjork's solution are the predictions of roughly hemispherical, "fluid-type" craters and penetration variation with velocity to the one-third power, which is to say crater volume proportional to projectile momentum. These were approximately the results found experimentally by Kinecke[5] at velocities over 1 km/sec in impacting pure lead with steel and lead projectiles. It would appear from this correlation that lead might be suitable as a convenient "model" material to investigate the problem of meteoroid penetration reduction. Based upon this assumption, this paper is a preliminary attempt to study the dependence of total particle penetration upon thickness and separation of a thin shield and to indicate optimum and minimum weight shield configurations, if any.

DESCRIPTION OF APPARATUS AND EXPERIMENTAL TECHNIQUES

The program was carried out with a standard smooth-bore gun chambered for the 0.243 caliber cartridge. The barrel assembly was purchased from the Utah Research and Development Company and enclosed in a range which was evacuated to a pressure of half a

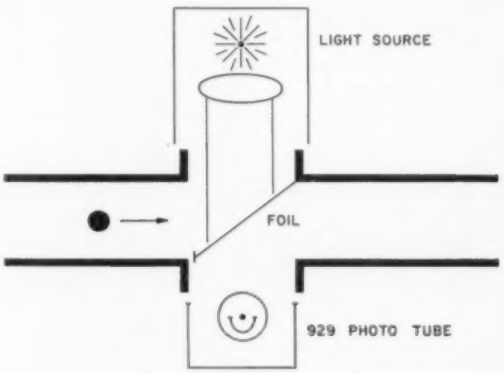

FIG. 1. Velocity signal station.

* S. M. thesis in the Department of Aeronautics and Astronautics, Massachusetts Institute of Technology.

† Presented to the Fourth Hypervelocity Impact Symposium, Eglin Air Force Base, Florida, April, 1960.

[1] L. E. Kaechele and A. E. Olshaker, "Meteoroids—implications for the design of space structures" (*Institute of Aeronautical Sciences Manned Space Stations Symposium, Los Angeles, California, April, 1960*).

[2] F. L. Whipple, "Possible hazards to a satellite vehicle" [Project RAND, Douglas Aircraft Corporation, Santa Monica, California, 1946 (Secret)].

[3] F. J. Willig and H. W. Semon, "A multistage H. E. actuated hypervelocity gun" (*Proceedings of Third Symposium on Hypervelocity Impact, Armour Research Foundation, February, 1959*), pp. 507–509.

[4] R. L. Bjork, "Effects of a meteoroid impact on steel and aluminum in space" (RAND Corporation, Santa Monica, California, paper P-1662, December, 1958); included in *Proceedings of the Tenth International Astronautical Congress, London, 1959* (Springer-Verlag, Vienna, 1960).

[5] J. H. Kinecke, Jr., "An experimental study of crater formation in lead" (*Proceedings of Third Symposium on Hypervelocity Impact, Armour Research Foundation, February, 1959*). pp. 157–182.

millimeter of mercury for all reported results. Muzzle to target distance was fifteen feet, including sabot barrier, velocity measurement stations, and target viewing ports.

Velocities were measured by two optically tripped signals, respectively, starting and stopping a microsecond counter. A signal generating station is shown schematically in Fig. 1. Velocity inaccuracies introduced by the inclination of the foil are below half a percent for two such stations spaced three feet apart. Velocities measured by this method were 2.55±0.05 km/sec for the lead projectiles and 2.60±0.10 km/sec for the steel projectiles. These velocities were not checked independently against another system, but agree with calibration values furnished with the barrel assembly. About

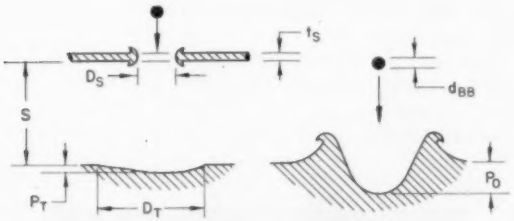

FIG. 2. Definition of symbols.

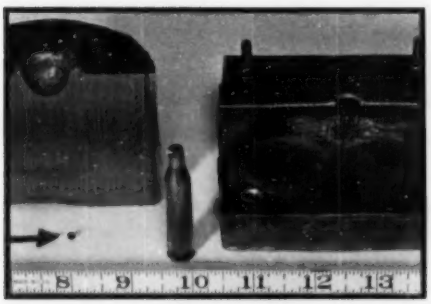

FIG. 3. Typical lead specimens.

30% of the total shots fired were arranged to furnish velocity data. These data are assumed to be a calibration of the gun performance for the entire experiment.

Projectiles fired were one-eighth inch diameter spheres held in the barrel by a phenolic sabot made in two halves. The sabot halves separated after leaving the barrel, permitting the projectile to pass alone through the center hole of a barrier. The lead projectiles were commercial BB shot, roughly one percent antimony, sorted to a weight of 0.188±0.001 g. Steel projectiles were hardened steel ball bearings, 0.133±0.001 g. Target and shield material was corroding lead, 99.9% pure.

In order to assume semi-infinite target depths, targets were always at least five times as thick as the penetration. Penetration was defined as the penetration of a

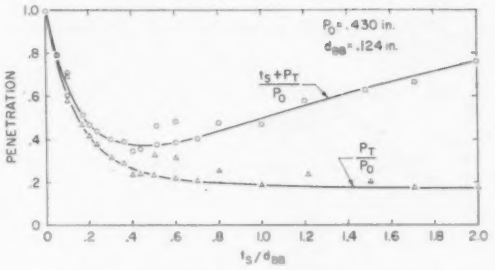

FIG. 4. Penetration vs shield thickness for constant shield separation of one-half inch.

probe with a hemispherical tip of 0.040 in. diam. The reason for this is that occasionally there would be small single pinpoint fissures at the bottom of what otherwise were well defined shallow pits. It was felt that the most reasonable description of the damage to the target was with such a probe, even though a needle point would have gone slightly deeper into a small percentage of the targets.

Nomenclature is defined by Fig. 2 and typical specimens are shown in Fig. 3. The shield shown is 0.054 in. thick and 1/2 in. from the target.

RESULTS AND DISCUSSION

Figure 4 shows penetration vs shield thickness for a constant shield separation. Figure 5 shows typical targets behind two different thickness shields at the half-inch separation.

A simple, physical explanation for the mechanism which makes this powerful effect possible has been proposed by David Lull of the A. D. Little Corporation in an unpublished note.[6] Assuming a thin shield, it follows that the shear plug punched out by the projectile will be the order of its cross-sectional area. Conserving axial momentum in an inelastic collision, there is seen to be a large "loss" of kinetic energy. Neglecting sound and light as well as shock energy in the shield leaves very few remaining energy-absorbing devices. Based upon the assumption that the strong shocks "bouncing around in the pellet" might have already fragmented it, Lull attempts equating the excess kinetic energy to

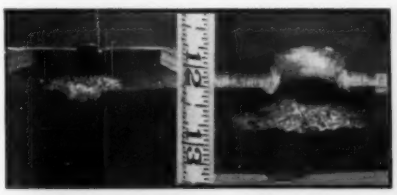

FIG. 5. 0.021-inch shield (0.17 d_{BB}) and 0.183-inch shield (1.47 d_{BB}) at one-half inch separation.

[6] D. B. Lull, "Analysis of impact of hypervelocity pellet with a thin shield" (Memorandum of A. D. Little Corporation, Cambridge, Massachusetts, December 29, 1959; Case 62509-1).

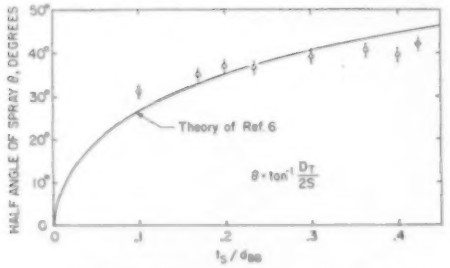

FIG. 6. Comparison of experimental half-angles of spray with those predicted by simplified analytical model.

spherical, radial expansion of the projectile fragments. The results of this calibration lead to the predicted half-angle of spray θ, which is a function of shield thickness only. Figure 6 shows this predicted angle variation compared to the angles measured from the crater diameters of the constant shield separation data.

The experimental values asymptote to 45° for shields thicker than those shown. The plot cannot be continued, however, because neglecting the energy in the shield shock is not possible for thick shields.

The penetrating power of the ball of fragments is not yet known analytically, but as Lull concludes, "Our argument does not show how or why the pellet shatters except to show that there is plenty of energy to explain the observed phenomena. The penetration or destructiveness of the individual grains is apparently very small."

The effect of separation on the minimum penetration shield thickness of Fig. 4 is shown in Fig. 7. A reason for the half-inch separation on the thickness variation plots is seen here. For the 0.054 shield, which is of most interest because of its maximum protective efficiency, the most protection for the least separation occurs at a separation of four or five projectile diameters. Figure 8 depicts typical target damage behind two different separations of the 0.054 shield.

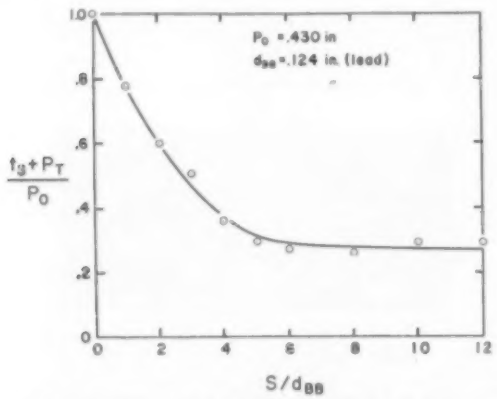

FIG. 7. Penetration vs shield separation for constant shield thickness of 0.054 inch.

An attempt to put effectiveness of the shield to a more severe test was made at the end of the program. Hardened steel ball bearings were fired at lead targets with shields separated one-half inch. Results almost identical to Fig. 4 were obtained. The minimum point was slightly higher than that of the lead projectiles, but the breakup of the projectiles and appearance of the target craters were indistinguishable from the soft projectile results. Since the impact velocity of 2.6 km/sec is below the "fluid" impact range for steel, it is the author's opinion that this result is a strong argument in favor of thin shield protection. It might even be that this similar result for different projectiles may indicate a possibility of designing for meteroid protection without exact knowledge of the particles' physical makeup.

One final point was considered. Would an effective shield become more so if divided into two half-thickness shields at the same over-all separation? The answer was found to be negative. Two 0.027 bumpers were spaced 1/4 in. and 1/2 in., respectively, from the target. The target penetration was twice as great as that behind a single 0.054 shield at 1/2 in. This result was obtained twice with the lead projectiles.

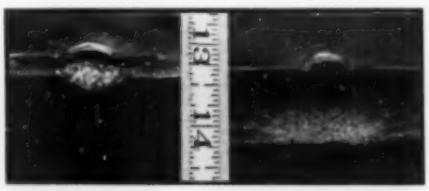

FIG. 8. 0.054-inch shield (0.43 d_{BB}) at one-quarter inch and one-inch separations.

CONCLUSION

Based on the assumption that the "fluid impact" penetration mechanism of lead at this velocity is qualitatively similar to that of structural materials at meteor velocities, it is concluded that the weight saving potential of the Whipple bumper will make its use mandatory for structures designed by the penetration condition.

ACKNOWLEDGMENTS

The author would like to gratefully acknowledge the guidance of his thesis supervisor, Professor Paul E. Sandorff of MIT's Department of Aeronautics and Astronautics, and that of Dr. Walter Herrmann of the Aeroelastic and Structures Research Laboratory. Professor Harold Edgerton of the MIT Strobe Laboratory was more than generous with equipment, as was Robert Schildkraut with his ideas and time.

JOURNAL OF APPLIED PHYSICS VOLUME 31, NUMBER 12 DECEMBER, 1960

Magnetic Viscosity Due to Solute Atom Pairs. Part I. Theory of the Effect*

G. Biorci, A. Ferro,† and G. Montalenti
Istituto Elettrotecnico Nazionale Galileo Ferraris, Centro Studi per l'Elettrofisica del C.N.R., Torino, Italy
(Received May 27, 1960)

It is shown that solute atom pairs in ferromagnetic alloys, as well as the interstitial atoms in iron, can give magnetic viscosity.

The viscosity field of the alloys vs wall displacement is determined for various crystal structures. The maximum value of the viscosity field is related to the anisotropy energy induced in the same materials by heat treating in a magnetic field.

INTRODUCTION

THE possibility of observing a magnetic viscosity in alloys, due to preferential orientation of pairs of solute atoms, has been foreseen by Néel[1] and Taniguchi.[2] Their qualitative considerations on this subject allow one to explain some results on anomalies of permeability observed by Ferro and Montalenti,[3] Külwein,[4] and Fahlenbrach.[5]

However, no quantitative theory of the magnetic viscosity due to solute atom pairs has been given, nor have proper experiments been performed, at least to our knowledge.

In Part I of this paper we give the theory of the effect. The experimental results obtained in various Fe-Si and Fe-Al alloys will be discussed in Part II.

MAGNETIC VISCOSITY IN ALLOYS

The theory of magnetic viscosity due to solute atom pairs is very similar to that of the viscosity due to interstitial atoms.[6] Néel[6] considers a small volume dv of the material, where the magnetization vector has rested in a given direction (α,β,γ) for a long time. If the magnetization vector in that small volume is suddenly turned to a new direction (α',β',γ'), this rotation requires an energy per unit volume

$$E_d = W_v(\alpha^2\alpha'^2+\beta^2\beta'^2+\gamma^2\gamma'^2), \quad (1)$$

the direction cosines being referred to the crystallographic axes. From this property of a small volume dv, Néel[6] deduced the existence of a viscosity field in a multidomain structure under proper condition.

On the other hand, if we anneal the material in a magnetic field the energy E_d appears throughout the specimen, and can be observed macroscopically as an uniaxial anisotropy energy still given by Eq. (1). Hence a specimen of α iron with interstitial atoms should show both magnetic viscosity and magnetic annealing. This point has been discussed by us in another paper,[7] and confirmed also by Graham.[8]

In the case of alloys, from a theory of Néel,[9] we know that the anisotropy energy induced by heat treating the alloy in a magnetic field, under the assumption that the interaction energy between a pair of solute atoms and the magnetization vector $\mathbf{J}_s$ is of the type $w\cos^2\varphi$ (φ being the angle between $\mathbf{J}_s$ and the axis of the pair), is given by

$$E_d = W_v'\left[\tfrac{1}{6}+S_{22}+(S_4-S_{22})(\alpha^2\alpha'^2+\beta^2\beta'^2+\gamma^2\gamma'^2) + 4S_{22}(\alpha\alpha'\beta\beta'+\beta\beta'\gamma\gamma'+\gamma\gamma'\alpha\alpha')\right], \quad (2)$$

where α, β, γ, α', β', γ' have the same meaning as in Eq. (1) and the S's are constants for each crystallographic structure.[9] Now we can refer this energy to a small volume dv, and ask if an anisotropy energy of this type can give rise also to magnetic viscosity.

To do this, we have simply to repeat the treatment of Néel[6] which leads from Eq. (1) to the existence of a magnetic viscosity, making use of Eq. (2) wherever Eq. (1) was present; or, more generally, we can replace Eq. (1) with a general $E_d(\alpha,\beta,\gamma,\alpha',\beta',\gamma')$.

Let us consider a Bloch wall separating two semi-infinite domains, and take three reference axes; the x axis perpendicular to the plane of the wall, the y axis parallel to the magnetization vector in one of the domains separated by that wall. In each point of the space, the magnetization vector is defined by its amplitude, which is constant and equal to J_s, and by the angle φ with the y axis, since the magnetization vector lies in planes parallel to the wall. Hence the direction cosines of the magnetization vector, at each point, become 0, $\cos\varphi$, and $\sin\varphi$, respectively.

Now let us consider two positions of the wall, in the first of which the middle plane of the wall has abscissa u. We assume that the wall has rested in that position for a long time. The second position, having abscissa u', is reached by a rapid displacement from the rest position. Obviously, in each point of space the magnetization

* This research has been sponsored by the U. S. Air Force Office of Scientific Research of the Air Research and Development Command, U. S. Air Force, through its European Office.
† Istituto Nazionale di Fisica Nucleare, Sezione di Torino.
[1] L. Néel, J. Appl. Phys. **29**, 3S (1958).
[2] S. Taniguchi and T. Ohmura, Sci. Repts. Research Insts. Tohoku Univ. **A6**, 330 (1954).
[3] A. Ferro and G. Montalenti, Nuovo Cimento Suppl. **6**, 1214 (1957).
[4] H. Külwein, Z. Physik **32**, 860 (1933).
[5] H. Fahlenbrach, Ann. Physik **2**, 355 (1948).
[6] L. Néel, J. phys. radium **13**, 250 (1952).
[7] G. Biorci, A. Ferro, and G. Montalenti, Nuovo Cimento (to be published).
[8] C. D. Graham, *Magnetic Properties of Metals and Alloys* (American Society for Metals, Cleveland, Ohio, 1959), p. 288.
[9] L. Néel, J. phys. radium **15**, 225 (1954).

vector, in general, rotates. If φ' is the new angle made with the y axis, in each elemental volume of the specimen the energy E_d can be expressed as

$$E_d = E_d(\varphi,\varphi'), \tag{3}$$

obtained from the original $E_d(\alpha,\beta,\gamma,\alpha',\beta',\gamma')$ by expressing all the cosines as functions of φ and φ'.

The total energy per unit surface of the wall required to make the displacement $(u'-u)$ is the integral of $E_d(\varphi,\varphi')$ for all values of x. That is,

$$W = \int_{-\infty}^{+\infty} E_d(\varphi,\varphi')dx. \tag{4}$$

The functions $\varphi(x)$, known from the theory of the Bloch walls,[10] are the following:

$$\begin{aligned} &\varphi = \arctan\exp[(x-u)/d] \quad \text{for} \quad 90^\circ \text{ walls} \\ &\varphi = \text{arctang}\sinh[(x-u)/d] \quad \text{for} \quad 180^\circ \text{ walls,} \end{aligned} \tag{5}$$

where $d = d_0(J/6K)^{\frac{1}{2}}$, d_0 is the atomic spacing, J the exchange integral, and K the anisotropy constant; and $g = \frac{3}{2}\lambda_{100}(C_{11}-C_{12})^{\frac{1}{2}}K^{\frac{1}{2}}$, in which λ_{100} is the magnetostriction constant along [100] and C_{11}, C_{12} are elasticity moduli. The numerical value of d and g in iron are: $d = 165$ A and $g = 0.0447$. If we put Eqs. (5) in Eq. (4), the integration becomes possible, at least in principle, and the resulting energy is a function of $U = u-u'$, only, since the amount of energy depends only on the displacement. Finally, the pressure P acting on the wall is simply the derivative of W. The pressure $P(U)$ is related to the viscosity field $h_t(U)$ since

$$\begin{aligned} P(U) &= h_t(U)J_s \quad \text{for} \quad 90^\circ \text{ walls,} \\ P(U) &= 2h_t(U)J_s \quad \text{for} \quad 180^\circ \text{ walls.} \end{aligned}$$

In the case of interstitial atoms,[6] the energy E_d is given by Eq. (1). If we rewrite Eq. (1) in the form

$$E_d = W_0 \cdot Q(\varphi,\varphi'),$$

where $Q(\varphi,\varphi') = \alpha^2\alpha'^2+\beta^2\beta'^2+\gamma^2\gamma'^2$, we can introduce the functions

$$\begin{aligned} F(U) &= W/W_0 = \int_{-\infty}^{+\infty} Q(\varphi,\varphi')dx; \\ f(U) &= P/W_0 = dF/dU. \end{aligned} \tag{7}$$

Equations (6) become

$$\begin{aligned} W_0 f'(U) &= h_t(U)J_s \quad \text{for} \quad 90^\circ \text{ walls,} \\ W_0 f''(U) &= 2h_t(U)J_s \quad \text{for} \quad 180^\circ \text{ walls.} \end{aligned} \tag{8}$$

Here the primes of the $f(U)$ indicate to which kind of wall the functions refer to. The functions $f'(U)$, $f''(U)$ have been computed by Néel.[6]

Now let us consider the case of pairs of solute atoms, where the anisotropy energy E_d is given by Eq. (2). By neglecting constant terms, Eq. (2) can be written in the form

$$E_d = W_0'[(S_4-S_{22})Q_1(\varphi,\varphi')+4S_{22}Q_2(\varphi,\varphi')], \tag{9}$$

where

$$\begin{aligned} Q_1(\varphi,\varphi') &= \alpha^2\alpha'^2+\beta^2\beta'^2+\gamma^2\gamma'^2 \\ Q_2(\varphi,\varphi') &= \alpha\alpha'\beta\beta'+\beta\beta'\gamma\gamma'+\gamma\gamma'\alpha\alpha'. \end{aligned}$$

By straightforward substitutions, Eq. (4) becomes

$$W = W_0'[(S_4-S_{22})F_1(U)+4S_{22}F_2(U)], \tag{10}$$

having put

$$F_1(U) = \int_{-\infty}^{+\infty} Q_1(\varphi,\varphi')dx; \quad F_2(U) = \int_{-\infty}^{+\infty} Q_2(\varphi,\varphi')dx.$$

Similarly, on taking the derivative of Eq. (10) and replacing dF_1/dU by $f_1(U)$ and dF_2/dU by $f_2(U)$, we have

$$P(U) = W_0'[(S_4-S_{22})f_1(U)+4S_{22}f_2(U)]. \tag{11}$$

Therefore the problem is reduced to finding functions $f_1(U)$ and $f_2(U)$ for the two classes of walls by operating on $Q_1(\varphi,\varphi')$ and on $Q_2(\varphi,\varphi')$.

The computations are reported in the Appendix. The result is that $P(U)$ is different from zero in all structures; hence we can draw the following conclusions.

(1) We have shown that the presence of an energy E_d of the form of Eq. (2) gives rise to magnetic viscosity under proper conditions. In other words, pairs of solute atoms can give a magnetic viscosity, as well as interstitial atoms.

(2) The above sentence can be generalized. Suppose that we have a ferromagnetic material which shows magnetic viscosity, i.e., that there is an element which diffuses in a way determined by the distribution of the Bloch walls. In other terms, the element has an interaction energy with the magnetization vector. This means that there is an energy E_d which depends, at each point, on the direction of $\mathbf{J}_s$, and may, or may not, be of the type of Eq. (2). Now if we make, on the same material, an experiment of magnetic annealing, the energy E_d will appear macroscopically, that is, the material will show an induced uniaxial anisotropy.

VISCOSITY FIELD AND INDUCED ANISOTROPY

In the case of interstitial atoms, since the maximum values of $f_1'(U)$ and of $f_1''(U)$ occur for the same U, and are 1 and 2, respectively, the maximum value H_t of the viscosity field is given, from Eqs. (8), by

$$H_t = W_0/J_s \tag{12}$$

for both classes of walls.

Now let us examine what happens in the case of solute pairs, on the basis of the calculations made in the preceding section and in the Appendix. We have to consider Eq. (2), neglecting the constant terms. Equa-

[10] C. Kittel, Revs. Modern Phys. **21**, 541 (1949).

tions (6) and (11) give

$$J_s h_t = W_0'[(S_4-S_{22})f_1'(U)+4S_{22}f_2'(U)], \quad (90° \text{ walls}),$$
$$2J_s h_t = W_0'[(S_4-S_{22})f_1'(U)+4S_{22}f_2''(U)], \quad (180° \text{ walls}). \quad (13)$$

From the values of the S's for the various structures,[9] we obtain

	Isotropic	Simple cubic	bcc	fcc
(S_4-S_{22})	2/15	1/3	0	1/12
$4S_{22}$	4/15	0	4/9	1/3

Now we have all we need to compute $h_t(U)$ in the various cases. In the case of interstitials, the first of Eqs. (8) shows that for 90° walls, $J_s h_t(U)/W_0$ is simply given by $f_1'(U)$ (plotted in Fig. 1). Similarly, for 180°, $J_s h_t(U)/W_0$ is given by $f_2''(U)/2$, immediately ducible from the curve of Fig. 2. In the case of pairs, we can compute $J_s h_t(U)/W_0$ by adding the curves of Figs. 1 and 2 multiplied by the factors given by the above table.

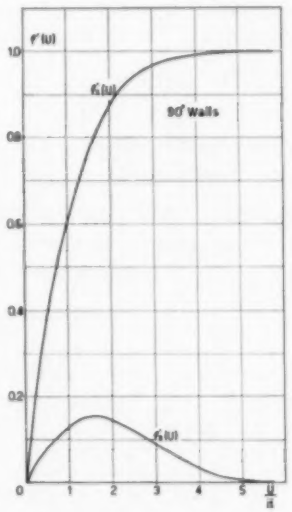

FIG. 1. The functions $f'(U)$ for 90° walls: $f_1'(U)$ corresponding to the angular term Q_1; $f_2'(U)$ corresponding to the angular term Q_2. The wall thickness D has been taken equal to 10 d. U is the wall displacement from the rest position.

Obviously, for the 180° walls, a further factor of $\frac{1}{2}$ has to be accounted for [see Eq. (6)].

The resulting $J_s h_t(U)/W_0$ for the two classes of walls in different structures are plotted in Figs. 3 and 4. Obviously, the descending branches of the curves of these figures are deeply modified by instability effects.[11]

Unfortunately, the occurrence of the same H_t for the two classes of walls happens only for the simple cubic lattice. Actually, the pairs of solute atoms in a simple cubic lattice behave exactly as the interstitial atoms in a bcc lattice. The fact that for interstitial atoms the curves of $J_s h_t(U)/W_0$ have maximum value of 1, whereas

[11] G. Biorci, A. Ferro, and G. Montalenti, Atti accad. naz. Lincei. Rend. Classe sci. fis. mat. e nat. **24**, 542 (1958).

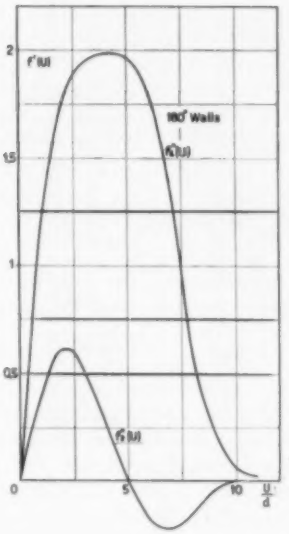

FIG. 2. The functions $f''(U)$ for 180° walls: $f_1''(U)$ corresponding to the angular term Q_1; $f_2''(U)$ corresponding to the angular term Q_2. The wall thickness D has been taken equal to 10 d. U is the wall displacement from the rest position.

for the pairs in simple cubic lattices $J_s h_t(U)/W_0$ has a maximum value of $\frac{1}{3}$, occurs because in the case of interstitial atoms the constant W_0 contains a term $\frac{1}{3}$ due to the distribution of atoms over the three axes, whereas, in the case of pairs, the distribution over the various axes is not accounted for by W_0', but by the S's which give the factor $\frac{1}{3}$. Since for the other cases it is hard to deduce the form of the macroscopic function $h_t(J)$ because the amounts of 90° and 180° walls are not known, we shall suppose the material composed of 180° domains only.

Under this assumption, the maximum viscosity field is given by

$$H_t = pW_0'/J_s. \quad (14)$$

The constant p has a different value in the various structures, as deduced from Fig. 4.

	Isotropic	Simple cubic	bcc	fcc
p	0.12	0.33	0.133	0.18.

Now we have to consider the anisotropy induced by annealing the same materials in a magnetic field.

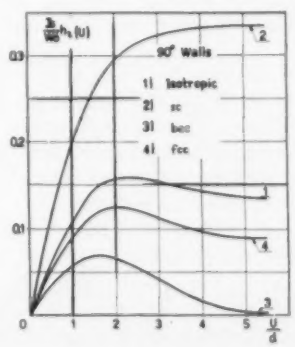

FIG. 3. Values of the function $J_s h_t(U)/W_0'$ as a function of the wall displacement U for walls at 90° and for different structures.

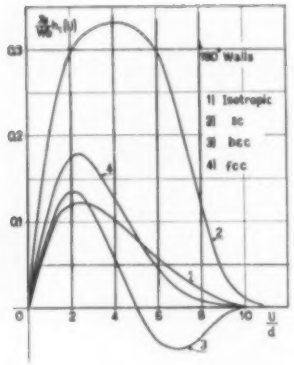

FIG. 4. Values of the function $J_s h_t(U)/W_0'$ as a function of the wall displacement U for walls at 180° and for different structures.

For the sake of generality, we shall treat the case of interstitial atoms together with the case of solute pairs. To do so, it is enough to express the variable part of E_d as

$$E_d = K_1 Q_1(\varphi,\varphi') + K_2 Q_2(\varphi,\varphi').$$

Thus, in the case of interstitials, $K_1 = W_0$ and $K_2 = 0$; whereas in the case of couples, $K_1 = (S_4 - S_{22})W_0'$ and $K_2 = 4.5_{22} W_0'$.

In order to find the expression for the uniaxial induced anisotropy in a polycrystalline specimen we take three reference axes, the x axis coinciding with the direction of the annealing field, and the other two at right angles to the annealing field. In this principal reference system let η_1, η_2, η_3 be the cosines of the direction along which we want to measure the anisotropy energy. Then let us consider, in each grain, a reference system with the axes coinciding with the crystallographic directions. In each of these systems the direction of the annealing field, and the direction η_1, η_2, η_3 have certain cosines α, β, γ and α', β', γ'. So, for each grain, one can write E_d as a function of η_1, η_2, η_3 and the angles between the axes of that grain and the axes of the principal reference system. By averaging the expression obtained over all values of the latter angles, one obtains a function of η_1, η_2, η_3 only, which is the desired macroscopic anisotropy energy function w_a (η_1,η_2,η_3). This calculation can be done by standard methods, using the Euler angles, or more rapidly with a procedure similar to that used by Galissot and Vèrgne.[12] It turns out that w_a is given by

$$w_a = (\tfrac{2}{5}K_1 + \tfrac{3}{10}K_2)\eta_1^2 = K_u \eta_1^2, \qquad (15)$$

where K_u is the induced anisotropy constant of the polycrystal and η_1 is the cosine of the angle between the chosen direction and the direction of the annealing field. The other two cosines η_2 and η_3 do not appear since w_a has cylindrical symmetry.

Therefore, in the case of interstitial atoms, using the proper value of K_1 we obtain

$$K_u = 2W_0/5; \qquad (16)$$

whereas, in the case of solute pairs

$$K_u = W_0'[\tfrac{2}{5}(S_4 - S_{22}) + (6/5)S_{22}]. \qquad (17)$$

By making use of the values of S_4 and S_{22} for the different structures we obtain

$$K_u = 2W_0'/15 \qquad (18)$$

for all structures. The fact that the coefficient takes the value 2/15 for all structures is not surprising, since it results from an average over the links (which gives the S's)[9] and from another average over all possible orientations. At this point, the relationship between viscosity field and anisotropy induced by annealing in a magnetic field becomes very simple. In the case of interstitials, it is enough to compare Eq. (12) and Eq. (16). They give

$$H_t = 2.5K_u/J_s. \qquad (19)$$

In the case of solute pairs one has to compare Eq. (14) and Eq. (18), taking into account the values of the coefficient p. The results are, for

$$\begin{aligned} &\text{isotropic crystals,} && H_t = 0.9K_u/J_s;\\ &\text{simple cubic crystals,} && H_t = 2.5K_u/J_s;\\ &\text{body-centered cubic crystals,} && H_t = K_u/J_s;\\ &\text{face-centered cubic crystals,} && H_t = 1.35K_u/J_s. \end{aligned} \qquad (20)$$

Equations (20) are deduced in the hypothesis that only 180° walls are present. However, they are approximately valid also if the specimen contains 90° walls.

CONCLUSION

In this paper we have given the theory of the magnetic viscosity due to solute atom pairs in a ferromagnetic alloy. The anisotropy energy has been taken as that given by Néel.[9] Taking into account the instability effects[11] we conclude that the effect is similar to that due to interstitial atoms in bcc structures.

Furthermore, we have stressed a general property: If a material shows magnetic viscosity it also exhibits magnetic annealing, whatever is the source of viscosity.

In the case of solute pairs we have found the relationship between viscosity field and induced anisotropy for various structures. The constant of the interaction energy between a pair of solute atoms and the magnetization vector remains unknown, whereas that of the interstitial atoms in iron has been computed by us[13] in a satisfactory approximation.

The experiments performed to verify the present theory will be reported in Part II of this paper.

APPENDIX

Computation of the Functions $f_1(U)$ and $f_2(U)$

We may first observe that $Q_1(\varphi,\varphi')$ is identical to Q for the case of interstitial atoms. Therefore the functions

[12] G. Galissot and R. Vèrgne, Compt. rend. **248**, 703 (1959).

[13] G. Biorci, A. Ferro, and G. Montalenti, Air Research Development Command Tech. Note 1c, March, 1958.

$f_1'(U)$ and $f_1''(U)$ are those computed by Néel, and reported in Figs. 1 and 2. Now let us examine the term $Q_2(\varphi,\varphi')$. With the usual substitutions $\alpha=\alpha'=0$, $\beta=\cos\varphi$, $\gamma=\sin\varphi$, $\beta'=\cos\varphi$, and $\gamma'=\sin\varphi'$, Q_2 becomes

$$Q_2(\varphi,\varphi')=\tfrac{1}{4}\sin 2\varphi \sin 2\varphi'.$$

At this point we have to express φ and φ' as functions of x, by making use of Eqs. (5).

90° Walls

If we recall that

$$\tan\varphi=\frac{1-\cos 2\varphi}{\sin 2\varphi}=\frac{1-(1-\sin^2 2\varphi)^{\frac{1}{2}}}{\sin 2\varphi}$$

and make the substitution

$$e^{2x/d}=t$$

into a proper combination of Eqs. (5) and (7), we obtain

$$F_2'(U)=\frac{-(u-u')}{\exp[-(u-u')/d]-\exp[(u-u')/d]}=\frac{1}{2}\frac{U}{\sinh(U/d)}. \quad (21)$$

The desired function $f_2'(U)$ is obtained by taking the derivative of Eq. (21) and turns out to be

$$f_2'(U)=1/2\sinh(U/d)[1-(U/d)\operatorname{cotanh}(U/d)]. \quad (22)$$

This function is plotted in Fig. 1, together with $f_1'(U)$.

180° Walls

For this class of walls the function $\varphi(x)$ is given by the second of Eqs. (5). Using the same technique as before, we arrive at the integral of a rational function of fourth degree in the denominator, hence the computations become extremely complicated, even if simple in principle.

Therefore we have simplified the problem by assuming a linear dependence of φ on x inside the wall. In order to check the validity of this assumption, we have repeated the computation of $f_2'(U)$ for 90° walls making use of the linear approximation. The deviations of the curve obtained in this way from the exact curve previously computed turned out to be very small. The only remarkable difference was that the linear approximation obviously gives points of discontinuity, which are not present in the exact curve.

Being sufficiently confident of the linear approximation, we have taken, for the 180° walls,

$$\begin{aligned}&\varphi=(x-u)\pi/D+\pi/2 \quad \text{for} \quad (u-D/2)\leqslant x\leqslant(u-D/2)\\ &\varphi=0 \quad \text{for} \quad x<(u-D/2)\\ &\varphi=\pi \quad \text{for} \quad x>(u+D/2),\end{aligned} \quad (23)$$

where D is the wall thickness, equal to about $10d$. It is worth noticing that instability effects make the exact behavior of $f(U)$ above the maximum of no physical interest. In fact, as shown in a previous work,[11] if the material has very high permeability, as soon as the wall reaches the U at which $f(U)$ is maximum, any further increase of the field makes the wall jump forward, thus avoiding the descending branch of $f(U)$. By making use of Eq. (23), $Q_2(\varphi,\varphi')$ can be easily written as

$$Q_2=\tfrac{1}{4}\sin[2\pi(x-u)/D]\sin[2\pi(x-u')/D] \quad \text{for} \quad (u'-D/2)\leqslant x\leqslant(u+D/2);$$

$Q_2=0$, outside.

In writing the range where Q_2 is different from zero we have assumed $u'>u$. The case of $u'<u$ can be solved by symmetry consideration. The integration of Q_2 is straight forward, and gives $F_2''(U)$. Its derivative is the desired function $f_2''(U)$:

$$f_2''(U)=-(\pi/4)(1+U/D)\sin 2\pi U/D, \quad \text{for} \quad -D\leqslant U\leqslant D; \quad (25)$$

$f_2''(U)=0$, outside.

This function is plotted in Fig. 2 together with $f_1''(U)$. By having the required functions $f(U)$, the computation of the viscosity field $h_t(U)$ for the various structures becomes very simple, and is fully reported in the text.

Electron Optical Study of Basal Dislocations in Graphite

S. AMELINCKX AND P. DELAVIGNETTE
Centre d'Etude de l'Energie Nucléaire, MOL (Belgium)
(Received June 14, 1960)

Dislocations having a Burgers vector in the basal plane and lying in this plane, have been studied in graphite by the use of thin foil transmission electron microscopy. The dislocations are dissociated into ribbons consisting of two partials separated by a stacking fault. Specific models for these dislocations are presented. Hexagonal networks contain extended and contracted nodes. The presence of two types of stacking faults gives rise to singularities which are analyzed in terms of experimentally determined Burgers vectors. The dislocations and even the networks are very mobile along the basal plane. The stacking fault energy is determined as 3 to 5×10^{-2} ergs/cm^2.

1. INTRODUCTION

IN view of the importance of graphite as a nuclear material, and in order to understand its mechanical behavior, it seemed worth while to investigate its dislocation structure in some detail, making use of the techniques recently developed for metals by Hirsch, Whelan, Bollmann, and others.[1]

Glide along the basal plane of graphite is so easy that it is not obvious at first whether dislocations would actually be required in this process. From this study, it follows that basal dislocations do exist in graphite and behave like conventional dislocations. The same is found to be the case for talc,[2] another layer structure.

A preliminary account of these investigations has been made,[2,3] and a preliminary description of dislocation movement in the basal plane has been given by Grenall.[3a] A study of nonbasal dislocations by the use of Moiré patterns was already published by Dawson.[4] We therefore restrict ourselves in this paper to basal dislocations observed by straightforward transmission electron microscopy. The facts that the dislocations are dissociated into ribbons, and that the presence of two types of stacking faults gives rise to interesting patterns, are analyzed in some detail.

2. EXPERIMENTAL TECHNIQUES

Graphite is almost ideal for transmission electron microscopic work; the absorption coefficient is small, so that relatively thick foils can be tolerated. The optimum is therefore determined solely by the optimum contrast rather than limited by absorption. Moreover, thin foils can easily be obtained by cleavage. The procedure used to prepare the thin cleavage flakes has been described.[5]

The single-crystal graphite used in this investigation originated either from Ceylon or from the Ticonderoga limestone formation in the U. S. A. Some of the crystals were heated in a vacuum of 10^{-5} mm at some 2500°C by electron bombardment for a few minutes, and then quenched to room temperature in an attempt to obtain quenched-in point defects. (This work will be discussed separately.) The well developed net patterns were found almost exclusively in these heat treated crystals.

The observations were made with the standard Philips electron microscope operated at 100 kv.

3. THE GRAPHITE STRUCTURE

The graphite structure is shown schematically in Fig. 1(a). The most common variety consists of a hexagonal stacking of sheets of hexagonally linked carbon atoms in two different positions, *a* and *b*. The stacking sequence can be summarized as *abab*···. Figure 1(c) shows a projection on the *c* plane, which is a pronounced cleavage plane, while Fig. 1(a) shows a view along the direction *AB*.

A third stacking position, marked *c*, is, however,

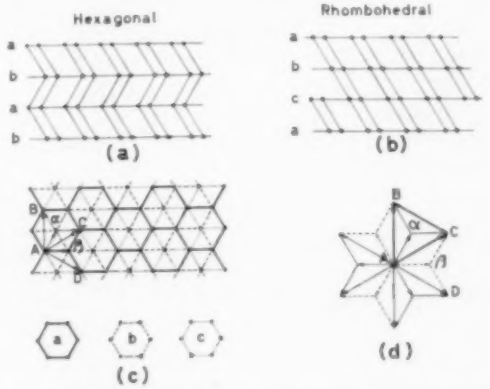

FIG. 1. Schematic view of the graphite structure. (a) The normal stacking is hexagonal: *a b a b* ··· as seen along *AB*; (b) rhombohedral stacking: *a b c a b c* ··· as seen along *AB*; (c) projection on the *c* plane; (d) the complete Burgers vectors are *AB*, *AC*, and *AD* as well as their negatives. Separation into partials according to the schemes $AC \rightarrow A\alpha+\alpha C$ and $A\beta+\beta C$ lowers the elastic energy.

[1] W. Bollmann, Phys. Rev. **103**, 1588 (1956); P. B. Hirsch, R. W. Horne, and M. J. Whelan, Phil. Mag. **1**, 677 (1956); P. B. Hirsch, J. Silcox, R. E. Smallmann, and K. H. Westmacott, *ibid.* **3**, 897 (1958); A. Berghezan and A. Fourdeux, Compt. rend. **248**, 1333 (1959).

[2] S. Amelinckx and P. Delavignette, Nature **185**, 603 (1960); Phil. Mag. **5**, 533 (1960).

[3] P. Delavignette and S. Amelinckx, J. Appl. Phys. (to be published).

[3a] A. Grenall, Nature **182**, 4633 (1958).

[4] I. M. Dawson and E. A. C. Follett, Proc. Roy. Soc. (London) **A253**, 390 (1959).

[5] P. Delavignette and S. Amelinckx, Phil. Mag. (to be published).

possible, and some graphites have the rhomobohedral structure *abcabc*···.[6] This stacking is the equivalent of the cubic stacking for layers of close-packed spheres; it is represented in Fig. 1(b) as seen along direction AB.

A consideration of the structure leaves little doubt about the localization of the glide plane, which is evidently between c planes, because the bonding between successive c layers is very weak. Since the cleavage plane, i.e., the foil plane and the glide plane, are parallel, extensive dislocation arrangements in the plane of observations are to be expected.

4. BASAL DISLOCATIONS, BURGERS VECTORS, STACKING FAULTS

Perfect dislocations in the graphite structure have a Burgers vector connecting crystallographically equivalent atoms. The shortest among these vectors are AB, AC, AD, and their negatives [Fig. 1(c,d)]. A dislocation with such a vector can, however, split into two Schockley partials according to the reaction $AC \rightarrow A\alpha + \alpha C$ or

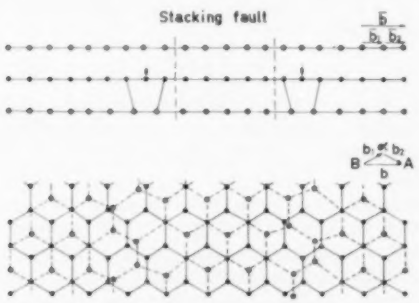

FIG. 2. Pure edge dislocation with a Burgers vector AB as seen along the direction αC (notation of Fig. 1), and in projection on c.

$A\beta + \beta C$ with a decrease in elastic energy. If the stacking fault has a sufficiently small energy this dislocation will really occur. From Fig. 1(c), the deduction can be made that the stacking fault associated with the first dissociation is a layer in c position. Since this "faulted" stacking is found to occur in certain graphites, the stacking fault energy associated with it is probably small, and therefore a visible dissociation will occur.

The stacking fault associated with the second dissociation consists of two layers vertically above one another. We expect the stacking fault energy associated with this stacking to be considerably larger than for the first type.

A visual illustration of a dislocation ribbon containing a low-energy stacking fault is presented in Figs. 2 and 3. Figure 2 represents the pure edge dislocation with a Burgers vector $AB = A\alpha + \alpha B$ as seen along the direction αC, while Fig. 3 on the other hand shows the 60° dislocation with a Burgers vector $AC = A\alpha + \alpha C$ as seen

[6] H. Lipson and A. R. Stokes, Proc. Roy. Soc. (London) **A181**, 101 (1942).

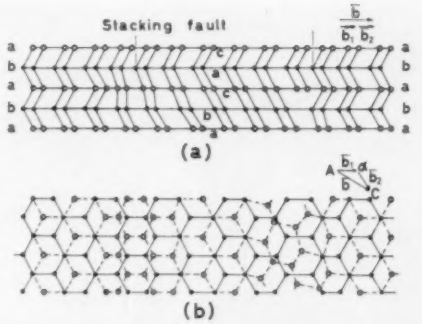

FIG. 3. (a) The 60° dislocation with a Burgers vector AC as seen along the direction AD (Fig. 1). Notice that between the partials, rhombohedrally stacked material is present. (b) Projection on the c plane.

along the direction AD. In this view it is clearly apparent that the ribbon contains two layers of rhombohedrally stacked material.

It should be pointed out that no C−C bonds in the graphite plane are broken; the strain is taken up by deformation of the hexagons. Only the weak bonds between the layers are, of course, broken.

One can consider two basic types of low-energy stacking faults, which can be generated by glide on the c plane. They are described by the sequences

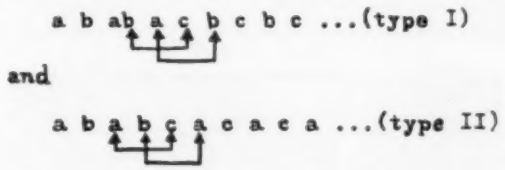

The second of these is shown in detail in Fig. 3(a). They both contain two violations of the second-nearest neighbor stacking, as shown by the arrows, and the energy should therefore be comparable. The difference consists merely that in type I a b layer is shifted into c position, whereas in type II an a layer has been displaced into c position. Stacking faults of the first type result on our scheme [Fig. 1(d)] from the movement of a partial like $A\alpha$, $B\alpha$, or $C\alpha$, while the second type of stacking fault is made from well-stacked crystal by a partial of the type αA, αB, or αC.

5. DETERMINATION OF THE BURGERS VECTOR

As outlined by Whelan,[7] the Burgers vector of a given dislocation can be determined by making use of the disappearance of contrast at that dislocation for certain Bragg reflections. The rule is as follows: A dislocation does not exhibit any contrast, when the latter is arising from Bragg reflection against a plane parallel to the Burgers vector. From the mobility of dislocations in the c plane (see Sec. 11) we already know that the Burgers

[7] M. J. Whelan, J. Inst. Metals **12**, 385 (1959).

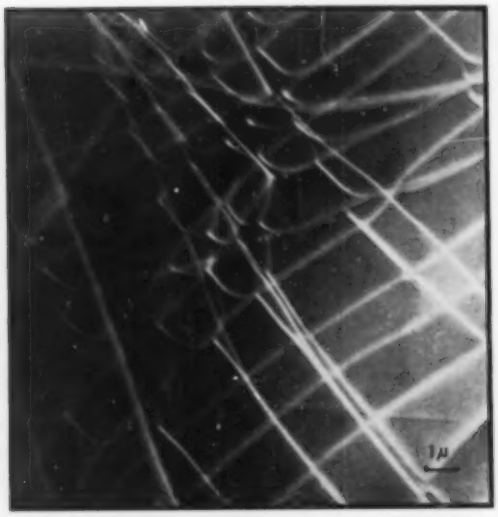

FIG. 4. Dark-field image of dislocation nets due to the $(11\bar{2}0)$ spot. Note the absence of one family of lines.

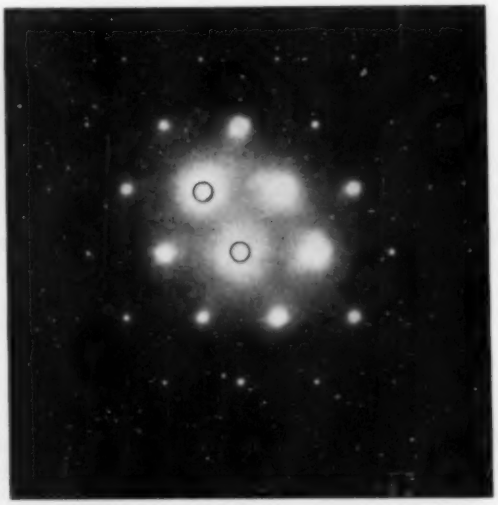

FIG. 6. Selected area diffraction patterns corresponding to Fig. 5(d). It is clearly apparent that the $(10\bar{1}0)$ spot gave rise to the stacking fault contrast.

vector of the dislocations considered here are in the c plane. It is therefore sufficient to know one other plane parallel to this vector in order to know, unambiguously, its direction. Such a plane can be found by looking for a specimen orientation which causes the dislocations of interest to disappear; without changing the foil orientation, one makes then a selected area diffraction pattern. It is then usually found that one low index diffraction spot is much more intense than the others. This is the spot corresponding to the reflection responsible for the contrast.

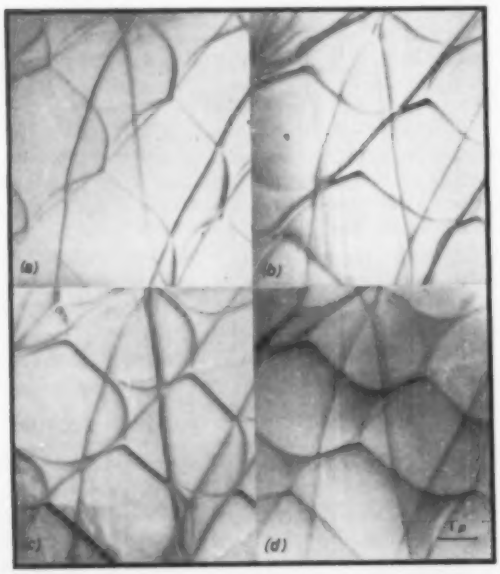

FIG. 5. Number of dislocation nodes. The sequence of photographs shows the disappearance of contrast for each one of the three families of partials, while the fourth photograph shows the stacking fault contrast inside the extended nodes. From these photographs and the corresponding diffraction patterns the Burgers vectors can be determined unambiguously.

Alternatively, as suggested earlier,[5] one can make a dark-field image using a reflection which one suspects to correspond to a plane passing through a Burgers vector. In the dark-field image the lines show up in reverse contrast, i.e., as light lines. The lines for which the extinction condition is satisfied will not appear in the image. The second method is somewhat less ambiguous than the first, where sometimes more than one spot is intense, and where occasionally *two* sets of dislocations disappear. An example of such an image is shown in Fig. 4, using the $(11\bar{2}0)$ reflection.

Using these procedures, the Burgers vectors of the dislocations in Fig. 5(a) were determined. In Fig. 5 (a), (b), and (c) are three different aspects of the same area. It is now clear that the pattern consists of three different families of dislocations, and it is further evident that in each of the photographs another family of lines is lacking. The indices of the diffraction spots responsible for the contrast in (a) (b) and (c) of the figure were, respectively, $(11\bar{2}0)$, $(1\bar{2}10)$, $(\bar{2}110)$. One example of a diffraction pattern is reproduced in Fig. 6. The center of the pattern as well as the intense $(10\bar{1}0)$ spot are surrounded by a circle. The directions of the Burgers vector as deduced from these are $A\alpha$, $B\alpha$, and $C\alpha$ in accordance with the theoretical picture. The magnitude of the Burgers vectors can of course not be determined directly, but this value follows immediately from a consideration of the structure.

Other examples of extinctions are shown in Fig. 7(a)

and in Fig. 7 (b), (c), and (d), which represent the same area, also shown in Fig. 8 schematically. From Fig. 7(d) it is now evident that the three dislocations marked (1) in Fig. 8 have the same Burgers vectors. The same applies to the dislocations marked (2).

Comparing Fig. 9(a) and Fig. 9(b), it is evident that the ribbon consisting of three lines and marked R has disappeared completely, showing that the three components of the ribbon have the same Burgers vector and also that the stacking faults do not show up for the same reflection. We will discuss the geometry of the ribbon in detail later.

6. THE STACKING FAULT ENERGY

The stacking fault energy γ can be estimated in two different ways: (a) by measuring the distance d between partials in a ribbon; (b) by measuring the radius of curvature of a partial in an extended node.[8]

The first method is based on a formula expressing the equilibrium distance between partials[9] in elastically isotropic material:

$$\gamma=\frac{\mu b^2}{8\pi d_0}\frac{2-\nu}{1-\nu}, \tag{1}$$

where $d_0=d[1-(2\nu/2-\nu)\cos 2\alpha]^{-1}$. The angle α is the angle between the total Burgers vector and the dislocation; b is the magnitude of the Burgers vector of a partial; μ is the rigidity modulus, and ν Poisson's ratio. With $\alpha=90°$, $d_0=2d$; while with $\alpha=0$, $d_0=d$ and $\gamma=\frac{1}{16}(\mu b^2/d_0)$.

In the second method one makes the assumption that the crystal is elastically isotropic and that the interaction between partials can be neglected in a point like P of the extended node (Fig. 9).

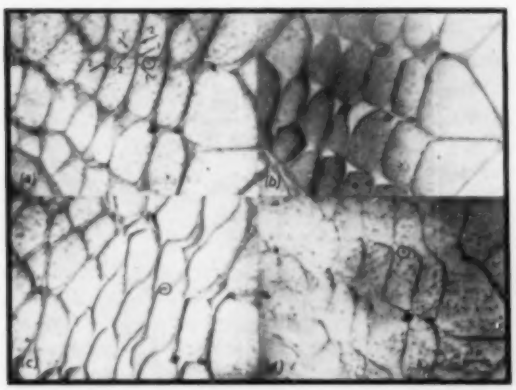

FIG. 7. Four aspects of the same network containing two types of stacking faults: (a) all elements visible; (b) inverted contrast: notice differences in stacking fault contrast; (c) all lines lettered $C\alpha$ (in Fig. 8) are lacking; (d) all dislocations lettered αA are lacking.

[8] M. J. Whelan, Proc. Roy. Soc. (London) **A249**, 114 (1958).
[9] W. J. Read, *Dislocations in Crystals* (McGraw-Hill Book Company, Inc., New York, 1953).

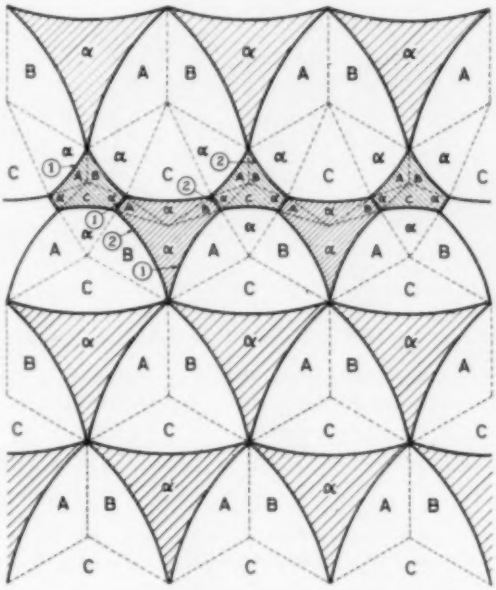

FIG. 8. Lettering pattern of network observed in Fig. 18 (and Fig. 7).

The line tension of the dislocation is then given by

$$T=\frac{\mu b^2}{2\pi(1-\nu)}\ln\frac{r_1}{r_0}\simeq 0.5\mu b^2.$$

A dislocation with a radius of curvature R is in equilibrium with a shear stress $\sigma=\gamma/b$ if $\sigma=T/bR$ and hence

$$\gamma=\mu b^2/2R. \tag{2}$$

There is obviously a relation between R and d_0; $R\simeq 5d_0$, i.e., $5d<R<10d$.

Measurements on enlarged micrographs of Fig. 9(a) and Fig. 5 lead to mean values for $d=0.1\,\mu$ and $R=0.9\,\mu$; these are within the limits given. To find γ on an absolute scale we must know μ and ν. The best value of

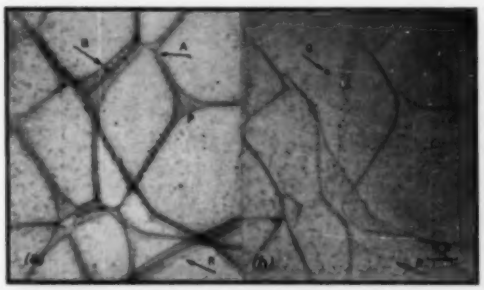

FIG. 9. Pattern showing several types of interactions: (a) all elements visible, (b) all dislocations lettered $C\alpha$ are lacking. Notice disappearance of ribbon marked R in (b).

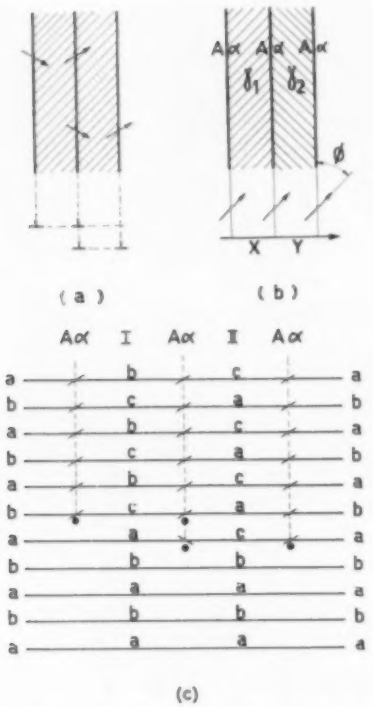

FIG. 10. (a) Possible dislocation configuration for the ribbon shown in Fig. 7. The three dislocations do not have the same Burgers vector, however. (b) Probable configuration of dislocations in the three-dislocation ribbon of Fig. 7. (c) Arrangement of layers in three dislocation ribbons.

μ is one deduced from specific heat measurements by Bowman and Krumhansl,[10] $\mu=2.3\times10^{10}$ dynes/cm^2.

Using this value and putting $\nu=\frac{1}{3}$, we find $\gamma=3.5\times10^{-2}$ ergs/cm^2.

7. THREE-DISLOCATION RIBBON

The observation of a ribbon consisting of three partial dislocations with the same Burgers vector, as pointed out in Sec. 5, implies the occurrence of two types of stacking faults. In order to make this clear let us consider the different conceivable interpretations of this observation.

(i) A ribbon consisting of two outer partials and a perfect dislocation in the center. In this case the two stacking faults would be of the same kind. However, the central dislocation would certainly split in partials, since it is helped to do so by the stacking faults. No splitting is observed, however. Moreover, the three dislocations would not have the same Burgers vector as required.

(ii) The ribbon is in fact a superposition of two ribbons. It is, however, not possible to find a model which could give rise to a stable situation as, for example, that shown in Fig. 10(a) and which would give the three dislocations the *same* Burgers vector.

(iii) The only remaining model, as far as we can see, is shown in Fig. 10 (b). It consists of three partials of the type $A\alpha$ [Fig. 10(c)]. They may, for example, result from the reaction of $AB\rightarrow A\alpha+\alpha B$ with $AC\rightarrow\alpha C+A\alpha$ to form $\alpha B+\alpha C=A\alpha$. A detailed picture of the arrangement of layers in such a double ribbon is symbolically represented in Fig. 10(c). The first partial transforms the normal stacking into a type I stacking fault while the second partial transforms it further in a type II stacking fault. The last partial puts the stacking back to normal. In the following we will present further experimental evidence for the occurrence of two kinds of stacking faults. First, it will be shown that the assumptions made here lead to a width of the three-dislocation ribbon in agreement with the experiment.

We therefore calculate the equilibrium separation of partials in the model of Fig. 10(b).

We call $\alpha=\mu/2\pi$, $\beta=\mu/2\pi(1-\nu)$; we can then write down the following equilibrium conditions:

$$b^2A\left(-\frac{1}{x}-\frac{1}{x+y}\right)+\gamma_1=0, \tag{3}$$

$$b^2A\left(\frac{1}{x}-\frac{1}{y}\right)+\gamma_2-\gamma_1=0, \tag{4}$$

$$b^2A\left(\frac{1}{y}+\frac{1}{x+y}\right)-\gamma_2=0, \tag{5}$$

where $A=\alpha\cos^2\phi+\beta\sin^2\phi$. These equations express the fact that the sum of all the forces on each dislocation is zero.

This is a set of three compatible equations with two unknowns; the solution is

$$x=(3Ab^2)/[(2\gamma_1-\gamma_2)+g],$$
$$y=(3Ab^2)/[(2\gamma_2-\gamma_1)+g],$$

where $g=(\gamma_1^2+\gamma_2^2-\gamma_1\gamma_2)^{\frac{1}{2}}$.

In the case where $\gamma_1\sim\gamma_2=\gamma$, one finds

$$x=y=3Ab^2/2\gamma. \tag{6}$$

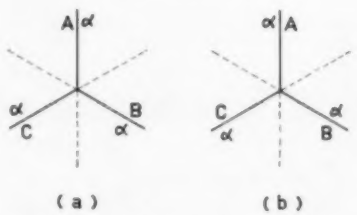

FIG. 11. The two possible types of nodes according to the lettering scheme used in this paper. Nodes (*a*) and (*b*) correspond, respectively, to the *K* and *P* nodes introduced by Frank (footnote 11).

[10] M. G. Bowman and J. A. Krumhansl, J. Phys. Chem. Solids **6**, 367 (1958).

With $\nu=\frac{1}{3}$, $\beta=\frac{2}{3}$, and $A\simeq\mu/2\pi$, we find by combining Eqs. (6) and (1) $x+y\simeq 5d$ which is of the right magnitude, since the measured values are $d\sim 0.1\,\mu$ and $x+y=0.5\,\mu$. From the symmetry of the ribbon we can further deduce that $\gamma_1\approx\gamma_2$. We conclude that the model discussed is also quantitatively in agreement with the observation since it yields a good value for the width of the ribbon.

8. NODES BETWEEN PARTIAL DISLOCATIONS

Using the notation introduced in Fig. 1(d), we can distinguish two types of threefold nodes among partial dislocations. They are represented in Fig. 11.

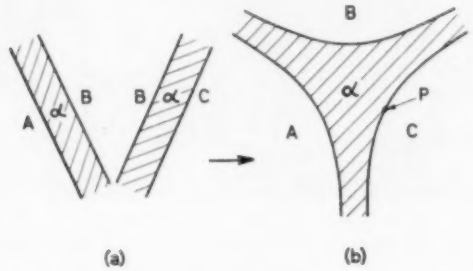

FIG. 12. Fusion of two ribbons both containing a type I stacking fault. An extended node containing a type I fault is formed.

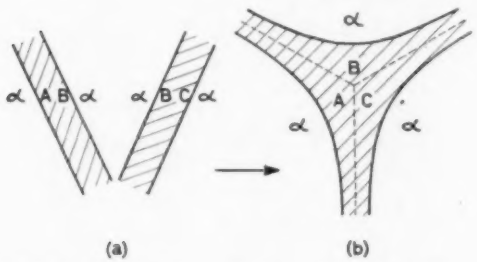

FIG. 13. Fusion of two ribbons both containing a type II stacking fault; again an extended node is formed. It now contains a type II stacking fault.

The corresponding node conditions are, respectively,

$$\alpha A+\alpha B+\alpha C=0 \quad \text{and} \quad A\alpha+C\alpha+B\alpha=0.$$

It is clear that this distinction is only possible when giving a sense in which the symbols will be read. We adopt the convention given earlier by Frank[11] for the face-centered cubic lattice. When looking out from the node point we read from left to right of the line. The two nodes described here are the analogs of the K and P nodes introduced by Frank.[11] In a stable net, adjacent nodes have the opposite type, while parallel segments have to repel. In deriving equilibrium configurations we have further to take into account the presence of stacking faults of two types. Since the stacking fault energy is very small in any case, the partials can practically be treated as independent dislocations.

[11] F. C. Frank, *Report of Conference on Defects in Crystalline Solids* (The Physical Society, London, 1955), p. 159.

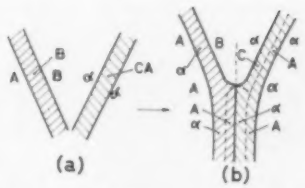

FIG. 14. Fusion of two ribbons containing a different type of stacking fault. The Burgers vectors of the interacting ribbons are $A\alpha+\alpha B$ and $\alpha C+A\alpha$.

9. REACTIONS BETWEEN TWO RIBBONS IN THE SAME OR ADJACENT LATTICE PLANES

Some of the simpler configurations which are often observed can be considered as resulting from the interaction between ribbons in the same or successive lattice planes.

9.1. Fusion of Two Ribbons

The Two Ribbons Contain the Same Stacking Fault

Let us first consider the interactions between two ribbons containing the same stacking fault: Two ribbons with a type I stacking fault like $A\alpha+\alpha B$ and $B\alpha+\alpha C$ can react in the way shown in Fig. 12 and form an extended node, as illustrated by Fig. 9. The interior of the triangular region is faulted according to type I. If the two ribbons both have a type II stacking, e.g., $\alpha A+B\alpha$ and $\alpha B+C\alpha$, the result is essentially the same, except that the enclosed area is now a type II stacking fault (Fig. 13). For all other combinations of Burgers vectors the ribbons either repel, react in the way described, or annihilate mutually.

The Two Ribbons Contain a Different Stacking Fault

A greater variety of possibilities now arises; we will only consider nontrivial ones: (a) For ribbons with Burgers vector $A\alpha+\alpha B$ and $\alpha C+A\alpha$ a Y-shaped symmetrical configuration results, the main feature being the equality of the Burgers vectors in the three dislocation ribbons. The larger width of this ribbon is in agreement with the formula deduced in Sec. 7. It con-

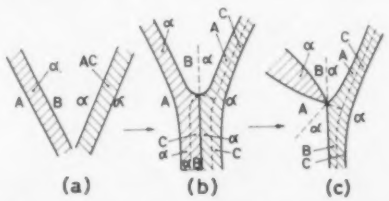

FIG. 15. Fusion of two ribbons containing a different type of stacking fault. The Burgers vectors of the two ribbons are now $A\alpha+\alpha B$ and $\alpha A+C\alpha$.

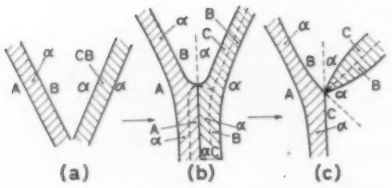

FIG. 16. Fusion of two ribbons containing a different type of stacking fault and having Burgers vectors $A\alpha+\alpha B$ and $\alpha C+\alpha B$. The configuration is symmetrical with respect to the one represented in Fig. 15.

tains two different stacking faults. The reaction is represented schematically in Fig. 14. Examples of observations can be found on many photographs; we refer especially to Fig. 9. (b) Ribbons with Burgers vectors $A\alpha+\alpha B$ and $\alpha A+C\alpha$ will react in much the same way, but the situation as represented in Fig. 15(b) is not in equilibrium, since $A\alpha$ and $C\alpha$ will further react to form αB. The final stable situation is therefore as pictured in Fig. 15(c). It contains again two types of stacking faults. A number of configurations of this kind can easily be found, for example, in Fig. 9 (arrow A).

If the interacting ribbons have a Burgers vector $A\alpha+\alpha B$ and $\alpha C+B\alpha$ the configuration is symmetrical with respect to the one just derived; it is illustrated in Fig. 16.

9.2. Intersection of Two Ribbons

We will now consider the possible intersections of two ribbons and the resulting equilibrium configuration of the nodes. Two essentially different cases arise, depending on whether the stacking faults are of the same or of different type.

If they are of the same type, the interaction gives rise to an extended and a contracted node as represented in Fig. 17. It is the regular repetition of this pattern which gives rise to the hexagonal grids containing one type of stacking fault (visible in Fig. 18 and drawn schematically in the lower part of Fig. 8).

If the two stacking faults are of different types, the configuration of Fig. 19(b) results; this is relatively stable as a consequence of the repulsion between the three partials with the same Burgers vector αA. It is, however, only stable as long as the mutual annihilation

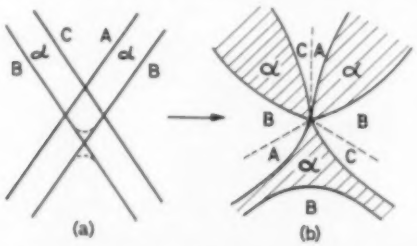

FIG. 17. Intersection of two ribbons containing the same stacking fault. One extended and one contracted node are formed.

of the partials with Burgers vectors αA has not taken place at their intersecting point. If this occurs the two dislocations with Burgers vector $A\alpha$ below the contracted node will glide away from this node and form, after interaction, the configuration represented in Fig. 19(c). This is now the final equilibrium situation, as can easily be checked. All parallel segments are repelling, and adjacent nodes are alternatively of the P and K type.

FIG. 18. Hexagonal nets containing singularities marked by arrows (see also Fig. 8): (a) line contrast, (b) stacking fault contrast.

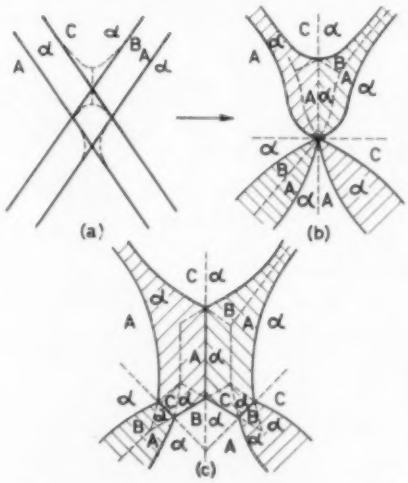

FIG. 19. Intersection of two ribbons containing a different stacking fault.

The regular repetition of this pattern would give rise to a hexagonal grid containing two kinds of stacking faults. Some singularities in hexagonal grids of the first type are most probably due to intersection with a dislocation ribbon containing a different type of stacking fault (Figs. 8 and 18).

9.3. Combined Patterns

A combination of the described reactions allows us to explain most of the observed patterns. As an example we

have analyzed the feature represented in Fig. 9; the result is given in the lettering pattern of Fig. 20. The correctness of the pattern was verified by making use of the contrast causing the extinction of certain dislocations. Such a photograph is reproduced in Fig. 9(b). It is clearly apparent that all dislocations lettered $C\alpha$ have disappeared.

10. DISLOCATION NETS

The main type of net to be expected in this structure is the hexagonal net in the c plane. As a consequence of the small stacking fault energy the dislocations will dissociate, and extended and contracted nodes similar to those observed in stainless steel will form.[8] Large nets of this type have been observed and Fig. 18(a) gives an example where the dislocations show up as lines. Figure 18(b), on the contrary, exhibits stacking fault contrast. The Burgers vectors of the different dislocations could be determined, as described in Sec. 5, using the sequence of photographs of Fig. 5. The result is summarized in the lettering pattern of the bottom part of Fig. 8.

The nets often contain singularities, i.e., deviations from the ideal pattern. Examples are visible in Fig. 18 (arrows). The interesting feature is redrawn in the upper part of Fig. 8. The same figure also conveniently summarizes the analysis in terms of Burgers vectors, using an adaptation of the lettering scheme proposed by Thompson[12] for the face-centered cubic lattice.

The singularities shown here can be considered as

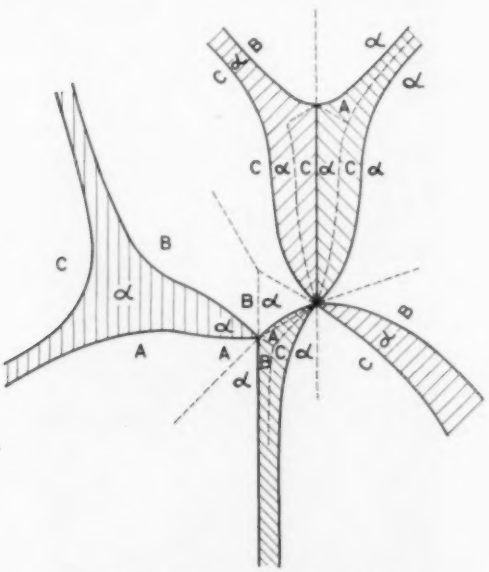

FIG. 20. Analysis of pattern shown in Fig. 9.

[12] N. Thompson, Proc. Phys. Soc. (London) **B66**, 481 (1953); *Report of Conference on Defects in Crystalline Solids* (The Physical Society, London, 1955), p. 153.

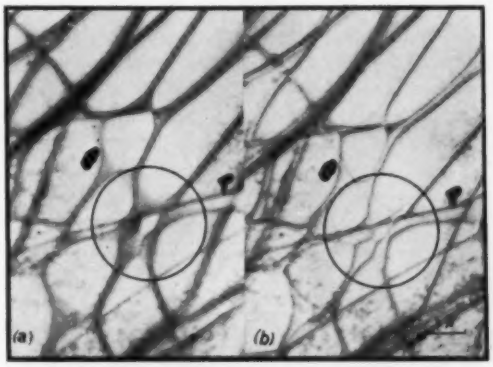

FIG. 21. Star pattern: (a) all lines visible; (b) one family of lines has disappeared.

resulting from a parallel displacement of one dislocation of the family $C\alpha$ in such a way that it no longer intersects with the two outer families in a common point. The result of the displacement of a partial dislocation with Burgers vector αC is to reconvert material containing a type I stacking fault into a normally stacked crystal. On the other hand, normally stacked regions will be transformed into regions containing a type II stacking fault. If the difference in energy between types I and II is small, as it certainly is, such displacements may be frequent and the singularity just described may occur more or less in a systematic fashion. This then gives rise to patterns as observed in Fig. 7. In reality the singularity probably results from the intersection of a "foreign" dislocation ribbon, i.e., one containing a stacking fault of a different type from the rest of the net (Sec. 9.2).

It is apparent from the lettering pattern of Fig. 8 that the three dislocation segments marked (1) should have the same Burgers vector αA as well as the three segments marked (2), which should have αB as a vector. From Fig. 7(d) we see that these segments have the same Burgers vector since they all disappear simultaneously. It is further clear from Fig. 7(c), which shows the same region but with a different line contrast, that all segments which have the same Burgers vector $C\alpha$ have disappeared. We have therefore proved that the lettering pattern is correct.

The same region was also observed with inverted contrast as shown in Fig. 7(b). It is now apparent that the two regions between the three dislocations (1) exhibit a different shade, in agreement with the fact that they contain different stacking faults. This distribution in shades corresponds exactly to the distribution of type I and type II stacking faults.

Figure 21(a) shows a further striking pattern, the star pattern redrawn somewhat ideally in Fig. 22, which at the same time summarizes the analysis in terms of Burgers vectors. The stability of the configuration can be checked on this lettering pattern. Parallel disloca-

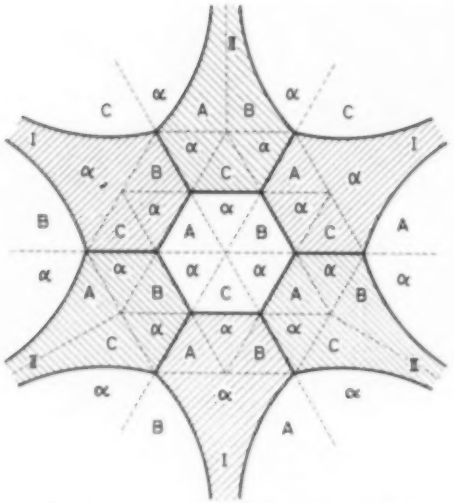

FIG. 22. Analysis of the star pattern of Fig. 21.

tions of the central hexagon repel since they have the same Burgers vector, preventing this from collapsing. Further extension of this hexagon is also hampered, since this would necessitate an increasing stacking fault area. The corner points of the hexagon are alternatively of the K and P type, assuring stability in this way. This pattern also implies the presence of two types of stacking faults in alternating sectors of the star, as indicated in Fig. 22 by a different cross hatching. Figure 21(b) shows a different contrast, with one set of lines lacking; it is clear that all these lines have the same Burgers vector $C\alpha$ in the lettering pattern, proving it correct.

11. MOVEMENT OF DISLOCATIONS

The basal dislocations in graphite are extremely mobile along the c plane and multiplication of dislocations is often observed after a few minutes of irradiations. This is probably due, as pointed out earlier by Hirsch,[13] to the stresses set up by deposition of a carbon layer on the specimen. The sources of dislocations are usually cleavage steps or the border of the specimen. No evidence for Frank-Read sources was found.

Figure 23 demonstrates in a striking way the glissile character of the nets. The interaction due to the crossing over of the row of extended nodes by another basal dislocation is sufficient to cause a very noticeable deformation.

These photographs also reveal that contracted and extended nodes can be formed by glide in the c plane only. It is, in particular, clearly visible that between Fig. 23 (a) and Fig. 23(b) the number of nodes between the point P which remained fixed, as can be judged from the identity of the configuration of vertical lines with respect to reference dust particles and the point Q, has increased by two. Whelan[8] has described in detail a mechanism whereby such nodes form in face-centered metals. This mechanism involves cross slip. It appears that this is not necessary, at least in graphite.

DISCUSSION

The observations presented here give direct evidence that dislocations in graphite behave like conventional dislocations in metals except that the stacking fault energy is very small. This explains why rhombohedral stacked graphite is occasionally found.

Also, as a consequence of the small stacking fault energy, the hexagonal nets consist of alternating extended and contracted nodes. A number of singularities have been explained in a consistent manner by assuming the occurrence of two kinds of low-energy stacking faults. In principle the same features could be explained; the lettering patterns would even remain the same, assuming that the second kind of stacking fault is the high-energy stacking fault mentioned in Sec. 1. The latter explanation is, however, less probable.

All the lettering patterns have actually been proved by making use of contrast effects as described in Sec. 5. The frequent occurrence of the hexagonal networks in

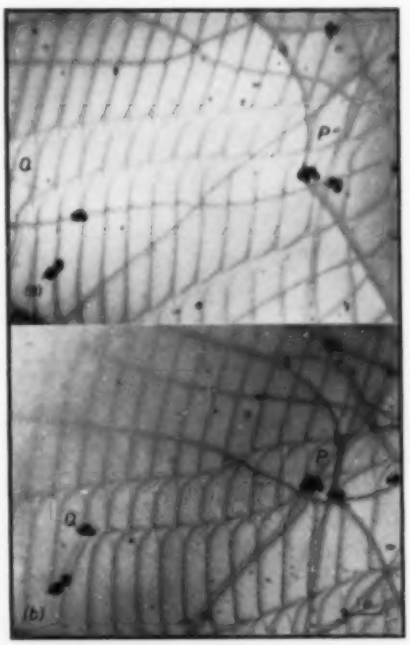

FIG. 23. Movement of dislocations. Between the two photographs a number of dislocations have moved, resulting in the formation of two *more* extended and contracted nodes between points P and Q.

[13] P. B. Hirsch, R. W. Horne, and M. J. Whelan, *Dislocations and Mechanical Properties of Crystals* (John Wiley & Sons, Inc., New York, 1957), p. 92.

the heat-treated samples suggests that an appreciable amount of rearrangement or even climb must take place at high temperatures (2500°C).

ACKNOWLEDGMENTS

We are indebted to Mr. Goens, director of the C.E.N., Mol, for permission to publish this paper. We also wish to thank Mr. Nicasy for his skillful preparation of specimens, Mr. Beyens for careful photographic work, Mr. Modave for preparing the drawings and, last but not least, we would like to express our gratitude to Dr. Henning and Mr. Dickerson of the Argonne National Laboratory for providing us with single crystals of graphite.

JOURNAL OF APPLIED PHYSICS VOLUME 31, NUMBER 12 DECEMBER, 1960

Mechanical Properties of Thin Single-Crystal Gold Films*

AVERY CATLIN AND WALTER P. WALKER
University of Virginia, Charlottesville, Virginia
(Received June 30, 1960)

Single-crystal gold films were grown by vacuum deposition on heated (375°C) sodium chloride substrate blanks. Completely oriented films with thicknesses between 1000 and 3000 A were obtained, with the plane of the film being the {100} crystallographic plane. A small hole was drilled through the substrate with a water jet, and the mechanical properties were determined by stressing the unsupported film over this hole. The films were observed to undergo considerable plastic deformation, accompanied by the appearance and growth of mechanical twin bands as the stress was increased. X-ray diffraction studies were made to determine the twin orientation. Both the ultimate tensile stress and the elastic modulus were found to increase as the thickness of the films was reduced.

INTRODUCTION

INVESTIGATIONS of the mechanical properties of thin gold and silver films have been in progress at the University of Virginia for several years. Previously published work by Beams[1] and associates on polycrystalline films indicates that there is a large increase in the strength as the thickness of the films is decreased below 2500 A. These thin films also show an indication of an increase in the elastic modulus as the thickness is reduced.

The series of experiments reported in this article was undertaken to examine the mechanical properties of thin single-crystal gold films. The results show that in these films there is also an increase in both ultimate tensile stress and elastic modulus as the thickness is reduced, similar to the increase observed in the polycrystalline films. Such a relatively large tensile strength for very thin single-crystal gold films has already been reported by Pashley.[2] In our experiments, mechanical twinning was observed at room temperature in the region of plastic flow, and this phenomenon was investigated in more detail. Other investigators have reported such twinning in copper at low temperatures,[3] and in silver-gold alloys at temperatures up to 0°C.[4]

* This work was supported in part by the Office of Ordnance Research, United States Army.
[1] J. W. Beams, W. E. Walker, and H. S. Morton, Phys. Rev. **87**, 524 (1952); J. W. Beams, H. S. Morton, and E. F. Turner, Science **118**, 567 (1953); J. W. Beams, J. B. Breazeale, and W. L. Bart, Phys. Rev. **100**, 1657 (1955).
[2] D. W. Pashley, Proc. Roy. Soc. (London) **A255**, 218 (1960).
[3] T. H. Blewitt, R. R. Coltman, and J. K. Redman, J. Appl. Phys. **28**, 651 (1957).
[4] H. Suzuki and C. S. Barrett, Acta Met. **6**, 156 (1958).

EXPERIMENTAL PROCEDURE

The gold films used in this work were prepared by vacuum deposition on sodium chloride crystal substrate blanks. Blanks with {100} surfaces were cleaved from larger crystals. Samples were selected which had large areas of the cleaved surface free from visible cleavage steps. These blanks were approximately 10 mm square and two mm thick. They were maintained at a temperature of 350° to 400°C by means of an induction furnace installed in the vacuum system. The gold was evaporated from an electrically heated molybdenum filament, and deposited at a rate of 500 to 1500 A per minute. A thin circular stainless steel plate was placed in the crystal holder with the crystals. The weight of this plate was determined both before and after evaporation, and from the difference in weight the thickness of the gold film could be calculated.

Samples were prepared for testing by drilling a small hole through the sodium chloride substrate with a water jet. The drilling apparatus was mounted beneath the stage of an optical microscope and a hole was drilled perpendicular to the plane of the film. Before drilling started, an area of the film was selected that was free from visible defects or steps. Drilling was stopped as soon as a circular area of gold film, approximately 0.5 millimeters in diameter, was no longer supported by the substrate. A remarkable feature of this drilling procedure is that such perfectly circular holes are produced. Figure 1 shows the appearance of a typical film. After drilling, the crystal was immersed in a series of ethyl alcohol and ether baths to remove all traces of water and

FIG. 1. Area of gold film over drilled hole. Note wrinkles due to compressive strain in film. (×90).

prevent crystallization of small sodium chloride crystals on the surface of the film.

Since the coefficient of thermal expansion of sodium chloride is about three times that of gold, the film is under considerable compressive strain when the sample cools down from the deposition temperature to room temperature. Wrinkles appear in the area of the film not supported by the substrate, as shown in Fig. 1. It is thus necessary to apply some pressure difference to the film before the major wrinkles disappear and the film assumes the shape of a spherical cap. Our measurements were made from this initial pressure difference, which defined zero strain. The actual testing was carried out by bulging the film downward through the hole in the substrate. The sample was mounted in a holder on the optical microscope stage so that the pressure on the bottom side of the film could be reduced with a vacuum pump. The pressure difference between the top and bottom of the film was measured with a calibrated water manometer.

An interference method was used to measure the radius of curvature of the bulged area. A thin cover glass was placed over the area of the gold film above the hole in the substrate, and the film was illuminated through the microscope objective with monochromatic light. Circular interference fringes, such as those shown in Fig. 2, were observed, and by counting each new fringe as it appeared at the center of the circular area, the change in the depth of the spherical cap could be determined. A photograph was taken of the interference fringes at the initial pressure difference, and from this photograph the initial radius of curvature and depth of the spherical cap were computed.

DISCUSSION

A. Epitaxial Growth of Films

Single-crystal gold films were grown on sodium chloride substrate blanks cleaved on a {100} plane, the plane of the deposited film also being a {100} plane. The process of epitaxial growth under these conditions has been previously reported in the literature.[5]

One of the first problems encountered in this work was that of producing very thin single-crystal films that were free from holes. It was found that films as thin as 1000 A could only be produced if the substrate temperature was maintained in the narrow range between 370° and 380°C. The deposition rate was varied between 500 and 1500 A per minute. If the temperature was too high, the film was not continuous, but contained holes. If the temperature was too low, the film was not a perfect single crystal, but contained disoriented grains. Using this technique of direct deposition of gold on sodium chloride, the minimum thickness of a good film seemed to be about 1000 A. Similar difficulties in producing very thin single-crystal films in this manner have been encountered by other workers.[6]

It is interesting to note here that in one experimental run, a sodium chloride blank was partially shadowed during evaporation. When this particular crystal was examined with the electron microscope, it was easy to observe the transition from material that was free from holes to material that contained holes. In both parts of the sample, the orientation was the same; the part free from holes was a good single crystal, while the part containing holes seemed to consist of many individual crystals that had started their growth at different nucleation centers and had not completely coalesced. Proceeding further toward the more heavily shadowed part of the sample, the holes became larger and the film appeared to consist of isolated individual crystals with the same orientation.

As mentioned earlier, the prepared films were badly wrinkled. This wrinkling indicated that the gold film was under compression when cooled from the deposition temperature to room temperature. However, there is some evidence that the film was originally under tension

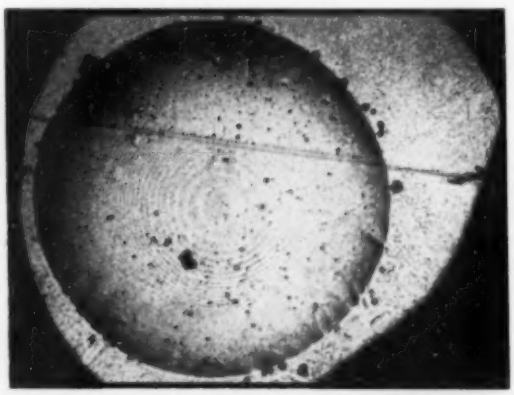

FIG. 2. Appearance of interference fringes used to determine depth of bulge. (×90).

[5] D. W. Pashley, Advances in Physics **5**, 19 (1956).
[6] Private conversation with D. W. Pashley.

when deposited. When the samples were reheated after drilling, the wrinkles all disappeared at about 150° to 200°C, which was considerably below the deposition temperature of 375°C. Furthermore, there was a large difference between the measured and calculated values of initial strain. Assuming a constant radius of curvature, the measured value of initial compressive strain was approximately 0.25%. An initial strain of about 1.0% was computed from the difference in the coefficients of thermal expansion of gold and sodium chloride. While this discrepancy could be explained by the presence of wrinkles around the edge of the hole, the two observations taken together suggest that the original stress in the film at the deposition temperature was a tensile stress.

B. Observation of Mechanical Twinning

One of the most interesting results of these experiments was the appearance of bands due to mechanical twinning. It is difficult to specify the stress at which twinning first occurred, since the initial bands that appeared were probably too small to be resolved by the optical microscope. These very small bands were later observed with the electron microscope. However, at a stress just below the ultimate tensile stress, small twin bands suddenly became visible, with their long dimension oriented in a ⟨110⟩ direction. These bands grew slightly in length and width with increasing stress. Some mechanism which is not completely understood served to impede the propagation of a twin band once it had formed, and a new band was then nucleated.

Upon application of further stress, the small bands grouped together into one or more large or major twin bands. A laminated fine structure was often visible in these major bands. Since twin bands oriented in the [110] direction can be formed by twinning on either the (111) or ($\bar{1}11$) plane, this laminated appearance is probably due to the junction of these twins formed on different planes. Where several small bands that had twinned on the same plane joined together to form a large band, the latter did not exhibit a laminated fine structure. Two major bands, extending almost all the way across the bulged area, often appeared at right angles to each other. Their appearance is shown in the optical micrograph of Fig. 3. The small bands had lengths of up to 50 μ, while the large bands were often as long as 1000 μ.

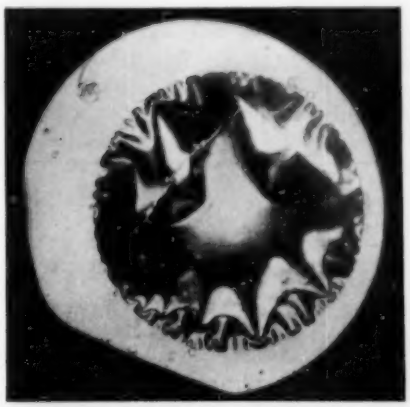

FIG. 3. Optical micrograph showing appearance of twin bands. (×90).

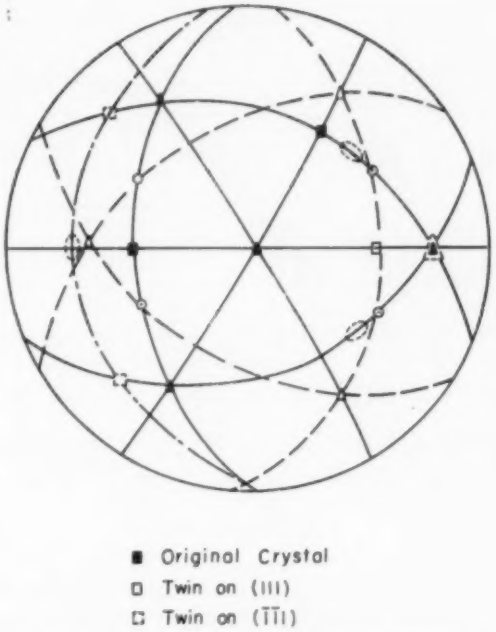

FIG. 4. Stereographic plot of x-ray diffraction photograph.

X-ray diffraction studies were made to determine crystallographic orientation within the bands. Transmission Laue photographs were taken using a highly collimated x-ray beam. The gold films were oriented so that the beam was incident on a deformed area along a ⟨111⟩ direction. The diffraction patterns showed a set of spots that correspond to rotations of the crystal through 180° about the ⟨111⟩ directions. Appearance of these additional spots indicated that the bands were twin bands, and that twinning had occurred on {111} planes in ⟨112⟩ directions. The stereographic plot of a typical diffraction photograph is shown in Fig. 4. Further details of this twinning process have been discussed in a separate article.[7]

C. Stress-Strain Curves

Stress and strain were computed from the measured pressure difference between the two sides of the film,

[7] A. Catlin, K. R. Lawless, and W. P. Walker, Acta Met. (to be published).

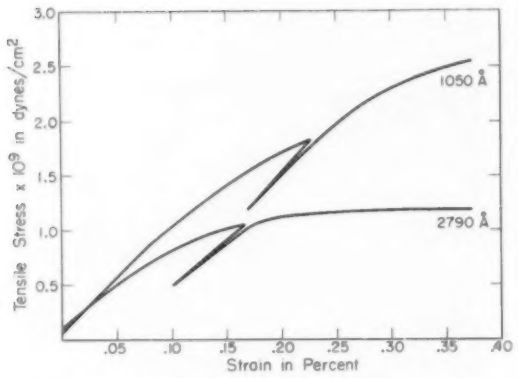

FIG. 5. Stress-strain curves for two films of different thickness.

and the measured change in deflection of the center of the bulged test area. The expressions used were[8]:

$$\text{stress} \quad \sigma = \frac{Pr}{2h} = \frac{Pa^2}{4hd},$$

$$\text{and strain} \quad \epsilon = \frac{2(d^2 - d_0^2)}{3a^2},$$

where P = differential pressure across film,
r = radius of curvature of spherical cap,
h = thickness of film,
a = radius of hole in substrate,
d = deflection of film from original plane,
d_0 = initial deflection of film.

The equation for stress is quite accurate, since the radius of curvature at the center of the spherical cap can be precisely determined from photographs of interference fringes. The equation for strain is less accurate, since our derivation assumed constant strain throughout the bulged test area. A few wrinkles always remained around the periphery of the hole, and they presented such a complex geometry that their effect could not be taken into account in calculating the strain. However, these computed strains are useful in comparing films of different thicknesses.

A plot of the stress-strain characteristics of two representative films is shown in Fig. 5. The small value of stress at zero strain is due to the initial pressure difference required to remove wrinkles at the center of the film. As the stress is increased, it is observed that there is no well-defined elastic region with a constant slope. Stress relaxation steps were taken at higher values of stress in order to determine the elastic modulus. These steps could be accurately reproduced and exhibited no hysteresis effects. The separation at the top of these steps can be accounted for by short-time creep in the films. Stress is normally increased at a rate of approximately 5×10^8 d per cm² per min. When the pressure difference between the two sides of the film was maintained constant, the film was observed to creep, the change in strain being of the order of 5×10^{-3} % over a period of 15 sec. Although changes in the strain of less than 10^{-3}% could have been observed by following the displacements of the interference fringes, no further creep was noticed over a period of one hour.

In the region of low stress, the apparent work hardening of the specimen is partially due to rearrangement of wrinkles around the boundary of the bulged film. There is also some plastic flow and consequent work hardening due to twinning in areas of high local stress concentration in the wrinkled boundary. Occasional small twin bands have been observed in this area at quite low values of applied stress. These effects introduce a negative curvature in what would normally be the linear elastic portion of the curve. However, it should be noted that the initial slope of each curve agrees fairly well with the slope of the stress relaxation step.

In the region of higher stresses, the shape of the curves indicates further plastic flow and work hardening. It is interesting to compare the two curves for samples of different thickness. The thinner film (1050 A) shows considerable work hardening up to the point of fracture. Only small twin bands were observed, and the fact that these bands seemed to be pinned down at their ends, so that additional stress had to be applied to cause further twinning, probably accounts for this work hardening. The large or major twin bands did not appear in this film.

The thicker film (2790 A) shows some work hardening, but also a considerable amount of plastic flow, especially at stresses just below the ultimate tensile stress. Each incremental increase in applied stress produced a greater number of small twin bands than in the case of the thinner film. It would appear here that conditions for the nucleation of the twinning process were more favorable. Furthermore, there was the sudden appearance of the large twin bands, shown in Fig. 3, accompanied by an increase in strain with no appreciable increase in stress. This is the portion of the curve for strains greater than about 0.33%.

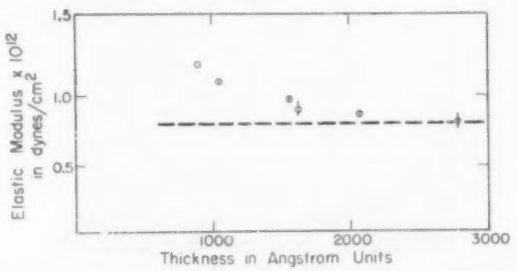

FIG. 6. Variation of elastic modulus with film thickness.

[8] R. Hill, Phil. Mag. 41, 1133 (1950).

Very thin single-crystal gold films have been previously tested, and it has been reported[9] that these films deformed elastically almost up to the point of fracture. The films we have tested all showed considerable plastic deformation before fracture, and in most cases twin bands were observed.

D. Changes in Strength and Elastic Modulus

The variation of elastic modulus with film thickness is shown in Fig. 6. The modulus increases with decreasing thickness in the range observed. Several samples of the same thickness were tested, and the spread of values at each thickness was quite small. We have no theoretical explanation for this increase in elastic modulus as the thickness is reduced.

The elastic modulus for orthogonal applied stresses in the principal plane of a cubic crystal is invariant under rotation in the plane. We have this situation in our samples, where the area at the center of the spherical cap is subjected to biaxial tensile stress, and where the plane of the film is a principal plane of the crystal. Using the reported compliance tensor components[10] for gold, we have calculated the value of elastic modulus for a single crystal of gold under these conditions. This value is 0.785×10^{12} d per cm^2, and is indicated by the dashed line in Fig. 6. There is close agreement between this calculated value and the measured elastic modulus in the thicker films.

Variation of ultimate tensile stress with film thickness is shown in Fig. 7. The resolved shear stress on the (111) plane in the $[10\bar{1}]$ direction is 41% of the tensile stress. The ultimate tensile stress increases by about 100% over the thickness range observed, and this increase is very similar to that reported[11] for thin polycrystalline gold films.

It has been suggested that the increased strength of thin films could be due to their small grain size.[12] Since our thin single-crystal films contained no individual grains and still exhibited high strength, it would appear that this effect is not lost when grain boundaries are absent. The increased strength of thin films is probably due to their thinness and the proximity of the two surfaces of the film, rather than to small grain size.

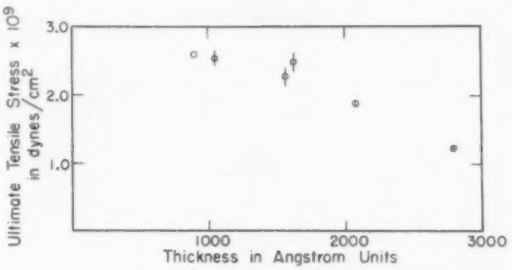

FIG. 7. Variation of ultimate tensile stress with film thickness.

SUMMARY

The results of this investigation show that mechanical twinning will occur in thin single-crystal gold films that are subjected to tensile stress. The nucleation and propagation of twin bands accounts for a large part of the plastic flow and work hardening observed in the stress-strain curves. The measured values of ultimate tensile stress and elastic modulus both increase as the thickness of the film is reduced, in substantial agreement with the results obtained for thin polycrystalline films.

ACKNOWLEDGMENTS

The authors wish to acknowledge that this research was carried out under the guidance and supervision of Dr. J. W. Beams. We are grateful to Dr. N. Cabrera and Dr. J. W. Mitchell for help and advice in interpreting the results of these experiments. Our thanks are due to Dr. K. R. Lawless for the electron microscope observations.

[9] J. W. Menter and D. W. Pashley, *Structure and Properties of Thin Films*, edited by C. A. Neugebauer, J. B. Newkirk, and D. A. Vermilyea, (John Wiley & Sons, New York, 1959), p. 111.

[10] H. B. Huntington, *Solid State Physics*, edited by F. Seitz and D. Turnbull (Academic Press, New York, 1958). Vol. 7, p. 274.

[11] W. K. Ford, A. L. Stampler, and J. W. Beams, Bull. Am. Phys. Soc. Ser. II, **1**, 333 (1956).

[12] W. K. Ford, doctoral dissertation, University of Virginia (1957).

Experimental Investigations of the Cesium Plasma Cell*

W. A. Ranken, G. M. Grover, and E. W. Salmi
Los Alamos Scientific Laboratory, Los Alamos, New Mexico
(Received December 16, 1959; and in final form July 25, 1960)

Some aspects of the performance of a cesium plasma cell with tantalum emitter are evaluated in terms of experimental determinations of the effects of variations in such parameters as cesium vapor pressure, emitter temperature, and emitter-collector separation distance. Experiments relating to the effect of collector serrations and to the feasibility of radiation shielding are described. Voltage-current characteristics are presented for several emitter temperatures and for a wide range of cesium vapor pressure.

I. INTRODUCTION

THE direct conversion of heat to electricity through the use of what has been called either a thermionic converter or a plasma thermocouple, depending primarily on the pressure of cesium vapor used to neutralize the electronic space charge, has been reported by several research groups.[1–5] Basically, the device is a simple diode with a hot filament or button serving as an electron emitter and a cold surface serving as an electron collecting electrode. The region between the electrodes is filled with cesium vapor which is ionized either upon contact with the hot high work function emitter, or by other processes, and hence serves to neutralize the electronic space charge so that saturated Richardson emission currents can be obtained. The source of the voltages observed across the cell terminals has been attributed to the contact potential difference existing between the high work function emitter and the low work function collector by Hernqvist *et al.*[2] when cesium pressures are sufficiently low so that electrons making the transit from the emitter to the collector do so with few or no collisions with ions or atoms in the gas. In applying this model it is assumed that the low work function collecting electrode is maintained at a temperature sufficiently low for its thermionic emission to be negligible compared to emission from the hot electrode. For cesium pressures where the number of collisions made in the region between electrodes is large, the situation becomes more obscure. Lewis and Reitz[6] have treated the cell as a plasma thermocouple and when no current flows have used transport theory and thermodynamical considerations to calculate the thermoelectric voltage generated when an electron temperature gradient exists. Pidd *et al.*[4] have demonstrated that the zero current voltages of the cell follow roughly the behavior predicted from this theory for cesium pressures of the order of 0.3 mm Hg and above.

This paper describes experiments performed with cell configurations where tantalum is used as the emitter. The general purpose of these experiments was primarily to determine optimum operating conditions for such a cell and secondarily to obtain a measure of understanding of the physical mechanisms involved in its performance at high (on the order of 1 mm Hg) cesium pressure. Reported herein are investigations relating to the effects on cell performance of modifications of the geometrical configuration of the cell, including the effect of varying the separation distance of the emitter and collector, the effect of serrations of the collector electrode (designed to double the effective collecting area exposed to the cesium plasma), and the effect of introducing radiation shielding between the emitter and collector. In the process of these investigations the behavior of the voltage-current characteristics and power outputs of the cell were studied over a wide range of cesium vapor pressure and emitter temperature.

II. EXPERIMENTAL CELL CONFIGURATIONS

The basic design features of the cell have been described in an earlier report[1] but for the sake of clarity these will be presented again insofar as they relate to the present set of experiments.

Figure 1 shows the more important aspects of the design of the cell with adjustable emitter-collector spacing. A tantalum button $\frac{1}{8}$ in. thick and $\frac{3}{8}$ in. in diameter is welded into a 0.012-in. thick tantalum disk and the assembly is mounted between two circular knife edges thus dividing the cell into two chambers. The upper chamber, which is continuously evacuated, houses the electron gun used to heat the tantalum button. In the normal range of operation the gun bombards the tantalum button with electron currents of from 0.3–0.8 amp at voltages up to 2600 v. Considering that the resistance of the button and disk is less than 10^{-3} ohm it can be seen that the extraneous voltages associated with button heating are very small.

The quartz viewport mounted on the insulator at the top of the gun chamber allows pyrometric observation of the button temperatures. For this purpose, also, small holes are drilled four-fifths of the way through the

* This work was performed under the auspices of the U. S. Atomic Energy Commission.
[1] G. M. Grover, D. J. Roehling, E. W. Salmi, and R. W. Pidd, J. Appl. Phys. **29**, 1611 (1958).
[2] K. G. Hernqvist, M. Kanefsky, and F. H. Norman, RCA Rev. **19**, 244 (1958).
[3] V. C. Wilson, J. Appl. Phys. **30**, 475 (1959).
[4] R. W. Pidd, G. M. Grover, E. W. Salmi, D. J. Roehling, and G. F. Erickson, J. Appl. Phys. **30**, 1861 (1959).
[5] R. Fox and W. Gust, Bull. Am. Phys. Soc. Ser. II, **4**, 322 (1959).
[6] H. W. Lewis and J. R. Reitz, J. Appl. Phys. **30**, 1439 (1959).

tantalum button. The length to diameter ratio of these holes is 5 to 1, and hence only small emissivity corrections to the pyrometrically observed temperatures are required. Of more importance, however, is the fact that temperatures can be measured without regard to changes in emissivity of the button surface brought about by prolonged bombardment heating. In addition, the effect of reflected light, from the tungsten filament in the electron gun, on the observed temperature is negligible. Temperature drops of up to 200°C occur from one face of the button to the other and hence a calibration must be made of the temperature of the lower face of the button (the emitting surface of the cell) vs observed hole temperatures.

The emitting area of the cell is taken to be that of the tantalum button (2 cm²). Justification for this assumption is given in Fig. 2, which shows a typical temperature profile for the button and disk geometry. Since electron emission falls off exponentially with temperature, the

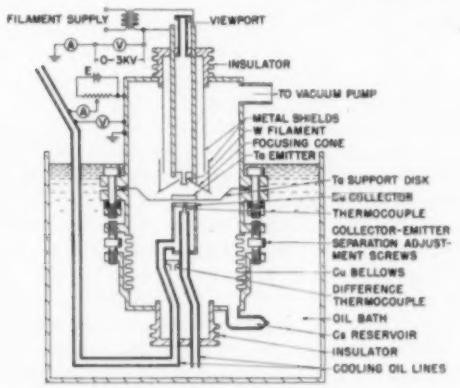

FIG. 1. Schematic illustration of experimental cell showing assembly details and electrical circuits.

error made in neglecting the emission from the disk is small insofar as this emission is characterized by the work function of tantalum. For cesium pressures on the order of 10^{-2} mm Hg and higher, the possibility exists that annular regions of the disk are partially coated with cesium with the resulting formation of low work function surfaces.[3] In this instance it is likely that the emission per unit area of portions of the disk is comparable with the emission per unit area of the button and the emitter area is no longer well defined. This effect will be further discussed in Sec. III. The region of the button and disk where positive ion formation takes place is not generally well defined.

The lower chamber depicted in Fig. 1 forms the thermoelectric cell. The collector is a $\frac{3}{8}$-in. diam capped copper tube through which silicone oil is circulated. Thermocouples are inserted in the oil stream, as shown, to determine the oil inlet and outlet temperatures, thus providing a somewhat rough calorimetric measure of the total heat flow to the collector. The oil is circulated by

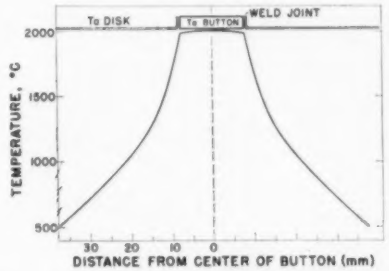

FIG. 2. Temperature profile of tantalum button and mounting disk as viewed from cesium side of cell.

a centrifugal pump driven by an air motor. The latter is used so that no problem arises from pickup voltages appearing across the cell terminals when open circuit voltages are being measured.

The spacing between the emitter and collector may be changed by means of three adjusting screws which expand or contract the copper bellows. The cesium is encapsulated in glass and placed in a side tube as shown. After the cell has been thoroughly baked out at a temperature of about 350°C the copper pumping tube is pinched off in a hydraulic press, forming a reliable cold-weld joint, and the cesium capsule is crushed. The whole assembly is immersed in a thermostatically controlled silicone oil bath by means of which the cesium pressure in the cell can be controlled over a range of 10^{-5}–6 mm Hg. The insulator through which the collector leads pass is maintained about 50°C hotter than the oil bath to combat the formation of a cesium coating. When this precaution is taken the leakage resistance across this insulator is generally in the range of 1×10^5 to 3×10^5 ohms.

The cell configuration shown in Fig. 1 is that used to obtain data on the effect of emitter-collector spacing on

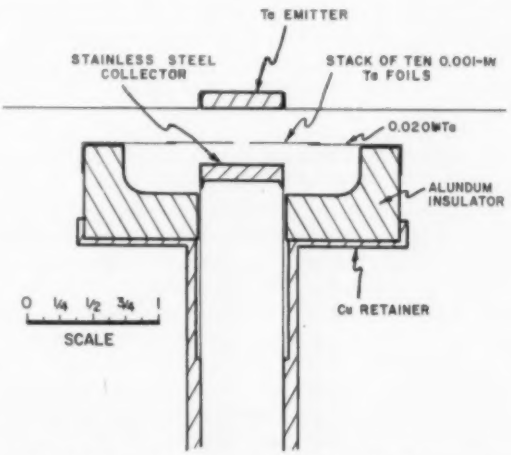

FIG. 3. Schematic illustration of radiation shield mounting. Scale is in inches.

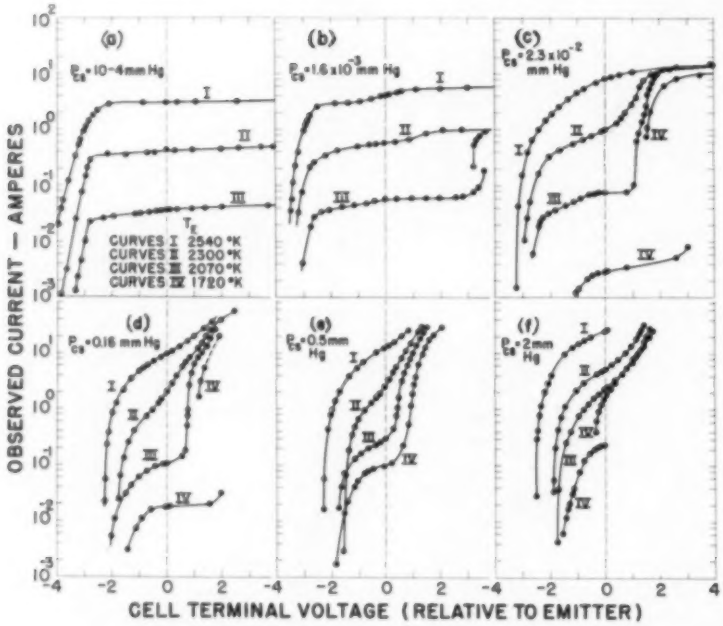

FIG. 4. Current-voltage characteristics of cell with tantalum emitter and serrated copper collector. Curves I through IV cover the emitter temperature range of 2540 to 1720°K. Figures 4(a) through 4(f) cover the cesium vapor pressure range of 10^{-4} to 2 mm Hg.

cell performance. The experimental configuration used in the experiments on the value of collector serrations is identical to that shown in Fig. 1 with the exception of circular serrations in the face of the copper collector. These circular grooves were 0.032 in. deep and served to double the surface area of the collector face.

The experimental arrangement used to obtain some idea of the feasibility of improving the cell efficiency through the use of radiation shields is sketched in Fig. 3. The radiation shield consists of 10 circular 1-mil thick tantalum foils spot welded together at several points. Through the center of the stack is a $\frac{1}{8}$-in. diam hole. This arrangement is mounted on a tantalum support disk which is mounted, in turn, on an alumina insulator. The shield is allowed to float electrically. The collector used in this experiment was fabricated from stainless steel.

III. VOLTAGE CURRENT CHARACTERISTICS OF THE SERRATED COLLECTOR CELL

Of the various cell configurations, that which was studied most extensively was the cell with the serrated copper collector described in Sec. II. This cell had a collector-emitter separation distance of 2.5 mm. Current-voltage characteristics were obtained for a voltage range of -24 v to $+24$ v except where cell currents exceeded 30 amp.

The voltage source consisted of a 6-ohm rheostat placed across two 12-v storage batteries. Such a voltage source has the disadvantage of variation of the load across the cell as the voltage is changed, but this is of consequence only in the region of high cesium pressure and positive applied voltages where arc discharges are encountered. In the working region of the cell the voltage current relations obtained by this method duplicate exactly those obtained by varying a load resistor.

In measuring most of the voltage-current characteristics of the cell it was not found necessary to correct the emitter temperature for the variation in Peltier cooling occurring as electron currents were varied from zero to short circuit values. The geometry of this cell is sufficiently inefficient for the amount of heat removed by Peltier cooling to be small compared to the amount lost by radiation and conduction from the button and disk. As a result, changes of emitter temperature occurring as the cell current was changed from zero to values up to about 20 amp were too small to be detected with the optical pyrometer, (less than about 10°K). When cell currents significantly larger than 20 amp were obtained (Sec. IV) it was necessary to vary the power supplied to the emitter in order to obtain a constant emitter temperature current-voltage characteristic.

Voltage-current characteristics obtained for the serrated collector cell in the range of net electron current are presented in Fig. 4 for emitter temperatures (T_E) ranging from 1720°K to 2540°K and for cesium pressures P_{Cs} covering the range of 10^{-4} to 2 mm Hg. For the two lowest cesium pressures [Fig. 4(a) and 4(b)] the curves are similar to those observed by Hernqvist *et al.*[2] Even for these low cesium pressures the electron currents are completely space-charge neutralized. In fact, with the exception of the curve for emitter temperature equal to 2540°K and cesium pressure of 10^{-4}

mm Hg, the electron space charge is over-neutralized; more positive ions are being produced than are required for space charge neutralization. The observed currents rise from zero with a behavior dependent upon electron temperature until they essentially level off at a voltage close to the contact potential difference between the cesium-coated copper collector and the uncoated tantalum emitter. The magnitudes of the currents at the points where current saturation occurs are slightly more than half the expected thermionic emission from tantalum. At these low pressures this discrepancy can be partially ascribed to the fact that some of the electrons from the emitter travel to the walls of the vacuum chamber rather than to the collector. Except for the curve with $T_E = 2070°K$ and $P_{Cs} = 1.6 \times 10^{-3}$ mm, the currents increase slowly with applied positive voltage in the range of 4–24 v not shown in Fig. 4. The behavior of the excepted curve is unusual in that the cell apparently goes into a thermionic arc discharge at a lower applied voltage (3.5 v) than the voltages (>24 v) for which breakdown occurs at higher emitter temperatures.

For a cesium pressure of 2.3×10^{-2} mm [Fig. 4(c)] the voltage at which the transition from the normal operating mode of the cell to the discharge mode occurs decreases with emitter temperature in accord with early experiments on thermionic arcs in cesium vapor.[7] The most striking behavior at this pressure occurs for $T_E = 1720°K$, where an abrupt increase of current of more than three orders of magnitude takes place in the voltage range of 1—3 v positive. The currents obtained in the discharge region show very little dependence on emitter temperature.

It is difficult to explain the magnitude of the electron currents obtained for positive cell voltages on the basis of effects occurring at the button surface. It is more probable that these high current values result from the coating of the support disk with cesium. This formation of fractions of a monolayer of cesium on tantalum produces low work function surface areas even if the tantalum is at a relatively high temperature, provided the cesium pressure is sufficiently high. Hence, portions of the emitter support disk may be prolific electron emitters. However, these surface regions, because of their low work function, are not good ion producers. Hence the emitted electrons cannot reach the collector until the collector is made positive relative to the emitter and the accelerating field between the electrodes becomes large enough to enable ionization by impact of electrons with neutral cesium atoms to take place.

Extension of the emitting area beyond the confines of the emitter button apparently has little effect on the shape of the current voltage characteristics in the working region of the cell, at least for the higher emitter temperatures. This conclusion is based on a series of measurements in which a small, cooled, Langmuir plane probe was mounted flush and central with respect to the collector surface in a cell with tantalum emitter and a 3-mm collector-emitter separation distance. The collector diameter was 0.625 in. When the collector and probe were maintained at the same voltage the collector served as a guard ring for the probe and shielded it from any effects of emission from the support disk. Under these conditions, and for an emitter temperature of 2540°K, the ratio of short circuit currents to the probe and the collector was just the ratio of their areas for values of cesium pressure up to 0.5 mm Hg, the highest pressure at which probe measurements were made. This result is not to be expected if the collector is drawing appreciable current from the support disk. Measurements of this type were not made at the lower emitter temperatures.

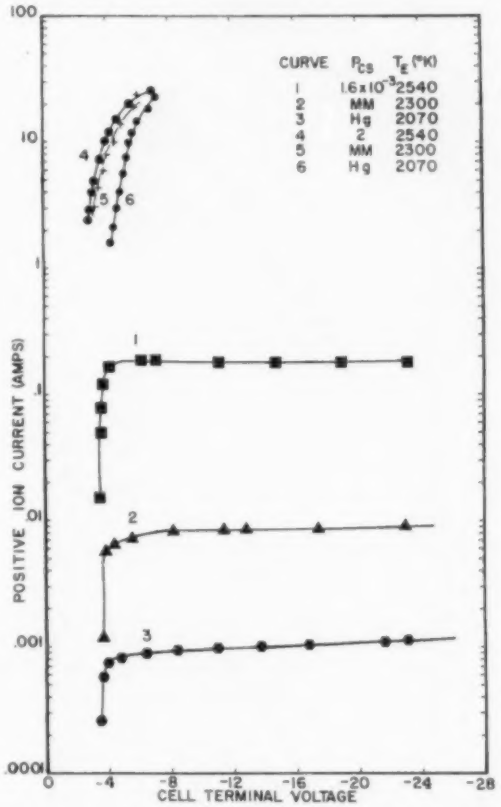

FIG. 5. Positive ion current versus negative potential applied to cell terminals. Curves 1 through 3 were obtained for a cesium vapor pressure of 1.6×10^{-3} mm Hg. Curves 4 through 6 are for a cesium vapor pressure of 2.0 mm Hg.

The behavior of the current-voltage characteristics in the region of reverse (positive ion) currents for pressures on the order of 10^{-1} mm and less is typified by curves 1, 2, and 3 which are presented in Fig. 5. These curves were obtained at a cesium pressure of 1.6×10^{-3} mm Hg. Above 10^{-1} mm pressure, arclike discharges are en-

[7] F. H. Newman, Phil. Mag. **50**, 463 (1925).

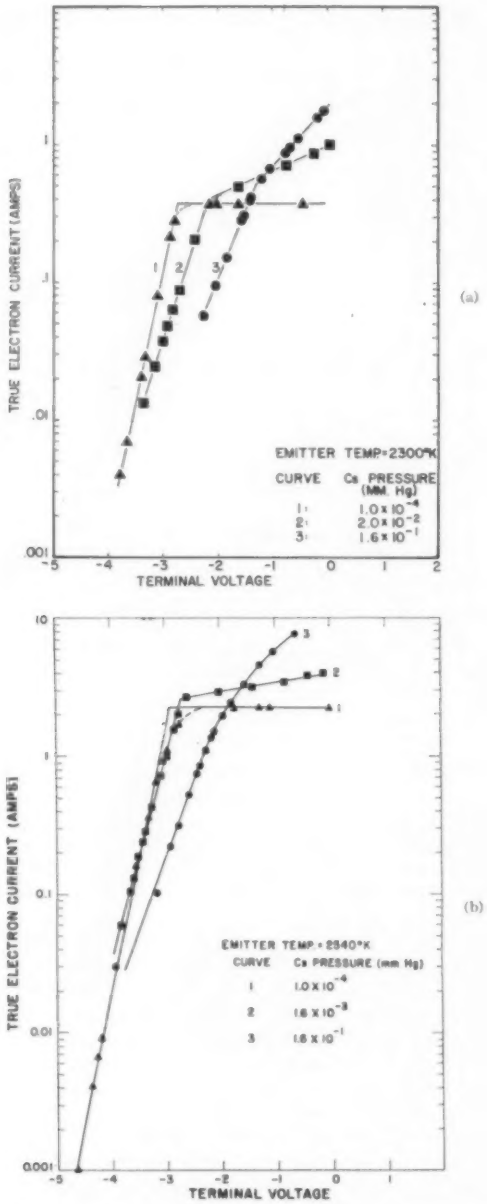

FIG. 6. Plot of true electron current (observed current corrected for magnitude of positive ion current) versus cell terminal voltage. (a) Emitter temperature = 2300°K, cesium vapor pressures of 1×10^{-4}, 2×10^{-2}, and 1.6×10^{-1} mm Hg. (b) Emitter temperature = 2540°K, cesium vapor pressures of 1×10^{-4}, 1.6×10^{-3}, and 1.6×10^{-1} mm Hg.

countered, with breakdown voltages decreasing with increasing pressure until at 2-mm pressure the behavior demonstrated by curves 4, 5, and 6 in Fig. 5 is encountered. The reverse current increases from zero (at equivalent open circuit voltage) to 25 amp with no sign of a transition region.

Low and intermediate pressure ion curves show the behavior expected from a plane Langmuir probe in a plasma.[8] Carrying the similarity a little further, one can extrapolate the flat region of the ion curves to less negative voltage values and add the magnitudes of the extrapolated ion currents to the observed electron currents to obtain curves of true electron current vs collector voltage. This is, of course, the procedure followed in constructing Langmuir probe characteristics. When collector characteristics are plotted in this manner, curves of the type shown in Fig. 6(a) and (b) are obtained. The similarity to probe characteristics is obvious. The initial increase of true electron current with voltage is indeed exponential. For a true probe the slope of this portion of the characteristic is (on a semilogarithmic plot) proportional to the reciprocal of the electron temperature in the plasma. Electron temperatures obtained from the curves in Fig. 6(a) and (b) for a pressure of 10^{-4} mm are within 100 deg (Kelvin) of the emitter temperatures. This result has been predicted by Hernqvist *et al.*[2] However, as the cesium pressure increases, the behavior of the collector characteristics in Fig. 6(a) and (b) suggests that the electron temperature increases to values on the order of twice the emitter temperature. That such high electron temperatures should exist in the cell plasma is reasonable enough for large currents flowing through the cell, but the collector characteristics do not give evidence of electron temperature depending on the current.

The relatively abrupt change in slope of the characteristics is identified, in the case of true probes, with the point at which probe voltage is equal to the plasma potential. Ideally this is the potential for which all electrons in the plasma are able to diffuse to the probe and further increase in probe voltage will not increase the electron current. In the case of the collector the change in slope (pseudosaturation of electron current) occurs, at low pressures, when the electron current reaches the value of Richardson emission of the emitting surface. The voltage at which this break occurs is not necessarily related to the plasma potential. For high cesium pressures diffusion limiting may also falsify apparent space potentials. (Diffusion limiting refers to the case where the collector drains electrons from the plasma adjacent to it at a rate limited by the electron replacement by field free diffusion from more remote regions in the plasma.) In any case, measurements of plasma potentials and electron densities obtained from the collector characteristics in the usual manner are likely to be in error. Plasma densities may, however, be estimated from the saturation values of the positive ion

[8] A complete discussion of the Langmuir probe and probe characteristics is given in L. B. Loeb, *Basic Processes of Gaseous Electronics* (University of California Press, Berkeley, California, 1955), pp. 332–370.

currents.[9] That these estimates are reliable, at least for cesium pressures below 10^{-1} mm Hg, has been verified by results obtained with the Langmuir probe mentioned earlier. In principle, if the electron velocity distribution is indeed Maxwellian then once the electron densities are established the plasma potential may be obtained. In most cases this procedure involves large extrapolations of the initial portions of the collector characteristics and hence is subject to considerable error. The general trend of plasma potential with cesium pressure is from a value of about zero for a Cs pressure of 10^{-4} mm Hg to values of about 2 v positive (relative to the emitter) for 10^{-1} mm Hg.

It is perhaps worthwhile to point out that although the short circuit currents for a given emitter temperature increase with cesium pressure, as can be gleaned from the curves in Figs. 4 and 6, the maximum power does not follow this behavior. Figure 7 depicts the dependence of maximum power output on cesium pressure for several emitter temperatures. The power maximum is seen to decrease slightly with increasing cesium pressure until at a pressure of about 2×10^{-1} mm Hg a rapid rise occurs. This pressure is in the range for which cesium coating of the emitter is expected to become appreciable. It can be seen that the rate of increase of power with pressure is greater for lower emitter temperatures.

The improvement of the power density of the cell brought about by doubling the effective area of the collector through the use of serrations was about a factor of two for high cesium pressure and high emitter temperature operation. At the lower emitter temperatures little or no improvement was observed. Hence the evaluation of the effect of the serrations is not straightforward. For low pressure operation, where the cell currents are known to be emission limited, there was no increase in power density nor does one expect any.

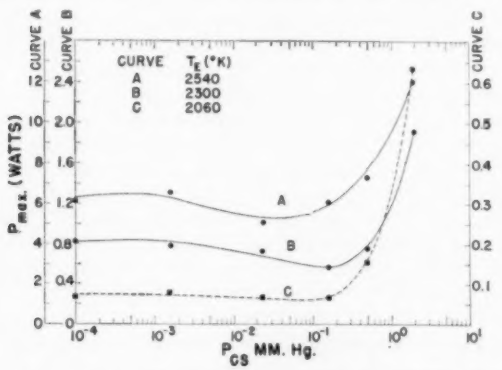

FIG. 7. Maximum output power in watts (P_{max}) versus cesium vapor pressure (P_{Cs}). Note separate ordinate scale for each emitter temperature.

[9] J. E. Allen, R. L. F. Boyd, and P. Reynolds, Proc. Phys. Soc. (London) **B70**, 297 (1957).

IV. EFFECT OF EMITTER-COLLECTOR SPACING ON CELL PERFORMANCE

The two phenomena expected to influence the amount of current drawn at a given cell terminal voltage (in the working region of the cell) and at a given emitter temperature are the emission limit of the emitter and the effective impedance of the plasma, be it due to multiple scattering of electrons by ions or to negative space charge formation resulting from positive ion deficiency. It has been seen in Sec. III that for cesium pressures below about 10^{-2} mm the electron currents drawn are definitely emission limited. For the higher pressures it was found that the current was a strong function of the collector voltage in the range of -2 to 0 v and indeed, at the latter voltage, exceeded the expected Richardson emission for tantalum.

At the low pressures the plasma impedance should be negligible since electron and ion mean free paths are large compared with the dimensions of the cell and the electron space charge is completely neutralized. For high pressures the interaction of electrons and ions with each other and with the neutral atoms can no longer be neglected and it becomes of interest to determine the relative importance of emission and plasma impedance in limiting the current output of the cell.

The behavior of the current output of the cell as a function of emitter collector spacing can be used as an indication of the importance of plasma impedance in limiting the current flow, provided that this impedance is associated with the bulk of the plasma between the electrodes rather then confined to thin layers adjacent to one or both of the electrodes.[4,6] Figure 8(a) gives the dependence of maximum power vs electrode separation for a cesium pressure of 0.5 mm Hg and for four emitter temperatures. The curves are normalized to the value for $T_E=2540$°K at 6.7-mm separation. These measurements were obtained with the cell configuration shown in Fig. 1. Since for this pressure the cell voltages were nearly independent of spacing the behavior of zero-voltage (short circuit equivalent) current with spacing is similar to that shown in Fig. 8(a). It can be seen that as the spacing is decreased from 6.7 mm to 1.2 mm the maximum power is increased by an average of only 50%. Much of this effect can be attributed to increased loss of positive ions and electrons from the working region of the cell as the spacing is increased. It appears that the bulk impedance of the plasma has a negligible effect in limiting the cell's performance in this range of operation.

Some experimental data were also taken at a cesium pressure of 2.0 mm Hg. The results are presented in Fig. 8(b). Again the curves are normalized to a point at 6.7 mm and $T_E=2540$°K. As compared to the results in Fig. 8(a) the increase of power with the reciprocal of electrode separation is somewhat more pronounced for an emitter temperature of 2420°K and much more pronounced for the emitter temperature equal to

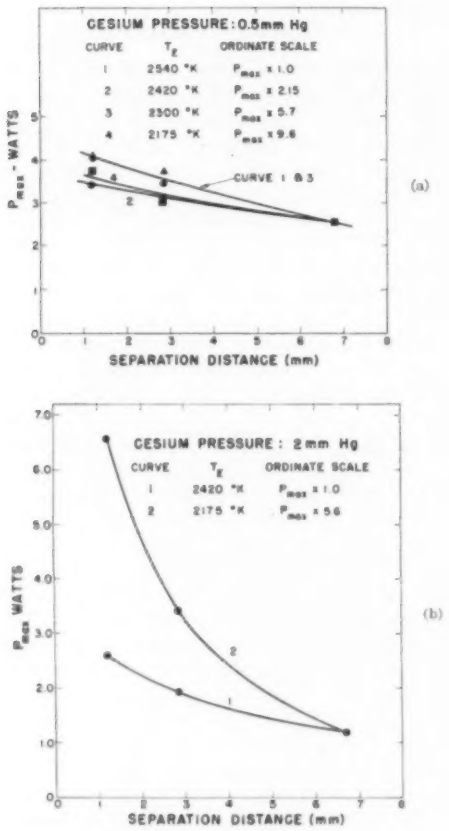

FIG. 8. Effect of emitter-collector separation distance on maximum output power (P_{max}) for several emitter temperatures. (a) Cesium vapor pressure=0.5 mm Hg. (b) Cesium vapor pressure=2 mm Hg. Power values have been multiplied by the factors given in the columns labeled "ordinate scale" in order to normalize the curves for different emitter temperatures to the same value for a separation distance of 6.75 mm.

2175°K. The latter behavior may result from a space charge limiting effect near the collector and will be discussed in Sec. VII.

Electrode separation for the cell with the serrated collector was reduced to about 0.1 mm and the cell was operated at a cesium pressure of 6 mm Hg and an emitter temperature of 2710°K. This operating point represented the highest value of cesium pressure that could be safely attained with the silicone oil bath and the highest controlled emitter temperature attainable. The zero-voltage current was 110 amp and the maximum power produced in an external load was 60 watts, representing an approximate efficiency of 15%. The method of measuring a value for the efficiency is discussed in Sec. V. At this close spacing there was no indication that the power would not continue to increase with increase in cesium pressure or emitter temperature.

V. CELL WITH RADIATION SHIELD

The parallel requirements of high electron emission and sufficient ionization of cesium necessitate high temperature operation of the plasma cell emitter. At the temperatures required, radiation transport from the emitter to the collector constitutes a major effect in limiting cell efficiency. The spacing experiments described in Sec. IV indicated that limitation of cell performance by plasma impedance at the optimum operating point was not a major consideration. This being the case, it was of interest to investigate the feasibility of placing shields between the emitter and collector which would intercept radiant energy while allowing the flow of electrical current.

The initial experiment to explore the value of the radiation shielding concept was done with the cell configuration depicted in Fig. 3 and discussed in Sec. II. The tantalum shield was allowed to assume the wall potential (potential at which electron and positive ion currents to the shield are equal) determined by some average value of the parameters of the plasma in contact with it. The flow of radiation is restricted to that which passes through the $\frac{1}{8}$-in. diam hole in the center of the radiation shield. The temperature of the collector side of the radiation shield rides about 800°K below that of the emitter.

Observations made with this cell configuration revealed some unexpected results. Perhaps the most surprising was the fact that at high cesium pressures the maximum power obtained was equal to that of an unshielded cell with identical electrode spacing performing at the same pressure and the same emitter temperature. Hence the cell efficiency was considerably higher. The relationship of efficiency and emitter temperature for optimum cesium pressures for the shielded and comparable unshielded cell are shown in Fig. 9. It must be emphasized that the efficiencies shown are not typical of the values that can be obtained with the cell at lesser electrode separations and higher cesium pressures. The large value of the spacing used was necessitated by the crudity of the initial radiation shield design.

Efficiency values quoted are those obtained by dividing the maximum measured electrical power by the total power received by the collector. The heat transfer to the collector is measured through the use of a differential thermocouple measurement of the temperature rise of the cooling oil as it passes by the collector. This efficiency measurement neglects heat loss through the electrical (and mechanical) connections to the emitter.

The efficiency curves demonstrate the effectiveness of radiation shielding. However, the maximum efficiency obtained with the shielded cell is still considerably below the maximum value attained with an unshielded cell (Sec. IV). It is to be presumed that an improved design for the radiation shield (one which, in particular, allows smaller electrode separations) will increase the cell efficiency. However, attention must be given to the

problem of exposing too much surface area to the plasma and hence draining its supply of positive ions through recombination on the exposed area.

The behavior of the voltage-current characteristics of the cell for a cesium pressure of 0.5 mm Hg is demonstrated in Fig. 10. It is seen that the introduction of the constriction between the electrodes has resulted in pronounced double mode behavior. The results of positive ion measurements indicate that for cesium pressures above 10^{-2} mm and emitter temperatures above 2100°K the positive ion densities are of approximately the right magnitude to support the electron currents observed in the low current modes. There are not nearly enough ions to provide neutralization for the electron flow observed in the high current modes. Thus it is apparent that for these high current modes additional ions are being produced. It is reasonable to expect that as the cell terminal voltage is brought toward zero, electric fields are built up in the vicinity of the hole in the radiation shield so that eventually the cell current jumps to the high current mode, with the ion deficiency now removed by the formation of ions as a result of electron impact with neutral cesium atoms. In this regard it is of interest to note that the current voltage relations in the high current mode are quite similar, in shape and magnitude, especially in the range of −0.5 to 0.5 v, to those obtained for the unshielded cell

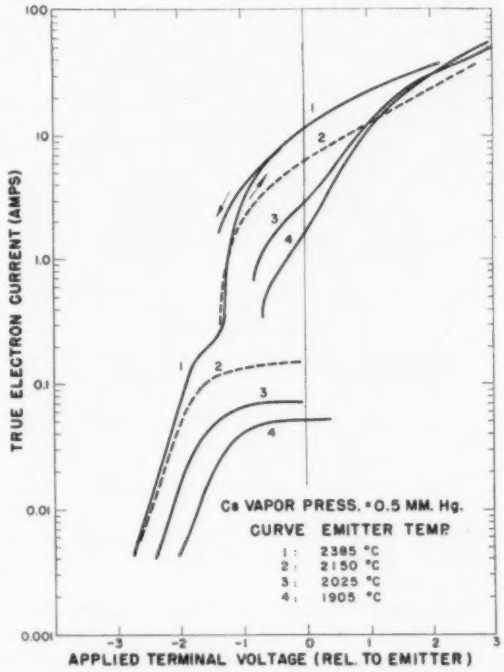

FIG. 10. Current-voltage characteristics of cell with radiation shield for a cesium vapor pressure of 0.5 mm Hg and several emitter temperatures.

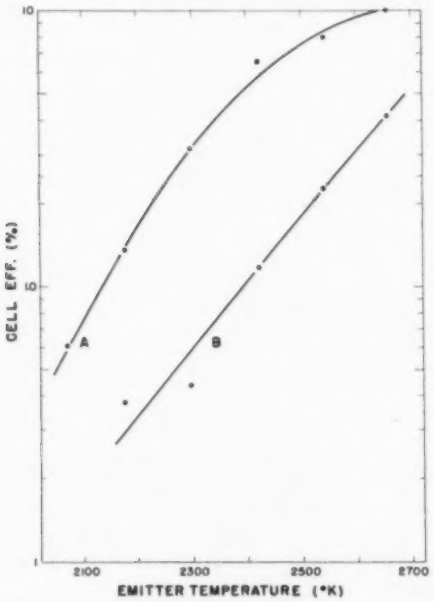

FIG. 9. Measured cell efficiency versus emitter temperature for tantalum emitter cells with and without radiation shielding. The cesium vapor pressure was 0.5 mm Hg for each curve. Efficiency measurements neglected thermal losses through the electrical connection to the emitter. The maximum measured efficiency for the unshielded cell is comparatively low because of the large emitter-collector spacing (10.8 mm).

in the same range of high emitter temperature and cesium pressure.

On referring to Fig. 3 it can be seen that a possible current path exists from the emitter, around the outside of the radiation shield support insulator, to the copper retainer. However, it is quite unlikely that electrons would choose this path because of its length and because the temperature of the cesium vapor in the region between the outside of the insulator and the vacuum chamber wall must be near that of the oil bath. Hence the plasma density in this region should be very low. On the other hand, since the emitter-radiation shield combination can be considered as an approximation to a cavity emitter, it is obvious that the distance from the hot plasma (at a temperature near that of the emitter) to the collector is only about 4 mm by way of the hole in the radiation shield.

VI. POSITIVE ION CURRENT MEASUREMENTS

Since the existence of a copious supply of positive ions is essential to the operation of the plasma cell, a certain amount of effort has been devoted to the study of the behavior of ion currents as a function of emitter temperature and cesium pressure for various cell configurations.

Another reason for studying these ion currents is that, as indicated earlier, a plot of saturated ion currents as a

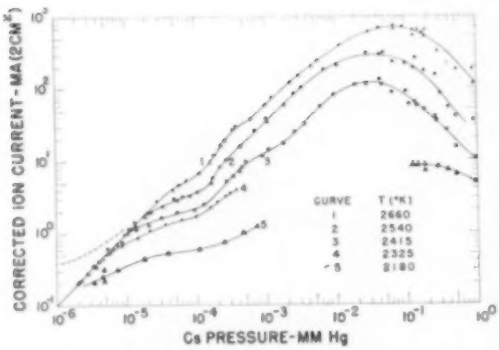

FIG. 11. Saturation magnitudes of positive ion current versus cesium vapor pressure for several emitter temperatures as observed for a tantalum emitter cell with an emitter-collector separation distance of 13 mm. The areas of the emitter button and copper collector were each 2 cm². Measured ion current values have been corrected for a background of photoelectron current from the collector. The dashed line indicates the behavior of the uncorrected data obtained for an emitter temperature of 2540°K.

function of cesium pressure is essentially a plot of the dependence of the plasma density at the collector on cesium pressure.

The dependence of ion current on cesium pressure is shown in Fig. 11. The various curves were obtained for five different emitter temperatures in the range of 2180–2660°K. The range of cesium pressure is from 2×10^{-6}–1 mm Hg. The cell used to obtain these results was of the type shown in Fig. 1. The copper collector was $\frac{5}{8}$ in. in diam and was spaced 13 mm from the tantalum emitter. The cylindrical surface of the collector was coated with a 0.015-in. thick layer of alumina.

In the pressure region of 10^{-6}–10^{-5} mm Hg it was necessary to wait 1 or 2 hr, for each change of emitter temperature, in order to allow the cesium vapor pressure in the cell to reach equilibrium with the cesium in the reservoir. A similar waiting period of 20- to 30-min duration followed each small change in the bath temperature.

The observed ion currents have been corrected for background currents of photoelectrons ejected from the cesium coated collector by thermal radiation from the emitter. The dashed line in the pressure range of 10^{-6}–10^{-5} mm Hg (Fig. 11) shows the behavior of the uncorrected data for the emitter temperature of 2540°K. The background corrections were first estimated roughly from the shape of the uncorrected data. Values thus obtained were modified slightly in order to give the corrected curves the expected linear dependence of ion current on cesium pressure in this pressure region. This correction procedure produced the result apparent in Fig. 11 where the data for each emitter temperature can be represented at the lowest cesium pressures by the same straight line. Further justification of the correction procedure arises from the fact that the photoelectron background current obtained in this manner had the correct dependence on the temperature of the emitter.

In the cesium pressure range of 10^{-2}–10^{-1} mm Hg it can be seen that the ion currents rise to values as high as 350 ma/cm². There is little doubt but what this current magnitude represents a flow of ions to the collector rather than a flow of electrons away from it. In the latter instance the mechanism of electron production is restricted to the possibility of significant thermionic emission from the low work function collector (since the order of magnitudes of photoelectron currents have already been reasonably well established as much less than the reverse currents obtained at 10^{-1} mm Hg cesium pressure). Since the collector temperature is known it is possible to calculate the collector work function required to obtain a thermionic current of the magnitude observed for the reverse currents. This work function is found to be about 0.6 v. Even in the very unlikely event that the collector work function was this low (the current voltage characteristics indicate it is more like 1.4 v) the dependence of the reverse current magnitude on emitter temperature cannot be explained on a basis of thermionic emission because the variation in collector temperature with varying emitter temperature is not sufficiently great.

When potassium is used in place of cesium in a cell of the same geometry used to obtain Fig. 11, the current-voltage characteristics indicate a collector work function greater than 2 v. Yet the magnitude of the reverse current at the maximum is only about 25% less than that obtained with cesium when the emitter temperature is 2540°K for both cells. Thus the invoking of thermionic emission to explain the observed reverse currents is not rewarding.

For cesium pressures higher than about 5×10^{-2} mm Hg the ion current data is not very reproducible, both from one run to another and from one experimental cell to another. At the 13-mm emitter-collector spacing the data are consistent in that the decrease in ion current with cesium pressure invariably occurs. However, the pressure at which the decrease begins may vary by a factor of 2 or 3 from one cell to another and the slope of the decreasing portion of the ion current shows some variation. These difficulties arise from the instability of the cell at these high pressures for voltages at which saturation of the ion current appears (about -5 to -6 v). A voltage transient, such as opening and closing a switch, may produce an arclike mode of discharge with currents on the order of tens of amperes being drawn. For emitter-collector spacings of 3 mm this discharge behavior occurs so readily (see Fig. 5) that it is impossible to obtain any realistic measurements of the true ion current for cesium pressures higher than 0.1 mm Hg.

VII. DISCUSSION

A full understanding of the behavior of the plasma cell as exemplified by the various experiments reported in the previous sections cannot as yet be said to exist. However, there are a number of features about cell

operation which are understood qualitatively if not quantitatively.

The role of potential barriers formed both at the emitting and collecting surfaces is an important consideration in the interpretation of cell characteristics. Some of the effects of potential barriers at the emitting surface can be seen in Fig. 11. For the lowest cesium pressures the rate of ion production is insufficient to neutralize the electron emission. Hence, there is formed at the emitter surface a negative potential barrier whose magnitude is sufficient to limit the number of electrons entering the plasma per second to approximately the rate required to neutralize the ions. (For cesium this rate is about 500 times the ion production rate. However, when ion currents are being measured it drops to 250 times the ion production rate since electrons are reflected from the collector back to the emitter whereas ions are neutralized at the collector.) Since more than enough electrons are generated to neutralize the ions, the ion currents measured at the collector are independent of the emitter temperature.

As the cesium pressure in the cell is increased, with the emitter temperature held constant, the negative potential barrier decreases in magnitude and eventually becomes a positive potential barrier when the rate of ion production exceeds that required to neutralize the electron emission. This positive potential barrier forms because, in a plane parallel geometry and in the absence of collisions, the plasma density in the region between the emitter collector is established by the rate at which electrons are emitted. The emitted electrons are accelerated by the emitter potential sheath, reflected by the collector potential sheath (when ion current is being collected) and returned to the emitter, having suffered no net energy gain or loss in transit.

The potential diagram for the plasma cell, for the case of a positive potential barrier at the emitter and noncolliding electrons, is shown in Fig. 12(a). In the diagram the cell is at open circuit voltage so that the height of the collector barrier is established by the condition that the magnitude of the electron current reaching the collector must be limited to the magnitude of the positive ion current. This means that approximately 249 out of 250 electrons are reflected by the barrier and return to the emitter. For this particular case the energy of the electrons impinging against the collector barrier consists of the usual thermal energy imparted to them by the hot emitter, plus the directed energy component imparted by the emitter potential sheath.

The formation of the positive potential barrier at the emitter surface means that, even though the rate of formation of ions increases about linearly with increasing cesium pressure, the ion current obtained at the collector should remain constant, at the value determined by the electron emission rate. As this rate is increased, by increasing the emitter temperature, the pressure at which the transition from negative to positive potential sheath occurs is naturally higher.

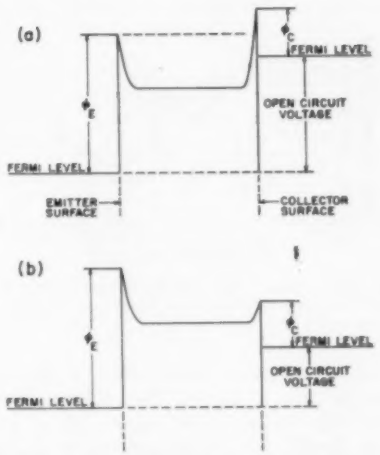

FIG. 12. Schematic diagram of electron potential energy versus distance for plasma cell at open circuit when ion production rate is significantly greater than that required to neutralize electron emission. (a) Case where electrons make no collisions in transit to and from the collector. (b) Many-collision case.

The type of behavior described in the foregoing appears to be occurring in Fig. 11 for cesium pressures between 10^{-6} and 10^{-4} mm Hg. However, the ion currents never become truly constant with increasing cesium pressure, possibly as a result of electron-electron and electron-ion collisions not being entirely negligible.

A change in the behavior of the saturation ion currents with cesium pressure can be seen to occur in Fig. 11 at a cesium pressure of 10^{-4} mm Hg. The slopes of the ion curves increase rather abruptly at this pressure. For the higher emitter temperature the ion currents once more approach a linear dependence on cesium pressure. This effect is not well understood. Certainly the discussion of ion current behavior at low pressure does not apply when collisions become an important consideration. In fact, for the many-collision case, the simple procedure of equating both inward and outward going electron currents and inward and outward going ion currents at the emitter-plasma boundary suggests that, for a Maxwellian distribution of particles, the plasma density should increase as the square root of the pressure.

If one takes the collision cross section for ions with neutral cesium atoms to be 0.14×10^{-8} at 0°C and 1 mm Hg,[10] then one finds that, at 1.4×10^{-4} mm Hg, the mean free path of the ions is equal to the emitter-collector spacing.[11] Presumably, the electron mean free path for

[10] A. Von Engel, *Ionized Gases* (Oxford University Press, New York, 1955), p. 27.

[11] In calculating this mean free path the temperature of the neutral cesium is taken to be that of the oil bath used to establish the cesium vapor pressure. This procedure is reasonable since only a small fraction of the cesium particles leaving the hot emitter are neutral atoms and until such time as the mean free paths for ion-neutral and neutral-neutral collisions become considerably smaller

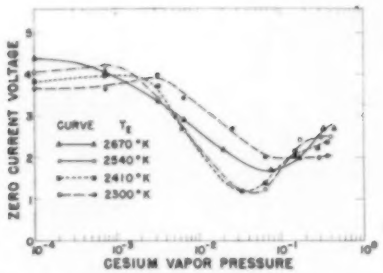

FIG. 13. Zero current (open circuit) voltage of plasma cell as a function of cesium vapor pressure for several emitter temperatures. Cesium pressure is given in mm Hg.

scattering by neutrals is comparable. Thus, it appears that for a pressure of 10^{-4} mm Hg collisions of ions and electrons with neutral cesium atoms can no longer be neglected. Hence, a correlation of the change in slope of the ion current curves with the onset of charged particle-neutral atom collisions seems reasonable, especially when note is taken of the fact that the pressure at which the change in slope occurs is independent of emitter temperature, and, thus, also independent of plasma density.

Another effect correlated with the change of slope of the ion currents is the onset of a decrease of open circuit voltage with increasing cesium pressure. This behavior is shown in Fig. 13, which presents open circuit voltage as a function of cesium pressure for four emitter temperatures. These data were taken with a cell having a 3-mm emitter-collector separation distance. The minima in the open circuit voltages which occur between 4 and 8×10^{-2} mm Hg cesium pressure are considerably smaller in magnitude than these observed for the serrated collector cell with 2.5-mm spacing (Fig. 4). This difference may be an effect of the collector serrations, but it appears more likely that it represents a difference in the emitter-collector spacings of the two cells. It is known that the magnitudes of the open circuit voltage minima are dependent on the emitter-collector spacing. For instance, at a spacing of 12.5 mm the open circuit voltage obtained for an emitter temperature of 2540°K dips to a value of 0.6 v. The difference in the emitter-collector spacing of the two cells in question has been quoted as 0.5 mm. However, this value may be in error by an amount on the order of a millimeter, since the spacing is determined when the emitter is cold and procedures undertaken to correct for the change in spacing as the emitter is brought up to temperature are not always accurate.

In any case, Fig. 13 shows the general behavior of open circuit voltage as a function of cesium pressure. A direct comparison of Fig. 13 and Fig. 11 is not possible because of the difference in emitter-collector spacing. However, it is known from other experiments that the decrease in open circuit voltage begins at the same cesium pressure for which the ion current renews its almost linear rise with cesium pressure for a given emitter-collector spacing.

The commencement of the decrease of open circuit voltage at the same pressure for which the ion currents change slope is expected on the basis of the development of a Maxwellian electron distribution when the effect of electron collisions with neutrals becomes important. Such collisions serve to increase the time a given electron spends in the region between the emitter and collector and, hence, the time during which this electron can exchange energy with other electrons. For cesium pressures sufficiently low for collision effects to be treated as negligible, the voltage picture is that shown in Fig. 12(a). The collector barrier is larger than the emitter potential sheath by an amount required to turn back 249 of 250 electrons with a velocity distribution equivalent to electrons at emitter temperature. However, as the electron distribution becomes more random with increasing cesium pressure the anode barrier decreases. The component of velocity in the direction of the collector is gradually reduced until eventually the energy distribution of electrons in the plasma is completely Maxwellian with an electron temperature approximately that of the emitter. Although the plasma density is now much greater, the collector barrier consists only of the kinetic energy term approximately equal to the voltage required to repel now on the order of 499 of 500 electrons. The fact that the rise in ion current in this pressure region is linear with pressure implies that the height of the emitter barrier has not changed. As a result, the open circuit voltage has decreased as shown in Fig. 12(b). While the mechanism suggested here can account for the correlation between the rise of plasma density and decrease in open circuit voltage, it can only account for a voltage drop of the order of a volt or less. Hence some other effect is required to explain the full magnitude of the voltage drop shown in Fig. 12.

It is possible to relate the behaivor of the ion current with pressures above 10^{-2} mm Hg (Fig. 11) to the combined effect of ion diffusion and the recombination of ions and electrons. The calculational procedure involves three assumptions. The first of these is that the source of ions in the plasma cell is restricted to the net number per second which enter the plasma through the potential sheath at the emitter. The second is that the loss of ions from the plasma occurs only through recombination and through neutralization at the collector surface. The third assumption is that the mean free path for ion-neutral scattering does not vary in the region

than the emitter-collector spacing, the neutral cesium vapor must be considered as a Knudsen gas whose temperature is determined by the cell walls and the collector surface. As the number of free paths between the emitter and collector increases, the average temperature of the cesium vapor between the two electrodes will increase until it approaches a value midway between that of the emitter and the collector. Note that a consequence of this effect is that a region of pressure will exist for which the macroscopic cross section for ion-neutral scattering will increase more slowly than linearly with increasing cesium pressure.

between the emitter and collector. This assumption is not very realistic, since the temperature of the neutral cesium atoms certainly varies in this region. However, it is required if the mathematical treatment of the problem is to be at all tractable.

With the foregoing assumptions, the transfer of ions from the emitter to the collector can be represented by the steady-state diffusion equation

$$D_a\nabla^2 N-\rho N^2=0. \tag{1}$$

Here N is the ion or electron density and ρ is the recombination coefficient for ions and electrons. D_a is the ambipolar diffusion coefficient for the ions and electrons. When the ion and electron temperatures are equal, D_a is just twice the ion diffusion coefficient and can be represented by the relation $D_a=(\lambda v)/3$, where λ is twice the ion-neutral scattering mean free path and v is the mean ionic velocity. When the electron temperature is greater than the ion temperature, D_a is greater than twice the ion diffusion coefficient. This effect can be more than compensated for by calculating D_a in the plasma region immediately adjacent to the emitter and, in keeping with the third assumption made above, taking this value as representative of the entire plasma region. In calculating the ambipolar diffusion coefficient, collisions of ions with electrons and with other ions are not considered. The neglecting of ion-electron collisions is of little consequence, and it seems apparent that the effect of an individual ion-ion encounter in impeding the flow of ions from emitter to collector is of much less importance than an ion-neutral encounter, since in the former instance there can be no distinction made as to which particle is which. An ion proceeding in the direction of the emitter may lose its momentum in this direction through collision with another ion, but the second ion will gain the momentum lost by the initial ion.

In Eq. (1) it can be seen that the first term represents the net rate at which ions diffuse into a unit volume of plasma while the second term is the rate at which ions are lost as a result of recombination. For a plane parallel geometry the equation can be restricted to one dimension and integrated. This procedure yields

$$\frac{dN}{dx}=-\left(\frac{2\rho N^3}{3D_a}+A\right)^{\frac{1}{2}}, \tag{2}$$

where A is the constant of integration.

As a first boundary condition, the diffusion current at the collector is set equal to the ion current received by the collector. This conditions may be written as

$$-D_a\frac{dN}{dx}\bigg|_{x=x_1}=\frac{n_1 v}{4}=I, \tag{3}$$

where n_1 refers to the ion density immediately adjacent to the collector sheath. This relation evaluates the constant A and Eq. (2) may be rewritten and integrated yielding

$$-\int_n^{n_1}[(n_1 v/4D_a)^2-(2\rho/3D_a)n_1^3+(2\rho/3D_a)N^3]^{-\frac{1}{2}}dN=\int_0^{x_1}dx, \tag{4}$$

where n is the ion density in the plasma region adjacent to the emitter. With the following substitutions

$$D_a=\lambda v/3,\quad a=32\rho\lambda n_1/9v,\quad \eta=a/(1-a),$$

and

$$z=\eta^{\frac{1}{3}}(N/n_1),$$

Eq. (4) may be rewritten as

$$-\int_{(n/n_1)\eta^{\frac{1}{3}}}^{\eta^{\frac{1}{3}}}\frac{dz}{(1+z^3)^{\frac{1}{2}}}=a^{\frac{1}{2}}(1-a)^{1/6}\frac{3x_1}{4\lambda}. \tag{5}$$

The range of interest of values of the dimensionless parameter a is from 10^{-1} to 10^{-9} so that with little error $\eta^{\frac{1}{3}}$ and $a^{\frac{1}{2}}(1-a)^{1/6}$ can be replaced by $a^{\frac{1}{2}}$. The integral in Eq. (5) represents an elliptic function of the first kind which may be written as

$$\int\frac{dz}{(1+z^3)^{\frac{1}{2}}}=-0.75984F(\alpha,\phi)+\text{constant}, \tag{6}$$

where $F(\alpha,\phi)$ is given by

$$F(\alpha,\phi)=\int_0^{\phi}(1-\sin^2\alpha\,\sin^2\psi)^{-\frac{1}{2}}d\psi.$$

In the solution [Eq. (6)] above, α is 75° and ϕ is given by the relation

$$\cos\phi=\frac{z+1-\sqrt{3}}{z+1+\sqrt{3}},$$

where $-1\leqq z\leqq\infty$.

The simplest calculational procedure is to evaluate the integral in Eq. (6) by making a binomial expansion of $(1+z^3)^{-\frac{1}{2}}$ for the two cases of $z<1$ and $z>1$ and combining the two solutions obtained by the use of the exact result for the value of the integral from zero to infinity, this value being obtained from tables of elliptic functions. Once a graph of the value of the integral in Eq. (5) has been plotted as a function of z, it is a straightforward procedure to obtain graphs of $a(n/n_1)$ as a function of $\frac{3}{4}(x/\lambda)$ for various values of a. These graphs form a set of master curves from which the behavior of the ion density as a function of $\frac{3}{4}(x/\lambda)$ may be obtained for various assumed dependences of the ion density at the emitter on cesium pressure.

These master curves are shown in Fig. 14. If the ion density adjacent to the emitter is assumed to increase linearly with pressure (and λ is assumed inversely proportional to pressure) then $a(n/n_1)$ is a constant.

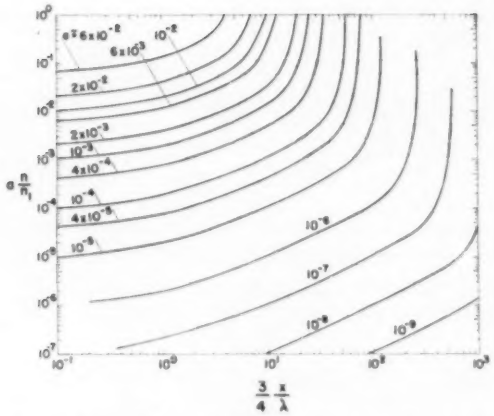

FIG. 14. Curves showing the behavior of the quantity $a(n/n_1)$ as a function of $\frac{3}{4}(x/\lambda)$ for several values of the parameter $a=32\rho\lambda n_1/9v$. The ordinate is essentially a constant times $n\lambda$, where n is the ion density at the emitter and λ is twice the mean free path for ion-neutral elastic scattering. Hence a constant value of the ordinate describes the case where the ion density at the emitter increases linearly with cesium vapor pressure if λ is taken to be inversely proportional to this pressure.

Various values of $a(n/n_1)$ then correspond to various emitter temperatures and curves of $\frac{3}{4}(x/\lambda)a$ vs $\frac{3}{4}(x/\lambda)$, obtained from Fig. 14, are essentially plots of the ion current versus cesium pressure. A set of such curves is shown in Fig. 15. It can be seen that the behavior of ion current versus cesium pressure is similar to that shown in Fig. 11. It has been found that the assumption of a linear increase of the ion density at the emitter with cesium pressure results in a considerably better fit to the observed data than does the assumption of a square root dependence of the ion density on cesium pressure. Fits to experimental curves such as shown in Fig. 11 require that λ be evaluated as discussed previously, and that ρ be given a value of from 1 to 4×10^{-12} cm^3/sec instead of the accepted value for cesium of 3×10^{-10} cm^3/sec.[12] The ion current curve for the highest emitter temperature shown in Fig. 11 (curve number 1) cannot be fitted with the same parameters which fit curves 2, 3, and 5 obtained at lower emitter temperatures. It may be that this discrepancy results from a breakdown of the assumption that the ion source is restricted to ions entering the plasma from the emitter, that is, photoionization and ionization by electron impact with cesium atoms may be relatively more important for very high emitter temperatures.

In Fig. 15, it is apparent that for high cesium pressures the ion density at the collector becomes independent of the ion density at the emitter. This limiting curve is given by the relationship

$$n_1=14.6(v/\rho)(\lambda^2/x^3)$$

for $a\ll1$. The equation indicates that the ion current at the collector eventually falls off as the inverse square of the cesium pressure for a given emitter-collector spacing.

In Fig. 4(e) and Fig. 10 there appeared instances of a double valued dependence of current on voltage. This double mode behavior of the plasma cell in the region of high pressure and relatively large electrode spacing can be understood, in part at least, in terms of positive ion deficiency and hence electron space charge limitation in the region near the collector. The results of the experiments with the radiation shielded cell (Sec. V, Fig. 10) demonstrated that the positive ion currents obtained at the high pressures are of about the right magnitude to neutralize the electron current obtained in the low current mode. The high current mode requires a source of ionization other than the formation of ions at the emitter.

A similar situation exists for the cell with 12-mm electrode spacing at high cesium pressure. As a result of recombination, the ion density at the collector can fall below the level required to pass all the electron current from the emitter. Hence a space charge barrier will become established in the region near the collector and the cell current will satuarate at a level determined by the ion density at the collector. As in the radiation shielded cell, if an additional source of ions is provided, the current will increase to values apparently limited by the emission of the electron source.

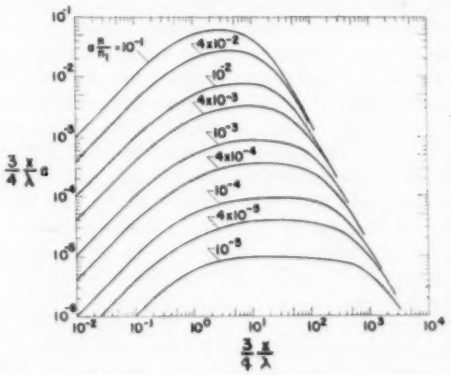

FIG. 15. Behavior of the quantity $\frac{3}{4}(x/\lambda)a$ as a function of $\frac{3}{4}(x/\lambda)$ for various values of $a(n/n_1)$, corresponding to various emitter temperatures. The ordinate is equal to a constant times the ion density at the collector for the case of $x=x_1$, the emitter-collector separation distance. Hence these curves represent the behavior of collector ion current as a function of cesium vapor pressure when the ion-neutral scattering mean free path is taken to be inversely proportional to the cesium pressure.

The double mode behavior which occurs for a tantalum emitter cell with 12-mm spacing and a 51-mm diam collector is depicted in Fig. 16. With emitter temperature at 2175°K [Fig. 16(a)] two modes are not observed. At a pressure of 0.5 mm the current increases continuously with voltage. For the two higher pressures the current levels off at values which decrease with pressure. Electron accelerating fields in the cell are not sufficient

[12] See p. 141 of work cited in footnote 10.

to increase the electron temperatures to the point where ionization by collision can occur frequently enough to maintain the high current discharge mode. At the next higher emitter temperature [Fig. 16(b)] a double mode exists for $P_{Cs}=1$ mm. For the lower pressure only the high mode exists and for the higher pressure only the low mode is observed.

Further increase in emitter temperature [Fig. 16(c)] brings about the appearance of double modes at $P_{Cs}=2$ mm. For $T_p=2540°K$, $P_{Cs}=1$ mm, a discontinuity in the slope of the current voltage characteristic is the only indication of the tendency for double mode operation. It can be seen that the minimum voltage for which the high current can be sustained increases with increase in cesium pressure and decreases (becomes more negative) with increasing emitter temperature. Other experiments have demonstrated that for a given emitter temperature the double mode behavior will first appear at a fixed

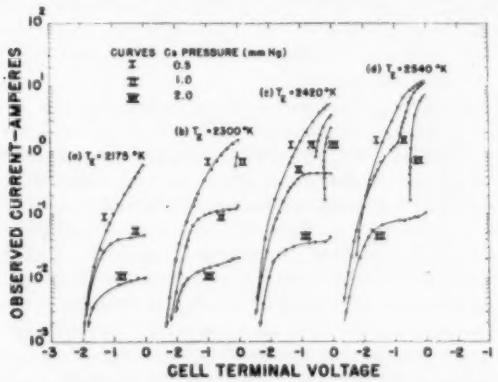

FIG. 16. Current-voltage characteristics at high cesium pressures for tantalum emitter cell having collector-emitter separation distance of 12-mm and 51-mm diam copper collector. Each set of curves represents the characteristics at the given emitter temperature for cesium pressures of 0.5, 1.0, and 2.0 mm Hg.

value of pressure times electrode separation distance, a result to be expected from similarity considerations.

The general behavior of the transitions from low to high current modes is closely analogous to the transitions to temperature limited arcs described by Malter *et al.*[13] as occurring in rare gases. Malter also observed that such arcs could be maintained even when the voltage applied across the gas was reduced to negative values.

[13] L. Malter, E. O. Johnson, and W. M. Webster, RCA Rev. **12**, 415 (1951).

The identification of cell behavior at high cesium pressures as arclike suggests a potential distribution observed by Compton and Eckart[14] for a mercury vapor arc wherein the emitter barrier is about equal to the ionization potential (of cesium, in this case) and the plasma potential decreases from this maximum to values near zero at the collector. For the case where the emitter work function is higher than that of the collector the voltage at the collector can be negative.[13,15] In the body of the plasma the electron current is sustained by forces of thermoelectric origin, i.e., electron temperature and concentration gradients.

Confirmation that the plasma cell is generating a temperature limited arc discharge at high cesium pressure and low cell voltage has recently been obtained from observations made in the Los Alamos Laboratory.[16] These observations were made through the use of a tantalum emitter cell equipped with a sapphire window to permit visual (and spectrographic) observation of the plasma region between the emitter and collector. Visual inspection of this region demonstrated that the discontinuous transition from the low current to high current mode was accompanied by the abrupt appearance of a yellow glow which filled the region between the emitter and collector. In the low current mode of cell operation no light from the plasma region would be distinguished from the background of scattered light originating from the emitter. In the high current mode increasing the cell voltage in a positive sense (to and beyond the condition of short circuit) resulted first in the intensification of the glow. In the region from zero to one volt positive the cell current increased rapidly with voltage while at the same time the light from the discharge could be seen to spread across the tantalum support disk. This indicates, as suggested in Sec. III, that the high currents obtained at high cesium pressure for positive cell voltages result from the fact that a large region of the tantalum support disk is furnishing electrons to the plasma under these conditions.

ACKNOWLEDGMENTS

The authors would like to acknowledge the assistance of D. J. Kelly, R. E. Aamodt, D. J. Roehling, and G. F. Erickson in obtaining various portions of the experimental data described herein.

[14] K. T. Compton and C. Eckart, Phys. Rev. **25**, 139 (1925).
[15] See p. 254 of work cited in footnote 10.
[16] L. E. Agnew, Los Alamos Scientific Laboratory (private communication).

Correlation of Low-Temperature Caloric and Magnetic Effects in TiFe

K. SCHRÖDER AND C. H. CHENG
Department of Mining and Metallurgical Engineering, University of Illinois, Urbana, Illinois

(Received June 20, 1960)

Magnetic measurements by Nevitt on TiFe can be interpreted on the assumption that his specimen is superparamagnetic. It is possible to calculate from his measurements approximate values of the size and number of ferromagnetic clusters. The magnetization vector of these clusters oscillates at very low temperatures within directions given by the energy of crystal anisotropy. This gives rise to the term C_{el} in the specific heat at low temperatures, due to the clusters, which is to be added to the lattice and electronic terms. The calculation gives reasonable agreement of C_{el} with experimental values found in specific heat measurements.

ISOTHERMAL magnetization curves of TiFe were recently given by Nevitt.[1] His magnetization values M are replotted as a function of H/T in Fig. 1. For low values of H/T the experimental values of M follow a common curve, except for magnetization values measured at 9°K and 110°K. A Langevin function $L=L(H/T)$ is given in Fig. 1 as a solid line. The dotted line shows its initial slope. It can be seen that the magnetization M, measured at different temperatures, follows qualitatively the solid line of the Langevin function except at $T=9$°K and 110°K. All values of M should coincide with this function L for an ideal paramagnetic gas, but Bean and Livingston[2] pointed out that deviations from the Langevin function should be observed in a superparamagnetic material, if the size of the particles and their corresponding magnetic moment varies. Clusters also could have different Curie temperatures due to a variation in chemical composition. The magnetization moment of a cluster decreases very rapidly if the temperature is raised above the Curie temperature, because then the cluster breaks up. This means that the number of clusters decreases with increasing temperature. The magnetization moment of the specimen should therefore be smaller for identical H/T values at higher temperatures. For this reason, we neglect the low magnetization values found by Nevitt at 110°K. The magnetization curve at $T=9$°K is a special case and will be discussed later. We need for the calculation of an average size and concentration only the initial slope of the Langevin function, for which the measured values of M give practically the same value, as can be seen in Fig. 1. A detailed discussion as to which Langevin function would give the best fit to these values is therefore unnecessary.

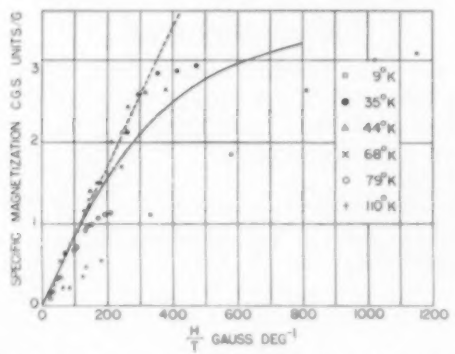

FIG. 1. Magnetic moment of TiFe as given by Nevitt (work cited in footnote 1).

Bean and Jacobs[3] have demonstrated recently the superparamagnetic behavior of fine iron particles suspended in mercury. They also found a residual induction at very low temperatures. Bean and Livingston[2] attributed this residual induction to the fact that some iron particles are stable and cannot rotate freely. Because Nevitt observed also magnetic remanence at 5°K in TiFe, it is probable that small ferromagnetic clusters of iron atoms with unpaired electron spins exist in this TiFe specimen, and that they are kept at low temperatures in certain orientations by the energy of crystal anisotropy. An external magnetic field has in such a case to overcome not only the thermal oscillation of the clusters, but also the crystal energy. Therefore, the magnetization $M=(H/T)$ measured at $T=9$°K is below values measured at higher temperatures, as shown in Fig. 1. It should be pointed out that Bean and Jacobs[3] found also that M was smaller for certain H/T values at 4.2°K than at 77°K.

Nevitt gives a saturation moment M_s of 3.3 cgs units/g for his specimen. Therefore, the initial slope of the magnetization curve is

$$\frac{dM}{M_s d(H/T)}=\frac{dL(H/T)}{d(H/T)}=\frac{\mu}{3k}$$

$$=26.0\times10^{-4}\ \text{deg gauss}^{-1}. \quad (1)$$

If we assume that a cluster has n iron atoms with 2.2 free Bohr magnetons β each, then $2.2\times n\times\beta$ should be equal to μ. Equation (1) gives therefore as the average number of iron atoms per cluster

$$n=(3\times26.0\times10^{-4}k)/2.2\beta=52.8. \quad (2)$$

[1] M. V. Nevitt, J. Appl. Phys. **31**, 155 (1960).
[2] C. P. Bean and J. D. Livingston, J. Appl. Phys. **30**, 120S (1959).
[3] C. P. Bean and I. S. Jacobs, J. Appl. Phys. **27**, 1448 (1956).

The saturation moment M_s is, according to Nevitt,[1] 0.061 Bohr magnetons/unit cell. The number of free iron atoms with 2.2 Bohr magnetons is therefore 27×10^{-3}/unit cell, and the concentration of clusters N is $27\times10^{-3}/52.8=52.4\times10^{-5}$.

The system of a ferromagnetic cluster in a nonferromagnetic matrix would, in the classical picture, be kept in a position of minimum energy. If a force acts on such a cluster and alters the direction of its magnetization vector, then the potential energy of the system is increased. This energy could be stored, e.g., in the elastic deformation of the matrix and the cluster, and in magnetostriction energy. Therefore, if the ferromagnetic cluster oscillates due to thermal agitation, the system absorbs per degree of freedom of rotation an energy of $(k/2)T$ for each possible potential energy value which is larger than $(k/2)T$. This means that the specific heat per mode of rotation per possible potential energy value is $k/2$ (N. B., a nonclassical approach to this problem should give an approximately similar result[4]). The contribution C_{el} of all clusters in a mole to the specific heat is therefore

$$C_{el}=z\times k/2\times L\times N=z\times5.24\times10^{-4}\text{ cal mol}^{-1}\text{ deg}^{-1},\quad(3)$$

where L is Avogadro's number, z is the product of the number of degrees of freedom of rotation z_1, times the possible number of potential energy states. z_1 should be either 2 or 3.

Circles in Fig. 2 represent experimentally found specific heat values of a TiFe specimen, a portion of which was used by Nevitt for his magnetic measurements. The chemical composition and thermal history was therefore in both measurements the same. If one assumes that the lattice contribution to the specific heat in TiFe is the same as that is measured in a $V_{0.8}Fe_{0.2}$ alloy[5] ($\beta=0.035\times10^{-4}$ cal mol^{-1} deg^{-4}), because both alloys consist of the same or very similar atoms, and that the electronic contribution is γT, then one gets a best fit curve of the form

$$C(T)/T=\gamma+\beta T^2+(C'/T),\quad(4)$$

with $\gamma=0$ and $C'=21.5\times10^{-4}$ cal mol^{-1} deg^{-1}. The alloy $V_{0.8}Fe_{0.2}$ was chosen for comparison, because its specific heat can well be separated into the electronic and lattice contribution. The lattice contribution should not depend very much on the actual composition of the alloy. For instance, one could use the β value of the alloy $V_{0.55}Fe_{0.45}$,[5] which is 0.047×10^{-4} cal mol^{-1} deg^{-4}. This would not change the best fit curve (4) very much, because the term βT^2 is small compared with C'/T in the temperature range up to 4°K.

The best fit curve (4) is shown in Fig. 2 as the solid line and it can be seen that this curve agrees very well with the experimental values. C' would be practically equal to C_{el} for $z=4$. This is a very reasonable value for z, e.g., it could mean that the number of modes of rotation is two, and that two possible forms of energy are absorbed. But because the model we used for the calculation is oversimplified, it is not sensible to attach much importance to the fact that z is nearly an integer.

C' and C_{el} are of the same order of magnitude. This indicates strongly that ferromagnetic clusters exist in this TiFe specimen and that each cluster has at low temperatures a specific heat of the order of k.

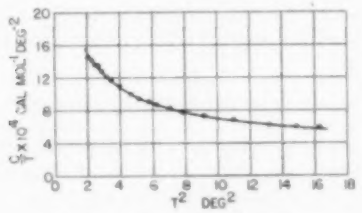

FIG. 2. Specific heat of TiFe.

[1] R. M. Thomson (private communication).

ACKNOWLEDGMENTS

The authors wish to thank Professors P. A. Beck and R. M. Thomson, and Dr. R. J. Weiss for fruitful discussions, and Dr. C. T. Wei for collaboration in the specific heat measurements. This investigation was supported by the Office of Ordnance Research, U. S. Army, and U. S. Air Force under contract.

[5] C. H. Cheng, C. T. Wei, and P. A. Beck, Phys. Rev. **120**, 426 (1960).

Effects of Irradiation on the Thermal Conductivity of Synthetic Sapphire

R. BERMAN, E. L. FOSTER,* B. SCHNEIDMESSER,† AND S. M. A. TIRMIZI‡
Clarendon Laboratory, Oxford, England

(Received June 15, 1960)

The thermal conductivity between 2° and 100°K has been measured on synthetic sapphire single crystals and on sintered alumina, before and after reactor and γ-ray irradiations. Reactor irradiation appears to introduce two types of thermal resistivity-producing defects, one of which is dominant at low temperatures. The only effect of γ irradiation is an extra thermal resistivity at low temperatures which saturates for quite small doses. This saturation value seems to depend on the initial perfection of the crystal and is increased by reactor produced damage. At present, detailed information about the defects cannot be derived from thermal conductivity measurements alone.

INTRODUCTION

GEBALLE[1] recently discussed the difficulties involved in deriving information about the nature of irradiation damage in nonmetallic solids from measurements of heat conductivity alone. We have, from time to time[2,3] measured the heat conductivity of irradiated crystals, but we have more recently concentrated on studying the influence of defects with more precisely known characteristics. The theoretical difficulty of relating conductivity to defect concentration even for the simplest type of defects (isotopic variation of mass[4]) is so great that it indeed seems unlikely that irradiation effects on conductivity will be properly understood in the near future. However, it seems worth reporting very briefly on that part of our work on irradiated crystals which has not yet been published.[5]

The increase in thermal resistivity of both quartz[2] and synthetic sapphire[3] single crystals after irradiation in a reactor seems to be made up of two parts, one varying only slightly with temperature ($T^0 - T^1$) and the other more rapidly ($T^{-2} - T^{-3}$). For quartz these two resistivities are equal at about 15°K and for sapphire they are equal at about 30°K. These resistivities were originally ascribed to point or line defects and to larger scale defects, respectively, because of the frequency dependences which could be deduced for the cross sections for phonon scattering (see, e.g., work cited in footnote 8). In view of the uncertainty as to the defects actually responsible and the extent to which resistivities are additive, we will here refer to the two components merely as the "high"-and "low"-temperature resistivities.

The influence of γ irradiation was first measured in order to test the interpretation of the reactor irradiation effects. 1-Mev γ rays should only yield single atomic displacements or very small groups, since the atoms knocked-on by the ejected electrons would not have sufficient energy to produce many further displacements. It was therefore expected that the only observable effect would be a small high-temperature resistivity. In fact, only a low-temperature resistivity was produced, and no change at high temperatures was detected. There was a significant difference between the low-temperature resistivity produced by γ rays and by reactor irradiation—whereas this resistivity increased with irradiation dose for reactor irradiation, the resistivity produced in a given crystal by ^{60}Co γ rays does not vary significantly for doses ranging from 3×10^5 to 10^8 r. A similar saturation has been found in optical absorption experiments.[6,7]

The experiments to be described were designed mainly to find the connection between the low-temperature resistivities produced by reactor and by γ-ray irradiation.

LOW-TEMPERATURE RESISTIVITY

It was shown previously[3] that, for sapphire irradiated in a reactor, the increase in the high-temperature resistivity with dose was slightly less than linear and could be extrapolated to pass through the origin quite well. However, if we plot the low-temperature resistivity against dose we obtain a curve of similar shape but it does not extrapolate to the origin. For any temperature there is now a finite positive intercept on the resistivity axis. In Fig. 1 we have plotted these intercepts as a function of temperature; this curve must represent the resistivity due to very readily produced defects, and it bears a striking resemblance to the temperature variation of the resistivity produced by γ irradiation. The effect of γ irradiation varies slightly from crystal to crystal, but a typical result is also shown in Fig. 1.

A further relationship between the effects of reactor and γ irradiation is found in the effect of annealing. It

* Now at I.C.I. Fibres Division, Wilton, England.
† Now at Scientific Department, Ministry of Defense, Israel.
‡ Now at Physics Department, University of Karachi, Pakistan.

[1] T. H. Geballe, J. Appl. Phys. **30**, 1153 (1959).
[2] R. Berman, P. G. Klemens, F. E. Simon, and T. M. Fry, Nature **166**, 864 (1950).
[3] R. Berman, E. L. Foster, and H. M. Rosenberg, "Defects in crystalline solids," *Report of Bristol Conference* (The Physical Society, London, 1954).
[4] R. Berman, P. T. Nettley, F. W. Sheard, A. N. Spencer, R. W. H. Stevenson, and J. M. Ziman, Proc. Roy. Soc. (London) **A253**, 403 (1959).
[5] We will not mention here some of our work on quartz which has been discussed by King [J. C. King, Bell System Tech. J. **38**, 573 (1959).]
[6] G. J. Dienes and P. W. Levy, "Defects in crystalline solids," *Report of Bristol Conference* (The Physical Society, London 1954).
[7] R. A. Hunt and R. H. Schular, Phys. Rev. **89**, 664 (1953).

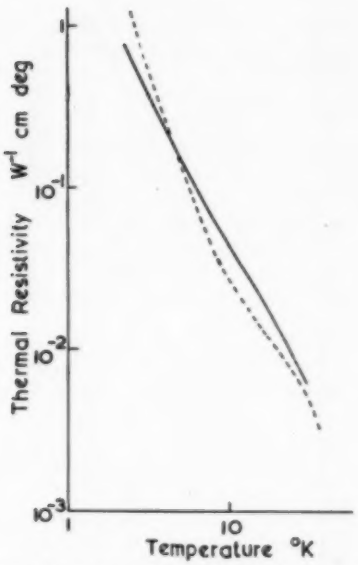

FIG. 1. Extra thermal resistivities produced in synthetic sapphire single crystals by irradiation.——Saturation resistivity produced by γ rays.····Resistivity derived by extrapolating reactor irradiation effect to zero dose.

has already been noted[2] that on heating a crystal after reactor irradiation, the low-temperature resistivity anneals relatively more rapidly than the high-temperature resistivity. We find that the resistivity produced in sapphire by γ irradiation is completely removed by heating at 750°C for 18 hours.

These results suggest that at least part of the defects responsible for the low-temperature resistivity caused by reactor irradiation are of the same nature as the defects produced by γ irradiation. We carried out further experiments to see whether the extra low-temperature resistivity which appears with increasing reactor irradiation is of the same nature too.

A synthetic sapphire was given the same γ-ray dose as had been used in previous experiments (3×10^7 r) and the change in resistivity was measured: this was exceptionally small. This extra resistivity was then removed by heating, and the crystal was irradiated in a reactor for a dose about 50% greater than the total irradiation (5×10^{18} fast neutrons per cm²) of the previous reference.[3] At 20°K the resistivity introduced was a little over 50% greater than previously, corresponding to the greater dose, but at 4°K the extra resistivity in the two cases were about equal. This can again be explained by assuming that the low-temperature resistivity produced in a reactor is the sum of a resistivity which can also be produced readily by γ irradiation and a resistivity dependent on reactor dose. For this crystal, the readily produced resistivity had been found to be small (presumably the initial concentration of the appropriate defects was small) and the 50% increase in reactor dose must just make up for this smaller initial resistivity.

The crystal was heated and a large part of the low-temperature resistivity was removed, as well as some of the high-temperature resistivity. The crystal was then given the same γ irradiation as in the first instance and the increase in resistivity measured. This was five times greater than the resistivity produced by γ irradiation of the virgin crystal. In addition, the shape of the resistivity-temperature curve was now again similar to the curve which would be produced by an appropriate reactor dose, whereas just before the final γ irradiation the shape reflected the relatively greater annealing of the low-temperature resistivity. The measured resistivities are illustrated in Fig. 2, and Fig. 3 shows the resistivities at every stage after the resistivity of the virgin crystal has been subtracted.

It seems, therefore, that the low-temperature resistivity produced by reactor irradiation comes from the same kind of defects as are produced by γ irradiation, but in the former case its increase with dose is in some way related to the displacement damage being produced simultaneously.

We made two experiments to see whether the effect of γ rays is influenced by other forms of defect. In the first, a crystal was heated *in vacuo* at 1000° to 1100°C for about 12 hr, and after cooling, the effect of γ irradiation was measured. Artificial sapphires, as produced, usually contain excess oxygen relative to the stoichiometric proportion, some of which can be removed by high-temperature vacuum annealing. There was, how-

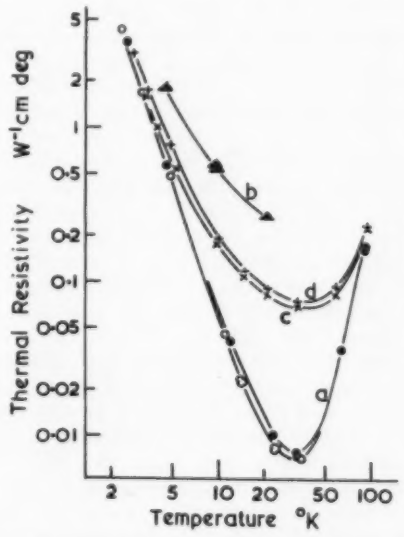

FIG. 2. Thermal resistivity of synthetic sapphire after various irradiations and annealing. o Original crystal. ● (a) After γ irradiation. ▲ (b) After reactor irradiation. × (c) After some annealing of reactor damage. + (d) After γ irradiation of partially annealed crystal.

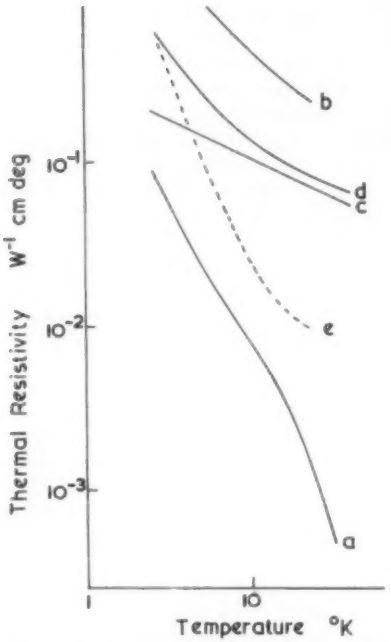

FIG. 3. Extra thermal resistivity produced in synthetic sapphire by irradiation. (a) Resistivity produced by γ irradiation of virgin crystal. (b) Resistivity produced by reactor irradiation. (c) Extra resistivity remaining after some annealing of reactor damage. (d) Extra resistivity produced after γ irradiation of partially annealed crystal. (e) Difference between (d) and (c), representing the effect of γ irradiation on the already damaged crystal.

ever, no change in the resistivity produced in such a crystal greater than the experimental uncertainties.

In the second experiment, a synthetic sapphire crystal was stretched at 1400°C in order to introduce dislocations. The great change in thermal conductivity produced by this 15% elongation can be seen in Fig. 4. The increase in resistivity is proportional to T^{-2} and from Klemens' formula[8] the dislocation density derived is $\sim 10^9/\text{cm}^2$. This formula, however, appears[9] to overestimate the density by a factor of 10^2-10^3. The stretched crystal was γ irradiated and a small change in thermal conductivity was produced. The extra resistivity was only slightly greater than was produced by γ irradiation of the virgin crystal.

The low-temperature resistivity was originally ascribed to large scale defects because its temperature dependence could be explained by a uniform distribution of such defects, scattering phonons nearly independently of wavelength. The mean free path for the scattering would be a few millimeters. At an early stage of the work we carried out an experiment to test a possible view that the effect of γ irradiation might be to

[8] P. G. Klemens in *Solid State Physics*, edited by F. Seitz and D. Turnbull (Academic Press, Inc., New York, 1958), Vol. 7.
[9] R. L. Sproull, M. Moss, and H. Weinstock, J. Appl. Phys. **30**, 334 (1959).

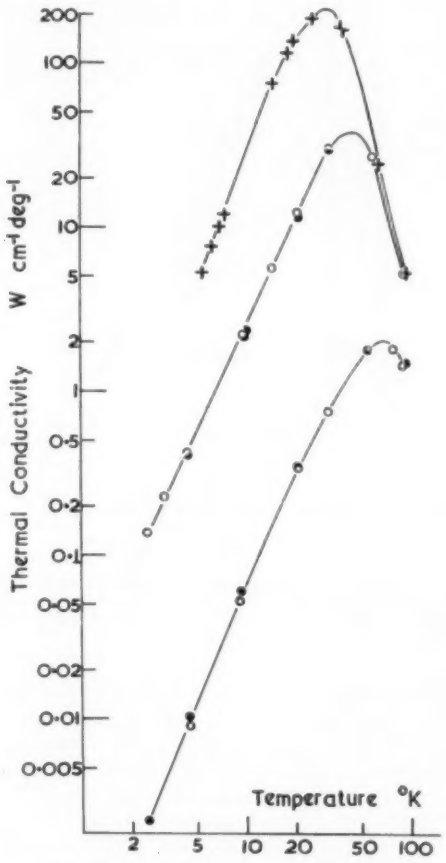

FIG. 4. Effect of irradiation on the thermal conductivity of a stretched sapphire and of sintered alumina. Upper and middle curves: + Original single crystal; ○ Stretched single crystal; ● γ-irradiated stretched crystal. Lower curve: ○ Sintered alumina; ● γ-irradiated sintered alumina.

cause some severe damage confined to the outer layer of the crystal, thereby reducing the effective specimen cross section. Such an effect would give about the right temperature dependence of the resistivity, although it would not explain the variation of the effect among different specimens. At the temperatures concerned, the conductivity (derived from the usual quantities measured) is proportional to the crystal diameter, so that a reduction in effective diameter by a factor x would reduce the conductivity by this amount and would also introduce a factor x^2 into the specimen cross-sectional area. The conductivity calculated from the measurements would then be proportional to x^3 and would, for example, be halved if the effective radius were reduced to about 80% of the crystal radius (2.5 mm in these experiments). This possibility could be tested by measuring the effect of irradiation on single crystals of various diameters. We actually examined the effect on a rod of

sintered alumina of the same diameter as the single crystals. The crystallites were about 20 μ in size, and the conductivity correspondingly smaller at low temperatures, as can be seen in Fig. 3. Severe damage to an outer 20% of the specimen radius would, however, still reduce the apparent conductivity to 65% of its initial value, but if γ irradiation only produced uniformly distributed defects scattering phonons with a mean free path of a few millimeters, this would not be noticeable for the polycrystalline rod in which the mean free path is limited to tens of microns. On irradiation with γ rays, no change in conductivity of the sintered rod was indeed found.

CONCLUSIONS

The experiments suggest that the low-temperature resistivity is produced by defects spread throughout the crystal. The number of these defects which can be produced by γ rays is determined in some way by the initial perfection of the crystal, and is greater in a crystal which has been damaged by neutron bombardment. If these defects were purely displaced atoms, then they would have to be in large groups to give the observed temperature dependence of resistivity. Such groups are unlikely to be produced by 1-Mev γ rays. The similarity of the effect to that observed in germanium with various impurity concentrations,[10] and to the extra thermal resistivity at low temperatures found for an electrically conducting diamond,[11] as well as the ease with which the defects are removed by heating, suggests that the scattering may be electronic in origin. The theory of the scattering of phonons by relatively small concentrations of charge carriers is not certain enough for definite conclusions to be drawn from our present experiments,[12] but we present the results in the hope of stimulating further theory and experiments on irradiation effects.

ACKNOWLEDGMENTS

We would like to thank F. P. Clarke and Dr. J. H. O. Varley of the Atomic Energy Research Establishment, Harwell, for arranging irradiations and high temperature vacuum annealing, and Dr. M. Kronberg of the General Electric Company, Schenectady, New York, for providing the stretched crystal.

[10] J. A. Carruthers, T. H. Geballe, H. M. Rosenberg, and J. M. Ziman, Proc. Roy. Soc. (London) **A239**, 502 (1957).

[11] R. Berman, E. L. Foster, and J. M. Ziman, Proc. Roy. Soc. (London) **A237**, 344 (1956).

[12] Similar, but much more detailed conclusions have been drawn from measurements of optical absorption in irradiated sapphires (P. Levy, private communication).

Measurement of Thermal Conductivity by Utilization of the Peltier Effect. II. Correction for Wire Radiation and Determination of Specimen Radiation Emissivity*

R. SIMON, R. T. BATE, AND E. H. LOUGHER
Battelle Memorial Institute, Columbus, Ohio

(Received August 2, 1960)

The analysis in the first article on measurement of thermal conductivity by utilization of the Peltier effect [T. C. Harman, J. H. Cahn, and M. J. Logan, J. Appl. Phys. **30**, 1351 (1959)] is extended to correct for radiation of heat from the lead wires. It is shown how the radiation emissivity of the semiconductor specimen can also be determined from the measured temperatures.

INTRODUCTION

IN the work cited in footnote 1, the heat equation is solved to obtain the axial and radial distribution of temperature in a cylindrical semiconductor specimen with an assumed uniform Joule heating throughout the specimen, and by approximating the radiation flux per unit surface area of the specimen by $4\sigma\epsilon_s\bar{T}^3(T-T_a)$, where σ is the Stefan-Boltzmann constant, ϵ_s is the surface emissivity of the specimen, $\bar{T}=(T_h+T_c)/2$ is the average of the hot and cold junction temperatures, T is the surface temperature of the specimen as a function of the axial coordinate, and T_a is the ambient temperature. It is shown, from a consideration of the heat-balance equations at the two junctions, how the thermal conductivity of the specimen may be computed from the measured hot- and cold-junction temperatures. Joule heating of the lead wires and the conduction of heat along the lead wires are taken into account in this treatment, but radiation of energy from the surface of the lead wires is assumed to be negligible.

In a subsequent article[2] the case of semiconductor specimens of rectangular cross section is treated in the same manner as that described above for cylindrical specimens.

For many measurement applications, radiation from the lead wires has a significant effect on the magnitude of the lead wire correction in the determination of the thermal conductivity of the semiconductor specimen. The present treatment includes radiation from the lead wires, as well as that from the specimen, and utilizes an improved linearized approximation to the heat equation with the radial temperature distribution neglected. Neglect of the radial temperature distribution is justified for both the specimen and the lead wires for the ranges of the geometrical and physical variables of interest. Finally, it is shown how the radiation emissivity of the specimen can also be determined from the measured temperatures. The value of the specimen emissivity is required for the thermal conductivity determination.

THEORY

Consider a cylinder of length ℓ, radius a, thermal conductivity κ, surface emissivity ϵ, and electrical resistivity ρ. The end $z=0$ is at temperature T_2 and the end $z=\ell$ at temperature T_1. The ambient temperature is T_a. An electrical current $\pi a^2 j$ flows axially through the cylinder. This cylinder may represent either the semiconductor specimen or lead wire. It is desired to compute the flow of heat into the cylinder at $z=0$.

It is shown in the work cited in footnote 1 that the heat equation reduces to $\nabla^2 T=-j^2\rho/\kappa$ for assumed negligible gradients of κ, ρ, and the thermoelectric power α. It is seen in Appendix A that the variation of T with r can be neglected for the experimental conditions involved. Hence, the heat equation becomes

$$\kappa d^2T/dz^2=-j^2\rho+(2/a)(\epsilon\sigma)(T^4-T_a^4), \qquad (1)$$

where σ is the Stefan-Boltzmann constant. The first term on the right of Eq. (1) is the Joule heat generated per unit volume and the second term is the heat dissipated by radiation from the surface of the cylinder per unit cylinder volume.[3] The latter term becomes relatively more important as the radius of the cylinder is decreased. Thomson heat generation along the cylinder is excluded by the assumption that $\nabla\alpha$ is negligible.

In terms of $T_c^4\equiv T_a^4+(j^2\rho a/2\epsilon\sigma)$ and $\beta^2\equiv 8T_c^3\epsilon\sigma/\kappa a$, Eq. (1) becomes

$$d^2T/dz^2=(\beta^2/4T_c^3)(T^4-T_a^4). \qquad (2)$$

T_c represents the equilibrium temperature at which the Joule heat generated is balanced by the radiative dissipation. T would equal T_c at distances $\gg 1/\beta$ from

* Research supported by the Thermoelectric Cooling Research Group.

[1] T. C. Harman, J. H. Cahn, and M. J. Logan, J. Appl. Phys. **30**, 1351 (1959).

[2] J. H. Cahn and J. C. Bell (to be published).

[3] The emissivity of the containing vessel can be neglected if the surface area of the cylinder is much less than that of the vessel, and if the emissivity of the latter is not too small. The rate of radiation of energy per unit area from a cylinder or sphere of radius a, temperature T_1, and emissivity ϵ_1 located concentrically within a cylinder or sphere of radius a_2, lower temperature T_2, and emissivity ϵ_2, is given by $\epsilon\sigma(T_1^4-T_2^4)$, where $(1/\epsilon)=(1/\epsilon_1)+(a_1^2/a_2^2)\times[(1/\epsilon_2)-1]$. (See, for example, R. B. Scott, *Cryogenic Engineering*, D. Van Nostrand Company, Inc., New York, 1959, p. 148.) Both of the above conditions are fulfilled by the experimental arrangement.

the ends of the cylinder if the cylinder were long enough for $\beta\ell \gg 1$. $1/\beta$ represents a length for which the longitudinal heat flow per unit temperature difference $\pi a^2\beta\kappa$ would equal the radial heat flow per unit temperature difference above ambient $(2\pi a/\beta)4T_e^3\epsilon\sigma$. Equation (2) is further reduced to

$$\partial^2\tau/\partial(\beta z)^2=\tau, \tag{3}$$

by substituting $\tau\equiv(T-T_e)/T_e$ and assuming $\tau\ll 1$.

The constants of integration C_1 and C_2 in the solution of Eq. (3),

$$\tau=C_1\cosh(\beta z)+C_2\sinh(\beta z), \tag{4}$$

are determined by using the boundary conditions $T=T_2$ at $z=0$, and $T=T_1$ at $z=\ell$, obtaining for the temperature distribution

$$T-T_e=(T_2-T_e)\cosh(\beta z)+[(T_1-T_e)-(T_2-T_e)\cosh(\beta\ell)]\cdot\sinh(\beta z)/\sinh(\beta\ell) \tag{5}$$

and

$$(dT/dz)_{z=0}=[-\beta/\sinh(\beta\ell)]\times[(T_2-T_e)\cosh(\beta\ell)-(T_1-T_e)]. \tag{6}$$

For the limiting case $\beta\ell\ll 1$, Eq. (6) reduces to $(dT/dz)_{z=0}=-(T_2-T_1)/\ell$. For the other limiting case of $\beta\ell\gg 1$, $(dT/dz)_{z=0}=-\beta(T_2-T_e)$, independent of T_1. $\tau\ll 1$ is a much better approximation for the latter limiting case, for which most of the length of the cylinder is at temperature T_e, than the approximation made in the work cited in footnote 1 that $(T-\bar{T})/\bar{T}\ll 1$. For the wire, T_e can be considerably greater than $(T_1+T_2)/2$. For the former limiting case, the two approximations are equally good, since the temperature distribution is insensitive to the values of T_e or β.

Application to *Z* Meter

The experimental arrangement for the measurement of thermal conductivity by utilization of the Peltier effect has become known as the "*Z* meter" because of its use in determining the figure of merit $Z=\alpha^2/\kappa\rho$ of semiconductor materials for thermoelectric applications. This arrangement consists of the semiconductor specimen of length ℓ_s and radius a_s, cylindrical copper end caps on both ends, each of length ℓ_c and radius equal to that of the specimen, and copper electrical lead wires attached concentrically to the end caps, each of length ℓ_w and radius a_w.

By applying Eq. (6), the heat balance relationship at the hot end of the specimen $(T=T_h)$ becomes

$$[\kappa_s\beta_s/\sinh(\beta_s\ell_s)][(T_h-T_{es})\cosh(\beta_s\ell_s)-(T_c-T_{es})]+(a_w/a_s)^2[\kappa_w\beta_w/\sinh(\beta_w\ell_w)]\times[(T_h-T_{ew})\cosh(\beta_w\ell_w)-(T_a-T_{ew})]+[1+2\ell_c/a_s]\epsilon_c\sigma(T_h^4-T_a^4)=j_s\alpha T_h+j_s^2\rho_c(\ell_s/2). \tag{7}$$

In Eq. (7) the subscript s refers to the specimen, and the subscript w to the wire. The first term on the left is the rate of heat flow into the specimen from its hot end per unit cross-sectional area of the specimen; the cold end is at temperature T_c. The second term is the rate of heat flow into the lead wire from the hot end of the specimen per unit cross-sectional area of specimen; the other end of the wire is at ambient temperature T_a. This term is negative if T_{ew} exceeds $(T_h-T_a)/[\cosh(\beta_w\ell_w)-1]$. The third term on the left is the radiation loss from the end cap per unit cross section of specimen, where ϵ_c is the radiation emissivity of the end cap. The entire end cap is assumed to be at uniform temperature T_h. The first term on the right of Eq. (7) represents the rate of Peltier heat generation per unit cross section of specimen, where α is the difference between the absolute thermoelectric powers of the specimen and the metal end cap. The second term on the right represents the Joule heat generated by the contact resistances at the junctions between the specimen and the end caps per unit cross-sectional area of specimen, the quantity ρ_c being defined by $\rho_c\equiv 2\pi a_s^2R_c/\ell_s$, where R_c is the contact resistance of each junction.

In a similar manner, Eq. (6) is applied to establish the heat balance equation for the cold end of the specimen, obtaining

$$[\kappa_s\beta_s/\sinh(\beta_s\ell_s)][(T_c-T_{es})\cosh(\beta_s\ell_s)-(T_h-T_{es})]+(a_w/a_s)^2[\kappa_w\beta_w/\sinh(\beta_w\ell_w)]\times[(T_c-T_{ew})\cosh(\beta_w\ell_w)-(T_a-T_{ew})]+[1+2\ell_c/a_s]\epsilon_c\sigma(T_c^4-T_a^4)=-j_s\alpha T_c+j_s^2\rho_c\ell_s/2. \tag{8}$$

It is assumed that the lead wire and end cap on the cold end are of the same length, diameter, resistivity, and surface emissivity as those on the hot end in writing Eq. (8).

Determination of Thermal Conductivity

The difference between Eqs. (7) and (8) is

$$\kappa_s\beta_s\coth(\beta_s\ell_s/2)\Delta T+(a_w/a_s)^2\kappa_w\beta_w\coth(\beta_w\ell_w)\Delta T+(1+2\ell_c/a_s)\epsilon_c\sigma(T_h^4-T_c^4)=2j_s\alpha\bar{T}, \tag{9}$$

where

$$\Delta T=T_h-T_c \quad\text{and}\quad \bar{T}=(T_h+T_c)/2.$$

Equation (9) may be written as

$$\kappa_s=\phi_s\ell_s[j_s\alpha\bar{T}/\Delta T-\tfrac{1}{2}(a_w/a_s)^2(\kappa_w/\ell_w\phi_w)-2(1+2\ell_c/a_s)\epsilon_c\sigma\bar{T}\bar{T}^2], \tag{10}$$

or

$$K_s/\phi_s+K_w/\phi_w+A_c\epsilon_c\sigma\bar{T}\bar{T}^2=I\alpha\bar{T}/\Delta T, \tag{11}$$

where

$$\phi_s\equiv\tanh(\beta_s\ell_s/2)/(\beta_s\ell_s/2)$$

$$\phi_w\equiv\tanh(\beta_w\ell_w)/\beta_w\ell_w$$

$$\bar{T}^2=(T_h^2+T_c^2)/2$$

$$K_s=(\pi a_s^2/\ell_s)\kappa_s$$

$$K_w=(\pi a_w^2/2\ell_w)\kappa_w$$

$$A_c=2\pi a_s^2(1+2\ell_c/a_s).$$

K_w is the thermal conductance of the two lead wires in series, and A_e is the total exposed area of both end caps.

For the semiconductor materials and geometry of interest in this application $\phi_s \cong 1$, which means that the radiation correction is small, except perhaps for some materials at temperatures well above room temperature. A good first approximation to the value of κ_s can then be obtained by employing either Eq. (10) or (11) with $\phi_s = 1$. Since the electrical resistivity and radiation properties of the material are contained only in ϕ_s, it is not necessary to know the values of ρ_s and ϵ_s in order to obtain a first approximation to κ_s.

Essentially the same problem was solved by M. A. Kaganov *et al.*[4] by assuming that the rate of dissipation of heat from the surface of the specimen per unit length of specimen is given by the product of a heat-transfer coefficient that is considered constant along the specimen, the perimeter of the specimen, and the difference between the temperature of the specimen at the longitudinal position in question and the ambient temperature. In this respect their treatment is similar to that of footnote reference 1, except that the radial temperature gradients is considered to be negligible, as is done in the present treatment. Kaganov *et al.* also took into account the dissipation of heat from the surface of the electrical lead wires in the same manner as for the heat dissipation from the surface of the specimen. However, although not specifically stated, it is evident from the resultant expressions that the lead wires are assumed to be effectively infinitely long in the work cited in footnote 4, corresponding to $\beta_w \ell_w \gg 1$. An assumption corresponding to $\beta_s \ell_s \ll 1$ is made for the specimen in obtaining the expression for κ_s. Correction for dissipation of heat from end caps is not considered.

Determination of Emissivity

The sum of Eqs. (7) and (8) is

$$2\kappa_s\beta_s \tanh(\beta_s\ell_s/2)(\bar{T}-T_{cs}) + 2(a_w/a_s)^2[\kappa_w\beta_w/\sinh(\beta_w\ell_w)] \times[(\bar{T}-T_{cw})\cosh(\beta_w\ell_w)-(T_a-T_{cw})] + (1+2\ell_c/a_s)\epsilon_s\sigma(T_h^4+T_c^4-2T_a^4) = j_s\alpha\Delta T + j_s^2\rho_s\ell_s. \quad (12)$$

The first term on the left side of Eq. (12) is equivalent to

$$(8\epsilon_s\sigma T_a^3\ell_s\phi_s/a_s)[(1+j_s^2\rho_s a_s/2\epsilon_s\sigma T_a^4)^{\frac{1}{4}}(\bar{T}-T_a)] - 4j_s^2\rho_s\ell_s\phi_s.$$

Since $j_s^2\rho_s a_s/2\epsilon_s\sigma T_a^4 \ll 1$ for the ranges of values of the quantities involved at the temperatures for which the determination of ϵ is of interest, the first-order expansion of the binomial to the $\frac{1}{4}$ power is a good approximation. With this expansion, the first term becomes

$$(8\epsilon_s\sigma T_a^3\ell_s\phi_s/a_s)(\bar{T}-T_a) + 3j_s^2\rho_s\ell_s(\bar{T}-T_a)\phi_s/T_a - j_s^2\rho_s\ell_s\phi_s.$$

Equation (12) may be further simplified somewhat by using alternating current[5] of rms current density j_s instead of direct current for the emissivity measurement, in which case the $j_s\alpha\Delta T$ term vanishes and $T_h = T_c = \bar{T}$. The result of solving Eq. (12) for ϵ_s is

$$[8\sigma T_a^3(\bar{T}-T_a)\ell_s\phi_s/a_s]\epsilon_s = j_s^2\ell_s\left[\rho_s\left(4-\frac{3\bar{T}}{T_a}\right)\phi_s+\rho_s\right] - 2\left(\frac{a_w}{a_s}\right)^2\left(\frac{\kappa_w}{\ell_w}\right)[(\bar{T}-T_{cw})/\phi_w+(T_{cw}-T_a)/\theta_w] - 2\left(1+\frac{2\ell_c}{a_s}\right)\epsilon_s\sigma(\bar{T}^4-T_a^4), \quad (13)$$

where $\theta_w \equiv \sinh(\beta_w\ell_w)/\beta_w\ell_w$. Alternatively, Eq. (13) may be written as

$$E\phi_s\epsilon_s = I^2[R_s(4-3\bar{T}/T_a)\phi_s+2R_c]-4K_w[(\bar{T}-T_{cw})/\phi_w + (T_{cw}-T_a)/\theta_w]-A_e\epsilon_s\sigma(\bar{T}^4-T_a^4), \quad (14)$$

where

$$E \equiv (2\pi a_s\ell_s)(4\sigma T_a^3)(\bar{T}-T_a).$$

A first approximation to the value of ϵ_s may be obtained from Eq. (13) or (14) by setting $\phi_s = 1$. A better value of ϕ_s may then be computed from this approximate value of ϵ_s and the first approximation to κ_s obtained from Eq. (10) or (11). Improved values of both ϵ_s and κ_s may then be obtained by substituting the more accurate value of ϕ_s into the appropriate equations. Successive approximations may be needed if ϕ_s differs appreciably from unity.

The fact that ϵ_s and the radiation correction to κ_s can be calculated thus from the experimental data is a consequence of the good thermal isolation of the sample from its surroundings in the Z meter, and illustrates an advantage of the Z meter over other techniques for measuring κ_s.

End Cap Correction

For the end caps, $\ell_c \cong 0.6a_s$ in order to obtain a desired degree of uniformity of current flow in the semiconductor specimen.[6] For $\ell_c \cong 8a_s$, the surface area of the specimen is about 3.6 times that of the end caps. Furthermore, the emissivities of the specimens range from about 0.5–1, whereas that of the end cap at room temperature and above can probably be made to be about 0.05 or less by suitable polishing and/or plating. Consequently, the terms in the formulas for κ_s and ϵ_s that result from radiation of heat from the end caps would be comparatively small and probably could be

[4] M. A. Kaganov, I. S. Lisker, and I. B. Mushkin, Fiz. Tverdogo Tela **1**, 988 (1959) [translation in Soviet Physics—Solid State **1**, 905 (1959)].

[5] W. C. Myers and R. T. Bate (to be published).

[6] R. Simon, J. H. Cahn, and J. C. Bell (to be published).

neglected in most cases. At any rate, an accurate value of ϵ_s is not needed.

Lead Wire Correction

It is desirable to minimize the lead wire correction, not only to achieve greater accuracy in the determination of κ_s, but also to decrease the amount of current through the semiconductor specimen needed to obtain a given ΔT. It is seen from Eq. (14) that $\bar{T}-T_a$ varies approximately as I^2, whereas Eq. (11) shows that ΔT varies approximately as I. It is seen from Eq. (11) that minimization of the lead wire correction would entail an experimental arrangement for which $K_w/\phi_w \ll K_s/\phi_s$.

Typical specimen parameters at room temperature might be $a_s=0.25$ cm, $\ell_s=2$ cm, $\alpha \cong 10^{-4}$ v/°K, $\epsilon_s \cong 1$, $\rho \cong 10^{-3}$ ohm-cm, and $\kappa_s \cong 10^{-2}$ w/(cm)(°K). The lead wire parameters for a typical experimental arrangement might be $a_w=0.0040$ cm (40-gauge wire), $\ell_w=6$ cm, $\rho_w=1.7\times10^{-6}$ ohm-cm (copper), $\kappa_w=4.2$ w/(cm)(°K), and $\epsilon_w \cong 1$ (wire surface treated to obtain high emissivity). Now $K_s=9.8\times10^{-4}$ w/°K and $K_w=1.76\times10^{-5}$ w/°K. To obtain a first approximation to I, set ϕ_s and ϕ_w at their maximum values of unity and $\bar{T}=T_a=293$°K. The result is $I=34$ ma for $\Delta T=1$°K. Hence, $T_{cs}=293$°K, $\beta_s\ell_s=1.35$, and $\phi_s=0.87$. Also $T_{cw}=296$°K, $\beta_w\ell_w=1.58$, and $\phi_w=0.58$. Hence K_w/ϕ_w is only about 3% of K_s/ϕ_s. A better value of $\bar{T}$ can be obtained from Eq. (15), but $\bar{T}$ should not be significantly different from T_a for the values of T_{cs} and T_{cw} obtained. The corrected value of I is 40 ma for $\Delta T=1$°K.

It is often desired to determine the value of κ_s as a function of temperature down to liquid nitrogen temperature, $T_a=77$°K. At this temperature, typical values of ρ_s and α_s are assumed to be $\frac{1}{4}$ of the above room temperature values and the value of κ_s is assumed to be the same as the above room temperature value. The values of ρ_w and κ_w for the copper lead wires are about $\frac{1}{8}$ and $\frac{3}{4}$ times their room temperature values, respectively. Now $K_s=9.8\times10^{-4}$ w/°K, $K_w=2.4\times10^{-5}$ w/°K, and the first approximation to I is 522 ma for $\Delta T=1$°K. Hence $T_{cs}=92$°K, $\beta_s\ell_s=0.24$, and $\phi_s=0.99$. Likewise $T_{cw}=302$°K, $\beta_w\ell_w=1.42$, and $\phi_w=0.63$. At liquid nitrogen temperature K_w/ϕ_w is about 4% of K_s/ϕ_s. Thus the condition that $K_w/\phi_w \ll K_s/\phi_s$ can also be met at liquid nitrogen temperature by using 40-gauge copper wire for the leads. The maximum temperature of each lead would be much less than T_{cw}; the magnitude of $\beta_w\ell_w$ would have to exceed about 3.0 for the temperature away from the ends of the leads to approach T_{cw}.

If bare copper wire with $\epsilon_w \cong 0.05$ is used for the leads, the value of T_{cw} at $T_a=77$°K would be in the neighborhood of 600°K or more, because of the increase of ρ_w at the higher wire temperature. Not only would a considerable amount of heat flow from the lead wires into the specimen, thereby raising the temperature of the latter appreciably, but also the theory of the lead wire correction developed herein, based on the assumption of constant ρ_w, κ_w, and ϵ_w along the length of the wire, would be inadequate.

Generalization to Specimens and Lead Wires of Noncylindircal Geometry

All equations also apply to specimens and lead wires of noncircular cross section if the quantities a_s and a_w are replaced by $2A_s/P_s$ and $2A_w/P_w$, respectively, where A is the cross-sectional area and P is the perimeter, except that the expression $(a_w/a_s)^2$ in Eqs. (7), (8), (9), (10), (12), and (13) must be replaced by A_w/A_s.

ACKNOWLEDGMENT

The authors wish to thank Drs. A. C. Beer and H. L. Goering for their helpful comments on the manuscript, and Mr. M. J. Logan for the experimental work described in Appendix B.

APPENDIX A

Radial Temperature Gradient

The substitution of Eq. (1) for $\nabla^2 T=-j^2\rho/\kappa$ is equivalent to separating the variables by writing

$$(1/r)(\partial/\partial r)(r\partial T/\partial r)=-(2/a)(\epsilon\sigma/\kappa)(T_0^4-T_a^4), \quad (A.1)$$

where T_0 is the surface temperature of the cylinder. The solution of this equation with the boundary condition $\kappa(\partial T/\partial r)_{r=a}=-\epsilon\sigma(T_0^4-T_a^4)$ is

$$T-T_0=(\epsilon\sigma a/2\kappa)(T_0^4-T_a^4)(1-r^2/a^2). \quad (A.2)$$

If T_i is the temperature at the axis of the cylinder ($r=0$), we have $T_i-T_0=(\epsilon\sigma a/2\kappa)(T_0^4-T_a^4)$, or

$$(T_i-T_0)/(T_0-T_a)=2a\epsilon\sigma T_{0a}^3/\kappa, \quad (A.3)$$

where

$$T_{0a}^3=(1/4)(T_0+T_a)(T_0^2+T_a^2).$$

For 40-gauge copper lead wires at $T_{0a}=750$°K and $\kappa_w=4.2$ w/(cm)(°K), $(T_i-T_0)/(T_0-T_a)=2.3\times10^{-7}$ for $\epsilon_w=0.05$ (bare wire) and 4.6×10^{-6} for $\epsilon_w=1$. Hence, the wire temperature can certainly be considered to be uniform throughout the cross section, since the variation is minute as compared with the difference between the wire temperature and ambient temperature at any point along the length of the wire.

For a semiconductor specimen of $a_s=2.5$ mm, $\epsilon_s=1$ and $\kappa_s=10^{-2}$ w/(cm)(°K) at $T_{0a}=300$°K, $(T_i-T_0)/(T_0-T_a)=8\times10^{-3}$. The temperature variation throughout any cross section of the semiconductor specimen is thus of the order of 1% of the difference between its outer surface temperature and ambient.

Hence, the approximation made in Eq. (1) by considering T as independent of r is a good one for the lead wires at any temperature of interest, and for the specimen at least up to room temperature.

Usefully accurate values of κ_s are obtained by using Eq. (10) or (11), even under conditions for which the

radial temperature gradient would not be expected to be negligible, i.e., for specimens with small length-to diameter ratios at high temperatures. For example, for κ_s as low as 0.005 w/(cm)(°K), $\ell_s=2$ cm, $a_s=0.5$ cm, and $\epsilon_s=1$, $1/\phi_s=2.85$ for $T_{ss}=760$°K. The correction factor for K_s in which the effects of the radial temperature gradient are taken into account is given by the summation in Eq. (17) of the work cited in footnote 1. The value of this summation is 2.65 for $\gamma\equiv h_s a_s/\kappa_s = (\beta_s a_s)^2/2=1$, corresponding to the above conditions. Hence, for this case, $1/\phi_s$ overcorrects by about 8%. (For the more favorable specimen parameters of $\kappa_s=0.01$ w/(cm)(°K), $\ell_s=2$ cm, $a_s=0.25$ cm, and $\epsilon_s=0.5$, equally accurate results would be obtained at $T_{ss}=1520$°K, for which γ also $=1$.)

It is readily shown that the first term of the summation in Eq. (17) of the work cited in footnote 1 is identical to $1/\phi_s$ for $\gamma\ll 1$ and the other terms are relatively small. As γ increases, the value of the summation becomes smaller than $1/\phi_s$. Hence, the correction factor $1/\phi_s$ to K_s tends to overcompensate for the effects of radiation from the surface of the specimen, as is shown in the above example. Some overcompensation is to be expected, since the surface temperature at any longitudinal position would be less than the average temperature throughout the cross section at that position.

APPENDIX B

Experimental Emissivity Measurement

A 1.105-cm-diameter, 1.80-cm-long specimen of a 67% Bi_2Te_3 − 33% Sb_2Te_3 alloy was coated with a thin layer of commercial flat black lacquer, for which the emissivity should be between 0.95 and 1. The specimen was provided with 0.476-cm-long copper end caps of the same diameter as the specimen and 30-gauge bare copper lead wires each six cm in length (diameter—0.0254 cm). The end caps and lead wires were cleaned and polished. The room temperature values of the thermal conductivity and of the resistivity of the specimen are 1.42×10^{-2} w/(cm)(°K) and 8.74×10^{-4} ohm-cm, respectively.

When using an alternating current of 300 ma, a value of $\bar{T}-T_a=0.65$°K was obtained. The computed values of ϵ_s are 1.05, 1.0, and 0.95 for assumed values of ϵ_w of 0.04, 0.05, and 0.06, respectively. It would be preferable to treat the surface of the wire to obtain an ϵ_w of close to unity, since a few percent decrease of the actual emissivity of the wire from unity would make an insignificant error in the determination of ϵ_s, whereas an uncertainty in the value of a small ϵ_w makes an appreciable error in the determination of ϵ_s, as seen above.

Determination of Electrode Shapes for Axially Symmetric Electron Guns*

KENNETH J. HARKER
Microwave Laboratory, W. W. Hansen Laboratories of Physics, Stanford University, Stanford, California
(Received August 1, 1960)

The determination of the electrode shapes for an electron gun involves solving Laplace's equation subject to specified boundary values of voltage and normal field on an open curve. Past attempts to solve this problem for the case of axial symmetry by mathematical methods have met with considerable difficulties because the problem is improperly set and leads to unstable solutions. Following Garabedian, we have reformulated the problem in such a manner that it becomes properly set, and have applied it to a curvilinear space-charge limited flow gun. First, a conformal transformation is made which maps the beam boundary into a coordinate axis. The second step, which constitutes the essence of the method, is accomplished by making an analytic continuation of Laplace's equation and its boundary values into a fictitious complex domain. Laplace's equation, which is elliptic in the real domain, is thereby converted into a set of hyperbolic equations. This leads to a stable scheme of computation by finite differences. This method should find particular application to curvilinear flow guns, where the use of analogs, such as the electrolytic tank, requires the use of involved experimental techniques. The method is very general, however, being applicable to any configuration where the boundary conditions are given through analytic functions. If one desires, these specifications for the boundary conditions may be given implicitly, as, for example, through a set of differential equations.

INTRODUCTION

THE determination of the electrode shapes for axially symmetric electron guns with space-charge limited flow has been of particular concern ever since the inception of these devices. Although this problem has been solved analytically for the two-dimensional case,[1,2] there are no known analytic solutions for the potential about beams with axial symmetry. The electrode shapes have commonly been found with analog methods, such as electrolytic tanks and resistance networks.[3–5]

It would seem that the time is at hand, now that high-speed computers are readily available to most people, for one to seek a solution through numerical computation. Some workers[6,7] have approached the problem through the use of Taylor series expansions around the beam edge, but of course their results are only valid within the restricted region determined by the domain of convergence of the expansions. Others[8] have attempted to solve the problem by stepping procedures. Their results are open to question, since Laplace's equation is elliptic and unstable under the Cauchy boundary conditions prescribed by this problem. (By instability, we are, of course, referring to the fact that the solution does not converge to the exact solution as the mesh size of the calculation is reduced towards zero.)

Following recent work by Garabedian,[9,10] we intend to show, however, how the problem may be reformulated in order to obtain stable solutions. This will be done by continuing Laplace's equation into the complex domain, so that it becomes hyperbolic. One is then able to obtain a stable solution on an electronic computer by stepping procedures which will converge to the exact solution.

We will develop our method around a particular curvilinear flow electron beam described by Kirstein and Kino.[11] The theory behind the method, the numerical methods used, and finally, results obtained on a digital computer, will be presented in order. Although the method at hand will be directed to a particular gun, it should be emphasized again that it is quite general and can be applied to any gun whose boundary conditions are specified analytically.

THEORY FOR REAL DOMAIN

Kirstein and Kino[11] have shown that a number of exact solutions can be obtained to the equations of space-charge limited electron flow in addition to Langmuir's[12,13] original solutions. In particular, we shall concentrate on a hollow beam gun with a cylindrical cathode. Kirstein and Kino have shown that there exists a flow which is described by an analytic solution in which the voltage and electric fields vary exponentially with respect to distance along the axis. Figure 1 shows a finite beam embodiment of this type of flow drawn in a meridian plane with the usual cylindrical coordinates r and z. Since it is characteristic of this type of flow that any electron trajectory can be generated from any other by a translation in the z direction, both beam edges have identical shapes. We will assume that the beam edge is defined by a relation of the form

$$z=\phi(r). \tag{1}$$

* The research reported in this document was supported in whole or in part by the Rome Air Development Center, Air Research and Development Command, United States Air Force.

[1] P. T. Kirstein, Proc. I.R.E. **46**, 1716 (1958).
[2] R. J. Lomax, J. Electronics and Control **7**, 482 (1959).
[3] J. R. Pierce, *Theory and Design of Electron Beams* (D. Van Nostrand Company, Inc., Princeton, New Jersey, 1954), p. 179.
[4] K. R. Spangenberg, *Vacuum Tubes* (McGraw-Hill Book Company, Inc., New York, 1948), p. 456.
[5] E. J. Cook, Proc. I.R.E. **46**, 497 (1958).
[6] I. Sugai, Proc. I.R.E. **47**, 87 (1959).
[7] R. Hechtel, Telefunken-Zeitung **28**, 222 (1955).
[8] Kuo-Chu Ho and R. J. Moon, J. Appl. Phys. **24**, 1186 (1953).
[9] P. R. Garabedian and H. M. Lieberstein, J. Aeronaut. Sci. **25**, 109 (1958).
[10] P. R. Garabedian, *Studies in Mathematics and Physics Presented to Richard von Mises* (Academic Press, Inc., New York, 1954), p. 149.
[11] P. T. Kirstein and G. S. Kino, J. Appl. Phys. **29**, 1758 (1958).
[12] I. Langmuir, Phys. Rev. **2**, 450 (1913).
[13] I. Langmuir and K. Blodgett, Phys. Rev. **22**, 347 (1923), and Phys. Rev. **24**, 49 (1924).

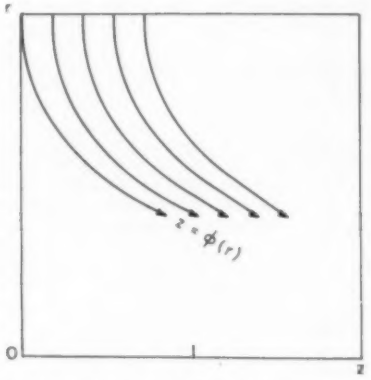

FIG. 1. A finite embodiment of curvilinear flow from a hollow cylindrical cathode.

Let us now examine the equations governing the region within the electron beam. Assuming that the voltage varies as $e^{2\beta z/a}$, Poisson's equation in MKS units is given by

$$\frac{\partial^2 V}{\partial r^2}+\frac{1}{r}\frac{\partial V}{\partial r}+\frac{4\beta^2 V}{a^2}=\frac{\rho}{\epsilon}, \tag{2}$$

where a is the beam radius, β is a dimensionless constant, ρ is the electron charge density, and ϵ is the dielectric constant of free space. It will be convenient for our purpose to transform to the new coordinates

$$\begin{aligned} u&=r \\ \xi&=z-\phi(r), \end{aligned} \tag{3}$$

in which all electron trajectories correspond to constant values of ξ. In this new coordinate system, Poisson's equation becomes

$$\frac{dP}{du}=\frac{2\beta(\psi P+Q)}{a}+\frac{2\beta}{a}\frac{d\psi}{du}V+\frac{2\beta\psi V/a-P}{u}+\frac{\rho}{\epsilon}, \tag{4}$$

where

$$P=\frac{dV}{du}, \tag{5}$$

$$\psi=\frac{d\phi}{du}, \tag{6}$$

$$Q=\psi P-\frac{2\beta}{a}(1+\psi^2)V. \tag{7}$$

By the law of current conservation and simple geometrical considerations, it can be seen that the charge density is given by

$$\rho=\frac{J}{(2eV/m)^{\frac{1}{2}}}=\frac{J_0 a}{(2eV/m)^{\frac{1}{2}}u}(1+\psi^2)^{\frac{1}{2}}, \tag{8}$$

where J is the current density, J_0 is the cathode emission density, e is the electron charge, and m is the electron mass.

In order to completely describe the flow, we need the equation

$$\frac{(d\psi/du)}{(1+\psi^2)^{\frac{1}{2}}}=\frac{V_n}{2V}, \tag{9}$$

where V_n is the normal derivative of the voltage on the concave side of the beam boundary, stating the equality between the centrifugal and normal electric forces. Again from geometrical considerations, it is clear that

$$V_n=\frac{1}{(1+\psi^2)^{\frac{1}{2}}}\left[-\psi\frac{\partial V}{\partial r}+2\beta\frac{V}{a}\right]. \tag{10}$$

From Eqs. (3), (5), and (6) it is also clear that

$$P=\frac{\partial V}{\partial r}+\frac{2\beta}{a}\psi V. \tag{11}$$

Substituting Eqs. (7), (10), and (11), we obtain from Eq. (9) the relation

$$\frac{d\psi}{du}=-(1+\psi^2)\frac{Q}{2V}. \tag{12}$$

For the remainder of this paper we shall use normalized quantities in order to simplify our formulas. In particular, all distances shall be measured in units of the cathode radius a, V in terms of the voltage unit

$$\left[\frac{243}{500}\frac{J_0 a^2}{(2e/m)^{\frac{1}{2}}\epsilon}\right]^{\frac{2}{3}},$$

and P and Q in terms of the field unit

$$\left[\frac{243}{500}\frac{J_0 a^1}{(2e/m)^{\frac{1}{2}}\epsilon}\right]^{\frac{1}{3}}.$$

If we choose J_0 as the current density at the cathode edge, then the equations of space-charge limited flow along the beam edge reduce to the normalized equations below:

$$\frac{d\phi}{du}=\psi, \tag{13}$$

$$\frac{d\psi}{du}=-(1+\psi^2)\frac{Q}{2V}, \tag{14}$$

$$\frac{dV}{du}=P, \tag{15}$$

$$\frac{dP}{du}=2\beta(\psi P+Q)-\beta(1+\psi^2)Q + \frac{2\beta\psi V-P}{u}+\frac{500}{243u}\left[\frac{1+\psi^2}{V}\right]^{\frac{1}{2}}, \quad (16)$$

$$Q=\psi P-2\beta(1+\psi^2)V, \quad (17)$$

with the initial conditions

$$\psi=V=P=Q=0 \quad \text{at} \quad u=1. \quad (18)$$

In the charge-free region around the beam, Laplace's equation

$$\frac{\partial^2 V}{\partial r^2}+\frac{1}{r}\frac{\partial V}{\partial r}+\frac{\partial^2 V}{\partial z^2}=0 \quad (19)$$

determines the voltage. It will be necessary for us to make a conformal transformation to new coordinates (u,v) so that the beam boundary maps into one of the coordinate axes. Rembering that the beam edge is defined by the equation

$$z=\phi(r), \quad (20)$$

an appropriate conformal transformation is given by

$$z+ir=\phi(u+iv)+i(u+iv). \quad (21)$$

Inspection of this equation indeed verifies that the beam edge is mapped into the line $v=0$. A sketch of the conformal coordinate system is shown in Fig. 2.

As the reader may verify, Eq. (19) transforms under this conformal transformation into

$$\frac{\partial^2 V}{\partial u^2}+\frac{\partial^2 V}{\partial v^2}+\frac{1}{r}\frac{\partial r}{\partial u}\frac{\partial V}{\partial u}+\frac{1}{r}\frac{\partial z}{\partial u}\frac{\partial V}{\partial v}=0. \quad (22)$$

This, along with the Cauchy-Riemann equations

$$\frac{\partial r}{\partial v}=\frac{\partial z}{\partial u} \quad (23)$$

$$\frac{\partial z}{\partial v}=-\frac{\partial r}{\partial u}, \quad (24)$$

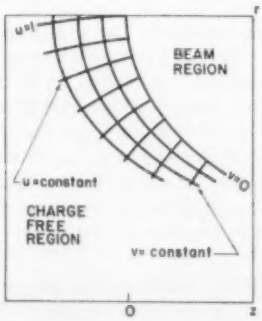

FIG. 2. Conformal coordinate system in region outside the beam.

constitutes the complete set of equations determining the voltage.

It is furthermore desirable to reduce Eqs. [(22)–(24)] to a set of first order equations by defining

$$P=\partial V/\partial u \quad (25)$$

$$Q=\partial V/\partial v. \quad (26)$$

This leads us to the following set of equations:

$$\frac{\partial Q}{\partial v}=-\frac{\partial P}{\partial u}-\frac{Q}{r}\frac{\partial z}{\partial u}-\frac{P}{r}\frac{\partial r}{\partial u} \quad (27)$$

$$\frac{\partial P}{\partial v}=\frac{\partial Q}{\partial u} \quad (28)$$

$$\frac{\partial r}{\partial v}=\frac{\partial z}{\partial u} \quad (29)$$

$$\frac{\partial z}{\partial v}=-\frac{\partial r}{\partial u}. \quad (30)$$

The boundary values of r, z, V, P, and Q for these partial differential equations are given by the values of u, ϕ, V, P, and Q, respectively, generated by Eqs. [(13)–(17)]. On the beam boundary it is clear from the Cauchy-Riemann equations that

$$P=\frac{\partial V}{\partial r}+2\beta\psi V \quad (31)$$

and

$$Q=\psi\frac{\partial V}{\partial r}-2\beta V. \quad (32)$$

Combining these equations, we find that

$$Q=\psi P-2\beta(1+\psi^2)V. \quad (33)$$

Since this is identical with Eq. (17), it is clear that Q generated by Eqs. [(13)–(17)] is indeed the boundary value of Q required in Eqs. [(27)–(30)].

THEORY FOR COMPLEX DOMAIN

Any attempt to integrate the partial differential equations of the previous section as such would be subject to sure failure, inasmuch as they are elliptic and consequently unstable. It is the essence of the method we are proposing here to reformulate the problem in such a manner that it is properly set and the instability is eliminated. This is accomplished by making an analytic continuation into the complex domain. Our partial differential equations become hyperbolic in the process and stability is thereby obtained for computation by finite differences

Figure 3 illustrates the process. The p axis is the old u axis and represents the beam boundary. The plane

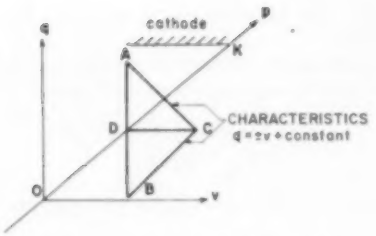

FIG. 3. Geometry of characteristic coordinates in the complex domain.

$q=0$ represents the region of the original real problem, while the region above and below this plane represents the region into which the analytic continuation is to be made.

A solution is obtained by first continuing the boundary conditions along the p axis into the complex domain. The boundary conditions for the problem are thereby generated over the surface $v=0$. One then uses these boundary conditions to integrate the partial differential equations in the planes $p=$ constant outward from the boundary and between the characteristics $q=\pm v+$constant. In general, complex values of V will be generated through the domain. Those values of V in the plane $q=0$ will be the only ones of physical relevance. They will be real and will represent the values of voltage being sought.

To be more specific, suppose it is desired to know the voltage along the line DC. We recall from the theory of complex variables that if $u=p+iq$, then

$$\partial/\partial u=\partial/i\partial q=\partial/\partial p. \tag{34}$$

One first integrates Eqs. [(13)–(17)] from K to D in the form

$$d\phi/dp=\psi \tag{35}$$

$$\frac{d\psi}{dp}=-(1+\psi^2)\frac{Q}{2V} \tag{36}$$

$$dV/dp=P \tag{37}$$

$$\frac{dP}{dp}=2\beta(\psi P+Q)-\beta(1+\psi^2)Q + \frac{2\beta\psi V-P}{u}+\frac{500}{243u}\left[\frac{1+\psi^2}{V}\right]^{\frac{1}{2}} \tag{38}$$

$$Q=\psi P-2\beta(1+\psi^2)V. \tag{39}$$

Real values of ϕ, ψ, V, P, and Q are obtained at the point D.

One next obtains the boundary conditions along AB by integrating Eqs. [(13)–(17)] from D to A and D to B in the following form:

$$d\phi/dq=i\psi \tag{40}$$

$$\frac{d\psi}{dq}=-i(1+\psi^2)\frac{Q}{2V} \tag{41}$$

$$dV/dq=iP \tag{42}$$

$$\frac{dP}{dq}=i\left\{2\beta(\psi P+Q)-\beta(1+\psi^2)Q + \frac{2\beta\psi V-P}{u}+\frac{500}{243u}\left[\frac{1+\psi^2}{V}\right]^{\frac{1}{2}}\right\} \tag{43}$$

$$Q=\psi P-2\beta(1+\psi^2)V. \tag{44}$$

Since the differential equations are now complex, complex values of ϕ, ψ, V, P, and Q are obtained along the line AB.

Starting from AB, we next integrate our partial differential equations outward between AC and BC. None of the results will have physical relevance, except along DC, where real values of r, z, V, P, and Q will be obtained as functions of the conformal coordinates u and v. Since we are integrating along a plane $p=$ constant, our partial differential equations will have the form

$$\begin{vmatrix} \frac{\partial P}{\partial v} \\ \frac{\partial Q}{\partial v} \\ \frac{\partial r}{\partial v} \\ \frac{\partial z}{\partial v} \end{vmatrix} = \begin{vmatrix} 0 & -i & 0 & 0 \\ i & 0 & i\frac{P}{r} & i\frac{Q}{r} \\ 0 & 0 & 0 & -i \\ 0 & 0 & i & 0 \end{vmatrix} \begin{vmatrix} \frac{\partial P}{\partial q} \\ \frac{\partial Q}{\partial q} \\ \frac{\partial r}{\partial q} \\ \frac{\partial z}{\partial q} \end{vmatrix} \tag{45}$$

and

$$\frac{\partial V}{\partial v}=Q. \tag{46}$$

The boundary values of r, z, V, P, and Q are given by the values of $(p+iq)$, ϕ, V, P, and Q, respectively, generated by Eqs. [(40)–(44)].

The characteristic roots of the matrix in Eq. (45) are $+1$ and -1. According to the theory of characteristics, our partial differential equations are hyperbolic and therefore stable, since the above characteristic roots are real. Furthermore, the characteristic roots give the slope of the characteristics, so that the characteristic curves are given by the family of straight lines given by

$$q=\pm v+\text{constant}.$$

Stable solutions for our partial differential equations will be obtained as long as the integration is adjusted to

stay within the influence region bounded by the characteristics.

NUMERICAL ANALYSIS

We shall base our solution of Eq. (45) on a central difference scheme. If we let $v=jh$, $q=kh$, where h is the mesh interval, and define $\phi(jh,kh)=\phi_{jk}$, then we may approximate our partial differential equations by the difference equations

$$\left.\begin{aligned}
P_{m+1,n}&=P_{m-1,n}-i(Q_{m,n+1}-Q_{m,n-1})\\
Q_{m+1,n}&=Q_{m-1,n}+i\Bigg[P_{m,n+1}-P_{m,n-1}\\
&\quad+\frac{Q_{m,n+1}+Q_{m,n-1}}{r_{m,n+1}+r_{m,n-1}}(z_{m,n+1}-z_{m,n-1})\\
&\quad+\frac{P_{m,n+1}+P_{m,n-1}}{r_{m,n+1}+r_{m,n-1}}(r_{m,n+1}-r_{m,n-1})\Bigg]\\
r_{m+1,n}&=r_{m-1,n}-i[z_{m,n+1}-z_{m,n-1}]\\
z_{m+1,n}&=z_{m-1,n}+i[r_{m,n+1}-r_{m,n-1}].
\end{aligned}\right\}\quad(47)$$

In order to start the calculation, we must calculate the data for the first column. This is done by using Eq. (45) in the modified form:

$$\left.\begin{aligned}
P_{1,n}&=\tfrac{1}{2}[P_{0,n+1}+P_{0,n-1}-i(Q_{0,n+1}-Q_{0,n-1})]\\
Q_{1,n}&=\frac{1}{2}\Bigg[Q_{0,n+1}+Q_{0,n-1}+i\Bigg\{P_{0,n+1}-P_{0,n-1}\\
&\quad+\frac{Q_{0,n+1}+Q_{0,n-1}}{r_{0,n+1}+r_{0,n-1}}(z_{0,n+1}-z_{0,n-1})\\
&\quad+\frac{P_{0,n+1}+P_{0,n-1}}{r_{0,n+1}+r_{0,n-1}}(r_{0,n+1}-r_{0,n-1})\Bigg\}\Bigg]\\
r_{1,n}&=\tfrac{1}{2}[r_{0,n+1}+r_{0,n-1}-i(z_{0,n+1}-z_{0,n-1})]\\
z_{1,n}&=\tfrac{1}{2}[z_{0,n+1}+z_{0,n-1}+i(r_{0,n+1}-r_{0,n-1})].
\end{aligned}\right\}\quad(48)$$

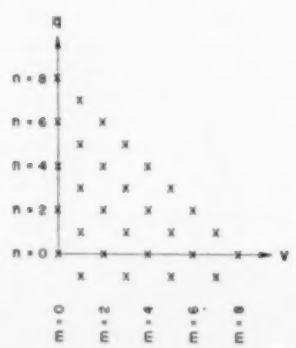

FIG. 4. Mesh points for the finite difference scheme.

TABLE I. Electrode coordinates.

Left cathode electrode $V=0$		Right cathode electrode $V=0$	
r	z	r	z
1.0000	0.0000	1.0000	0.2000
0.9896	−0.0242	0.9905	0.2248
0.9665	−0.0679	0.9742	0.2736
0.9412	−0.1066	0.9618	0.3202
0.9143	−0.1398	0.9527	0.3619
0.8863	−0.1679	0.9461	0.3979
0.8577	−0.1913	0.9413	0.4286
0.8287	−0.2104	0.9377	0.4547
0.7995	−0.2255	0.9350	0.4772
0.7703	−0.2369	0.9328	0.4968
0.7414	−0.2450	0.9310	0.5139
0.7128	−0.2498	0.9299	0.5249
0.6846	−0.2516	0.9296	0.5291
0.6570	−0.2504	0.9284	0.5427
0.6301	−0.2463	0.9273	0.5549
0.6040	−0.2394	0.9265	0.5658
0.5788	−0.2297	0.9257	0.5758
0.5548	−0.2170	0.9251	0.5849
0.5321	−0.2016	0.9245	0.5932
0.5108	−0.1831	0.9240	0.6008
0.4910	−0.1617	0.9231	0.6141
0.4731	−0.1373	0.9225	0.6253
0.4572	−0.1099	0.9219	0.6346
0.4435	−0.0798		
0.4319	−0.0472		
0.4226	−0.0130		
0.4154	0.0220		
0.4099	0.0567		
0.4058	0.0899		
0.4026	0.1206		
0.4004	0.1479		
0.4013	0.1757		

In practice, it is only necessary to use values of n and m in Eqs. (47), whose sum is even. Furthermore, since $P_{m,0}$, $Q_{m,0}$, $r_{m,0}$, and $z_{m,0}$ are all real, the Schwarz principle of reflection shows that

$$\begin{aligned}
r_{m,-1}&=r_{m,1}^*\\
z_{m,-1}&=z_{m,1}^*\\
P_{m,-1}&=P_{m,1}^*\\
Q_{m,-1}&=Q_{m,1}^*,
\end{aligned}\quad(49)$$

where the asterisk denotes the complex conjugate. This symmetry property allows us to solve Eq. (47) using only mesh points for $n\geq 0$ since, when $n\geq 1$, we do not need any mesh points in the lower half plane in order to evaluate Eq. (47), while for $n=0$ the mesh points in the lower half plane can be eliminated from Eq. (47) by means of Eqs. (49).

Figure 4 shows the mesh in which the numerical calculation is carried out. The initial conditions determine the points in column $m=0$ for $n=0, 2, 4, \cdots, 2N-2$. Equations (48) are used to determine the column with $m=1$ for $n=1, 3, 5, \cdots, 2N-3$. Equations (47) and (49) are then applied in succession to find columns $m=2, 3, 4, \cdots$ such that $m+n$ is even and does not exceed $2N-2$.

Equation (46) may be approximated by the difference equation

$$V_{m+1,0}=V_{m-1,0}+h(Q_{m,1}+Q_{m,-1}).\quad(50)$$

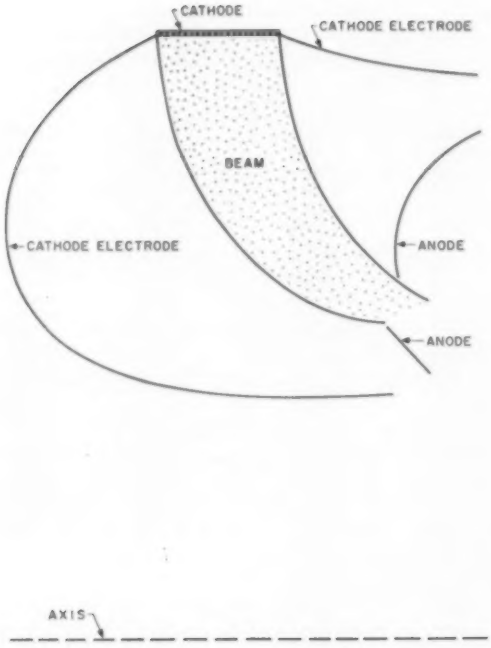

FIG. 5. Electrode shapes for a hollow beam gun with $\beta=3$.

Using the values of Q obtained from Eqs. (47), it can be evaluated in order to yield the desired values of voltages in the real domain.

RESULTS

The method developed in the previous section was applied to an electron gun with $\beta=3$. The mesh size h was chosen to be 0.005. The calculation was carried out in five hours' time on a Burroughs 220 digital computer. Our equations were integrated by the numerical methods discussed above, yielding V, r, and z as functions of v for fixed values of p. A quadratic interpolation with respect to v was then used to yield r and z as functions of V. Since our numerical method used central differences, the truncation error of our results should be of the order of magnitude of the square of our mesh size h.

In Tables I and II are given the coordinates for four equipotentials, one pair corresponding to the cathode electrodes and another to the anode electrodes. The electrode configuration determined by this data is shown in Fig. 5. The cathode width has been taken to be 0.2000.

TABLE II. Electrode coordinates.

Outer anode electrode $V=4.4210$		Inner anode electrode $V=2.8286$	
r	z	r	z
0.6128	0.3886	0.5223	0.3585
0.6412	0.3861	0.5119	0.3678
0.7163	0.4023	0.5037	0.3762
0.8072	0.4773		
0.8355	0.5234		
0.8476	0.5498		

SUMMARY AND ACKNOWLEDGMENTS

A numerical method has been developed which we feel can be applied with greater ease, accuracy, and economy than that given by presently existing methods for calculating the electrode shapes for an electron gun. This method is completely general and can be applied to any gun configuration in which the beam boundary values are given in analytic form. It should be of especial value for guns with curvilinear trajectories, where analog methods become especially complicated.

The author wishes to thank Dr. Paul R. Garabedian and Dr. Gordon S. Kino for their help and encouragement during the course of this project. The author also wishes to thank Mr. Jan Hennel for his assistance during an appreciable part of the effort.

Multiple Tube Collimator for Gas Beams

G. R. Hanes
Division of Applied Physics, National Research Council, Ottawa, Canada
(Received May 27, 1960; and in final form August 15, 1960)

A multiple tube gas collimator is described which consists of a bundle of tubes with 20-μ radii, made by electrolytic removal of copper wires from the plastic matrix in which they were embedded. Details of construction are given, as well as measurements of the angular distribution of gas flow from the collimator, which are determined with a helium mass spectrometer leak detector. The theory of flow through multiple tube sources is discussed, and a figure of merit giving relative values of beam intensity for fixed collimator area and flow rate is derived. The collimator described in this paper compares favorably with those used by previous workers.

I. INTRODUCTION

A NUMBER of papers[1–4] have appeared recently describing the use of bundles of small tubes as sources of molecular beams of high intensity. The flow from these sources is concentrated in the axial direction, so that for a given available pumping capacity, a higher beam density may usually be obtained than is the case with simple apertures. Most of this work has been inspired by the requirements of the ammonia maser. The author has been working along similar lines during the production of an atomic beam light source in which the spectra of permanent gases could be excited with reduced linewidth. It is particularly desirable to study the 6056-A line of Kr^{86} as part of the contribution of this laboratory to the international work on the redefinition of the meter in terms of the wavelength of this line.

This paper presents the construction details of a multiple tube source made from readily available materials, which compares favorably with those described by previous workers. Experimental measurements of the flow from one of these collimators are given, and the theory of flow through multiple tube gas collimators is discussed.

II. EXPERIMENTAL

A. Collimator Construction

The collimator is made from a bundle of fine enameled copper wires embedded in a plastic matrix. A wafer of thickness equal to the desired tube length is cut perpendicular to the wires, and the copper is removed electrolytically.

The wire bundle is produced by winding the wire on a form which has part of its circumference cut away, as shown in Fig. 1. After winding, the free part of the coil at A is wetted with a liquid epoxy resin. The press shown in Fig. 1(b), with a coating of silicone grease on the inside to prevent sticking, is slipped over the wires at A. The rest of the press is assembled and tightened, the coil is cut at B and removed from the form, and the press with the bundle of wires is put in an oven until the resin polymerizes. The loose ends of wire are then cut off, and the pressed stick is removed from the press and placed in a cylindrical mold. More resin is poured around the stick to form a rod with the wires parallel to the axis. A wafer of the required thickness is cut from the rod with a jeweler's saw, and the faces are smoothed by grinding on fine emery paper placed on a flat surface. The last step before electrolysis is the cementing of the wafer to the end of a glass tube, care being taken that no cement covers the end of any wires.

The electrolysis proceeds easily when a suitable electrolyte is used. With the acid electrolytes initially tried (phosphoric, sulphuric+copper sulphate), the current

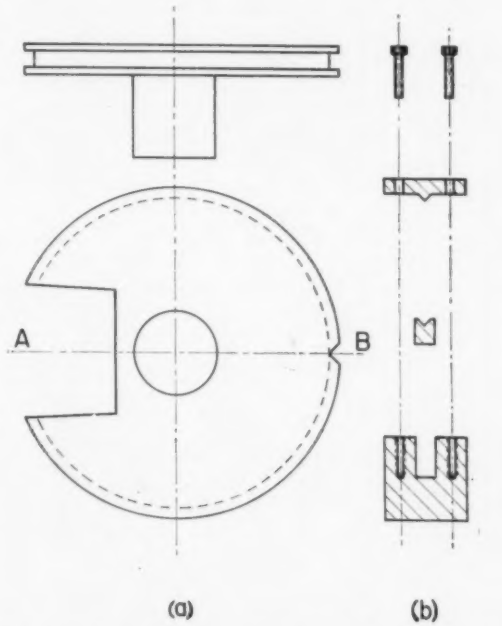

FIG. 1. (a) The coil form on which the wire bundle is wound. (b) The press used to compress the bundle while the resin binder is curing.

[1] J. P. Gordon, H. Zeiger, and C. H. Townes, Phys. Rev. **99**, 1264 (1955).
[2] J. G. King and J. R. Zacharias, Advances in Electronics and Electron Phys. **6**, 1 (1956).
[3] J. C. Helmer, F. B. Jacobus, and P. A. Sturrock, J. Appl. Phys. **31**, 458 (1960).
[4] J. A. Giordmaine and T. C. Wang, J. Appl. Phys. **31**, 463 (1960).

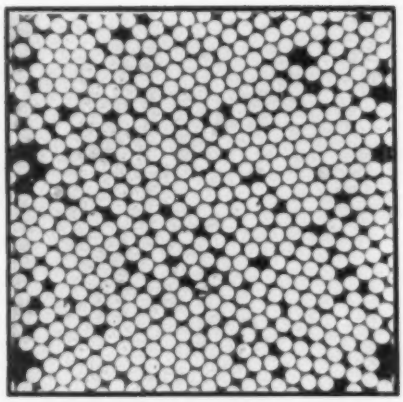

FIG. 2. One square mm of a finished collimator, with tube lengths of 32 radii, photographed by transmitted light (×60).

always fell to very small values after the wires had been etched to a depth of a few diameters. Copper salts were precipitated in the tubes, most likely because conditions became alkaline when diffusion could not keep up with the release of hydroxyl ions. Experiments were then tried with alkaline solutions, using chelating agents to prevent precipitation; this proved successful after a few trials. The electrolyte now being used contains about 100 ml of ammonium hydroxide (30% NH_3 by weight), 50 g of glycine, and four ml of hydrogen peroxide (30% H_2O_2) in one liter of solution. The concentrations are not critical, but each component seems to be necessary for satisfactory removal of the copper.

The electrolysis is performed with electrolytic contact to both ends of the wires. The end of the glass tube with the wafer is inserted into electrolyte in a beaker containing a platinum cathode. Electrolyte and a platinum anode are placed in the tube above the wafer. The electrodes are connected to a source of about five volts dc, and with the electrolyte at 60°C the current density is approximately 0.1 amp/cm² of copper. A wafer 0.7 mm thick is etched through in about two days. It appears necessary to use enameled wire, since with bare wire the epoxy resin is squeezed out so thinly that when the copper is removed the webbing is too fragile to be practical.

A photograph of one square mm of a finished collimator made with No. 46 enameled wire is shown in Fig. 2. It has about 4000 tubes in an area 1.4×5.4 mm, each tube being 630 μ long and 19.7 μ in radius. It can be seen that some of the wires have not been completely removed, but they represent only a few percent of the total. The axial transmission T, defined as the ratio of the area of the holes to the total area, is about 65%.

B. Performance Test

To test the finished collimators, the angular distribution of gas flowing into a vacuum chamber has been measured with the apparatus sketched in Fig. 3. I am indebted to C. J. Van der Hoeven for suggesting the use of a helium leak detector; it makes this type of measurement very simple. In addition, by measuring the dimensions of the probe carried on the hollow rotating arm, and calibrating the helium detector with a standard leak, absolute measurements of beam density, etc., can be made. The noise level of the particular detector used, with a two-second response time, corresponded to a flow rate into the measuring probe of about 5×10^9 atoms/sec.

The results of the tests are given in Figs. 4 and 5. In Fig. 4, (a) is a theroetical curve, and (b), (c), and (d) some experimental curves, of the angular distribution of atoms from the collimator. The theoretical curve

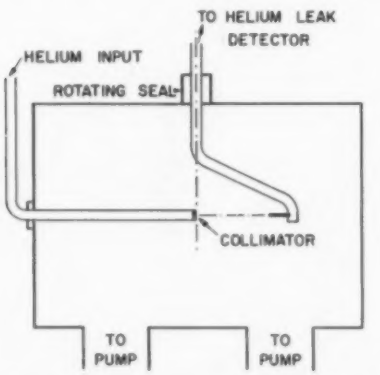

FIG. 3. Sketch of the apparatus used to measure the gas flow from a collimator.

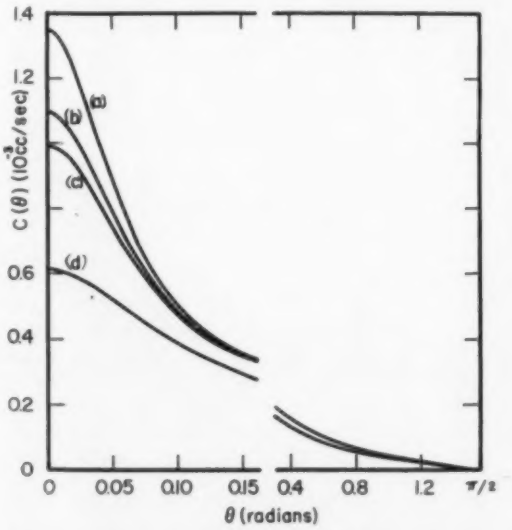

FIG. 4. Flow from collimator divided by driving pressure as a function of angle; (a) theoretical, low pressure; (b), (c), and (d) experimental, with increasing driving pressure.

is discussed in the next section. The abscissa in Fig. 4 is the angle θ that the receiving probe makes with the axes of the collimator tubes, and is therefore the angle at which the detected atoms leave the collimator. The ordinate is the number of atoms per second collected by the probe, divided by the number of atoms per cm³ in the oven, i.e., it is the conductance $C(\theta)$ of the collimator-receiving probe combination in cm³/sec. In describing the experimental curves, it is convenient to define a relative driving pressure $P=p/p_o$, where p is the pressure behind the collimator (the "oven" pressure), and p_o is that pressure at which the mean free path of the gas atoms in the oven is equal to the length of the tubes. In this test the tube length was 0.63 mm; therefore, p_o for helium was 0.22 mm Hg. Curves (b), (c), and (d) were taken with $P=0.1$, 0.7, and 3.5, respectively.

Figure 5 shows the measured values of the axial conductance $C(0)$, and the angle $\theta_{\frac{1}{2}}$ at which the conductance falls to one half the axial value, as a function of the relative driving pressure P.

Two other experiments of some interest have been done. In the first, the receiving probe was replaced by an electron gun which projected a narrow beam of electrons at right angles to an argon atomic beam. Light emitted in the third perpendicular direction was photographed through a 10-cm Fabry-Perot etalon and a prism spectrograph. A portion of the spectrum in the region of 4250 A is shown in Fig. 6. The etalon length was large enough that light emitted from atoms moving at random at room temperature would give no fringes. The observed reduction in linewidth by a factor of six shows that the atoms are, for the most part, moving perpendicular to the line of sight.

In another experiment the helium detector apparatus was used to test a commercial "molecular" filter as a possible gas collimator. This was suggested by an idealized drawing in an advertisement.[5] No beam formation was observed from either side of the material, indicating that either the holes have a very large spread of angles at the surface, or that they are not straight at the surface for even one diameter, or both.

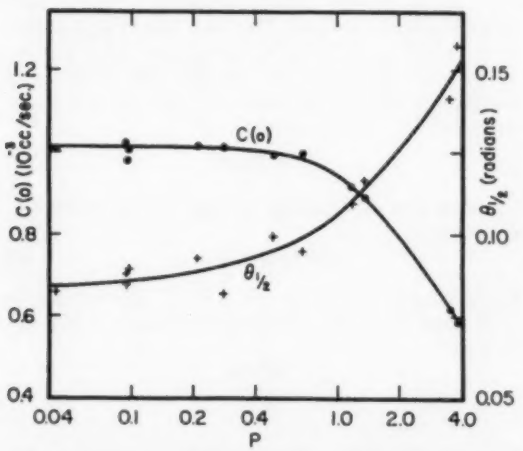

FIG. 5. $C(0)$, the axial flow divided by the driving pressure, and $\theta_{\frac{1}{2}}$, the angle at which the flow is one half the axial value, as a function of driving pressure.

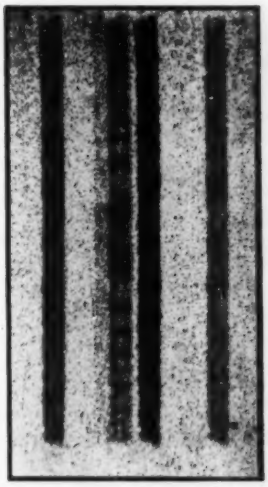

FIG. 6. Fringes obtained with a 10-cm Fabry-Perot etalon in light emitted from an argon beam from a collimator; excitation by electron bombardment.

III. THEORY AND DISCUSSION

A. Theoretical Angular Distribution

In order to determine theoretically the results to be expected in this experiment, we need first an expression for the angular distribution of the flow of gas from a single tube. As shown by Clausing,[6] this problem can be solved at low pressures (collisions between atoms negligible) by a straightforward geometrical calculation if the number of atoms impinging on the wall of the tube is known as a function of the distance along the tube. Clausing[7] had previously derived an integral equation for this function, but could obtain only an approximate solution, which is exact in the limit of very short tubes. Essentially the same integral equation was considered by Buckley[8] when discussing the interreflection of light in a well with a diffuse reflection coefficient ρ. For $\rho=1$ the problem is identical to that of low-pressure molecular flow. By approximating the kernel in the integral equation with an exponential function, Buckley was able to obtain an exact solution to the approximate equation. His solution is almost identical to Clausing's, and lends support to the idea that the angular distribution determined by Clausing from his

[5] Science **130**, 1140 (1959).
[6] P. Clausing, Z. Physik **66**, 471 (1930).
[7] P. Clausing, Physica **9**, 65 (1929).
[8] H. Buckley, Phil. Mag. **6**, 447 (1928); see also P. Moon, J. Opt. Soc. Am. **31**, 301 (1941).

solution will give acceptable predictions, within the accuracy required for usual molecular beam calculations, for arbitrary tube length at sufficiently low pressures.

Mention might also be made of a numerical solution of essentially the same integral equation, obtained by White[3] for a square tube of relative dimensions $1\times1\times4$, giving the average values around the perimeter of the square. Values obtained from Clausing's solution for a length of four diameters agree with White's to better than 1%. Finally, in the limit of very long tubes, Clausing's equations for the angular distribution of the flow at low pressure reduce to Eqs. (17) and (18) of Giordmaine and Wang.[4] Lacking an exact solution to the problem, the angular dependence of the flow given in Clausing's Eqs. (8) and (10) in footnote reference 6 is used. This function for the flow from one tube is written here $B(\theta)$ and is normalized such that $B(0)=1$.

In principle, the theoretical conductance curve (a) is given simply by $C(\theta)=A_s A_r \bar{c} B(\theta)/4\pi Z^2$, where A_s and A_r are the areas of the source and receiver, $\bar{c}$ is the mean velocity of the gas atoms, and Z is the source-receiver distance. However, several corrections have to be applied in order to make a fair comparison with the experimental curves. First, the collimator subtends a substantial angle at the receiver, which therefore discriminates against atoms coming from the edges of the collimator. Secondly, the receiver is only on the axis of tubes at the center of the collimator; this further discriminates against atoms from the edges. These effects lead to a correction of $B(\theta)$ by a constant factor of 0.52 for $\theta\geq0.10$ radian. For θ near zero the correction is more complicated, since it removes the cusp at the origin of $B(\theta)$, the axial value being reduced from 1 to 0.37. The calculated theoretical curve is given in Fig. 4(a).

The experimental curve for low driving pressure, Fig. 4(b), agrees quite well with the theory. The discrepancy in the ordinates of curves (a) and (b) can have arisen in several ways. The standard helium leak has a calibration uncertainty of 10%. The receiving probe is only 150 μ in diameter, and therefore its area A_r is difficult to determine to better than about 5%. The tubes in the collimator are not exactly parallel, and while this produces little effect on the curve for $\theta\geq0.05$ radian, it causes a broadening and lowering of the peak, and hence an increase in the measured half-width. Taking into account these uncertainties in the experiment, and those mentioned previously in the theory, the agreement is quite good.

The effect of the driving pressure on the performance of multiple tube collimators is demonstrated in Fig. 5. In the region in which $C(0)$ is flat ($P\lesssim1$), the beam intensity increases linearly with the driving pressure, and the angular distribution is essentially independent of pressure. In the region $P>1$, the axial beam density no longer increases as fast as P, and the angular distribution broadens, so that the ratio of beam intensity to total flow is decreased.

While these experiments were not designed as a stringent test of the theory, but as a check on the performance of the collimator, they show that Clausing's equations provide a good approximation to the flow for tube lengths of 32 radii, and that the flow has essentially the same angular distribution and is linearly proportional to pressure for all $P\gg1$.

B. Collimator Theory

It was mentioned previously that Clausing's[6] expressions for the angular distribution of the flow from a single tube at low-pressure reduce, in the limit of the tube length L very much greater than the radius a, to those obtained by Giordmaine and Wang[4] (hereafter referred to as GW). This is case one of GW, i.e., $P<1$. We now wish to show that the essential details of case two flow of GW ($P>1$) can be obtained from the low-pressure theory.

Consider a tube being operated with $P>1$. At some position along the tube z_1, the density will be such that the mean free path is equal to the remaining length of the tube L_1, to the low pressure end. Provided that L_1 is still much greater than a, this part of the tube is approximately equivalent to a tube of length L_1 being operated with $P=1$. Now, it can be seen from Fig. 5 that for this equivalent tube with $P=1$ the axial intensity I (molecules per second steradian) and the angle $\theta_{\frac{1}{2}}$, at which the intensity is reduced to half the axial value, will be given to a good approximation by I^*, $\theta_{\frac{1}{2}}^*$, the values predicted by low-pressure theory.

The axial intensity is given simply by

$$I=\bar{c}a^2n_o/4, \tag{1}$$

where n_o is the density (molecules/cm^3) in the oven, since at low pressure I is the same for a tube as for a thin hole of the same area. The oven density n_o is limited by the condition that the mean free path at n_o is equal to the tube length L_1. From the definition of the mean free path in terms of the molecular collision diameter σ, this condition may be written

$$n_o=1/2^{\frac{1}{2}}\pi\sigma^2L_1. \tag{2}$$

The total flow rate through the tube N (molecules/sec) is given by

$$N=2\pi\bar{c}a^3n_o/3L_1. \tag{3}$$

Eliminating L_1 from Eqs. (2) and (3), and solving for n_o in terms of N, which is then substituted in Eq. (1), we have

$$I^*=\frac{2^{\frac{1}{2}}3^{\frac{1}{2}}\bar{c}^{\frac{1}{2}}a^{\frac{1}{2}}}{8\pi\sigma}N^{\frac{1}{2}}. \tag{4}$$

This intensity I^* has the same functional form as the intensity expression obtained by GW for case two flow [their Eq. (12)], but is $(2/\pi)^{\frac{1}{2}}=0.80$ times as great. It

[3] W. T. White, J. Opt. Soc. Am. 31, 308 (1941).

might be expected that I^* would be somewhat too small since in case two flow the molecules crossing the plane at z_1 will already have some degree of collimation. Eliminating n_o from Eqs. (2) and (3) we obtain

$$L_1=\frac{2^{\frac{1}{2}}c^{\frac{1}{2}}a^{\frac{1}{2}}}{3^{\frac{1}{2}}\sigma}N^{-\frac{1}{2}}. \tag{5}$$

From this we can calculate θ_1^* from the expression for θ_1 at low pressures given by GW [their Eq. (19), which is the same as would be obtained from Clausing with $L_1 \gg a$]. The expression so obtained again has the same functional form as those obtained by GW for case two flow [their Eqs. (24) and (27)] and is intermediate in size between their two values (1.50 times θ_1 and 0.75 times θ_1').

Ignoring numerical factors of the order of one, it is evident that for a collimator A, operated with $P>1$, there is an equivalent but shorter collimator B operated with $P=1$. Collimator B has tubes of length L_1 given by Eq. (5), and gives essentially the same axial intensity and beam half-width as A for the same flow rate. In collimator A, the part of the tubes upstream from the point z_1 contributes little to the collimation, but acts mainly as a series resistance to the gas flow.

The above argument suggests that collimators with shorter tubes than have often been used will perform as well. However, it can readily be seen that a collimator should never have tubes so short that it is operated with $P<1$. Eliminating n_o from Eqs. (1) and (3), (with L in place of L_1), we have for the axial intensity in this pressure region

$$I=3LN/8\pi a,$$

which holds up to $P\sim 1$. If $L<L_1$ given by Eq. (5), the intensity can be increased at fixed N by increasing the tube lengths to L_1 and raising the oven pressure to keep the same flow rate.

A collimator of area A containing M tubes will give a total intensity I_c and flow rate N_c that are M times I and N for a single tube. As is obvious from the definition of the axial transmission T, the number of tubes is given by $M=AT/\pi a^2$. Then, from Eq. (4) we obtain

$$I_c^*=\frac{2^{\frac{1}{2}}3^{\frac{1}{2}}c^{\frac{1}{2}}}{8\pi^{\frac{1}{2}}\sigma}\frac{A^{\frac{1}{2}}T^{\frac{1}{2}}}{a^{\frac{1}{2}}}N_c^{\frac{1}{2}}.$$

TABLE I. Comparison of various multiple tube collimators.

Source (see text)	Radius of single tubes, a (10^{-3} cm)	No. of tubes per 10^{-2} cm^2	Axial transmission T (%)	Figure of merit, $F=\left(\frac{T}{a}\right)^{\frac{1}{2}}$ (cm$^{-\frac{1}{2}}$)
A	16.5	11	94	7.6
B	2.35	96	15	7.9
C	2.7	190	27	10.0
K and Z	3.8	110	50	11.5
K-5	5.9	81	85	12.0
K-1	1.27	530	27	14.6
This work	1.97	530	65	18.2

From this expression it can be seen that for a given collimator area A and flow rate N_c, which are usually fixed by other considerations, the available beam intensity is proportional to $(T/a)^{\frac{1}{2}}$. This relation was suggested in some of the earlier works.[3,4] The parameter $F=(T/a)^{\frac{1}{2}}$ may then be used as a figure of merit for comparing different collimators in situations where A and N_c are fixed, and maximum beam intensity is desired.

In Table I, the collimator material described in this work is compared with some of those which have been used by others. Some of the numbers given here were not supplied directly in the original works, and therefore may be subject to some correction. The first column in the table identifies the source: A, B, and C were described by Giordmaine and Wang.[4] They were made, respectively, from a klystron grid, an aligned stack of photographically etched metal foils, and "crinkly foil." K and Z is a "crinkly foil" collimator described by King and Zacharias.[2] K-5 and K-1 were made from klystron grid stock with tubes of 0.005 in. and 0.001 in., respectively; they were described by Helmer, Jacobus, and Sturrock.[3] The next three columns in the table give, respectively, the effective radius a of the individual tubes, the number of holes per mm^2, and the axial transparency T. The last column contains values of the figure of merit defined above, $F=(T/a)^{\frac{1}{2}}$.

IV. ACKNOWLEDGMENTS

The able technical assistance of Miss B. A. Rogers and W. E. E. Berger contributed greatly to the successful preparation of the collimators.

JOURNAL OF APPLIED PHYSICS VOLUME 31, NUMBER 12 DECEMBER, 1960

Corbino Disk

D. A. KLEINMAN AND A. L. SCHAWLOW
Bell Telephone Laboratories, Incorporated, Murray Hill, New Jersey
(Received July 19, 1960)

When a disk with concentric inner and outer electrical contacts is placed in a magnetic field parallel to its axis, and current is made to flow through the disk, the lines of current flow have a spiral shape. This spiral current flow produces its own magnetic field, which interferes constructively or destructively with the applied field, depending upon whether the carriers spiral inward or outward, respectively. For ordinary conductors and ordinary currents the effect of the self-field of the current is very small. But the effect should be large in materials of very high mobility such as has been recently reported for bismuth at 4.2°K. In this paper the theory of the effect is given for the case in which the mean free path of the carriers is small compared to the inner radius of the disk. The analysis shows that the disk behaves as a rectifier. The easy direction of flow corresponds to outward spiraling of the carriers, which at large currents results in the explusion of the magnetic field from the disk. In the hard direction of flow the magnetic field at the center of the disk may be several orders of magnitude larger than the applied field. It is suggested that the corbino disk may be a useful rectifier in applications requiring extremely low impedance. It may also be a useful voltage regulator in a very low-voltage high-current power supply. A device consisting of the disk and a coil to provide the magnetic field is discussed in some detail. The static characteristics when the coil is connected through a suitable resistance in parallel with the disk exhibits a negative resistance. This negative resistance is useful in ac operation if a condenser is also connected in series with the coil. The equations and boundary conditions which determine the electrical properties of the disk in the time-dependent case are formulated. In the small-signal approximation the complex impedance is obtained for the limiting cases of low and high frequency. At low frequency the reactance is that of a negative inductance ($-i\omega L$). At high frequencies there is a skin effect on the tangential component of current, which causes most of the signal current to be radial and causes the impedance to reduce to the resistance of the disk.

1. INTRODUCTION

IN 1911 O. M. Corbino[1] reported magnetoresistance measurements on several metals in which the specimens were disks with inner and outer concentric ring contacts. The disk was placed in a magnetic field along its axis and the resistance between the contacts was measured as a function of magnetic field. The resistance is given by

$$R(H)=R(0)[1+\tan^2\Psi], \tag{1}$$

where $R(0)$ is the resistance in zero magnetic field, and

$$\tan\Psi=(\mu/c)H, \tag{2}$$

where μ is the mobility (more precisely, the Hall mobility). The increase in resistance represented by Eq. (1) may be ascribed to the increase in the length of the current path resulting from the current flowing at the angle Ψ to the radial electric field. The magnetoresistance effect does not depend on the sign of the magnetic field or the current.

We see from Eq. (2) that if the mobility is very large, the Hall angle can be made to approach 90° for moderate magnetic fields. This is the situation in the high mobility semiconductors (Ge, GaAs, InSb) and especially the semimetals (Sn, Bi) at low temperatures. When the Hall angle is large there may be a considerable magnetic field associated with the current itself. This self-field interferes *constructively* with the applied field if the carriers flow inward, and *destructively* if the carriers flow outward, regardless of the sign of the field or the carriers. As a result of this interference the magnetic field is not constant over the disk but varies as some power of the radius. In the constructive direction of current flow the field is very high at the inside of the disk and falls off to the applied field at the outside; in the destructive direction the field is very low at the inside and rises to the applied field at the outside. It follows that the resistance in the constructive direction is higher than that given by Eq. (1), if Ψ is the Hall angle for the applied field, and the resistance in the destructive direction is lower. The disk, therefore, would have rectification properties. All of the effects due to the self-field of the current vanish at very small currents; for small currents Eq. (1) is valid and H in Eq. (2) is the applied field. In this paper we shall derive the electrical properties of the disk taking the self-field into account.

It may be well at the outset to mention several effects which do *not* occur. It might be thought that there would be some conditions under which a current in the constructive direction could maintain its spiral flow by its own magnetic field. One can easily see, however, that if the external field vanishes the tangential component of current must decay to zero beginning at the outside. In the destructive direction at large currents the magnetic field is very small over most of the disk and rises rapidly at the outside. The resistance, therefore, at large currents is $R(0)$, which may be several orders of magnitude smaller than $R(H)$, the resistance at small currents. It might be thought that there would be a region of negative differential resistance in the transition from $R(H)$ to $R(0)$. It turns out, however, that the differential resistance is always positive.

The Corbino disk and a coil to provide the applied field together constitute the essential elements of a four terminal device with interesting properties. This device,

[1] O. M. Corbino, Atti accad. nazl. Lincei **20**, 342, 416, 569, 746 (1911). See also D. K. C. MacDonald, Commissions 1 and 2, Louvain, 1956, Annexes 1956-2, Suppl. Bull. inst. int. du froid, p. 15.

herein named the *corbinotron*, is discussed in Sec. 4 and further in the Appendix. It somewhat resembles the *cryotron*,[2] in that the coil may be likened to the *control* and the disk to the *gate* of the latter. Although it would be possible to connect the coil and disk in the same way as the control and gate of the cryotron to form computer elements, the device seems to offer no advantages over the cryotron for this application. On the other hand, there may arise applications in which the extremely low impedance level of Corbino disk devices can be used to advantage.

2. THE STEADY STATE

We start out by considering a cylinder of altitude h, inner radius r_1, and outer radius r_2. We assume that current can flow without appreciable resistance along the inner and outer surfaces. Inside the cylinder ($r_1<r<r_2$) the current density $\mathbf{J}$ is perpendicular to the axis. We assume that $\mathbf{J}$ obeys the phenomenological equation,[3,4]

$$\mathbf{J}=\sigma\mathbf{E}+(\mu/c)\mathbf{J}\times\mathbf{H}, \tag{3}$$

where $\mathbf{E}$ is the electric field; σ, the conductivity; μ, the mobility; and $\mathbf{H}$, the magnetic field. This equation has been written for positively charged current carriers; in general the second term in Eq. (3) is preceded by a sign which is the same as the sign of the carriers. Throughout the discussion we will be assuming that the current is carried by a single kind of carrier. The magnetic field satisfies

$$\nabla\times\mathbf{H}=(4\pi/c)\mathbf{J}. \tag{4}$$

Because of the cylindrical symmetry there will be no dependence on the angle θ in the cylindrical coordinates r, θ, z. Thus Eq. (4) becomes

$$(4\pi/c)J_r=-(\partial H_\theta/\partial z) \tag{5}$$

$$(4\pi/c)J_\theta=-(\partial H_z/\partial r). \tag{6}$$

The radial component of magnetic field is zero $H_r\equiv 0$. From Eq. (4) it follows that the divergence of $\mathbf{J}$ vanishes, which implies that J_r varies as r^{-1}. Therefore we write

$$J_r(r,z)=-(2\pi r)^{-1}[dI(z)/dz], \tag{7}$$

where $I(z)$ is the current carried in the positive z direction by the inner surface and the negative z direction by the outer surface. The tangential component of magnetic field H_θ is due to the current on the inner surface, and is given by

$$H_\theta(r,z)=(2/cr)I(z). \tag{8}$$

It may be seen from Eq. (3) that H_θ gives rise to an electric field (Hall field) in the z direction. It then follows that E_r must be a function of z, since $\mathbf{E}$ in the steady state is irrotational. These complications, however, can be neglected in a preliminary treatment such as this. It is then permissible to regard $dI(z)/dz$ as a constant and write

$$J_r=-(2\pi r)^{-1}(I/h), \tag{9}$$

where I is the total current flowing in the circuit. The sign of I is so chosen that positive I corresponds to the constructive direction for positive carriers.

We now imagine that the cylinder is placed in an external applied field H_0 in the z direction. Therefore we have $H_z(r)=H_0$ for $r>r_2$. A differential equation for $H_z(r)$ in the region $r_1\leq r<r_2$ may be obtained from Eqs. (3), (5), and (9) in the form

$$(dH_z/dr)+B(H_z/r)=0, \tag{10}$$

where

$$B=(2\mu/c^2)(I/h). \tag{11}$$

If the current in the outer surface has no θ component, $H_z(r)$ must be continuous at $r=r_2$; the solution is then

$$H_z(r)=\begin{cases} H_0(r_2/r)^B & r_1\leq r\leq r_2 \\ H_0 & r\geq r_2. \end{cases} \tag{12}$$

We see that the dimensionless parameter B characterizes the self-field effect in the Corbino disk. For very small currents B is very small and $H_z(r)=H_0$ over the whole disk. On the other hand if $B\gg 1$ the field at the inside surface may be several orders of magnitude higher than H_0. For $B\ll -1$ the field vanishes over most of the cylinder and rapidly increases to H_0 at the outer surface. For computations it is convenient to rewrite Eq. (11) in the form

$$\begin{aligned} &B=2\times 10^{-9}(\mu I/h), \\ &\mu \text{ in cm}^2/\text{v-sec}, \\ &I \text{ in amp}, \\ &h \text{ in cm}. \end{aligned} \tag{13}$$

From Eqs. (2) and (3) we obtain the radial electric field

$$\sigma E_r=J_r[1+\tan^2\Psi]. \tag{14}$$

We define the voltage drop V by the formula

$$-V=\int_{r_1}^{r_2}E_r dr, \tag{15}$$

so chosen that positive voltage drop corresponds to the constructive direction. Integration of Eq. (15) gives

$$V=IR(0)[1+f(\zeta,B)\tan^2\Psi_0], \tag{16}$$

where $\zeta=r_2/r_1$, $\tan\Psi_0=(\mu/c)H_0$, $R(0)=(\ln\zeta)/2\pi h\sigma$ is the resistance in zero field, and $f(\zeta,B)$ is the function

$$f(\zeta,B)=(\zeta^{2B}-1)/(2B\ln\zeta). \tag{17}$$

[2] D. A. Buck, Proc. I.R.E. **44**, 482 (1956).
[3] R. F. Wick, J. Appl. Phys. **25**, 741 (1954); W. T. Read, Phil. Mag. **46**, 111 (1955); R. A. Logan, G. L. Pearson, and D. A. Kleinman, J. Appl. Phys. **30**, 885 (1959).
[4] B. Abeles and S. Meiboom, Phys. Rev. **101**, 544 (1956).

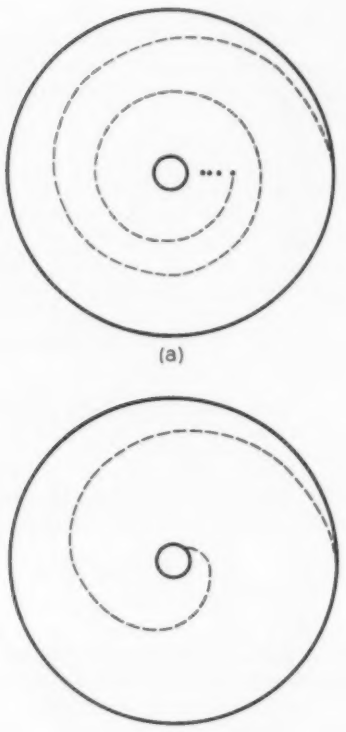

FIG. 1. Steady-state current streamlines for constructive case (a) and destructive case (b). In (a) two loops are shown and dots indicate the next three loops. In all the path makes eleven rotations before reaching the inner contact.

This function has the following properties:

$$f(\zeta,B)>0 \quad \text{all } B,$$
$$f(1,B)=1 \quad \text{all } B,$$
$$f(\zeta,B)\to 1 \quad B\to 0,$$
$$f(\zeta,B)\to 0 \quad B\to -\infty.$$

We see that for small currents ($|B|\ll 1$), or thin cylinders $\zeta\sim 1$, Eq. (16) reduces to (1) with $H=H_0$. The differential resistance dV/dI may be readily obtained from Eq. (16)

$$dV/dI=R(0)[1+\zeta^{2B}\tan^2\Psi_0]. \tag{18}$$

This function is positive for all B. It should be mentioned here in anticipation of Sec. 4 that Eq. (18) gives the slope of the *static characteristic*, but does not necessarily give the ac resistance except under special circumstances. Finally we may observe that if $H_0=0$ the magnetic field $H_z(r)$ is everywhere zero.

The path followed by the current (current streamlines) is determined by the differential equation

$$r(d\theta/dr)=(\mu/c)H_z(r),$$

which may be integrated to obtain the equation for the path in polar form

$$\theta(r)=B^{-1}\tan\Psi_0[\zeta^B-(r_2/r)^B]. \tag{19}$$

A plot of the streamlines for the constructive and destructive directions of flow is shown in Fig. 1. The figure is drawn for the case discussed in Sec. 3 and specified by Eq. (29) in which $\zeta=r_2/r_1=10$, $\tan\Psi_0=8$, and the current is assumed to be such that $|B|=1$.

3. THE APPROXIMATE TREATMENT OF THE DISK

The usual Corbino disk would not be a long cylinder ($h\gg r_2$) but a flat disk ($h\ll r_2$). The disk shape is more difficult to analyze because of the more complicated magnetic field. Qualitatively we may expect that the disk behaves much the same as the cylinder. The self-field effects should be characterized by a parameter proportional to the current and the mobility like B in Eq. (11). The principal difference should be the replacement of the altitude h of the cylinder by a radial dimension of the disk. To see how this comes about in the theory we shall formulate the disk problem. If $\mathbf{R}$ is a radial vector from the center of the disk the magnetic field can be written[5]

$$\mathbf{H}=\mathbf{H}_0+\frac{1}{c}\int\int\int\frac{\mathbf{J}(\mathbf{R}')\times(\mathbf{R}-\mathbf{R}')}{|\mathbf{R}-\mathbf{R}'|^3}d\mathbf{R}', \tag{20}$$

where $\mathbf{H}_0$ is the externally applied field. Let the disk be a short cylinder bounded by the planes $z=\pm h/2$; then in the plane $z=0$ the field is

$$\mathbf{H}(z=0)=\mathbf{H}_0+\frac{1}{c}\int\int\int\frac{\mathbf{J}(\mathbf{R}')\times(\mathbf{r}-\mathbf{r}')}{[|\mathbf{r}-\mathbf{r}'|^2+z'^2]^{\frac{3}{2}}}dz'd\mathbf{r}', \tag{21}$$

where $\mathbf{r}$ is the cylindrical radial vector. The integration over z' gives

$$\mathbf{H}(z=0)=\mathbf{H}_0+\frac{h}{c}\int\int\frac{\mathbf{J}(\mathbf{r}')\times(\mathbf{r}-\mathbf{r}')d\mathbf{r}'}{|\mathbf{r}-\mathbf{r}'|^2[|\mathbf{r}-\mathbf{r}'|^2+h^2/4]^{\frac{1}{2}}}. \tag{22}$$

The z component of magnetic field is

$$H_z=H_0+\frac{h}{c}\int_{r_1}^{r_2}\int_0^{2\pi}\frac{J_\theta(r')(r'-r\cos\theta')}{|\mathbf{r}-\mathbf{r}'|^2[|\mathbf{r}-\mathbf{r}'|^2+h^2/4]^{\frac{1}{2}}}r'dr'd\theta', \tag{23}$$

where $|\mathbf{r}-\mathbf{r}'|^2=r^2+r'^2-2rr'\cos\theta'$ and θ' is the angle between the vectors $\mathbf{r}$, $\mathbf{r}'$. We now eliminate $J_\theta(r)$ by means of Eqs. (3) and (9) to obtain an integral equation for $H_z(r)$,

[5] See, for example, J. A. Stratton, *Electromagnetic Theory* (McGraw-Hill Book Company, Inc., New York, 1941), p. 232.

$$H_z(\mathbf{r})=H_0 + \frac{\mu I}{2\pi c^2}\int_{r_1}^{r_2}\int_0^{2\pi}\frac{H_z(r')(r'-r\cos\theta')}{|\mathbf{r}-\mathbf{r}'|^2[|\mathbf{r}-\mathbf{r}'|^2+h^2/4]^{\frac{1}{2}}}dr'd\theta'. \quad (24)$$

This equation is considerably more complicated than the differential equation (10) obtained for the cylindrical case. The complication arises because H_r is a function of z so that Eq. (6) does not hold.

For comparison purposes it is instructive to write $H_z(r)$ for the cylinder problem in the form of Eq. (24). This can be done by taking the limit $h\gg r_2$ in Eq. (24), which gives

$$H_z(r)=H_0 + \frac{\mu I}{\pi c^2 h}\int_{r_1}^{r_2}\int_0^{2\pi}\frac{H_z(r')(r'-r\cos\theta')}{r^2+r'^2-2rr'\cos\theta'}dr'd\theta'. \quad (25)$$

This expression contains the discontinuous factor

$$\int_0^{2\pi}\frac{(r'-r\cos\theta')}{r^2+r'^2-2rr'\cos\theta'}d\theta'=\begin{cases}0 & r'<r\\ 2\pi/r' & r'>r.\end{cases} \quad (26)$$

Therefore Eq. (25) reduces to

$$H_z(r)=H_0+\frac{2\mu I}{c^2 h}\int_r^{r_2}\frac{H_z(r')}{r'}dr', \quad (27)$$

which is satisfied by the cylinder solution [Eq. (12)]. In fact, Eq. (27) is immediately obtained from Eq. (10) and the boundary condition $H_z(r_2)=H_0$ by a formal integration. This shows that the solution for the cylindrical case may be written in the form of Eq. (25). This goes over into the disk equation (24) if one replaces h by $2[|\mathbf{r}-\mathbf{r}'|^2+h^2/4]^{\frac{1}{2}}$ under the integral sign. It is therefore a reasonable approximation to replace h by $2r_2$. This gives an approximate theory for the disk formally identical with the cylinder theory except that B is given by

$$B=(\mu I)/(c^2 r_2) \quad \text{(disk)}. \quad (28)$$

Armed with this approximate theory for the disk we can now discuss a numerical example. The effects we are considering become important for $B\gtrsim 1$. In a good conductor such as copper[6] (good electrical grade) the mobility at room temperature is about 40 cm²/v-sec; at 13°K it increases to a maximum of about 5×10^3. To achieve $B=1$ in a disk with $r_2=1$ cm would require the enormous current $I\sim 2\times10^5$ amp at 13°K, or 2×10^7 amp at room temperature. In the ordinary good conductors, therefore, it would be practically impossible to make B approach unity. To observe the self-field effects the disk must be made of a material having an extremely high mobility. Recently it has been found that in extremely pure copper the mobility may be as high as 2×10^5 at liquid helium temperature.[6] The compound semiconductor InSb[7] has an exceptionally high mobility (6×10^4) at room temperature. The maximum mobility reported for this material is about 4×10^5 at 60°K. Mobilities of this order can also be obtained in germanium[8] at 12°K. Still higher mobilities are found in bismuth[4,9] single crystals. Since bismuth is very anisotropic we limit discussion to the case where the disk is cut from a single crystal of bismuth normal to the trigonal axis. The mobility is then independent of the direction of current flow in the plane of the disk. In very pure bismuth there are[9] 4.9×10^{17} electrons/cm³ and an equal number[4] of holes, and the two carriers have comparable mobilities. Therefore the disk should not be made from pure bismuth, because the self-field effects would largely cancel. But like the semiconductors bismuth can be doped,[10] p-type with tin or n-type with tellurium. The electrons have somewhat higher mobility so we shall assume the disk is n-type. Abeles and Meiboom[4] have defined three mobility parameters μ_1, μ_2, μ_3 from which the mobility tensor can be constructed. If the z axis is along the trigonal axis the mobility tensor is

$$\begin{pmatrix}\mu & 0 & 0\\ 0 & \mu & 0\\ 0 & 0 & \mu_3\end{pmatrix},$$

where $\mu=\frac{1}{2}(\mu_1+\mu_2)$ is the mobility with which we are concerned in the disk. The value of μ is 1.6×10^4 cm²/v-sec at 300°K,[4] 2.9×10^5 at 80°K,[4] and 7.8×10^6 at 4.2°K[9] Associated with the very high mobility at 4.2°K is a very long mean free path for the carriers. Smith[11] finds $\ell\sim0.18$ cm for electrons, which is the longest mean free path yet known in any material. In the present treatment we are considering the disk as an Ohm's law conducting continuum which can be described by Eq. (3). This treatment is valid if the mean free path is short compared to the dimensions of the disk. The case we have chosen to treat numerically is specified as follows:

$$\begin{aligned}&\text{bismuth } (n\text{-type}) \text{ 4.2°K},\\ &r_1=0.1, \quad r_2=1.0 \text{ cm},\\ &\mu=8\times10^6 \text{ cm}^2/\text{v-sec},\\ &H_0=100 \text{ oe}.\end{aligned} \quad (29)$$

[6] Estimated on the assumption of one conduction electron per atom and data on the conductivity of copper from *Handbook of Chemistry and Physics* (Chemical Rubber Publishing Company Company, Cleveland, Ohio, 1956), 38th ed. Unpublished data on extremely pure copper by J. E. Kunzler.

[7] H. J. Hrostowsky, F. J. Morin, T. H. Geballe, and G. H. Wheatley, Phys. Rev. **100**, 1672 (1955).

[8] P. P. Debye and E. M. Conwell, Phys. Rev. **93**, 693 (1954).

[9] A. L. Jain, Phys. Rev. **114**, 1518 (1959).

[10] N. Thompson, Proc. Roy. Soc. (London) **A155**, 111 (1936); **A164**, 24 (1938); J. K. Galt, W. A. Yager, F. R. Merritt, B. B. Cetlin, and A. D. Brailsford, Phys. Rev. **114**, 1396 (1959).

[11] G. B. Smith, thesis, University of Chicago, 1959; Phys. Rev. **115**, thesis, University of Chicago, 1959; Phys. Rev. **115**, 1561 (1959).

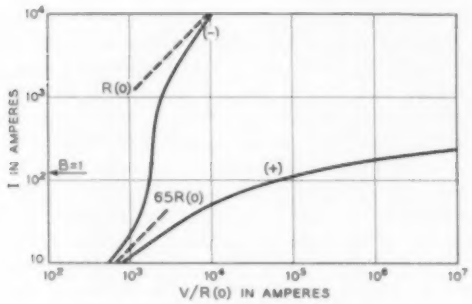

FIG. 2. Current-voltage characteristic for Corbino disk described by (29).

For H in oe, I in amperes, V in volts, and R in ohms, formulas (2), (11), (16), and (17) become in this special case

$$\begin{aligned} \tan\Psi &= 0.08H, \\ B &= 0.008I, \\ V/R(0) &= I[1+64f(I)], \\ f(I) &= [\exp(0.0368I)-1]/0.0368I. \end{aligned} \tag{30}$$

Since the resistance at zero magnetic field $R(0)$ depends on the doping and thickness of the disk we shall express the voltage V in terms of the current $V/R(0)$. The current-voltage characteristic is plotted in Fig. 2 for the two directions of current flow. The curves are labeled (+) and (−) in accordance with our sign convention for V and I in which the constructive (inward flow) direction is considered positive. The arrow on the current scale indicates the current for which $|B|=1$. At low currents both branches are asymptotic to the dotted line labeled $65R(0)$. This line is the magnetoresistance characteristic (1). The (−) branch again becomes linear in V at high currents as it asymptotically approaches the line labeled $R(0)$ corresponding to the expulsion of the external field from the disk. At high currents in the (+) direction the voltage increases exponentially with current.

We see that the Corbino disk might be used as a rectifier. Although fairly high rectification ratios can be achieved, the device would not be suitable for most present applications of rectifiers because of its extremely low impedance. The resistance of the disk $R(0)$ depends on the thickness h. In order to maintain the high mobility of the electrons this thickness should not be made much less than the mean free path $\ell\sim 0.1$ cm. If we take for example $h=0.1$, $r_1=0.1$, $r_2=1.0$ cm we find $R(0)=2.7\times 10^{-6}$ ohm, which will be the resistance for large currents in the (−) direction. The resistance in the (+) direction will be several orders of magnitude greater than this, but still will probably be much less than 1 ohm. The Corbino rectifier would therefore be limited to very special applications. The actual construction of the rectifier would have to be according to the principle discussed at the end of the next section and in the Appendix.

Another possible application is as a voltage regulator. The (−) characteristic in Fig. 2 has a region in which the current increases by an order of magnitude while the voltage increases by only 50%. The regulator performance is improved by increasing the magnetic field, because the height of the nearly constant voltage region increases as H_0^2. Again application would be limited to special low impedance situations.

4. THE CORBINOTRON

It will be noticed that in the example just given the external magnetic field $H_0=100$ oe is a rather small field easily produced with air-core coils. As mentioned in the introduction the coil and the disk may be considered as elements of a single device. The name *corbinotron* is suggested for this device. The magnetic field applied to the disk is proportional to the current I_c in the coil so we may write

$$(\mu/c)H_0=\alpha I_c, \tag{31}$$

where α is a parameter characteristic of the device. Two terminal devices are obtained if the coil is connected in series or in parallel with the disk. The current voltage characteristic for the series connection is shown in Fig. 3 for $\alpha=0.032$ amp^{-1}. The designations (±) again refer to the direction of current flow. In the (−) direction the voltage varies as I^2 for large currents according to the relation

$$V^{(-)}/R(0)\rightarrow(\alpha^2c^2r_2/2\mu)I^{(-)2}. \tag{32}$$

The characteristic for the parallel connection is shown in Fig. 4. If the coil has a resistance $R\neq 0$ the equations for the device are

$$\begin{aligned} I &= I_d+I_c \\ V/R(0) &= I_d[1+\alpha^2I_c^2f(I_d)] \\ &= I_cR/R(0), \end{aligned} \tag{33}$$

where I_d and I_c are the currents in the disk and coil, respectively, and I is the total current. Solving for I_c gives

$$I_c=\frac{R/R(0)}{2\alpha^2f(I_d)I_d}\left\{1\pm\left[1-\frac{4\alpha^2f(I_d)I_d^2}{[R/R(0)]^2}\right]^{\frac{1}{2}}\right\}. \tag{34}$$

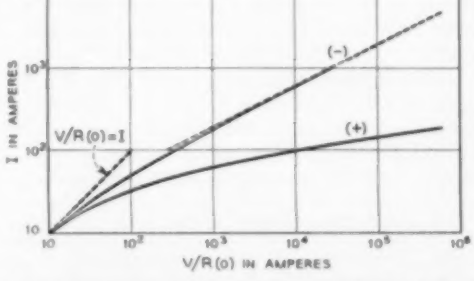

FIG. 3. Current-voltage characteristic for series Corbinotron.

The I-V characteristic shown in Fig. 4 has been calculated for the case $\alpha=0.0634$ amp^{-1}, $R/R(0)=14.47$. The most interesting feature is the appearance of a negative resistance in the $(-)$ branch. The $(+)$ branch has an extremely flat $(dI/dV=0,\ d^2I/dV^2=0,\ d^3I/dV^3\sim 0)$ region which may also prove to be of interest. At low currents both branches are asymptotic to the line representing the resistance $RR(0)/[R+R(0)]$, which is the resistance of the coil and disk in parallel at no magnetic field. In this region most of the current flows through the disk [if $R\gg R(0)$]. At large currents the two branches again approach a common asymptote corresponding to R. In this range the magnetic field is large and essentially all of the current flows through the coil. [The voltage at which the current divides equally is indicated by an arrow.] A linear plot of the $(-)$ characteristic is shown in Fig. 5 to aid in appreciating the magnitude of the anomaly.

The static characteristic of Fig. 5 indicates that the corbinotron with parallel connection may be an interesting and potentially useful device. The present analysis, however, is insufficient to determine how this device would behave with alternating current. The inductance of the coil would have to be taken into account, but this would require only a minor generalization of Eqs. (33) (see Appendix). There is a more basic difficulty, however, which can only be overcome by constructing the device somewhat differently than we have imagined so far; this remark applies also to the Corbino rectifier. To obtain the characteristic of Fig. 5 it is necessary for the magnetic field H_0 applied to the disk to vary proportional to the current in the coil. The highly conducting outer contact of the disk, however, will effectively shield the interior of the disk from these changes in magnetic field except at very low frequencies. Thus the effect of an alternating current in the coil will be simply to induce currents in the outer ring contact. This could be prevented by breaking the contact at some point. There would then be an electric dipole at this point producing an electric field in the disk of a rather complicated form. The analysis of such a geometry would be difficult and cannot be given here.

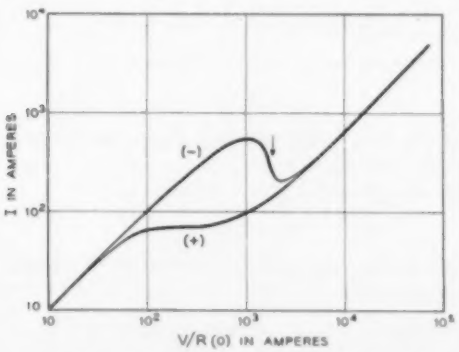

FIG. 4. Current-voltage characteristic for parallel Corbinotron.

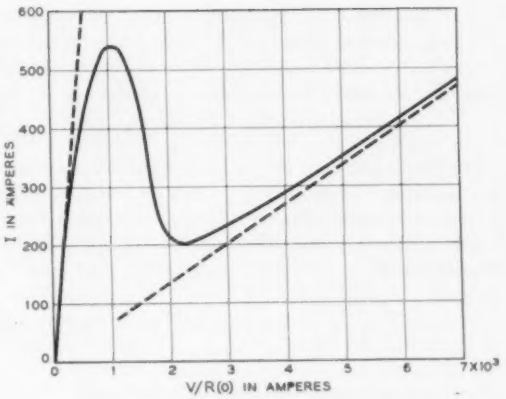

FIG. 5. Negative resistance characteristic of Fig. 4 on linear scale.

There is another way of overcoming the difficulty which reatins the cylindrical symmetry of the disk. This is to make the coil with a radius intermediate between r_1 and r_2. The outer contact will maintain a constant value of the flux

$$\Phi=2\pi\int_{r_1}^{r_2} rH(r)dr. \tag{35}$$

A current in the coil will then produce a field of one sign inside the coil and the opposite sign over the rest of the disk. Since the sign of H does not come into Eq. (14), this is equivalent to producing an external field over the whole disk. This device is discussed in the Appendix where it is shown that Fig. 5 represents a typical static characteristic. The Corbino rectifier would also have to be constructed in this way with interior coil or magnet.

5. THE CORBINO CYLINDER IN THE TIME DEPENDENT CASE

We now consider the time dependent theory for the Corbino cylinder of Sec. 2. The assumption that the inner and outer surfaces have negligible resistance gives the boundary condition

$$E_\theta(r_1,t)=E_\theta(r_2,t)=0 \tag{36}$$

for the tangential electric field, which satisfies the equation[12]

$$\frac{1}{r}\frac{\partial}{\partial r}(rE_\theta)+\frac{1}{c}\frac{\partial H}{\partial t}=0. \tag{37}$$

The tangential current density according to Eq. (3) is

$$J_\theta=\sigma E_\theta-(\mu/c)J_r H, \tag{38}$$

where $H(r,t)$ is the z component of magnetic field. The radial current density is given by Eq. (9) with $I(t)$ a function of time. We are neglecting the displacement

[12] See work cited in footnote 5, Chap. 1.

current density $K\partial E/\partial t$, where K is a (rationalized) dielectric constant; this is valid if the frequency is not too high, the condition being $\omega \ll \sigma/K$. On combining Eqs. (6), (9), and (38), we get

$$(4\pi\sigma/c)E_\theta + B(t)(H/r) + (\partial H/\partial r) = 0, \tag{39}$$

where $B(t)$ is given by (11) with $I(t)$ a function of time. This equation differs from Eq. (10) by the addition of the induced current density $\sigma E_\theta(r,t)$. On eliminating E_θ between Eqs. (37) and (39) we get the equation for the magnetic field

$$\frac{1}{r}\frac{\partial}{\partial r}\left\{r\frac{\partial H}{\partial r} + B(t)H\right\} = \frac{4\pi\sigma}{c^2}\frac{\partial H}{\partial t}. \tag{40}$$

The boundary conditions (36) can be written

$$(\partial \ln H)/(\partial \ln r) = -B(t), \quad r = r_1, r_2. \tag{41}$$

Equation (40) and the conditions (41) determine $H(r,t)$ to within an arbitrary factor independent of r or t.

Physically the arbitrary factor represents an arbitrary circulating current in the contacts. In the static case this factor was determined by the requirement $H(r_2) = H_0$, which corresponds to zero circulating current in the outer contact. In the time-dependent case we must permit $H(r,t)$ to be discontinuous at $r = r_2$, but the total flux crossing the disk must be a constant,

$$\int_{r_1}^{r_2} rH(r,t)dr = \text{const.} \tag{42}$$

This equation holds even if the source of the applied field is a coil carrying an alternating current, providing that we do not consider frequencies so low that the shielding depends on the resistance of the contacts. The constant in Eq. (42) may be regarded as the arbitrary factor yet to be determined. The applied external field H_0 may now be introduced by requiring that the flux have the same value as the static case for B equal to the mean value of $B(t)$. Thus the specification of the problem is completed by the condition

$$\int_{r_1}^{r_2} rH(r,t)dr = H_0 r_2^2 \frac{\zeta^{B-2} - 1}{B-2}, \tag{43}$$

where $B = \text{av}B(t)$.

Let us consider a line integral of the electric field which follows a current streamline from the outer to the inner contact (the positive direction of flow) and returns along a radius to the outer contact. According to the Faraday induction law[12] we have

$$\int \mathbf{E}\cdot d\mathbf{s} = -(d\Phi_c/dt), \tag{44}$$

where Φ_c is the flux enclosed by this path. Since E_r is independent of θ it follows that this can be written

$$\int_C E_\theta r d\theta = -\frac{d\Phi_c}{dt}. \tag{45}$$

Now consider a contour C' which is the same as C except that the return along a radius from r_1 to r_2 is through a battery of voltage $V(t)$. For this contour the Faraday induction law becomes

$$\int_{C'} \mathbf{E}\cdot d\mathbf{s} = -\int_{r_1}^{r_2} E_r dr + \int_C E_\theta r d\theta - V(t) = -\frac{d\Phi_{c'}}{dt}. \tag{46}$$

Since $\Phi_c = \Phi_{c'}$ we finally

$$V(t) = -\int_{r_1}^{r_2} E_r(r,t)dr, \tag{47}$$

which is the same as Eq. (15) used previously for the static case. From Eq. (3) we find the relation

$$\sigma[E_r + E_\theta \tan\Psi] = J_r[1 + \tan^2\Psi], \tag{48}$$

which reduces to Eq. (14) for the static case. The second term in the bracket on the left is the Hall field arising from the induced current.

We now assume that the time variation is a small signal superposed on a steady-state solution. Therefore let

$$\begin{aligned} H(r,t) &= \bar{H}(r) + h(r)e^{i\omega t} \\ B(t) &= B \times be^{i\omega t} \\ E_r(r,t) &= \bar{E}_r(r) + e_r(r)e^{i\omega t} \\ E_\theta(r,t) &= e_\theta(r)e^{i\omega t} \\ V(t) &= \bar{V} + ve^{i\omega t}, \end{aligned} \tag{49}$$

where $\bar{H}(r)$, B, $\bar{E}_r(r)$, and $\bar{V}$ refer to the steady-state solution of the cylinder problem. The equation for $h(r)$ is

$$-(b/r)(dz/dr) + \beta^2 h = 0, \tag{50}$$

where

$$\beta^2 = -(4\pi\sigma\omega/c^2)i, \tag{51}$$

and

$$-bz(r) = r(dh/dr) + Bh + b\bar{H}(r). \tag{52}$$

The boundary conditions (41) become

$$z(r_1) = z(r_2) = 0. \tag{53}$$

Since the form of Eq. (46) was chosen for the solution, it is not necessary to impose Eq. (43) as a separate condition. From Eq. (39) it follows that

$$e_\theta = b(c/4\pi\sigma)z/r. \tag{54}$$

By eliminating $h(r)$ from Eqs. (50) and (52), we get the equation for $z(r)$,

$$(d^2z/dr^2) + [(B-1)/r](dz/dr) + \beta^2 z = -\beta^2\bar{H}(r), \tag{55}$$

which together with Eq. (53) completely determines

[12] See for example Electrical Engineering Staff, M.I.T., *Electrical Circuits* (John Wiley & Sons, Inc., New York, 1943), Chap. I.

$z(r)$. The radial electric field obtained from Eqs. (48) and (54) is

$$-e_r=\frac{\mu}{4\pi\sigma}\frac{\bar{H}(r)}{r}[bz(r)+2Bh(r)]+\frac{c^2b}{4\pi\sigma\mu}\frac{1}{r}[1+\tan^2\Psi]. \quad (56)$$

Finally the signal voltage is obtained in the form

$$v=\frac{c^2b}{4\pi\sigma\mu}[1+f(\zeta,B)\tan^2\Psi_0]\ln\zeta+\frac{\mu b}{4\pi\sigma}\int_{r_1}^{r_2}\left[1+\frac{2B(B+2)}{\beta^2r^2}\right]\frac{\bar{H}(r)z(r)}{r}dr. \quad (57)$$

It will be noted that Eq. (57) is independent of the sign of H_0, since Eq. (55) shows that changing the sign of H_0 also changes the sign of $z(r)$.

6. THE LOW-FREQUENCY BEHAVIOR

In this section we shall consider the limit $\beta\to 0$. Nevertheless the frequencies we are considering are still high enough that the perfect shielding condition (43) is valid. Such a limit is meaningful if the ring contacts are made of a material having a much higher conductivity than the disk; for example, the contacts might be superconducting. The solution of Eq. (55) can be developed as a power series in β^2 in which the boundary conditions (53) are satisfied in each order.

$$\begin{aligned}&z(r)=z_0(r)+\beta^2z_1(r)+\beta^4z_2(r)+\cdots,\\&z_n(r_1)=z_n(r_2)=0,\quad n=0,\ 1,\ \cdots.\end{aligned} \quad (58)$$

It is evident that $z_0(r)\equiv 0$. The equation for $z_1(r)$ is

$$\frac{d^2z_1}{dr^2}+\frac{B-1}{r}\frac{dz_1}{dr}=-\bar{H}(r). \quad (59)$$

This equation may be integrated directly by writing it in the form

$$\frac{1}{r^{B-1}}\frac{d}{dr}\left(r^{B-1}\frac{dz_1}{dr}\right)=-\bar{H}(r). \quad (60)$$

By two integrations and the use of the boundary conditions one obtains (for $B\neq 2$)

$$z_1(r)=\frac{H_0r_2^2}{B-2}\left\{\frac{\ln\zeta}{1-\zeta^{B-1}}\left[\left(\frac{r_2}{r}\right)^{B-1}-1\right]-\left(\frac{r_2}{r}\right)^{B-1}\ln\frac{r_2}{r}\right\}. \quad (61)$$

In order to calculate v to order β^2 it is necessary to obtain $z_2(r)$ which satisfies the equation

$$\frac{1}{r^{B-1}}\frac{d}{dr}\left(r^{B-1}\frac{dz_2}{dr}\right)=-z_1(r). \quad (62)$$

This may also be integrated by elementary methods but the result is so complicated it will not be given here. The integrals over z_1 and z_2 in Eq. (57) are also elementary, so the voltage to order β^2 can be obtained analytically, although the result is very complicated.

We shall be content here to deduce the algebraic sign of $z_1(r)$ and $z_2(r)$ which will tell us the sign of the reactance term in Eq. (57), whether it is inductive (positive imaginary part) or capacitative (negative imaginary part). Let us suppose that $\bar{H}(r)$ in Eq. (60) is positive. Then $r^{B-1}(dz_1/dr)$ must be a monotonically decreasing function of r. Now we know that (dz_1/dr) must change sign at least once, since $z_1(r)$ vanishes at r_1 and r_2. Therefore dz_1/dr vanishes at just one point in the interval $r_1\leq r\leq r_2$ and is positive to the left (smaller r) of this point. It follows that $z_1(r)$ is positive in the interval $r_1\leq r\leq r_2$. More generally we may say $z_1(r)\bar{H}$ is nonnegative regardless of the sign of H_0. The same reasoning applied to Eq. (62) shows that $z_2(r)\bar{H}(r)$ is also nonnegative.

The impedance of the disk is defined as the voltage v divided by the current, which may be written as $(hc^2/2\mu)b$ according to Eq. (11); thus the impedance is

$$Z=R+iZ=(2\mu/hc^2)v/b. \quad (63)$$

To order β^2, which is to say to first order in ω, the real (resistive) and imaginary (reactive) parts of Z are

$$R=R(0)[1+f(\zeta,B)\tan^2\Psi_0]+\frac{B(B+2)\mu^2}{\pi\sigma hc^2}\int_{r_1}^{r_2}\frac{\bar{H}(r)z_1(r)}{r}dr \quad (64)$$

$$X=-i\omega\frac{2\mu^2}{hc^4}\int_{r_1}^{r_2}\left[z_1(r)+2B(B+2)\frac{z_2(r)}{r^2}\right]\frac{\bar{H}(r)}{r}dr. \quad (65)$$

By means of Eq. (62) and two integrations by parts this can be reduced to the form (writing $z_2'=dz_2/dr$)

$$X=-i\omega\frac{2\mu^2}{hc^4}\left\{\frac{\bar{H}(r_1)z_2'(r_1)}{r_1}-\frac{\bar{H}(r_2)z_2'(r_2)}{r_2}\right\} \quad (66)$$

in which B does not appear explicitly. Since $\bar{H}(r)z_2(r)$ is nonnegative and has only one maximum the quantity in brackets in Eq. (66) is positive for all B. The reactance is therefore that of a *negative inductance*. It should be remembered that Eq. (66) does not include the positive inductance of the leads and external circuit. It may be noted that the resistance Eq. (64) is quite different from the differential resistance Eq. (18) of the static characteristic. This is because the boundary conditions under which Eq. (64) was obtained require a constant magnetic flux over the disk. To observe Eq. (18) the frequency would have to be low enough to permit the flux to change according to the static solution for each instant of time. The criterion for the validity of retaining only the z_1 and z_2 terms in Eq. (58) is $|\beta r_2|^2<1$. For

bismuth at 4.2°K and a carrier density $n\sim 10^{18}$ cm^{-3} the condition becomes $\nu<10^7/r_2^2$ (r_2 in cm, ν in cps).

7. THE HIGH-FREQUENCY BEHAVIOR

We shall now consider the limit $|\beta|\to\infty$, but nevertheless we assume that the frequency is low enough so that we can continue to neglect the displacement current. Actually the error of neglecting the displacement current can be removed to a large extent by including the impedance of a capacitor in parallel with the disk representing the condenser formed by the concentric ring contacts. This in effect takes into account the radial displacement current but neglects the tangential component. The validity of our assumption is certain, however, for the bismuth disk considered in Sec. 3, which would have a conductivity of the order 10^6 mho/cm and negligible displacement current for frequencies less than 10^{17} sec^{-1}.

It is possible to write a formal solution of Eq. (55) satisfying Eq. (53) as an integral over Bessel functions of order $\pm B/2$ and argument βr. This solution is not of much use and will not be given here. A much simpler solution can be obtained for the special case $B=1$, since for this case the first derivative term drops out of Eq. (55). The solution is then

$$z(r)=\beta H_0 r_2\left\{\frac{\sin\beta(r-r_1)}{\sin\beta(r_2-r_1)}\int_{r_1}^{r_2}\sin\beta(r_2-r')\frac{dr'}{r'}-\int_{r_1}^{r}\sin\beta(r-r')\frac{dr'}{r'}\right\} \quad (67)$$

valid for all β. In the general case $B\neq 1$ we may anticipate that $z'=dz/dr$ is of order β and z'' of order β^2. Therefore the first derivative term can be neglected in the high-frequency range $|\beta|\gg|B|$, and the solution is

$$z(r)=\beta H_0 r_2^B\left\{\frac{\sin\beta(r-r_1)}{\sin\beta(r_2-r_1)}\int_{r_1}^{r_2}\sin\beta(r_2-r')\frac{dr'}{r'^B}-\int_{r_1}^{r}\sin\beta(r-r')\frac{dr'}{r'^B}\right\}. \quad (68)$$

For $|\beta r_1|\gg 1$ it is permissible to evaluate the integrals according to the formulas

$$\int_{r_1}^{r}\sin\beta(r-r')\frac{dr'}{r'^n}\sim\frac{1}{\beta r^n}-\frac{\cos\beta(r-r_1)}{\beta r_1^n}$$
$$\int_{r_1}^{r_2}\cos\beta(r-r_1)\frac{dr}{r^n}\sim\frac{\sin\beta(r_2-r_1)}{\beta r_2^n}, \quad (69)$$

which neglects terms of orders β^{-2} and higher. By use of Eq. (68) and Eq. (69) the voltage Eq. (57) can be evaluated in the high frequency limit; the result may be written as a complex impedance

$$Z(\omega)=R(0)\left[1+(1-i)\frac{c\tan^2\Psi_0}{(8\pi\sigma\omega)^{\frac{1}{2}}r_2}\frac{(1+\zeta^{2B+1})}{\ln\zeta}\right], \quad (70)$$

which is valid for $|\beta|\gg B$, $|\beta|r_1\gg 1$.

We see that the reactance is negative at high frequencies just as at low frequencies; this may mean that the reactance is negative at all frequencies. The most interesting point about Eq. (70) is that $Z(\omega)$ approaches the zero field resistance $R(0)$ as $\omega\to\infty$. The reason for this is that the tangential component of current is confined to a thin "skin" at the inner and outer contacts. Except in these "skins" the time dependent part of the current flows radially. As the frequency increases the "skins" become thinner, eventually forcing all of the signal current to flow radially, and the impedance for radial flow is just $R(0)$.

8. SUMMARY

The principles which govern the behavior of the Corbino disk have been set forth for the static and time-dependent cases.[15] Solutions have been obtained for the static case and for the low- and high-frequency cases. It is suggested that a device consisting of the disk and a coil to provide the magnetic field may have interesting and useful properties. The static current-voltage characteristic of this device, the corbinotron, is shown to have a negative resistance region when the coil is connected in parallel with the disk. This is only a static characteristic, however, and may not apply at radio frequencies. However, an appendix is included in which the main effects to be expected at radio frequencies are discussed and a circuit is proposed for using the device. Principally this paper is addressed to the problem of the electrical properties of the Corbino disk itself in a constant applied magnetic field.

The results obtained indicate that the Corbino disk, when made of a suitable material, is a good rectifier and voltage regulator. It is also capable of expelling an external field such as the earth's field, which might be of use in some experiments. It can amplify an external field by a large factor, which might be of use in detecting and measuring weak fields. The best material known for making the Corbino disk is tellurium-doped bismuth at liquid helium temperature; the disk must be cut from a single crystal normal to the trigonal axis. The reactance at low frequencies is surprising in that it is that of a negative inductance, which may also prove useful. At high frequencies the impedance is governed by a skin effect on the tangential current, which causes the impedance to approach the resistance of the disk at zero magnetic field. Again the reactance is negative in sign, suggesting that this is the case at all frequencies.

[14] See work cited in footnote 5, p. 520.

[15] After this manuscript had been completed the following note appeared on the Corbino disk: D. Midgely, Nature **186**, 377 (1960).

The theory presented is only valid if the mean free path of the carriers is small compared to the dimensions of the disk. Since in very pure bismuth single crystals the mean free path is of the order of a millimeter, it seems likely that devices could be constructed which are small compared to the mean free path. The theory for this case is beyond the scope of the present paper.

ACKNOWLEDGMENTS

It is a pleasure to thank W. S. Boyle and G. W. Weinreich for several very helpful discussions.

APPENDIX

The Practical Corbinotron

It was proposed in Sec. 4 that the disk and a coil for producing the magnetic field may constitute a useful device. In particular, a negative resistance device is obtained when the coil (with suitably matched resistance) is connected in parallel with the disk and current flows in the (−) direction. It was pointed out, however, that alternating current operation would only be possible if the device were modified by making the coil radius intermediate between the inner and outer radii of the disk. The analysis of Sec. 4, therefore, does not strictly apply to the practical corbinotron. In the Appendix we shall derive the static characteristic and small signal impedance of the (practical) corbinotron. The analysis shows that a condenser should be placed in series with the coil to form a series resonant circuit. One then obtains the negative resistance corresponding to a chosen operating point on the static characteristic over a narrow band near the resonant frequency of the coil and condenser. The usefulness of the device is in doubt because of the very low impedances involved.

The effect of the coil is to produce a discontinuity in the axial component of magnetic field. Let us define H_0 in terms of this discontinuity

$$H_0=H(a-)-H(a+), \tag{A.1}$$

where a is the radius of the coil. This definition is so written that if the disk and its contacts were not present the field inside the coil would be H_0. The total flux Φ cutting the disk is given by Eq. (35). If the contacts are perfectly conducting this flux will be constant. The solution of Eq. (10) satisfying Eq. (A.1) and Eq. (35) is

$$H(r)=\begin{cases} A_1H_0(a/r)^B, & r_1\leq r<a \\ A_2H_0(r_2/r)^B, & a<r\leq r_2, \end{cases} \tag{A.2}$$

where

$$A_1=\frac{1}{\xi^{B-2}-1}\left\{\frac{(B-2)\Phi}{2\pi H_0a^2}\left(\frac{r_2}{a}\right)^{B-2}+\left[\left(\frac{r_2}{a}\right)^{B-2}-1\right]\right\}$$
$$A_2=\frac{1}{\xi^{B-2}-1}\left\{\frac{(B-2)\Phi}{2\pi H_0r_2^2}+\left(\frac{a}{r_2}\right)^2\left[1-\left(\frac{a}{r_1}\right)^{B-2}\right]\right\} \tag{A.3}$$

with $\xi=r_2/r_1$. By evaluating Eq. (15) we find that the voltage can be written

$$V=IR_1(0)\left[1+A_1^2f\left(\frac{a}{r_1},B\right)\tan^2\Psi_0\right]$$
$$+IR_2(0)\left[1+A_2^2f\left(\frac{r_2}{a},B\right)\tan^2\Psi_0\right], \tag{A.4}$$

where Ψ_0 is defined by Eq. (2), the function $f(\xi,B)$ by Eq. (17), and $R_1(0)$ and $R_2(0)$ are zero-field, cylindrical-spreading resistances

$$R_1(0)=\ln(a/r_1)/2\pi h\sigma,$$
$$R_2(0)=\ln(r_2/a)/2\pi h\sigma, \tag{A.5}$$
$$R_1(0)+R_2(0)=R(0).$$

The previous analysis of Sec. 4 corresponds to the situation

$$a=r_2,$$
$$\Phi=2\pi H_0r_2^2(\xi^{B-2}-1)/(B-2), \tag{A.6}$$
$$A_1=1, \quad A_2=0.$$

Since Φ must be constant this solution is possible only if H_0 is constant.

The static characteristic of the parallel corbinotron (the interesting case) can now be obtained from circuit equations like Eq. (33), although the coil current I_c now enters in a more complicated way through H_0 in Eq. (A.3). This does not occur, however, if we choose $\Phi=0$; for $\Phi=0$ the circuit equations can be solved by means of Eq. (34) if $f(I_d)$ is given by

$$R(0)f(I_d)=R_1(0)A_1^2f(a/r_1,B)$$
$$+R_2(0)A_2^2f(r_2/a,B). \tag{A.7}$$

We now limit ourselves to the interesting case $B<0$, which is the (−) case of Fig. 4. For this case (A.3) shows that A_2^2 varies as $(a/r_2)^4$ and therefore may be neglected in a qualitative treatment. In the same approximation $A_1\sim1$ and (A.7) becomes

$$f(I_d)\sim[R_1(0)/R(0)]f(\eta,B), \tag{A.8}$$

where $\eta=a/r_1$. If the factor $[R_1(0)/R(0)]=\ln\eta/\ln\xi$ is absorbed in the coil constant α^2, the static characteristic is obtained in exactly the same form as in Eqs. (33) and (34). The effective outer radius becomes a and the effective coil constant becomes $\alpha[\ln\eta/\ln\xi]^{\frac{1}{2}}$. Therefore, Fig. 5 applies to a corbinotron with $a=1.0$ cm and $\alpha=0.0725$ amp^{-1}. The outer radius of the disk could be taken as $r_2\sim2$ cm but is not critical. The resistance $R(0)$ is still taken to be the total resistance of the disk. In calculating B by Eq. (28) one may use a instead of r_2.

If the coil has N turns the flux linking the coil is

$$\Phi_c=A_12\pi NH_0a^2(1-\eta^{B-2})/(2-B). \tag{A.9}$$

For $B<0$, $a\gg r_1$, $A_1\approx 1$ this becomes

$$\Phi_c=\pi NH_0a^2/(1+\lambda I_d)$$
$$\lambda=\mu/2c^2a. \tag{A.10}$$

This can also be written

$$\Phi_c=(1/c)[LI_c/(1+\lambda I_d)], \tag{A.11}$$

where L is the inductance (emu) of the coil

$$L=(N\pi a^2c^2/\mu)\alpha, \tag{A.12}$$

and α is the coil constant defined by Eq. (31). The voltage drop across the coil is

$$V_c=RI_c+(1/c)(d\Phi_c/dt). \tag{A.13}$$

Later it will be found that it is very desirable to insert a condenser in series with the coil and connect the combination in parallel with the disk. Therefore, we write

$$V=RI_s+\frac{1}{c}\frac{d}{dt}\Phi_c+\frac{1}{C}\int I_c dt. \tag{A.14}$$

The voltage across the disk can be written down very simply in the quasi-static approximation

$$V=I_dR(0)[1+\alpha^2I_c^2f(I_d)]. \tag{A.15}$$

Here, V, I_d, and I_c are functions of time. This approximation corresponds to neglecting the induced current σE_θ in Eq. (39), which causes that equation to have the same form as Eq. (10). The validity of this approximation demands $|\beta a|^2\ll 1$ where β is defined by Eq. (51). We use it here because it is the simplest approximation which is correct in the limit of zero frequency. In Sec. 6 this approximation would correspond to setting $z_1=z_2=0$, and would lead to the first term of Eq. (64) for the impedance. In the region of negative resistance it is a good approximation to write

$$f(I_d)\approx[4(\ln\xi)\lambda I_d]^{-1}, \tag{A.16}$$

so that (A.15) becomes

$$V\approx R(0)[I_d+\gamma I_c^2]$$
$$\gamma=\alpha^2/4\lambda\ln\xi. \tag{A.17}$$

We now consider small signal ac currents and voltages

$$I_c(t)=I_c+xe^{i\omega t}$$
$$I_d(t)=I_d+ye^{i\omega t}$$
$$I(t)=I+ze^{i\omega t}$$
$$V(t)=V+ve^{i\omega t}$$
$$z=x+y, \tag{A.18}$$

where I_c, I_d, I, V now represent dc components corresponding to an operating point in the negative resistance region. We consider that only the signal component of coil current flows through the condenser. The signal quantities then satisfy

$$R_s+\frac{i\omega L}{c^2(1+\lambda I_d)}\left\{x-\frac{\lambda I_c}{1+\lambda I_d}y\right\}+\frac{1}{i\omega C}x$$
$$=R(0)[y+2\gamma I_cx]=v. \tag{A.19}$$

The negative resistance $-R_s$ of the static characteristic is obtained by setting $\omega C\to\infty$ and $\omega L\to 0$, which gives

$$R_s=-RR(0)/[R+R(0)(1-2\gamma I_c)]. \tag{A.20}$$

This is a convenient unit of impedance for expressing $Z(\omega)=v/z$. If the bias conditions are properly chosen $R_s>0$. The impedance can be written

$$Z(\omega)=-R_s\frac{1+iQ_L-iQ_c}{1-iQ_L'+iQ_c'}, \tag{A.21}$$

where

$$Q_L=\frac{\omega L}{Rc^2(1+\lambda I_d)}\left[1+\frac{2\gamma\lambda I_c^2}{1+\lambda I_d}\right]$$
$$Q_L'=\frac{\omega L}{Rc^2(1+\lambda I_d)}\left[1+\frac{\lambda I_c}{1+\lambda I_d}\right]\frac{R_s}{R(0)} \tag{A.22}$$
$$Q_c=1/\omega RC$$
$$Q_c'=Q_cR_s/R(0).$$

Consider first the case in which the condenser is omitted $Q_c=Q_c'=0$. The condition for negative resistance is then

$$Q_LQ_L'<1. \tag{A.23}$$

For the example of Fig. 5 this becomes $\omega L/R<0.6$. The coil constant $\alpha\sim 0.07$ amp^{-1} implies a coil of inductance about 10^{-7} henry. If the disk has a thickness $h\sim 10^{-3}$ cm, the resistance is $R(0)\sim 3\times 10^{-4}$ ohm, so that $R\sim 4\times 10^{-3}$ ohm. The upper frequency limit for negative resistance is then $\nu_{\max}\sim 7000$ cps. This shows that the Corbinotron without condenser is limited to very low frequencies.

With the condenser it is possible to have real $Z(\omega)=-R_s$ at any frequency by properly choosing C so that $Q_L'=Q_c'$. Therefore, the condenser should be considered an essential part of the practical corbinotron. Again considering the previous example we find that 10 Mc operation would require a condenser of capacitance about $C\sim 0.005$ μf. The resistance R of course includes the condenser resistance.

The extremely low impedance of the Corbino rectifier has been pointed out in Sec. 3. Likewise the corbinotron is an extremely low impedance active device. This difficulty can be overcome insofar as the signal is concerned by transformers, but there remains the difficulty of providing the dc bias conditions. Here the static Corbino disk in a uniform applied field may prove to be of value. By means of a Corbino voltage regulator operating on the (−) characteristic, it should be possible to provide the voltage stabilized bias for a corbinotron.

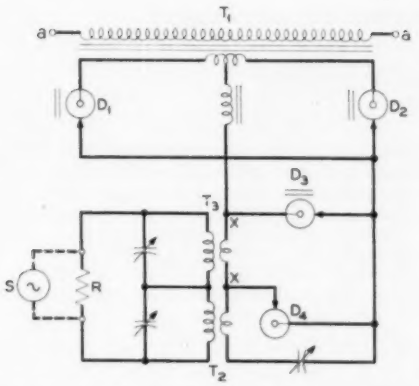

FIG. 6. Circuit diagram of corbinotron negative resistance amplifier or oscillator with power supply employing Corbino disks.

The dc magnetic field could be obtained from a permanent magnet. The power delivered to the coil resistance would not necessarily constitute a loss; the coil resistance could be provided by a load inductively coupled to the coil to improve the efficiency. It would seem that considerable advantage would result from the use of superconducting coils, condenser, and leads in view of the low impedance of the disk.

A circuit utilizing the corbinotron and a power supply consisting of a full-wave Corbino disk rectifier and Corbino disk voltage regulator is shown in Fig. 6. Line voltage ac is applied to a step-down transformer T_1 the secondary of which is connected to disks D_1 and D_2 serving as rectifiers. The full-wave rectified output is applied to a Corbino disk D_3 acting as voltage regulator through an inductance. The magnetic field for D_1, D_2, and D_3 is supplied by permanent magnets. The regulated output is applied to the corbinotron circuit consisting essentially of disk D_4 and coil T_2. For practical reasons T_2 is made a transformer and the necessary impedance in the coil circuit is introduced into the secondary circuit of T_2. The negative resistance appears across the terminals marked x, and again for practical reasons is transformed by T_3. If the circuit is suitably designed and adjusted the load R can serve as the resistance in the coil circuit. It may be necessary to tune the transformers as shown in the circuit. If the load resistance R is not too great the corbinotron will oscillate and deliver high-frequency power to the load. If the load resistance is too high for oscillation the corbinotron acts as a narrow band negative resistance amplifier. When a generator or signal source is connected to the load, as shown by the dotted part of the circuit, greater power is delivered to the load than the generator could deliver alone.

Study of Initial Conditions in Constant Velocity Impact

JAMES F. BELL
The Johns Hopkins University, Baltimore, Maryland
(Received July 1, 1960)

Diffraction grating measurements are made of dynamic plastic strain within a few thousandths of an inch from the impact face of 1-in. diameter, annealed aluminum specimens in free flight undergoing constant velocity impact. From these data it has been established that initial nondispersive shock fronts are present, even in low-velocity impact. This initial nondispersive front develops in the first $\frac{1}{4}$ diameter in two sections, each involving $\frac{1}{2}$ the initial kinetic energy; the first section is that of the deviatoric, or shear, component, and the second is associated with the hydrostatic stress. It is shown that the dynamic stress-strain curves obtained experimentally in annealed aluminum and copper may be computed directly from the theory, using information supplied by the static stress-strain curve. The von Karman critical velocity for annealed aluminum is found to be a dividing point between two types of initial wave development.

INTRODUCTION

IN a recent paper[1] this investigator gave experimental evidence that the one-dimensional strain rate independent theory of plastic wave propagation is applicable in annealed aluminum. Those experiments, which were for constant velocity impact of identical large-diameter cylindrical rods, indicated that the slopes of the static stress-strain curve may be used for determining the velocities of strain propagation and the maximum strain amplitudes. It also was observed that this mode of wave propagation applies in all details only after the first diameter. It is the purpose of the present paper to give the results of an investigation of the behavior in the first diameter itself, with particular emphasis upon strain-time and surface angle-time measurements, obtained by the diffraction grating method,[2] between 0.020 diameter and $\frac{5}{32}$ diameter from the impact face.

Earlier experimental studies in annealed aluminum by Johnson, Wood, and Clark[3] and by Campbell,[4] and in copper by Habib[5] and by Simpson, Fireman, and Koehler[6] have indicated that a dynamic stress-strain curve differing considerably from the static curve must be considered in constant velocity impact. Since the diffraction-grating experiments conducted by this author in aluminum and in copper have shown that the wave propagation is governed by the strain rate independent theory and the static stress-strain curve, an apparent contradiction is presented. In this author's studies, however, it was observed that the strain maxima and strain-time detail differed in the first diameter from the behavior which would be expected from applying the strain rate independent theory following an infinite step at the origin. It was thought, and it has indeed proved to be the case, that the dynamic stress-strain curve is associated primarily with the development of the plastic wave in the region of the impact face.

In this paper it is shown that at the instant of impact a nondispersive shock front is inaugurated, which develops in the first $\frac{1}{4}$ diameter into a dispersive plastic wave front. It is shown, further, that this front develops in two separate sections, each involving $\frac{1}{2}$ the initial energy. The first front is associated with the deviatoric component of the initial stress, and the second portion of the front, which develops much more slowly into a dispersive plastic wave, is associated with the hydrostatic stress.

Measurements from 30 diffraction grating tests within a few thousandths of an inch from the impact face have provided experimental evidence for this behavior. Using the equations of the initial shock front, the Johnson, Wood, and Clark dynamic stress-strain curve in annealed aluminum, as well as the Habib dynamic stress-strain curve in copper, have been determined from the static stress-strain curve. These dynamic curves also have been computed from observations of the surface angle maxima associated with the development of the deviatoric component of the plastic wave.

The von Karman critical velocity in annealed aluminum is found to be a dividing point between two distinct types of initial wave formation. The initial shock front and its subsequent development into a dispersive plastic wave are shown to account for most of the observed phenomena in the first diameter.

EXPERIMENTAL DATA

The diffraction grating measurements discussed in this paper offer some special difficulties when compared with measurements made at larger distances from the impact face. The most important of these is the envelopment of the grating by the air shock escaping from between the impact faces just prior to impact. This air shock effect has been referred to before,[1] and indeed has been used to verify the dynamic alignment of the specimens. In the previous measurements the introduction of a deflection shield in the vicinity of the impact face was sufficient to eliminate the refraction of

[1] James F. Bell, J. Appl. Phys. **31**, 2 (1960).
[2] James F. Bell, Proc. Third U. S. Nat'l Congr. Appl. Mech. (June, 1958).
[3] J. E. Johnson, D. S. Wood, and D. S. Clark, J. Appl. Mech. **20**, 4 (1953).
[4] J. D. Campbell, J. Mech. Phys. Solids **1**, (1952–53).
[5] E. T. Habib, J. Appl. Mech. **15**, 3 (1948).
[6] O. C. Simpson, E. L. Fireman, and J. S. Koehler, NDRC, Armor & Ordnance Repts. No. A-257 (1944).

the diffraction images caused by the rising shock front. When measurements are made within a few thousandths of an inch from the impact face, great care must be taken in introducing this shield since it now lies in the light field itself and may introduce errors in the measurement.

A second difficulty in measurements close to the origin is seen if one considers the errors due to gauge length for dispersive waves. It may be shown that this error is approximately equal to the gauge length divided by the distance from the origin. In the present tests a gauge length of 0.005 in. has been used, which for a position $\frac{3}{32}$ in. from the impact face introduces an error of approximately 5%. Tests run at 0.020 diameter and at $\frac{1}{16}$ diameter have required the use of gauge lengths of 0.001 in., with somewhat of a decrease in sensitivity. A 0.001-in. long, 30 720 lines/in. grating contains a total of 30 lines, and is sufficiently long for making strain and surface angle measurements provided special care is used in polishing the specimen surface.

A number of tests have been run for different impact velocities at $\frac{3}{32}$ diameter and at $\frac{1}{8}$ diameter. If one compares tests for a given impact velocity at these two positions, it is seen that a general trend toward the development of the dispersive wave is observed, which development continues at $\frac{3}{32}$ diameter to a maximum at $\frac{1}{4}$ diameter. A comparison of tests at a particular position, however, has shown considerable variation. These tests near the impact face have shown that only the lower strain levels propagate as a dispersive plastic wave in the first $\frac{1}{4}$ diameter. One type of test, which occurs much less frequently and is consistent with observations of a few tests at large distances from the origin, involves the development of a double wave front. The dispersive wave measurements may be compared with the extrapolation of tests at large distances from the origin back to $\frac{3}{32}$ diameter by means of the strain rate independent theory.

DISCUSSION OF RESULTS

If one examines the energy aspect of a propagating dispersive wave front produced by a constant velocity impact and governed by the strain rate independent theory, it is seen that the energy of deformation per unit volume for the maximum strain is considerably larger than the kinetic energy per unit volume prior to impact. This effect, of course, is due to the dispersive nature of the wave and the fact that the static stress-strain curve is concave downward. At the impact face, when the time $t=0$, one might expect that the energy of deformation would be equal to the initial kinetic energy. If this assumption is made, and moreover, the energy of deformation is assumed to be determinable from the static stress-strain curve, the equations of mass and momentum conservation give

$$\epsilon_0 = v_0/D + v_0, \tag{1}$$

$$P = \rho(D+v_0)v_0, \tag{2}$$

where D is the shock velocity, v_0 the impact velocity, ρ the initial mass density, P the stress, and ϵ_0 the axial strain here considered as a change in the linear density. The elimination of D from Eqs. (1) and (2) gives

$$\tfrac{1}{2}P\epsilon_0 = T_0, \tag{3}$$

where $T_0=\frac{1}{2}\rho v_0^2$ is the kinetic energy per unit volume prior to impact. The impact considered is that of two identical specimens moving in opposite directions with an impact velocity in axial collision of v_0. The energy of deformation for this case would be expected to be equal to T_0 since the wave is nondispersive. Thus we may write Eq. (4)

$$\tfrac{1}{2}P\epsilon_0 = \int_0^{\epsilon_0} \sigma_x d\epsilon_x, \tag{4}$$

where the integral on the right-hand side represents the area under the static stress-strain curve, and the limit ϵ_0 is chosen so that the energy of deformation represented by this area will be equal to T_0. Since the static stress-strain curve is given, it is possible from Eq. (4) to compute the expected stress level P for a given impact velocity v_0. It is found (Fig. 1) that this computation based upon the foregoing equations and the static stress-strain curve gives a very close agreement with the dynamic stress-strain curve of Johnson, Wood, and Clark in annealed aluminum.

In order to be certain that this agreement was not a coincidence, a similar calculation was made from Habib's dynamic and static stress-strain curve in copper. It may be seen that similar results are obtained, even though in this case maximum strain levels of as high as 25% are involved. The circles in Figs. 1 and 2 represent values computed from Eq. (4) from the static stress-strain curve. The higher solid lines are the experimental dynamic stress-strain curves, and the lower solid lines

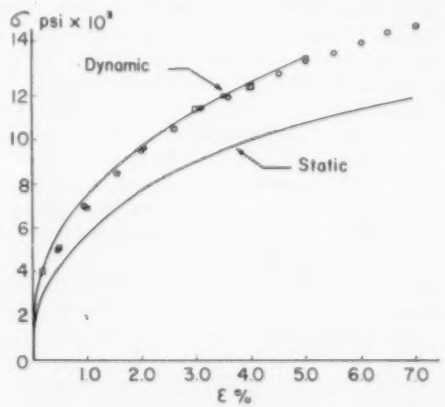

FIG. 1. A comparison of the theoretical dynamic stress-strain curve in annealed aluminum, with the experimental (solid line) curve of Johnson, Wood, and Clark. The lower solid line is the static stress-strain curve.

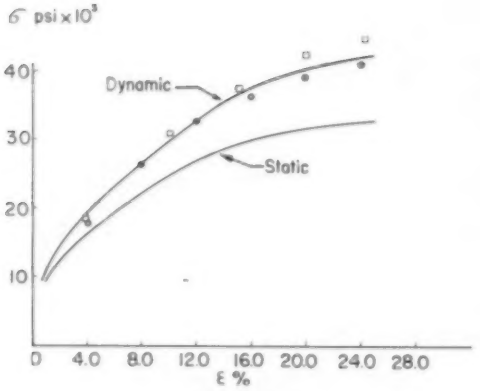

FIG. 2. A comparison of the theoretical dynamic stress-strain curve in copper, with the experimental (solid line) curve of Habib. The lower solid line is the Habib static stress-strain curve.

are the corresponding static stress-strain curves. In Fig. 1, the static stress-strain curve is the average of eight tests conducted by this author.

Experiments also were carried out by this author similar to those of Johnson, Wood, and Clark, in which a hard elastic aluminum specimen was struck in axial collision by a soft annealed aluminum hitter of the type used in the present wave propagation studies. Velocities were adjusted to give strain maxima in the annealed specimen corresponding to that obtained from the impact of identical annealed specimens at 66.5 ft/sec. Measurements were made in the hard aluminum specimen using wire resistance strain gauges. These experiments gave remarkably close agreement with the Johnson, Wood, and Clark stresses, despite the fact that their specimens had rounded ends and were $\frac{1}{2}$ in. in diameter, whereas square-ended, 1-in. diam specimens were used in the present study. The aluminum used by this author was 1100F, annealed for 2 hr at 1100°F, and furnace cooled. Checks were made of grain size after annealing to be certain that at least 20 to 25 grains were in the grating area optically studied.

Figure 3 illustrates a typical strain-time and surface angle-time curve obtained from diffraction-grating measurements at $\frac{1}{2}$ diameter, for an impact velocity of 66.5 ft/sec. The theoretical maximum strain for this impact velocity is 2.2% which, as has been shown before,[1] is the value obtained between two and four diameters in 10-diameter specimens.

If one examines the surface angle behavior, it is seen to undergo a maximum at a strain of approximately 1.35% and a subsequent minimum which corresponds very closely to the maximum strain. By computing the surface angle from the strain rate independent theory of a wave proceeding from an infinite step at the origin and governed by the static stress-strain curve, the surface angle maxima would be expected to coincide with the arrival of maximum strain and would be followed by a very sharp decrease in angle. The experimental maxima, however, are found to occur at the flex point of the strain-time curve, and the level of strain ϵ_1 varies with impact velocity. When a large number of tests are averaged for each impact velocity, it is found that this strain level ϵ_1 always coincides with that strain for which the area under the static stress-strain curve is $\frac{1}{2}$ the total area, or the energy of deformation for the theoretical maximum strain for the given impact velocity. Furthermore, it is also invariably the case that the stress σ_1 of the static stress-strain curve corresponding to ϵ_1 is always $\frac{2}{3}$ the stress of the dynamic stress-strain curve for that impact velocity. This has been found to be true for both aluminum and copper.

The value of ϵ_1 may be determined in two ways: first, by determining the time of propagation of the surface angle maxima at many different positions along the specimen and finding the strain whose propagation velocity is such as to give equivalent times of propagation. A second method is to average the measured strains on the strain-time curves at the corresponding time of surface angle maximum for the particular test involved. For the case of 66.5 ft/sec. the former procedure gives a strain ϵ_1 of 1.35% when over 50 tests are averaged, whereas the latter gives 1.38% strain. Hence either method may be used in making this determination. The calculation of the dynamic stress-strain curve from the measured values of ϵ_1 and the static stress-strain curve are shown as squares in Figs. 1 and 2. Here, again, the agreement is excellent.

Figure 4 shows a particular case of annealed aluminum at 66.5 ft/sec.

In order to understand why the stress at a strain corresponding to $\frac{1}{2}$ the total energy of deformation should invariably be $\frac{2}{3}$ the dynamic stress for the corresponding impact velocity, it is necessary to look again at the nature of the initial shock front. Since this nondispersive wave front involves a plane stress front in the axial direction, it may be divided into a deviatoric and a hydrostatic portion. The axial component of the deviatoric stress is $\frac{2}{3}P$, whereas the hydrostatic component is $\frac{1}{3}P$. The ratio of the energy of deformation

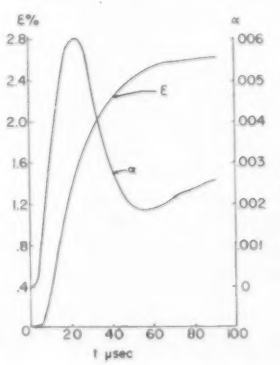

FIG. 3. Strain-time and surface angle-time at $\frac{1}{2}$ diameter, for 0.990 diameter annealed aluminum, with an impact velocity of 66.5 ft/sec.

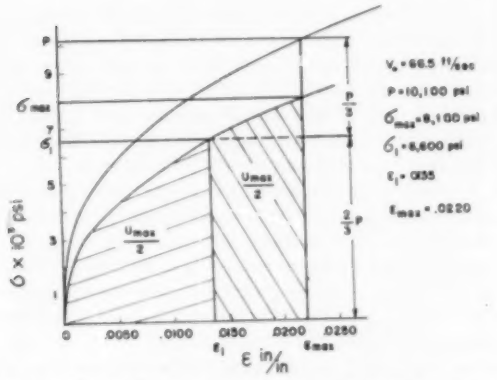

FIG. 4. Relation between the dynamic and static stress-strain curves at the strain ϵ_1 corresponding to the surface angle maximum.

per unit volume to the kinetic energy per unit volume prior to impact may be computed from the strain rate independent theory from the area and slopes of the static stress-strain curve. For an impact velocity of 66.5 ft/sec a maximum strain of 2.2% is obtained. The ratio U/T_0 is approximately $\frac{3}{4}$ for this impact velocity. A dispersive wave whose final strain level is ϵ_1 corresponding to $\frac{1}{2}$ the maximum energy of deformation would then be seen to develop from $\frac{1}{2}$ the initial kinetic energy.

Thus the initial nondispersive shock front develops into a dispersive plastic wave in two stages. The first stage is that associated with the deviatoric stress of $\frac{2}{3}P$, corresponding to $\frac{1}{2}$ the initial kinetic energy. The second stage is the much slower evolution of the hydrostatic portion of the initial front. Although the second half of the initial kinetic energy must be associated with this hydrostatic component, neither the observed maximum of approximately 2% strain of the partly developed wave fronts at $\frac{3}{32}$ diameter, nor an examination of the initial shock front have permitted of computations providing an energy balance based solely upon strain energy considerations. It is important to note that the maximum strain amplitude occurring at $\frac{1}{4}$ diameter is nearly always equal to $2\epsilon_1$, indicating that when the upper half of the wave front has developed, it possesses an amplitude equivalent to the lower wave. Thus for a 66.5 ft/sec impact velocity where $\epsilon_1 = 1.35\%$, the experimental maximum observed at $\frac{1}{4}$ diameter is 2.75%, whereas the theoretical maximum observed at two or more diameters is 2.2%.

Approximately 4% of the tests in annealed aluminum at room temperature and 15% of the tests in annealed copper have shown the presence of a double wave structure at positions from two to eight diameters from the impact face. Preliminary high-temperature tests in aluminum at 800°F indicate that this two-wave structure is much more likely to occur at elevated temperatures. In every case the strain level of the initial front is ϵ_1 whereas the second maximum is the theoretical value given by the strain rate independent theory. The lower wave arrives at the position in question at times agreeing with all other measurements, whereas the arrival time of the upper wave is unpredictable, except that it is always later than that of the more usual strain front. In some cases, a distinct flat is observed at the maximum of the first wave. Thus it would appear that in these cases, the formation of a dispersive plastic wave from the hydrostatic portion of the initial front is sufficiently delayed so as to involve a separate wave structure.

Thirty diffraction grating tests were conducted at positions inside the first $\frac{1}{4}$ diameter. The largest number of tests were run at $\frac{3}{32}$ diameter, although a few tests were run at 0.02 diameter, $\frac{1}{16}$, $\frac{1}{8}$, and $\frac{5}{32}$ diameters. As was pointed out already, variations in strain-time detail are observed from one test to another for the same impact velocity and distance from the impact face.

Figure 5 illustrates several tests at $\frac{3}{32}$ diameter and $\frac{1}{8}$ diameter. All tests in Fig. 5 were for an impact velocity of 66.5 ft/sec, although measurements also were made at 44.5 ft/sec and 78.5 ft/sec. The solid lines in Fig. 5(a), (b), and (d) are the extrapolation to $\frac{3}{32}$ diameter of a large number of experimental strain-time curves obtained between one and four diameters. These values are extrapolated back to the $\frac{3}{32}$-diameter position, using the velocities of strain propagation obtained from the slopes of the static stress-strain curve. For a number of these tests, as may be seen in Fig. 5(a) where two tests are given, the average experimental strain-time curve and the data at $\frac{3}{32}$ diameter are in good agreement.

In an earlier paper[1] it was emphasized that strain maxima at positions of two or more diameters differed very little from the theoretical value of the strain rate independent theory. Nevertheless, the variations in the time of arrival of the various strain levels were such that it was necessary to average in time a large number of tests at each position to determine the veloc-

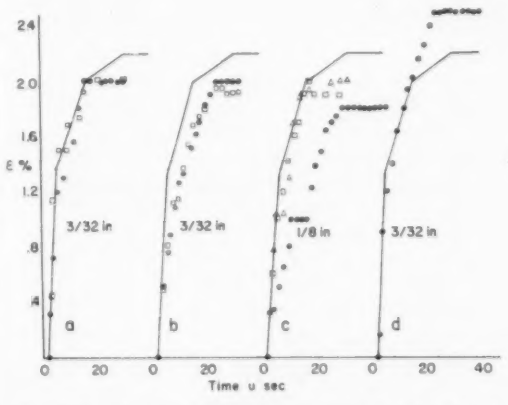

FIG. 5. Experimental strain-time data in the vicinity of the impact face. The impact velocity is 66.5 ft/sec.

ities of propagation for each level of strain. The typical strain-time curves shown in Fig. 1 of that paper were selected from over 50 tests in such a way as to emphasize the statistical aspect of this problem. When data from 50 tests between $\frac{1}{2}$ and $3\frac{1}{2}$ diameters were averaged, the velocities of strain propagation were in very close agreement with the predictions from the slopes of the static stress-strain curve. An additional 150 tests have now been conducted in annealed aluminum at many positions in the first eight diameters. The average strain arrival times have given an even closer agreement with the strain rate independent theory of wave propagation in every section of the rod as far as the constancy of the velocities of propagation of strain are concerned. The results shown in Fig. 5(a) indicate that these velocities of propagation are constant and in agreement with the static stress-strain curve from as close as $\frac{3}{32}$ diameter from the impact face.

The tests of Fig. 5(b) represent the latest arrival times found in these data, other tests at this impact velocity falling between Figs. 5(a) and 5(b). Of course, nonaxiality will have an important effect upon strain-time curves in the immediate vicinity of the impact face. In Fig. 5(d) is shown at $\frac{3}{32}$ diameter a strain-time curve which is more like that obtained at $\frac{5}{32}$ diameter or $\frac{1}{4}$ diameter from the impact face. Strains up to 2% are similar to those of Fig. 5(a).

In Fig. 5(c) are shown three tests at $\frac{1}{8}$ diameter from the impact face. Two of these tests resemble those at $\frac{3}{32}$ diameter of Fig. 5(a). The third test, shown as circles in Fig. 5(c), contains a definite two-wave structure. The strain amplitude of the first wave is 1%. One test at $\frac{1}{16}$ diameter and two tests at $\frac{3}{32}$ diameter have exhibited a similar two wave structure, with the first strain level varying between 0.75% and 1% strain. One test at $\frac{1}{4}$ diameter has shown a small flat occurring at ϵ_1. A few tests between one and $3\frac{1}{2}$ diameters also have exhibited a two-wave structure, where the height of the first wave is invariably ϵ_1.

If one studies the surface angle behavior of these tests at $\frac{1}{16}$, $\frac{3}{32}$, and $\frac{1}{8}$ diameters, it is found that the maxima occur at a strain less than ϵ_1 except for tests of the type shown in Fig. 5(d), where the surface angle maximum occurs at ϵ_1. The strain at which maxima occur varies all the way from 0.8% to 1.35% for this impact velocity of 66.5 ft/sec. For this impact velocity ϵ_1 is 1.35%. The average strain at surface angle maxima for all 66.5 ft/sec tests at $\frac{3}{32}$ and $\frac{1}{8}$ diameters is 1.08%.

Figure 6 shows a number of tests between $\frac{3}{32}$ diameter and $1\frac{1}{2}$ diameter from the impact face. The rise to a maximum of $2\epsilon_1$ for nearly all strain-time curves at $\frac{5}{32}$ diameter or $\frac{1}{4}$ diameter occurs at a rate such that the higher levels of strain certainly have not propagated from the $\frac{3}{32}$ position. The individual test shown at $\frac{3}{32}$ diameter is similar to those of Fig. 5.

All tests at $\frac{3}{32}$ and $\frac{1}{8}$ diameters have developed in a fashion shown in Fig. 6, most of them having developed to a strain of 2% for this impact velocity at a time of approximately 20 μsec. The lower strain levels, which are those of the deviatoric front, propagate from the origin as would be expected. If one examines the higher levels of strain at $\frac{1}{4}$ diameter, it is seen that it is not until $\frac{1}{2}$ diameter from the impact face that a constant velocity of propagation begins.

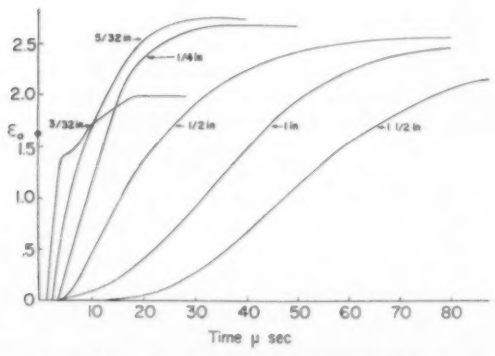

FIG. 6. Strain-time behavior in the first $1\frac{1}{2}$ diameters.

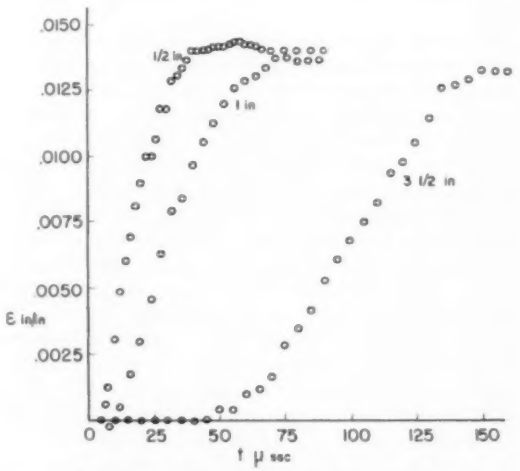

FIG. 7. Strain-time data for different distances from impact face for impact velocity of 44.5 ft/sec.

For this impact velocity of 66.5 ft/sec, the extrapolated average strain-time curves definitely indicate a change of slope occurring at 2%, which is the maximum for tests at $\frac{3}{32}$ and $\frac{1}{8}$ diameters. The low values at which the surface angle maxima occur and the detail of the higher strain suggest that the dispersive plastic wave front, including the deviatoric portion, is a gradual development in this region. All of the data discussed above was obtained from 0.990-diam specimens.

Tests conducted in $\frac{1}{2}$-in. diameter specimens and in 1-in. diameter hollow tubes with a $\frac{1}{8}$-in. wall thickness have shown that the strain level ϵ_1 is independent of the

geometry and therefore the initial partition of energy is not primarily associated with the effects of radial kinetic energy. An ϵ_1 for annealed copper is found experimentally which is similar in all respects to the behavior in aluminum. Although both lead and magnesium have shown themselves to be materials to which the strain rate independent theory does not apply, nevertheless the same type of surface angle behavior is observed in both cases in measurements at large distances from the impact face, although a similar relationship with the static stress-strain curve has not been established.

Dynamometer experiments indicate that the dynamic stress level is maintained for at least 80–100 μsec. Experiments on the unloading wave, to be reported elsewhere, have shown, however, that the final unloading stress is that of the static stress-strain curve. Thus in the process of developing through the first diameter, a lowering of stress levels must be involved.

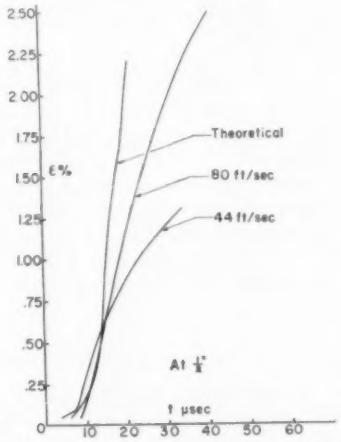

FIG. 8. Averaged strain-time data at 80 ft/sec and 44 ft/sec compared with theoretical result if an infinite step were present at origin.

These experiments near the impact face have been carried out for several impact velocities. As had been observed earlier, strain-time detail below an impact velocity of 48.5 ft/sec varies to a marked degree from that above this velocity. This impact velocity of 48.5 ft/sec has been shown by calculations from a large number of static tension tests conducted by Professor Robert Pond of the Johns Hopkins University[7] to be the von Karman critical velocity in tension. The differences in strain-time detail for lower velocity tests is seen in measurements from $\frac{1}{2}$ to four diameters, as well as in measurements at $\frac{3}{32}$ diameter. It is generally characterized by a much slower development of plastic strain near the impact face and practically no mushrooming, or excess maximum strain, in the first diameter except at the position of $\frac{1}{4}$ diameter. In fact the theoretical maxima are obtained at all positions between $\frac{1}{2}$ diameter and $3\frac{1}{2}$ diameters, as may be seen in Fig. 7 where

[7] Private communication.

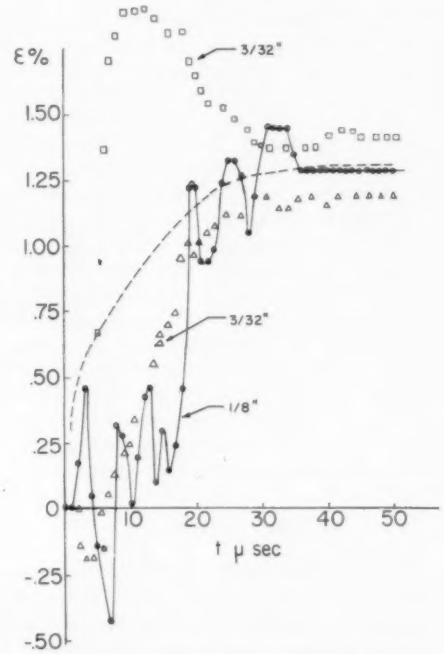

FIG. 9. Strain-time data near the impact face for 44.5 ft/sec and 46 ft/sec.

three tests are shown for an impact velocity of 44.5 ft/sec. The theoretical maximum is 1.3% strain.

Figure 8 shows a number of tests' results which have been averaged and extrapolated to $\frac{1}{2}$ diameter for 80 ft/sec and 44 ft/sec. For all tests above 48.5 ft/sec the initial strain arises to some point along the strain-time curve shown for 80 ft/sec, whereas for tests below 48.5 ft/sec, as shown in Fig. 8, a different rise time is seen at all strain levels. Both of these velocities are compared with the theoretical strain-time curve which would be obtained if the strain were to propagate from an infinite step at the origin with velocities of propagation calculated from the slopes of the static stress-strain curve.

One characteristic of tests in the vicinity of the impact face at these lower velocities is the lack of reproducibility. Three tests are shown in Fig. 9, two at $\frac{3}{32}$ diameter and one at $\frac{1}{8}$ diameter from the impact face. The dashed curve is the extrapolated average strain-time curve for this impact velocity at a position of $\frac{1}{8}$ diameter.

One feature which all of these tests have in common is that the final strain maximum always approximates the theoretical strain maximum for this impact velocity. The strain-time curve shown as squares in Fig. 9, which rises rapidly to a high strain level and then falls to the theoretical maximum strain, is for an impact velocity of 46 ft/sec, or 2 ft/sec higher than the other two tests shown. It is not known whether the rapid oscillations of the test at $\frac{1}{8}$ diameter are significant since it has not been possible to reproduce this result. This interesting

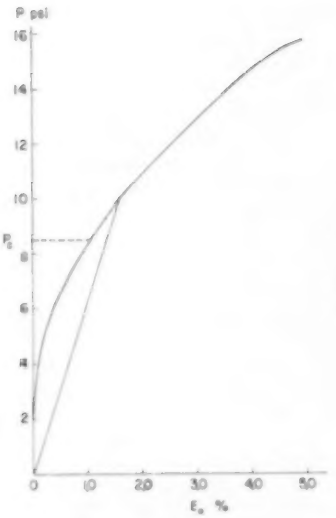

FIG. 10. The dynamic stress-strain curve for which the strain is that of the nondispersive wave front rather than that of the dispersive wave front of Fig. 1.

inconsistency of low-velocity tests when compared to the more consistent higher velocity strain-time curves suggests some alternate form of development is present. The surface angle maximum occurs at a strain ϵ_1 of 0.79% for 44.5 ft/sec. The dynamic stress P, determined from this ϵ_1, is not in as good agreement in this low-velocity region. Tests at $\frac{1}{4}$ diameter have shown a strain rise to a value of $2\epsilon_1$ or higher, similar to the high-velocity behavior. Only a relatively small amount of low-velocity data has been obtained when compared with impact velocity data above 50 ft/sec.

In the many tests which have been run from very close to the impact face to eight diameters in 10-diameter specimens, a large number of values of Poisson's ratio have been obtained by the method discussed in an earlier paper.[1] Although a study of these data has not as yet been completed, it is found, in general, that Poisson's ratio for one or more diameters increases from $\frac{1}{3}$ to $\frac{1}{2}$ with increasing rapidity, with an increase of the distance from the origin. Much lower values of Poisson's ratio at large strains are found, however, at positions within the first diameter. Calculations at $\frac{3}{32}$, $\frac{3}{32}$, and $\frac{1}{4}$ diameters have given values of the apparent Poisson's ratio of approximately $\frac{1}{4}$ for strains up to 1% and in some cases even higher. Initial values of Poisson's ratio at $\frac{1}{2}$-diameter tests have given a Poisson's ratio betewen $\frac{1}{4}$ and $\frac{1}{3}$ up to strains of approximately 1%.

If one computes the corresponding dilatation from these values of Poisson's ratio, it is seen that a significant amount of dilatation is present in the first diameter, decreasing to very small values by two diameters. If the axial component of these calculated dilatations are subtracted from the measured strains of the experimental strain-time curves in the first diameter, the resulting deviatoric strain-time curves are found to be very straight up to strain levels in the vicinity of the theoretical strain maxima.

A consideration of the bulk modulus for aluminum, as determined by Bridgman,[8] would give values of dilatation far below those obtained from these computations. A thermoplastic theory which included thermal effects created by strain rates of between 500 and 5000 in./in./sec which are found in these tests, might account for the observed differences. It also is possible that these values of Poisson's ratio are associated primarily with a surface effect. However, the studies of hollow tubes, as well as the fact that at one or more diameters the computed Poisson's ratio increases from $\frac{1}{3}$ to $\frac{1}{2}$, suggest that this is not the case.

One point which might shed some light on the nature of the decaying amplitude of the plastic wave in the first diameter is that maximum strains in copper, whose mass is considerably greater than that of aluminum, decreased to the theoretical value at a much slower rate, indicating that radial acceleration may play an important role.

If the dynamic stress of Fig. 1 is plotted against ϵ_0 obtained from Eq. (4), instead of against maximum strains at large distances from the origin, we obtain the stress-strain curve of Fig. 10. The nondispersive wave velocity D of Eq. (2) is then obtainable from the square root of the secant modulus devided by the mass density ρ. The modulus is shown for 66.5 ft/sec. The velocity D for 66.5 ft/sec is 50 000 in/sec, or $\frac{1}{4}$ the elastic velocity c_0. The value P_c of 8 500 psi is the stress corresponding to the von Karman critical velocity of 48.5 ft/sec.

SUMMARY AND CONCLUSIONS

In this paper it has been shown possible to determine the dynamic stress-strain curves in both annealed aluminum and copper from the consideration of initial nondispersive shock fronts as well as from an interpretation of the surface angle detail at large distances from the origin. An impact velocity of 48.5 ft/sec agreeing with the von Karman critical velocity for this material determined from tension tests, would appear to be a dividing line between two types of initial plastic wave fronts.

A number of tests conducted in the first $\frac{1}{4}$ diameter indicate that a plastic wave front develops between the impact face and $\frac{1}{4}$ diameter, with a rising maximum until $\frac{1}{4}$ diameter is reached. The maximum of this plastic wave then decreases to the theoretical value between $1\frac{1}{2}$ and two diameters. Six tests at $\frac{3}{4}$ diameter have indicated that a minimum occurs at this position.

Although a detailed theory for this behavior in the first diameter is not provided insofar as the development of the upper portion of the wave front is concerned, sufficient information is given to show that there is no

[8] P. W. Bridgman, *The Physics of High Pressure* (G. Bell and Sons, London, England, 1931).

contradiction between earlier experiments of others in obtaining dynamic stress-strain curves and this author's results using the static stress-strain curve. The dynamic stress-strain curves for annealed aluminum and copper do not appear to be a measure of material properties in the same sense as the static stress-strain curve, but rather to reflect the mechanics of the development of initial plastic wave fronts.

Experiments currently in progress are extending the impact velocity to 500 ft/sec or to the lower levels of the explosive shock wave studies, with the hope that the initial front may propagate to larger distances from the impact face and provide sufficient information for a theoretical analysis of the development of the entire dispersive wave front.

It has been noted elsewhere[9] that magnesium exhibits an interesting two-wave structure in the first $1\frac{1}{2}$ diameters, the upper wave of which rapidly decreases in the first $1\frac{1}{2}$ diameters. Since the static stress-strain curve of magnesium, whose crystal structure differs from that of aluminum and copper, possesses a very long and flat region above the yield stress, it is hoped that a series of experiments now in progress will reveal a much more drastic difference between the dynamic and static stress-strain curves than is the case for aluminum and copper, thus providing the opportunity experimentally for a much more detailed examination of the development of the plastic wave.

This paper has accounted experimentally for some of the first diameter effects observed earlier[1] and, in particular, has shown that the delaying effects in the area of large strains at positions from one to eight diameters are introduced in the development of the plastic wave in the first $\frac{1}{8}$ diameter. The strain rate independent theory thus may be seen to account for the detail of the plastic wave, as far as the velocities of propagation are concerned, from $\frac{1}{8}$ diameter to the end of finite length annealed aluminum and copper rods. The mushrooming in the first diameter and the delay in the development of the upper portion of the plastic wave, on the other hand, are a consequence of the development of dispersive plastic waves from an initial nondispersive shock wave.

[9] James F. Bell, Tech. Rept. No. 5, U. S. Army Office of Ordnance Research (March, 1960).

ACKNOWLEDGMENTS

The author wishes to acknowledge the sponsorship of the U. S. Air Force, Office of Scientific Research, and to thank Mr. John Suckling and Mrs. Patricia Jones, research assistants.

Prediction of Fatigue Life*

A. M. FREUDENTHAL
Columbia University, New York, New York
(Received June 22, 1960)

On the basis of the relation between the "reliability-function" (probability of surviving beyond age N in cycles or t in time) and the "risk" of failure (as a function of age), the physical interpretation of the latter can be used to extrapolate the former beyond the range of possible observation. It is shown that the asymptotic distribution of smallest values is compatible with the physical concept of (dynamic or static) fatigue, while the logarithmic-normal distribution is not.

THE number N of load cycles that can be repeated or the time t during which a steady load can be sustained before failure of a metallic structural part of a mechanical system is conveniently referred to as its (dynamic or static) "fatigue life"; it is a statistical variable of relatively wide range of variation[1] even under rather stringent control of load-amplitude or load-intensity and environmental conditions. The wide scatter in observed fatigue lives under nominally identical conditions is mainly due to the fact that the progressive damage which leads to (dynamic or static) fatigue fracture after N load cycles or after t hours originates at the surface and propagates within the microstructure before a crack of critical macroscopic size can develop.[2] The number of cycles or the time required for such development are therefore extremely surface- and structure-sensitive, so that the prediction of fatigue lives of a "population" of nominally identical parts under closely similar conditions can only be made at specified probability levels $R(N)$ or $R(t)$, where $R=(1-P)$ denotes the probability of survival at N cycles or at age t, while $P(N)$ or $P(t)$ denote the probability of failure.

Problems of prediction of fatigue life are encountered whenever mechanical systems are designed for long operational lives under actual service conditions, rather than for sudden failure under a very rarely encountered and therefore unlikely "ultimate" load. Since it is desirable to keep the probability of failure P of the designed system reasonably low, (and therefore R very close to unity) the survival- or "reliability"-functions $R(N)$ or $R(t)$ should be known throughout the significant range which extends at least to $R=0.95$ for easily replaceable parts of the system, and to $R=0.99$ or even closer to unity for parts or systems the failure of which would have castastrophic consequences. On the other hand, direct observation of this function by destructive testing of representative samples of the required magnitude of n test replications is impossible: with a mean "plotting position" $R_m=1-m/(n+1)$ of the result of the mth replication (arranged in ascending order),[3] it is obvious that more than 100 test replications would be required if $R=0.99$ is to be exceeded. Therefore, for the prediction of fatigue lives of any but the simplest and most easily replaceable parts that can be tested in large numbers, extrapolation from the observable central range toward the significant "tails" of the distribution function remains the only realistic procedure.

Within the central range, however, no valid distinction can be made between the various non-symmetrical probability functions by which the actual observations of $N>0$ could be represented. Thus the differences between the Logarithmic-Normal, Extremal and Gamma-distribution functions become significant only beyond the range of $0.1<R<0.9$, while actual observation, for all practical purposes, is limited to this, or in most cases, to even narrower ranges because of limited sample sizes. Extrapolation toward the tails of the distribution functions of fatigue lives $p(N)=-dR(N)/dN$ or $p(t)=-dR(t)/dt$ must therefore have a more realistic basis than that provided by the standard (analytical or graphical) statistical procedures.

It is obvious that such a basis cannot be derived by probabilistic reasoning alone, without consideration of the relevant physical aspects of fatigue. In order to discriminate between probability functions that can not be distinguished from each other within the range of actual observation it is necessary to introduce a concept that combines the physical and statistical aspects and that permits to base the differentiation between statistical functions on physical considerations. Such a concept is the "risk" of failure or the "failure rate" $r(N)$ or $r(t)$, which expresses the probability of failure at the $(N+1)$th cycle or during the time interval dt of those members of the "population" of parts or systems that have survived N cycles or reached the "age" t. In statistical theory the function $r(x)$ is known as the "intensity function," its inverse as Mill's ratio.[4]

* This research was supported by the U. S. Air Force under contract.

[1] A. M. Freudenthal and E. J. Gumbel, Adv. in Appl. Mech. 4, (1956), pp. 117–158.

[2] A. M. Freudenthal, "Fatigue," *Handbuch der Physik*, edited by E. Flügge (Springer-Verlag, Berlin, 1958), Vol. 6, p. 596.

[3] See work cited in footnote 1, p. 133.

[4] E. J. Gumbel, *Statistics of Extremes* (Columbia University Press, New York, 1958), p. 20.

According to its above definition

$$r(x)dx=\frac{p(x)dx}{R(x)}=-\frac{dR(x)}{R(x)} \tag{1}$$

and therefore

$$R(x)=\exp-\int_0^x r(z)dz \tag{2}$$

where the variable x represents either N or t. Equation (2) relates the reliability function $R(x)$ with the risk function $r(x)$, the trend of which can be related to the physical aspect of fatigue.

When the risk of failure remains constant and thus independent of the number of load cycles or the duration of sustained load, $r(x)=\text{const}=1/T$, (where T denotes the "return period" of or the mean interval between chance failures) $R(x)=\exp[-(x/T)]$. The simple exponential survivorship function is thus characteristic of failure due to pure chance, unaffected by the number N of load cycles or the period t of loading preceding it.

On the other hand, fatigue as a process of progressive damage terminated by actual failure must necessarily be associated with a risk function that increases with N or t. Moreover, the risk of failure in a fatigue process vanishes, by definition, over an initial finite period $x_0=N_0$ or $x_0=t_0$, the "minimum life,"[5] which is just too short for the propagation of a fatigue crack throughout a finite cross section. The simplest risk function that satisfies both conditions is a power function

$$r(x)=c\alpha(x-x_0)^{\alpha-1}, \quad \alpha>1; \tag{3}$$

according to Eq. (2) with $z=(x-x_0)\geq 0$ it is associated with the reliability function

$$R(x)=\exp\left[-\left(\frac{x-x_0}{v-x_0}\right)^{\alpha}\right] \tag{4}$$

if c is identified with $c=(v-x_0)^{-\alpha}$ and v, considered as a "return period" of fatigue failures, denotes the value of x at the quantile $R=1/e$. Equation (4) is easily identified as the third asymptotic probability function of extreme (smallest) values,[6] which thus emerges as the survivorship function in fatigue associated with the simplest possible assumption of risk increasing with number of load cycles or age. The scale parameter α is inversely proportional to the standard deviation of $(\log x)$, so that the rate of increase of the risk of failure is reflected in the range of variation of fatigue life: the higher this rate the narrower the expected scatter range. Figure 1 shows risk functions as well as reliability functions and their derivatives according to Eqs. (3) and (4) for the values $\alpha=2, 3, 4$; for $\alpha=1$ the function $r(x)=c$ is a constant and $R(x)$ and dR/dx degenerate into the simple exponential function with $c=1/T$ as the inverse of the return period T of chance failure.

In the interpretation of and extrapolation from observed distribution functions of fatigue life under repeated and under sustained load the logarithmic-normal distribution is very widely used; its use is recommended in practically all existing specifications for planning of fatigue and creep-rupture tests and interpretation of their results.[7] It is therefore of interest to derive the associated risk function according to Eq. (1). In Fig. 2 the results of this analysis have been plotted for 4 logarithmic-normal distribution functions selected so as to match the standard deviations of $\log[(x-x_0)/(v-x_0)]$ used in Fig. 1; the value v at $R=1/e$ of the extreme value distribution has been replaced by the median $\breve{x}$ at $R=0.5$.

A comparison of Figs. 1 and 2 shows the significant physical difference between the extremal and logarithmic-normal representations of the distribution of fatigue lives: logarithmic-normal distributions imply a risk of failure decreasing in the long-life range while the extremal distributions show the opposite trend. It appears doubtful, therefore, whether logarithmic-normal distributions are physically relevant to the phenomenon of fatigue and thus suitable for representation and extrapolation of observed fatigue lives; it does not seem reasonable to associate a wear-out process such as fatigue with the possibility of the risk of failure decreasing with increasing life, while even for chance failures this risk remains constant. However, the doubts can be finally resolved only by fatigue tests with sufficient replications to reach the range of divergence between the two types of risk function.

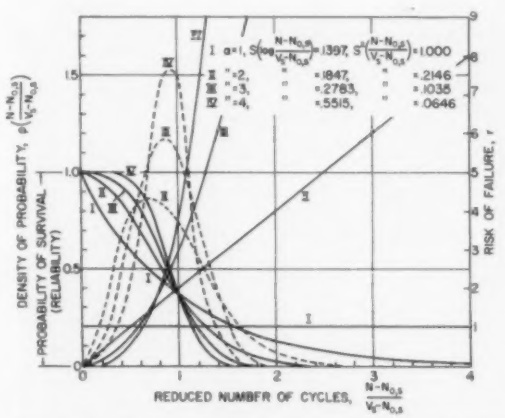
DENSITY OF PROBABILITY, $p\left(\frac{N-N_{0.5}}{v_c-N_{0.5}}\right)$
PROBABILITY OF SURVIVAL (RELIABILITY)
RISK OF FAILURE, r
REDUCED NUMBER OF CYCLES, $\frac{N-N_{0.5}}{v_c-N_{0.5}}$
I α=1, $S\left(\log\frac{N-N_{0.5}}{v_c-N_{0.5}}\right)$=1397, $S'\left(\frac{N-N_{0.5}}{v_c-N_{0.5}}\right)$=1.000
II " =2, " =.1847, " =.2146
III " =3, " =.2783, " =.1035
IV " =4, " =.5515, " =.0646

FIG. 1. Risk-functions, probability-densities and reliability-functions of third asymptotic extreme value distribution for different standard deviations S.

[5] A. M. Freudenthal and E. J. Gumbel, J. Am. Statist. Assoc. 49, 575 (1954).

[6] See work cited in footnote 1. p. 278.

[7] "Manual on Fatigue Testing" American Society for Testing Materials, (Philadelphia, 1959).

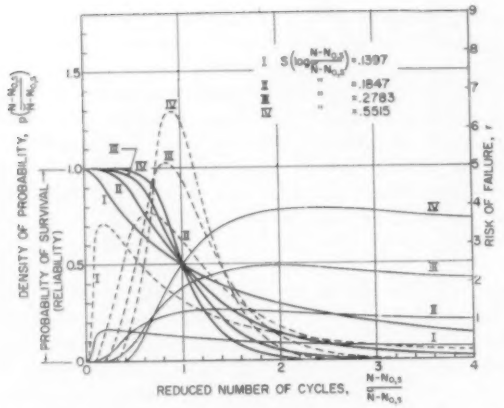

FIG. 2. Risk functions, probability densities, and reliability functions of logarithmic-normal distribution for different standard deviations S.

In papers on reliability analysis[8] it is frequently claimed that the difference between reliability functions $R(x)$ representing the distribution of chance failures and functions representing "wear-out" (including fatigue) failures is the existence in the latter of a mode $\tilde{x}>0$, while pure chance failures (or failures in complex systems governed by so many deterioration mechanisms with different rates that they appear to be chance failures and can only be treated as such) are characterized by simple exponential distributions. Figure 2 shows this conclusion to be a fallacy; logarithmic-normal distributions, in spite of their distinct modes, are even less suited to represent fatigue failures than are exponential distribution because of the decrease toward zero of the associated risk functions. On the other hand, it can be shown that a uniform distribution of fatigue lives having no mode is characterized by a sharply increasing risk-function.

[8] M. P. Fayerhern, IRE Fifth National Symposium on Reliability, (Philadelphia, 1959), p. 119; G. R. Herd, *ibid.*, p. 126.

Other distribution functions having both modes and increasing risk functions as, for instance, the normal and the gamma distributions, have been used to represent fatigue lives. Of these the normal distribution is symmetric and unlimited and therefore physically irrelevant. The gamma distribution

$$p(x)=(\alpha!\beta^{\alpha+1})^{-1}x^{\alpha}\exp(-x/\beta) \tag{5}$$

which is physically relevant[9] has a risk function that for $\alpha>1$ increases at a decreasing rate, approaching asymptotically a limit. In this respect it differs so significantly from the extreme value distribution that small-specimen experiments might be designed to discriminate between these two distributions.

The actual life of mechanical systems or parts depends in fact on the combined risk of failure due to the chance-occurrence of the (very rare) ultimate load of return period T and the development of fatigue. Simplifying Eq. (3) by setting $x_0=0$, this combined risk

$$r(x)=1/T+(1/v)(x/v)^{\alpha-1}, \tag{6}$$

where v is the mode of the distribution (4); therefore

$$R(x)=\exp(-x/T)\exp(-x/v)^{\alpha}. \tag{7}$$

The mode $\tilde{x}$ of the associated distribution function $p(x)=-dR(x)/dx$ is determined by the equation $dp(x)/dx=0$, or:

$$[(\alpha-1)/\alpha]^{\frac{1}{2}}(\tilde{x}/v)^{(\alpha-2)/2}-(\tilde{x}/v)^{\alpha-1}=v/\alpha T. \tag{8}$$

Because of the added risk of chance failure $\tilde{x}<v$; for instance for $\alpha=2$ the mode $\tilde{x}=v(1/\sqrt{2}-v/2T)$. Unless $v<T\sqrt{2}$, chance failure is critical since $\tilde{x}=0$; as $(v/\alpha T)$ tends asymptotically towards zero $\tilde{x}\to v\cdot\alpha[(\alpha-1)/\alpha]^{\frac{1}{2}}$. The ratio $(v/\alpha T)$ can be considered as a design and performance parameter delimiting fatigue-sensitive and fatigue-insensitive mechanical systems.

[9] A. M. Freudenthal and R. A. Heller, *Fatigue in Aircraft Structures* (Academic Press, Inc., New York, 1956), p. 170.

Electron Microscope Observations of Fission Fragment Tracks in Thin Films of UO_2

T. S. NOGGLE AND J. O. STIEGLER
Solid State Division, Oak Ridge National Laboratory, Oak Ridge, Tennessee*
(Received July 18, 1960)

Electron microscope studies of the tracks produced by fission fragments in thin films of UO_2 have established a 100% detection efficiency for fission events in films 100 A or less in thickness. A background texture decreases the efficiency in thicker films. The tracks register in the films primarily as a result of a redistribution of surface material arising from the disturbance produced by the continuous loss of energy of the fragment by electron excitation and ionization. The minimum rate of energy loss which registers as a track in the film is on the order of 1000 ev/A. Track length distributions, however, suggest that as yet unrecognized free surface effects may also contribute to the track registration.

I. INTRODUCTION

VISUAL observations of the tracks produced by the passage of fission fragments through matter have been realized with the aid of Wilson cloud chambers[1] and photographic emulsions.[2] Recent work has shown that the passage of fission fragments in and through thin films of UO_2 gives rise to a similar type of track structure which may be studied in the electron microscope.[3] Electron microscope studies have also revealed fission fragment tracks in mica[4]; however, differences between mica and UO_2 and in the specimen preparations employed suggest that there may be basic differences in the nature of the damage detected. The present study indicates that the fission fragment tracks observed in the UO_2 films arise from a disturbance of the surface and as such represent a special aspect of radiation damage in solids.

An extension of the earlier observations[3] to a more quantitative basis is reported here. The correlation between expected and observed densities of the structure has been evaluated for a number of experimental conditions, and statistics on the track lengths have been obtained. Attempts have been made to elucidate the conditions which determine registration of a track in the films. These latter studies logically lead to concern with the mutual interaction between the fission fragments and the matter they traverse, and the results obtained to date suggest that explanations based on current theories of charged particle penetration of matter will qualitatively account for the observations.

All observations reported here have been made at very low track densities. This restriction was made to minimize the superposition of the tracks in order to allow the study of individual tracks in the film. It is of interest from a radiation damage standpoint to study these films at very high burnup levels for which a substantial volume of the film will have been affected by the passage of the fission fragments. It is, of course, no longer possible at the high doses to relate observations to individual events, and only the net effect of the passage of numerous fragments is observed. Work in this area of interest has been carried out by Bierlein and Mastel.[5]

II. EXPERIMENTAL PROCEDURE

Films of UO_2 on the order of 100 A thick were prepared by the vacuum evaporation of U_3O_8 or UO_2 from a tungsten filament at pressures of less than 5×10^{-5} mm of mercury. The U_3O_8 decomposes upon heating so that films prepared from both U_3O_8 and UO_2 showed the crystal structure of UO_2 as determined by electron and x-ray diffraction. The films were formed on fresh cleavage surfaces of NaCl and mica. Fine grained,

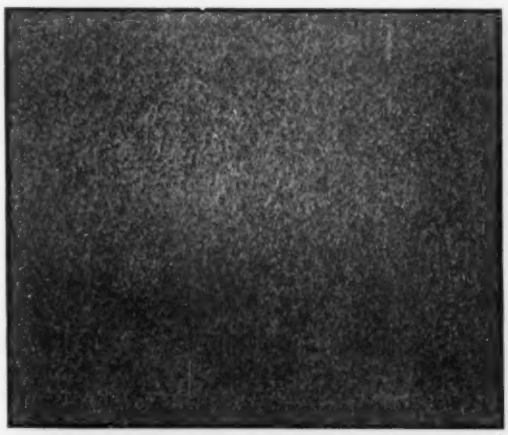

FIG. 1. Typical microstructure of evaporated UO_2 film, unirradiated. 50 000×.

* Oak Ridge National Laboratory is operated by Union Carbide Corporation for the U. S. Atomic Energy Commission.

[1] D. R. Corson and R. L. Thornton, Phys. Rev. **55**, 509 (1939); K. J. Brostrøm, J. K. Bøggild, and T. Lauritsen, Phys. Rev. **58**, 651 (1940); J. K. Bøggild, O. H. Arrøe, and T. Sigurgeirsson, Phys. Rev. **71**, 281 (1947); W. Gentner, H. Maier-Leibnitz, and W. Bothe, *An Atlas of Typical Expansion Chamber Photographs* (Pergamon Press, London, 1954), p. 116.

[2] P. Demers, Phys. Rev. **70**, 974 (1946); E. O. Wollan, C. D. Moak, and R. B. Sawyer, Phys. Rev. **72**, 447 (1947).

[3] J. O. Stiegler and T. S. Noggle, Bull. Am. Phys. Soc., Ser. II, **4**, 141 (1959).

[4] E. C. H. Silk and R. S. Barnes, Phil. Mag. **4**, 970 (1959).

[5] T. K. Bierlein and B. Mastel, HW-61656 (September 9, 1959).

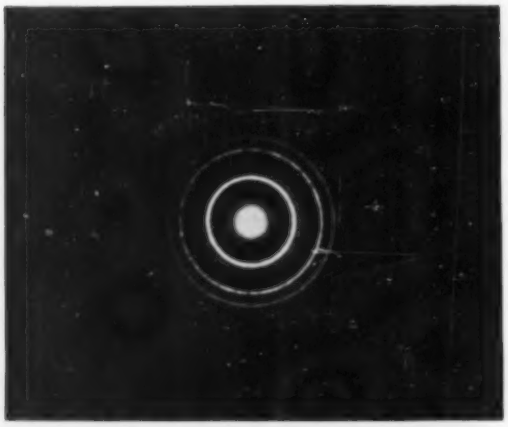

FIG. 2. Selected area electron diffraction pattern from unirradiated UO_2 film.

polycrystalline films were obtained with either source material on either substrate. A typical microstructure and the corresponding electron diffraction pattern obtained from these films are shown in Figs. 1 and 2. The grain size of the films increases with the film thickness, but the average grain diameter is less than the film thickness. The increase in grain size with thickness interferes to some extent with the observations in the thicker films since diffraction contrast associated with individual grains gives a background structure which cannot readily be distinguished from fission events registering as small spots.

The thicknesses of the films were determined from alpha-counting rates taken from a series of cover glasses which were arranged closely around a group of specimens during the evaporation; from a calibration available[6] the counts were converted to the number of uranium atoms per unit area. The thickness was then calculated by assuming the bulk density of UO_2 for the material in the films. Measurements of film thickness were made in the electron microscope for comparison and, within experimental error, confirmed the estimated thickness determined by counting. It is worth noting that for the correlation studies the film thickness does not enter explicitly; one needs to know only the number of U^{235} atoms per unit area. In the case of the track length distributions, however, the film thickness is an important parameter.

The substrates on which the films are formed are very thick ($\sim$1 mm) and, hence, opaque to the electron beam. The films, therefore, must be stripped from them for examination in the microscope. This is readily effected with the films formed on NaCl by floating small crystals (1–2 mm square) onto water with the UO_2 surface facing up. The salt quickly dissolves, leaving the UO_2 film floating on the water. The film is then picked up on a 200 mesh, $\frac{1}{8}$-in. diameter specimen grid, and all subsequent handling is carried out with the film on this grid. Usually the UO_2 films on mica will detach themselves from small plates 2–3 cm square which are slowly inserted edgewise into water; however, after irradiation the films will not strip from mica surfaces in this manner. In general, NaCl has proved to be the most easily handled substrate and consequently has been most frequently employed.

FIG. 3. Transmission micrograph of a 45 A thick $U^{235}O_2$ film after thermal neutron irradiation of $\sim 2\times10^{21}$ nvt. 25 000×.

The UO_2 films produced in this way are quite fragile and become more so after irradiation. Even with the most careful handling considerable breakage occurs. It has been found desirable, particularly with the thinner films, to evaporate on the surface of the film a 100–200 A thick layer of carbon to support the UO_2. This reinforcement with carbon is normally made after irradiation with the films still in place on the substrate; under these conditions the contrast can be enhanced by shadowing with a 10–20 A layer of platinum before evaporating the carbon. Observations have been made on bare films, carbon-reinforced films, and carbon-reinforced films preshadowed with platinum. The basic appearance of the structure is unchanged under these different conditions. By dissolving the UO_2 in nitric acid after freeing the composite film from the substrate, the preshadowed, carbon-reinforced films also serve as replicas for ob-

[6] A weighed quantity of the enriched uranium oxide was dissolved, and aliquot portions of the solution containing approximately the same mass of uranium as the films were dried down and counted to determine the disintegration rate per microgram. The specific activity of natural uranium was assumed for the natural uranium films. These activities along with the known counter geometry and detection efficiency were used to determine the uranium mass per unit area. The estimated errors in the measurement of uranium atoms per unit area are $\pm1\%$ for the enriched films and $\pm5\%$ for the natural uranium films. Since monitors located adjacent to the films were counted rather than the films themselves, the estimated errors should be slightly greater than the values quoted above.

serving the topographical features of the free surface of a specimen. Replicas from UO_2 on mica can be obtained by using nitric acid to dissolve the UO_2 and free the preshadowed carbon replicas. As noted above, the inability to strip films of UO_2 from mica after irradiation has limited the use of mica to a convenient source of free films of unirradiated UO_2 and to replica studies of the free surfaces of irradiated films.

Irradiations of the films have been carried out with the films mounted on their substrates and as free films supported on the 200 mesh specimen grids. All irradiations have been at the pile ambient temperature (approximately 35°C) in Holes 10 and 51 of the Graphite Reactor at the Oak Ridge National Laboratory. The integrated thermal neutron fluxes were determined by γ-counting cobalt foils irradiated adjacent to the specimens to give the dose received by each specimen to within about 5%.

In the correlation and track length studies the principle source of error arises from uncertainty in the magnification of the photomicrographs employed. As a consequence of the inherent characteristics of the electron microscope, the magnification can normally be specified to no better than about $\pm 10\%$. This uncertainty arises from the nonreproducibilities of the specimen plane and of lens strengths, from long-term drifts in reference circuits, and the accuracy of the calibration standard. In this work the uncertainty in magnification was minimized by using extra care in positioning specimens in the instrument, by normalizing lens circuits for improved reproducibility of lens strengths, and by recalibrating the microscope frequently with a 28,800 line per inch grating replica.[7] Under these conditions it is estimated that the uncertainty in magnification is less than $\pm 10\%$ but no better than $\pm 5\%$.

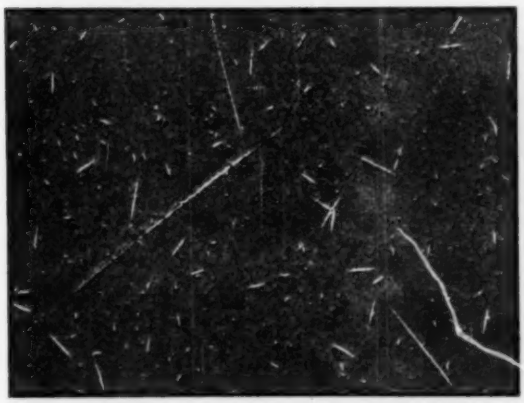

FIG. 4. Transmission micrograph of a 100 A thick UO_2 film after thermal neutron irradiation of $\sim 5\times 10^{15}$ nvt. 25 000×.

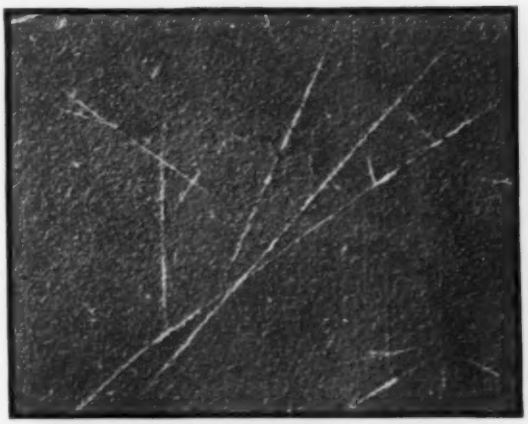

FIG. 5. Transmission micrograph of a 156 A thick UO_2 film after thermal neutron irradiation of $\sim 8\times 10^{15}$ nvt. 25 000×.

The electron microscope work was performed on an RCA-EMU-3B instrument operated at 100 kv.

III. RESULTS AND DISCUSSION OF RESULTS

A. Correlation Studies

Films which are essentially structureless after forming (Fig. 1) show a system of lines and spots after exposure to thermal neutrons (Figs. 3, 4, 5, and 6). The density varies directly with the thermal neutron dose and with the concentration of U^{235} in the films. This is taken as evidence that the structure is some manifestation of individual fission events occurring in the films.

The results of the correlation between the observed number of fission events and the number expected on the basis of calculations for fission of U^{235} are presented in Table I. These data show that within experimental error the detection of fission events is substantially

FIG. 6. Transmission micrograph of a 350 A thick UO_2 film after thermal neutron irradiation of $\sim 10^{15}$ nvt. 25 000×.

[7] Item No. 115 obtained from E. Fullam, Inc., P. O. Box 444, Schenectady 1, New York.

TABLE I. Summary of correlation studies.

Plate number	Film thickness	U^{235} concentration	Irradiation atmosphere	Integrated thermal flux nvt	Calculated fissions	Observed tracks	Ratio of observed to calculated
726	100 A	Normal	Air	1.14×10^{16}	2550	2501	0.98
722	100 A	Normal	Air	1.14×10^{16}	1870	2055	1.10
746[a]	100 A	Normal	Air	1.14×10^{16}	645	679	1.05
729	100 A	Normal	Air	9×10^{14}	222	192	0.86
724	45 A	>90%	Air	9×10^{14}	1701	1347	0.79
774	45 A	>90%	Air	2×10^{15}	319	272	0.85
806	156 A	Normal	Air	8.6×10^{15}	470	182	0.39
748[a]	100 A	Normal	Helium	1.14×10^{16}	370	421	1.14
749[a]	100 A	Normal	Vacuum	1.14×10^{16}	485	432	0.89

[a] Specimens irradiated as free films. All others were irradiated in place on the NaCl substrates on which they were formed.

100% for the films 100 A or less in thickness. These data also indicate that there is no significant difference in the efficiency of registration of the fission events between free films and films irradiated in place on the substrates upon which they were formed. In addition, within the limits of environmental conditions established here, i.e., vacuum ($\sim10^{-5}$ mm Hg), air, and helium, no significant effect is noted on the registration efficiency. The experimental error in these measurements arises in the determination of the density of fission fragment tracks from photomicrographs. The possible error in magnification leads to an error in area determination of about $\pm15\%$, which combined with the estimated uncertainties in the determination of U^{235} atoms per unit area ($\sim5\%$) and the dose ($\sim5\%$) gives a total possible error of about $\pm25\%$.

B. Track Structure Observations

1. Transmission Studies

The apparent one-to-one correspondence noted above indicates that each fission event registers as a single, continuous disturbance in the film. The disturbance appears as a spot or line depending on the inclination with respect to the plane of the film of the trajectory of the recoil atoms born in the fission event. Careful examination of the examples of the structure present in these films after irradiation in Figs. 3, 4, 5, and 6 indicates that it is not possible to identify any point along a track with the point at which fission occurred, not to conclude whether the passage of a light or heavy fission fragment gave rise to any particulat line segment. Thus, in the examination of this structure it is not possible to determine the following factors of interest:

1. point at which fission occurred;
2. direction of travel and mass number of the fission fragment associated with any line segment;
3. sense of the inclination of the trajectory of the fission fragment, i.e., which direction along a line emerges through the free surface.

The lack of information on these points hampers the interpretation in many instances; unfortunately these points cannot be resolved with the techniques currently in use.

It is of considerable interest from a radiation damage standpoint to investigate the nature of the disturbances in the films which give rise to the contrast effects which permit observation of this structure. As may be noted in Figs. 3–6 the structure identified as fission tracks invariably appears as light lines or spots. This indicates that the films are more transparent to electrons in the regions of a track than eleswhere. In addition, examination of the longer lines shows that not infrequently the film is broken along the track. This, along with the contrast decrease with increasing film thickness (Figs. 3–6), suggests that local thinning of the film is responsible for the contrast effects observed.

2. Replica Studies

The structure observed in the replicas is shown in Figs. 7 and 8. In that the contrast effects observed here are the result only of the topographical features of the replicated surface as revealed by the shadowing material, the interpretation that the surface has been disturbed by the fission fragment is direct. In Fig. 7 a well-defined furrow may be observed with a more or less regular array of small particles lined up on both sides of the furrow. These furrows are about 100 A in width and 50 A deep, while the displaced material is present as particles 50–100 A in size. The volume of material represented by these particles in many cases approximately equals the volume estimated to fill the furrow; it is not uncommon, however, to observe furrows or portions of a furrow in which there is a complete absence of the displaced material. In Fig. 8 the tracks appear as a linear array of particles or small bulges frequently having a doublet appearance but without a distinguishable furrow. A continual graduation of appearance of the tracks between the structures of Figs. 7 and 8 has been observed, and tracks showing gradual transitions along their lengths are not uncommon. The differences in the disturbances of the surface possibly arise from the variation in depth below the free surface of the path which a fission fragment

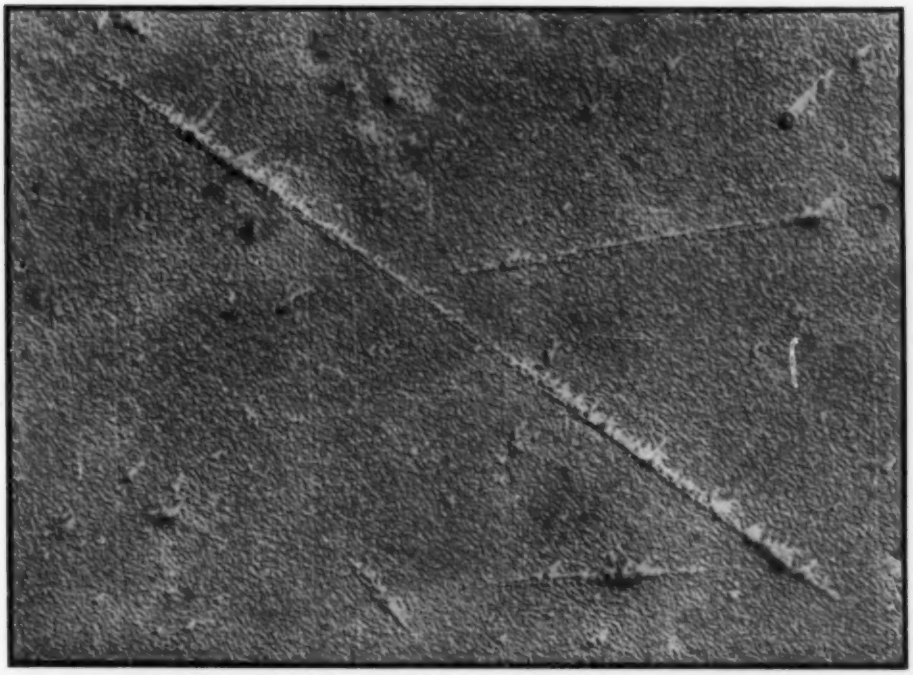

FIG. 7. Electron micrograph of an Au-Cr preshadowed carbon replica taken from the surface of a UO_2 film after thermal neutron irradiation of $\sim 10^{15}$ nvt. 30 000×.

takes in traveling through the material and from the variation in the specific rate of energy loss by a fission fragment along its range. In this interpretation the furrow type of track arises from the passage of the fission fragments in the regions closest to the surface and/or from the higher rates of energy input to the material. The unfurrowed track arises from passage at deeper levels and/or from lower rates of energy input.

The isolated particles and clumps of particles randomly distributed over the surface are present in amounts approximately equivalent to the spot structure observed in transmission. These particles probably represent the surface disturbance resulting from fission fragment trajectories nearly perpendicular to the film. It would be expected that this displacement of material to the surface would be accompanied by the formation of a crater or pore; however, to date such structures have not been detected.

Many of the tracks observed are asymmetrical in that one end tapers gradually while the other end is relatively blunt with clumps of particles and bulging of the film. The relative frequency of this class of tracks appears consistent with the expected frequency of scattering of fission fragments out of the plane of the film. In this case the blunt end is the region in which a scattering event has occurred which deviates the fragment either into the substrate or out through the free surface, either case resulting in termination of the track in a relatively short distance.

The principal result of these replica studies is the observation of the displacement of material at the free surface. The appearance of the track structures indicates that lateral as well as vertical displacement of material occurs, leading to effective local thinning of the film

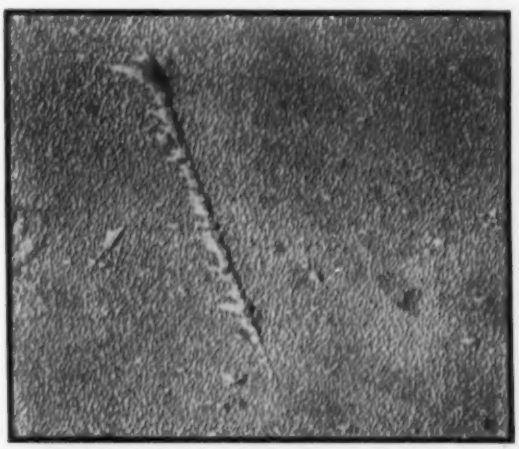

FIG. 8. Electron micrograph of a Au-Cr preshadowed carbon replica taken from the surface of a UO_2 film after thermal neutron irradiation of $\sim 10^{15}$ nvt. 30 000×.

in agreement with the deductions from transmission studies.

In the light of the observations of the replicas, reexamination of the transmission micrographs indicates several features which may be missed with more casual examination. First, many of the longer tracks display to some extent narrow, dark regions immediately adjacent to the light lines. This results from the buildup of material adjacent to the track. Second, in many instances the appearance of a track is different at the two ends; one end is tapered while the other is frequently blunt. This appearance parallels that which is observed in the replicas and suggests that the tapered end is associated with one fragment gradually running out of the surface and the blunt end with the scattering of the other fragment out of the plane of the film.

Observations of this structure have not indicated changes in the films other than those arising from local redistribution of matter along the paths of the fission fragments. The electron diffraction patterns of these films are not detectably changed by the fission fragment damage, at least up to doses an order of magnitude greater than those reported in this investigation. This does not rule out possible changes in the structure of the films that might occur in the close vicinity of the path of the fission fragments since the fractional volume of the film affected at these low doses is very small.

C. Track Length Distribution Studies

It was noted quite early in this work that the frequency of occurrence of long track lengths was significantly less than that which was expected.[8] Tracks in excess of 5 μ in length are quite rare, although track lengths approaching the combined range of the fragments (about 12 μ)[9], should be observed. The expected distribution of track lengths can be easily derived from geometrical considerations. For the case under consideration here of a thin film of thickness, t, which intersects an isotropically distributed system of fission fragment trajectories, the distribution of track lengths in the observational plane is given by

$$F(l)=\frac{t}{(l^2+t^2)^{\frac{1}{2}}}, \qquad (1)$$

where $F(l)$ is the fraction of the tracks having projected lengths greater than l. It is assumed here that each fission event gives rise to a single straight track that competely traverses the film; the finite range of the fragments is neglected. For the case where the track lengths are appreciably greater than the thickness, Eq. (1) can be written in the simpler, approximate form

$$F(l)\approx(t/l). \qquad (2)$$

This is a more useful form of the distribution function, and little error is introduced by its use [for $l>5t$, Eq. (2) differs from Eq. (1) by less than 2%].

The statistics obtained on the track length distributions are presented in Figs. 9, 10, and 11. In examining these curves it is convenient to consider the behavior for short track lengths (0.05 μ to about 1 μ) separately from the long track lengths (greater than 1 μ). For comparison, curves corresponding to Eq. (2) are inincluded in Figs. 9 and 10. In Fig. 10 the experimental curves obtained from films irradiated in situ on rock-salt substrates covering a thickness range of a factor of three are compared.[10] The superposition of these curves in the short track length region is a somewhat surprising result since the theory indicates that the curves for different film thicknesses should have the same slope, as is observed, but should be displaced vertically. This indicates that under these conditions regardless of the actual film thickness an essentially constant effective thickness of about 200 A determines the track length distribution. This suggests that after a fission fragment has penetrated into the substrate, the disturbance of the material along its path affects the film enough to register as part of the track. The

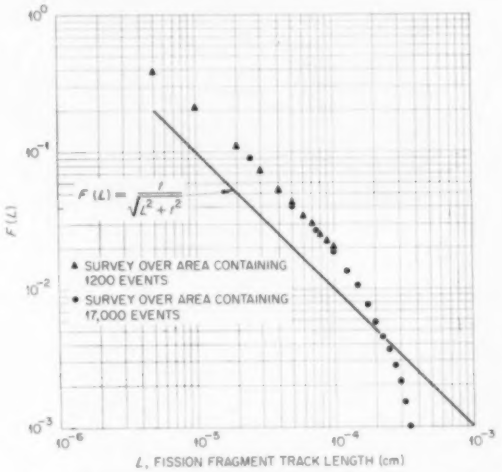

FIG. 9. Fission fragment track length distribution curve for a 100 A thick film of UO_2.

[8] The longest track observed to date is about 6 μ long. In a 100 A thick film we would expect that about 0.2% of the fission events would give initial fission fragment trajectories which, if undeviated, would give rise to tracks 5 μ or longer. In a mosaic type of survey area which was made there was only one track longer than 5 μ in an area containing 40 000 events. If the expected frequency of tracks longer than 5 μ was observed, there should have been about 80 tracks longer than 5 μ as against the one observed. Observations such as this suggested that there were factors limiting the maximum length registered and indicated the need of statistical studies on the track length distribution.

[9] J. D. Eichenberg *et al.*, WAPD-183, pp. 25 and 158 (October, 1957).

[10] The calculated total number of events was used in obtaining the experimental distribution curve for the 156 A thick film owing to the low detection efficiency for tracks having trajectories nearly normal to the plane of the film. All other distribution curves are based on the experimentally determined total number of events.

curve obtained from free films shown in Fig. 11 indicates that this interpretation is probably not correct since the experimental curve lies well above the curve for the same thickness of film irradiated on the substrate, whereas in the absence of the substrate one would expect the curve to follow the theoretical distribution. In addition, the curve obtained with an external source of fission fragments, shown in Fig. 11 and which shows the best agreement with theory, does not support this supposition. The results using an external source tend to rule out significant substrate-film interaction, while the free film results suggest that the solid-gas interface contributes in some manner to the experimentally determined track lengths. One can qualitatively account for the magnitude of the displacement of the experimental curves from the theoretical curves by assuming that the passage of a fission fragment outward through the free surface leads, in some unexplained manner, to

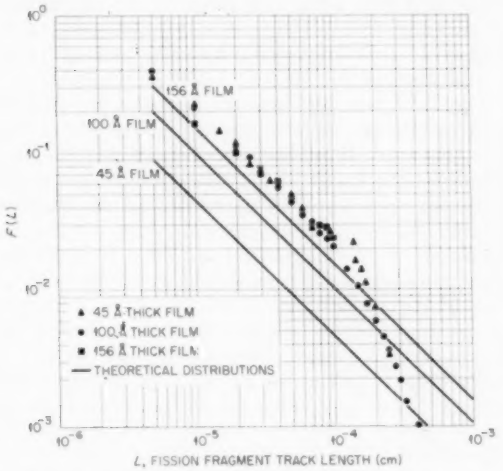

FIG. 10. Fission fragment track length distribution curves for various UO_2 films.

the registration of an extra length of track equivalent to passage through an additional thickness of film t'. One must further assume that the passage of a fission fragment into the film through the free surface does not register any extra track length and that passage of a fragment into the substrate also does not register any extra length. Under these conditions, a value of t' of approximately 100 A for all the experimental conditions gives the approximate magnitude of the deviation from simple geometrical theory. This interpretation is not particularly satisfying; nevertheless, it provides the only relation that appears to reconcile the experimental results in a consistent manner.

The low frequency of occurrence of the long tracks manifests itself in Fig. 9 by the rapid down turn of the curve slightly above 1 μ and by an effective cutoff at a track length of about 4 μ. In the case of the free films ripples

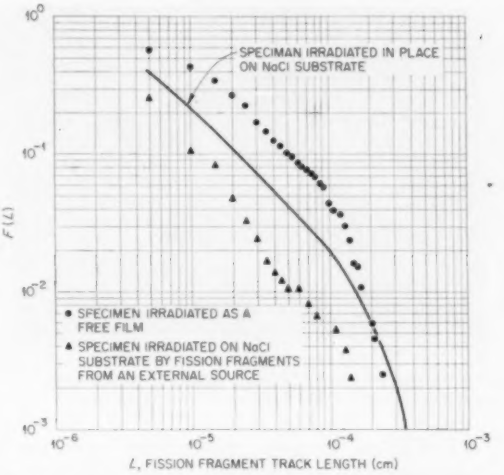
SPECIMAN IRRADIATED IN PLACE ON NaCl SUBSTRATE
● SPECIMEN IRRADIATED AS A FREE FILM
▲ SPECIMEN IRRADIATED ON NaCl SUBSTRATE BY FISSION FRAGMENTS FROM AN EXTERNAL SOURCE
F(L)
L, FISSION FRAGMENT TRACK LENGTH (cm)

FIG. 11. Fission fragment track length distribution curves for 100 A thick UO_2 films irradiated under various conditions.

in the films limit the maximum track length and lead to cutoff at a slightly shorter length. The external source geometry similarly limits the flux of fragments traveling at small angles to the plane of the film and results in shifting the cutoff to a shorter track length. It is not worthwhile to attempt to evaluate the effect of ripples in the film or external source geometry on the long track lengths until a better interpretation is obtained of the results with the simpler geometry of the irradiations on the substrate.

The rapid decrease in $F(l)$ for track lengths greater than about 1 μ probably results from scattering of the fission fragments by nuclear encounters. Encounters for which a fission fragment is scattered in excess of about 2° will in most cases result in the fragment being scattered out of the plane of the film, thereby terminating the track.

The tailing off is more rapid than would be expected for a constant scattering cross section; however, the cross section for Rutherford scattering increases as the energy of the fission fragment decreases. A distribution function calculated in this way using experimental range-energy curves[11] is in qualitative agreement with the observed distribution. Scattering should have some effect on the distribution for track lengths less than 1 μ, but the displacement of the distribution from the theoretical function prevents identification of any scattering component in this region. It is not certain at present whether or not a similar modification is occurring on the long track lengths. This, along with the uncertainty of the cross sections for scattering through angles of less than 2° and the cumulative effect of small angle scatterings, inhibits a quantitative treatment of this problem.

[11] C. B. Fulmer, ORNL-2320, pp. 61–62 (August 1957).

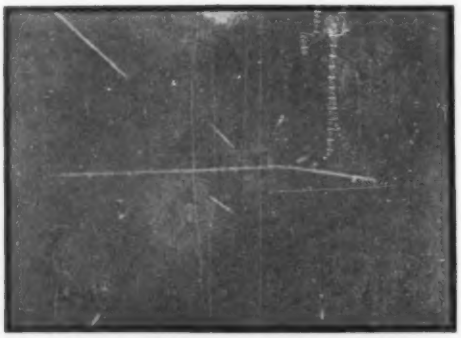

FIG. 12. Transmission electron micrograph of a bent track produced by the interaction of a light fission fragment with a uranium lattice atom. 25 000×.

It is of interest to note that for these conditions the oxygen atoms in UO_2 contribute very little to the scattering process. The mean free path for a scattering event which deflects the fission fragment $\sim 2°$ is approximately ten times greater for scattering from oxygen than from uranium. The energy transfers also differ greatly for the two cases; an encounter of this type involving a fission fragment of mass 100 results in a transfer of about 50 kev to a uranium atom and about 1 Mev to an oxygen atom.

D. Bent Tracks

Examination of large numbers of tracks about 1 μ or longer in length has shown that a portion, on the order of 5%, shows bends representing abrupt changes in direction in excess of about 2°. Small angle bends are most frequent although angles as large as 12° have been observed. Figure 12 is an example of such a track. Bent tracks such as this arise as a result of nuclear encounters of the fission fragments with lattice atoms in which the fragment is scattered in the plane of the film. Figure 12 is typical of most of the bent tracks observed in that there is no indication of a track left by the struck atom, although for a two-body collision the path of the ejected atom must lie in the plane of the film. A very rare type of bent track is shown in Fig. 13 in which it appears that the struck atom has also left a track. In the cases where the paths of the particles are determined before and after the collision, it is possible to carry out a mechanical analysis on the event. The analysis for this event, included in Fig. 13, gives the result that a fission fragment of mass 85 collided with an oxygen atom (mass 16).[12] For this collision about one-half of the energy of the fission fragment was transferred to the oxygen atom. Since the fission fragment must have traveled less than $\frac{1}{10}$ its range, it is estimated that it carried in excess of 70 Mev of kinetic energy,[11] and hence the oxygen atom received about 35 Mev. The estimated rates of energy loss of the fission fragment before and after the collision and of the ejected oxygen atom are high enough to allow registration of all three tracks. A very small number of events of this type have been observed (6), and of these only four have had sufficiently long tracks that meaningful angle measurements could be made. Of these, one did not give a reasonable estimate of the mass number of the fission fragment.

[12] In Fig. 13 θ is the relative deflection angle in the center of mass. For details of the mechanics of the collision process see N. Bohr, Kgl. Danske Videnskab. Selskab, Mat.-fys. Medd. 18, 8 (1948).

E. Energy Input Necessary to Produce Tracks

The general absence of forking of the bent tracks raises questions as to the conditions necessary for the registration of the tracks in the film. The continuous nature of the furrows suggests that we must primarily be observing the consequences of the continuous ionization loss to the material of the film and that the nuclear encounters that impart pulses of energy to the material at several hundred angstrom intervals along the track[13] probably contribute only in a minor manner to the disturbance of the film. In addition the correlation studies indicate that nuclear encounters must contribute little to the track registration since the detection efficiency with the thinnest films is sensibly 100% even though a considerable fraction of the tracks have lengths in the film which are less than the mean free path for encounters which transfer more than 100 ev. The observations on the longest tracks (4–6 μ) indicate that registration occurs for track lengths of the order of one-half the combined range of the fragments. Estimates of the rate of energy loss in solids from typical range-energy curves[11] give an initial rate of about 3000 ev/A and a value of about 1000 ev/A at one-half the range. From this one may estimate that registration occurs for energy inputs down to 1000 ev/A but may not accurately determine the lower limit.

A survey experiment designed to evaluate the possibilities of the present technique with alpha particle and proton bombardments employed a 100 A film of UO_2 depleted in U^{235} upon which a thin layer of lithium oxide enriched in the Li^6 isotope had been evaporated. After irradiation of this composite film no tracks were detected which could be ascribed to the passage through the film of the 2.1-Mev alpha particles or the 2.7-Mev H^3 nuclei formed by the reaction

$$Li^6 + n \rightarrow He^4 + H^3 + 4.8 \text{ Mev}.$$

The alpha particles lose energy to the UO_2 initially at a rate of about 100 ev/A.[14] From this we may conclude that the lower limit of energy input for track registration is in excess of 100 ev/A.

This lower limit on the energy input necessary for track registration accounts for the basic difference between the bent and forked tracks in Figs. 12 and 13.

[13] F. Seitz and J. S. Kohler in *Solid State Physics*, edited by F. Seitz and D. Turnbull (Academic Press, Inc., New York, 1956), Vol. 2, p. 322. A. H. Cottrell, Met Rev. 1, 487 (1956).

In Fig. 12 the angle of deviation is 11.5°. This probably represents an encounter of a fission fragment with a uranium atom since an angle of deviation this large could not occur from an encounter with an oxygen atom by a fission fragment of mass greater than 80. Since the fission yield of fragments with mass number less than 80 is about 0.1%, the probability that this is a fission fragment-oxygen encounter is extremely small. For the case of a fission fragment-uranium atom encounter the mass number of the fission fragment cannot be specified; however, for typical light and heavy fission fragments an energy transfer to the uranium atom of 1.5 to 2 Mev would deflect the fragment by the amount observed. A uranium atom with this amount of energy would dissipate an estimated 400 ev/A by ionization[14] and would not register a track if the lower limit for registration is in the vicinity of the 1000 ev/A deduced above. If this were an encounter with an oxygen atom, the situation would be similar to that given for the forked track in Fig. 13, and registration would be expected. One can account for the very low frequency of forked tracks if the lower limit for the energy loss by ionization necessary for track registration is taken to be 1000 ev/A. On this basis the frequency of occurrence of forked tracks would at most amount to only a few per hundred thousand fission events. This is in line with the observed frequency of forked tracks of which six have been observed in micrographs, which in aggregate represent roughly one-half million events.

The rather large energy input required for track registration is certainly adequate to give rise to the furrow structure observed. If all of the energy appeared as thermal energy it would be sufficient to heat a cylindrical region along the track about 40–60 molecules in diameter to the melting temperature (2176°C). This corresponds to a cylindrical region about 100 A in diameter and corresponds quite well with the experimentally observed size of the tracks. The appearance of the furrows indicates that more than simple melting is involved since material is displaced in the form of discrete particles rather regularly arrayed along the fission track trace. The thermal spike would exert a large hydrostatic pressure which could cause plastic flow in the vicinity of the surface, probably accompanied by extrusion of heated material and perhaps would even "blast" away the material between it and the surface. The more or less regular position of the displaced material along the track suggests that the particular process which leads to the furrowing and bulging must operate in such a fashion that the material is not physically detached (sputtered) while undergoing displacement. If the latter case occurred, one would expect to see the particles distributed laterally over a wider range than is actually observed.

Recent measurements[15] have shown that the passage

$\phi = 5\frac{1}{2}°$
m_1, v_1
m_1, v
m_2, v_2
$\psi = 12\frac{1}{2}°$
$\tan\phi = \frac{m_2 \sin\theta}{m_1 + m_2\cos\theta}$
$\theta = \pi - 2\psi$
IF $\phi = 5\frac{1}{2}°$ AND $\theta = 155°$, $\frac{m_1}{m_2} = 5.3$
IF $m_2 = 16$, $m_1 = 85$

FIG. 13. Transmission electron micrograph of a forked track produced by the interaction of a fission fragment of mass 85 with an oxygen lattice atom. 25 000×.

[14] The average energy loss by ionization per unit path length from charged particles passing through matter is given by

$$-\frac{dE}{dx} = \frac{4\pi e^4 (Z_1^{\text{eff}})^2}{mv^2} NB,$$

where v is the velocity and (Z_1^{eff}) the effective charge on the particle, m the mass, e the charge of the electron, N the number of atoms per unit volume of the stopping material, and B the stopping number of the material. The effective charge on an alpha particle is 2. For a fission fragment Z_1^{eff} may be estimated from

$$Z_1^{\text{eff}} = Z_1{}^{\frac{1}{3}}(hv/2\pi e^2),$$

where Z_1 is the atomic number of the fragment and h is Planck's constant. For fission fragments passing through heavy atoms B is approximately equal to:

$$(4Z_2{}^{\frac{1}{3}}hv)/(2\pi e^2),$$

where Z_2 is the atomic number of the stopping material. For natural alpha particles $Z_2{}^{\frac{1}{3}}$ gives better agreement with experiment. For charged particles passing through light materials B is given by

$$Z_2 \ln(1.123mv^3/\omega e^2 Z_1^{\text{eff}}),$$

where ω is some average oscillation frequency of the electrons in the atom. For UO_2 the uranium and oxygen contributions are calculated separately and then added to give the over-all dE/dx. These equations are only approximately correct but give results which differ by no more than a factor of two from values determined from experimental range-energy curves. For a discussion of the development and use of these relationships see H. A. Bethe and J. Ashkin in *Experimental Nuclear Physics*, E. Segrè, Editor (John Wiley & Sons, Inc., New York, 1953), Vol. I.

[15] B. V. Ershler and F. S. Lapteva, J. Nuclear Energy II, 4, 471 (1957). This is a translation of an article which originally appeared in Atomnaya Energiya I, 63 (1956).

of fission fragments through metal surfaces results in the evaporation of a large number of atoms from the surface. In the case of oxidized uranium surfaces, however, an average of only about 50 uranium atoms was evaporated per fission fragment. If this is the case some evaporation probably occurs during the irradiation of these films, but the magnitude of the number of atoms evaporated per fragment is too small for it to be the major source of contrast. It is not clear, however, that this figure can be directly extrapolated to our system. Some experiments currently in progress are designed to measure the evaporation of uranium atoms from thin films of UO_2 by fission fragments.

IV. SUMMARY

The correlation between the observed and expected number of fission fragment tracks in irradiated thin films of UO_2 has been established as sensibly unity. Detection efficiency less than this was found for the films thicker than 100 A owing to a background texture in the films.

The registration of the tracks in the films is a result of the displacement of material at the surface arising as a consequence of the thermal spike which is associated with the loss of energy by the fission fragment to the film material by electron excitation and ionization. A rate of energy loss in excess of about 1000 ev/A is required to give track registration.

The track length distributions obtained in this work are not well understood at the present time. The distribution for long track lengths can qualitatively be accounted for on the basis of scattering theory. The distributions for short track lengths suggest that some as yet unrecognized free-surface effect may contribute significantly to the track registration.

Observations on bent and forked tracks representing encounters of fission fragments with lattice atoms have been made, and from these observations estimates of the rate of energy loss required for track registration yield a value of about 1000 ev/A. Further observations on bent and forked tracks should be useful in arriving at better estimates of the energy input required for registration.

V. ACKNOWLEDGMENTS

The authors wish to express their thanks to D. K. Holmes for many helpful discussions on the track length statistics and to S. A. Reynolds for the measurements of the alpha counting rates used in estimating the film thicknesses.

JOURNAL OF APPLIED PHYSICS VOLUME 31, NUMBER 12 DECEMBER, 1960

Direct Measurements of the Surface Energies of Crystals

JOHN J. GILMAN
*General Electric Research Laboratory, Schenectady, New York**

(Received July 25, 1960)

By means of quantitative cleavage experiments, the surface energies of several simple crystals have been measured at −196°C. The crystals and their cleavage planes are: LiF(100), MgO(100), CaF_2(111), BaF_2(111), $CaCO_3$(10$\bar{1}$0), Si(111), and Zn(0001). Measured values of their respective surface energies (ergs/cm²) are: 340, 1200, 450, 280, 230, 1240, and 105. The measured values for LiF and MgO are in good agreement with simple ionic lattice theory. Values for the other crystals seem consistent with their binding energies.

Under irreversible conditions an effective surface energy is measured. This quantity increases rapidly with increasing temperature for the metallic crystals, Zn and Fe(3% Si). The increase correlates with increasing plastic flow in these crystals. In contrast, the effective surface energy of LiF and MgO is only moderately dependent on temperature.

A small amount of cadmium (0.1 at.%) markedly increases the cleavage surface energy of zinc.

INTRODUCTION

IN the experiments reported here surface energy measurements were made by the most direct of all methods. Although the surface energy of a solid is one of its most fundamental properties, there is a dearth of experimental values for it. This is because many difficulties are associated with measuring it; especially when indirect methods are used. Therefore, it seemed to be worthwhile to apply cleavage techniques that have been developed in other studies to this purpose. Since the surface energy can be defined as the work that is required to separate a crystal into two parts along a plane, cleavage is a particularly direct way of measuring it. The method consists of measuring the work that is required to cause cleavage per unit area of cleaved surface. If the cleavage is carried out in a reversible fashion, the work of cleavage is equal to the intrinsic surface energy of the crystal. If the cleavage is not carried out in a reversible fashion, the work of cleavage is increased and one speaks of an *effective* cleavage energy.

The cleavage method for measuring surface energies has been previously applied to the case of mica crystals

* Now at Brown University, Providence, Rhode Island.

by Obreimov.[1] Derjaguin *et al.*,[2] and Bailey[3]; but it has not been applied to simpler crystals. Some particularly simple crystals (LiF, MgO, $CaCO_3$, Zn, CaF_2, BaF_2, Si) have been used in the present study so the results can be readily compared with theoretical calculations.

Other methods that have been used for surface energy measurements are: (a) measurements of energy absorption during impact cleavage by Kusnetsov and Teterin[4]; (b) comparisons of the heats of solution of large and small particles of crystal, most recently by Benson, Schreiber, and van Zeggeren[5]; and (c) measurement of the force required to balance the surface tensions of metal wires near their melting points, by Udin, Shaler and Wulff.[6] Method (a) suffers from difficulties associated with achieving reversibility and precision under impact conditions. Both methods (a) and (b) have not yet been applied under conditions where irreversible plastic flow did not accompany the production of new surfaces. Therefore, they have yielded values too high by a factor of about two. Method (c) can only be used at high temperatures, and it does not yield values for individual crystallographic faces.

For historical reviews of the subject, the reader is referred to the books by Partington[7] and Kusnetsov.[8]

EXPERIMENTAL TECHNIQUE

The method used for measuring the work of cleavage is the same principle as the one used by Obreimov[1] for mica. The geometry has been modified somewhat, however, so it can be used for a variety of crystals. A schematic view of the experimental arrangement is shown in Fig. 1. The specimens had the form of rectangular blocks that were partially bisected by cracks. In preliminary experiments, the forces F were applied by slowly pushing wedges into the cracks. However, this method gave poor reproducibility (even when the wedges were carefully made and lubricated) so it was abandoned. The method that was finally adopted for

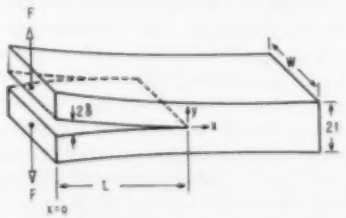

FIG. 1. Schematic cleavage of a crystal.

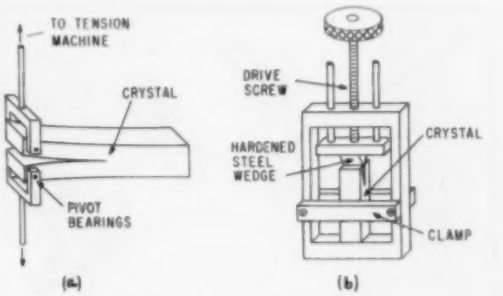

FIG. 2. Methods for applying force to specimens and for making partially cleaved crystals.

applying the forces was to attach a small yoke to each "arm" of a specimen by means of pivot pins. This is shown schematically in Fig. 2(a). The length L of each lever arm then becomes the distance between the crack tip and the pivot point.

Crystals were initially cracked part way along their lengths by means of the jig shown in Fig. 2(b). It consists of a screw-driven hardened steel wedge for starting cracks, and rubber-padded clamps for applying compressive forces to the crystal near the middle of its length. The wedge was ground to a 30° chisel edge with convex curvature so it made initial contact with a crystal at only one point. Compressive stresses produced by the clamps stopped the cracks from running the entire lengths of crystals. The entire jig was immersed in liquid nitrogen for starting cracks at a low temperature.

Measured forces were applied to the partially cracked specimens by means of an Instron tensile-testing machine. The cross-head of the machine moved at constant speed so as to increase the applied force at a rate of about 8 g/sec. When the cracks began to increase in length the applied forces decreased suddenly because of the increased deflections of ends of the crystals. These deflections relaxed the stiff elastic spring of the loading machine. The forces at which this happened were recorded as critical forces for crack propagation.

The dimensions of the crystals were measured by means of a standard micrometer. The crack lengths were measured approximately before each test and more accurately afterwards by microscopic examination of the cleaved surfaces. When a cleavage crack stops moving and later starts to move again, the small cleavage steps that it leaves behind suffer a discontinuous change in direction. These microscopic markings indicate the position of the stopped crack tip.

Several different kinds of crystals were studied: LiF, MgO, CaF_2, BaF_2, $CaCO_3$, Zn, Si, and Fe-Si. The LiF, CaF_2, and BaF_2 crystals were purchased from the Harshaw Chemical Company, MgO from the Norton Company, and the $CaCO_3$ crystals were natural Iceland Spar crystals purchased from Ward's Natural Science Establishment. The silicon crystals were high-purity semiconductor grade crystals provided by the Semi-

[1] J. W. Obreimov, Proc. Roy. Soc. (London) **A127**, 290 (1930).
[2] B. V. Derjaguin, N. A. Krotova, V. V. Karassev, and Y. M. Kirillova, Second Int. Cong. Surf. Act. **III**, 417 (1957).
[3] A. I. Bailey, Second Int. Cong. Surf. Act. **III**, 406 (1957).
[4] V. D. Kusnetsov and P. P. Teterin in *Surface Energy of Solids* (Her Majesty's Stationery Office, London, 1957), pp. 39–42.
[5] G. C. Benson, H. P. Schreiber, and F. van Zeggeren, Can. J. Chem. **34**, 1553 (1956).
[6] H. Udin, A. J. Shaler, and J. Wulff, Trans. AIME **185**, 186 (1949).
[7] J. R. Partington, *An Advanced Treatise on Physical Chemistry* (Longmans, Green and Company, London, 1952), Vol. 3, p. 242.
[8] V. D. Kuznetsov, *Surface Energy of Solids*, translation from the Russian (Her Majesty's Stationery Office, London, 1957).

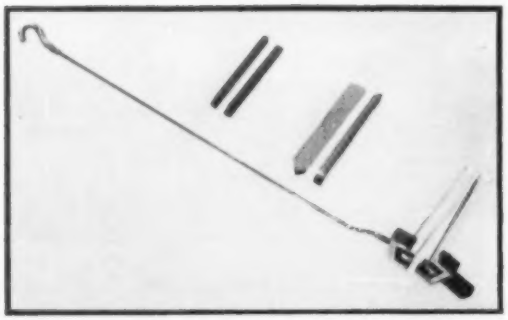

FIG. 3. Specimen holder and typical cleaved crystals. From left to right are shown a silicon, a zinc, and a lithium fluoride crystal.

conductor Products Department of the General Electric Company. The Fe-Si crystals were grown at the General Electric Research Laboratory by Dr. C. Dunn, and the zinc crystals were prepared by the author from 99.999% pure zinc purchased from the New Jersey Zinc Company. This particular collection of crystals was selected primarily on the basis of availability in large enough sizes to allow the present experimental methods to be applied, but an effort was made to include representatives of the ionic, metallic, and covalent types.

Specimens were initially prepared by cleavage or abrasive cutting followed by deep chemical polishing (at least $\frac{1}{4}$ mm removal from all surfaces) to remove the damaged surface layers. At this stage they were rectangular bars 2–6 cm long and with w and $2t$ (Fig. 1) in the range 2–6 mm. They were oriented with their cleavage planes parallel to one set of side surfaces. Cracks 1–3 cm long were then made in them with the jig of Fig. 2(b). Some of the actual specimens are shown in Fig. 3 together with the jig that was used to apply forces to them.

CLEAVAGE MECHANICS

In order to convert the measured critical forces for crack propagation into fracture surface energies one must analyze the mechanics of the system shown in Fig. 1. This has been done using isotropic elasticity theory and following the method of Benbow and Roesler.[9] Except for the selection of reasonable elastic modulus values for the various crystals, their elastic anisotropy was not taken into account. This seems justified because the experimental results show an amount of scatter that exceeds the error that might be expected from using the simple analysis instead of something more elaborate.

Mechanically, a partially cracked crystal is nearly equivalent to two built-in cantilever beams of length L, height t, width w, and moment of inertia $I=wt^3/12$. If a force F is applied at $x=0$, then the bending moment in each beam is $M(x)=Fx$, and the strain energy U due to this bending moment (in each beam) is

$$U=\frac{1}{2EI}\int_0^L M^2(x)dx=\frac{F^2L^3}{6EI}.$$

Then by Castigliano's theorem, the deflection δ due to bending of each beam at the point of application of the force is

$$\delta_0=\frac{\partial U}{\partial F}\bigg|_{x=0}=\frac{FL^3}{3EI}.$$

According to elasticity theory,[10] the deflection curve of the top cantilever in Fig. 1 will be

$$\delta(\text{along } y=t/2)=\frac{Fx^3}{6EI}-\frac{FL^2x}{2EI}+\frac{FL^3}{3EI}+\frac{Ft^2}{8GI}(L-x),$$

where the first three terms give the deflection caused by bending, and the last term gives the deflection caused by shearing; E and G are the Young's modulus and the shear modulus, respectively. The deflection caused by shearing depends on the boundary condition at the built-in end. At most, at the free end ($x=0$) it will be $\delta_1=Ft^2L/8GI$; or, since $G\simeq 3E/8$, $\delta_1\simeq(t/L)^2\delta_0$, and hence will be small in most cases. The strain energy V caused by the shearing stress will be

$$V=(F^2Lt^2/16GI)\simeq(t/L)^2U,$$

and hence also small in most cases. (In the most extreme case of the present work, that of zinc with its small shear modulus, this correction to the measured surface energy amounts to less than 5%.) The boundary condition for this maximum effect of shearing is that at the point $x=L$, $y=t/2$, a vertical element of the cross section is held fixed. A photoelastic study of the stress distribution near a cleavage crack, made by Guernsey and Gilman,[11] indicated that there is not much disturbance of the neutral bending planes on either side of the crack. Therefore, the boundary condition mentioned above is probably not suitable. The actual situation seems to be closer to the condition that at $x=L$, $y=t/2$, a horizontal element of the cross section remains fixed. Then there is no deflection caused by shear.[10] Since the effect of shear is small at most, and perhaps completely negligible, it will be neglected in what follows, and the deflection curve will be taken to be

$$\delta=(F/6EI)(x^3-3L^2x+2L^3).$$

For a moving crack, there is kinetic energy associated with the sidewise deflections of the cantilevers. The mass of an elemental volume in one of the cantilevers is $\rho wtdx$, where ρ is the density, and the velocity of the element is $(d\delta/dt)$, so its kinetic energy is $dT=\frac{1}{2}$

[9] J. J. Benbow and F. C. Roesler, Proc. Phys. Soc. **70**, 201 (1957).

[10] S. Timoshenko, *Theory of Elasticity* (McGraw-Hill Book Company, Inc., New York, 1934), p. 33.

[11] R. Guernsey and J. Gilman, Proc. Soc. Exper. Stress Anal. (1960).

TABLE I. Elastic moduli used in this study.

Crystal	Cleavage plane	Parallel to cleavage plane $1/E_{\parallel}$	Parallel to cleavage plane $E_{\parallel}$ (10^{11} d/cm^2)	Perpendicular to cleavage plane $1/E_{\perp}$	Perpendicular to cleavage plane $E_{\perp}$ (10^{11} d/cm^2)
LiF[a]	(100)	S_{11}	10.2	S_{11}	10.2
MgO[b]	(100)	S_{11}	26.1	S_{11}	26.1
Fe(3% Si)[c]	(100)	S_{11}	13.2	S_{11}	13.2
CaF_2[d]	(111)	$S_{11}-\frac{1}{3}[(S_{11}-S_{12})-S_{44}/2]$	8.62	$S_{11}-\frac{2}{3}[(S_{11}-S_{12})-S_{44}/2]$	11.4
BaF_2[e]	(111)	$S_{11}-\frac{1}{3}[(S_{11}-S_{12})-S_{44}/2]$	6.53	$S_{11}-\frac{2}{3}[(S_{11}-S_{12})-S_{44}/2]$	6.52
Si[f]	(111)	$S_{11}-\frac{1}{3}[(S_{11}-S_{12})-S_{44}/2]$	16.8	$S_{11}-\frac{2}{3}[(S_{11}-S_{12})-S_{44}/2]$	18.6
Zn[g]	(0001)	S_{11}	13.5	S_{33}	4.13
$CaCO_3$[d]	(001)	[h]	14.0	[h]	9.45

[a] C. V. Briscoe and C. F. Squire, Phys. Rev. **106**, 1175 (1957).
[b] M. A. Durand, Phys. Rev. **50**, 449 (1936).
[c] E. Schmid and W. Boas, *Plasticity of Crystals* (F. A. Hughes & Company, Ltd., London, 1950).
[d] H. B. Huntington, *Solid State Physics* (Academic Press, Inc., New York, 1958), Vol. 7.
[e] L. Bergman, Z. Naturforsch. **12a**, 299 (1957).
[f] M. E. Fine, J. Appl. Phys. **26**, 862 (1955).
[g] G. A. Alers and J. R. Neighbours, Bull. Am. Phys. Soc. **2**, 121 (1957).
[h] In the trigonal system, $1/E=(1-n^2)^2S_{11}+n^4S_{33}+n^2(1-n^2)(S_{44}-2S_{13})+2mn(3l^2-m^2)S_{14}$, where l, m, n are direction cosines of the direction of E. For calcite in the perpendicular direction: $l=0$, $m=0.701$, $n=0.713$; in the parallel direction: $l=0$, $m=0.897$, $n=0.442$.

$\rho wtdx(d\delta/dt)^2$. Then the kinetic energy of the whole cantilever is

$$T=\frac{\rho wt}{2}\int_0^L\left(\frac{d\delta}{dt}\right)^2dx$$

but

$$\frac{d\delta}{dt}=\frac{\partial\delta}{\partial L}\left(\frac{dL}{dt}\right)=\left(\frac{\partial\delta}{\partial L}\right)v_c,$$

where v_c is the crack velocity. Upon substitution and integration, one finds that

$$T=12(L/t)^2(v_c/v_s)^2U,$$

where v_s is the velocity of sound $(E/\rho)^{\frac{1}{2}}$. From this it can be seen that for the usual specimen dimensions ($L\simeq 10t$), the kinetic energy is small compared with the strain energy unless the crack velocity is greater than about $v_s/100$.

The energy of the new surfaces that are created when the crack moves forward a distance dx can be found by forming an energy balance for the whole system. This requires that the motion is reversible; a condition that obtains only for slow motion of the crack. This latter condition was obtained in the present work by forming the energy balance at the critical point when crack motion just begins. The work dW done when the crack length increases by dL, must then equal the increase in strain energy dU plus the energy of the newly created surfaces dS if the process is reversible. That is,

$$dW=dU+dS.$$

The incremental work is $Fd\delta_0=(F^2L^2/EI)dL$; and $dU=(F^2L^2/2EI)dL=dW/2$; and, if γ is the specific surface energy per unit area, $dS=\gamma wdL$. Then, the above condition becomes

$$S=3U$$

or

$$\gamma=6F^2L^2/Ew^2t^3. \qquad (1)$$

This is the equation that was used to interpret the measured critical force values in this study. The value of γ that it yields is a minimum when the cracking is reversible, and equals the intrinsic surface energy γ_s of the crystal. When the cracking is accompanied by irreversible processes, the value of γ given by Eq. (1) will take some larger value γ_p which includes the energy absorbed irreversibly plus the intrinsic surface energy.

The value of E that was used throughout is the Young's modulus in the direction of propagation of the crack. It is calculated from the elastic constants. For the cubic crystals with {100} cleavage (LiF, MgO, Fe-Si) it is simply $1/S_{11}$. For the cubic crystals with {111} cleavage (CaF_2, Si) it is $[\frac{1}{3}(S_{11}+S_{12}+S_{44}/2)]^{-1}$. For hexagonal zinc, it is $1/S_{11}$. For calcite ($CaCO_3$) it is $[0.65S_{11}+0.04S_{33}+0.16(S_{44}+2S_{13})-0.64S_{14}]^{-1}$. Wherever values of the elastic constants at 78°K were available (LiF, MgO, Si, and Zn) they were used; otherwise it was necessary to use room temperature values. The various values are listed in Table I.

RESULTS

The experimental results will be described for each crystal species in turn.

a. Lithium Fluoride

The most extensive work was done on LiF crystals because they were more readily available and easily cleaved than the other crystals. At room temperature, plastic flow occurs near the tips of slowly moving cracks in them. Therefore, in order to measure their intrinsic surface energies, it was necessary to carry out the measurements at the boiling point of liquid nitrogen (−196°C) where plastic flow is almost completely suppressed. Proof that flow is suppressed was obtained by etching the cleaved surfaces to look for dislocations, and by examining the patterns of cleavage steps on the same surfaces. It was found that cracks could be stopped and started again in crystals at −196°C causing only barely perceptible changes in the directions and

TABLE II. Cleavage surface energies measured for LiF crystals.

Specimen number	Test conditions	Dimensions (cm) w	t	L	F^* (g)	γ (ergs/cm^2)	Author's choice
LF-2	As-grown crystal No. 3—cracked in $N_2(l)$ and immediately tested in $N_2(l)$	0.262	0.322	2.85	164	530	
6		0.242	0.322	2.30	175	472	
4		0.244	0.338	2.05	210	450	
8		0.242	0.310	2.35	158	450	
9		0.264	0.330	2.35	172	370	
5		0.279	0.325	2.50	166	370	
3		0.274	0.328	2.15	186	360	
10		0.269	0.337	2.15	182	350	
7		0.294	0.322	2.10	195	330	
							340
LF-C	As-grown crystal No. 3—cracked in $N_2(l)$ and then warmed to room temp. in $N_2(g)$ and cooled again in $N_2(l)$ for testing	0.274	0.315	3.0	193	800	
B		0.292	0.317	2.9	185	600	
A		0.290	0.327	1.9	290	580	
G		0.498	0.330	1.6	580	550	
D		0.277	0.319	2.8	174	530	
E		0.508	0.366	2.6	412	510	
F		0.485	0.368	2.5	390	460	
LF-R6	As-grown crystal No. 1—cracked in $N_2(l)$ and then warmed to room temp. in $N_2(g)$ for testing	0.122	0.100	2.4	205	830	
R3		0.284	0.333	2.3	270	730	
R4		0.292	0.332	3.0	188	580	
R7		0.422	0.345	1.1	785	580	
R5		0.269	0.332	2.9	178	570	
R2		0.259	0.332	2.8	150	390	
R1		0.259	0.342	1.6	220	260	
LF-BK5	Crystals compressed ~2.5% in compression at room temp and then cracked and tested in $N_2(l)$	0.290	0.322	2.2	350	1140	
BK2		0.224	0.345	2.5	250	1080	
BK1		0.233	0.350	1.9	335	980	
BK4		0.233	0.322	2.1	255	860	
LF-NA1	Crystals given neutron dose of 32×10^{14} nvt and then cracked and tested in $N_2(l)$	0.307	0.160	1.4	107	330	
NA2		0.312	0.157	0.9	160	310	

numbers of cleavage steps. Dislocation etch pits were observed, but these were confined to thin layers on the cleavage surfaces (less than 10^{-4} cm thick). Estimates of the amount of energy that could have been absorbed by forming and moving the dislocations indicate that it is negligible in comparison with the intrinsic surface energy. The estimates were based on the plastic work done by each dislocation as it moved into a crystal under a stress approximately equal to the flow stress. The amount of plastic flow that occurs depends, of course, on the hardness of a crystal. In the present work the crystals were moderately hard (room temperature bending yield stress equal to 890 g/mm^2).

At the top of Table II, the measured values for nine specimens that were cleaved from the same large crystal are given. These specimens were all partially cracked while they were immersed in liquid nitrogen, and then were quickly transferred to a liquid nitrogen bath that was mounted on the testing machine. It may be seen that the measured surface energy values spread over the range of 330–530 ergs/cm^2. Part of this spread is caused by experimental error, but much of it can be correlated with the density of cleavage steps on the cracked surfaces. This ranged from 7–66 step-lines/cm. The steps were introduced by errors in the alignment of the initial crack with respect to the cleavage plane, or by twist-type subgrain boundaries. Even without correcting for the effect of cleavage steps, the majority of the results lie in the range of 330–400 ergs/cm^2; and, since the *lowest* values measured by this method should approach the reversible value most closely, it is believed that 340 ergs/cm^2 represents the intrinsic surface energy of the {100} planes of LiF.

The second set of data in Table II shows the effect of warming up a crystal between the time it was initially cracked and the time of testing. Plastic relaxation occurred near the crack tips while they were warm, and this raised the subsequently measured surface energy values. The effect is measurable but not large, indicating that small amounts of plastic relaxation would not change the first set of data discussed above.

A surprising result is presented by the third set of data. It was expected that large amounts of energy would be absorbed by slowly moving cracks at room temperature in LiF because these crystals are quite plastic at this temperature. However, this is not the case. The measured values have a considerable spread, but even the highest one is only about two and one-half times the intrinsic surface energy of LiF. Such low cleavage surface energy reflects the brittleness of LiF at room temperature even though it exhibits plasticity in slow bend tests.

TABLE III. Cleavage surface energies measured for MgO crystals.

Specimen number	Test conditions	Dimensions (cm) w	t	L	F^* (g)	γ (erg/cm^2)	Author's choice
MG-2	As-grown crystal cracked	0.360	0.224	2.4	381	1370	
3	in N_2(1) and immediately	0.363	0.319	1.8	876	1270	
X2	tested in N_2(1)	0.386	0.250	2.3	1089	1140	
							1200
MG-Y1	As-grown crystal cracked in	0.363	0.238	1.8	863	3000	
Y3	air at 25°C and tested in	0.238	0.266	2.6	413	2380	
Y2	air at 25°C	0.238	0.266	2.3	404	1790	
MG-X1	As-grown cracked in N_2(1) and tested in air at 25°C	0.386	0.250	2.3	590	1720	
MG-4	As-grown cracked in air at	0.323	0.238	2.7	375	1610	
5	25°C and tested in N_2(1)	0.231	0.211	1.3	410	1260	

The fourth set of data in Table II shows how prestrain affects cleavage in liquid nitrogen. It increases the energy absorption by a factor of about three by markedly increasing the density of cleavage steps on the fractured surfaces.

Finally, it can be seen from the last set of data in the table that substantial radiation damage has but little effect on the surface energy. In other words, the surface energy of LiF is not very structure sensitive. As would be expected, the surface energy depends simply on the atomic binding strength per unit area of surface, and if a small fraction of the atomic bonds is damaged by radiation, this has only a small effect on it.

b. Magnesium Oxide (Periclase)

The results given in Table III for MgO follow the same pattern as for LiF, but the numbers are larger. The specimens in this case were cleaved out of large irregular chunks that were purchased from the Norton Company. The chunks were colorless, but not more than about 99.9% pure. Specimens were obtained by first sawing rectangular blocks from the chunks with the flat sides parallel to {100} planes. Then, by successively bisecting the blocks by means of cleavage, several slender rods could be obtained from each block. From tests of these rods it is concluded that the surface energy of the {100} planes of MgO is about 1200 ergs/cm^2. As in the case of LiF, although MgO exhibits plasticity at room temperature, its fracture surface energy is quite low. This is consistent with its brittle behavior at room temperature.

c. Calcium Fluoride (Fluorite)

Large crystals of CaF_2 were sawed into slabs with the large faces of the slabs parallel to (111) planes. The large faces were then optically polished with aluminum oxide powder. Next the slabs were sawed into rectangular rods, and the sawed faces were polished. Finally the rods were partially cleaved and tested. Their top and bottom faces were cleaved {111} surfaces while their side surfaces were polished {112} surfaces, and the direction of crack propagation was ⟨110⟩.

The cleavage surfaces of the CaF_2 crystals showed very few cleavage steps, and no evidence at all of plastic relaxation at the tips of stopped cracks. This is consistent with the relatively small amount of scatter in the data of Table IV. The surface energy of the {111} planes of CaF_2 is about 450 ergs/cm^2.

d. Barium Fluoride

Barium fluoride specimens were prepared in the same way as calcium fluoride. The formation of cleavage cracks was quite reversible in this case because plastic flow and cleavage steps were nearly absent. In fact, the most perfect crystal surfaces that the author has ever seen resulted. This made it difficult to determine the initial lengths of cracks and caused scatter in the results (Table V). The average of the measured values is taken to be the surface energy of the {111} plane of BaF_2; 280 ergs/cm^2.

TABLE IV. Cleavage surface energies measured for CaF_2 crystals.

Specimen number	Test conditions	Dimensions (cm) w	t	L	F^* (g)	γ (erg/cm^2)	Author's choice
CA-2a	As-grown crystal, cracked in	0.246	0.465	2.1	313	490	
4a	N_2(1) and immediately	0.236	0.454	1.5	405	470	
3	tested in N_2(1)	0.233	0.452	1.8	336	440	
4b		0.236	0.223	1.3	154	440	
2b		0.246	0.229	1.4	152	420	
							450
CA-1	As-grown cracked and tested	0.241	0.229	1.3	154	390	
2	in air at 25°C	0.243	0.452	2.3	222	320	

TABLE V. Cleavage surface energies measured for BaF_2 crystals.

Specimen number	Test conditions	Dimensions (cm) w	t	L	F^* (g)	γ (ergs/cm²)	Author's choice
BA-1	As-grown crystal, cracked in liquid N_2 and immed. tested in liquid N_2	0.188	0.257	1.68	86	304	
2		0.188	0.257	1.52	78	207	
3		0.188	0.258	1.60	79	230	
5		0.185	0.254	1.35	108	333	
6		0.183	0.250	3.31	43	335	
							280

e. Calcium Carbonate (Calcite)

Slabs about $\frac{3}{16}$-in. thick were cleaved from natural Iceland Spar rhombs. This can be readily accomplished if a rhomb is cut with two parallel faces that are perpendicular to the remaining four cleavage faces. Such a block of crystal can be successively bisected parallel to one set of cleavage faces if a convex chisel is driven into the center of one of the ground faces (excessive crushing occurs if one tries to drive a chisel into an edge).

The slabs (with cleavage planes as their largest faces) were cemented to glass slabs with glycol pthalate, while being careful to avoid thermal stresses by heating and cooling the whole assembly uniformly. After the slabs had been sawed into rods, the side faces of each rod were optically polished with carborundum powder.

After many attempts it was found that longitudinal cracks would not run straight through mechanically polished specimens. Therefore, several crystals were given additional chemical polishing treatments. They were repeatedly dipped into conc HCl for 5–10 sec followed by an alcohol rinse and drying in an air blast. This treatment was successful in eliminating the defects that had previously caused premature cracking.

Table VI shows the data for calcite crystals that were partially cracked in liquid nitrogen and then tested while they were still immersed in liquid nitrogen. Their cleavage surfaces were quite flat and only a few new cleavage steps appeared at the places where the cracks stopped in them. It is concluded that the surface energy of $\{10\bar{1}0\}$ planes in calcite is about 230 ergs/cm².

f. Silicon

Of all the crystals, silicon was the most difficult to test because longitudinal cracks in it have a strong tendency to turn and run out the side of a specimen on one of the transverse {111} planes. Out of 12 specimens that were completely prepared for testing, only two yielded good results. Rectangular specimen rods were cut out of a cylindrical crystal of silicon that had been grown by the floating-zone technique. One set of side faces were cut parallel to a (111) plane and the lengths of the bars were parallel to ⟨112⟩ directions. A narrow slot was cut into one end of each bar parallel to the oriented (111) plane as a means for starting a crack. Small holes for the pivot points were ultrasonically drilled on either side of each slot. The specimens were then chemically polished in "white polish" ($HF+HNO_3$). Next the base of each slot was scratched by gently drawing a SiC-coated thread over it. The purpose of this was to facilitate the initiation of cleavage. Finally, each specimen was initially cleaved while immersed in liquid nitrogen, and then immediately tested in liquid nitrogen.

The results of the two successful tests on silicon in Table VII agree with each other quite well so it is concluded that the surface energy of the {111} planes of silicon is about 1240 ergs/cm².

g. Zinc

High purity zinc crystals were grown by the author in the form of 6-mm square rods with the (0001) basal plane lying parallel to one set of side faces. Specimens

TABLE VI. Cleavage surface energies measured for $CaCO_3$ crystals.

Specimen number	Test conditions	Dimensions (cm) w	t	L	F^* (g)	γ (ergs/cm²)	Author's choice
CA-1	Natural Iceland spar cracked in $N_2(l)$ and immediately tested in $N_2(l)$	0.282	0.386	1.30	431	280	
2		0.261	0.320	1.42	254	240	
3		0.259	0.312	1.12	297	220	
							230

TABLE VII. Cleavage surface energies measured for silicon crystals.

Specimen number	Test conditions	Dimensions (cm) w	t	L	F^* (g)	γ (ergs/cm²)	Author's choice
S-10	Semiconductor grade silicon, silicon, cracked and tested in $N_2(l)$	0.220	0.284	0.85	749	1250	
4		0.193	0.310	1.01	622	1230	
							1240

TABLE VIII. Cleavage surface energies measured for Zn and for (Zn+$\frac{1}{10}$% Cd) crystals.

Specimen number	Test conditions	Test temperature (°C)	Dimensions (cm) w	t	L	F^* (g)	γ (ergs/cm²)	Author's choice
Zn-3a	High purity zinc, cracked in		0.574	0.283	0.6	890	143	
1	$N_2(l)$ and immediately		0.574	0.284	1.0	450	115	
2a	tested in $N_2(l)$		0.563	0.276	0.9	410	89	
ZN-3b	High purity zinc, cracked in		0.574	0.283	1.1	710	347	105
4B	$N_2(l)$ and tested in acetone at (−78°C)		0.594	0.292	1.3	635	324	
ZC-4a	Zinc +0.1% cadmium in $N_2(l)$ and then immediately tested at various temperatures	−196	0.568	0.279	0.9	1615	1150	
1		−196	0.541	0.264	2.4	417	780	
4b		−78	0.568	0.279	1.1	1920	2700	
4c		−25	0.568	0.279	1.2	2360	4570	
2a		+25	0.525	0.260	2.2	1180	5930	
4d		+25	0.568	0.279	1.2	2530	5620	

about 4 cm long were cut from these rods, and one end of each specimen was cut to a chisel shape as may be seen in Fig. 3. The purpose of this was to provide a place where cleavage could start at a point and would therefore tend to spread along a single cleavage plane. This is especially important for highly anisotropic crystals like zinc where the energies of cleavage steps are very high. After the chisel ends had been formed, the crystals were heavily chemically polished to remove the damaged surface layers. Finally, the zinc crystals were partially cracked, and then tested while they were immersed in liquid nitrogen. Table VIII gives the results.

The high purity zinc crystals were tested at −78°C in addition to the −196°C tests. At the higher temperature, the cleavage surface energy is considerably greater. At temperatures above −78°C the crystals were so soft that they bent excessively before enough force could be applied to them to cause cleavage.

Zinc crystals containing cadmium (0.1%) were also tested. They had considerably higher (an order of magnitude) yield strengths than the pure zinc crystals, so they could be tested at all temperatures from −196 to +25°C. A plot of the variation of the cleavage surface energy for zinc with temperature is shown in Fig. 4. It is not surprising that the cleavage surface energy increases rapidly with increasing temperature in the ductile-brittle transition range of zinc. However, it was surprising to find that cadmium increases the surface energy of zinc even at low temperatures. This seems to mean that the polarizable cadmium atoms form strong "bridges" between the (0001) cleavage planes of zinc.

As the cleavage surface energy of zinc increases with increasing temperature, characteristic changes in the appearances of the cleaved surfaces are observed. These have been interpreted as indications of plastic glide that occurs in directions transverse to the basal planes.[12] It is this transverse glide that absorbs increased amounts of energy during cleavage at higher temperatures.

[12] J. J. Gilman, J. Appl. Phys. **27**, 1262 (1956).

h. Iron-Silicon (3% Si)

The iron-silicon crystals were grown by the strain-anneal method in strip form with {100} planes parallel to the faces and edges of the strip. Specimens were sawed out of the strips and then heavily chemically polished. One end of each specimen was notched to facilitate crack initiation. Because of the large forces that had to be applied to these crystals in order to cleave them, they could not be held by pivot bearings. Instead, small holes were drilled near their notched ends, and hard steel pins were inserted in the holes, and used to apply the cleavage forces.

At −78°C the force required to make iron-silicon cleave is so large that specimens prefer to break on a transverse cleavage plane instead of giving longitudinal cleavage. The force at which this occurs corresponds to

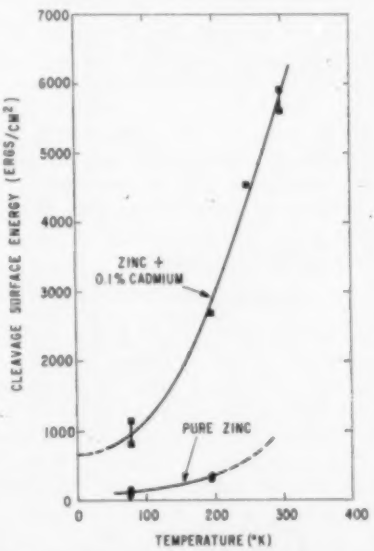

FIG. 4. Effect of temperature on the cleavage of zinc.

TABLE IX. Cleavage surface energies measured for Fe+3% Si crystals.

Specimen number	Test conditions	Dimensions (cm) w	t	L	F^* (g)	γ (erg/cm²)
SF-I	As-grown crystal, cracked and tested in H_2(l) (−250°C)	0.079	0.304	1.30	204	1360
SF-E	As-grown, cracked and tested in N_2(l) (−196°C)	0.078	0.312	1.04	1040	27 700
A		0.116	0.429	1.80	1410	26 400
C		0.081	0.310	1.36	726	23 000
D		0.086	0.312	1.23	863	23 000
B		0.081	0.302	0.90	1071	22 500
SF-G	As-grown, cracked and tested in acetone at −78°C	0.080	0.308	1.2	>2630	>240 000
SF-L	As-grown, prestrained 3% at 25°C, then cracked and tested in N_2(l)	0.084	0.313	1.4	976	40 000
J		0.084	0.312	1.5	472	10 000

a cleavage surface energy in excess of 240 000 ergs/cm² at −78°C (Table IX). At −196° the surface energy is still quite high but is at least an order of magnitude less than it is at −78°C. By the time −259°C (liquid hydrogen) has been reached the surface energy is down by another order of magnitude to about 1360 ergs/cm². This is about what would be expected for the intrinsic surface energy of iron, but only one test result was obtained so no conclusion about its significance can be reached.

The bottom set of data in Table VII show that, just as in the case of LiF, prestrain has little effect on the surface energy.

Much of the energy that is absorbed by cracks in iron-silicon crystals at −196°C is a result of twinning. Twinned regions are found near and on the edges of cracks.

COMPARISON WITH THEORY

An estimate of the work that is required to separate two internal surfaces of a crystal can be obtained by approximating the attractive stress between the two surfaces by a sine function. The stress is taken to be zero when the surfaces have their normal separation distance d_0. As the distance between the surfaces increases by an amount y greater than normal, the stress rises to a maximum value σ_0 and then drops to zero again when y exceeds the range a of the attractive forces. This can be expressed as

$$\sigma=\sigma_0 \sin[(\pi y)/a] \quad 0<y<a.$$

The strain between the surfaces is y/d_0 and for small strains the stress is given by Hooke's law; $\sigma=E(y/d_0)$. Therefore, since the sine is equal to its argument for small y, the value of the maximum stress can be evaluated; it is $Ea/\pi y$. The work that is done in moving the surfaces from their initial positions, $y=0$, to positions where they are no longer attracted by each other, $y=a$, is

$$\int_0^a \sigma dy=\frac{Ea}{\pi d_0}\int_0^a \sin\frac{\pi y}{a}dy.$$

Two surfaces are created by this amount of work, so the specific surface energy is

$$\gamma=(E/d_0)(a/\pi)^2.$$

Surface energy values estimated from the above elementary theory are listed in Table X. The d_0 values that were used in making the calculations are simply distances between the crystallographic cleavage planes. In the case of LiF and MgO, for example, d_0 equals one-half the cubic unit cell size. The a values were taken to equal the atomic radii of atoms lying in the cleavage planes. The elementary theory gives values that are uniformly high but of the same order of magnitude as the experimental values.

The simplest atomistic theory of surface energies is that of Born and Stern[13] which considers the electrostatic attractions between ions in rock-salt-type crystals, and hard-shell repulsions. The resulting surface energies for {100} and {110} surfaces are

$$\gamma_{100}=0.0145[(Ze)^2/r^3] \quad \text{(cgs units)}$$
$$\gamma_{110}=0.0394[(Ze)^2/r^3] \quad \text{(cgs units)},$$

where e is the electronic charge, Z is the valence, and r is the interionic distance. Table X shows that the agreement between values given by this theory and the present experimental results is fair. Better agreement is obtained with the theory of Glauberman[14] who used the same equation for the interionic potential as Born and Stern, but allowed some contraction of the surface layers to occur perpendicular to the surface plane. According to him, the cleavage surface energy should be

$$\gamma_{100}=0.0124[(Ze)^2/r^3],$$

which is in remarkably good agreement with the experimental values.

Similar calculations, using somewhat different potential energy equations have been made by Lennard-Jones

[13] M. Born and O. Stern, Sitzber. preuss. Akad. Wiss. Physik. math. Kl. 901 (1919).
[14] A. E. Glauberman, Zhur. Fiz. Khim. **23**, 124 (1949).

TABLE X. Comparison of experimental and theoretical surface energy values (ergs/cm²).

Crystal	NaCl	LiF	MgO	CaF_2	BaF_2	$CaCO_3$	Si	Zn	Fe(3% Si)
Cleavage plane	(100)	(100)	(100)	(111)	(111)	(1010)	(111)	(0001)	(100)
Experimental									
This study	···	340	1200	450	280	230	1240	105	1360(?)
Benson, Schreiber, Van Zeggeren	276	···							
Hutchinson, Manchester	366	···							
[a] Jura, Garland	···	···	1040						
Lipsett, Johnson, Mass	381	···	···						
[b] Kusnetsov, Teterin	300	···	···	146	···	78			
Liquid at melting point (extrapolated to 0°K)	190	350							
Atomic theory									
Born, Stern	150	420	1440						
Glauberman	130	360	1230						
Lennard-Jones, Taylor	96	···	1360						
Dent	77	···							
Biemuller	87	170							
Shuttleworth	155	···							
Van Zeggeren, Benson	188	···							
van der Hoff, Benson	···	560							
Klobe	···	···	···	<1019					
Ormont (from subl. energy)	···	···	···	···	···	···	1232		
Estimated from elastic modulus	310	370	1300	540	350	380	890	185	1400

[a] Heat of solution method.
[b] From impact cleavage.

and Taylor,[15] and by Dent.[16] Biemuller,[17] Verwey,[18] Shuttleworth,[19] and Van Zeggeren and Benson[20] used the complete Born-Mayer potential equation, thereby attempting to include the effects of ionic polarization on the surface energy. The results for LiF do not agree with the experimental values as well as do the simpler theories. A quantum-mechanical approach was used by van der Hoff and Benson,[21] but it gave a value for LiF that is too large. The results of these various atomic theories are summarized in Table X. Also included are an estimate for CaF_2 by Klobe[22] and for Si by Ormont.[23] Data for NaCl are included in the table because more work has been done for this crystal than for any other.

Although there is considerable spread in the various values given in Table X, they change in a consistent way from one crystal to another. This, together with the good agreement between the simple ionic theory and the experimental values, indicates that the present experimental method is suitable and reliable. The experimental value determined by Jura and Garland[24] for MgO smokes using the heat of solution method agrees quite well with the present work. For NaCl, the measurements by Lipsett, Johnson and Mass,[25] by Hutchinson and Manchester,[26] and by Benson, Schreiber, and Van Zeggeren[5] all are high in comparison with the theoretical values. This probably resulted because they used powders that were prepared by filing or crushing. Such damaged powders would be expected to contain a variety of defects that would contribute to an increasing heat of solution with decreasing particle size.

Comparison may also be made with estimates based on measurements by Jaeger[27] of the surface tensions of the alkali halides just above their melting points. Correction for the effect of temperature gives the two values listed in Table X for the surface energies of NaCl and LiF at 0°K.

Since the present measurements were carried out with the specimens immersed in liquid nitrogen rather than in vacuum, the effect of the environment on the measurements should be considered. It is known that the environment can markedly influence the cleavage of mica,[2] but this is associated with the fact that the cleavage surfaces are charged and discharging occurs between them through the environment. Perhaps the best evidence that the environment had no major effect on the present measurements is provided by the consistencies of the results and their good agreement with theory and other experiments. Also, since the molecular

[15] J. E. Lennard-Jones and P. A. Taylor, Proc. Roy. Soc. (London) **A109**, 476 (1925).
[16] B. E. Dent, Phil. Mag. **8**, 530 (1929).
[17] J. Biemuller, Z. Physik **38**, 759 (1936).
[18] E. J. W. Verwey, Rec. trav. chim. **65**, 521 (1946).
[19] R. Shuttleworth, Proc. Phys. Soc. (London) **A62**, 167 (1949).
[20] F. van Zeggeren and G. C. Benson, J. Chem. Phys. **26**, 1077 (1957).
[21] M. E. van der Hoff and G. C. Benson, J. Chem. Phys. **22**, 475 (1954).
[22] Reported by M. Born and M. Goeppert-Mayer in Handbuch der Physik **24-2**, 764 (1933).
[23] B. F. Ormont, Doklady Akad. Nauk. SSSR **106**, 687 (1956).
[24] G. Jura and C. W. Garland, J. Am. Chem. Soc. **74**, 6033 (1952).
[25] S. G. Lipsett, F. M. G. Johnson, and O. Mass, J. Am. Chem. Soc. **49**, 1940 (1927).
[26] E. Hutchinson and K. E. Manchester, Rev. Sci. Instr. **26**, 364 (1955).
[27] Jaeger, Z. anorg. u. allgem. Chem. **1010**, 1 (1917).

diameter of N_2 is about 2.2 A, it would not be able to absorb on the fresh cleavage surfaces in the immediate vicinity of the crack tip. It would only be able to adsorb some distance behind the crack tip where the surfaces were separated by more than 2.2 A. Thus the heat of adsorption would probably be lost as heat to the crystal and would not reduce the measured surface energy. Furthermore, at least for the ionic crystals the free energy change upon adsorption of N_2 is small. Measurements by Orr[28] for N_2 on KCl give a value of about 1 kcal/mol of surface at -196°C. Since the adsorption is due to van der Waals forces, it should be proportional to the polarizability of the substrate. This would reduce the free energy to about 0.2 kcal/mol for N_2 on LiF which is only about 5% of the total surface energy of 3.9 kcal/mol. The free energy of N_2 adsorption would be only about 2% of the total surface energy in the case of MgO.

FUTURE IMPROVEMENTS

The *precision* of the cleavage method is relatively low because of experimental scatter. The primary cause of this seems to be variations in the cleavage step densities amongst specimens. These variations could be reduced by (a) using more nearly perfect crystals with fewer subgrain boundaries in them; (b) cleaving at lower temperatures to further reduce plastic flow; (c) improving the technique used to start cracks so they are started more nearly parallel to a cleavage plane.

The *accuracy* of surface energy measurement could be improved by studying the elastic deflections in the cleavage specimens in detail. This can be done experimentally by means of the optical interference fringes that can be formed between the surfaces of a crack. Anisotropic elastic theory can be used to predict the deflections more accurately than was done in this study. Although the gaseous atmosphere does not seem to play an important role in these experiments, this should be investigated systematically.

Many pure crystals are so soft (even at low temperatures) that the cleavage method cannot be applied to them, but adding impurities to many of them would cause enough hardening to allow the method to be applied. By making measurements as a function of purity one could probably find the surface energy of the pure crystal by extrapolation.

[28] W. J. C. Orr, Proc. Roy. Soc. (London) **A173**, 349 (1939).

SUMMARY

By means of quantitative cleavage, the surface energies of LiF, MgO, CaF_2, BaF_2, $CaCO_3$, Zn, and Si crystals have been measured at -196°C. The measured values for LiF and MgO are in good agreement with simple ionic theory.

It has been found that the cleavage surface energy of LiF is only moderately dependent upon increasing temperature and upon plastic prestrain. It is quite independent of radiation damage. The cleavage surface energy of MgO is also relatively independent of temperature.

Zinc crystals that contain a small amount of cadmium (0.1%) are considerably more difficult to cleave than pure zinc crystals. The cleavage surface energy of zinc increases rapidly with increasing temperature, and the increase is accompanied by increasing nonbasal glide.

Iron (+3% Si) crystals absorb large amounts of energy through twinning when they are cleaved at -196°C, but they become completely brittle at -250°C. For temperatures of -78°C and greater these crystals cannot be cleaved under static conditions.

It is believed that the cleavage technique as described has been established as a reliable method for directly measuring crystal surface energies. Some suggestions for future improvement of the method are made.

ACKNOWLEDGMENTS

Considerable patience and skill were required to perform the experiments described here. These were provided by Mr. V. J. DeCarlo. Mr. R. Grubel of the Semiconductor Products Department of the General Electric Company kindly furnished a large silicon crystal. Dr. C. G. Dunn provided iron-silicon crystals. Mr. L. Nesbitt gave advice about performing tests in liquid hydrogen. Helpful comments on the manuscript were given by Dr. J. R. Low, Dr. G. W. Sears, Dr. G. Ehrlich and Dr. R. L. Fullman of the General Electric Research Laboratory. Dr. B. W. Roberts kindly checked the elastic moduli of calcite parallel and perpendicular to the cleavage plane by the pulse-echo technique.

JOURNAL OF APPLIED PHYSICS VOLUME 31, NUMBER 12 DECEMBER, 1960

Production of Dislocation Loops by a Combined Climb and Glide Mechanism

J. T. FOURIE* AND H. G. F. WILSDORF
The Franklin Institute Laboratories, Philadelphia 3, Pennsylvania
(Received July 25, 1960)

Studies of dislocations in elongated aluminum crystals by diffraction electron microscopy revealed narrow dislocation loops lying parallel to ⟨112⟩. These loops formed only behind screw dislocations, their long parts then having edge character. Four mechanisms have been proposed to account for the formation and stabilization of the narrow loops through the condensation of point defects.

INTRODUCTION

ELECTRON micrographs of thin metal foils gained from deformed bulk materials have repeatedly shown structures of tangled and kinked dislocation clusters which have been called "dislocation tangles," "bird nests," or "cotton wool structure." In a recent paper[1] such tangles were explained through the condensation of vacancies and possibly interstitials on glide dislocations initially present in the form of prismatic dislocation loops or voids, clusters, or simply in supersaturation. It was suggested that moving glide dislocations caused such defects to interact with themselves so as to produce isolated prismatic loops or large kinks pinning them locally. The dislocations would bow out between the pinning points; and, in addition, parts of the large kinks or loops were expected to emit dislocations by the Frank-Read mechanism. The final result of all these processes together is the formation of the typical dislocation tangles; and, in order to avoid repetitious descriptions, the simultaneous action of some or all of the above mechanisms was called dislocation "mushrooming."

In more recent experiments thin foils obtained from preoriented deformed single crystals have been examined. By and large, the previous results and conclusions have been substantiated. In addition, many narrow and comparatively very long dislocation loops were observed. Their evaluation made it possible to recognize additional processes which may take place in the mushrooming mechanism.

EXPERIMENTS

Experiments were carried out on aluminum single crystals of high purity (99.999%) with rectangular cross section (0.8×10 mm). Specimens for examination by diffraction electron microscopy 2000 A to 4000 A thick were obtained through electropolishing from both sides.[2] Crystal orientations were chosen for the present investigation which made it possible to distinguish the dislocations on the primary slip system from those on other systems and also to prepare, at will, thin specimens with predominantly edge or screw dislocations.

Examples of the most spectacular observation of this investigation, namely, the long narrow loops mentioned already, are shown in Figs. 1 and 2. The loops are mostly 1000 A to 5000 A long and a few hundred angstroms in width. They are present in specimens prepared from crystals strained 4–12%, but only if the thin films are of that orientation which allows dislocations of screw type to be seen. Obviously then, the loops have formed in conjunction with moving screw dislocations but not with edge dislocations. The loops were always parallel to a ⟨112⟩ direction and, being associated with the known first slip system, they were definitely determined as representing edge dislocations.

DISCUSSION

There will be little doubt that the described loops are closely related to the trails behind screw dislocations

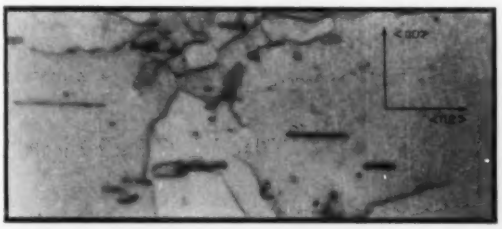

FIG. 1. Long and narrow dislocation loops in aluminum single crystal as revealed by diffraction electron microscopy. $\epsilon=0.1$. 29 000:1.

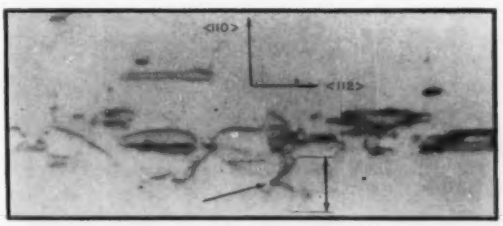

FIG. 2. Clearly resolved, narrow dislocation loops in aluminum single crystal (0.12 mm thick). $\epsilon=0.05$. Arrow points to screw dislocation with dragging semiloop, very likely corresponding to mechanism shown in Fig. 4. Extension mark indicates the projected length of original screw dislocation. 29 000:1.

* On study leave from the National Physical Research Laboratory, Pretoria, South Africa.

[1] H. G. F. Wilsdorf and D. Kuhlmann-Wilsdorf, Phys. Rev. Letters 3, 170 (1959).

[2] A detailed description of the experimental techniques will be given elsewhere.

observed by Dash[3] in silicon, and explained by Johnston and Gilman as being due to crossglide.[4] In their model a screw dislocation undergoes spontaneous double crossglide over a considerable width and depth. Since the two resultant kinks could then not move in a conservative fashion, they would leave behind strips of point defects; i.e., prismatic dislocation loops. Those portions of the screw dislocations which, by double crossglide, have reached the new slip plane, could act as Frank-Read sources, and this Johnston and Gilman believe to be the cause of the profuse multiplication which can result from even one dislocation loop in LiF.

While it may be too early to make definite statements in relation to the other materials under discussion, it seems most unlikely that the elongated loops found in the strained aluminum are due to this mechanism involving glide and crossglide only. The principal reason for rejecting the above theory is that it leaves a number of points unexplained, some of which are the same as previously discussed.[5] For instance, one fails to see what could cause screw dislocations to crossglide in such a spectacular fashion in the absence of any detectable obstacles. Also, why do the superjogs not move together by simple glide, leading to their annihilation as discussed by Seeger[6] and by Cottrell[7] for atomistic jogs.

Another consideration concerns the annihilation of the two resulting prismatic dislocation loops. The prismatic dislocation which represents a missing piece of atomic plane, and the other prismatic dislocation representing the corresponding additional portion of atomic plane would attract each other and, when moving together, annihilate. The theory also does not explain how dislocation tangles are produced, found even in pure single crystals strained only a few percent. Also, if the mechanism of double crossglide would create tangles, they should lead to tangles with a strongly preferred direction and only in conjunction with screw dislocations. Finally, and most important, one may raise the question why no such tangles nor isolated loops are formed if previously undeformed electron transparent foils of aluminum are strained while under observation in the electron microscope.[8,9]

The above questions can be answered in the context of the mechanism of "mushrooming." It is suggested that double crossglide of the simple kind does not take place spontaneously, but that the condensation of point defects on glide dislocations leads to super kinks[10] on the moving dislocations. In the particular case of Al this will most often happen when a moving dislocation meets a void caused by the agglomeration of vacancies.[1,11] Such superjogs cannot collapse and cannot be eliminated by glide. Depending on the concentration of point defects available, any smooth glide dislocation, even in pure single crystal almost free of other dislocations, could acquire super jogs.

Isolated prismatic loops have been observed close to the tangled dislocations which will have torn loose from the advancing dislocations, while others probably represent vacancy disks nucleated closely to but not in contact with a dislocation. Finally, the observation that no tangles are formed if a very thin foil is strained in the electron microscope represents a strong argument in favor of the idea that the mechanism of mushrooming is responsible for the tangles. Clearly, mushrooming cannot take place in very thin foils. In them the point

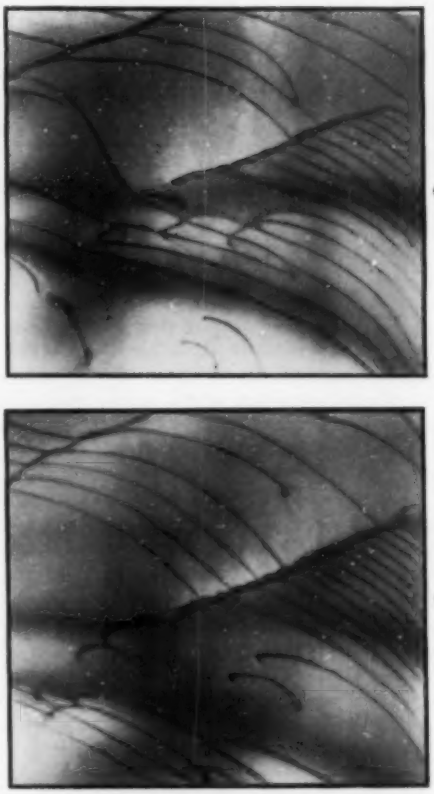

FIG. 3. Glide dislocations of considerable length produced in thin aluminum foil approximately 2000 A thick. 16 000:1. (a) Note that dislocations have no kinks and that no prismatic dislocation loops are present. (b) Some dislocations have moved a distance of more than 1 μ. This should be taken as further evidence that in thin foils dislocations acquire no kinks through vacancy condensation.

[3] W. C. Dash, J. Appl. Phys. **29**, 705 (1958).
[4] W. G. Johnston and J. J. Gilman, J. Appl. Phys. **31**, 632 (1960).
[5] D. Kuhlmann-Wilsdorf, R. Maddin, and H. Kimura, Z. Metallk. **49**, 584 (1958).
[6] A. Seeger, Phil. Mag. **46**, 1194 (1955).
[7] A. H. Cottrell, *Dislocations and Mechanical Properties of Crystals* (John Wiley & Sons, Inc., New York, 1957), p. 577.
[8] H. G. F. Wilsdorf, Am. Soc. Testing Material Spec. Tech. Pub. **245**, 43 (1958).
[9] A. Berghezan and A. Fourdeux, J. Appl. Phys. **30**, 1913 (1959).
[10] H. Kimura, R. Maddin, and D. Kuhlmann-Wilsdorf, Acta Met. **7**, 154 (1959).
[11] D. Kuhlmann-Wilsdorf and H. Wilsdorf, J. Appl. Phys. **31**, 516 (1960).

defects, congregating around the dislocation core, cannot be expected to form platelets, either in contact with or close to the dislocation core, since they will leave through the free surfaces by pipe diffusion along the dislocations.[12] In addition to results given in previous papers,[8,9] further evidence for this phenomenon is provided by Fig. 3, which shows an example in which the glide dislocations are relatively long.

The discovered narrow dislocation loops, trailing behind screw dislocations (Figs. 1 and 2), are interpreted as the result of a few particular processes contributing to the composite phenomenon of mushrooming. Four slightly different mechanisms are proposed which could be responsible, and it is believed that more than one of these, or other similar processes, may occur during plastic flow of aluminum at room temperature.

(i) If a screw dislocation is pinned temporarily by a void, its main portion will move on, dragging behind it two connecting sections of edge dislocation (Fig. 4). These, being of opposite sign and close to each other, could merge and thereby vanish; but, if the diffusion of vacancies from the void into the edge dislocation is sufficiently rapid, they will climb in opposite directions. Being on different slip planes, the edge dislocations no longer can annihilate mutually. As a consequence, a narrow prismatic loop would be dragged out behind the advancing screw dislocations, as long as the void and the surrounding material supply the necessary vacancies at a sufficient rate. Once the vacancy supply decreases below a critical level the loop terminates.

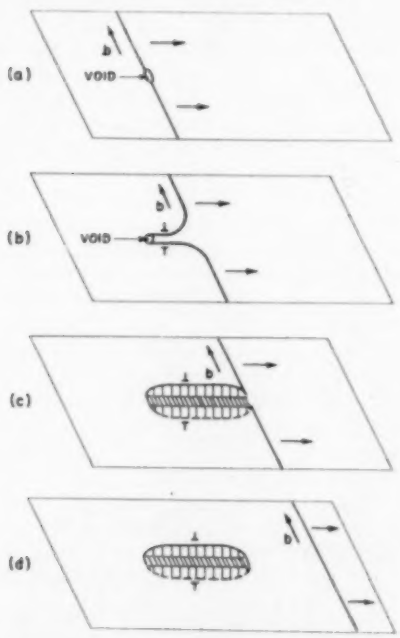

FIG. 4. Production of a long dislocation loop. (a) A screw dislocation meets a void lying symmetrically with regard to the glide plane. (b) On further movement of screw, edge dislocations are dragged behind. (c) Condensation of vacancies will cause the edges to climb. (d) Long loop is terminated and left behind when vacancy supply decreases below critical level.

[12] H. G. F. Wilsdorf, *Structure and Properties of Thin Films* (John Wiley & Sons, Inc., New York, 1959), p. 151.

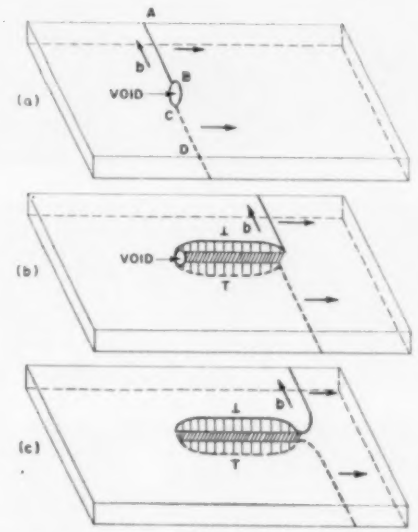

FIG. 5. Interaction of screw dislocation with irregular vacancy cluster. (a) Void is causing part of screw dislocation CD to leave glide plane on level AB. (b) Condensation of vacancies at dragging edge dislocations. (c) Explanation given in text. In this drawing as well as in Fig. 6 and 7 it has been assumed that the resulting loop has climbed out of its original rectangular shape; this, however, is not necessary.

(ii) A variation of the first mechanism will arise if the void is of irregular shape, causing the two parts of the screw to move into different slip planes in order to shorten their cores as much as possible (Fig. 5). This would lead to a super jog dragging out a prismatic loop as long as vacancies diffuse to it at a sufficient rate. After the supply of point defects is exhausted, the jog will be eliminated by glide, or will shift into a dislocation region which has mixed character, allowing it to glide conservatively.[6,13,14]

(iii) Similarly, point defects may precipitate in contact with the advancing screw dislocation, either in the form of one spiral turn,[15,16] or of a less regular shape. In either case, the resulting disturbance in the dislocation line has a slip surface other than the slip plane, and the main portion of the screw dislocation would move on as in (i), pinned only locally and dragging a narrow loop (Fig. 6). Again, this loop will not be removed by simple glide as long as the continuous supply of point defects

[13] J. Friedel, Phil. Mag. **46**, 1169 (1955).
[14] N. F. Mott, *Dislocations and Mechanical Properties of Crystals* (John Wiley & Sons, Inc., New York, 1957), p. 458.
[15] F. Seitz, Advances in Physics **1**, 43 (1952).
[16] S. Amelinckx, W. Bontinck, W. Dekeyser, and F. Seitz, Phil. Mag. **2**, 355 (1957).

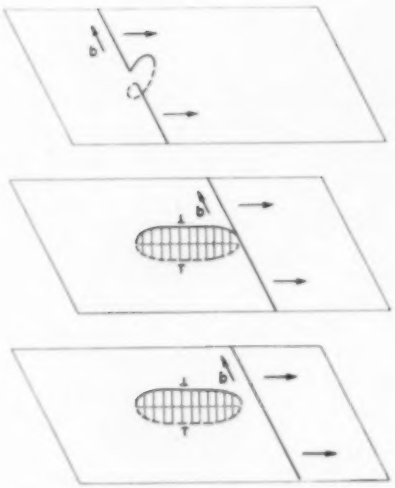

FIG. 6. Glide of "spiral" in screw dislocation and condensation of vacancies resulting in the formation of a long dislocation loop.

causes climb rapid enough to sustain the partly prismatic character of the dragged out loop.

(iv) Another mechanism is illustrated in Fig. 7. An obstacle close to the slip plane of the screw dislocation, for example, a precipitate or a prismatic loop, may cause a screw dislocation to execute double cross slip, resulting in a dislocation motion which geometrically is the same as described by Amelinckx and Dekeyser.[17] However, the jogs would move into a position allowing conservative glide; or the two resulting dragging portions of edge dislocation pairs would collapse; or the super jogs would move together and annihilate, unless fast defect condensation stabilizes them in the same manner as described under (i), (ii), and (iii).

To sum up: It is proposed that the presence and condensation of point defects is an important contribution to the formation of the observed narrow dislocation loops. These loops can be described as being the result of the combined action of dislocation climb and dislocation glide. They are not wholly prismatic loops nor wholly glide loops but combine the character of both. The separation of the two edge dislocations forming the loop sides, measured perpendicular to the slip plane, is governed by climb. Looking along the slip plane, parallel to the Burgers vector, a typical loop seems to be almost rectangular. This shape represents a form of comparatively low free energy as long as the loop ends are fixed, but it may also be due to a lack of atomistic jogs on the edge portions of the long loops. Glide will bring the dislocations close to their position of relative equilibrium, in which the radius vector connecting the two dislocation axes is under 45° to the slip plane.

[17] S. Amelinckx and W. Dekeyser, J. Appl. Phys. **29**, 1000 (1958).

Spontaneous double crossglide and the subsequent dragging of super jogs as postulated to account for the trailing loops[4] represent a mechanism which is highly unfavorable from energy considerations, except when very close to free surfaces so that the dislocation may shorten. By contrast, the process suggested in this paper will release energy through the condensation of the point defects. Thus we believe that many narrow loops and extensive dislocation tangles are only to be expected if point defects in sufficient concentration and with sufficient mobility are present.

In order to support the proposed explanation for the elongated loops experimentally, specimens were heated in a special furnace[18] while under observation in the electron microscope. Many of the isolated loops

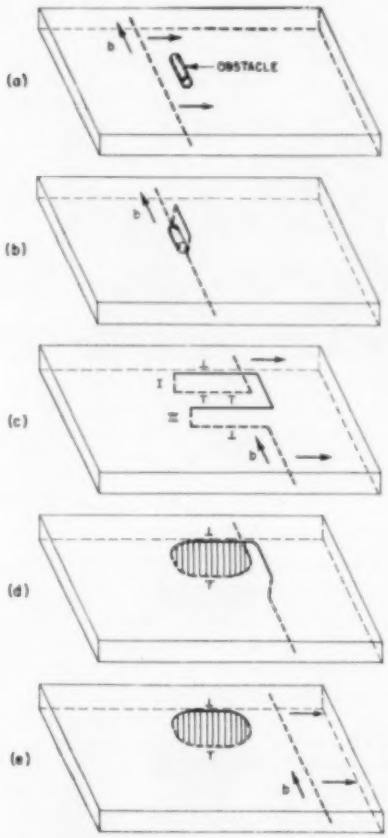

FIG. 7. Loop formation through double cross-slip and vacancy interaction. (a) Screw dislocation approaching obstacle. (b) Double cross-slip occurring near obstacle. (c) On further movement of screw, dragging edge dislocations are produced. (d) Interstitials in semiloop II are eliminated by vacancies, leaving only I. (e) Further glide of screw causes separation from I. [The obstacle has been omitted in (c), (d), and (e) for the sake of clarity.]

[18] B. Kear, Rev. Sci. Instr. **31**, 1007 (1960).

vanished, probably by prismatic glide through the specimen surfaces,[19] even before a temperature of 200°C was approached. Occasional loops, on the other hand, exhibited the expected behavior of prismatic dislocations as indicated by Fig. 8. From the micrographs it is evident that the loop shortens with rising temperature and, at the same time, assumes a rounder shape, actually increasing its width. Obviously, then, the area of the loop shrinks as vacancies migrate away, while the remaining vacancies rearrange to shorten the circumference, thereby lowering the loop energy.

A simplified calculation shows that the necessary climb rates may be easily reached in aluminum at room temperature. A screw dislocation pinned by a void is being considered. The vacancies from the void will move into or along the dislocation cores of the dragging edge dislocations with an activation energy of $U<0.5$ ev. The value of 0.5 ev represents an extreme upper limit since the energy of motion for a vacancy in an undisturbed crystal is just over $\frac{1}{2}$ ev. The linear rate of progress of the vacancies is

$$V_l=\nu b\epsilon^{-U/KT},$$

with $\nu\cong10^{13}$ sec^{-1}, the atomic frequency, and b, the nearest neighbor distance equal to about 3 A. At room temperature V_l then becomes 10^{13} sec$^{-1}\times3\times10^{-8}$ cm$\times\epsilon^{-20}=5\times10^{-4}$ cm/sec. If the loop is dragged out with a velocity not exceeding V_l, climb will take place with sufficient speed to stabilize it. A void would have to contain about 10^5 vacancies to account for a typical loop; but, in reality, the vacancy atmosphere around the original dislocation will probably contribute much of this number.

In the context of the above it is not surprising why the slender loops are not found trailing after edge dislocations. Any prismatic loop in contact with an edge dislocation with the same Burgers vector will always be able to move by ordinary glide. It may, and probably will, cause a great deal of dislocation tangling, but there would be no reason for the formation of narrow loops.

The long portions of the discovered loops may act as dislocation sources. From their distribution, as seen in Figs. 1 and 2, it is clear that herewith one more possible explanation for the formation of slip bands is provided which is similar to the one given by Kuhlmann-Wilsdorf, Maddin and Kimura[5] in connection with the experiments on LiF by Gilman and Johnston.[20] Moreover, the analysis found in that paper[5] can be adapted easily to include the above mechanism.

[19] J. Silcox and M. J. Whelan, Phil. Mag. 5, 1 (1960).
[20] J. J. Gilman and W. G. Johnston, J. Appl. Phys. 27, 1018 (1956).

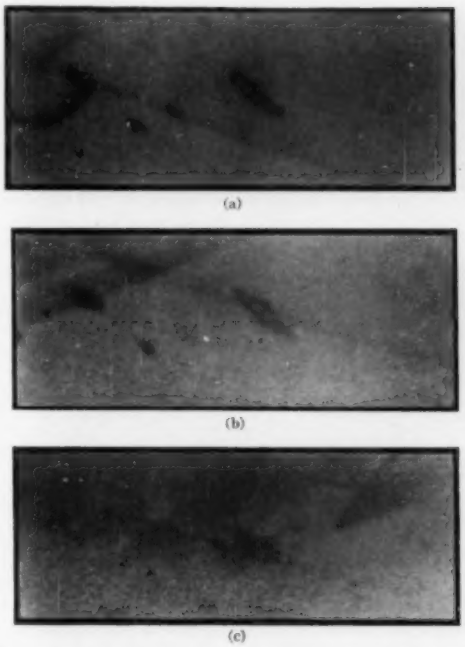

FIG. 8. Behavior of narrow loop on annealing. 40 000:1. (a) Narrow dislocation loop after deformation of single crystal. (b) and (c) Loop changes shape with increase of temperature to 200°C. Note that loop has decreased its length and increased its width.

CONCLUSIONS

1. Narrow dislocation loops lying parallel to ⟨112⟩ were found to form trailing behind screw dislocations of the primary glide system in strained aluminum crystals.

2. Four closely related mechanisms have been proposed to account for the formation of these narrow loops.

3. In all cases a sufficient supply of point defects is necessary for these mechanisms, in order to allow the edge portions of the long loops to climb and thus to stabilize the dragging loops.

ACKNOWLEDGMENTS

We are greatly indebted to Dr. Doris Wilsdorf, University of Pennsylvania, who contributed to the paper through many discussions. Thanks is also due to Mr. J. Schmitz for his able help with the experiments and to Mr. S. Borgese who assisted us with the annealing study.

The support of the Office of Naval Research is gratefully acknowledged.

Electron Microscope Studies of Colloids in KCl

R. E. SIMON* AND R. L. SPROULL
Laboratory of Atomic and Solid State Physics, Cornell University, Ithaca, New York
(Received August 1, 1960)

Electron microscope studies were made of surfaces of potassium chloride crystals containing excess potassium. The crystals were cleaved in a vacuum and the surfaces replicated in the same vacuum. Large potassium colloids were observed with distinctive shapes and orientations determined by the host lattice.

LARGE colloidal aggregates of potassium in potassium chloride have been observed with the electron microscope. The colloids were found to have distinct shapes and sizes which varied with the heat treatment. The shape and orientation of the colloids were found to be determined by the host lattice. Our observations differ from those recently reported[1] in that, probably because of our replication technique, we were able to determine the shape and size of the colloids.

The colloids were produced by cooling additively colored crystals from 700°C to room temperature at different rates. Harshaw KCl crystals were heated to 700°C for three hours in copper capsules which contained several grams of potassium metal in order to produce 10^{18} to 10^{19} F centers per cc.[2] The capsules were made of copper tubing, the ends of which were pinched to make vacuum tight seals. In successive experiments the copper capsules were cooled to room temperature as follows: (1) by reducing the oven temperature gradually over a period of 12 hours, (2) by allowing the oven to cool at its own rate, (3) by removing the capsule from the oven and allowing it to cool at its own rate in air, (4) by removing the capsule from the oven and cooling it in a jet of air, (5) by removing the capsule from the oven and quenching it in water.

FIG. 1. Electron micrograph showing a colloidal particle of K in additively colored KCl which was cooled to room temperature at oven's rate. The appearance of a metallic, ductile fracture of the colloidal particle should be noted.

The crystals were cleaved in a vacuum of 10^{-5} mm Hg, and the cleavage planes were replicated without being exposed to the atmosphere. The replicas were made by first evaporating a ~10 A film of uranium on the crystal from a source at an angle of 45° from the normal to the cleavage plane. This was followed by the evaporation of a ~100 A silicon monoxide backing layer. The replica was floated off the crystal on water and picked up on a screen for observation in the electron microscope. Although points less than 50 A apart could be resolved on these replicas, colloidal particles with dimensions less than about 100 A could not be distinguished from other imperfections on the crystal surface.

Colloidal particles were observed in all the crystals treated as described above, except in those which were cooled most rapidly from high temperature. The results of the electron microscope studies are summarized in Table I. Electron micrographs of the colloidal particles are shown in Figs. 1, 2, and 3. For each heat treatment colloids of a distinct size, rather than a large range of sizes, were observed. The slowest cooling rates resulted in the largest colloids. The colloids which were greater

TABLE I.

Run no.	Cooling treatment	Size of colloids (distance between parallel sides)	Shape of colloids [in cross-section parallel to (100) plane of KCl]
22	Cooled by reducing temperature of oven slowly over 12 hours	25 000 A	8-sided
5, 7	Cooled at same rate as oven	8000 A	8-sided
11	Cooled in air	2000 A	8- and 4-sided
23	Cooled in jet of air	200 A	···
1a	Cooled by dropping in water	None observed	···
25	Allowed to stand at 250°C for 14 hours then quenched in water	None observed	···
12	No excess K, cooled in air	None observed	···

* Now at RCA Laboratories, Princeton, New Jersey.
[1] T. Hibi and T. Tomiki, J. Phys. Soc. Japan **14**, 375 (1959).
[2] H. Rogener, Ann. Physik **29**, 386 (1937).

than 2000 A in lateral dimensions appeared eight-sided when observed in a cross section parallel to a (100) plane of the KCl. The 2000 A colloids appeared to be both eight-sided and four-sided. The shape of the smaller particles observed could not be distinguished. Optical microscope examination of the largest colloids showed that they were oriented so that their largest sides were parallel to (100) planes of the KCl. All the colloids observed on any one replica were identically oriented with respect to each other. These observations suggest that the KCl, rather than the metal, determines the shape and orientation of the colloids.

Optical absorption measurements on these crystals showed the existence of absorption peaks on the low-energy side of the F band which were especially pronounced in the crystals containing the smallest colloids. No correlation between the optical absorption measurements and the electron microscope observations have been found. Calculations by Savistianova[3] indicate that, except in the case of the smallest particles observed, the optical absorption should not be greatly affected by the observed colloids. Therefore, the peaks observed in the absorption measurements were probably caused by aggregates smaller than those observed with the electron microscope.

One sample prepared using the technique described by Scott *et al.*[4] was studied (Run No. 25). No colloidal particles were observed with the electron microscope in agreement with Scott's experience.

Only in Run No. 23, in which the 200 A particles were observed, were enough colloids observed to make possible an estimate of the number of potassium atoms which are in the form of colloids. Assuming that the cleavage plane was a random cut through a uniform distribution of colloids, and that the colloids had the density of bulk potassium, we should conclude that approximately 10^{19} potassium atoms per cc were in colloidal form, i.e., almost all of the excess potassium aggregated into colloids. Alternatively, the cleavage plane may have passed preferentially through regions of high density of colloids. The latter possibility is consistent with the observation of Amelinckx *et al.*[5] that colloids form along dislocations, since the cleavage plane would be expected to pass through regions of high dislocation density.

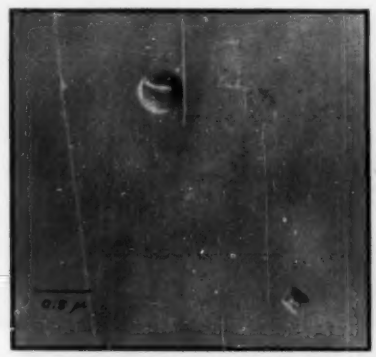

FIG. 2. Electron micrograph showing colloidal particles of K in additively colored KCl which was cooled to room temperature in air.

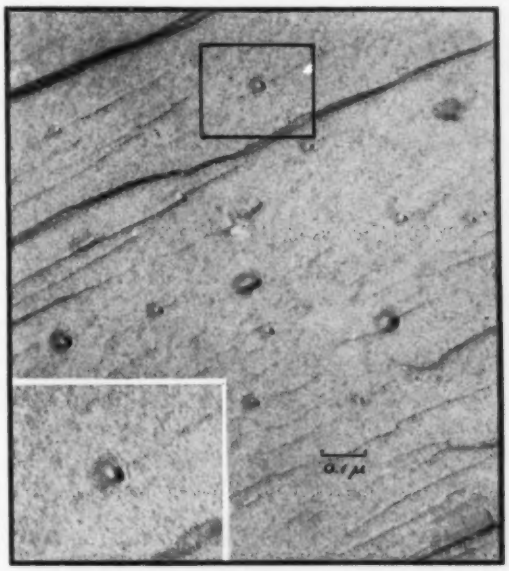

FIG. 3. Electron micrograph showing colloidal particles of K in additively colored KCl which was cooled to room temperature in a jet of air. The inset is enlarged by an additional factor of two.

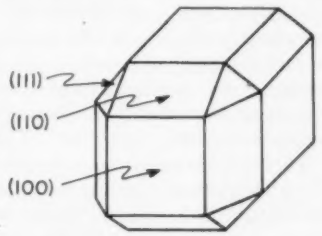

FIG. 4. Proposed model of large colloidal particle of K in KCl. The colloids are bounded by principal planes of KCl.

From the observation of the shape and orientation of the colloidal particles in two dimensions, a three-dimensional model of the larger colloids, shown in Fig. 4, has been derived. It satisfies the symmetry requirements that it appear eight-sided when cut by (100) plane and that one of its principal planes be a (100) plane. The colloidal particles which appear four-sided in two dimensions are probably cubes. It should be noted, however, that the eight-sided particles would appear to be four-sided if the cleavage plane passed through the colloid near its edge.

ACKNOWLEDGMENTS

The assistance of Dr. B. M. Siegel in the use of the electron microscope, and of Marvin Moss in the preparation of the figures, is gratefully acknowledged.

[3] M. Savistianova, Z. Physik **64**, 262 (1930).
[4] A. B. Scott, W. A. Smith, and M. A. Thompson, J. Phys. Chem. **57**, 757 (1953).
[5] S. Amelinckx, W. Van Der Vorst, R. Gevers, and W. Dekeyser, Phil. Mag. **46**, 450 (1955).

Some Effects Occurring in Dislocated Tellurium*

J. S. Blakemore, J. W. Schultz, and K. C. Nomura
Honeywell Research Center, Hopkins, Minnesota

(Received June 27, 1960)

Dislocation densities as small as 1000 cm^{-2} are sometimes found in carefully produced single crystals of tellurium, but since the material is very soft a quite mild stress can introduce 10^8 dislocations/cm^2 or more. Dislocation etch pits of sharply geometric shape can be developed on the cleavage $(10\bar{1}0)$ planes by the slow attack of sulphuric acid; their planar surfaces correspond to $(1\bar{1}00)$, $(10\bar{1}3)$, $(01\bar{1}1)$, and $(0\bar{1}1\bar{1})$ faces. Effects are noted on faces exposed by cleavage at 77°K which suggest that even at this temperature the material can suffer localized plastic damage, for brief etching of such faces produces small flat-bottomed pits; these may be interpreted by supposing that the mild stress of cleavage at 77°K generates shallow dislocation loops. The flat-bottomed pits disappear when a surface layer $\geq 25\,\mu$ is etched away. A marked increase in electron-hole recombination rate is noted in plastically deformed crystals. If the additional recombination occurs through the dislocations themselves, then each has a capture radius of some 4×10^{-6} cm at 300°K. Dislocated crystals also show more prominent trapping effects at low temperatures than structurally pure samples, and contain additional readily ionizable acceptor sites; these may be derived from the dislocations themselves or from other defects created or activated by plastic flow.

I. INTRODUCTION

THE element tellurium crystallizes in an interesting hexagonal lattice with atoms covalently held in chains spiraling around the [0001] direction (or c axis). Every third atom is directly above another atom in the same chain, so that a chain appears triangular on looking along the c axis. Chains are stacked with hexagonal symmetry, each atom having four next-nearest neighbors in adjacent chains. The binding between the chains is conventionally assumed to be mainly of the van der Waals type, and is certainly not very strong, since tellurium cleaves easily on any of the six planes equivalent to $(10\bar{1}0)$.

Purified tellurium is an intrinsic semiconductor at room temperature with a forbidden gap $E_i = 0.32$ ev. No doping agent has yet been discovered which will permit the material to be other than p type at lower temperatures. The free hole density provided by impurities seems to be unimpaired even at liquid helium temperatures.[1] Redistillation of the starting material and zone refinement are helpful in producing tellurium with a small extrinsic hole density, but passage of several hundred zones is necessary to make $N_a \lesssim 10^{14}$ cm^{-3}.

It is to be expected that the electrical properties of tellurium will be sensitive to departures from crystalline perfection, just as they are in other semiconductors. Indeed we should admit that our interests are largely associated with the properties of structurally perfect semiconducting crystals. When we noted the very marked adverse effect of dislocations on carrier lifetime in tellurium,[2,3] it became advisable to determine the conditions under which crystals can be damaged, and the range of effects produced by such damage.

II. MECHANICAL PROPERTIES

Tellurium is a very soft material. When it is desired to study the properties of perfect crystals, extreme care must be taken if dislocations are to be avoided. In studies where the effects of dislocations are observed, a very small applied stress can change the pattern.

For starting material, our studies have profited from the extensive program of purification and zone refinement of tellurium at these laboratories. More than 200 large single crystals have been grown using Davies' modification of the Czochralski method.[4] Many of these have dislocation densities as small as 1000 cm^{-2} when first examined.

In work related to our present topic, Stokes[5] has found that tellurium reacts purely elastically to stress along the [0001] direction, but that slip readily occurs in directions normal to the c axis. Slip can occur over any of the cleavage $(10\bar{1}0)$; thus the slip directions are

FIG. 1. Random distribution of dislocation etch pits on a $(10\bar{1}0)$ face of a tellurium crystal, as revealed by a hydrofluoric-nitric-acetic acid etch. $N_D = 8\times10^5$ cm^{-2} (×412).

* Work partly supported by the U. S. Air Force under contract.

[1] A. Nussbaum, Phys. Rev. **94**, 337 (1954).

[2] J. S. Blakemore, J. D. Heaps, K. C. Nomura, and L. P. Beardsley, Phys. Rev. **117**, 687 (1960).

[3] J. S. Blakemore and K. C. Nomura, Bull. Am. Phys. Soc. Ser. II, **5**, 62 (1960).

[4] T. J. Davies, J. Appl. Phys. **28**, 1217 (1957).

[5] R. J. Stokes, Acta Met. (to be published).

$[\bar{1}2\bar{1}0]$ and its equivalents. When a sample is exposed to compressional or tensional stress along either a $[\bar{1}2\bar{1}0]$ or $[10\bar{1}0]$ direction, relief can be obtained through slip along $[11\bar{2}0]$ and $[2\bar{1}\bar{1}0]$ directions. For the former direction of relief, we believe that dislocation loops are generated lying in the $(1\bar{1}00)$ plane which have essentially a screw character as they emerge on to a free $(10\bar{1}0)$ surface.

Sample preparation entails great care since dislocations can be introduced so easily. Sawing, grinding, lapping, and even optical polishing are prohibited. The $(10\bar{1}0)$ faces can readily be exposed by cleavage, but the operation must be carried out at a low temperature to minimize plastic damage. As described in the next section, and in contradiction to a statement made by Lovell *et al.*[6] we find that a surface layer suffers *some* damage even when tellurium is cleaved at 77°K.

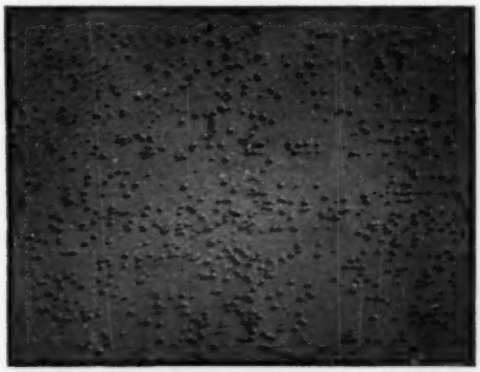

FIG. 2. Dislocation pits revealed with a sulfuric acid etch. $N_D = 2.4\times10^{3}$ cm^{-2} (×82).

For many of our samples we were interested in deliberately creating a large dislocation density. This could conveniently be done by applying a very moderate pressure in the $[10\bar{1}0]$ direction at room temperature. Such a procedure frequently resulted in a uniform distribution of dislocations through most of the bulk, but with a much more heavily worked layer some 50 μ (or more) thick on the front and rear surfaces. These layers (and the rather less thick worked layers produced by cleavage) were removed with a chemical polish consisting of one part chromic anhydride, one part concentrated hydrochloric acid and three parts of water—by weight. This mixture removes tellurium at a rate of 4 μ/min and yields a smooth bright surface, ready for preferential etching and exposure of dislocation patterns.

III. DISLOCATION ETCH PITS

A variety of chemical agents can be used to develop etch pits on $(10\bar{1}0)$ faces of tellurium. Figure 1 (for which, as in all the plates, the c axis runs horizontally across the picture) shows a typical example of pits which result from attack by a hydrofluoric-nitric-acetic acid mixture. A formulation of this type was used by Lovell *et al.*[6] in obtaining pictures of randomly distributed pits, low angle boundaries, and the pit distribution around mechanically worked regions. This kind of etch removes tellurium very rapidly at room temperature (approximately 5 μ/sec) and even when used refrigerated is, in our opinion, rather too active to permit optimum definition.

FIG. 3. The distinctive shape of tellurium etch pits developed by the sulfuric acid etch. (×198).

We find that pits of a more revealing shape can be produced with a very slow etch. In most of our work, the slow etch has been concentrated sulfuric acid, which at 150°C consumes tellurium at a rate of $\sim 1\,\mu$/min. (The rate is markedly temperature dependent.)

Figure 2 shows the typical result of the sulfuric etch for a crystal with many dislocations, viewed with a low magnification. It is preferable to etch for a longer time with a sample of small N_D; Fig. 3 provides a good example of the characteristic pit shape as viewed with moderate magnification. At first glance this shape may appear symmetrical about the c axis, but this is actually far from the case. It is in fact the *top edge* of the pit which lies along the c axis. Optical reflection techniques with a well-collimated beam have been used to determine the orientation of the pit faces. If the plane of the photograph is denoted as $(10\bar{1}0)$, then the large face sloping down from the upper edge of the pit is another cleavage plane, $(1\bar{1}00)$. The small area to the right of this is $(10\bar{1}3)$, and the lower surfaces are $(01\bar{1}1)$ and $(0\bar{1}\bar{1}1)$, which meet along the line $[2\bar{1}\bar{1}0]$.

Since our interest is physical rather than chemical, we have not pondered too deeply why these particular planes should be preferentially exposed. Rather we have appreciated that so characteristic a dislocation etch pit shape is not likely to be confused with any other surface structures.

When some tellurium single crystals are etched, lines of etch pits are revealed which run along the c axis, evidence of low angle twist or tilt boundaries. The

[6] L. C. Lovell, J. H. Wernick, and K. E. Benson, Acta Met. 6, 716 (1958).

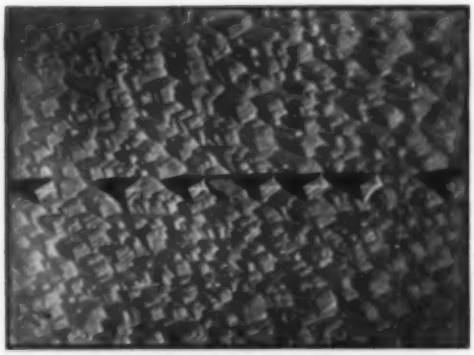

FIG. 4. Dislocations forming a subboundary, terminating as points along the [0001] direction in a $(01\bar{1}0)$ plane of tellurium. (×198).

crystal illustrated in Fig. 4 has a subboundary but contains very few other dislocations.

Lovell *et al.*[6] concluded that cleavage of tellurium at 77°K was *not* accompanied by any plastic damage. It is not surprising that they should have reached this conclusion, since with their very fast etch any damage in the immediate vicinity of the faces exposed by cleavage would be etched away in a very short time. In our work we have used a much slower etch, and see effects which could be attributed to very shallow dislocation loops created in the act of cleavage. For when a cleaved surface is etched in H_2SO_4 for a short time, many pits are seen, some having the form we have already described as characteristic of the bulk, but many having the same outline with a flat bottom. These flat-bottomed pits become progressively more shallow as etching proceeds, and disappear completely when a layer some 25 μ thick has been chemically removed. Figure 5 shows a good example of flat pits seen when a cleaved surface has been etched for a short time.

It is possible that a flat-bottomed pit represents the site of a microscopic dislocation loop generated through plastic deformation when the crystal is cleaved. (The material at the bottom of the pit is no longer preferentially attacked when the entire loop has been etched away.) If this is the explanation, we are left with the disquieting thought that tellurium is not safe from plastic damage even at 77°K. Such damage could conceivably be averted by performing cleaving operations at still lower temperatures, but we have not yet attempted to cleave tellurium crystals immersed in liquid helium.

IV. ELECTRICAL EFFECTS IN DISLOCATED TELLURIUM

In discussions of the electrical behavior of tellurium, care must be taken to distinguish between the *conductance* of a sample and the true bulk electrical *conductivity*. The two are related by the usual geometric factor only if the sample is free from a highly conducting surface layer. Caldwell and Fan[7] note how the conductance of tellurium in the extrinsic range is raised when the sample surfaces have been sandblasted or otherwise mechanically worked. They obtained the smallest conductance with an optically polished surface, and assumed that such a surface would not adversely affect measurements of the bulk electrical and optical properties. We find, alas, that even optical polishing results in a surface with some associated additional conductance, and which appreciably increases the opacity of a tellurium plate beyond the absorption edge.[8] On the other hand, the chromic-hydrochloric acid chemical polish yields a surface which is excellent for optical transmission and which is the best we have yet found for measurement of bulk electrical properties. It is not unreasonable to expect that further research could lead to even better surface treatments.

The electrical conductivity of a tellurium sample which is structurally almost perfect decreases on cooling from room temperature and typically becomes much less temperature sensitive in the extrinsic region below ~200°K. The lowest curve in Fig. 6 shows the behavior of a representative sample, measured with current parallel to the c axis. A much larger conductance is found when such a sample has been plastically deformed by compression along $[10\bar{1}0]$, as shown by the upper curve of the figure. Much of this increased conduction has its origin in the heavily worked surface layers; when these layers are removed by chemical polishing the sample conductivity exceeds that of the virgin state only by a small—but significant—amount. Conductivity and Hall effect studies suggest that some levels introduced by plastic deformation may become depopulated in the range between room temperature and 77°K, but that further supplies of free holes are maintained down to the lowest temperatures.

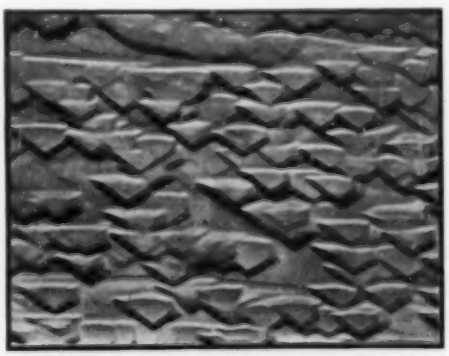

FIG. 5. Flat-bottomed pits which occur when a cleaved $(10\bar{1}0)$ face is etched for a short time. (×330).

[7] R. S. Caldwell and H. Y. Fan, Phys. Rev. **114**, 664 (1959).
[8] K. C. Nomura and J. S. Blakemore, Bull. Am. Phys. Soc. Ser. II, **5**, 62 (1960).

It is by no means certain that the additional acceptor levels arise from the dislocations themselves. For while Read[9] has shown that dislocations in the diamond lattice having any edge component have dangling unpaired electrons which are the seat of acceptors, rather different considerations apply to the tellurium lattice. A dislocation of either screw or edge character can lie in the slip planes of tellurium without disturbing any of the strong covalent bonds. Thus we should take into consideration the possibility that the additional acceptors seen come not from dislocations themselves but from point defects left behind by the motion of dislocations during plastic flow.[10]

Not only is the electrical conductivity larger for plastically deformed samples, so is the electron-hole recombination rate—and this to a much more drastic degree. The large increase in recombination rate is amply demonstrated in Fig. 7. (For convenience of comparison, Figs. 6 and 7 relate to the same sample, number T-320.)

The very purest tellurium samples have a lifetime of up to 60 μsec at room temperature, and are dominated by intrinsic transitions.[11] Sample T-320 was of slightly lower quality and the recombination rate appeared to be controlled by Shockley-Read processes at room temperature and below.[2] Upon plastic deformation and removal of the immediate surface layers, the etch-pit density was $N_D \sim 1.1\times10^6$ cm^{-2} and the room temperature recombination rate some 30 times larger than before. The new recombination rate was relatively insensitive to temperature down to $\sim$200°K, but declined steadily on further cooling in accordance with

$$\nu = \frac{10^6}{1+8T^{-1}\exp(770/T)}\ \text{sec}^{-1}. \qquad (1)$$

This form of temperature dependence indicates the onset of trapping at low temperatures. As we have previously reported,[2] low-temperature trapping occurs in tellurium samples which have *not* been deliberately deformed—and with a similar limiting temperature dependence. However, trapping always becomes much more prominent when a sample is deformed.

This does not necessarily mean that the traps originate in the dislocations themselves. Thus, Morrison[12] has developed a model for slow decay through dislocation levels, but this could only explain trapping in tellurium if a dislocation represents a line of *donor* levels considerably above the Fermi level. The traps could alternatively be of the kind studied in silicon by Haynes and Hornbeck,[13] centers which are present in the original material but which slow the photoconductive decay rate only when they compete with a very vigorous recombination mechanism (such as we find in deformed samples). Certainly the observed temperature dependence fits the Haynes-Hornbeck model for traps 0.066 ev below the conduction band, but only for an implausibly large trap density.[14]

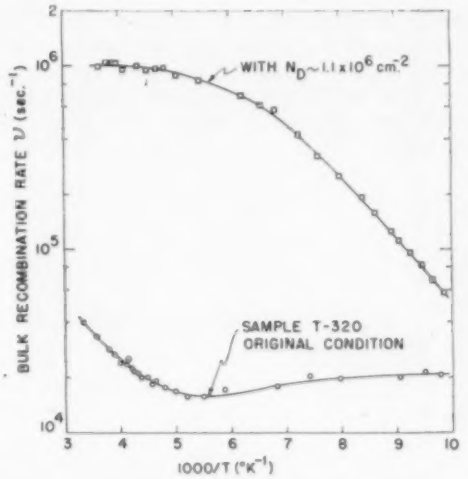

FIG. 7. Recombination rate as a function of temperature for small modulation ($\Delta n \leq 10^{12}$ cm^{-3}) in sample T-320, before and after introduction of a large dislocation density.

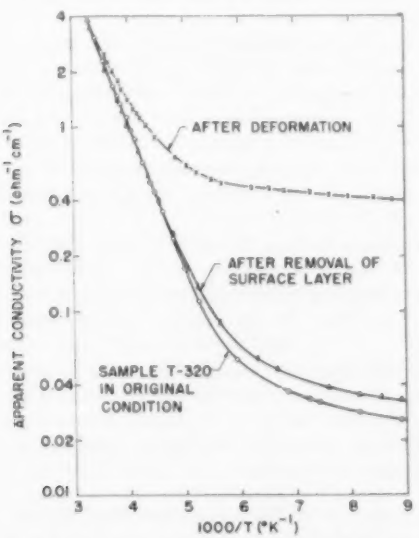

FIG. 6. Electrical conductivity (measured parallel to the c axis) of sample T-320; in its original state with an etch-pit density of 3000 cm^{-2}, after compression in the [1010] direction, and with the damaged surface removed—showing a small increase in the intrinsic conductivity when the etch-pit density is $N_D \sim 1.1\times10^6$ cm^{-2}.

[9] W. T. Read, Phil. Mag. **45**, 775 (1954).

[10] A. H. Cottrell, *Dislocations and Plastic Flow in Crystals* (Clarendon Press, Oxford, England, 1953).

[11] J. S. Blakemore, Prague Semiconductor Conference (August, 1960).

[12] S. R. Morrison, Phys. Rev. **104**, 619 (1956).

[13] J. R. Haynes and J. A. Hornbeck, Phys. Rev. **90**, 152 (1953).

[14] Thus the Haynes-Hornbeck model would require 2×10^{15} cm^{-3} traps in sample T-320, and comparable densities in other samples.

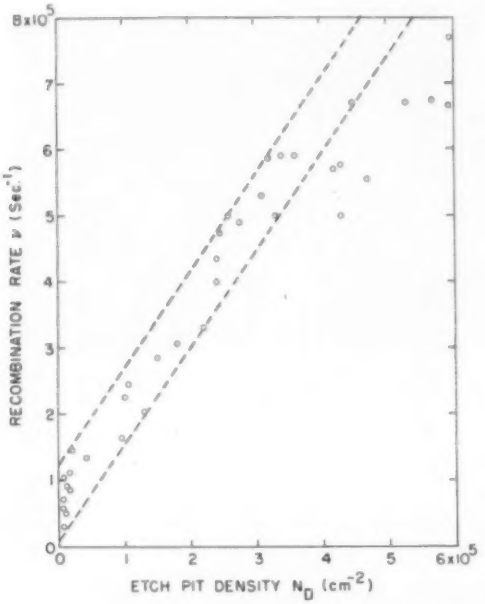

FIG. 8. Recombination rate at 300°K as a function of dislocation etch-pit density in tellurium samples.

At room temperature (300°K), trapping effects are apparently absent, and photoconductive decay does indicate the recombination rate. This will receive contributions from dislocations, from other defects and impurities, and from intrinsic mechanisms. Accordingly, one might expect that samples showing a dislocation etch-pit density N_D would have a recombination rate of 300°K of

$$\nu_{300} = \nu_i + A N_D, \tag{2}$$

where the quantity ν_i must lie between minimum and maximum values.[15] If this is the case, one would expect to find in a plot of ν_{300} vs N_D that points for various samples would be scattered between two parallel straight lines. Figure 8 shows the results of fitting some of our data to such a representation. The slope of the lines in this figure is $A = 1.45$ cm^2 sec^{-1}. If we are to view a dislocation as a cylinder of capture radius r_0, then $A = 2r_0\bar{v}$; for the expected thermal velocity this gives $r_0 = 4\times10^{-8}$ cm, a very plausible value.

It will be noted in Fig. 8 that the linear relationship Eq. (2) begins to fail when $N_D \gtrsim 4\times10^5$ cm^{-2}. Extension of the data to more seriously deformed samples of large

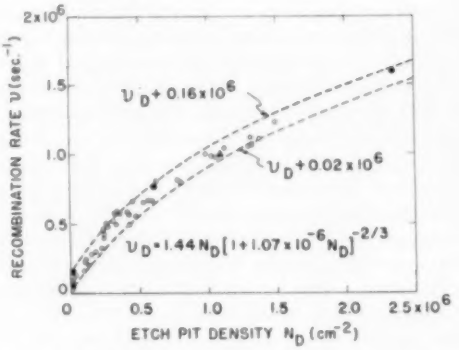

FIG. 9. Extension of the data in Fig. 8 to a broader range of ν and N_D, showing the apparent breakdown of a linear relationship.

N_D, shown in Fig. 9, demonstrates that $(d\nu/dN_D)$ becomes progressively smaller. The trend is clearly defined and the results have good internal consistency; thus the two solid triangles refer to one sample before and after deformation, while the three solid circles refer to another sample in its initial condition and following two successive plastic treatments. The curves of Fig. 9 have the form

$$\nu = \nu_i + \nu_D$$
$$= \nu_i + 1.44 N_D[1 + 1.07\times10^{-6} N_D]^{-\frac{2}{3}} \text{ sec}^{-1} \tag{3}$$

but obviously could be generated in a number of alternative analytic forms by appropriate choice of constants. A more crucial point is that for recombination *through dislocations themselves*, there is no reason to expect ν_D to be other than linear in N_D. Nonlinearity should only develop when the space-charge regions of adjacent dislocations overlap, and this should be inappreciable for $N_D < 10^8$ cm^{-2}.

This brings us back to the possibility that the trend of ν with N_D comes not from recombination through dislocation dangling bond levels, but through other defects created or activated by plastic flow. All the experimental points in Fig. 9 for $N_D > 10^5$ cm^{-2} relate to deliberately deformed samples, since our single crystals had small initial dislocation densities (usually $\lesssim 10^4$ cm^{-2}). The trend of ν with N_D for the deformed samples of Figs. 8 and 9 could come from phenomena *correlated* with plastic flow such as:

(a) vacancies generated by dislocation motion, or
(b) condensation of chemical impurities on dislocations.

Both of these phenomena are recognized as occurring to some extent when a sample is strained,[10] and it is interesting to note that for neither would the efficiency necessarily be independent of N_D (i.e., the recombination rate could then be sublinear with rising dislocation density).

Since $(N_a - N_d)$ is apparently $\sim 10^{14}$ cm^{-3} in our tellurium, the above result could be correct only if the extensive zone refining provides an almost perfectly compensated impurity distribution. This is hardly compatible with the fact that it has never been found possible to dope tellurium so as to make it n type.

[15] The minimum value of ν_i set by the rate of intrinsic processes $\approx 1.2\times10^4$ sec^{-1} at 300°K. With extensively zone refined material, the density of chemical recombination centers should be small enough to keep ν_i less than about 1.5×10^5 sec^{-1}.

A number of questions have been raised to which answers are not known at present. In view of the anisotropic behavior of tellurium, such answers will not be simple. Rather, different kinds of experiments will be required to ascertain more definitely which electrical effects are produced by dislocations themselves and which by other imperfections.

V. ACKNOWLEDGMENTS

T. J. Davies and A. W. Ryberg produced many beautiful crystals for this work, which we proceeded to subject to the most cruel treatments. Many stimulating and informative discussions were held with T. L. Johnston, C. H. Li, and R. J. Stokes of our metallurgy section.

JOURNAL OF APPLIED PHYSICS VOLUME 31, NUMBER 12 DECEMBER, 1960

Filled and Empty Dangling Bonds in III-V Compounds

D. B. HOLT
Department of Physics, University of the Witwatersrand, Johannesburg, South Africa
(Received June 23, 1960)

It is pointed out that the model of dangling bonds from the {111} and {$\bar{1}\bar{1}\bar{1}$} surfaces of III-V compounds proposed by Gatos, Moody, and Lavine is open to serious objection. The idea of resonance is introduced in order to develop a model which is not subject to the same difficulties. Certain implications of this model for dislocation theory are discussed.

GATOS, Moody, and Lavine[1] have put forward a model of the way in which atoms add onto the "*A*" {111}, and "*B*" {$\bar{1}\bar{1}\bar{1}$}, planes[2] of III-V compound crystals during growth, that is, for example, onto the III-element faced plane, (111), and onto the V-element faced plane, ($\bar{1}\bar{1}\bar{1}$). The observed differences in growth in the [111] and [$\bar{1}\bar{1}\bar{1}$] directions are ascribed to the fact that the "*B*" face presents filled dangling bonds (two electrons in each sp^3 hybrid tetrahedral bond) to the arriving III-element atom, whereas the "*A*" face presents empty dangling bonds (no electrons in any sp^3 tetrahedral bond) to the arriving V-element atom. This model has great heuristic value and is consistent with the observed differences in crystal growth behavior in the [111] and [$\bar{1}\bar{1}\bar{1}$] directions[1,3] and the differences of etching behavior of the (111) and ($\bar{1}\bar{1}\bar{1}$) planes.[1,4-6]

The model is open to serious objection, however. Each V-element atom has five valence electrons to be distributed over four tetrahedral bonds. Thus each bond from a V-element atom must contain on average $1\frac{1}{4}$ electrons and not 2 as assumed above. Similarly, on average each bond from a III-element atom contains $\frac{3}{4}$ electron and not zero as assumed above. Moreover the model neglects the small but real degree of ionicity of bonding in III-V compounds. That is, the bond is made up of atomic orbitals corresponding to a covalent bond and atomic orbitals corresponding to an ionic bond. The actual proportion of these orbitals present in the bond is the one giving the minimum energy. It should also be noted that on the Gatos, Moody, and Lavine model there will in general be an electrical dipole moment of the crystal as a whole. In Fig. 1 the Gatos, Moody, and Lavine model has been made symmetrical by considering the dangling bonds from all {$\bar{1}\bar{1}\bar{1}$} planes to be filled and those from all {111} planes to be empty. Since all dangling bonds from, for example, the (111) face are empty while all those from the ($\bar{1}\bar{1}\bar{1}$) face are filled the center of gravity of negative charge is shifted in the [$\bar{1}\bar{1}\bar{1}$] direction relative to the center of gravity of positive charge of the crystal as a whole. Thus there will be an electric dipole moment along each ⟨111⟩ direction, but if the crystal is a wafer cut parallel

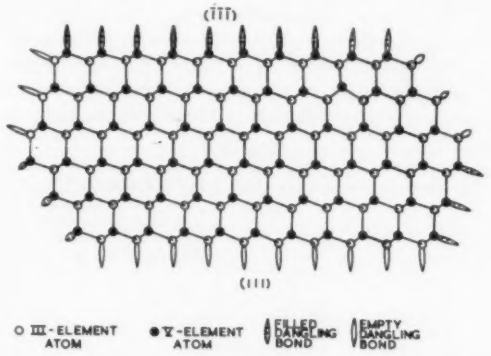

FIG. 1. Projection of the sphalerite structure onto the ($1\bar{1}0$) plane. The full and empty dangling bonds represent the model of Gatos, Moody, and Lavine. Note that the presence of electrons in the dangling bonds from the ($\bar{1}\bar{1}\bar{1}$) face of the crystal and the absence of electrons in the bonds from the (111) face implies a dipole moment of the whole crystal directed along [$\bar{1}\bar{1}\bar{1}$].

[1] H. C. Gatos, P. L. Moody, and M. C. Lavine, J. Appl. Phys. **31**, 212 (1960).
[2] J. F. Dewald, J. Electrochem. Soc. **104**, 244 (1957).
[3] S. G. Ellis, J. Appl. Phys. **30**, 947 (1959).
[4] J. G. White and W. C. Roth, J. Appl. Phys. **30**, 946 (1959).
[5] E. P. Warekois and P. H. Metzger, J. Appl. Phys. **30**, 960 (1959).
[6] J. W. Faust and A. Sagar, J. Appl. Phys. **31**, 331 (1960).

to (111) as shown in Fig. 1 the four dipole moments will not add up to zero. In the case shown in Fig. 1 there would be a net dipole moment of the whole crystal directed along [$\bar{1}\bar{1}\bar{1}$] and the ($\bar{1}\bar{1}\bar{1}$) face would be positively charged while the (111) face would be negatively charged. The III-V compounds are semiconductors, however, and this situation therefore cannot exist.

This situation may be dealt with by employing the idea of resonance. At the III-element face we may think of the bonds as made up by resonance between zero-electron and one-electron tetrahedral orbitals in the ratio of one to three, together with a four valence electron configuration of the ion present to an extent representing the degree of ionicity of the bonding in the compound. Similarly at the V-element face we may think of the bonds as made up by resonance between two-electron and one-electron tetrahedral orbitals in the ratio of one to three together with a four valence electron configuration of the ion present to the extent of the degree of ionicity. This viewpoint has the advantage that it can be extended to other types of zincblende-structure compounds such as the II-VI and I-VII compounds by altering the proportions of the various terms in the wave functions of the valence electrons.

There is a second field to which the filled and empty dangling bond model has application. This is to the core structure of dislocations. Haasen first pointed out that two types of edge dislocations are possible in the zincblende-structure III-V compounds, namely those in which the extra half-plane ends with a row of III-element atoms and those in which it ends with a row of V-element atoms.[7] Haasen also pointed out that one would expect the two sorts of dislocation to show different tendencies to trap conduction electrons and hence on Read's theory[8] to have different effects on the electrical conductivity. On the present model one can say that the III-element edged 60° dislocation (type II on Hornstra's classification[9]) has three one-electron dangling bonds to each zero-electron dangling bond in the dislocation core. Each of the former constitutes an acceptor level, as in the case of Read's treatment of dislocations in germanium, and each of the latter constitutes two acceptor levels one of which is probably very near the valence band. The V-element edged 60° dislocation will have three one-electron bonds to each two-electron bond. The former again constitute acceptor levels but the latter constitute donor levels one of which is probably very near the conduction band. Hence the III-element edged dislocation should acquire a stronger line charge and therefore a larger surrounding positive space charge region than that of a V-element edged 60° dislocation. There is evidence that the rate of etching in germanium at least depends among other things on the local electron or hole concentration and that it is the existence of the space charge region which is responsible for the revelation of edge dislocations by etching.[10] On this basis it may be assumed that with a suitable etchant and crystallographic plane it should be possible to reveal III-element but not V-element edged 60° dislocations. Observations of this type have been reported on the (110) surface of InSb.[11] Subsequent work has established that it is in fact the In-edged dislocations which are revealed by etching.[12]

Two points should be noted here. Firstly, by doping it is possible to alter the position of the Fermi level relative to the acceptor and donor levels of the dangling bonds. By raising the Fermi level the difference in line charge between the two types of dislocation will be minimized. Secondly, if the core bond rearrangements considered for dislocations in the diamond lattice[9] occur at all they can only do so in the III-element edged dislocation which has $\frac{3}{4}$ electron, on average, per bond. Such bond arrangement would eliminate the acceptor levels of the dangling bonds and would result in the V-element edged dislocation having the greater line charge and hence etching preferentially to the III-element edged dislocation. Therefore Venables and Broudy's observations[11,12] are evidence that core bond rearrangements do not occur in 60° dislocations in InSb.

ACKNOWLEDGMENTS

Thanks are due to Professor F. R. N. Nabarro for helpful discussions and to Professor M. H. L. Pryce for valuable suggestions for clarifying the presentation.

[7] P. Haasen, Acta Met. **5**, 598 (1957).
[8] W. T. Read, Phil. Mag. **45**, 775 (1954).
[9] J. Hornstra, Phys. Chem. Solids **5**, 129 (1958).
[10] J. W. Allen and K. C. A. Smith, J. Electronics **1**, 439 (1956).
[11] J. D. Venables and R. M. Broudy, J. Appl. Phys. **29**, 1025 (1958).
[12] J. D. Venables and R. M. Broudy (private communication).

Velocity Behavior of a Growing Crack

E. N. DULANEY AND W. F. BRACE
Department of Geology and Geophysics, Massachusetts Institute of Technology
(Received June 27, 1960)

An expression for the velocity behavior of a growing crack in a plate of brittle material is obtained by a mathematical refinement of the Mott energy balance around a moving crack. Crack velocity $\dot{c}$ is given by

$$\dot{c}=V_T(1-c_0/c),$$

where V_T is terminal crack velocity, c is instantaneous half-crack length, and c_0 is initial half-crack length. This predicts that velocity makes a hyperbolic asymtotic approach to terminal velocity. Growing cracks in large sheets of polymethyl methacrylate approach terminal velocity over three-quarters of their length as predicted by this theory but as though from an initial crack larger than the actual initiating crack. This is interpreted as due to energy losses at the very beginning of crack growth not included in the Mott energy balance.

I. INTRODUCTION

A NUMBER of theoretical predictions have been made of the maximum velocity of crack propagation in brittle material.[1-4] In recent reviews Anderson[5] and Gilman[6] conclude that those predictions based on Mott's energy balance for a moving crack[7] satisfactorily agree with most experimental observations of terminal crack velocity. However, Mott's theory in its original form cannot predict the entire velocity behavior of a crack as it accelerates from rest to terminal velocity, owing to a simplifying approximation made in the derivation of the theory. An expression for the complete velocity behavior can be readily found by a refinement of the mathematical analysis within the framework of the original Mott theory. Such an expression is obtained and compared with observed velocity behavior in polymethyl methacrylate.

II. ANALYSIS OF VELOCITY BEHAVIOR

For a moving crack in a brittle solid conservation of energy requires that

$$K+S+F=\text{constant}, \qquad (1)$$

where K is the kinetic energy of the time varying displacement field associated with the moving crack, S is the elastic energy in a material due to the presence of the crack minus the elastic energy in the same material without the crack, and F is the total surface energy associated with the new surface created by the crack. When properly evaluated the kinetic energy K includes disturbances radiating energy away from the region of the crack.

The foregoing energy balance, reported by Mott,[7] has been evaluated for conditions of plane stress under the important restriction that external forces do no work on the material during crack propagation. In other words, the theory is applicable to an originally static crack which grows in the interior of a thin infinitely large plate. A uniform tensile stress, applied at infinity normal to the long axis of the crack, is increased to a critical value σ at which the crack grows in the direction of its long axis. The tensile stress σ must remain constant during crack propagation.

For this model Eq. (1) is evaluated as follows: If c is the half length of a crack, approximated mathematically by a nearly flat elliptical hole (Fig. 1), T is the unit surface energy, assumed constant, and F is the surface energy of the crack per unit thickness of plate, then

$$F=4cT.$$

Evaluation of terms S and K depends on the stress and displacement fields around a moving crack. These fields are not known exactly but are usually assumed[2,8,9] to be the same as around a static crack. Considerable justification for this is given be a series of photographs

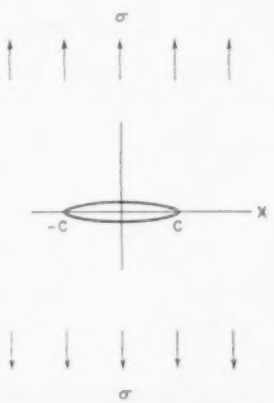

FIG. 1. Crack idealized as an elliptical cylindrical hole, under the single stress σ applied normal to the long axis of the crack. c is crack half-length.

[1] E. F. Poncelet, *Fracturing of Metals* (American Society for Metals, Cleveland, Ohio, 1948), p. 201.
[2] D. K. Roberts and A. A. Wells, Engineering **178**, 820 (1954).
[3] A. N. Stroh, Advances in Physics **6**, 418 (1957).
[4] J. W. Craggs, J. Mech. Phys. Solids **8**, 66 (1960).
[5] O. L. Anderson, *Fracture* (John Wiley & Sons, Inc., New York, 1959), p. 336.
[6] J. J. Gilman, *Fracture* (John Wiley & Sons, Inc., New York, 1959), p. 206.
[7] N. F. Mott, Engineering **165**, 16 (1948).
[8] E. H. Joffe, Phil Mag. **42**, 739 (1951).
[9] G. R. Irwin, in *Handbuch der Physik*, edited by S. Flügge (Springer-Verlag, Berlin, 1958), Vol. 6, p. 551.

taken by Wells and Post[10] of a moving crack in photoelastic material. These show clearly that dynamic and static stress fields do not differ significantly for a crack moving through a thin plate.

On using the stress and displacement fields of a static crack, S, the elastic energy difference resulting from the crack per unit thickness of plate and K, the kinetic energy per unit thickness of plate, are given by

$$S=-\pi\sigma^2c^2/E,$$

$$K=k\rho c^2\dot{c}^2\sigma^2/2E^2,$$

where E and ρ are the Young's modulus and density of the material, respectively, $\dot{c}$ is the velocity of propagation of the crack, and k is a numerical constant whose value depends on the stress and displacement fields about the moving crack. The form of the expression for kinetic energy was deduced by Mott on dimensional grounds independent of the numerical value of k.

On using these values of S, K, and F, Eq. (1) becomes

$$k\rho c^2\dot{c}^2\sigma^2/2E^2-\pi\sigma^2c^2/E+4Tc=\text{constant}. \quad (2)$$

If c_0 is half the initial crack length the Griffith theory of fracture[11] gives

$$4T=2\pi\sigma^2c_0/E,$$

which can be used to eliminate $4T$ in Eq. (2).

Mott differentiated with respect to c to remove the unknown constant on the right side of Eq. (2). Because he was primarily investigating terminal velocity he set $\partial\dot{c}/\partial c$ equal to zero to facilitate the analysis. This is only true near terminal velocity. This gave

$$\dot{c}=(2\pi E/k\rho)^{\frac{1}{2}}(1-c_0/c)^{\frac{1}{2}}$$

as the solution of Eq. (2). The constant k in Eq. (2) was evaluated by Roberts and Wells[2] using static crack expressions for stress and displacement. For material with Poisson's ratio of 0.25 their result is that

$$\dot{c}=0.38(E/\rho)^{\frac{1}{2}}(1-c_0/c)^{\frac{1}{2}}. \quad (3)$$

III. REFINEMENT OF THEORY

The approximation used by Mott and later by Roberts and Wells of setting $\partial\dot{c}/\partial c=0$ is only valid when $\dot{c}$ is very close to terminal velocity. Equation (2) may be solved rigorously without appealing to this simplification. First $4T$ in Eq. (2) is replaced as above by $2\pi\sigma^2c_0/E$; the constant term on the right is called U_0. Then

$$k\rho c^2\dot{c}^2\sigma^2/2E^2-\pi\sigma^2c^2/E+2\pi\sigma^2c_0c/E=U_0. \quad (4)$$

A boundary condition for the velocity is

$$\dot{c}=0 \text{ when } c=c_0.$$

Application of this boundary condition to Eq. (4) yields

$$0-\pi\sigma^2c_0^2/E+2\pi\sigma^2c_0^2/E=U_0,$$

from which

$$U_0=\pi\sigma^2c_0^2/E.$$

On substituting this value of U_0 the energy balance, Eq. (1), becomes

$$k\rho c^2\dot{c}^2\sigma^2/2E^2-\pi\sigma^2c^2/E+2\pi\sigma^2c_0c/E=\pi\sigma^2c_0^2/E. \quad (5)$$

This may be solved algebraically for $\dot{c}$, thus

$$\dot{c}=(2\pi E/k\rho)^{\frac{1}{2}}(1-c_0/c). \quad (6)$$

Equation (6) is the predicted velocity behavior and differs from that found by using the approximation $\partial\dot{c}/\partial c=0$ in that the term $(1-c_0/c)$ in Eq. (6) appears under a square-root sign in Eq. (3).

As the crack grows c_0/c will approach zero and the terminal velocity V_T will be $(2\pi E/k\rho)^{\frac{1}{2}}$. Equation (6) can be written

$$\dot{c}=V_T(1-c_0/c). \quad (7)$$

Velocity $\dot{c}$ plotted against $1/c$ gives a straight line (Fig. 2). The velocity axis intercept of the line is V_T and the reciprocal half-crack length axis intercept is c_0^{-1}. This type of plot is convenient for comparing velocity measurements with this predicted behavior. Figure 3 is a normal plot of $\dot{c}$ vs c from Eq. (7) showing the predicted velocity behavior. This mathematical refinement shows that according to Mott's theory crack velocity should make a hyperbolic asymptotic approach to terminal velocity.

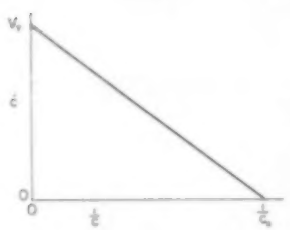

FIG. 2. Predicted velocity $\dot{c}$ of a growing crack as a function of inverse crack half-length. V_T is terminal velocity and c_0 is initial crack half-length.

IV. COMPARISON OF PREDICTED AND MEASURED VELOCITY

Data from unpublished studies of Professor E. Orowan were available for comparison of the foregoing theory with measured crack velocity. The experiments appear

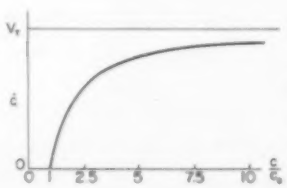

FIG. 3. Predicted velocity of a growing crack as a function of crack half-length.

[10] A. A. Wells and D. Post, Proc. Soc. Exptl. Stress Anal. **16**, 69 (1958).

[11] A. A. Griffith, *Proceedings of the First International Congress on Applied Mechanics*, J. Waltman, Jr., (Delft, Netherlands, 1924), p. 57.

to come close to fulfilling most of the requirements of the mathematical model.

Crack propagation was initiated at room temperature in sheets of polymethyl methacrylate (PMMA) measuring about 200 × 63 × 0.64 cm at a sawed slit halfway along one of the two long sides. The length of the slit c_0 varied from a fraction of a centimeter to 2 cm long. Tension was applied at the ends by means of a configuration of clamps suspended on knife edges. When rupture occurred the passage of the crack broke lines of printed-circuit paint placed normal to the path of the crack. The trace of a cathode-ray oscilloscope was photographed giving the time required for the crack to move from one painted line to another. From this, velocity of the crack was found as a function of distance from the edge of the sheet.

All of the cracks in the experiments propagated in a nearly straight line from the initial slit and branched about two-thirds of the way across the plate. Cracks which grew from the shorter initial slits appeared to approach a terminal velocity before branching; the others branched before reaching a terminal velocity, due possibly to edge effects. As Mott's theory is clearly not applicable after branching, only those cracks which appeared to approach a terminal velocity within the plate width will be considered here. The velocity behavior of two of these, specimens 10P and 11P, is shown in Fig. 4.

Comparison with theory is best done by replotting the data in $\dot{c}$ versus $1/c$ coordinates. This is done in Figs. 5 and 6 in which the small circles are points selected at 5-cm intervals and used for transcription of the data. The length c_0 of the slit, which was the initiating half-crack is shown as $1/c_0$ and includes a small crack which grew from the sawed slit as the specimen was brought up to load. Terminal velocity V_T is obtained

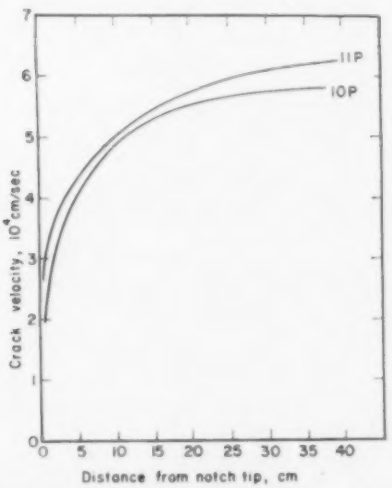

FIG. 4. Observed velocity behavior of two cracks, 10P and 11P, in PMMA sheets 63 cm wide. Cracks branched where curves end.

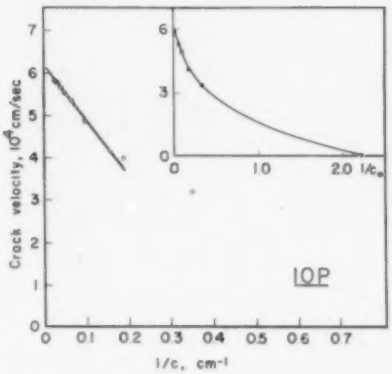

FIG. 5. Velocity behavior of crack 10P replotted as a function of inverse crack half-length. The figure in the upper right gives the entire behavior whereas the main figure shows the detailed behavior near terminal velocity.

using Maxwell's[12] value of Young's modulus of PMMA at room temperature for high strain rate (1000 cps) of 6.3×10^5 psi and density of 1.20. Thus

$$V_T=0.38(E/\rho)^{\frac{1}{2}}=7.1\times10^4 \text{ cm/sec}.$$

The transcribed points of Figs. 5 and 6 fall on a straight line between about 10 cm and 40 cm or for nearly $\frac{3}{4}$ the path length of the crack before branching. If this line is extrapolated, it intercepts the velocity axis at 6.2 and 6.7×10^4 cm/sec in Figs. 5 and 6, respectively. Call this intercept the "observed terminal velocity." Branching occurred when velocity was about 95% of observed terminal velocity.

If this straight line is extrapolated to the abscissa, the intercept is not c_0 but a distance four to five times greater than c_0.

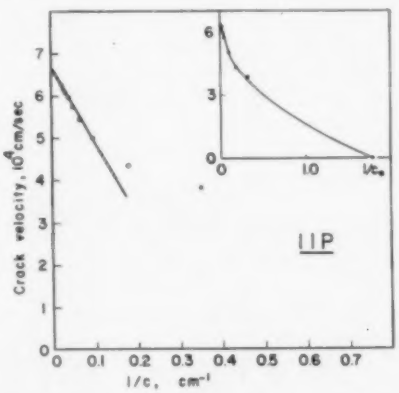

FIG. 6. Velocity behavior of 11P replotted as a function of inverse crack half-length.

[12] B. Maxwell, J. Soc. Plastics Engrs. **15**, 480 (1959).

V. DISCUSSION

The difference between predicted and observed terminal velocity is about 10% which is within the uncertainties in density, Young's modulus and Poisson's ratio used to calculate the predicted terminal velocity.

As to velocity behavior during crack growth, the cracks in the experiments behave as predicted by the theory, but as though having originated at an effective c_0 four to five times longer than the true c_0. This discrepancy can be explained qualitatively.

Inasmuch as the general approach of Mott, the application of the principle of conservation of energy, appears to be above reproach, the foregoing discrepancy must be due to improper evaluation of, or neglect of, terms in the energy balance equation. We must consider (1) the effect of letting the crack propagate from the edge, rather than, as prescribed by the theory, from the interior of the plate, (2) possible energy flux at the grips during crack propagation, and (3) any properties of PMMA different from those of the ideal brittle-elastic material of the theory.

Initiation of the crack from the edge rather than from the center of the plate is probably not responsible for the discrepancy. Inglis[13] found that the stresses near the tip of an elliptical crack were only slightly different for an interior crack and a half-crack at an edge.

As the crack starts to grow, an elastic disturbance travels from the crack to the grips holding the ends of the plate. This disturbance causes a displacement of the grips and an addition of energy to the plate. This energy added at the grips, which is not permitted in the mathematical model, must reach the vicinity of the crack to affect its velocity. Assuming that the energy flux occurs at a speed of approximately $(E/\rho)^{\frac{1}{2}} = 18.7 \times 10^5$ cm/sec, and using an observed average crack velocity of 3×10^4 cm/sec, the disturbance will not reach the vicinity of the crack tip until terminal velocity is nearly reached. Hence this effect will also be negligible, particularly in the early stages of crack growth.

Maxwell[12] found in a study of the elastic properties of PMMA that energy is lost as heat even at fairly high strain rates. This energy, measured as "loss factor," decreases rapidly with strain rate. For the experiments here, if we use reasonable values of duration of stress as the crack grows, then energy loss is significant during the first few centimeters of crack growth. The energy loss approaches zero within about 10 cm of the point of initiation of the crack. Expenditure of energy as either plastic work or as elastic energy which is not instantaneously recoverable is not included in the energy balance of Eq. (1). Such an energy loss appears to be present during crack propagation in PMMA and may be responsible for the discrepancy in predicted and observed velocity behavior.

The velocity behavior shown in Figs. 5 and 6 could be explained qualitatively by loss of energy as heat in the early stages of crack growth. Initial velocity on this basis should be lower than predicted. Initial velocity is lower than that given by points on a line joining $1/c_0$ and V_T. As crack velocity increases, strain rate increases and energy loss becomes zero. After traveling about 10 cm the crack behavior is described fairly closely by the theory, and the crack makes a hyperbolic asymptotic approach to terminal velocity.

VI. SUMMARY AND CONCLUSIONS

1. The theory of Mott as evaluated by Roberts and Wells is refined in order to predict the entire velocity behavior of a crack in brittle material. Cracks should make a hyperbolic asymptotic approach to terminal velocity.

2. Cracks in polymethyl methacrylate do make a hyperbolic asymptotic approach to terminal velocity but from an effective initial crack length some five times greater than the true one. This is qualitatively accounted for by considering the effect of heat loss during strain of this material known to be present even at high strain rates.

3. Terminal velocity may be difficult to measure for slow-moving cracks in brittle materials. Under these conditions a good estimate can be obtained by plotting velocity data in $\dot{c}$ vs $1/c$ coordinates, and finding the velocity intercept of the best straight line through the data points.

ACKNOWLEDGMENTS

We thank Prof. E. Orowan who generously made available unpublished data and freely discussed the experiments on PMMA. We must assume full responsibility for the correctness of the analysis, however, and for the interpretation of his experiments given here. Professors A. N. Stroh, S. M. Simpson, Jr., and T. R. Madden were very helpful in discussion of Mott's theory. Madden suggested the use of the $\dot{c}$ vs $1/c$ plot.

[13] C. E. Inglis, Trans. Inst. Naval Arch. (London) **55**, 223 (1913).

X-Ray Measurement of Grain Size*

B. E. WARREN
Massachusetts Institute of Technology, Cambridge, Massachusetts
(Received June 27, 1960)

When the number of crystals contributing to a powder pattern peak is small, changes in the position and orientation of the sample produce statistical variations in the measured integrated intensity. The statistics are those of a Poisson distribution, and the effect can be utilized in a very simple way for an absolute determination of grain size. Only relative intensity measurements are required. Grain sizes down to about one or two microns can be measured by this method. There is an interesting possibility of varying the experimental conditions in such a way as to distinguish between the sizes of grains and subgrains.

I. INTRODUCTION

DIFFRACTOMETER recordings of powder patterns are usually made with a flat-faced powder sample. In the ideal case, the individual crystals are so small that a large number contribute to each powder pattern peak, and the same peak area is obtained independent of the exact positioning of the sample. However, if only a small number of crystals contribute to a reflection, there will be large variations in the peak areas if the sample is given small changes in position and orientation. This statistical variation in peak area, which results from a coarse grained sample, is a well-known experimental effect. To the experimenter measuring integrated intensities it is a serious nuisance, but with properly chosen conditions, the effect can be made a convenient tool for the x-ray measurement of grain size. By the usual line broadening methods it is possible to measure crystal sizes up to about 1000 A. The statistical variation method, which we shall now develop, is suited to an absolute determination of grain size for crystals larger than about $1\,\mu = 10\,000$ A.

II. THEORY OF THE STATISTICAL VARIATION METHOD

We assume a collimated primary beam, of small cross-sectional area A_0, falling on a flat-faced powder sample made up of randomly oriented grains. The arrangement is shown schematically by Fig. 1. Imagine that the counter is set at the proper position for a reflection *hkl*. During the measurement the sample is made to rotate through a small angle ϕ. This angle ϕ and the length l of the receiving slit determine a small solid angle Ω which contains the normals $H(hkl)$ of all crystals contributing to the measured diffracted energy.

A small irradiated element of volume i, at a depth z, is shown by Fig. 1. It has a thickness Δz and volume $\Delta V_i = (A_0/\sin\theta)\Delta z$. The number of crystals in this volume is

$$n_i = (r\Delta V_i)/v_c = (rA_0\Delta z)/v_c \sin\theta,$$

where v_c = average volume per crystal, $r = \rho'/\rho$ = relative density of the sample, ρ' = density of the sample, ρ = density of a crystal.

If j is the *hkl* multiplicity, the average number of crystals in ΔV_i which contribute to the measured reflection is given by

$$\bar{m}_i = \frac{n_i j\Omega}{4\pi} = \frac{\beta r \Delta z}{\sin\theta} \tag{1}$$

where $\beta = (jA_0\Omega)/4\pi v_c$.

For different positions and orientations of the sample, the number of crystals m_i in the volume element ΔV_i at depth z_i which contribute to the reflection will vary above and below the average value $\bar{m}_i$. Since the fraction $j\Omega/4\pi$ is very small, the probability of a value m_i is given by the Poisson distribution law[1]

$$w(m_i) = \frac{(\bar{m}_i)^{m_i} \exp(-\bar{m}_i)}{m_i!}.$$

For a Poisson distribution, the statistical variations follow the simple law

$$\langle (m_i - \bar{m}_i)^2 \rangle = \bar{m}_i. \tag{2}$$

Let y_i be the number of counts recorded from the m_i crystals in ΔV_i for one setting of the sample, and let $\bar{y}_i$ be the average number of counts from the $\bar{m}_i$ average of crystals in ΔV_i.

$$y_i = \alpha_i m_i \quad \bar{y}_i = \alpha_i \bar{m}_i \tag{3}$$

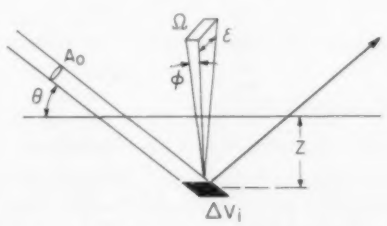

FIG. 1. Diffraction conditions for a fine primary beam falling on a flat-faced powder sample. The solid angle Ω contains the planar normals of all contributing crystals. The volume element ΔV_i is shown in section, it has a height ΔZ and top face $A_0/\sin\theta$.

* Research sponsored by the U. S. Atomic Energy Commission.

[1] H. Margenau and G. M. Murphy, *The Mathematics of Physics and Chemistry* (D. Van Nostrand Company, Inc., Princeton, New Jersey, 1943), pp. 422–425.

where μ is the linear absorption coefficient and

$$\alpha_z = K \exp[-(2\mu r z)/\sin\theta]. \quad (4)$$

From Eqs. (2) and (3) we can write

$$\langle (y_i - \bar{y}_i)^2 \rangle = \alpha_z^2 \bar{m}_i. \quad (5)$$

Let $Y = \sum_i y_i$ be the number of counts from the sample for any one of the sample settings, and let $\langle \bar{Y} \rangle = \sum_i \bar{y}_i$ be the average number of counts from the sample. Since the distributions in the different layers i are independent

$$\langle (Y - \langle \bar{Y} \rangle)^2 \rangle = \langle \sum_i (y_i - \bar{y}_i) \sum_j (y_j - \bar{y}_j) \rangle$$
$$= \sum_i \langle (y_i - \bar{y}_i)^2 \rangle = \sum_i \alpha_z^2 \bar{m}_i.$$

On replacing the sum by an integral

$$\langle (Y - \langle \bar{Y} \rangle)^2 \rangle = \int_0^\infty K^2 \exp\left[-\frac{4\mu r z}{\sin\theta}\right] \frac{r\beta}{\sin\theta} dz = \frac{K^2 \beta}{4\mu}. \quad (6)$$

In the same way

$$\langle \bar{Y} \rangle = \sum_i \alpha_z \bar{m}_i = \int_0^\infty K \exp\left[-\frac{2\mu r z}{\sin\theta}\right] \frac{r\beta dz}{\sin\theta} = \frac{K\beta}{2\mu}. \quad (7)$$

By combining Eqs. (6), (7), and (1)

$$\frac{\langle (Y - \langle \bar{Y} \rangle^2) \rangle}{(\langle \bar{Y} \rangle)^2} = \frac{\mu}{\beta} = \frac{4\pi\mu v_c}{j A_0 \Omega}. \quad (8)$$

If we approximate the crystals by spheres of diameter D, then $v_c = \pi D^3/6$ and the diameter cubed is given by

$$D^3 = \frac{3 j A_0 \Omega}{2\pi^2 \mu} \frac{\langle (Y - \langle \bar{Y} \rangle)^2 \rangle}{(\langle \bar{Y} \rangle)^2}. \quad (9)$$

To allow for a variation in crystal size, let m_{ik} be the number of contributing crystals of size v_k in the layer i.

$$y_i = \alpha_z \sum_k m_{ik} v_k \quad \bar{y}_i = \alpha_z \sum_k \bar{m}_{ik} v_k,$$

where $\alpha_z = K' \exp[-2\mu r z/\sin\theta]$. Since the orientations of the different sizes are random and independent

$$\langle (y_i - \bar{y}_i)^2 \rangle = \alpha_z^2 \sum_k v_k^2 \bar{m}_{ik}.$$

A weighted average crystal size can be defined by

$$\langle v_c \rangle = \sum_k v_k^2 \bar{m}_{ik} / \sum_k v_k \bar{m}_{ik}.$$

With the additional relation

$$\sum_k v_k \bar{m}_{ik} = j \Omega r A_0 \Delta z / (4\pi \sin\theta),$$

we arrive again at Eq. (9) with D^3 replaced by $\langle D^3 \rangle$. This is an average of D^3 weighted with respect to the volume of material having the size D.

If there is preferred orientation in the sample, the integrated intensity of the peak is γ times what it would have been for random orientation. The factor γ can be determined by comparing with other powder pattern peaks, or by comparing with a sample which has random orientation. Preferred orientation introduces an additional factor γ in Eq. (1). The final result allowing for size variation and preferred orientation is expressed by

$$\langle D^3 \rangle = \frac{3 j A_0 \Omega \gamma}{2\pi^2 \mu} \frac{\langle (Y - \langle \bar{Y} \rangle)^2 \rangle}{(\langle \bar{Y} \rangle)^2}. \quad (10)$$

III. EXPERIMENTAL PROCEDURE

The area A_0 is fixed by placing two small apertures in the primary beam, the second one close to the sample. The solid angle $\Omega = \phi\epsilon$ is the product of two angles; ϕ in the plane of the primary and diffracted beams, and ϵ perpendicular to this plane. The angle ϵ is conveniently fixed by the length l of the receiving slit $\epsilon = l/2R\sin\theta$, where R is the distance from the sample to the receiving slit. If the counter is held stationary, the angle ϕ can be provided by a rotation of the sample. If a commercial diffractometer is used, it is simpler to employ a very wide receiving slit and let both sample and counter rotate. The sample contributes only while the diffracted beam is within the receiving slit, and hence $\phi = w/2R$ where w is the width of the receiving slit. For this case the solid angle is given by

$$\Omega = (wl)/(4R^2 \sin\theta). \quad (11)$$

In the approximation for Ω given by Eq. (11), we are assuming that both ϕ and ϵ are large enough to neglect the variation in direction of the primary beam. We also assume that the 2θ width of the reflection is small compared to the width of the receiving slit. If a very broad receiving slit is used, it is necessary to employ a counter which has uniform sensitivity over the area of the receiving slit.

It is convenient to have the sample in the form of a disk pivoted to rotate. If the narrow primary beam strikes the flat face of the disk near the periphery, it is a simple matter to set the disk at say 24 different orientations and hence obtain 24 values of Y. For each setting, the total number of counts is registered for a fixed time which is a little greater than the time during which the reflected beam is within the receiving slit. Changing the counter orientation 2 or 3 degrees to exclude the *hkl* peak, and repeating the above procedure, gives a background correction.

From the form of Eq. (10), it is obvious that absolute intensity measurements are not required. Only ratios are involved, and hence the quantities Y are merely numbers proportional to the number of counts corrected for background which are received in each measurement. Since $\langle (Y - \langle \bar{Y} \rangle)^2 \rangle = \langle Y^2 \rangle - (\langle \bar{Y} \rangle)^2$, there are alternative ways for expressing the average.

IV. APPLICATION TO KCl POWDER

As an example of the method, a sample of finely ground KCl powder was examined with a Norelco diffractometer. By rough microscopic examination the powder had an approximate average size $D = 5\,\mu$. The reflection (200) was used with CoKα radiation. With

$w=0.05$ cm, $l=0.5$ cm, $R=17$ cm, $\sin\theta=0.29$, $A_0=0.04$ cm^2, $\mu=370$ cm^{-1}, $j=6$, and $\gamma=1$, Eq. (10) becomes

$$\langle D^3\rangle=7.3\times10^{-9}\frac{\langle(Y-\langle\bar{Y}\rangle)^2\rangle}{(\langle\bar{Y}\rangle)^2}.$$

With the counter turning at 1°/min, counts were taken for a fixed time of 64 sec. The measurements were made at 24 positions on the sample and corrected for background. To illustrate the magnitude of the statistical variation, the 24 corrected numbers proportional to Y are given: 128, 172, 140, 115, 83, 92, 141, 95, 120, 103, 142, 123, 83, 123, 132, 114, 121, 94, 99, 74, 102, 96, 105, 125. From these numbers $\langle(Y-\langle\bar{Y}\rangle)^2\rangle/(\langle\bar{Y}\rangle)^2=0.039$ and $\langle D^3\rangle^{\frac{1}{3}}=0.00065$ cm$=6.5\,\mu$.

V. DISCUSSION

Since it is really $\langle D^3\rangle$ which is measured, rather rough numbers suffice to give a satisfactory value of $\langle D^3\rangle^{\frac{1}{3}}$. To extend the method to very fine grains, it is advantageous to decrease the values of A_0 and Ω so as to maintain a significant statistical variation in the values of Y. However we are limited by the need for enough intensity to make the measurements. High values of the structure factor and absorption coefficient are favorable for a measurement of small grain size. For the average material, something like one or two microns seems to be the lower limit for the statistical variation method.

There is an interesting possibility of varying the quantity measured. Suppose that the grains in a sample are composed of subgrains with slight differences in orientation between the subgrains of any one grain. If we use small values of ϕ and ϵ, two adjacent subgrains will not be able to contribute to any one measurement and we will be measuring the subgrain size. By choosing much larger values of ϕ and ϵ, so that all of the subgrains of a grain can contribute, we will be measuring the whole grain size.

JOURNAL OF APPLIED PHYSICS VOLUME 31, NUMBER 12 DECEMBER, 1960

Mechanism of Photoconductivity in Microcrystalline Powders

RICHARD H. BUBE
RCA Laboratories, Princeton, New Jersey
(Received July 19, 1960)

Measurements on a variety of cadmium sulfide powder cells show that there are four different regions encountered as the applied voltage is varied. At low voltages an ohmic region is found in which barrier breakdown does not occur. At intermediate voltages a region is found in which barrier breakdown by a Process I occurs. At still higher voltages a region is found in which barrier breakdown by another Process II occurs in addition to that associated with Process I. At very high voltages another ohmic region is found where all barrier limitations have been removed. It is proposed, on the basis of the data, that Processes I and II are associated either with tunneling of electrons through interparticle barriers or with a reduction in barrier height assisted by the localized trapping of photo-excited or field-excited holes. A model constructed along these lines is applied to a variety of observations such as current-voltage curves, photocurrent lag after periods of no applied voltage or of opposite-polarity applied voltage, the existence of a semipermanent polarized set, ac properties of powders, and the hysteresis or storage effect.

INTRODUCTION

THE electrical properties of powders constitute a relatively unresolved field, at least as far as such properties as photoconductivity and electroluminescence are concerned. Photoconductive and electroluminescent cells employ mainly nonsingle-crystal forms of material, such as microcrystalline powders, sintered layers or pellets, and evaporated layers. Basic investigations of the mechanisms, however, have for obvious reasons been restricted largely to single crystals. Fortunately, the investigation of photoconductivity in single crystals bears enough similarity to the properties of powders suitably prepared and measured, to allow the conclusion that the fundamental processes are probably the same. In the field of electroluminescence, the differences between powder and single-crystal properties are still sufficiently large to prevent such a conclusion.

Even in the field of photoconductivity, however, the additional phenomena which characterize the properties of powders as distinguished from single crystals are sufficiently striking to merit consideration in their own right. It is the purpose of this report to present the results of such an investigation.

There are two major differences between the properties of powders and those of single crystals. (1) The ratio of surface to volume is much larger in the powders. (2) A current which flows through a powder sample must traverse many interparticle contacts which will not have the relatively simple properties of ohmic metallic contacts on a single crystal.

These differences are dramatically demonstrated if one takes photosensitive crystals and grinds them up to obtain a powder. The resulting powder shows only very low, if any, photosensitivity. Following this line

of reasoning, Kolomiets[1] suggested that failure to obtain a photosensitive powder of CdS was the result of high resistance between the particles; he subsequently showed that the photosensitivity could be materially improved by introducing a superficial oxidation which would form conducting CdO on the surfaces of the particles. Other authors[2] have also emphasized the importance of contact-controlled currents in powders.

Research at about the same time showed that photosensitive single crystals of CdS could be reproducibly prepared by the incorporation of approximately equal proportions of a donor, such as chlorine, and an acceptor, such as copper.[3] Several investigators were finally successful in preparing photosensitive CdS powders by using variations of phosphor-firing techniques with a chloride, usually present in large excess, and copper.[4-5] Later, others followed the lead of behavior in phosphor systems and showed that trivalent cations such as gallium, and other acceptors such as silver, could be used in preparing photosensitive CdS powders[6,7] just as in single crystals.[3] Such preparations normally require several firings in succession to produce the optimum product; a detailed summary of a typical method is given in the Experimental section of this paper. The delicacy of the art required in the preparation of such powders is additional evidence of the importance of surface effects.

Intermediate between powders and single crystals are sintered pellets, powder pressed into pellet shape and then fired to cause sintering. These may also be prepared to have high photosensitivity, starting with a mixture of CdS, a chloride, and copper as in the powder preparation.[8,9]

Perhaps the most outstanding difference between photoconductivity in powders and crystals is the dependence of photocurrent on voltage. Although single crystals may show rectification effects with certain types of metallic electrodes, it is usually possible to form an electrode contact for which the current will vary linearly with applied voltage. It is thus possible to operate a single crystal at very low voltages (such as millivolts) and still observe the same photosensitivity (defined as photoconductivity per unit light intensity) as at higher voltages. The same is by no means true of powders, for which the apparent photosensitivity varies markedly with applied voltage; to obtain the same photosensitivity as in single crystals, powders must be operated with applied fields in the range of 10^4 v/cm, which corresponds to an applied voltage of several hundred volts in a conventional powder cell. For lower voltages, the photocurrent of a powder photoconductor varies with a high power of the voltage, usually between 2 and 8. Thus in a manner of speaking the powder behaves like a single crystal would if it were fitted with very strongly rectifying contacts.

Another major difference between powder photoconductors and single crystals with ohmic electrodes is the photocurrent lag in following changes in *applied voltage*. All photoconductors show some photocurrent lag in following changes in *light intensity* because of trapping of free carriers with subsequent release after the cessation of excitation. But in single crystals with ohmic contacts changes in photocurrent with applied voltage are essentially instantaneous. In powder photoconductors, on the other hand, the photocurrent lag with changes in applied voltage can be much larger than the lag with changes in light intensity. This is particularly true if the polarity of the voltage is changed as well as (or instead of) its magnitude. This effect has manifested itself in the general inferiority of powers for ac operation as compared to dc. Using the same effect, DeVore[10] has suggested the possibility of erasing the long decay tail of photocurrent in a powder after the cessation of light excitation, by inserting a brief period of opposite-polarity voltage.

A third distinguishing characteristic of powders is the hysteresis or storage effect, as described by Nicoll.[11] When the applied voltage to a suitable cell is sufficiently high, brief exposure to light excitation will change the conditions in the powder so that a much higher current continues to be drawn even after the light excitation has been removed. Interrupting the voltage returns the powder to its initial condition. The effect is observed in CdSe powders at room temperature, but not at lower temperatures, in CdS powders at elevated temperatures, but not at room temperature. The temperature dependence of the effect has not been directly incorporated into previous speculation about its mechanism; this paper attempts to include particularly this feature of the hysteresis effect in its description of photoconductivity in powders. Investigations of the hysteresis effect by Smith[12] and by DeVore[13] have indicated that the induced high-conductivity state of the powder is accompanied by the emission of radiation, closely correlated with the current flowing. Such results have led North and Smith to propose hole injection as a possible important feature in the hysteresis process.[14]

This report presents the results of detailed measurements on a variety of photoconducting powders to give further insight into these various characteristic properties of powders. A descriptive picture of photo-

[1] B. T. Kolomiets, Doklady Akad. Nauk S.S.S.R. **83**, 561 (1952).
[2] A. Rose, Proc. I.R.E. **43**, 1850 (1955).
[3] R. H. Bube and S. M. Thomsen, J. Chem. Phys. **23**, 15 (1955).
[4] S. Rothschild, J. Opt. Soc. Am. **46**, 662 (1956).
[5] S. M. Thomsen and R. H. Bube, Rev. Sci. Instr. **26**, 664 (1955).
[6] W. van Gool, Phillips Research Repts. **13**, 157 (1958).
[7] R. H. Bube and A. B. Dreeben, Phys. Rev. **115**, 1578 (1959).
[8] S. Yoshimatsu, C. Kanzaki, S. Ibuki, and N. Murai, J. Phys. Soc. Japan **10**, 493 (1955).
[9] F. Gans, Bull. sci. A.I.M. (Belg). **11**, 897 (1953).
[10] H. B. Devore (unpublished data).
[11] F. M. Nicoll, R C A Rev. **19**, 77 (1958).
[12] R. W. Smith (private communication).
[13] H. B. DeVore (unpublished data).
[14] D. O. North and R. W. Smith (private communication).

conductivity processes in powders is constructed from the data which seem adequately to describe, at least qualitatively, the various phenomena. The picture involves three basic features: (1) the possibility of tunneling through interparticle barriers or of appreciably reducing the barrier height, (2) the possibility of field excitation of holes, and (3) the possibility of barrier penetration being modulated by the capture of photo-excited or field-excited holes near the barrier. Many of the same effects may result simply from the geometrical situation of small-area contacts between particles. In our discussion, however, we shall speak in terms of barriers.

EXPERIMENTAL

A summary of the various materials used in this investigation is given in Table I. Each of the samples has been identified for convenience with a letter of the alphabet, each figure showing experimental data has the identifying letter of the corresponding sample involved. The majority of the samples are based on the same photoconducting powder, a CdS:Cl:Cu powder; samples A through H are for this powder in various proportions of ethyl cellulose binder, sample M for this powder in polystyrene binder, sample N for this powder dry without binder, sample R for this powder after undergoing a cyanide wash, and sample S for this powder after undergoing an etch with HCl.

Because of the importance of this powder for the present investigation, it is desirable first to describe its preparation in a little detail.[15] This is essentially the same preparation technique as that described by Busanovich and Thomsen.[16] CdS powder (RCA 33-C-291A) was mixed in water with 20% $CdCl_2$ and 200 ppm Cu as a solution of the acetate, and then dried at 120°C for 16 hr. The dry mix was fired for 20 min at 600°C in air. The fired powder was washed free of chloride and dried for 2 hr at 120°C. As a second step, 1500 ppm chlorine as $CdCl_2$ were added and the sample was dried for 2 hr at 120°C. Then the sample was fired for 20 min at 675°C in air. Finally the material was fired at 500°C in S vapor, 10 min against a nitrogen background and then 10 min in vacuum. Powder samples were mixed with the indicated proportion of binder placed on gaps in TIC-coated glass slides, and dried at 50°C. The gaps were 0.5 mm in width and 5 mm in length.

TABLE I. Summary of materials.

Sample	Composition	Binder	Wt CdS/Wt binder
A	CdS:Cl:Cu[a]	Ethyl cellulose[b]	326
B	CdS:Cl:Cu[a]	Ethyl cellulose[b]	244
C	CdS:Cl:Cu[a]	Ethyl cellulose[b]	109
D	CdS:Cl:Cu[a]	Ethyl cellulose[b]	54
E	CdS:Cl:Cu[a]	Ethyl cellulose[b]	46
F	CdS:Cl:Cu[a]	Ethyl cellulose[b]	38
G	CdS:Cl:Cu[a]	Ethyl cellulose[b]	22
H	CdS:Cl:Cu[a]	Ethyl cellulose[b]	8
M	CdS:Cl:Cu[a]	Polystyrene[c]	198
N	Dry CdS:Cl:Cu[a]	None	...
R	Cyanide-washed CdS:Cl:Cu[a]	None	244
S	1 N HCl etched CdS:Cl:Cu[a]	None	244

[a] Preparation described in text.
[b] In amyl alcohol solution.
[c] In xylene solution.

[15] Powder samples were prepared by A. B. Dreeben and N. DiGuiseppe.
[16] C. J. Busanovich and S. M. Thomsen, U. S. Patent 2,876,209; March 3 (1959).

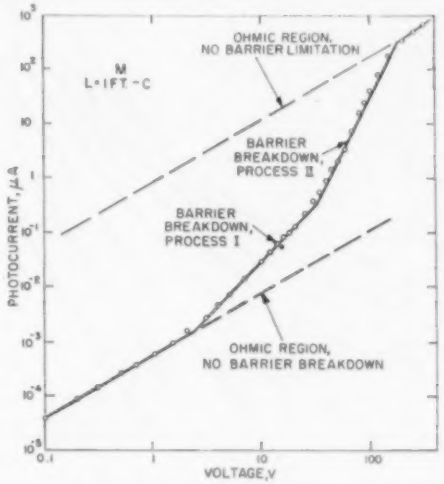

FIG. 1. Photocurrent as a function of voltage for CdS:Cl:Cu power in binder, sample M (see Table I). The curve illustrates the four basic regions of the current-voltage curve.

All measurements were made at room temperature, using either incandescent light for excitation, or where indicated, a Bausch and Lomb monochromator. Variations in light intensity were obtained with neutral density filters, reliable for seven orders of magnitude in light intensity. Current-voltage curves are equilibrium values, giving time at each voltage for such equilibrium to be reached. Transient behavior was recorded directly on a Leeds and Northrup X-Y recorder, or through a Leeds and Northrup micromicroammeter.

RESULTS

Current vs Voltage Curves

A typical current-voltage curve illustrating most of the principal features of such a curve is shown in Fig. 1. The current-voltage curve shows four separate sections: (1) at low voltages, below about 3 v (60 v/cm across the cell gap) the current varies linearly with applied voltage in an ohmic relationship; (2) for intermediate voltages, between about 3 v and 60 v (1.2×10^3 v/cm across the cell gap) the current varies as a higher power of the voltage, usually near 2; (3) for higher voltages, between 60 v and about 100 v (2×10^3 v/cm

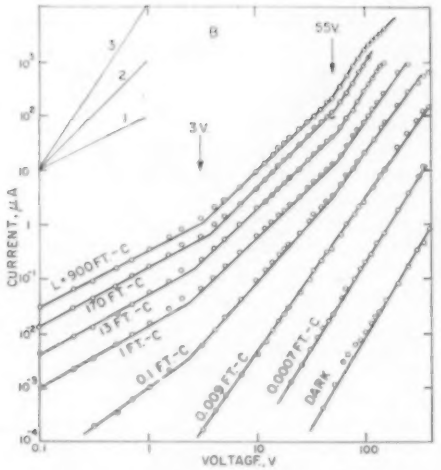

FIG. 2. Current as a function of voltage for CdS:Cl:Cu powder in ethyl cellulose binder, sample B (see Table I), for different values of light intensity.

across the cell gap) the current varies as a still higher power of the voltage, usually about 3 to 5; and (4) for voltages in excess of 100 v (dependent on light level as we shall see later), the current again varies with applied voltage in an ohmic manner. The basic nature of these four regions has been indicated on Fig. 1. The low-voltage ohmic region corresponds to the passage of a current which does not involve breakdown of barriers between particles. The second region corresponds to the breakdown of barriers according to Process I, left for the moment unspecified. The third region corresponds to the breakdown of barriers according to Process II in addition to Process I. The ohmic region for high voltages corresponds to no barrier limitation to the passage of current. If the high-voltage ohmic region is extrapolated back toward low voltages, we see the behavior we might expect if we were dealing with a single crystal with ohmic electrodes. If the low-voltage ohmic region is extrapolated up toward high voltages, we see the behavior we would expect if no barrier breakdown occurred. About three to four orders of magnitude in current separate the two ohmic limiting ranges.

One of the obvious variables is that of light intensity. Figure 2 shows similar curves for sample B measured in the dark and over six orders of magnitude of light intensity. Inspection of the data allows us to draw the following conclusions: (1) the threshold for the onset of the high-voltage ohmic region shifts to higher voltages with decreasing light intensity; (2) both the low-voltage ohmic region and breakdown by Process I require a certain light intensity for their occurrence, i.e., in the dark and at low light levels only breakdown by Process II occurs. Across the whole range of voltage, therefore, processes associated with light excitation are important. The ohmic low-voltage region and the breakdown by Process I region are not observed until the light intensity is sufficiently high; the breakdown by Process II region shows an almost linear variation of photocurrent with light intensity in the low light range; the threshold for the high-voltage linear range varies with light intensity. The data also indicate that breakdown by Process II occurs for much lower voltages than the observed transition from Process I to Process II would indicate at high light levels. It is safe to conclude that Processes I and II are both acting over the whole range from 3–100 v when the light intensity is high enough to permit Process I. In the dark, Process II is the only one of the four processes which is still detectable.

The effect of light can arise from two different mechanisms. First, excitation by light may simply reduce the resistivity of the bulk of the material, thus allowing greater concentration of the applied field at the barrier contacts, with whatever attendant increase in conductivity due to barrier reduction or tunneling may result. Secondly, excitation by light may result in the accumulation of a trapped space charge of such a sign as to increase the conductivity by the effects on the barrier.

The next question which comes to mind is: Are these different current-voltage regions basic to the properties

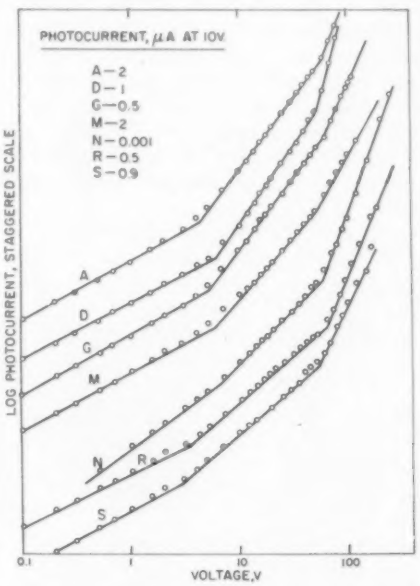

FIG. 3. Photocurrent as a function of voltage for seven different samples of CdS:Cl:Cu powder (see Table I for identifications) for excitation by 900 ft-c. All samples show similar behavior regardless of powder to binder ratio, type of binder, absence of binder, or surface treatments to powder. Note that the photocurrent scale is staggered; as indicated by the data listed, all samples have about the same photocurrent except sample N, the dry powder.

of the powder itself, or are they perhaps dependent on the binder? Figure 3 presents the data to answer this question. Current-voltage curves are given for seven different samples of the CdS:Cl:Cu powder, with different ratios of powder to binder, with a different binder, with no binder, and with two different surface treatments. Every one of these samples shows basically the same behavior, with the low-voltage ohmic region, the breakdown by Process I region, and the breakdown by Process II region, together with the voltages at which transitions from one region to another occur, all being independent of the binder or of surface treatments. All of the samples also show about the same sensitivity except for the dry powder; the low sensitivity in the case of the dry powder is at least partially explained by the realization that in this case excitation was through the powder, whereas in all other cases excitation was through the glass plate.

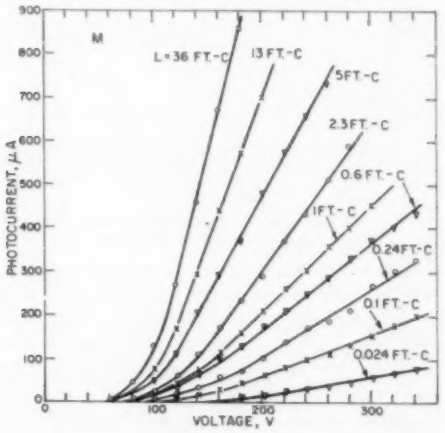

FIG. 4. Photocurrent as a function of voltage for CdS:Cl:Cu powder in polystyrene binder, sample M (see Table I), in the high voltage ohmic region, for different values of light intensity.

Let us now consider the high-voltage ohmic region. Figure 4 presents detailed data for sample M in this region, showing the variation with light intensity. If the linear portion of such a series of curves is carefully extrapolated back to the voltage axis, the intersection can be interpreted as the threshold voltage for complete breakdown of the barriers. The results of such an analysis are shown in Fig. 5 where the threshold voltage is plotted as a function of light intensity. Relatively independent of light intensity and equal to about 100 v above 1 ft-c, the threshold voltage increases very rapidly with decreasing light intensity below 1 ft-c until it is 280 v at 10^{-2} ft-c. The characteristics of the high-voltage ohmic region are summarized in Table II. It can be noted that the threshold current, i.e., that current corresponding to the threshold voltage, is relatively independent of light intensity or threshold voltage. The ohmic resistance in the high-voltage region

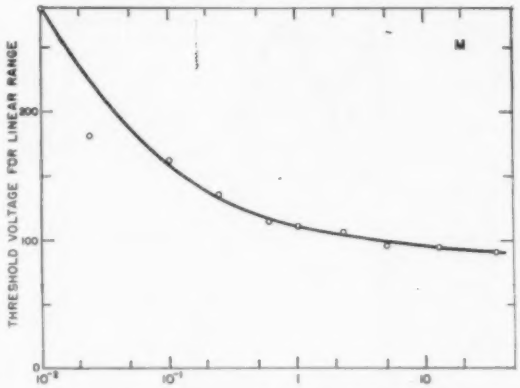

FIG. 5. The threshold voltage for the high-voltage ohmic region as a function of light intensity for sample M, as determined from data such as are shown in Fig. 4.

varies relatively slowly with light intensity, being approximately inversely proportional to the 0.4 power of the light (see Fig. 18).

A final item of interest relevant to the current vs voltage curves is the dependence of the spectral response of the powder on the applied voltage. Figure 6 shows spectral response curves for sample F, measured in the low-voltage ohmic region, in the breakdown by Process I region, and in the breakdown by Process II region. The only real difference shown by the curves is the considerably reduced excitation by strongly-absorbed light in the low-voltage ohmic region. All three curves show evidence of the peak at 5800 A which has been associated by Avinor[17] with uncompensated copper centers.

Photocurrent Lag Phenomena

The existence of photocurrent lag phenomena after a period of no applied voltage or a period of opposite-polarity voltage is the second indicative characteristic of the photoconductivity properties of powders. It is

TABLE II. Dependence of high-voltage ohmic region of light intensity.[a]

Sample M			
Light intensity, ft-c	Threshold voltage	Threshold current, μa	Ohmic resistance, ohms
9×10^{-3}	282	20	2.0×10^{6}
2.4×10^{-2}	181	15	2.0×10^{6}
10^{-1}	163	36	8.8×10^{5}
2.4×10^{-1}	136	29	6.2×10^{5}
6×10^{-1}	115	29	5.0×10^{5}
1	112	30	4.2×10^{5}
2.3	108	40	2.9×10^{5}
5	96	43	2.2×10^{5}
13	96	65	1.5×10^{5}
36	92	80	1.0×10^{5}

[a] See Figs. 4, 5, and 18.

[17] M. Avinor, thesis, University of Amsterdam, 1959.

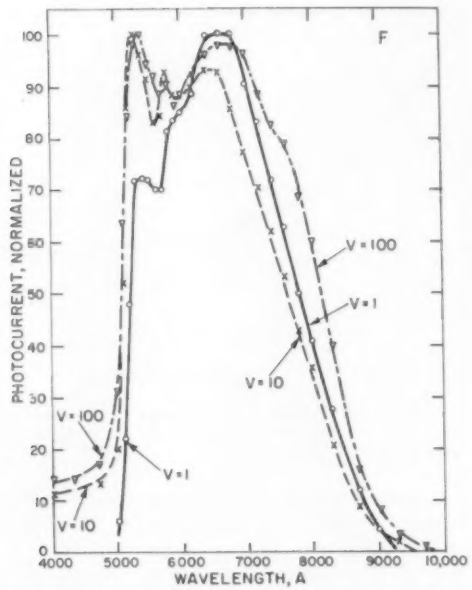

FIG. 6. Spectral response curves for CdS:Cl:Cu powder in ethyl cellulose binder, sample F (see Table I), measured in three different regions of the current-voltage curve.

the purpose of the data given here to explore these phenomena and to link them with the current-voltage curves.

Two types of measurements were devised to explore the photocurrent lag properties of powders. There are many ways of accomplishing the same purpose; Fig. 7 shows the two series of measurements that were used here. The first series is shown in Fig. 7 (a) and consists of the following steps: (1) a voltage V_0 has been applied to the powder for a time long enough for the current to reach equilibrium, (2) the voltage is turned off for a period of time t_1, usually 2.5 or 18 sec as designated in particular cases, (3) the original voltage V_0 was reapplied for a period t_1, (4) the voltage was again turned off for a period t_1, (5) a voltage of opposite polarity to the original voltage was applied for a period t_1, with magnitude either $\frac{1}{2}$, 1, or 2 times V_0, (6) another period t_1 of no applied voltage took place, and finally (7) there was a reapplication of the original voltage V_0. The following quantities were obtained from this series of measurements: (a) the rise time after a period t_1 of voltage being turned off (from the rise between t_1 and $2t_1$), (b) the rise time as affected by a previous period of opposite polarity (from the rise after $5t_1$), (c) i_1/i_0, the proportion of the initial current attained after a period t_1 of applied voltage V_0 following a period t_1 of no applied voltage, and (d) i_2/i_0, the proportion of the initial current attained after a period t_1 of opposite-polarity applied voltage.

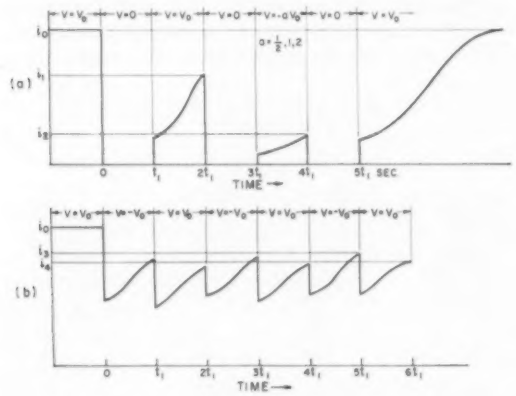

FIG. 7. Illustrative representation of two different types of measurements of importance to the discussion in this paper. The measurements are used to characterize slow recovery of photocurrent after periods of no voltage applied or periods of a voltage of reverse polarity applied.

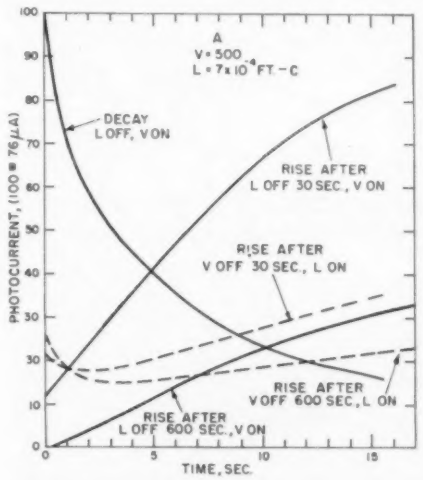

FIG. 8. Response curves for CdS:Cl:Cu powder, sample A (see Table I). A comparison is given between the response times for changing light intensity at fixed voltage with those for changing voltage at fixed light intensity.

The second series of measurements is shown in Fig. 7 (b): (1) a voltage V_0 has been applied to the powder for a time long enough for the current to reach equilibrium, (2) at $t=0$ the voltage is abruptly reversed to $-V_0$, (3) the voltage is abruptly reversed thereafter every t_1 seconds. Quantities measured are (a) i_3/i_0, the proportion of the initial current being drawn at the end of a period of opposite polarity at $t=7t_1$, and (b) i_4/i_0, the proportion of the initial current being drawn at the end of a period of same polarity as the initial voltage at $t=6t_1$. For convenience, the currents for both $+V$ and $-V$ are plotted on the same side of the axis.

Typical examples of simple rise and decay curves for sample A at a low light level are given in Fig. 8.

TABLE III. Summary of response to transients for sample A.[a]

	L, ft-c V, volts	7×10^{-4} 500	9×10^{-3} 200	10^{-1} 100	1 75	13 50	170 28	900 20
Photocurrent, μa		76	61	56	71	62	67	65
Decay time, sec	$\tau_{\frac{1}{2}}$	2.9	0.53	<0.1				
	$\tau_{\frac{1}{e}}$	9.0	2.9	0.65	<0.1			
Rise time, sec for V left on								
L off 30 sec		5.5	1.7	1.3	0.65	<0.1		
L off 600 sec		26.3	8.3	5.8	2.2	0.3	<0.1	
Rise time, sec for L left on								
V off 30 sec		29.5	10.2	11.4	9.5	7.5	3.7	0.43
V off 600 sec		64	31	57	44	31	18	5.1
Rise time, sec for L left on after:								
V off 18 sec		19	8.1	9.4	6.0	5.4	1.8	≤0.4
$V=-V_0/2$ for 18 sec		49	22	27	21	15	5.4	1.6
$V=-V_0$ for 18 sec		79	35	36	27	19	6.3	1.8
$V=-2V_0$ for 18 sec			51	58	45	23	5.4	1.6
Values of i_2/i_0 (see Fig. 7)								
$V=-V_0/2$		0	0	0.02	0.03	0.08	0.10	0.10
$V=-V_0$		0.02	0.12	0.39	0.43	0.62	0.90	0.93
$V=-2V_0$			1.26	1.8	4.2	6.0	4.6	6.0
Values of $\frac{i_3+i_4}{2i_0}$ (see Fig. 7)		0.07	0.18	0.28	0.45	0.70	1.0	1.0

[a] See Figs. 9 and 10.

Equivalent numerical data are summarized in Table III. The rise time is the time for the current to increase to one-half its equilibrium value; the decay time is the time for the current to decrease to one-half its equilibrium value. At this light level, the rise time after a period of light off with voltage on is longer than the decay time upon turning the light off, and the rise time after a period of voltage off with light on is longer still. The dependence of rise and decay times on light intensity is given in Fig. 9 and by the data of Table III. Measurements were made at constant photocurrent, decreasing the applied voltage with increasing light intensity to maintain this condition. All processes become faster with increasing light intensity. Response times with light off and voltage on are well known to become shorter with increasing light intensity because of a decreasing effect of trapping. The fact that the response times to changing voltage at constant light also become shorter with increasing light intensity shows that the time required to re-establish breakdown conditions by Process I and Process II is decreased by the effect of light excitation.

As previously indicated, the photocurrent lag after a period of opposite polarity is greater than after a period of no applied voltage. The data of Table III, for example, show that at 9×10^{-3} ft-c, the rise time after 18 sec of no applied voltage is 8 sec. The comparable rise times after 18 sec of an opposite-polarity voltage are 22 sec if the opposite-polarity voltage is ½ the initial voltage, 35 sec if the opposite-polarity voltage equals the initial voltage, and 51 sec if the opposite-polarity voltage is twice the initial voltage. This lag also decreases markedly with increasing light intensity.

Another way of characterizing the lag with reversing polarity is to consider the current i_2 of Fig. 7, measured after a period of opposite-poiarity voltage. The variation with light intensity of i_2/i_0 for $V=-V_0$, $-2V_0$, and $-V_0/2$ are summarized in Table III and in Fig. 10. The figure also shows the ratio $(i_3+i_4)/2i_0$ as a function of light intensity. With the use of suitable normalization

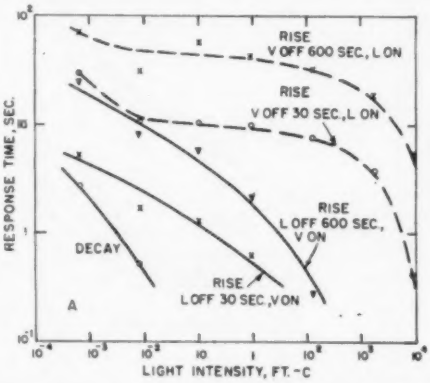

FIG. 9. Response times as a function of light intensity for CdS:Cl:Cu powder, sample A (see Table I). Measured for constant photocurrent by adjusting applied voltage for each light intensity (see Table III). A comparison is given between the response times for turning the light off and leaving the voltage on with those for turning the voltage off and leaving the light on.

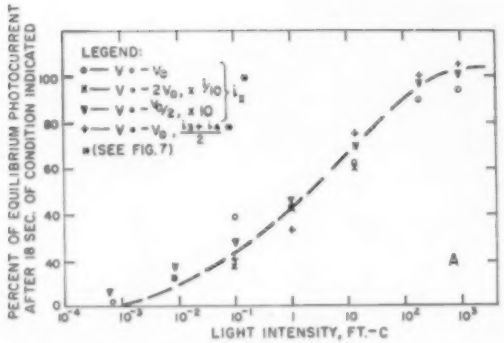

FIG. 10. The dependence of the ability of powder sample A (see Table I) to pass current upon reversal of the polarity of the applied voltage, as a function of the light intensity. The quantities i_2, i_3, and i_4 are defined in Fig. 7.

factors, all four sets of data can be represented by a single curve, rising from near zero at 10^{-3} ft-c to 100% above 10^2 ft-c. The achievement of 100% in these measurements means no more than that 100% modulation of the photocurrent is possible *with an 18-sec period*. For shorter periods of measurement (values of t_1) smaller modulation fractions would be observed.

Concept of Polarized Voltage Set

In addition to short-term effects of changing the applied voltage and its polarity, there are also certain long-term effects of considerable importance.

The first of these occurs only upon the very first application of voltage to a previously unmeasured cell. The drastic difference caused in an extreme case of such an initial effect is shown in Fig. 11 for sample H.

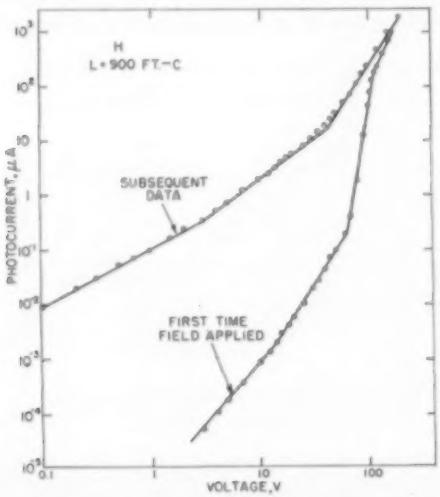

FIG. 11. An illustration of the change in the powder properties upon first application of a voltage, thereafter remaining unchanged. Data are for sample H (see Table I).

A freshly prepared cell was measured starting at low voltages and increasing the voltage for measurement of the current-voltage curve. After the breakpoint apparently corresponding to the region dominated by breakdown Process II, the current increases extremely rapidly with voltage. Equilibrium current-voltage curves after this first application of voltage are remarkably reproducible.

This last point is illustrated further by the data given in Fig. 12. Four sets of data are plotted here together, the maximum difference in the values being indicated on the figure: (1) after a long period of one polarity applied voltage, a curve for the same polarity applied voltage, (2) after a long period of one polarity applied voltage, a curve for the opposite polarity, (3) and (4), the same as (1) and (2) but with a long

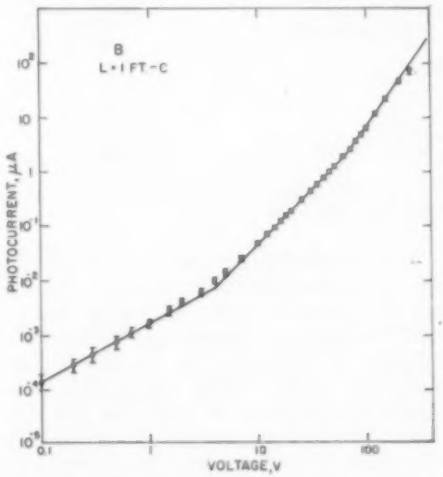

FIG. 12. Four sets of data for sample B (see Table I) plotted together, all lying within the limits indicated: (a) after long application of one polarity voltage, measurement for the same polarity; (b) after long application of one polarity voltage, measurement for the opposite polarity; (c) the same as (a) but with the opposite polarity being the one applied for a long time; (d) the same as (b) but with the opposite polarity being the one applied for a long time.

period of the opposite polarity voltage preceding the measurements. The equilibrium current-voltage curve is completely independent of polarity.

Although the equilibrium curve shows this independence, the same is not true at all of the photocurrent lag. In order to demonstrate the correlation between photocurrent lag, the polarity of the applied voltage, and the polarity of the voltage applied for a long time before the measurements are made, we use the type of plot shown in Fig. 13, which we shall call a "modulation profile." A modulation profile consists simply of the plotting of i_1/i_0, i_2/i_0, and i_4/i_0 as a function of the applied voltage; usually a light intensity of 1 ft-c and a period $t_1 = 2.5$ sec is used for uniformity.

In order to speak about the effect, we shall arbitrarily designate one polarity of the voltage as "plus" and the other polarity as "minus"; since the cell is perfectly symmetric before the application of a voltage, this designation has no meaning except to enable the discussion to be a little simpler. The data of Fig. 13 (a) indicate that after a long period of plus polarity, a "plus set" is built into the powder which manifests itself in a different transient behavior for plus voltages from that for minus voltages. The curve for i_1 is a kind of standard, indicating what the plus current would have been if the voltage had simply been turned off rather than being replaced by a period of minus voltage; it is relatively independent of applied voltage. The

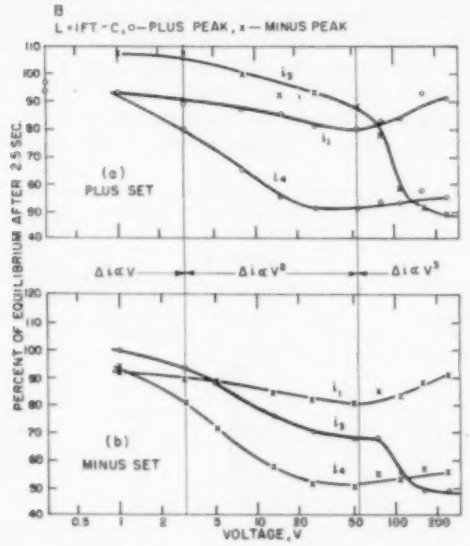

FIG. 13. Modulation profiles for sample B (see Table I) measured at 1 ft-c. The quantities i_1, i_3, and i_4 are defined in Fig. 7. Polarities of the applied voltage are arbitrarily designated plus for one direction and minus for the opposite direction. (a) is after a long application of plus polarity, thereby inducing a plus set to the powder. (b) is after a long subsequent application of minus polarity, thereby eliminating the plus set and causing an equivalent minus set.

following results are seen from Fig. 13 (a): (1) for very high voltages, in the region of breakdown by Process II and probably near the region of high-voltage ohmic behavior, the modulation current (i_3 and i_4) is independent of polarity and relatively constant with voltage; (2) the modulation current (i_4) for the same polarity as induced the set (plus in this case) remains at this low value or decreases slightly even further as the voltage is decreased into the region where breakdown by Process I is dominant; (3) the modulation current (i_3) for the opposite polarity (minus) to that which induced the set increases rapidly with decreasing voltage so that when the voltage is in the range where breakdown by Process I is dominant, 100% modulation

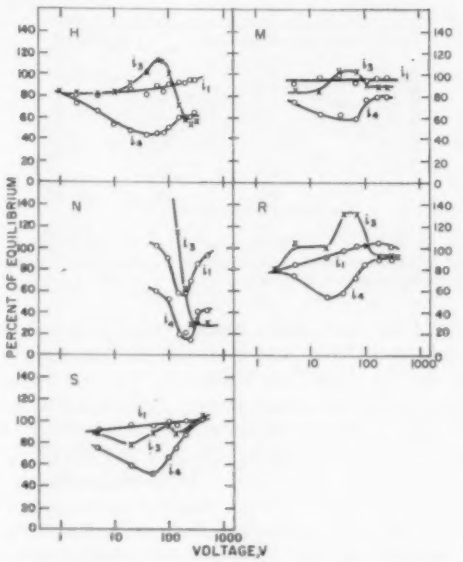

FIG. 14. Modulation profiles for the other samples of CdS:Cl:Cu powder identified in Table I. The quantities i_1, i_3, and i_4 are defined in Fig. 7.

is achieved; and (4) when the voltage is in the low-voltage ohmic range, all currents show approximately 100% modulation, i.e., there are no photocurrent lag effects in the low-voltage ohmic region.

The effect of the polarized set established by the long-term operation with a voltage of a given polarity is therefore to increase the speed with which the powder can establish equilibrium breakdown conditions when the *opposite* polarity is applied and breakdown is occurring primarily by *Process I*.

If the foregoing viewpoint concerning the observed effects is correct, it should be possible to reverse the set. Taking the same cell on which the measurements

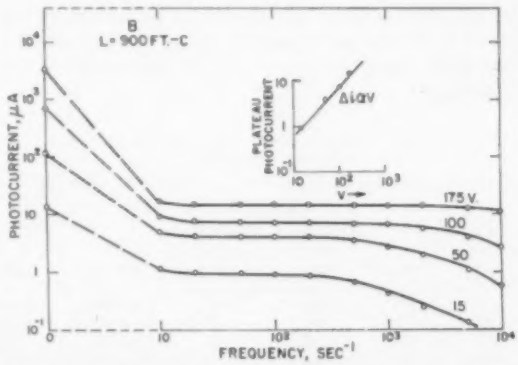

FIG. 15. Variation of the photocurrent of sample B (see Table I) for 900 ft-c excitation with the frequency of the applied voltage. The inset shows that the high-frequency photocurrent before the breakpoint varies linearly with the applied rms ac voltage.

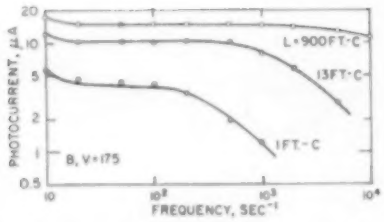

FIG. 16. Variation of the photocurrent of sample B (see Table I), for 175 volts applied, with frequency of the applied voltage at different intensities of excitation.

of Fig. 13(a) were made, a minus polarity voltage was applied for 90 min, and then the modulation profile given in Fig. 13(b) was measured. The curves for i_1 and i_4, now for the minus current, are identical with the same curves of Fig. 13(a) for the plus current. The curve for i_2 is qualitatively the same in both plots, its somewhat lower value in Fig. 13(b) indicating that a complete reversal of the set was not accomplished in 90 min. As mentioned before, the equilibrium current-voltage curve of Fig. 12 is completely independent of these changes in the transients.

Similar modulation profiles are found for the other samples of CdS:Cl:Cu powder we have discussed. Data for five such samples, all measured after a plus set, are given in Fig. 14, also for the dry powder, sample N. The dry powder shows a much stronger dependence of i_1 on voltage than the powder in binder, and also shows an extremely strong set. Values of i_2/i_0 greater than 100% imply simply that the transient current passed for the polarity opposite to the set is greater at the time it is measured than the initial current i_0.

Ac Photocurrent Data

The analysis of simple ac photoconductivity data on powder photoconductors can give additional evidence as to the nature of the ohmic low-voltage region. If this region is indeed the result of conduction processes not involving breakdown, the absence of photocurrent lag indicated by the previously presented modulation profiles should persist to relatively high frequencies of the applied field.

TABLE IV. Capacitance of powder cells from frequency breakpoint.[a]

Sample B					
Light intensity, ft-c	Voltage	Breakpoint frequency, sec^{-1}	Breakpoint current, μa	R, ohms	C, μμf
1	175	200	4	4.4×10^7	114
13	50	300	2	2.5×10^7	133
13	175	1100	10	1.8×10^7	52
900	15	470	1	1.5×10^7	143
900	50	1500	4	1.2×10^7	53
900	100	4200	7	1.4×10^7	17

[a] See Figs. 15, 16, and 18.

Figure 15 gives the dependence of photocurrent on frequency between 10 and 10^4 cps, relative to the photocurrent obtained for the same applied voltage under dc conditions. A component of the current is found which is independent of frequency over a wide frequency range. In this region where the photocurrent is independent of frequency, the current-voltage relationship is ohmic. Figure 16 shows the variation of the ac photoconductivity with frequency for a range of light intensities. The applied voltage (rms) was kept constant at 175 v. If the photocurrent breakpoint with increasing frequency is interpreted as resulting from an RC time constant of the cell, the corresponding values of cell capacitance can be calculated. Values are given in Table IV; they lie between about 20 and 150 μμf. The calculated capacitance varies about inversely as the applied voltage for fixed light intensity, and much more slowly with light intensity at fixed voltage.

Table V compares, for several values of light intensity and applied voltage, the actual dc photocurrent measured, the value of photocurrent which would be expected at the higher voltage by extrapolating the low-voltage ohmic photocurrent, and the value of photocurrent measured under ac conditions at the higher voltage. There is a close quantitative similarity between the extrapolated low-voltage dc values and the measured high-voltage ac values. We are therefore justified in concluding that the process responsible for the low-voltage ohmic behavior occurs for all voltages. By eliminating all breakdown processes, ac measurements reveal this ohmic behavior at higher voltages.

TABLE V. Comparison of high-voltage ac photocurrents with low-voltage dc photocurrents.

Sample B				
Light intensity, ft-c	Voltage	Observed dc photocurrent, μa	Low-voltage ohmic dc photocurrent extrapolated	Measured ac photocurrent, μa
1	175	350	8.0	4.3
13	50	40	3.6	1.7
13	100	73	7.8	4.4
13	175	1600	14	9.8
900	15	22	5.3	1.0
900	50	200	18	4.0
900	100	1600	38	7.2
900	175	4800	66	14

This conclusion can be strengthened further by the following consideration. It is clear from Fig. 15 that the ratio of dc photocurrent to ac photocurrent is decreasing with decreasing voltage. If we plot, therefore, the ratio of the dc to ac photocurrent as a function of the applied voltage, we should expect the curve to reach unity at a voltage corresponding to the transition between the ohmic low-voltage region and the first breakdown region. Figure 17 shows such a plot; the ratio becomes unity for an applied voltage of 3 v, which is the measured transition voltage in Fig. 1, 2, etc.

Finally, it is interesting to compare the variation of powder resistance with light intensity in the low-voltage ohmic region to that in the high-voltage ohmic region. The data are given in Fig. 18; both show a similar variation of resistance inversely with the square root of the light intensity. A similar behavior seems indicated by the ac resistance except at the higher light levels.

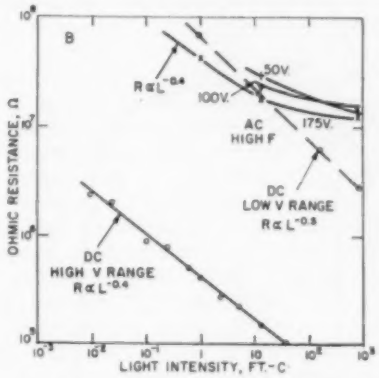

FIG. 18. A comparison of the variation of the ohmic resistance with light intensity (a) in the high-voltage dc region, (b) in the low-voltage dc region, and (c) in the high-frequency ac region. All show comparable variations with light intensity except at the highest light intensities.

Temperature Dependence

Some discrimination between mechanisms is possible on the basis of the temperature dependence of the current-voltage curves. Detailed measurements on sample C show that *equal or higher currents are measured at 90°K over the whole voltage range*, compared to values obtained at room temperature. In the low-voltage ohmic range, currents are about equal at the two temperatures, but since the low-voltage ohmic range comes to an end at about 0.5 v at 90°K instead of 3 v as at room temperature, measured currents at 10 v are an order of magnitude higher at 90°K than at room temperature. Except for the shift in the onset of breakdown by Process I, the curves are identical at the two temperatures; no shift in the onset of breakdown by Process II is found. The finding of such a temperature dependence for the photocurrent in the breakdown voltage range argues against such mechanisms as simple space-charge injection or voltage reduction of barrier height which should be much less effective at low temperature, since they depend on the magnitude of a high-energy tail in the electron distribution. Breakdown through the mechanism of tunneling should be reasonably temperature independent as long as the density of free electrons remains constant, and hence would be favored by these data except for the low voltage indicated for the onset of breakdown (about 0.005 v per particle). Physical contraction of the cell, binder, and powder at low temperatures may also play a role in the measured results, as it affects the particle-to-particle contacts.

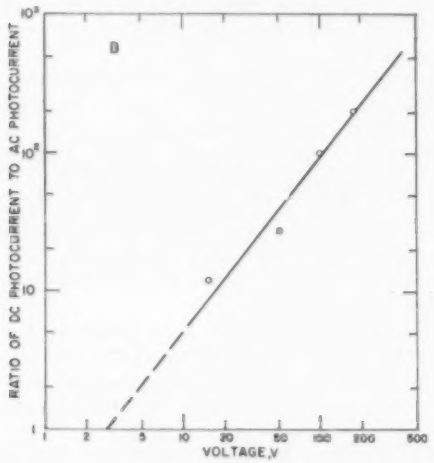

FIG. 17. The ratio of the dc photocurrent to the ac photocurrent, in the range where it is independent of frequency, as a function of the applied voltage. The two currents become equal for a voltage of about 3 v. Data are taken from Fig. 15 for sample B (see Table I).

Hysteresis

A typical hysteresis curve for a CdSe:Cl:Cu powder cell at room temperature is given in Fig. 19. All the data for the figure are obtained in the dark. If the voltage is increased in the dark, the current will increase continuously with voltage until a point B is reached where the current will suddenly rise very steeply to point C. If the voltage is now decreased, the current will decrease along the curve CD, and then for voltages lower than D decrease rapidly to A. If the voltage is turned off at some point between C and D during such a measurement, only the current corre-

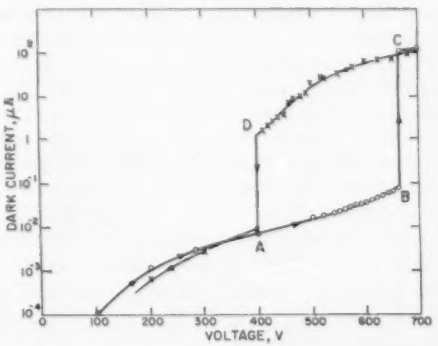

FIG. 19. Typical case of the hysteresis or storage effect in CdSe:Cl:Cu powder. Arrows indicate the direction of the measurements.

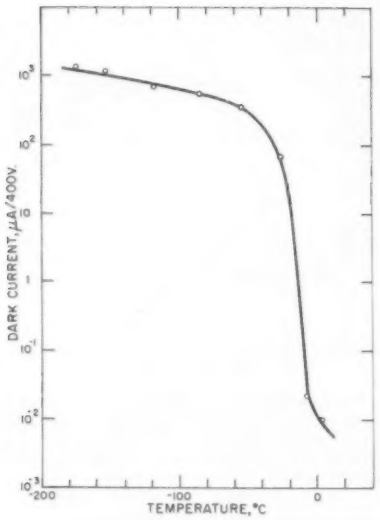

FIG. 20. The temperature dependence of the storage current induced in CdSe:Cl:Cu powder at low temperature by brief exposure to light, subsequently heated in the dark.

sponding to that voltage on the curve AB will be observed upon reapplication of the voltage. If a voltage between A and B is applied in the dark and the powder is then exposed to sufficient light, a triggering action occurs. The result is that the current is on the corresponding portion of the curve CD after removal of the light. We have then a quasi-stable high-conductivity state which can be created either by going to high enough voltage in the dark or by causing photoexcitation in a certain voltage range; the high-conductivity state can be destroyed by a period of interrupted voltage.

An interesting feature of this hysteresis effect is that it is found in the form described for CdSe at room temperature, but not at lower temperatures; for CdS at elevated temperatures, but not at room temperature. It is natural to ask what happens to the hysteresis effect at lower temperatures. All of the evidence at hand indicates that the hysteresis effect is not so much frozen out by lowering the temperature as it is brought about more slowly and at lower voltages, i.e., instead of observing a low current suddenly transforming to a high current when the voltage is raised high enough, thus clearly giving the recognized characteristics of the hysteresis effect, the high current is attained with long buildup times at lower voltages, thus giving the type of behavior we have been describing for CdS throughout this paper. The hysteresis effect occurs when barrier breakdown occurs suddenly; the phenomena described in this paper occur when barrier breakdown occurs gradually.

As a test of this viewpoint, measurements were made on CdSe:Cl:Cu powder at 90°K. A voltage of 400 v was applied at room temperature, a voltage insufficient to bring about the high-conductivity state at room temperature. As the powder was cooled to 90°K, the dark current decreased normally with decreasing temperature to a very low value at 90°K where it was perfectly stable in the dark. The cell was then exposed to a low light level for several minutes with no applied voltage and then returned to the dark. The dark current after turning off the light was over 10^5 times higher than the previous dark current, and about the order of magnitude of the high-conductivity state at room temperature. When the voltage was turned off and subsequently reapplied, the current was initially quite low but increased slowly and steadily until after several minutes it again read the high value. The high-conductivity state could thus be interrupted by turning off the voltage at 90°K, but could not be destroyed. In other words, there was a voltage-associated current lag exactly as we have discussed for CdS at room temperature.

With the CdSe powder in the high-conductivity state at 90°K, the powder was then heated in the dark with 400 v applied to the cell. The temperature dependence of the current is shown in Fig. 20. The high-conductivity state is relatively temperature insensitive until a temperature of about −50°C is reached. In the next 50°, the current drops by five orders of magnitude, as it must somewhere below room temperature since the high-conductivity state cannot be maintained by 400 v at room temperature.

The shape of the curve and the temperature of the breakpoint shown in Fig. 20 are exactly the same as that found for the temperature dependence of photoconductivity in CdSe.[18] In fact, the hysteresis effect is

TABLE VI. Phenomena in CdS and CdSe associated with the hole ionization energy of sensitizing centers.

Phenomenon	Temperature range of occurrence CdS	CdSe
Variation of photocurrent with a power of light intensity greater than unity (superlinearity)	Near 100°C (not at room temperature)	Near 0°C (not at low temperature)
Temperature quenching of photoconductivity	Near 100°C	Near 0°C
Optical quenching of photoconductivity	Below 100°C	Below 0°C
Hysteresis effect (abrupt transition to high-conductivity state)	Near 100°C (not at room temperature)	Near 0°C (not at low temperature)
Voltage-associated current lag (gradual transition to high-conductivity state)	Below 100°C	Below 0°C

[18] R. H. Bube, J. Phys. Chem. Solids **1**, 234 (1957).

just another of a series of phenomena previously described for CdS and CdSe which have a strong temperature dependence. These phenomena are summarized in Table VI. The relationship with temperature is associated with the value of the hole ionization energy of sensitizing centers in the two materials: 0.6 ev in CdSe and 1.0 ev in CdS. There can be little doubt but that *superlinearity, temperature quenching of photoconductivity, and the hysteresis effect (abrupt transition to high-conductivity state) occur in a temperature range where the sensitizing centers are being transformed from trapping centers to recombination centers*, i.e., in a temperature range where the demarcation level for the sensitizing centers is passing through the level associated with these centers. Likewise, *optical quenching of photoconductivity and voltage-associated current lag effects (gradual transition to high-conductivity state) occur in a temperature range where sensitizing centers are acting as recombination centers* and the demarcation level lies below the level associated with these centers.

DISCUSSION

Descriptive Model

In seeking to ascribe specific mechanisms to the four portions of the current-voltage curve found in photoconducting powders, we shall be thinking essentially in terms of the processes summarized in Fig. 21. Fig. 21 (a) shows the simple energy level scheme for a photoconducting insulator powder with interparticle barriers. A powder cell will consist of about 100 such particles in series.

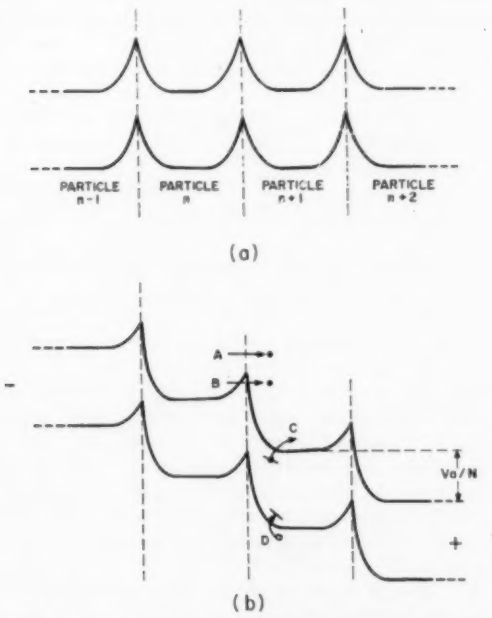

FIG. 21. (a) Schematic illustration of the energy bands of a CdS powder with barriers between particles. (b) Processes contributing to current flow when a voltage V_a is applied to the powder shown in (a), with N total particles across the cell gap.

Figure 21 (b) shows the general effects which may be expected upon the application of an external field to such a photoconducting system. There are particularly four processes which are singled out for consideration: A, electrons flowing over the cathode barrier or photo-excited in the region of the cathode barrier; B, electrons flowing into the crystal as the result of tunneling through the cathode barrier; C, thermal ionization of deep filled levels in the neighborhood of the barrier, producing free electrons and leaving behind a positive space charge; and D, capture of photo-excited or field-excited holes at sensitizing centers in the crystallite, where they will contribute to the positive space charge in the crystal, and where their presence will result in longer lifetimes for free electrons through the sensitization mechanism normally associated with hole capture at these centers.

We may next inquire as to the likely source of the field-excited holes mentioned in process D. It has been shown by Lampert[19] that the processes of no injection, single-carrier injection, and double-carrier injection of excess carriers into an insulator should be characterized by current-voltage ranges in which respectively $i \propto V$, $i \propto V^2$, and $i \propto V^3$. The apparent similarity between these theoretical dependencies and the experimental ranges as illustrated in Fig. 1 makes this interpretation attractive. The difficulty of identifying a source for the injected holes, however, and the fact that at still higher voltages another ohmic current-voltage region is encountered, makes a picture involving injection of holes undesirable. Such a picture would be quite reasonable for similar effects found with electrodes on a single crystal, where direct injection of holes from the anode is possible. In the powder it seems more likely that holes are formed by impact ionization at the cathode barrier when the field is sufficiently high. We therefore think primarily of electron flow into the crystallite over or through the cathode barrier, modulated by the effects of stably trapped holes near the barrier. These holes are formed either by optical excitation or by impact ionization.

Discussion of Four Current-Voltage Regions

1. Low-Voltage Ohmic Region

For applied fields below 60 v/cm in the powder cells, the current varies linearly with the voltage. The average voltage drop per particle is $\sim kT$. This region has in addition the following defining characteristics: (a) it does not occur in the absence of light, or at least the currents involved in the absence of light or at very low light levels are so small as to be below the level of detection; (b) there are no voltage-associated lag effects as evidenced directly by measurements on lag in the

[19] M. A. Lampert, R C A Rev. **20**, 682 (1959).

low-voltage range and by the detection of the same type of currents at frequencies of the applied field up to 10^4 cps; (c) it is poorly excited by strongly-absorbed light.

Two possible mechanisms for such a low-voltage ohmic region suggest themselves: (a) The ohmic current arises primarily from photoexcitation in the barrier region. Such a current may be likened to the ohmic current observed when a high resistance is inserted in series with a simple photovoltaic cell. (b) The ohmic current results from a decrease in interparticle barrier height caused by *the light*, at voltages low enough so that no tunneling or decrease in barrier height is caused by *the voltage*.

Both of these possible mechanisms show the dependence of the existence of the ohmic region on the presence of light excitation, and the absence of any voltage-associated lag effects since no barrier breakdown is associated with the application of a voltage.

2. *Breakdown Region of Process I*

When the applied field exceeds 60 v/cm ($\sim$0.03 v/particle), the current rises as a higher-than-unity power of the voltage, usually close to a variation as V^2. This range extends up to applied fields of about 10^3 v/cm ($\sim$0.5 v/particle) as a separate region but undoubtedly continues on up through the range dominated by breakdown Process II. It has the following defining characteristics: (a) it does not occur in the absence of light; (b) voltage-associated photocurrent lag is found for the same polarity voltage as that used in inducing the set, but not for the opposite polarity; (c) voltage-associated photocurrent lag is eliminated by a sufficient increase in the light intensity.

Two possible mechanisms are indicated by the characteristics of barrier breakdown Process I. (1) The barrier height is reduced by the applied *voltage*, over and above any effect in reducing the barrier height that the light alone may produce. (2) Tunneling through the barrier is induced by the applied voltage.

It is difficult to distinguish between these two mechanisms in such a nonhomogeneous system as that provided by powders. Light is necessary for the occurrence of Process I either because the voltage reduction of the barrier is dependent for its manifestation on a concurrent reduction in the barrier by light alone, or because the localization of photo-excited holes contribute additional positive charge in the vicinity of the barrier to increase the effective field across the barrier, thus increasing voltage-induced tunneling through the barrier. The temperature independence favors the tunneling mechanism.

This is the appropriate place to discuss the occurrence of voltage-associated photocurrent lag, which is applicable to both Process I and Process II. When the voltage is turned off and then reapplied at a later time, a considerable time will be required for the current to increase to its equilibrium value if the voltage is above the low-voltage ohmic region. In these higher-voltage regions, some degree of barrier breakdown is involved in the passage of current. The extent of barrier breakdown, whether by reduction in barrier height or by tunneling, depends directly on the width of the barrier and on the fraction of the externally applied field which is effective across the barrier. The slow increase in current is partly due to the slow thermal ionization of deep levels [C in Fig. 21 (b)], resulting in increased curvature of the bands and an increased effective field across the barrier. Photo-excited or field-excited holes may also contribute to the increase of current with time; holes captured at sites [D in Fig. 21 (b)] where they are thermally stable will have an effect similar to thermally ionized electron levels in increasing the effective field across the barrier. The schematic representation of the transformation in the energy levels with these various processes which tend to increase the field across the barrier is shown for a single particle in Fig. 22 (a).

When the voltage is turned off, reverse processes set in to undo the effects just described, as indicated in Fig. 22 (b). A reverse current flows to refill the thermally emptied levels, and the holes captured near the barrier are either thermally released without replacement to disappear eventually through recombination, or undergo recombination with free electrons directly. As a result, the reapplication of a voltage at some later time will find an initially much smaller field across the barrier than existed when the voltage was turned off.

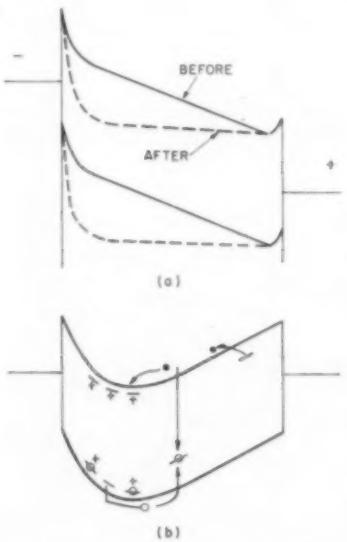

FIG. 22. (a) Schematic representation of changes in energy band configuration for a single particle resulting from slow emptying of electron levels and filling of hole levels. (b) Processes leading to a reversal of the changes indicated in (a) and to a transient current flow after the applied voltage is turned off.

To the extent that the reverse processes are not complete, an instantaneous rise to some fraction of the equilibrium current is expected upon reapplication of the voltage, to be followed by the slow re-establishment of those conditions pertinent to equilibrium.

If a voltage of opposite polarity is applied for a period, conditions will exist similar to those just described, but intensified in degree. The reapplication of a voltage of one polarity after a period of opposite polarity must first reverse all the charge and potential distributions favorable to the opposite polarity, and then must begin to develop the charge and potential distributions favorable to its own polarity. The rise to equilibrium will therefore be considerably slower in general than after a period in which the voltage is simply turned off, and will become progressively slower the larger the magnitude of the opposite-polarity voltage. This is the kind of effect indicated by the data given in Table III.

An exception to the inhibition of current flow by a voltage with polarity opposite to that just applied is found in Region 2 as a result of the phenomenon we have called a set. At least under moderate light excitation, the current is able to approach more rapidly to equilibrium for an applied voltage of opposite polarity to that used in the set than for an applied voltage of the same polarity used in the set. It seems likely that the voltage-induced set consists of a transport of ions or defects within the powder so that breakdown of the barrier at the contacts corresponding to the positive electrodes during the set becomes much easier. Such an ion transport, for example, might result in an appreciably increased density of centers in the neighborhood of the contacts which are able to stably capture photo-excited holes. This effect, illustrated best in the modulation profiles of Figs. 13 and 14, counteracts the effects tending to produce a lag upon reversal of the polarity of the voltage. It is significant to note that such an ion transport affects only breakdown by Process I and not by Process II.

When a high light intensity is creating photo-excitation of electrons and holes in the barrier and in the volume of the powder, a supply of electrons and holes is on hand to meet the necessary changes in charge and potential distribution upon reapplying a voltage after a period of no voltage, or upon applying a voltage of opposite polarity to that previously applied. Processes, which in the absence of high light intensity depend primarily on thermal emptying rates, can take place through capture and recombination with photo-excited carriers. The net result is that changes in applied voltage can be followed much more rapidly by the photocurrent, and the long rise times characteristic of dark and low-light photocurrents are no longer found.

3. The Breakdown Region of Process II

In the absence of light or at low light intensities, the current varies with a still higher power of the voltage than associated with Process I, usually as V^3 or V^4. In the presence of light intensities high enough so that Process I is also evident in current-voltage curves, the transition from Process I dominant to Process II dominant occurs for applied fields of about 10^3 v/cm ($\sim$0.5 v/particle). Breakdown by Process II is the basic breakdown mechanism over the whole voltage range covered by Regions 2 and 3, to which additional breakdown by Process I is added when sufficient light excitation is present. The region of breakdown by Process II extends on the high-voltage end up to fields of 2×10^3 v/cm and higher, depending on the light intensity, before the high-voltage ohmic region sets in. Breakdown by Process II has the following defining characteristics: (a) it does not require light for its occurrence, but the magnitude of the current in Region 3 is dependent on the light level; (b) it occurs for applied fields extending from 60 v/cm to 2×10^3 v/cm; (c) voltage-associated photocurrent lag occurs, alike for either polarity independent of the set; (d) voltage-associated photocurrent lag is eliminated by a sufficient increase in the light intensity.

Since voltage reduction of the barrier was considered an unlikely mechanism for Process I, due to the temperature independence of the current, it is likely that Process II is associated with field excitation of holes at the cathode by impact ionization by tunneling electrons. The role of holes as here conceived does not imply actual currents due to two-carrier current flow, but rather that the capture of field-excited holes near the cathode barrier supplements the effect of light at that barrier in increasing the effective field. Thus, penetration of the cathode barrier is modulated by the density of photo-excited or field-excited holes captured in the vicinity.

The lag characteristics of breakdown by Process II can be described in exactly the same manner used in the previous section for Process I, and need not be repeated here.

4. High-Voltage Ohmic Region

When the applied field exceeds 2×10^3 v/cm or higher, depending on the light intensity, an ohmic region is encountered which can be most simply ascribed to the complete breakdown of all barriers limiting current flow. The onset of this region is light sensitive, since photo-excited holes play a role in the breakdown of the barriers. Voltage-associated photocurrent lag is still present because interrupting or reversing the polarity of the voltage destroys the charge configurations which have been built up to allow complete penetration of the barriers. The resistance of the powder in this region is about three orders of magnitude lower than in the low-voltage ohmic region.

Hysteresis

In the section labeled Results, we have summarized the experimental evidence which indicates that the

occurrence of, and the form of, the hysteresis effect is intimately associated with the capture of holes by sensitizing centers under conditions of light, temperature, etc., for which these holes may be thermally stable in the captured state. Although there are a number of different mechanisms, some involving single carrier and some two-carrier effects, which may be proposed to give the formal characteristics of hysteresis, we are led by a consideration of the temperature dependence and of the observation of luminescence emission correlated with the hysteresis effect, as previously mentioned, to single out the following mechanism.

Consider the experimental data of Fig. 19. As the voltage is increased in the dark, little current flows until point B is reached, at which voltage the current increases almost spontaneously to a value three orders of magnitude higher. Examination of the current-voltage curve below point B indicates a variation of current with V^3. We suggest that, in the dark, barrier breakdown by Process II is occurring, i.e., breakdown augmented by the impact ionization of holes in the powder. We next concern ourselves with the fate of these holes. If they are stably held at sensitizing centers, they can contribute to the positive charge in the crystal. If they are thermally freed, they will be captured at fast recombination centers, where recombination with an electron will occur; no change in the positive charge affecting the cathode barrier results. Whether holes will be stable in sensitizing centers depends on the location of the demarcation level,[19] which depends in turn on the electron density. It is necessary for the hole demarcation level to lie below the level of the sensitizing centers in order for their effect to be felt. When the demarcation level lies above that of the sensitizing centers, i.e., for small free electron densities, these levels stay essentially occupied by electrons. There is therefore no buildup of trapped positive charge to increase the effective field on the barrier. (There is also a shorter lifetime for electrons in the CdSe, since any holes that are excited will be captured at recombination centers which favor recombination with free electrons, as mentioned already.) Once the current has increased to the value necessary to make the sensitizing centers effective, an abrupt increase in current to much higher values becomes possible, as the now stably captured holes increase penetration of the cathode barrier. If the voltage is now decreased, a high current will persist until the voltage has dropped to such a low value that, even with the support of the captured holes, the current can no longer be maintained. If in the dark a voltage is applied in the hysteresis range, a pulse of light will increase the density of free electrons sufficiently so that photo-excited holes may be captured at sensitizing centers to bring about the higher-conductivity state which will persist until after the light is turned off. But if the voltage is turned off for a period, the captured holes will be thermally freed and lost (in CdSe at room temperature), so that only a small current is found upon reapplication of the voltage.

The critical difference between CdS and CdSe comes from the fact that holes captured at sensitizing centers are effective in CdSe only if the density of free electrons is kept high, whereas in CdS they are effective over the whole range of light intensities and voltages used at room temperature. Thus a slow build-up with voltage occurs, rather than a sudden rapid increase at a critical voltage. Similarly, turning off the voltage for a period does not completely remove the conductivity, because many of the holes captured at sensitizing centers remain there unless directly involved in recombination. If CdS is heated so that the holes in sensitizing centers can be easily freed thermally, it behaves like CdSe at room temperature; if CdSe is cooled so that the holes cannot be easily freed, thermally it behaves like CdS at room temperature.

ACKNOWLEDGMENTS

The author wishes to express his indebtedness to A. Rose and R. Williams for the helpful discussions that led to the model formulated, to A. B. Dreeben and N. DiGiuseppe for their role in the preparation of samples and cells, and to H. E. MacDonald for assistance in making the ac measurements.

Field-Effect Modulation of Photoconductance in a Quasi-Intrinsic Semiconductor

R. R. BOCKEMUEHL
Research Laboratories, General Motors Corporation, Warren, Michigan
(Received July 12, 1960)

The field-effect modulation of conductance in a dark-insulating photoconductor is strongly dependent on the properties of carriers of both signs. An analysis of the equilibrium space charge density resulting from electron-hole pair generation in a "depletion layer" and the resulting influence on the terminal characteristics of a photoconductive field-effect transistor is presented. The derived relationships explain the optical and frequency response behavior of CdS field-effect modulation of photoconductance to be observed, and provide a method for evaluating the drift mobility of holes and other carrier properties in a quasi-intrinsic semiconductor.

1. INTRODUCTION

PREVIOUS analyses of the modulation of the bulk conductance of a semiconductor by application of a transverse electric field[1] have assumed the case where free carriers are mainly produced by ionization of donor or acceptor states. In such a case both conduction and depletion layer forming processes involve the majority carrier only. Minority carriers have negligible influence on the terminal characteristics of a unipolar field-effect transistor except for the I-V characteristic of the control terminal.[2]

Experimental field-effect transistors have recently been made from dark-insulating cadmium sulfide.[3] An analysis of these transistors shows that, when free carriers are produced mainly by thermal or optical pair production, the conductance is determined primarily by the carrier which has the greater drift mobility, while the depletion layer formation depends on the lower mobility carrier.

When a rectifying contact on one surface of a semiconductor slab is reverse biased, a space charge layer penetrates into the semiconductor bulk. If the formation of the space charge layer is such that the density of the mobile charge carriers within the layer is reduced, the conductance in the direction parallel to the rectifying contact surface is reduced accordingly.

In the ideal case all the mobile charge density is removed from the space charge layer. The cross section of the slab is effectively divided into two sections, a depletion layer which extends from the rectifying contact surface to the space charge layer boundary, and a conducting channel which extends from the space charge boundary to the oppostie surface of the slab.

The increase of space charge layer thickness resulting from an incremental increase in bias voltage, dh/dV, is inversely proportional to the space charge density ρ_s formed in the extended region dh. The resulting decrease in conductance is directly proportional to the free charge density ρ_f removed from the dh region. Therefore the incremental change in conductance per unit change in bias voltage $dg/dV=(dg/dh)(dh/dV)$ is proportional to the charge density ratio ρ_f/ρ_s.

When the mobile charge density is determined mainly by donor or acceptor concentrations, $\rho_f=-\rho_s=q(N_d-N_a)$ and the ratio $\rho_f/\rho_s=-1$. However, the following analysis shows that when carriers are produced mainly by thermal or optical generation the equilibrium value of $-\rho_s$ may be considerably different from ρ_f. This analysis is made on the basis of three simplifying assumptions: (1) the drift mobility of one type of carrier is at least one order of magnitude greater than that of the opposite carrier; (2) the drift velocity of the carriers in the depletion region is sufficient to permit diffusion and recombination to be neglected; and (3) the rate of electron-hole pair generation is uniform throughout the semiconductor. These conditions can be approximated in field-effect transistors made from many of the compound semiconductors, especially the insulating photoconductors included by the group II–VI sulfides, selenides, and tellurides.

2. SPACE CHARGE DENSITY IN A PHOTOCONDUCTOR

When electron-hole pairs are generated in the space charge region of an intrinsic semiconductor, equilibrium densities of free electrons and free holes will be reached which permit both types of carriers to be removed at a rate equal to their rate of generation. Removal processes include drift due to the field in the space charge layer, recombination, and diffusion.

If the hole mobility is much less than the electron mobility, the free hole concentration to establish the necessary drift current will be much greater than the corresponding free electron concentration. This difference is further emphasized if trapping levels and capture cross sections are such that the equilibrium ratio of trapped to free holes is greater than that ratio for electrons.

The analysis given in Appendix A shows that in regions where diffusion and recombination can be neglected, the space charge density is dependent on the drift mobility of the holes if that mobility is much less than the drift mobility for electrons. If pair generation is assumed constant throughout the semiconductor bulk, the equilibrium space charge density is uniform,

$$\rho_s=(qfk/\theta_p\mu_p)^{\frac{1}{2}}\ \text{coul/cm}^3, \qquad (1)$$

[1] W. Shockley, Proc. I. R. E. **40**, 1365 (1952).
[2] G. C. Dacey and I. M. Ross, Proc. I. R. E. **41**, 970 (1953).
[3] R. R. Bockemuehl, Proc. I. R. E. **48**, 875 (1960).

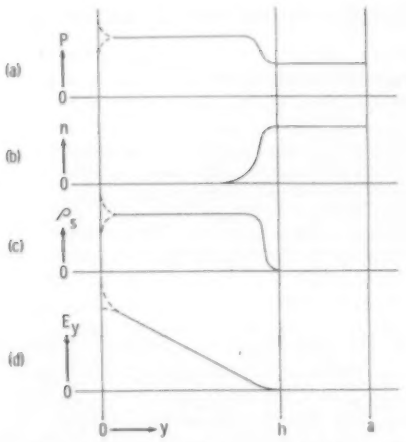

FIG. 1. Qualitative relationships as a function of distance y from the rectifying contact surface; (a) free hole density, (b) free electron density, (c) space charge density, (d) electric field.

where qf is the charge generation rate (coul/cm³ sec), k is the dielectric constant (farads/cm), and μ_p is the mobility of the free hole. For a given free hole density p there will be an additional hole density p_t, trapped in states which are in thermal equilibrium with the valence band. The product $\mu_p\theta_p$ represents drift mobility, where $\theta_p=p/(p+p_t)=$constant at a given temperature. A similar relationship exists for electrons, $\theta_n=n/(n+n_t)$.

The free carrier density ρ_f in the charge neutral region (conducting channel) can be assumed to consist entirely of electrons if $\mu_n\theta_n\gg\mu_p\theta_p$.

$$\rho_f=qn=qf\tau_n \text{ coul/cm}^3, \tag{2}$$

where τ_n (seconds) is the mean time interval that an electron remains in the conduction band before recombination occurs. The important relationship ρ_f/ρ_s results from Eqs. (1), (2),

$$\rho_f/\rho_s=(qf\tau_n{}^2\theta_n\mu_p/k)^{\frac{1}{2}}. \tag{3}$$

Values for the drift mobility of holes can be obtained from measurements of field-effect modulation characteristics which depend on the space charge density ρ_s and on the ratio ρ_f/ρ_s. Such measurements are sensitive to very low values of hole drift mobility. For example, typical properties of CdS are $k=10^{-12}$ farad/cm and $\tau_n=10^{-3}$ sec. With illumination yielding a charge generation rate $qf=10^{-3}$ coul/cm³-sec, the drift mobility $\theta_p\mu_p=10^{-3}$ $(\rho_f/\rho_s)^2$ cm²/vsec.

3. CHARGE DISTRIBUTION AT THE SPACE CHARGE BOUNDARIES

The analysis in Sec. 2 is valid in regions where diffusion and recombination can be neglected. This condition is met in the central region of the space charge layer because of the high electric field. However, variations in ρ_s may exist near the two boundaries of the space charge layer as shown in Fig. 1.

The hole current generated in the space charge layer must be collected at the rectifying contact surface. The collection velocity may be determined by a recombination velocity, a contact barrier height, a diffusion potential, or by a diffusion velocity through a surface barrier, depending on the properties of the contact. In any case the hole density at the contact surface must be sufficient to permit the required hole current to be collected. This value may differ from the equilibrium hole density in the bulk.

The electric field, Fig. 1(d), diminishes to zero at the boundary $y=h$. In the low field region near $y=h$ both recombination and diffusion are important. Although a rigorous mathematical analysis has not been made, it is obvious that electron density must increase rapidly near $y=h$ in order to maintain the required electron "collection" velocity at the $y=h$ boundary, Fig. 1(b). However, this value would not be expected to exceed that in the conducting channel, $h<y<a$. Qualitatively, the effective boundary of the carrier depletion layer penetrates slightly less than the space charge boundary.

4. TERMINAL CHARACTERISTICS OF A PHOTOCONDUCTIVE FIELD-EFFECT TRANSISTOR

Both the active and quiescent properties of a field-effect transistor are strongly dependent on charge densities ρ_s and ρ_f as shown by the analysis in Appendix B. They are also dependent on the manner in which the charges are distributed throughout the device. However, certain characteristics can be defined under limiting conditions which normalize the charge distribution functions.[3] This condition is characterized by operating at "pinchoff."

Pinchoff voltage is that voltage required to produce a space charge layer thickness h equal to the slab thickness a. Substituting the value for ρ_s from Eq. (1) into Eq. (23),

$$V_p=(a^2/2)(qf/k\mu_p\theta_p)^{\frac{1}{2}} \text{ volts}. \tag{4}$$

Pinchoff current is defined as the conducting channel current which results when the applied terminal potentials cause $h=0$ at one end of the conducting channel and $h=a$ at the other. From Eqs. (1), (2), and (27),

$$I_p=\frac{a^3c\mu_n\tau_n(qf)^{\frac{1}{2}}}{6L(k\mu_p\theta_p)^{\frac{1}{2}}}\text{amp}, \tag{5}$$

where c and L are slab width and length respectively (cm).

The mutual transconductance G_m is defined as the change in conducting channel current which results from an incremental change in potential at the rectifying contact. At pinchoff, from Eqs. (2) and (28),

$$G_{mp}=acq\mu_n f\tau_n/L \text{ mhos}. \tag{6}$$

The fact that G_m is influenced by ρ_s is not apparent in Eq. (6). However, G_{mp} is a special value obtained under certain bias conditions which are determined by ρ_s.

Equations (4), (5), and (6) are not independent for a given charge distribution. With the assumption that charge densities ρ_s and ρ_f in their respective regions do not vary with distance from the rectifying contact surface, the value $G_{mp}V_p/I_p=3$. The actual measured value serves to indicate the degree to which uniform distribution can be assumed in a specific characteristic determination.

TABLE I. The relationships between terminal characteristics, carrier properties, and material and geometric parameters permit determination of the carrier properties.

Hole drift mobility	$\theta_p\mu_p=(a^2/kcL)(I_{gp}/V_p^2)$ cm^2/vsec
Electron lifetime	$\tau_n=(L^2/2\mu_n)(G_{mp}/I_{gp})$ sec
Electron mobility	$\mu_n=(La/2kc)(G_{mc}/V_p)$ cm^2/vsec
Pair generation rate	$f=2I_{gp}/qcLa$ 1/cm^3 sec
Free charge density	$\rho_f=G_{mp}L/ac\mu_n$ coul/cm^3
Space charge density	$\rho_s=2kV_p/a^2$ coul/cm^3
Charge density ratio	$\dfrac{\rho_f}{\rho_s}=\dfrac{G_{mp}La}{2V_pkc\mu_n}=G_m(\mathrm{dc})/G_m(\mathrm{ac})$

5. TRANSIENT EFFECTS IN THE SPACE CHARGE LAYER

The relationships discussed in Sec. 4 represent equilibrium values for active and quiescent terminal characteristics. However, substantially different active characteristics result when signal frequencies do not permit sufficient time for equilibrium to be established.

Upon application of a step function of reverse bias voltage, electrons are removed from the depletion layer much more rapidly than holes (assuming $\mu_n\gg\mu_p$). Initially the space charge density is produced by the charge remaining after extraction of the highly mobile electrons $\rho_s=-\rho_f$. Several time-dependent processes take place before the equilibrium value of ρ_s given by Eq. (1) is reached. These include (1) the time required for electrons trapped in states which are in thermal equilibrium with the conduction band to reach a new equilibrium value, (2) the time required to reach hole trap equilibrium, (3) the time for any adjustment of recombination center population which may result, (4) the time required for excess holes to be conducted out of the region or for hole deficiencies to be satisfied by generation. No single one of these effects has obvious domination over the equilibrium process.

If $\mu_n\gg\mu_p$ the transit time for electrons across the space charge layer can be expected to be much less than any of the listed equilibrium times. Therefore, *four* frequency zones characterize the frequency response of the active terminal parameters. At dc and very low frequencies the active gain is determined by the equilibrium value of ρ_s. At higher frequencies which do not permit equilibrium to be maintained, a transition to the gain determined by $\rho_s=-\rho_f$ begins. This value will be maintained until frequencies are reached where the effects of the dielectric relaxation time of the semiconductor become important.

The high-frequency performance is not dependent on hole mobility. The ratio of mutual transconductances at low and high frequencies is independent of the value of quiescent terminal potentials by the equation

$$G_m(\mathrm{dc})/G_m(\mathrm{ac})=\rho_f/\rho_s=(qf\tau_n^2\theta_p\mu_p/k)^{\frac{1}{2}}. \quad (7)$$

6. CURRENT AT THE RECTIFYING JUNCTION

The reverse current at the rectifying contact must be at least equal to the charge generation rate times the volume of the space charge layer.[4] Additional current may result from leakage around the contact or through "weak" points in an imperfect barrier. If the latter sources of current are neglected and if light intensity is sufficient to make dark current negligible, the current density can be related to bias voltage from Eq. (22). With uniform pair generation,

$$J_g=qfh=qf(2kV/\rho_s)^{\frac{1}{2}}\ \mathrm{amp/cm^2}. \quad (8)$$

This indicates a half-power dependence of J_g on V and serves as a check of the quality of the rectifying contact.

When current flows in the conducting channel, variation of h with x must be considered as shown in Appendix C. The generated current I_{gp} at pinchoff conditions is

$$I_{gp}=qfcLa/2\ \mathrm{amp}. \quad (9)$$

Equations relating the dynamic conductance G_g of the rectifying contact and the short circuit current gain β of the device as a function of hole mobility are obtained by substituting ρ_s, ρ_f from Eqs. (1) and (2) into Eqs. (32) and (33). At pinchoff,

$$G_{gp}=(3cL/a)(qfk\theta_p\mu_p)^{\frac{1}{2}}\ \mathrm{mhos} \quad (10)$$

$$\beta_p=(a^2\mu_n\tau_n/3L^2)(qf/k\theta_p\mu_p)^{\frac{1}{2}}. \quad (11)$$

7. VALIDITY OF THE ASSUMPTIONS USED IN THE ANALYSIS

Operational equations which permit evaluation of carrier properties from measured terminal characteristics are tabulated in Table I. Typical values obtained for CdS are shown in Table II. Although the principles which determine field effect in a photoconductor were discussed in general, the equations relating the device parameters were derived on the basis of several assumptions. These must be recognized before valid conclusions can be drawn from the equations.

A high ratio of light to dark current insures that carriers are produced mainly by pair production. The condition requiring a large difference between drift mobilities of holes and electrons is not only necessary for the analysis presented but is necessary to permit an appreciable conductance modulation to be observed. However, most relatively wide band gap materials ex-

[4] W. W. Gärtner, Phys. Rev. **116**, 84 (1959).

TABLE II. Approximate values of carrier properties derived from known geometric parameters and measured terminal characteristics of a cadmium sulfide field-effect transistor.

Known device parameters	
Length	$L=10^{-1}$ cm
Width	$c=10^{-1}$ cm
Thickness	$a=10^{-2}$ cm
Dielectric constant	$k=10^{-12}$ farad/cm
Measured terminal characteristics (at pinchoff)	
Mutual transconductance	$G_{mp}=2\times10^{-6}$ mho
Pinchoff voltage	$V_p=10^{2}$ v
Channel current	$I_p=7\times10^{-5}$ amps
Rectifying contact current	$I_{gp}=5\times10^{-8}$ amps
Mutual transconductance (ac)	$G_m(\text{ac})=4\times10^{-6}$ mho
Derived carrier properties	
Hole drift mobility	$\mu_p\theta_p=5\times10^{-4}$ cm²/vsec
Electron lifetime	$\tau_n=10^{-3}$ sec
Charge generation rate	$qf=10^{-3}$ coul/cm³ sec
Electron mobility	$\mu_n=2\times10^{2}$ cm²/vsec
Free charge density	$\rho_f=10^{-6}$ coul/cm³
Space charge density	$\rho_s=2\times10^{-6}$ coul/cm³
Additional terminal measurements used for checks	
Rectifying contact conductance	$G_{gp}=2\times10^{-9}$ mho
Short circuit current gain	$^{ac}\beta_p=10^{3}$
Charge distribution test	$G_{mp}V_p/I_p\approx3$

hibit this property, with electron mobility greatly exceeding hole mobility.

A more questionable approximation is that of a geometrically uniform pair generation rate. The optical absorption coefficient of the material and inhomogeneities in the stoichiometric and impurity defects in the crystal preclude ideal realization of this assumption. However, terminal characteristics at pinchoff are not strongly dependent on charge distribution unless sharp discontinuities are present. Furthermore the relationship $G_{mp}V_p/I_p=3$ serves as an indication of the degree to which uniform distribution can be assumed. Experimental analysis has shown that illumination of thin crystals (100 μ) with polychromatic wavelengths longer than the absorption edge permits uniform distribution to be assumed without introducing excessive error into the parameter evaluations.

The rectifying contact is assumed to exhibit no leakage currents. This can be verified experimentally by testing the $I:V^{\frac{1}{2}}$ relationship, Eq. (8). Furthermore, the contact should collect holes freely in order to avoid a large value of space charge at the contact surface. This condition can also be checked by the $G_{mp}V_p/I_p$ test.

Recombination in the space charge region can be neglected to the approximation given by the ratio of the transit time of the electron across the space charge layer to the lifetime of the free electron. Typical values for this ratio in CdS are of the order of 10^{-5}. Diffusion is also neglected in the space charge region. Current density due to hole diffusion is equal to $J=D_p dp/dy$, where D_p is the diffusion coefficient for holes. However Eq. (19) shows that $dp/dy=0$, which indicates that if the derivation included hole diffusion its effect would be negligible. Both recombination and diffusion of electrons are appreciable in the region near the space charge boundary. However, the resulting error is negligible, as shown in Appendix A.

APPENDIX A. DEPENDENCE OF SPACE CHARGE DENSITY ON HOLE MOBILITY

Assuming that a space charge layer has been formed, the photogenerated holes in that layer drift toward the rectifying contact surface $y=0$ while the generated electrons drift toward the space charge boundary $y=h$. If the electron-hole pairs are generated at a constant rate f/cm³ sec, the current density $J_n(y)$ due to electrons at any point $0<y<h$ is equal to the total generation rate in the region from 0 to y. The electron current density must also equal the electron charge density times the drift velocity as follows:

$$J_n(y)=qfy=qn\mu_nE_y \text{ amp/cm}^2, \tag{12}$$

where n is the density of electrons in the conduction band at y and E is the electric field. A similar argument for holes shows that the current density due to holes at y is

$$J_p(y)=qf(h-y)=qp\mu_pE_y. \tag{13}$$

The space charge density $\rho_s(y)$ is equal to the difference between the charge densities due to holes and electrons. This must include the trapped charge which is in thermal equilibrium with the free carriers, represented by $\theta_n=n/(n+n_t)$ and $\theta_p=p/(p+p_t)$. This space charge is related to electric field by Poisson's equation by the equation

$$\rho_s=(qp/\theta_p)-(qn/\theta_n)=-kdE_y/dy. \tag{14}$$

By substituting p and n from Eqs. (12), (13) and rearranging,

$$E_ydE_y=-\frac{qfdy}{k}\left[h\left(\frac{1}{\mu_p\theta_p}\right)-y\left(\frac{1}{\mu_p\theta_p}+\frac{1}{\mu_n\theta_n}\right)\right]. \tag{15}$$

If drift mobility $\mu_p\theta_p\ll\mu_n\theta_n$, Eq. (15) reduces to

$$E_ydE_y=-qf(h-y)dy/k\mu_p\theta_p. \tag{16}$$

Solution of Eq. (16) under the boundary condition $E_y=0$ at $y=h$ gives

$$E_y=(h-y)(qf/k\mu_p\theta_p)^{\frac{1}{2}}. \tag{17}$$

Then, from Eqs. (14) and (17),

$$\rho_s=(qfk/\mu_p\theta_p)^{\frac{1}{2}}. \tag{18}$$

Therefore, with the assumptions made, ρ_s is not a function of h, y, or $\mu_n\theta_n$. Also, from Eqs. (12), (13), and (17),

$$p=(kf\theta_p/q\mu_p)^{\frac{1}{2}} \tag{19}$$

and

$$n=p\mu_py/\mu_n(h-y). \tag{20}$$

Equation (20) shows that electron density is a function of y while Eq. (18) indicates a constant value for

ρ_s even though ρ_s is a function of n in Eq. (14). This apparent incongruity can be explained by the fact that, with the assumption $\mu_n\theta_n \gg \mu_p\theta_p$, the space charge due to holes ρ_p is so much greater than that due to electrons ρ_n over most of the space charge region that the latter can be neglected and $\rho_s=\rho_p$ can be assumed.

However, inasmuch as recombination and diffusion were neglected in the derivation, Eq. (20) approaches infinity as y approaches h. The magnitude of the error which results is indicated by solving for a value $y=h'$ where ρ_s differs from ρ_p by a given amount, for example 10%. In this case,

$$(h-h')/h=10\mu_p\theta_p/\mu_n\theta_n. \tag{21}$$

The region $h'<y<h$ is effectively a finite transition region between the space charge layer and the conducting channel. Both recombination and diffusion take place in this region. Furthermore, free electron densities in this region contribute to the conducting channel current. However, the extent of the transition region defined by Eq. (21) is negligibly small in cases where the original assuption $\mu_p\theta_p \ll \mu_n\theta_n$ is valid.

APPENDIX B. DEPENDENCE OF TERMINAL PARAMETERS ON FREE CHARGE AND SPACE CHARGE DENSITIES

Previous analyses[1,3] of field-effect parameters assumed $\rho_s=-\rho_f$. A similar analysis can be made for $\rho_s \neq -\rho_f$. The following derivation assumes constant values of ρ_s in the space charge region $0<y<h$ and constant ρ_f in the conducting channel $h<y<a$.

By solving Poisson's equation $d^2V/dy^2=-\rho_s/k$ with the boundary conditions $dV/dy=0$ at $y=h$ and $V=0$ at $y=0$ and solving for $V(h)$ at $y=h$,

$$V(h)=\rho_s h^2/2k. \tag{22}$$

Pinchoff potential is defined for $h=a$:

$$V_p=\rho_s a^2/2k. \tag{23}$$

Current density in the direction x along the conducting channel is

$$J_x=\frac{dV}{dx}\mu_n\rho_f dy. \tag{24}$$

Inasmuch as dV/dx is finite, the value of h also varies with x. The channel current is obtained by introducing slab width c and length L and substituting $dV/dx=dVdh/dxdh$,

$$Idx=c\mu_n\rho_f(a-h)(dV/dh)dh. \tag{25}$$

By substituting dV/dh from (22) and satisfying boundary conditions $h=H_s$ at $x=0$ and $h=H_d$ at $x=L$,

$$I=\frac{c\mu_n\rho_f\rho_s}{6kL}[3a(H_d^2-H_s^2)-2(H_d^3-H_s^3)]. \tag{26}$$

Pinchoff current is defined when $H_s=0$ and $H_d=a$:

$$I_p=a^3c\mu_n\rho_f\rho_s/6kL. \tag{27}$$

The mutual transconductance at pinchoff is obtained from Eqs. (22) and (26) when $H_s=0$ and $H_d=a$:

$$G_{mp}=dI/dV_g=(dI/dH_s)(dH_s/dV_g)=ac\mu_n\rho_f/L. \tag{28}$$

APPENDIX C. RECTIFYING CONTACT CURRENT AND CONDUCTANCE

The current generated in the space charge layer is equal to the charge density generation rate times the volume of the layer. With uniform generation,

$$dI_g=qfch(x)dx=qfch(dx/dh)dh. \tag{29}$$

The expression dx/dh can be derived from Eqs. (25) and (26). Solution of Eq. (29) with boundary conditions $h=H_s$ at $x=0$ and $h=a$ at $x=L$ (upper end of channel pinched off), yields

$$I_g=\frac{qfcL}{2}\frac{(a^4-4H_s^3a+3H_s^4)}{(a^3-3H_s^2a+2H_s^3)}. \tag{30}$$

Under the defined pinchoff conditions, $H_s=0$,

$$I_{gp}=qfcLa/2. \tag{31}$$

The dynamic conductance of the rectifying contact at pinchoff is obtained by differentiating Eqs. (22) and (30) with $H_s=0$,

$$G_{gp}=dI_g/dV_g=(dI_g/dH_s)(dH_s/dV_g)=3qfcLk/a\rho_s. \tag{32}$$

The short-circuit current gain β at pinchoff is,

$$\beta_p=dI/dI_g=G_{mp}=a^2\mu_n\rho_f\rho_s/3L^2kfq. \tag{33}$$

Uniform Avalanche Effect in Silicon Three-Layer Diodes*

A. GOETZBERGER
Shockley Transistor Unit of Clevite Transistor, Palo Alto, California
(Received June 30, 1960)

Interaction of current gain and avalanche multiplication in three-layer diodes is utilized to produce uniform avalanche effect, indicated by uniform light emission over the area of a junction. Proof that the effect is caused by the three-layer action is furnished by removing the emitter layer, which changes the light emission to the usually observed microplasma pattern.

AVALANCHE breakdown in *pn* junctions is generally not uniform due to small variations of breakdown voltage from point to point. Certain surface conditions, dislocations, and other crystal imperfections can lower the breakdown voltage locally, an effect which can be studied by observation of light emission from thin diffused junctions at breakdown.[1] There are also theoretical indications that complete uniformity of breakdown is impossible because statistical fluctuations of donors and acceptors will produce at least one small area of localized breakdown about 0.7 v below the average breakdown for the junction.[2] Only one observation of nearly uniform avalanche effect has been reported so far.[3] Another similar case reported recently[4] was found to be mainly caused by the effect described here.

This letter describes a possibility of obtaining uniform avalanche effect in *npn* or *pnp* three-layer diodes which does not require extremely uniform diffusion and crystal conditions. Uniformity of avalanche effect is indicated by uniform light glow over the area of a junction (Fig. 1). This uniform glow is caused by interaction of current gain and avalanche effect. In a three-layer diode the relation $M\alpha=1$ holds for current levels which are high in comparison to the collector saturation current (M is the multiplication factor and α the current amplification).[5] In silicon devices α increases with increasing current; M, therefore has to decrease and, according to the relationship

$$1/M=1-(V/V_B)^n, \qquad (1)$$

the voltage V across the junction decreases (V_B = breakdown voltage, n = const). The current voltage characteristic of this device, therefore, shows a negative resistance. (See Fig. 2 which was obtained from the same device whose light emission is shown in Fig. 1.) Uniformity of current over the area can occur if V_B-V is relatively large compared to the variations of V_B over the junction area.

Due to the lower operating voltage arising from the negative resistance effect, uniformity of multiplication over the area occurs. This is illustrated in a numerical example using Eq. (1) with $n=2$: A junction of 30 v breakdown voltage has localized areas of 29 v breakdown. When 28.9 v are applied to this junction the current density through the 29 v area is more than 10 times higher than through the 30 v area. The same ratio is 1.05 for an applied voltage of 23 v. This voltage drop occurs easily in three-diodes (Fig. 2). Another effect that aids uniformity of current distribution is uniform injection from the emitter layer.

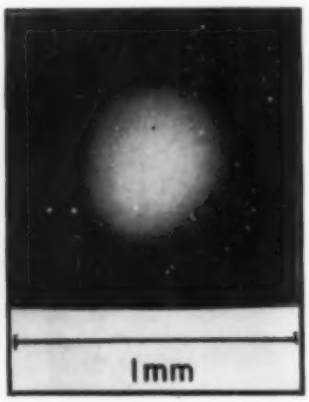

FIG. 1. Light emission from three-layer diode.

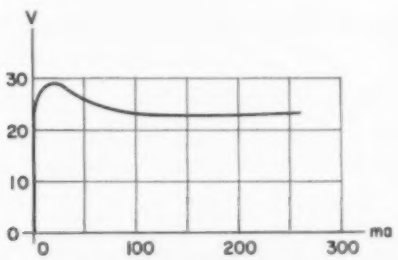

FIG. 2. V-I characteristic of same diode.

* Research supported by Air Force Cambridge Research Center.
[1] A. G. Chynoweth and G. L. Pearson, J. Appl. Phys. **29**, 1103 (1958).
[2] W. Shockley, Bull. Am. Phys. Soc. Ser. II, **5**, 3, 161 (1960).
[3] R. L. Batdorf, A. G. Chynoweth, G. C. Dacey, and P. W. Foy, J. Appl. Phys. **31**, 7, 1153 (1960).
[4] B. McDonald, A. Goetzberger, and C. Stephens, Bull. Am. Phys. Soc. Ser. II, **4**, 8, 455 (1959).
[5] W. Shockley, Proc. I.R.E. **106**, B Suppl. 15, 270 (1959).

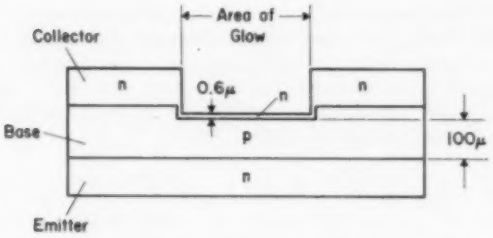

FIG. 3. Geometry of guard ring structure for observation of light emission.

FIG. 4. Light emission of diode after removal of emitter n-layer.

The structure of the device that was used to observe this effect is shown in Fig. 3. The main feature is a guard ring of higher breakdown voltage that eliminates surface effects.

That the uniformity of light glow in Fig. 1 requires the three-layer structure was shown by etching off the bottom n-layer. Then a typical microplasma light emission pattern was obtained (Fig. 4). At the same time the negative resistance in the V-I characteristic disappeared.

JOURNAL OF APPLIED PHYSICS VOLUME 31, NUMBER 12 DECEMBER, 1960

Theoretical and Experimental Study of the Backscattering Cross Section of an Infinite Ribbon*

MICHAEL S. MACRAKIS†
Cruft Laboratory, Harvard University, Cambridge, Massachusetts
(Received February 11, 1960)

The geometrical optics approximation is derived for the backscattering cross section per unit length of an infinite ribbon. A comparison is made with the exact theory, the approximate theory of Sommerfeld, the variational method, and with experimental results obtained through the space-separation method for the measurement of backscattering cross sections in a parallel-plate region.

1. INTRODUCTION

THE present report is an outcome of a study by the author of some problems connected with the diffraction of a plane electromagnetic wave from a slotted cylinder. An approximate theory had been developed for the determination of the backscattering cross section per unit length of a slotted cylinder and an experimental verification of the results therefore became necessary.

Many methods were reviewed in order to find the one best suited to measurements on slotted cylinders. Previous work on the Doppler-shift method[1] demonstrated that this method was extremely accurate, but it could not be used for the slotted cylinders since it requires mechanical motion of the obstacle whose cross section is to be measured. It was decided instead to use the space-separation method[2] for measuring the cross sections.

In order to calibrate the equipment and to check on the region where it would give reliable results, extensive measurements were performed on ribbons and complete cylinders. An account of this work is given in the present report, which is divided into two parts. The first part is devoted to the theoretical determination of the backscattering cross section per unit length of an infinite ribbon as a function of ka when the incident wave is polarized parallel to the ribbon edge. An interesting deduction is that the geometrical optics approximation of the cross section is $\sigma_B k = 1 + (2ka)^2$ for $ka > 1.0$, where $k = 2\pi/\lambda$, λ is the wavelength, and $2a$ is the width of the ribbon. The second part is devoted to the experimental method as adapted to the parallel-plate region.

* Prepared for Air Force Cambridge Research Center under a U. S. Air Force contract.

† Now at Lincoln Laboratory, Massachusetts Institute of Technology, Lexington 73, Massachusetts.

[1] C. C. Tang, Sci. Rept. No. 6, Cruft Laboratory, Harvard University (1956) and J. Appl. Phys. **28**, 628 (1957).

[2] H. J. Schmitt, IRE Trans. on Antennas and Propagation, **AP-7**, 15–22, January (1959).

2. BACKSCATTERING FROM RIBBON (THEORY)

Morse[3] gives the following expression for the scattered field from a thin ribbon of half-width a, extending from $-\infty$ to $+\infty$, when the polarization of the incident wave is parallel to the ribbon edge:

$$E_z^{sc} = -i(8\pi)^{\frac{1}{2}} \sum_{m=0}^{\infty} \frac{i^m Se_m(ka, \cos u)}{M_m^{e}(ka)} \times \exp(-i\delta_m^{e}) \sin\delta_m^{e}. \quad (1)$$

$$Se_m(ka, \cos\theta) He_m(ka, \cosh\mu),$$

where Se_m, He_m, M_m^{e}, δ_m^{e} are the known Mathieu functions[3] and where u and θ are angles connected with the geometry of the ribbon, as indicated in Fig. 1. The far field can be computed if He in Eq. (1) is substituted with its limiting value when $\mu \to \infty$, which has the form

$$He_m(kc, \cosh\mu) \underset{\mu\to\infty}{\longrightarrow} (ka, \cosh\mu)^{-\frac{1}{2}} \times \exp\{i[ka\cosh\mu - (\tfrac{1}{2}\pi)(m+\tfrac{1}{2})]\}.$$

For perpendicular incidence ($u=\frac{3}{2}\pi$), the backscattered field ($\theta=\frac{1}{2}\pi$), is

$$E_z^{sc} \underset{\mu\to\infty}{\longrightarrow} -i(8\pi/kiy)^{\frac{1}{2}} \times e^{ikiy} \sum_{m=0}^{\infty} \frac{[Se_m(ka,0)]^2}{M_m^{e}(ka)} \exp(-i\delta_m^{e}) \sin\delta_m^{e} = (i/4)(2/\pi iky)^{\frac{1}{2}} e^{iky} 8\pi Q(ka), \quad (2)$$

where $Q(ka)$ represents the infinite sum. By definition, the backscattering cross section σ_B of an obstacle is a measure of the power scattered back from the obstacle and in the direction of the source. More precisely, σ_B effectively gives a measure of the power radiated by an isotropic scatterer,[4] radiating the same amount of power in all directions as that of an obstacle in the direction opposite to that of the incident field. In cylindrical geometry, then,

$$\sigma_B = 2\pi r \frac{|\bar{S}^{sc}(r, u\pm\pi)|}{|\bar{S}^{in}(0)|} = 2\pi r \frac{|\bar{E}^{sc}(r, u\pm\pi)|^2}{|\bar{E}^{in}(0)|^2},$$

where $S^{in}(0)$ is the incident Poynting vector at the geometric center of the scatterer; $S^{sc}(r, u\pm\pi)$ is the scattered Poynting vector at a distance r from the center of the scatterer and at an angle $u\pm\pi$; and u is the angle determining the orientation of the incident field. With an incident field of the form $E_z^{i}(\bar{r}) = \exp[ikr\cos(\phi-u)]$ it can be shown after some algebra that the backscattering cross section per unit length of the infinite ribbon has the form

$$\sigma_B = (\tfrac{1}{4}k)(8\pi)^2 Q(ka) Q^*(ka)$$

or

$$\sigma_B k = (4\pi)^2 Q(ka) Q^*(ka),$$

where an asterisk denotes the conjugate of a complex quantity.

For the computation of $\sigma_B k$, the tables given in the Appendix of the work cited in footnote 3 have been used. These tables cover the range $1.0 \le ka \le 3.0$. In this range the series $Q(ka)$ converge rapidly. However, for large values of ka the convergence of the series is slow, tabulated values of the Mathieu functions do not exist, and other methods have to be used for the determination of the cross section.

In a recent work, Levine[5] derives a solution for the problem of the infinite slit when the boundary condition on the screen ($y=0$, $|x| \ge a$) is $\partial\psi(x,y)/\partial y = 0$. This problem, which is equivalent to the case of an H^{i}-field parallel to the slit edge, is the complementary problem to the one considered here; this can be seen if Levine's function $\psi(x,y)$ is identified as a quantity proportional to the magnetic field $H_z(x,y)$. Levine discusses the complementary problem through an integral equation to which the following integral equation[6] for the electric field E_z in the slit is an alternative:

$$\int_{-a}^{a} E_z(\xi) H_0^{(1)}[k|\xi - x|]\, d\xi = 2/k\eta, \quad (3)$$

where $H_0^{1}(k|\xi-x|)$ is the kernel of the integral equation and a Hankel function of the first kind and of zero order, and $\eta^{-1} = \zeta = (\mu/\epsilon)^{\frac{1}{2}}$. The integral equation

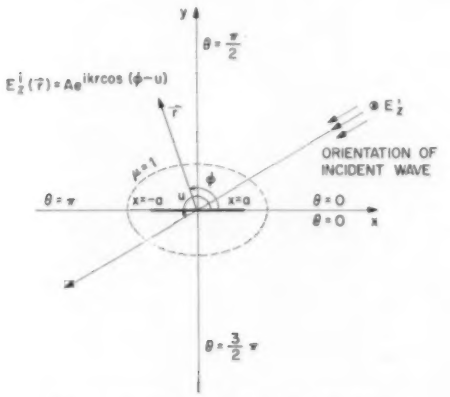

FIG. 1. Geometry for scattering from strips.

[3] P. Morse and H. Feshback, *Methods of Theoretical Physics* (McGraw-Hill Book Company, Inc., New York, 1958) Vol. II, p. 1428. The problem of the ribbon is also treated in N. W. McLachlan, *Theory and Applications of Mathieu Functions* (Oxford University Press, New York, 1947); Y. Nomura and S. Katsura, J. Phys. Soc. (Japan), **XII**, 190 (1957).

[4] For example, see R. W. P. King, *Theory of Linear Antennas* (Harvard University Press, Cambridge, Massachusetts 1956), p. 507.

[5] H. Levine, J. Appl. Phys. **30**, 1673, (1959).

[6] H. Levine's integral equation is for the current on the screen, and the alternative integral equation for the electric field E_z in the slit is given by Sommerfeld in *Optics* (Academic Press Inc., New York, 1954).

for the current on the ribbon, when, at perpendicular incidence, the incident electric field E_z^i is polarized parallel to the ribbon edge, can be written[7] as

$$\int_{-a}^{a} I_z(\xi) H_0^{(1)}[k|\xi-x|]d\xi = -4/k\zeta, \tag{4}$$

where $I_z(\xi)$ is the current flowing on the ribbon and induced by the incident field. The backscattered far field at normal incidence is[7]

$$E(r) \underset{r\to\infty}{\rightrightarrows} (k\zeta/4)(2/\pi ikr)^{\frac{1}{2}} e^{ikr} \int_{-a}^{a} I_z(x)dx. \tag{5}$$

Denoting, then, by $\bar{I}(0)$ the integral of Eq. (5), the backscattering cross section per unit length can be determined from Eq. (2) to have the value

$$\sigma_B k = (k\zeta/2)^2 \bar{I}(0)\bar{I}^*(0). \tag{6}$$

On the other hand, for the complementary case described by Levine, the far field at an angle θ from the screen and for the shadow region only, has the form reproduced here from Eq. (33) of the work cited in footnote 5:

$$\psi(r,\theta) \underset{r\to\infty}{\rightrightarrows} -(i/2)(2/\pi ikr)^{\frac{1}{2}} \times e^{ikr} \int_{-a}^{a} \exp(-ikx\cos\theta) E(x)dx$$

$$= -(i/2)(2/\pi ikr)^{\frac{1}{2}} e^{ikr} \bar{E}(k\cos\theta). \tag{7}$$

$\bar{E}(k\cos\theta)$ is the Fourier transform of a quantity proportional to the electric field in the slit and is explicitly given by Eq. (36) of the same reference. The similarity of integral equations (3) and (4) which can lead to the proof of Babinet's principle, establishes the fact that the quantity $(k\zeta/2)\bar{I}_z(0)$ in Eq. (5) can be exchanged for the quantity $\bar{E}(k\cos\theta)$ for $\theta=\frac{3}{2}\pi$. Here the interest is in the field at the slit or the current distribution at the ribbon, and therefore the fact that the far field in the illuminated region of the slit is given by Eq. (7) with an additional contribution of the field when there is no slit present, does not affect the above discussion. It should be noted at this point that in the notation of Levine[5] the angles differ by π from the angles of Fig. 1, and that his quantity $E(x)$ is equal to $ik\eta E_x$, where E_x is the actual electric field perpendicular to the edges. Thus the backscattering cross section per unit length of the ribbon is $\sigma_B k = \bar{E}(0)\bar{E}^*(0)$.

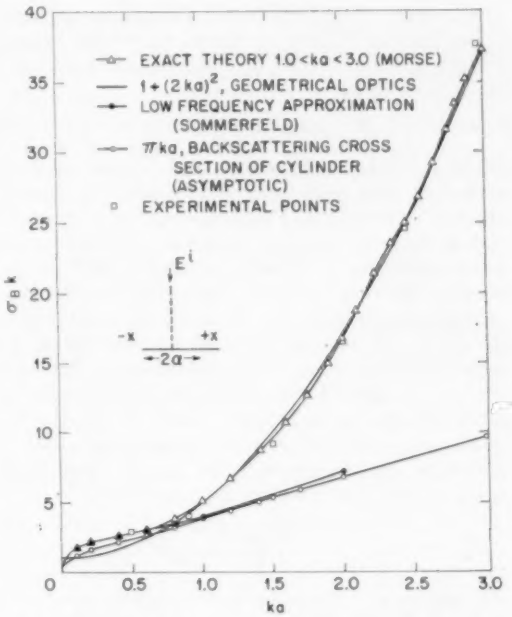

FIG. 2. Backscattering cross section per unit length for strip.

The geometrical part of the cross section is given by Eq. (36) of the work cited in footnote 5:

$$\bar{E}(f) = \frac{k\sin\theta}{f-f_0}\left\{\left(\frac{k-f}{k-f_0}\right)^{\frac{1}{2}} \exp[i(f-f_0)a] - \left(\frac{k+f}{k+f_0}\right)^{\frac{1}{2}} \exp[-i(f-f_0)a]\right\}$$

$$= k\sin\theta \frac{d}{df}\left\{\left(\frac{k-f}{k-f_0}\right)^{\frac{1}{2}} \exp[i(f-f_0)a] - \left(\frac{k+f}{k+f}\right)^{\frac{1}{2}} \exp[-i(f-f_0)a]\right\}. \tag{8}$$

For $f=f_0=k\cos\theta$, it follows that

$$\bar{E}(k\cos\theta) = k\sin\theta(-1/k\sin\theta + 2ia), \tag{9}$$

and, for backscattering, $\theta=\frac{3}{2}\pi$ in the notation of Levine; therefore $\bar{E}(0)=-1-2ika$, and thus

$$\sigma_B k \doteq 1+(2ka)^2. \tag{10}$$

For the low-frequency case ($ka\leq 1.0$), the first term of $Q(ka)$ in Eq. (2) must be retained for the calculations, and then

$$\sigma_B k = (4\pi S e_0^2/M_0^e)^2 \sin^2\delta_0^e, \quad ka\leq 1.0, \tag{11}$$

which reduces to

$$\sigma_B k = \pi^2[\ln(0.4453)]^{-2}$$

for $ka\leq 0.1$. This is the backscattering cross section of an infinite cylinder of radius a for very small ka. For comparison, $\sigma_B k$ is plotted in Fig. 2 as given by the

[7] F. Borgnis and C. Papas, *Randwertprobleme der Microwellenphysik* (Springer Verlag, Berlin, 1955).

exact theory ($1.0 \leq ka \leq 3.0$) by the geometrical optics approximation ($0 \leq ka < +\infty$) and by the first approximation of Sommerfeld[6] as corrected by Bouwkamp[8] which is given by

$$(\sigma_B k)_{\text{Som}} = (\pi^2/pp^*)[1+(ka/2)^2], \qquad (12)$$

where $p = \ln(ka) - 0.81 - i(\frac{1}{2}\pi)$. In addition, the backscattering cross section per unit length of a complete cylinder is included in Fig. 2. A variational determination of the cross section with the assumption of a constant current on the ribbon gives $\sigma_B k \doteq (2ka)^2$ for very large ka. However, for small values of ka the error in the cross section is very large. It should be noted that for the same type of approximation for the current, the variational method applied to the determination of the *total cross section* of the ribbon yields much better results (compare with footnote reference 7). The stationary expression for $\sigma_B k$ can be built with the help of integral equation (4) using the standard procedure.[7] It can be shown to have the following form,

$$\sigma_B k = 4 \frac{\left[\int_{-a}^{a} I(x)dx\right]^2}{\left[\int_{-a}^{a}\int_{-a}^{a} I(\xi)H_0^{(1)}[k|x-\xi|]I(x)dxd\xi\right][\text{same}]^*},$$

which reduces to

$$\sigma_B k = \frac{4a^2k^2}{\left\{\int_0^{2ka} H_0(\alpha)d\alpha - H_1^{(1)}(2ka) + 1/i\pi ka\right\}\{\text{same}\}^*}$$

when it is assumed that the current is a constant over the ribbon. It is believed that if the edge singularities of the current are accounted for with a trial current of the form $[1-(x/a)^2]^{-\frac{1}{2}}$, the results will be considerably improved. In view of the excellent approximation of the geometrical optics cross section with the exact cross section in a large range of the variable ka, it can only be concluded that the variational method is often of limited accuracy.

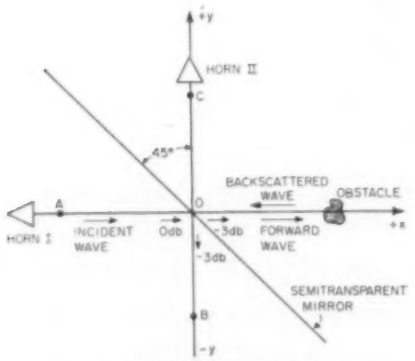

FIG. 3. Space separation method for backscattering measurements.

3. BACKSCATTERING FROM RIBBON (EXPERIMENTAL)

In the past, adequate experimental techniques have been studied and developed for diffraction problems,[9] especially for those in which the diffracting obstacles have some symmetry. For diffraction measurements, Row has developed the parallel-plate image-plane technique[10] for obstacles that exhibit cylindrical geometry. For backscattering measurements, the parallel-plate region has been used by Tang[1] in connection with the Doppler-shift method and for cylindrical obstacles. Backscattering measurements are limited for a number of reasons. The inability to completely decouple the forward from the backward wave, the inability to reduce to a minimum the reflections from obstacles other than the ones to be measured, and the difficulty in realizing a plane-incident wave pose limitations on both the accuracy and the range of measurements.

The problem of decoupling and of spurious reflections can be eliminated, to a large extent, by the use of the Doppler-shift method. However, measurements on the ribbon have been unsuccessfully attempted with this method[11] when the motion of the obstacle against the source has been achieved with a large rotating disk (despite the fact that the commutation time has been decreased to the lowest minimum possible consistent with the requirement of obtaining at least one period of the beat frequency). The reasons for the limitation of the Doppler-shift method will be given later in this paper. We now proceed in the description of the space-separation method.

Schmitt[2] has experimented with the space-separation technique. His measurements have been performed on an image plane and the obstacles have been disks. His results are very good and he claims an ability to measure a backscattering cross section of about $0.01\lambda^2$ without exhausting the sensitivity of the equipment. In principle, his method can be described as follows: a signal is propagating in the x direction (see Fig. 3). A semitransparent mirror at 45 deg from the x axis reflects half of the incident power towards the $-y$ axis and transmits the other half towards the $+$ axis in the direction of the obstacle. The backscattered wave, propagating in the direction of the $-x$ axis, is again transmitted and reflected by the mirror in the directions of the $-x$ and $+$ axes, respectively. The available signal at $x=-0$ is 3 db down from the one incident on the mirror at $x=+0$.

[8] J. Bouwkamp, Research Rept. No. EM-50, New York University (1953).

[9] For a review of related work performed at Harvard University, see R. W. P. King and T. T. Wu, Sci. Rept. No. 12, Cruft Laboratory, Harvard University (1957).

[10] R. V. Row, Tech. Rept. No. 153, Cruft Laboratory, Harvard University (1952).

[11] C. Tang (private communication).

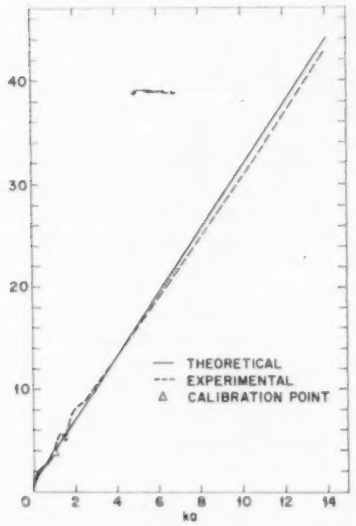

FIG. 4. Theoretical and experimental values of the backscattering cross section of cylinders.

The space-separation method has been adapted for measurements of the back-scattering cross sections in the parallel-plate region. Two similar horns have been inserted at right angles between the parallel plates, and tightly clamped. The receiving horn is positioned in such a way as to be at the center between the transmitting horn and the obstacle. The mirror, inclined 45 deg from the center line of the parallel-plate region, is a thin strip of commercially available plate glass, with a dielectric constant of about $\epsilon=3.5$. Since both ϵ and the thickness of the mirror are given, the 3 db split of power is not achieved. Graphs for the transmission coefficient of a plane dielectric sheet, as a function of thickness at 45 deg as well as curves of constant transmission coefficients, can be found in Figs. 2 and 3 of the work cited in footnote 2. The power available from a 3K29 klystron was more than enough to compensate for the fact that the system was not operating at its maximum efficiency, which is obtained only when the power is half-reflected and half-transmitted. Resistive wedges spaced every 2.5 cm have been placed all around the parallel-plate region in order to avoid reflections. The amount of reflection has been reduced to a minimum by making the wedges long (30 cm) and continuously tapered. The voltage standing-wave ratio was 1.05 for $\lambda=\pi$ inside the region.

To calibrate the equipment for measurements of unknown obstacles, a single measurement of a complete cylinder of known radius is required. In order to test the effectiveness and the range of the space-separation technique, however, a whole set of cylinders has been measured. A small field-measuring probe inserted in the region gave an appreciable backscattered signal, and the smallest cylinder that could be positioned without any difficulties (1 mm radius) gave a large backscattered signal. Two consecutive measurements of the same obstacle showed a variation of about 2% on the average.

The results of the computations and of the measurements on a cylinder are given in Fig. 4. The calculations for the cross section of the circular cylinder have been made, using the well-known expression

$$\sigma_B k=4\left|i\sum_{n=0}^{\infty}(-i)^n J_n(ka)/H_n^{(1)}(ka)\right|^2$$

for $ka=1.0$, $\sigma_B k=3.863$. A cylinder with $ka=2.0$ is inserted in the parallel-plate region, and the output from the receiving horn is adjusted for a reading of 3.86 on a Ballantine voltmeter. The detecting crystal is a square-law device and the readings of the voltmeter are therefore proportional to $\sigma_B k$. After these initial adjustments, cylinders with a ka above and below 1.0 are measured. The maximum error is observed in the region $1.5<ka<3.5$. After a long experimentation with cylinders and other obstacles, it has been concluded that the space-separation method has some inherent limitations which may be difficult to surmount. We see in the next paragraph that the experimental results for the cross section of ribbons are almost perfect for all values of the variable ka. This suggests that, for specific ranges of ka, obstacles with large, scattered intensities in directions other than the backward direction (pronounced intensity lobes in directions other

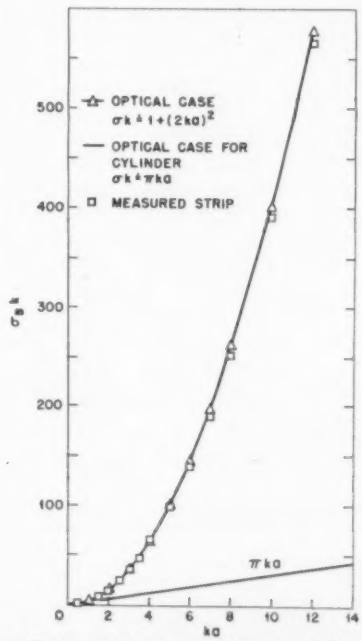

FIG. 5. Backscattering cross section per unit length of ribbon at normal incidence.

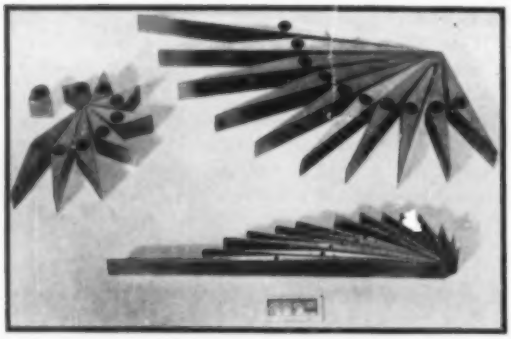

FIG. 6. Profiles of measured ribbons.

than π) will yield experimental values of the cross section not corresponding to the correct ones. And there are, for example, two specific reasons for which this may be so. A cylinder with $ka=3.0$ has a scattered intensity at an angle $\pi\pm\frac{1}{3}\pi$, which is 3.8 times larger than the backscattered intensity. Thus, the two possibilities are (a) that the scattered wave in the direction $\pi+\frac{1}{3}\pi$ will be scattered back from the mirror to the cylinder and again rescattered, this time in the backward direction (this effect can be avoided if the width of the mirror is $\frac{1}{2}\lambda$); and (b) that the scattered wave in the direction $\pi-\frac{1}{3}\pi$ will be directed towards the receiving horn. In both cases, the distances traveled are not great enough to be neglected because of attenuation.

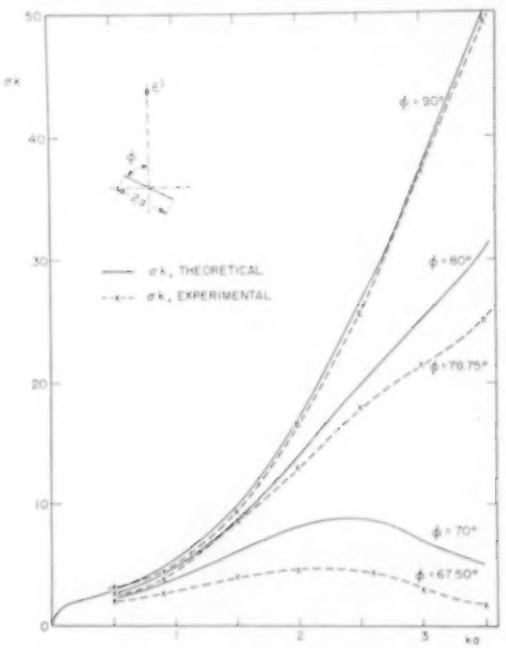

FIG. 7. Backscattering cross sections of ribbons for incidence other than normal.

The results of the measurements on the ribbon are shown in both Fig. 2 and Fig. 5. An interesting deduction of Sec. 2 of the present report was that the geometrical optics approximation of the backscattering cross section per unit length of the ribbon at normal incidence has the form $\sigma_B k=1+(2ka)^2$ for $ka\to\infty$. Taking as the starting point the geometrical value for $ka=10.00$, which is 401, the remaining values of the cross sections come out with extremely small errors, which can be ascribed to the inaccuracy in the positioning of the ribbons in the parallel-plate region. The ribbons measured were different from the theoretical ribbons in that the thickness of the former was finite. The geometrical profile of the measured ribbons was triangular (Fig. 6), but ribbons of different triangular profile did not give different results for $ka>1.0$, as long as the ribbon edges were sharp.

In addition to measurements when the incidence is perpendicular, results are presented in Fig. 6 that pertain to other orientations of the ribbon with respect to the incident field. The measurements were taken at intervals of 11.25 deg and comparison is made with theory at 260- and 250-deg incidence, and scattering of 80 and 70 deg respectively, with $ka=3.0$. The value of the cross section depends critically upon the orientation of the ribbons, and falls off rapidly with small increases in the angle of incidence. It can now be seen why the Doppler shift method did not give satisfactory results on the cross section of the ribbons: during the commutation time the ribbon changes orientation with respect to the incident field and the measured cross section is only an average.

4. CONCLUSION

An experimental and theoretical study has been presented in this report concerning the backscattering cross section per unit length of cylinders and ribbons. The experimental results obtained through the application of the space-separation method have been compared with the theoretical, and the agreement has been shown to be excellent for ribbons, but less good for the cylinders. Reasons for this have been given.

5. ACKNOWLEDGMENTS

The author is indebted to Professors R. W. P. King and H. J. Schmitt for their valuable suggestions.

JOURNAL OF APPLIED PHYSICS VOLUME 31, NUMBER 12 DECEMBER, 1960

Observation of Domains in Iron Whiskers Under High Fields*

C. A. Fowler, Jr., E. M. Fryer, and David Treves†
Department of Physics, Pomona College, Claremont, California
(Received July 1, 1960)

An improved instrument utilizing the longitudinal Kerr magneto-optic effect is used to observe the magnetic domain development in iron whiskers undergoing a magnetization cycle. It is found that domains persist at the tip of the whisker even under conditions for which the crystal is usually assumed to be saturated. Under applied fields of a few thousand oersteds these persistent domains at the tip, in all of the specimens observed, are magnetized perpendicular to the axis of the whisker and in the same sense around its lateral faces. It is proposed that these domains are caused by the high fields localized near the sharp corners and edges of the crystal.

INTRODUCTION

THE problem of the nucleation of regions of reversed magnetization in a previously saturated single crystal of high anisotropy has received considerable attention but with little success.[1,2] Brown[3] has shown that for ellipsoidal single crystals nucleation cannot occur until there is applied a reverse field larger than $2K/I_s - NI_s$, where K is the magnetocrystalline anisotropy constant, I_s is the saturation magnetization, and N is the demagnetizing factor. For ellipsoidal specimens the maximum value of N is 4π. Thus, in highly anisotropic materials, one can neglect $4\pi I_s$ with respect to the first term and therefore a coercive force of $2K/I_s$ would be expected. Experiments with magnetic powders, however, give a much lower value,[4] suggesting that the ellipsoical model is not a satisfactory one to account for the observed coercive force.

Shtrikman and Treves[5] have recently proposed that the extremely high demagnetizing fields localized near the sharp edges and corners of crystallites may be responsible for domain nucleation. These fields may theoretically attain values approaching infinity and thus should be able to nucleate domains even in materials of high anisotropy where $2K/I_s \gg 4\pi I_s$. The coercive force will then be related to domain growth and wall movement rather than to rotation of magnetization from an easy direction and will usually be lower[3] than the expected value of $2K/I_s$.

Because a rigorous mathematical solution involves formidable computations, it was decided to observe experimentally the ferromagnetic domains near the corners of single crystals with the purpose of determining whether such domains exist even under conditions in which the crystal is usually assumed to be saturated, and also how they develop when the applied field is reduced.

In order to observe the domain development near saturation the specimen must be at remanence if it is a highly anisotropic material or, in case of lower anisotropy, under a strong saturating field. In either of these cases the colloidal magnetite or "powder pattern" technique seemed not very suitable inasmuch as the colloidal particles tend to agglomerate over the entire pole of the specimen and details of the domain structure are thus obscured. Scott and Coleman[6] did succeed in seeing some evidence of structure near the tip of an iron whisker under a moderate field of 650 oe, although the cloud of colloid already covers a large portion of the tip. The electron beam techniques[7–9] being also sensitive to magnetic fields, experience similar difficulties. The Kerr magneto-optic technique,[10] on the other hand, is sensitive to the magnetization in the ferromagnetic material rather than to magnetic fields and should, therefore, be well suited to the observation of domains as saturation is approached.[11]

We have, therefore, undertaken to visually and photographically observe, by means of the Kerr technique, the domain development in a single crystal, particularly near the ends and corners, as it is subjected to magnetizing fields ranging in value from zero to 6000 oe. As samples for this investigation, iron whiskers seemed the most suitable for several reasons: they are single crystals and are often free from imperfections that affect the magnetic properties; some have very simple domain structures, enabling the observations on all faces to be easily correlated, as the beautiful work of DeBlois and Graham has demonstrated[12]; some have the good reflecting surfaces required by the Kerr meth-

* Supported by the U. S. Office of Naval Research.
† On leave from the Weizmann Institute of Science, Rehovot, Israel and now at the Bell Telephone Laboratories, Murray Hill, New Jersey.
[1] A. Aharoni, J. Appl. Phys. **30**, 70S (1959); Phys. Rev. **119**, 127 (1960).
[2] G. W. Rathenau, J. Smit, and A. L. Stuyts, Z. Physik, **133**, 250 (1952).
[3] W. F. Brown, Jr., Revs. Modern Phys. **17**, 15 (1945).
[4] K. J. Sixtus, K. J. Kronenberg, and R. K. Tenzer, J. Appl. Phys. **27**, 1051 (1956).
[5] S. Shtrikman and D. Treves, J. Appl. Phys. **31**, 72S (1960).
[6] G. G. Scott and R. V. Coleman, J. Appl. Phys. **28**, 1512 (1957).
[7] M. Blackman, G. Haigh, and N. D. Lisgarten, Proc. Roy. Soc. (London) **A251**, 117 (1959).
[8] M. E. Hale, H. W. Fuller, and H. Rubinstein, J. Appl. Phys. **30**, 78S (1959); H. W. Fuller and M. E. Hale, ibid. **31**, 238 (1960).
[9] L. Mayer, J. Appl. Phys. **28**, 975 (1957); ibid. **29**, 658 (1958); ibid. **30**, 1101 (1959).
[10] C. A. Fowler, Jr., and E. M. Fryer, Phys. Rev. **94**, 52 (1954).
[11] Another technique which has the same property and might be useful in highly magnetostrictive material is the x-ray method used by K. M. Merz, J. Appl. Phys. **31**, 14S (1960).
[12] R. W. De Blois and C. D. Graham, Jr., J. Appl. Phys. **29**, 93I (1958).

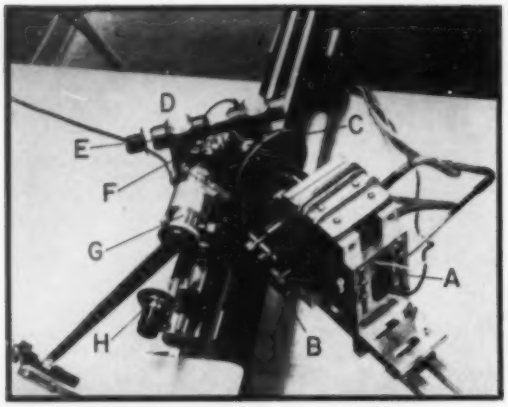

FIG. 1. Kerr instrument for microscopic observation. A, light source; B, condenser lens manipulator; C, polarizer; D, magnet; E, sample manipulator; F, microscope objective; G, analyzer with control arm; H, holder for eyepiece or camera.

od, making polishing unnecessary; a few are fairly perfect parallelopipeds with square cross sections, are terminated by a flat surface perpendicular to the whisker axis, and possess the sharp corners and edges required for the proposed observations.

EXPERIMENTAL PROCEDURE

The Kerr technique (longitudinal effect) has proved useful heretofore for the examination at low magnifying powers of relatively large domains such as occur in large single crystals and in evaporated films,[12–15] but little or no success has been reported with domain structure that is truly microscopic. We have considered the optical factors that limit high resolution in this technique, and by minimizing these, a resolution of a few microns has been attained.[16] Moreover, because the employment of large specimens will permit observation of the nucleating process in greater detail, we have given considerable attention to the technique of growing large iron whiskers.

Specimens

The whiskers were grown by the usual reduction method[17] from ferrous chloride in a hydrogen atmosphere within a Vycor tube of 2-in. i. d. To determine the best conditions for the growth of large and reasonably perfect whiskers, experimental runs were made at various temperatures from 630°–800°C, and with rates of hydrogen flow from 100–4000 ml/min. The best results were obtained at about 670°C with a flow of 1500 ml/min. The boats used were of Armco Magnetic Ingot Iron, and each charge of hydrated iron chloride was about 20 g. Such a run yields hundreds of whiskers and sometimes among these were a few which met the several requirements of the investigation; good surfaces, square cross section, and a width of 100 μ or more. Preliminary experiments with the whisker growing technique described by Wiedersich[18] did not show a marked advantage and were not further pursued.

Instrument

The most important factor operating against a high resolving power with the Kerr method seems to be the fact that for metallic reflection only these rays having the electric vector polarized parallel or perpendicular to the plane of incidence are reflected as plane polarized; for all other azimuths of the electric vector, the reflected ray becomes elliptically polarized.[19] Good microscope resolution requires a large "numerical aperture" which in turn requires for this technique that a significantly divergent beam be specularly reflected from the specimen into the microscope objective. Although the beam is plane polarized, each of the rays constituting the beam has a different plane of incidence and angle of incidence. Therefore the reflected beam consists mainly of rays whose elliptical polarizations are inhomogeneous and cannot be compensated with a quarter-wave plate. The ellipticity increases the amount of light transmitted by the pair of crossed-polarizing crystals, and this residual light obscures the contrast upon which the technique depends. This inhomogeneity of the polarization in the reflected beam is a minimum for a mean angle of incidence of zero degrees, and increases with the incidence angle. On the other hand, the longitudinal Kerr rotation, upon which contrast depends, is zero for zero angle of incidence and increases to a maximum at an incidence of about 60°.[10,16,20] Consequently, good resolution together with satisfactory contrast involves a compromise between these competing effects. We have found that for a beam divergence of about 10° (permitting resolution of approximately 5 μ), maximum contrast is obtained at an angle of incidence of about 20°.

The Kerr apparatus employed was a refined version of the standard design developed in this laboratory.[10] The light source is a 100-w high-pressure mercury arc (Osram type HBO-109) having a short constricted arc of about 0.3 mm × 0.3 mm. The condensing lens is mounted on a three-dimensional manipulator to permit accurate centering and focusing of the light spot on the sample. The polarizer and analyzer are a pair of Glan Thompson prisms of cross section 10 mm × 10 mm

[12] C. A. Fowler, Jr., E. M. Fryer, and J. R. Stevens, Phys. Rev. **104**, 645 (1956).
[14] M. Prutton, Phil. Mag. **4**, 1063 (1959).
[15] O. W. MucKenhirn, A. E. LaBonte, and P. J. Besser, J. Appl. Phys. **31**, 304S (1960).
[16] An account of this work will be published elsewhere.
[17] S. S. Brenner, Acta. Met. **4**, 62 (1956).
[18] H. Wiedersich, J. Electrochem. Soc. **106**, 810 (1959).
[19] F. A. Jenkins and H. E. White, *Fundamentals of Optics* (McGraw-Hill Book Company, Inc., New York, 1957), 3rd ed., p. 520.
[20] *International Critical Tables* (McGraw-Hill Book Company, Inc., New York, 1929), 1st ed., Vol. VI, p. 438.

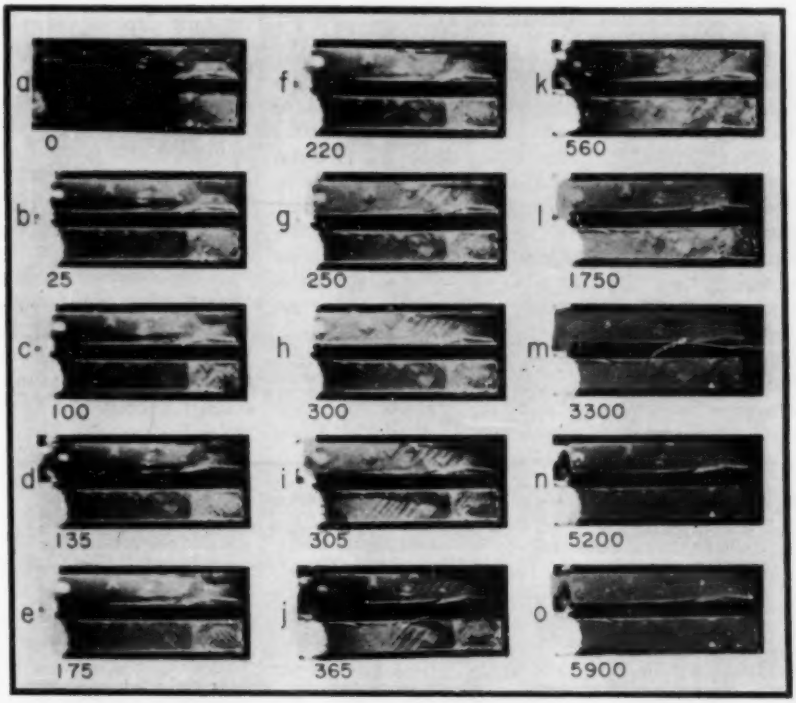

FIG. 2. Domain structure on two adjacent faces of a 2 mm × 0.16 mm whisker under a varying magnetic field. The common edge is the one between each pair. Fields are given in oersteds.

which, when placed directly in series and crossed, transmitted a few parts per million of the total intensity, (as compared to about one part in ten thousand for the best polaroid films available in this laboratory). The viewing system consists of a low-power microscope objective, the analyzer, and an ocular or camera. The illuminating and viewing arms are mounted on two horizontal rails connected through a pivot, permitting illumination at angles of incidence between 10° and 90°. Color-corrected optical components were used throughout the system. A green filter did not noticeably improve the contrast, showing the dispersion of the rotation to be only slight. For the reasons mentioned above, no quarter-wave compensator was used.

The whisker samples were handled as described by Fontanella and DeBlois,[21] the cut end inserted in a capillary tube and the naturally terminated end available for observation. A small electromagnet, capable of reaching fields of 6000 oe for short periods, was designed to fit the optical system and interfere as little as possible with the optical observation of the sample. A 3-mm brass rod was drilled at its tip to hold the capillary tube in which the whiskers are mounted. The rod in turn fits in a hole drilled through one pole piece. Alignment of any face of the sample is accomplished by rotating the entire magnet about a vertical axis and by rotation of the brass rod. Figure 1 is a photograph of the entire instrument including the magnet and specimen mount.

It should be noted that no transverse Kerr effect could be detected in these whiskers. Therefore, since the axis of the whisker was parallel to the plane of incidence, an ambiguity existed with respect to the determination of the direction of the magnetization in case the latter was perpendicular to the axis of the whisker. In order to eliminate this ambiguity the mount of the magnet was designed to permit observation of the whisker with its axis perpendicular, as well as parallel, to the plane of incidence.

Although the longitudinal Kerr rotation between saturation in two opposite directions at an angle of incidence of 20° was only about three minutes for the iron whiskers, with this apparatus the domain structure could readily be observed visually at powers up to about 100×. For photographing the domains a direct magnification of about 20 was used, and with Adox KB14 film the exposure time was from a few seconds to a minute. The smoothness of the whisker faces made the positive-on-negative "noise-reduction" technique[22] quite unnecessary. "Blooming" of the whiskers[15] was not attempted.

[21] E. L. Fontanella and R. W. De Blois, Rev. Sci. Instr. **30**, 982 (1959).

[22] C. A. Fowler, Jr., and E. M. Fryer, J. Opt. Soc. Am. **44**, 256 (1954).

RESULTS OF OBSERVATION

Specimens selected for observation were those that were 100 μ or more in width and showed the simple structure of closure domains characteristic of whiskers having (100) faces and with the axis parallel to a [100] direction. Figure 2(a, top) shows on such a face the typical structure consisting of antiparallel domains in the axial direction associated with a square-faced domain near the center and a triangular closure at the tip. The fact that the Kerr technique reveals the entire domain surface with an intensity related directly to the magnetization direction makes the interpretation of the domain structure straight forward and unambiguous. The advantage is particularly evident in Fig. 2(a, bottom) which shows the face adjacent to that of Fig. 2(a, top). In this face the surface magnetizations in two opposite directions meet at a line which is actually the intersection of two plane walls that bound the prism-shaped closure domain. This type of "V line" collects magnetic colloid very weakly or not at all,[12,23] but the true structure is revealed here with clarity.

Photographs of the domain development under controlled field conditions were taken of several specimens, and many more were observed visually. In all of these the behavior was identical, and the general features of a typical development are described later in terms of Figs. 2–7, which include photographs of specimens in various stages of the magnetization process. In particular, Fig. 3 is a sequence of photographs of one face of a whisker undergoing a change of magnetization from an unmagnetized state to magnetic saturation and thence through one half of a hysteresis cycle: Fig. 2 compares

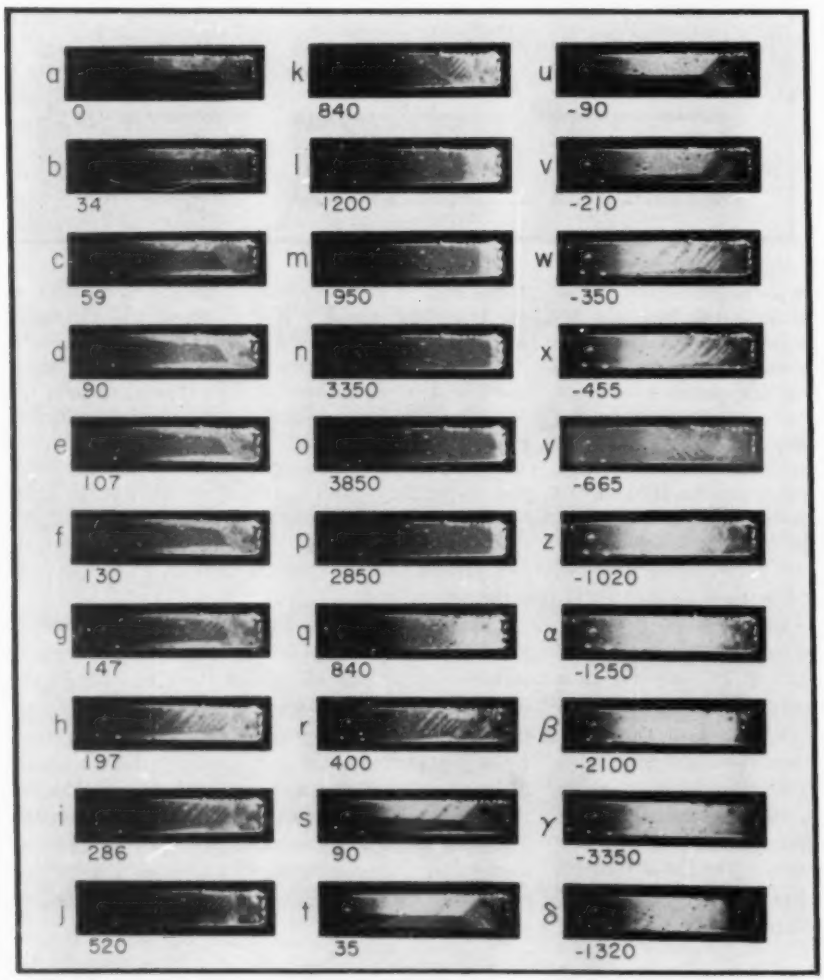

FIG. 3. Domain structure on one face of a whisker (2.2 mm × 0.14 mm) undergoing a magnetization cycle. Fields are in oersteds.

[23] R. V. Coleman and G. G. Scott, J. Appl. Phys. **29**, 526 (1958).

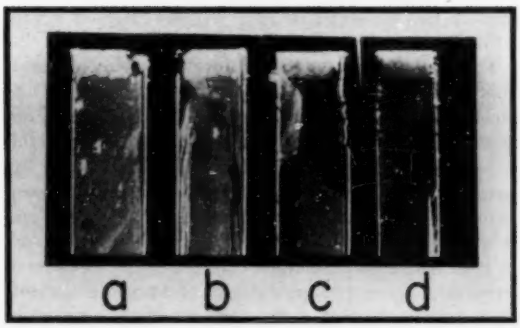

FIG. 4. Four sides of a whisker (2.5 mm × 0.17 mm) showing the closure domain "cap" under a field of 3300 oe. The structure seen in (c) is of crystalline nature and not magnetic.

two adjacent faces at each stage of the magnetization curve; Fig. 4 compares all four faces at a whisker tip under a "saturating" field. All of the whiskers observed had practically zero remanence, as can be seen in Fig. 3(t) and (u). This is probably due to the dimensions of the samples observed.

1. Low Values of the Impressed Field (0–200 oe)

From 0–200 oe, the magnetization proceeds by movement of the principal 180° wall and a corresponding change in shape of the closure domains. The manner, schematically indicated in Fig. 5, is very similar to one predicted in the work cited in footnote 5. A typical structure equivalent to Fig. 5(c) is seen in the photographs (b) and (c) of Fig. 6 (the curved shadow in (c) is due to a surface defect), and similar developments are seen in Fig. 2(a)–(h) and in Fig. 3(a)–(f). It should be noted that the domains of reversed magnetization are often merely needles along the edges of the whisker, as can be seen in the two adjacent crystal faces of Fig. 6(a) and (b). At other times these reversed domains are thin sheets covering the entire width of one face. This latter case is seen in Fig. 2 where the thickness of the reverse domain in one face (upper photograph of each pair) decreases from (a)–(h) at which point it can no longer be seen, while on the adjacent face (lower photographs) the width continues to cover the entire face. A damaged tip, such as seen in Fig. 3, does not alter the general domain development but does give rise to a somewhat more complicated closure structure at the tip.

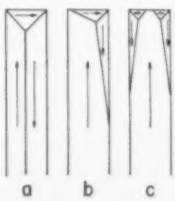

FIG. 5. Schematic diagram of the observed development of closure domains under a low magnetic field. The field increases from (a) to (c).

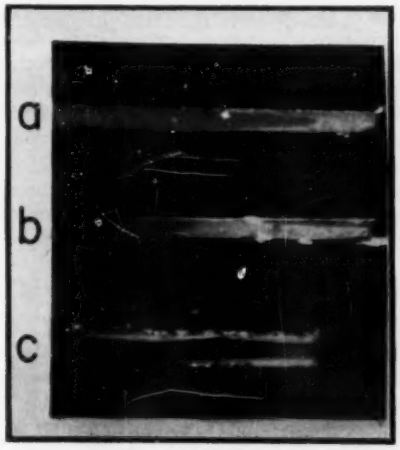

FIG. 6. Typical closure domains at fields of about 150 oe (a) and (b) are two adjacent faces of the same whisker (5.5 mm × 0.07 mm) while (c) is of another whisker (0.10 mm width).

2. Very High Values of the Field (1000–6000 oe)

The domain configuration, which at intermediate fields undergoes a complicated development [see Sec. (3) below], becomes very simple again under fields of magnitudes generally considered to be much greater than necessary for saturation. In all specimens there appears at the tip a "cap" whose magnetization in each surface is perpendicular to the axial magnetization in the body of the whisker. As the magnetizing field is increased, this cap reversibly retreats toward the tip and can still be observed at the limiting value of our field (6000 oe). Figure 2(l)–(o) and Fig. 3(l)–(q) and (α)–(δ) show the cap and its behavior as the field is increased, and Fig. 4 is a photograph of all four sides of a whisker in a field of 3300 oe.

In order to determine the absolute direction of the magnetization in the cap, the whisker was also observed with its axis perpendicular to the plane of incidence. Although the cap had appeared at first to be practically homogeneously magnetized, it was found by this perpendicular observation to be actually composed of a complicated domain structure magnetized mainly perpendicular to the whisker's axis. Only under fields of such magnitude as to restrict the length of the cap to

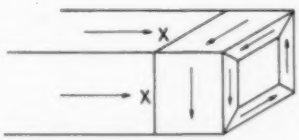

FIG. 7. Diagram showing the interpretation of the cap domain structure in which the end domains form a closed flux path and their thickness tapers off to zero at the boundaries X. The arrows show the direction of magnetization in the individual domains.

a fraction of the whisker's width, was the cap magnetized homogeneously on each face and in the same sense around the four faces. Figure 7 is an interpretation of the cap structure, in which the end domains form a closed flux path and their thickness tapers off to zero at the boundaries (X). These domains presumably lower the energy of the system by effectively eliminating the corners of the region saturated parallel to the external field, reducing this region to an approximate ellipsoid having much lower local demagnetizing fields.

3. Intermediate Values of the Field (200–1000 oe)

The domain structure changes from the simple pattern of 1 (low fields) to the simple pattern of 2 (high fields) in a complicated but typical manner. Spiked domains appear in which the magnetization is 90° to the axial field. These increase in number and retreat toward the tip as the magnetizing field is increased, finally coalescing in a complex fashion to become the cap described in 2. This phase of the development is evident in Fig. 2(g)–(k) and in Fig. 3(g)-(l) and (w)–(α). In each of these pictures the three directions of magnetization can be assigned with certainty. For example, Fig. 3(g) has an elongated domain of reversed magnetization at the bottom edge together with a few spikes near the tip (lightest shade); the main body of the whisker and some spikes are magnetized in the direction of the field (darkest shade); the large spikes and most of the surface near the tip are magnetized at 90° to the whisker axis (intermediate gray shade).

Decreasing the field from saturation to zero and to saturation in the negative direction is illustrated in Fig. 3(o)-(γ).

CONCLUSIONS

The observations show conclusively that magnetic domains in iron whiskers persist in the neighborhood of the tip and its corners even under a field of several thousand oersteds, whereas the average demagnetizing fields for the whiskers being studied is from about 10 to a few hundred oersteds. Particularly important is the fact that at equal fields the length of the cap relative to the width of the whisker is almost independent of the ratio of the whisker's length to width. Whiskers with ratios between 12 and 80 were observed.

The fact that the mode of development of domains from a quasi-saturated state is the same for all of the whiskers observed indicates that the mechanism is not connected with imperfections or a damaged end but rather with the macroscopic shape of the whisker's tip, through the high demagnetizing fields related to sharp corners. Such fields can, with sufficiently sharp edges, be many times greater than $4\pi I_s$ and might therefore be responsible for the nucleation of domains even in previously saturated crystallites of very high anisotropy, such as barium ferrite and manganese bismuth. Although the volume of such domains at remanence may be a very small fraction of the total volume of the crystal, their effect on the coercive force can be very great. Additional evidence as to the validity of the interpretation of these observations could probably be obtained by the study of the nucleation of domains in highly anisotropic single crystals, and by the effect of shape on the coercive force of relatively large single crystals, as by gradually etching the sharp edges of whiskers.

It should be noted that the lowering of the coercive force by the "corner effect" was avoided in the experiments of De Blois and Bean[24] by the application of a bias field. This field localized the domains in the neighborhood of the tips; the high values of the coercive force actually found were measured in the middle section which was presumably saturated.

It is recognized that these observations involve single isolated crystal samples. In dealing with polycrystalline materials, in which the magnetostatic interaction between crystallites must be taken into account, the present study can only serve as a guide for future work.

ACKNOWLEDGMENTS

The authors wish to thank Dr. S. Shtrikman for very valuable discussions which stimulated much of the present work, Prof. B. Henke for several important suggestions, Mr. R. J. De Blois for furnishing some of the whiskers, and Mr. M. Lu for his technical assistance.

[24] R. W. De Blois and C. P. Bean, J. Appl. Phys. **30**, 225S (1959).

Subsidiary Resonance in the Coincidence Region in Yttrium Iron Garnet

F. C. Rossol
Bell Telephone Laboratories, Inc., Murray Hill, New Jersey
(Received May 23, 1960; and in final form August 15, 1960)

The measurement of h_{crit}, the threshold rf field for subsidiary resonance, as a function of frequency throughout the coincidence region, and the behavior of μ''_{max} at rf fields exceeding h_{crit} are presented for a single-crystal yttrium iron garnet sphere at room temperature. The sphere has a linewidth of 480 moe measured at 3000 Mc. The h_{crit} curve obtained was quite flat at approximately 0.3 moe from 2000 Mc to 3300 Mc and increased by more than a factor of 6 within 150 Mc of either end; a much more sudden increase than was the case for previously measured spheres of wider linewidth. The measured curve is compared to a curve computed from Suhl's theory of subsidiary resonance at high power levels, and the effects of the linewidths ΔH and ΔH_k on the shape of the curve are considered. The variation of μ''_{max} with rf power above the threshold followed Suhl's $P^{-\frac{1}{2}}$ law rather closely for frequencies above 2700 Mc but exhibited fine structure and a slower fall-off for frequencies below.

INTRODUCTION

As the rf power applied to a ferromagnetic sample is increased beyond a certain threshold, the generation of spin waves causes the uniform precession to become unstable. In general, at lower dc fields a subsidiary resonance can also be generated for rf power greater than another threshold value. Throughout the range of frequencies known as the "coincidence region" in which the dc magnetic field required for the observation of subsidiary resonance is identical to that required for the uniform precession, this threshold is particularly low and the instability appears in the form of spin waves generated at half the applied frequency. The purpose of this paper is to present observations of these effects in a polished, single-crystal, narrow linewidth, yttrium iron garnet sphere at room temperature. The behavior of μ''_{max}, the imaginary part of the complex permeability at resonance is observed at rf magnetic fields above the threshold h_{crit}. A measurement of the curve of h_{crit} vs frequency is presented and discussed in terms of Suhl's theory of nonlinear effects at high signal power levels and in relation to other factors affecting the shape of this curve. The coincidence region includes frequencies in the range $\omega_M N_Z$, $<\omega<2\omega_M N_Z$ where $\omega_M=\gamma 4\pi M$, M is the saturation magnetization, γ is the gyromagnetic ratio, and N_Z is the demagnetizing factor for the axis parallel to the applied dc field.

Spencer, LeCraw, and Porter[1] reported similar measurements of h_{crit} as a function of frequency, made in a tunable resonant cavity, using a relatively unpolished yttrium iron garnet sphere with a linewidth of 5.7 oe at 3000 Mc. Narrower linewidth samples now available permit these measurements to be made in a coaxial transmission structure which requires no tuning as the frequency is varied. The sphere reported in this paper has a diameter of 0.016 in., a $4\pi M$ of 1890,[2] and a linewidth of 480 moe measured at 3000 Mc.

According to the ferromagnetic resonance theory developed by Suhl,[3] instability in the coincidence region for a spherical sample occurs at rf magnetic fields which exceed

$$h_{crit}=\frac{\gamma\omega_H}{\omega_M}\left[\frac{\Delta H_k \Delta H}{\sin\Theta_k\cos\Theta_k(\frac{3}{4}\omega_H-\frac{1}{2}\omega_M+\omega_{ex}\ell^2k^2)}\right]. \quad (1)$$

In this equation $\omega_H=\gamma H$, where H is the dc magnetic field, Θ_k is the angle between the direction of propagation of the spin wave ω_k of wave number k and the dc field; $\omega_{ex}=\gamma H_{ex}$, where H_{ex} is the exchange field, ℓ is the lattice constant, ΔH is the measured linewidth; and $\Delta H_k=1/\gamma T_{1k}$ where T_{1k} is the spin-lattice relaxation time averaged over the spin waves involved.

The spin wave spectrum for a sphere given by

$$\omega_k^2=(\omega_H-\tfrac{1}{2}\omega_M+\omega_{ex}\ell^2k^2)(\omega_H-\tfrac{1}{2}\omega_M+\omega_{ex}\ell^2k^2+\omega_M\sin^2\Theta_k) \quad (2)$$

is shown in Fig. 1.

EXPERIMENTAL RESULTS AND CONCLUSIONS

The sphere was placed approximately at the short (50 mils away to avoid wall effects) in a shorted rectangular coaxial transmission line so that it was located at

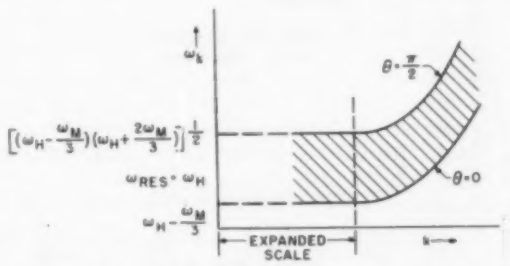

FIG. 1. The general spin-wave spectrum of a sphere as a function of wave number k.

[1] E. G. Spencer, R. C. LeCraw, and C. S. Porter, J. Appl. Phys. 29, 429 (1958).

[2] Although the reason is not understood at present, the particular batch of material from which this sample was chosen exhibited a somewhat higher value of $4\pi M$ than is usual for yttrium iron garnet.

[3] H. Suhl, J. Phys. Chem. Solids 1, 209 (1957).

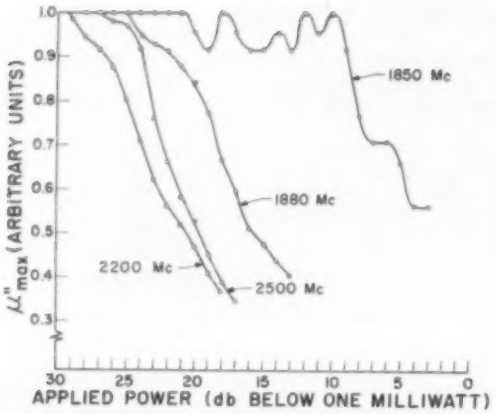

FIG. 2. The measured fall-off of μ''_{max} as a function of rf power applied to the structure for frequencies in the lower half of the coincidence region. Irregularities are present and the behavior of the curve at 1850 Mc is believed to result from the formation of domains.

a point of maximum rf magnetic field directed perpendicular to the dc magnetic field. The rf power was applied through one arm of a hybrid junction and the changes observed in the power reflected from the short as the dc field was adjusted from off resonance to resonance yielded a curve of μ''_{max} in arbitrary units as a function of the power level of the applied signal. It is interesting to note that the threshold appeared with as little as 2 μw applied to the shorted coaxial structure.

For frequencies above 2700 Mc, the curves of μ''_{max} vs applied rf power break sharply at P_{crit} and follow a $P^{-\frac{1}{2}}$ variation for applied power P greater than P_{crit}. Figure 2 illustrates the variation of μ''_{max} with rf power applied to the coaxial structure for a number of the frequencies in the lower portion of the coincidence region. These curves tend to roll off in the region near $P=P_{crit}$ rather than to break sharply as in the case for the higher frequencies. This roll-off effect introduces some difficulty in ascertaining the exact value of P_{crit}. At 1850 Mc, the dc field is at a value such that the sphere is approaching the point of becoming unsaturated and the additional structure might reasonably result from the formation of domains.

The values of P_{crit} determined from the μ''_{max} curves yielded values of h_{crit} which appear plotted as a function of frequency by the solid curve in Fig. 3. The measured value of h_{crit} is nearly constant at approximately 0.3 moe throughout most of the coincidence region, but

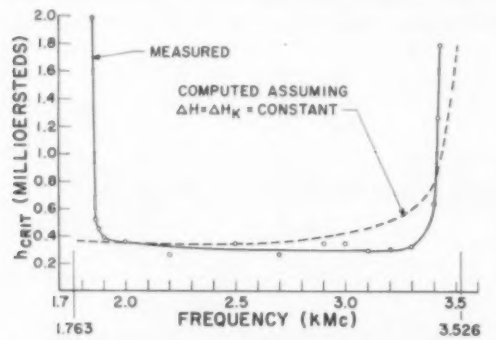

FIG. 3. The solid curve is the measured curve of h_{crit} as a function of frequency in the coincidence region. The dashed curve is the curve of h_{crit} computed from Eq. (1) excluding any effects of variations in linewidth ΔH or ΔH_k. This is accomplished by setting $\Delta H=\Delta H_k=$const.

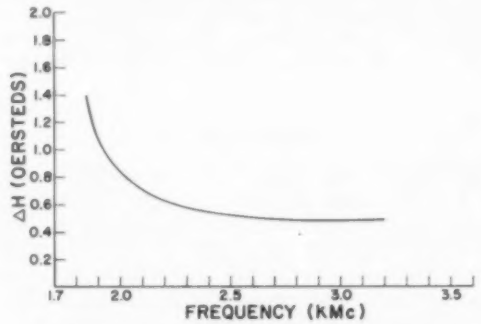

FIG. 4. The measured variation of linewidth ΔH with frequency in the coincidence region.

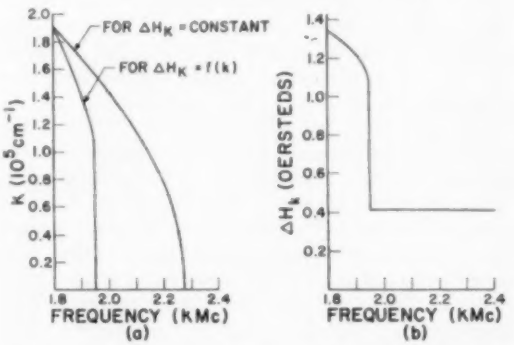

FIG. 5. (a) A comparison of the wave number k determined by minimization (allowing ΔH_k to assume values according to the discussion in the text) with the wave number k obtained by minimization, assuming ΔH_k to be constant. (b) The frequency dependence of ΔH_k as a result of the minimization of Eq. (1) including the k dependence of ΔH_k.

exhibits an extremely sharp rise at either end. The slight scattering of measured points about the smooth curve was determined to result from standing wave effects in the coaxial structure. The frequencies 1763 Mc and 3526 Mc correspond, respectively, to the limits $\frac{1}{3}\omega_M$ and $\frac{2}{3}\omega_M$ of the coincidence region for the sphere which has a $4\pi M$ of 1890. The dashed curve of Fig. 3 shows the variation of h_{crit} computed by minimizing Eq. (1) with respect to k and Θ_k such that Eq. (2) is also satisfied. In computing this curve, it was assumed that $\Delta H=\Delta H_k=480$ moe for all frequencies considered.

A lower limit exists for the value of wave number k of the generated spin waves; however, it was found that no essential error is involved in representing k equal to zero in the data described.

Figure 4 shows the variation of linewidth ΔH with frequency as measured at an rf power level below the threshold and with the dc field along the easy, [111], axis. Modifying the computed h_{crit} curve to include this variation of ΔH results in a rise at the low-frequency end of the region, but not nearly as rapid as the rise in the measured h_{crit} curve.

Measurements of spin-wave relaxation time T_{1k} reported by Fletcher, LeCraw, and Spencer[4] for an yttrium iron garnet sample show that T_{1k} varies with wave number k. Since $\Delta H_k = 1/\gamma T_{1k}$, we have from this reference the values of ΔH_k as a function of k. The minimization of Eq. (1) using these values of ΔH_k results in k remaining zero for lower frequencies than was the case for minimization, assuming ΔH_k to be constant. The values of k vs frequency determined by both minimization processes are compared in Fig. 5(a). Figure 5(b) shows the curve of ΔH_k vs frequency computed from the values of k in the left-hand curve of Fig. 5(a).

The variation of ΔH_k with frequency shown in Fig. 5(b) together with the measured variation of ΔH with frequency shown in Fig. 4 are sufficient to explain the steep rise in the measured h_{crit} curve at the low-frequency end of the coincidence region.

ACKNOWLEDGMENT

The author wishes to express thanks to E. G. Spencer for many helpful and stimulating discussions concerning this work.

[4] R. C. Fletcher, R. C. LeCraw, and E. G. Spencer, Phys. Rev. 117, 955 (1960).

JOURNAL OF APPLIED PHYSICS VOLUME 31, NUMBER 12 DECEMBER, 1960

Gold-Induced Climb of Dislocations in Silicon*

W. C. Dash
General Electric Research Laboratory, Schenectady, New York

(Received August 9, 1960)

Studies were made of the climb of dislocations in silicon crystals induced by the diffusion of gold in the temperature range from 1000°C to 1300°C. For some studies, dislocations were introduced into previously dislocation-free crystals by indentation at room temperature and deformation at about 900°C in order to predetermine both Burgers vector and the direction of deformation. It was possible in this way to introduce left-handed screw dislocations in small concentrations. The left-handed screw dislocations were found to form right-handed helices upon the diffusion of gold during subsequent heat treatment at temperatures above 1000°C. This observation is shown to be consistent with the idea that gold diffuses as an interstitial atom and causes a vacancy deficiency in the neighborhood of dislocations. Further evidence of the structure sensitivity of the diffusion of gold is shown by autoradiographic techniques. Studies were made of the effect of heat-treatment times and quenching rates upon the diameter of helices. The diameter of the helices increases with time at a given temperature, and increases with temperature during a given time of heat treatment. Variation of the cooling time by a factor of 10^3 has no apparent effect on the diameter. Therefore, the helices form as a result of a gradient in the concentration of gold rather than by a quenching process. Impurities introduced by heat treatment at 900°C strongly modify climb in crystals which are relatively free from oxygen. Precipitates believed to be formed during this heat treatment act as nucleation sites for the formation of prismatic loops. Crystals grown from quartz crucibles and thus containing about 10^{+6} atom fraction of oxygen have complicated climb mechanisms believed to be associated with the pinning effect of the oxygen on the dislocations. Modified Bardeen-Herring sources have been found in these cases.

I. INTRODUCTION

THE climb of dislocations in crystals results from the acquisition of vacancies or interstitial atoms at the dislocation core. In simplest terms, the climb of an edge dislocation will occur in such a way as to cause the "extra plane" to decrease in size by interaction with vacancies, and to increase in size by interaction with interstitial atoms.[1] A screw dislocation can also climb by the acquisition of vacancies or interstitial atoms, but the absence of an extra plane in this case causes a screw dislocation to form a helix with axis parallel to the Burgers vector.[2] If sufficient information about a dislocation and its direction of climb are known, it is possible to determine whether the point defects responsible for climb are vacancies or interstitial atoms.

In this investigation, attention will be paid primarily to helical dislocations because it is much simpler to introduce a pure screw than a pure edge dislocation in silicon in a predetermined way. This is a result of the tendency of all parts of a glissile dislocation loop to lie along ⟨110⟩ crystallographic directions under appropriate conditions of deformation.[3] Another important

* This research was supported by Wright Air Development Division.

[1] W. T. Read, *Dislocations in Crystals* (McGraw-Hill Book Company, Inc., New York, 1953), p. 49.

[2] W. Bontinck and S. Amelinckx, Phil. Mag. 2, 94 (1957). See also R. deWit, Phys. Rev. 116, 592 (1959) and references cited therein.

[3] W. C. Dash, J. Appl. Phys. 27, 1193 (1956).

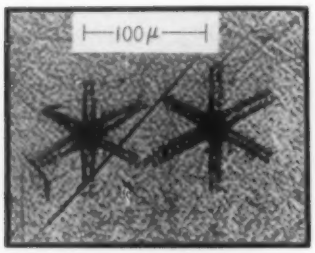

FIG. 1. A lightly indented (111) silicon surface after heating to 1000°C and etching. Closely spaced prismatic loops extend in all ⟨110⟩ directions.

reason for confining attention to helices is that their formation by climb is simple to recognize, whereas it is more difficult to determine that an edge dislocation has climbed.

Silicon crystals appear to have a very low concentration of vacancies, even at temperatures near the melting point. For this reason, climb is difficult to observe in as-grown crystals. It is possible, however, to induce effects similar to those of an excess of vacancies by the diffusion of gold into crystals at high temperature.[4]

The experiments described herein demonstrate a unique way in which the direction of climb induced by the diffusion of gold can be determined. This is made possible by the availability of large crystals of very pure silicon free from dislocations, as well as the ability to introduce small numbers of dislocations in a controlled manner. A number of correlated effects have been investigated in order to determine the mechanism by which gold diffusion induces climb.

II. EXPERIMENTAL PROCEDURE

The silicon crystals used in this study are grown by one of two different pulling techniques: the pedestal technique,[5] which has the advantage that dislocation-free, oxygen-free crystals can readily be grown, and the ordinary Czochralski technique which uses a quartz crucible and results in a crystal containing of the order of 10^{-5} atom fraction of oxygen.[6] In addition to dislocation-free crystals grown by both these methods, crystals containing about 10^3 dislocations per cm^2 were very useful in this study.

In order to have good control of the geometric properties of the dislocations, it was necessary to introduce them deliberately into dislocation-free crystals. This was done by first indenting the surface with a diamond point at room temperature.[7] An indentation of this sort is a rich source of dislocations. Upon heating to elevated temperature, dislocation loops are emitted from the center of the indentation, as shown in Fig. 1. The application of a shear stress at elevated temperature expands the dislocation loops which originate at the indentation, as shown in Fig. 2. By proper choice of crystallographic axes and mode of deformation, it is possible therefore to predetermine the geometry of the dislocation loops which are formed. This is essential in order that conclusions can be drawn about the direction of climb in subsequent measurements of this property. The details of the geometry of deformation will be given in a later section.

To induce climb in a silicon crystal containing dislocations, a layer of gold is chemically deposited onto a brightly etched surface from a solution of a small amount of gold cyanide in concentrated hydrofluoric acid. Alternatively, droplets of a water solution of gold chloride can be applied to the sample for better control of concentration and direction of diffusion. If it is desired to decorate the dislocations, droplets of dilute copper nitrate solution are applied to the specimen, as described in the work cited in footnote 3. The crystal is then heated to a temperature of 1000°C to 1300°C for a length of time which varies according to the experiment performed. To achieve proper decoration of the dislocations when copper has been applied to the specimen, it is necessary to quench from the temperature of diffusion. This is usually done by dropping the specimen directly out of the furnace onto a copper plate. Although cooling is rapid, it is largely one-demensional and unconstrained, with the result that proper decoration occurs without deformation. The decorated dislocations are examined by the use of a microscope and infrared image tube. In cases where no decoration of the dislocations is desired, they can be examined by etching techniques which have also been described in the reference given in footnote 3. No visible decoration occurs when gold alone is diffused into the crystals.

Measurements of the diffusion coefficient of gold in silicon crystals grown from quartz crucibles have been made by Struthers.[8] At the time of this writing, some

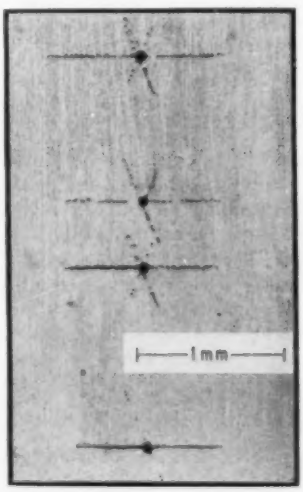

FIG. 2. Etch pattern on a (112) indented silicon surface after deformation by torsion at 900°C.

[4] W. C. Dash, Phys. Rev. Letters **1**,400 (1958).
[5] W. C. Dash, J. Appl. Phys. **31**, 736 (1960).
[6] W. Kaiser, P. H. Keck, and C. F. Lange, Phys. Rev. **101**, 1264 (1956).
[7] W. C. Dash, *Properties of Elemental and Compound Semiconductors*, edited by H. C. Gatos (Interscience Publishers, New York, 1960), p. 195.

preliminary studies by the authors of the diffusion coefficient of Au^{198} indicate that the diffusion is structure sensitive. Some qualitative experiments using autoradiographic techniques have been performed in order to establish the position of the diffused gold with respect to concentrations of dislocations.

III. RESULTS

A. An As-Grown Pedestal Crystal Containing Dislocations

In crystals which contain of the order or 10^3 dislocations per sq cm and an oxygen concentration less than 10^{16} per cubic cm, the observed climb is relatively simple. Figure 3 is a typical example of climb in such a crystal at 1200° with simultaneous copper decoration. The inset shows an end-on view of a "helix," indicating that they are usually polygonized with all elements parallel to ⟨110⟩ directions. The helices which are seen in this figure make an angle of the order of 30° with the plane of the specimen. They are relatively uniform in pitch along the length of each helix, although there is a considerable variation from one helix to another. As contrasted with crystals which contain oxygen described herein, the observed climb in pedestal crystals is characterized primarily by the formation of polygonized helices. Occasionally, isolated hexagonal or circular dislocation loops on (111) planes are found. Formation of prismatic loops with ⟨110⟩ Burgers vectors by mutual repulsion of the turns of a helix has been described in the work cited in footnote 4.

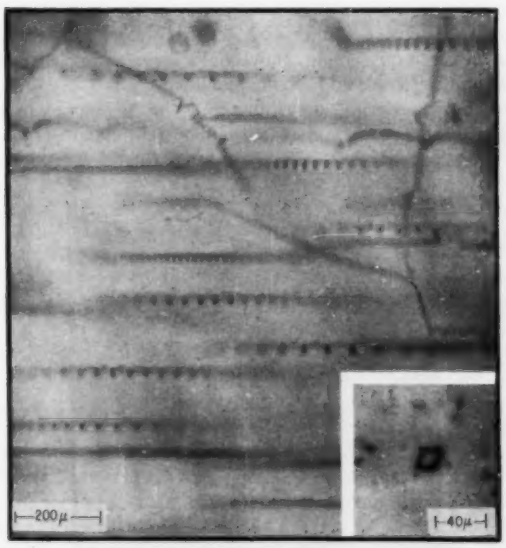

FIG. 3. Group of helical dislocations formed by the diffusion of gold into a pedestal-grown crystal at 1200°C. Inset shows a view along the axis of a typical helix to demonstrate the polygonal structure.

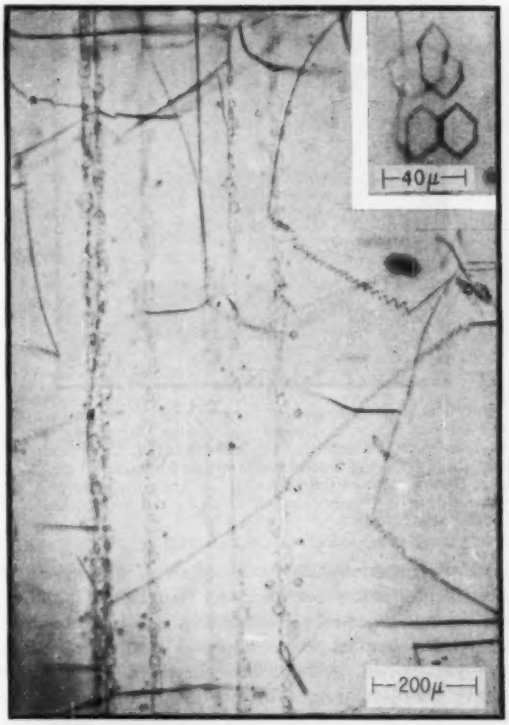

FIG. 4. Climb of ⟨110⟩ dislocations in a crucible-grown crystal induced by gold diffusion at 1200°C. The inset shows a closed loop and a figure 8 formed by the climb. The original ⟨110⟩ dislocation was apparently not a screw.

B. Climb in Crucible-Grown Crystals

The climb observed in crystals which contain about 10^{-5} atom fraction of oxygen is frequently found to be much more complicated than that in pedestal crystals. This is believed to be the result of the pinning effect of oxygen on the dislocations.[9] Figure 4 is a typical view of a decorated dislocation subjected to a heat treatment similar to that of the specimen in Fig. 3. The climb illustrated in Fig. 4 is a somewhat special case in that the original dislocation lines were parallel to ⟨110⟩ close-packed directions in the diamond lattice. The initial stages of climb apparently occurred in segments, each of which was pinned at the original position of the dislocation. The result is a set of loops which appear to have been formed by a modification of the Bardeen-Herring mechanism.[10] The inset in Fig. 4 shows

[8] J. D. Struthers, J. Appl. Phys. **27**, 1560 (1957). Erratum: The values of the diffusion constant of gold in silicon in this reference are low by a factor of ten.

[9] Pinning effects interfering with glide of dislocations in crucible-grown crystals have been described by the author in J. Appl. Phys. **29**, 705 (1958).

[10] J. Bardeen and C. Herring, *Imperfections in Nearly Perfect Crystals*, edited by W. Shockley (John Wiley & Sons, Inc., New York, 1952), Chap. 19.

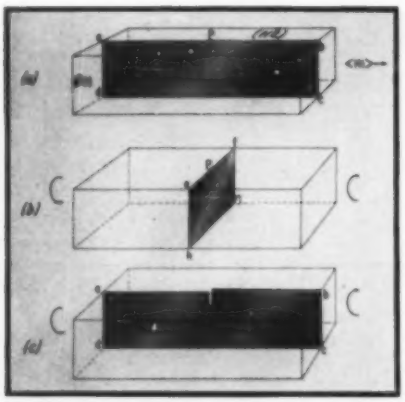

FIG. 5. Schematic diagram of the geometry of deformation used to introduce left-handed screw dislocations. (a) shows the undeformed crystal which has been indented at *P*. Upon heating to 900°C and applying a torsional stress as indicated in (b), loops enter the crystal from the source at *P* on the glide plane *efgh*. The plane *abcd* in (a) becomes an element of a left-handed helicoidal surface, as shown in (c).

some of these loops in early stages of formation. In later stages, it is often observed that closed loops are left behind and a straight dislocation continues to climb away from them. A more complete description of these observations will be published elsewhere. Well-formed helices are often formed in crucible-grown crystals on dislocations with a large screw component. Several of these can be seen in Fig. 4.

C. Deformed Crystal Containing Left-Handed Screws

A dislocation-free crystal approximately $\frac{1}{4}$ in.$\times\frac{1}{4}$ in. $\times 1$ in. was deformed following indentation at room temperature. The geometry of deformation is illustrated in Fig. 5. The plane *abcd* in Fig. 5(a) represents a $(1\bar{1}0)$ plane which is perpendicular to the Burgers vector. In Fig. 5(b) the glide plane is sketched as *efgh*. The letter *P* indicates the point as which an indentation was made at room temperature. At elevated temperature, which was about 900°C in this case, the specimen was twisted in the direction indicated by the arrows. Dislocation loops, whose sides are parallel to $\langle 110\rangle$ crystallographic directions, move into the interior of the crystal as shown in Fig. 5(b). The lower portion of the dislocation loop illustrated is a pure screw dislocation. This is consistent with the geometry of deformation and also with the x-ray results of Newkirk[11] using the Berg-Barrett technique. In Fig. 5(c) the atomic displacement in the plane *abcd* is illustrated. It can be seen that the plane which was originally parallel to the $(1\bar{1}0)$ crystallographic plane now has the form of a left-handed helicoidal surface.

For reasons which will be discussed in the next section, it was necessary to cool the specimen which has been deformed in the manner described from a temperature of 900° to room temperature over a period of a half-hour or longer. The specimen thus treated was then plated with gold and heat-treated in the way described earlier, in order to cause climb of the screw dislocations. In every case it was found that the left-handed screw dislocations thus formed were converted into right-handed helical dislocations. A discussion of the interpretation will be given in Sec. IV.

D. Effects of Heat Treatment Before the Gold Diffusion

Early experiments to produce climb of freshly introduced dislocations by the diffusion of gold resulted in failure. Instead, these specimens were found to contain large numbers of randomly scattered hexagonal dislocation loops on (111) planes. Since similar problems do not occur in as-grown crystals, it was suspected that contamination by some impurity occurred when the crystal was deformed.

Copper and nickel are typical impurities which diffuse rapidly into silicon at elevated temperatures and precipitate when it is cooled. Impurities such as these, deposited on the surface of the crystal in preparation, are a likely source of precipitates during the heat treatment required for deformation. In the case of copper, about 10^{16} atoms per cc are sufficient to produce visible decoration. A monolayer on a crystal with 1 cm^2 surface area consists of about 10^{15} atoms. If a substantial number of these enter the crystal during deformation, and precipitate on cooling, they could serve as nuclei from which the observed loops might form.

The geometrical distribution of the hexagonal prismatic loops observed in subsequent diffusion of gold

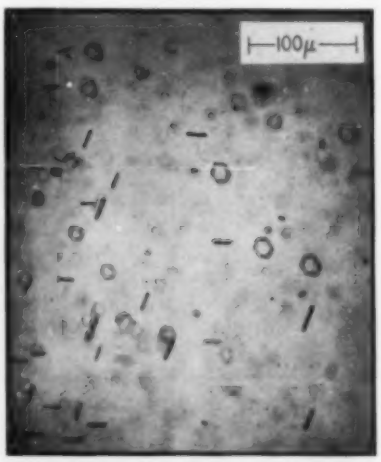

FIG. 6. Prismatic dislocation loops near the outer surface of a crystal which was heated briefly to 900°C and cooled prior to the diffusion of gold. The loops are believed to be nucleated by precipitated impurities resulting from the initial heat treatment.

[11] J. B. Newkirk, Phys. Rev. **110**, 1465 (1958).

is good evidence that these precipitates act as nuclei for the climb and formation of prismatic loops. Figure 6 shows a typical group of hexagonal loops formed in an oxygen-free specimen which was heat treated briefly at 900°C, cooled in air to room temperature, coated with gold and copper, heated to 1200°C for 30 min, and quenched. Randomly distributed loops from 10 to 25 microns in diameter are formed to a depth of about one millimeter from the original surface. The interior of the crystal more than one millimeter from the surface is completely free from the loops.

In order to avoid the formation of these dislocation loops, precautions must be taken to eliminate the rapidly diffusing impurities immediately following deformation. One possible solution to this problem is prevention of surface contamination. No satisfactory way has been found to do this as yet.[12] Another solution, which was well suited to these experiments, involves cooling the crystal at a sufficiently slow rate so that impurities are not trapped in the interior where they can precipitate. A cooling time of about 30 min was found to be adequate for the purposes of these experiments, although a small amount of contamination was evidently still present.

Further studies of the prismatic loops, though outside the scope of the present investigation, would be of some interest. It is desirable to know whether they are stacking faults surrounded by partial dislocations, or whether they are full dislocations. Electron microscopy of thin sections or x-ray image methods may be useful to determine this. It has also been suggested that they may be gold platelets.[13] Because the loops are analogous to collapsed vacancy disks, it would be instructive to study their behavior when a stress is applied. Full or partial dislocations should cause plastic deformation,[14] whereas the dislocation surrounding a gold platelet would presumably be sessile.

E. The Effect of Heating Times and Cooling Rates

A series of 1 mm-thick disks cut from the same pedestal crystal containing a concentration of the order of 10^3 dislocations per cm^2 was studied to determine the effect of heating times and cooling rates upon the amount of climb observed. Although it was difficult to get a quantitative evaluation of these parameters, certain qualitative relationships did emerge. A series of specimens was plated with gold; each specimen was heat treated at a given temperature for a period of time ranging from 30 sec to 17 hr. The quoted time represents total time in the furnace, uncorrected for about 5 to 10 sec required to bring the sample to the desired temperature. Each specimen was treated with copper nitrate to decorate the dislocations upon cooling. The results of these experiments are shown in Table I.

TABLE I. Helix diameters at various temperatures and times.

Temperature °C	Time in furnace	Diameter of helices
1000	3 min	$<1\ \mu$
	30 min	2 to 3 μ
	2 hr	2 to 3 μ
	17 hr	3 to 5 μ
1050	3 min	1 to 2 μ
	10 min	2 to 4 μ
	1 hr	4 to 5 μ
1100	75 sec	2 to 3 μ
	30 min	2 to 5 μ
	17 hr	4 to 7 μ
1200	30 sec	2 to 3 μ
	5 min	5 to 10 μ
	30 min	8 to 15 μ
	15 hr	8 to 15 μ
1250	75 sec	10 to 15 μ
1300	30 sec	3 to 5 μ
	3 min	$>100\ \mu$

Although Table I does not take into account some important parameters such as distance from a free surface and variations in dislocation concentration, two interesting trends are clearly shown. At a given temperature the diameter changes rapidly at first, and approaches a fixed value after a long time of heat treatment. In addition, higher temperatures produce larger diameter helices for given times of heat treatment.

The effect of cooling rate was also studied. It was found that the presence of helices did not depend upon the rate of cooling. There was no apparent difference between the diameter of helices in crystals cooled from a given temperature of diffusion in a few seconds and those cooled in several hours. Undecorated specimens which were cooled over a period of several hours from the temperature of diffusion of gold contained helices which could be observed either by etching at room temperature or by subsequent copper decoration at about 900°C. Following the slow cooling from the temperature of diffusion, there was no observable precipitation in the interior of the crystal. The gold does not decorate the dislocations during this treatment. Other rapidly diffusing impurities which might have been present had sufficient time to diffuse out of the crystal, leaving none detectable with the infrared microscope.

F. Minimum Gold Concentration Required to Form Helices

The minimum surface gold concentration required to produce detectable helices in specimens containing dislocations was determined for a 5-min heat treatment at 1200°C. A series of water solutions of $HAuCl_4 \cdot 3H_2O$ with different Au concentrations was made and applied in known amounts to a group of disks cut from the same crystal. The results are summarized in Table II. From Table II it can be seen that about 5×10^{15} gold atoms per cc, calculated on the basis

[12] A. Goetzberger, Bull. Am. Phys. Soc., Ser. II, 5, 160 (1960), has suggested several gettering treatments which might be useful for this purpose. Such methods have not been tried in the present work.

[13] J. W. Mitchell (private communication).

[14] D. Kuhlmann-Wilsdorf, Phil. Mag. 3, 125 (1958).

TABLE II. Minimum gold concentration for helix formation.

Au Concentration*	Diameter of helix (five min at 1200°C)
1.5×10^{14}/cc	$<1\ \mu$
4.5×10^{15}/cc	2 to 3 μ
1.5×10^{16}	5 to 10 μ
1.5×10^{17}	5 to 10 μ

* Computed on the assumption that the gold is uniformly distributed in the crystals.

of uniform distribution, is required to make climb detectable. This would thus be an upper limit of the internal concentration. Preliminary results from studies of diffusion of Au^{198} indicate that the concentration is approximately 10^{15} per cc when climb is directly observable.

G. Diffusion of Au^{198}

An experiment using radioactive Au^{198} was used to obtain qualitative information about the interaction of gold and dislocations. The purpose was to determine whether the concentration of gold in the immediate vicinity of dislocations was different from that found in regions remote from dislocations. This was found to be the case.

The experiment was carried out as follows: One end of a cylindrical section of a crystal containing a nonuniform distribution of dislocations was coated with a solution of Au^{198}. It was then heated for one hour at 1150°C and cooled to room temperature in a few minutes. There is no evidence that precipitation of gold on dislocations occurs during this heat treatment, as contrasted with the behavior of copper and other elements. An autoradiograph of a 50 μ slice cut 1 mm from the Au-coated surface is shown in Fig. 7(a). Figure 7(b) shows for comparison the dislocation etch-pit pattern on the untreated part of the crystal nearest to the slice in Fig. 7(a). Two features of Fig. 7 are of interest: The amount of gold in the area containing the highest concentration of dislocations is distinctly greater than elsewhere, and crystallographically oriented patterns corresponding to different glide systems are distinguishable. Individual dislocations are not resolved in the autoradiograph, either because the decay products of Au^{198} have sufficient range to blur the pattern, or the gold is not strongly localized near the dislocations.

IV. DISCUSSION

One of the primary results of this investigation is the observation that left-handed screw dislocations form right-handed helices when gold is diffused into silicon at high temperature. It will now be shown by a geometrical model that this result is consistent with a mechanism whereby the dislocation core serves as a sink for interstitial gold atoms or, in an atomically equivalent but otherwise more probable manner, serves as a source of vacancies wherein diffusing gold atoms become trapped. A comparison will be made between the direction of climb produced by acquisition of vacancies and the acquisition of interstitial atoms at the core of the dislocation.

Consider first the case of an excess of vacancies. For simplicity, the vacancies are assumed to collapse into a prismatic loop surrounded by an edge dislocation; the loop is then moved to the core of the dislocation. Figure 8 shows three adjacent planes of a crystal threaded by a left-handed screw dislocation. For convenience, the vertical separation of the planes is expanded after cutting them with an arbitrary plane extending from the original crystal surface to the core of the dislocation. The prismatic loop formed by the aggregation of vacancies, shown isolated in Fig. 8(b), is moved to the core of the dislocation in Fig. 9(b). The letters on the parts of Fig. 9 indicate how the expanded drawing is to be reassembled, with the primed letters in one layer to match the unprimed letters in the adjacent layer. Figure 9(d) shows a line drawing

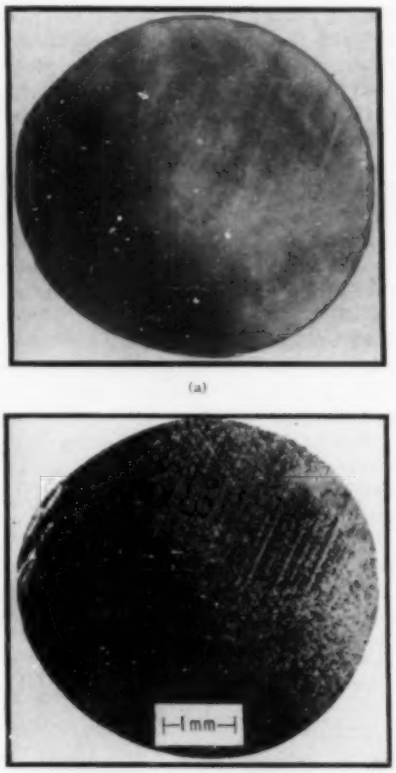

(a)

(b)

FIG. 7. (a) Autoradiogram of a 50 μ slice about one mm away from the surface on which Au^{198} was placed prior to diffusion at 1150°C for one hour. Light areas represent a higher concentration of Au^{198}. (b) Etch-pit pattern of a part of the untreated crystal nearest the surface coated with Au^{198}.

of the dislocation. It can be seen immediately that this step in the vacancy-induced climb of a left-handed screw dislocation forms an elementary part of a left-handed helix.

The case of climb induced by interstitial atoms is illustrated in Figs. 10 and 11. The construction used is similar to that in Figs. 8 and 9, but a prismatic loop of condensed interstitial atoms is used instead of vacancies. When the prismatic loop in Fig. 10(c) is moved to the dislocation core, it displaces the portion *CD* in Fig. 11(b) from contact with its adjoining atoms,

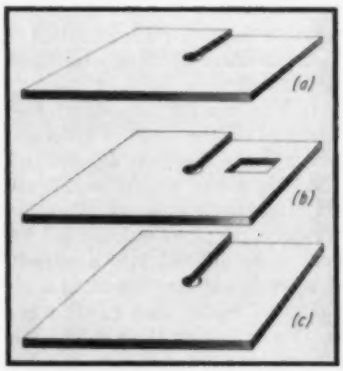

FIG. 8. Expanded model of three adjacent planes of crystal threaded by a left-handed screw dislocation. Plane (b) contains a prismatic dislocation loop formed by the aggregation of vacancies.

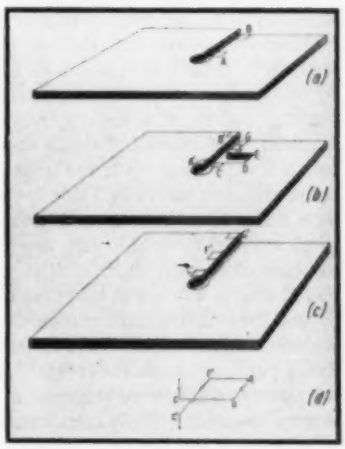

FIG. 9. Element of a helical dislocation formed by moving the prismatic dislocation loop in Fig. 8(b) to the core of the screw dislocation. *A* and *A'*, *B* and *B'*, etc., represent adjacent atoms in the crystal when the planes (a), (b), and (c) are brought together. The result of this construction is the formation of one turn of a left-handed helix shown in (d).

thus forming an edge dislocation along *CD*. Similarly, the three unattached sides of the prismatic loop also form edge dislocations. The construction is summarized in Fig. 11(d). The net result is that the acquisition of condensed interstitial atoms at the core of a left-handed screw dislocation causes the formation of a right-handed helix.

This result is consistent with the idea that interstitial atoms become substitutional atoms at the core of the dislocation. Although this process is energetically feasible if the interstitials are silicon atoms, the trapping

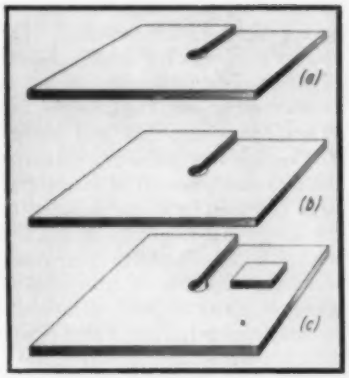

FIG. 10. Expanded model of three adjacent planes of a crystal threaded by a left-handed screw dislocation. A prismatic dislocation loop formed by the aggregation of interstitial atoms between planes (b) and (c) is shown on top of plane (c).

of interstitial impurities at substitutional sites at the core of the dislocation is probably more difficult. The net effect of the formation of a helical dislocation by conversion of interstitial gold to substitutional gold at the core of a screw dislocation is the introduction of a helicoidal surface of gold into the crystal. Such a helicoid would have a large surface energy, and therefore it would be quite surprising that it sould form. It is necessary to consider alternative ways of explaining the net effect which is observed without gold atoms actually being deposited at the core of the dislocation.

This apparent difficulty with the proposed mechanism of the inducement of climb by the diffusion of gold is probably not real. The apparent ease of prismatic glide along the axes of the helices helps to rule out a gold helicoid. The phenomena associated with the diffusion of copper in germanium observed by Tweet and Gallagher[15] and by Fuller and Ditzenberger,[16] and interpreted by Frank and Turnbull,[17] appear to have ap-

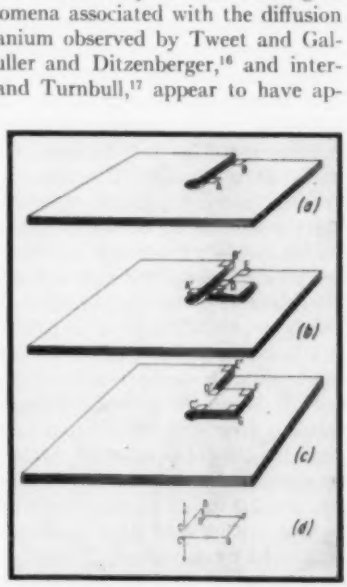

FIG. 11. Element of a helical dislocation formed by moving the prismatic dislocation loop in Fig. 10(c) to the core of the screw dislocation. *A* and *A'*, *B* and *B'*, etc., represent adjacent atoms in the crystal when the planes (a), (b), and (c) are brought together. The result of this construction is the formation of one turn of a right-handed helix shown in (d).

[15] A. G. Tweet and C. J. Gallagher, Phys. Rev. **103**, 828 (1956).
[16] C. S. Fuller and J. A. Ditzenberger, J. Appl. Phys. **28**, 40 (1957).
[17] F. C. Frank and D. Turnbull, Phys. Rev. **104**, 617 (1956).

plication to the current investigation. These investigators explained the formation of increased concentrations of copper in the neighborhood of free surfaces and of dislocations in germanium by the dissociative diffusion mechanism. The essential features of this mechanism, following Frank and Turnbull, are as follows: The equilibrium vacancy concentration is very small; the diffusion constant of interstitial impurities is very large and may be of the order of 10^{-3} cm^2 per second; the interstitial solubility is small, but the product of solubility and diffusivity is greater than for the substitutional atoms; the substitutional solubility of the diffusing impurity is much greater than the equilibrium vacancy concentration. There is reason to believe that these conditions are fulfilled in the present case.

With an initial vacancy concentration C_v' and no immediate supply of additional vacancies, the introduction of Au causes a reduction in the vacancy concentration, since

$$C_s+C_v=C_v', \tag{1}$$

where C_s=concentration of substitutional Au and C_v=concentration of vacancies. From (1), we obtain

$$C_v=C_v'/(1+kC_i), \tag{2}$$

where

$$k=C_s'/C_i'C_v'=Cs/C_iC_v. \tag{3}$$

Here C_i=concentration of interstitial Au, C_i'=solubility of interstitial Au, and C_s'=solubility of substitutional Au.

Since C_v' is apparently much less than C_s', C_v is correspondingly smaller than C_v'. This causes the generation of additional vacancies at dislocations and at free surfaces. From the point of view of climb, the generation of vacancies by a dislocation is atomically equivalent to the acquisition of interstitial atoms. Therefore, the geometry of the observed helices discussed in connection with Figs. 8, 9, 10, and 11 is accounted for by dissociative diffusion. Moreover, Au atoms need not actually become attached to the dislocation core in this mechanism, but need only approach the dislocation within the diffusion distance of vacancies. On the basis of this mechanism, the data in Table II lead one to the conclusion that the equilibrium vacancy concentration in silicon at 1200°C is less than 10^{15} per cc.

It is interesting to consider the case of crystals which are doped with a saturation concentration of gold during growth. When the grown-in dislocations in these crystals are decorated with copper at 950°C, there is no sign that climb has occurred. Since the gold atoms can be accommodated directly into substantial positions at the growing interface, climb processes are not required to supply vacancies. If gold is diffused in from the surface under conditions which readily cause climb in undoped crystals, no climb is observed. Both of these observations are additional indications that a concentration gradient of gold is necessary to cause climb in undoped crystals.

Precipitated impurities greatly modify the climb of the dislocations. This has been shown to be true in crucible-grown crystals. Apparently this is caused by the precipitation of specks of oxide along the dislocation line, pinning it at many points. Between these pinning points the dislocation is free to climb, resulting in configurations greatly different from those in pure crystals. Other impurities, such as those which are introduced by heat treatment at 900°C prior to the diffusion of gold, appear to produce randomly distributed precipitates which can act as nuclei for the generation of prismatic dislocation loops. These impurities also can precipitate on dislocations and prevent the climb normally observable in pure crystals. These experiments demonstrate an effect which may be important in other materials as well.

It is interesting to compare the influence of copper and gold on the climb of dislocations. Although statements in the literature suggest that copper behaves in silicon in a way similar to copper in germanium, it is doubtful that this is the case. Control experiments in which copper alone was diffused into one specimen and gold alone diffused into a second specimen indicated completely different interaction with dislocations. Precipitation, rather than climb, was observed in crystals containing copper alone. Climb, and not precipitation, is observed when gold alone is diffused into the crystals. This is consistent with a very small substitutional solubility of copper relative to that of gold in silicon.[18,19]

Other indications that the two elements behave differently in their interaction with dislocations is shown by the studies of heat-treatment temperature, times of heating, and rates of cooling from the temperature of diffusion. The amount of climb observed with gold diffusion is dependent upon the length of time at a given temperature as shown in Table I. Cooling times ranging from a few seconds to several hours do not change the climb induced by gold in any way yet determined. For the case of copper, there is little variation of the observed effects with length of time at high temperature beyond the first few minutes required to get a reasonably uniform concentration. There is little or no dependence on temperature above about 900°C. In contrast to gold, the rate of cooling very strongly affects the decoration of the dislocations.[3] Fully consistent with this difference in behavior is the fact that gold introduced by diffusion at high temperature remains atomically dispersed on being cooled to room temperature,[18] whereas only a very small fraction of the copper remains atomically dispersed.[19] These results suggest that gold can diffuse rapidly as an interstitial at low concentration, whereas the solubility of substitutional gold is much higher and the diffusivity probably much lower. On the other hand, copper apparently exists almost entirely as an interstitial atom at elevated temperature. The rapid diffusion

[18] C. B. Collins and R. O. Carlson, Phys. Rev. **108**, 1409 (1957).
[19] C. B. Collins, R. O. Carlson, and C. J. Gallagher, Phys. Rev. **105**, 1168 (1957).

and the decreasing solubility upon cooling would account for the precipitation of copper.

Although some light is shed on the configuration of a climbing dislocation as a function of time by the data in Table I, no clear understanding of the changes of configuration can be formulated on the basis of the present work. Table I shows that the suggestion in the work cited in footnote 4, to the effect that rapid cooling of the specimen was responsible for the climb, is incorrect because climb continues as a function of time at the elevated temperature. The driving force is not supersaturation as a result of quenching, but rather a concentration gradient of the impurity. Thus, there still remains unexplained the reason why helices and dislocation loops of small diameter can exist in the close proximity of edge dislocations which have a large diameter. According to Friedel's theory of climb,[20] discussed by Silcox and Whelan,[21] for the case of quenched aluminum crystals, dislocation loops with large curvature should disappear in favor of those with small curvature. A large amount of evidence indicates that there is no appreciable interchange between small and large diameter loops, at least in the sizes which are observable by the infrared technique.

Another observation of some interest is the fact that the loops, as well as the helical dislocations, persist during heat treatment times which are long compared with the time required to achieve saturation of the gold impurity in the sample. At 1200°C the time required to achieve saturation of a 1 mm-thick sample is a few hours. It is to be expected that the elastic forces would tend to cause a redistribution of the curvatures during long heating times. This observation is at least self-consistent with the observation that dislocations of small diameter can coexist in close proximity to dislocations of large diameter as mentioned previously. Although there is an apparent discrepancy between these observations and those of Silcox and Whelan on the annealing of prismatic loops in quenched aluminum specimens, it should be pointed out that these authors studied loops which were of the order of 100 times smaller in diameter than those in silicon. Therefore, the net transfer of vacancies required for an observable change of distribution of sizes of dislocation loops is much smaller in aluminum than in silicon.

V. CONCLUSIONS

It has been shown that gold diffusing into the crystal from the surface is responsible for the formation of helices and other manifestations of climb of dislocations in silicon. In order to form readily detectable helices, the surface concentration of gold at 1200°C must be of the order of 5×10^{18} per cc. Preliminary results with radioactive tracers suggest that the internal concentration is 10^{15} per cc or less. The theory of Frank and Turnbull leads one to the conclusion that the equilibrium vacancy concentration at this temperature is less than 10^{15} per cc.

It was shown that it is possible to introduce screw dislocations which have a predetermined geometry into dislocation-free crystals. In the case described, left-handed screws were formed. The diffusion of gold produced right-handed helices from these screws. It was found that all segments of the resulting dislocations are parallel to ⟨110⟩ crystallographic directions, resulting in polygonalized helicoids. From geometrical considerations alone, these results indicate that either interstitial atoms or a vacancy deficiency was responsible for the formation of a right-handed helix from a left-handed screw dislocation.

The diffusion of radioactive tracers indicates an increased concentration of gold near dislocations. Although the sensitivity of the experiment was not sufficient to localize the gold, it is possible to tell that the areas which contained the larger concentration of dislocations also had a higher concentration of gold. This is similar to the results obtained for the diffusion of copper in germanium.[15] These results suggest that dissociative diffusion is a likely mechanism to account for the observed effects, since vacancies can be generated in the neighborhood of dislocations.

The precipitation of impurities such as oxygen on the dislocations in silicon grown from quartz crucibles causes a considerable modification of the climb of the dislocations. Pinning of the dislocations occurs at random points. Where the dislocation becomes unpinned and is thereafter free to climb, closed loops are formed by a process apparently analogous to the Bardeen-Herring mechanism. In addition, precipitation occurs at random throughout the crystal in regions well removed from dislocations. These precipitates can serve as the sources of prismatic loops usually found to be parallel to {111} planes. The Burgers vector of these loops has not been determined as yet. Further experiments are required to determine whether or not they consist of sheets of gold atoms coherent with the silicon matrix.

VI. ACKNOWLEDGMENTS

The author wishes to thank L. J. Keifer for his help in preparation of the specimens used in this investigation. He is indebted to R. O. Carlson and G. D. Brower for their aid in some of the studies involving radioactive tracers. He is also grateful to J. W. Mitchell for stimulating discussions, and to A. G. Tweet for criticism of the manuscript.

[20] J. Friedel, *Les Dislocations* (Gauthier-Villars, Paris, 1956), p. 72.

[21] J. Silcox and M. J. Whelan, *Structure and Properties of Thin Films*, edited by C. Neugebauer *et al.* (John Wiley & Sons, Inc., New York, 1960), p. 164.

Changes in Macroscopic Shape, Lattice Parameter, and Density in Crystals Due to Point Defects*

R. W. Balluffi and R. O. Simmons
University of Illinois, Urbana, Illinois

(Received July 11, 1960)

It is demonstrated that a crystal of arbitrary shape filled with a fine random distribution of centers of dilatation will dilate homogeneously. No elastic approximations are made, and the results should hold for strains of any magnitude. By use of an average and perfect reference lattice embedded in the strained crystal, it is then shown that the lattice dilatation as measured by x-ray lattice parameter measurements and by macroscopic dimensional measurements should be the same along any direction when the number of substitutional atomic sites remains constant. Perturbing effects due to x-ray diffuse scattering should cause negligible error in determining the positions of the Laue-Bragg maxima under usual conditions. All results should apply also to the case of thermal dilatation at temperatures up to the melting point. The use of density measurements in the determination of point defect concentrations is discussed. Experimental data are reviewed.

I. INTRODUCTION

THE demonstration by Eshelby[1] that a body of arbitrary shape, containing a finely distributed random distribution of point defects which act as centers of dilatation, undergoes a uniform dilatation without change in shape is based upon the assumption of an elastically strained continuum and the use of linear elasticity theory. There has been some concern[2] that Eshelby's results may not be exactly true in actual crystals, because the displacements around point defects are generally large, and the assumption of usual linear elasticity may not hold throughout the volume. This question may be particularly important in crystals containing a very high density of defects where a large fraction of the total volume of the material may be strained beyond the elastic range.[3]

The purpose of the present work is to present simple arguments which prove the intuitive expectation that a body of arbitrary shape filled with a finely distributed random distribution of point centers of dilatation will be homogeneously dilated regardless of whether the strains are elastic or not. The arguments also apply to a uniformly heated body, which of course is known to undergo homogeneous dilatation. Eshelby[1] has already pointed out the correspondence between these two effects. After these results further arguments are given to establish that the lattice dilatation as measured experimentally by macroscopic length measurements or by means of x-ray lattice parameter measurements will be the same in all cases when the number of substitutional atomic sites remains constant. These results are of some importance, since they may be used to obtain valuable information about point imperfections in crystals when suitable simultaneous measurements of their linear dimensions (or density) and lattice parameter are available.[2,4–10]

Measurements on stressed samples need to be treated with caution. Stresses can arise from inhomogeneity of defect content (as in nonuniform radiation damage), from external constraint of the sample, or from a combination of the two. Measurements on exceedingly small samples containing very few defects (e.g., x-ray line broadening from small crystallites elastically deformed by inhomogeneous defect distributions) of course fall outside the scope of our discussion. The case of relatively large crystals containing very small defect concentrations has not yet arisen in practice because of the limited sensitivity with which actual dimensional measurements can be made.

II. CHANGES IN MACROSCOPIC SHAPE

Suppose a strain-free crystal of cubic crystal structure and of arbitrary shape which is to be filled with a fine random distribution of point centers of dilatation. Before introducing the centers of dilatation we divide the crystal into a large number of identical small cubical blocks where the block walls are taken parallel to the unit cell faces (Fig. 1). Each block is physically separated, with free surfaces, and is large enough so that it will contain the average density of centers of dilatation. Also, the size is chosen so that each block will contain a large number of centers of dilatation but will still be very small compared to any of the linear dimensions

* This work was supported by the U. S. Atomic Energy Commission.

[1] J. D. Eshelby, J. Appl. Phys. **25**, 255 (1954); in *Solid State Physics*, edited by F. Seitz and D. Turnbull (Academic Press, Inc., New York, 1956), Vol. 3, p. 79.

[2] R. Feder and A. S. Nowick, Phys. Rev. **109**, 1959 (1958).

[3] An extreme example of solids subject to severe internal stress is furnished by certain metamict minerals [A. Pabst, Am. Mineralogist **37**, 137 (1952)]. These are uranium- or thorium-bearing compounds, originally crystalline, which have been so heavily irradiated by alpha-particle decay over geologic time intervals that they no longer yield crystalline x-ray diffraction patterns.

[4] E. C. Ellwood, J. Inst. Metals, **80**, 217 (1951–52).

[5] E. C. Ellwood and K. Q. Bagley, J. Inst. Metals, **80**, 617 (1952).

[6] J. A. Lee and G. V. Raynor, Proc. Phys. Soc. (London), **67B**, 737 (1954).

[7] D. Binder and W. J. Sturm, Phys. Rev. **96**, 1519 (1954); **107**, 106 (1957).

[8] R. O. Simmons and R. W. Balluffi, J. Appl. Phys. **30**, 1249 (1959).

[9] R. O. Simmons and R. W. Balluffi, Phys. Rev. **117**, 52 (1960).

[10] R. O. Simmons and R. W. Balluffi, Phys. Rev. **119**, 600 (1960).

of the body.[11] Next, we fill the component parts of the body with a finely distributed random distribution of centers of dilatation which we shall take to possess cubic symmetry. Each block will in general undergo a volume change and we shall make the very general *a priori* assumption that the blocks may also change shape in such a way that they are no longer cubes. It is clear, however, that the shape of each block will be the same, and that the symmetry of the problem requires that the external shape will retain cubic symmetry. We note that each block may have a microscopic bumpiness on its surface due to the presence of centers of dilatation randomly located very near the surface. This bumpiness may be removed by applying a distribution of suitable surface forces to each block in such a way that the sum of the forces on each face is zero.

We now reassemble the entire crystal by joining the blocks so that all points on neighboring surfaces which were joined in the original unstrained body are again joined and are then welded together. Symmetry considerations require that the joined interfaces be planar and parallel to the original block surfaces. The crystal at this stage will, therefore, have the same shape as in its original state but will be uniformly dilated over distances which are large compared to the spacing between centers of dilatation.

The situation at the external surface of the crystal must be considered in further detail. In order to maintain symmetry everywhere during the reassembling operation, it is necessary to apply a distribution of external force to all block surfaces facing the external surface of the crystal which is the same as the distribution of force exerted on each mated internal surface. The applied forces necessary to eliminate the previously described bumpiness and the forces necessary to maintain symmetry at the surface are still present, and the body is therefore not free of applied forces. These applied forces may be removed by applying equal and opposite forces at every necessary point. Since the sum of applied forces on each block face is zero, the result, according to St. Venant's principle, is merely local straining without any change in the macroscopic shape of the crystal. The final result is a force-free crystal uniformly dilated without change in shape.

So far only the particularly simple example of a uniformly dilated cubic crystal containing cubically symmetric centers of dilatation has been considered. Actually, atomic centers of dilatation in cubic structures may not possess cubic symmetry (e.g., the crowdion[12]), and somewhat different effects may, therefore, occur. In general, however, the defects will have sufficient symmetry so that the problem can be handled by the previous method. Let us take the crowdion in the fcc structure as an example. We consider first the case where all of

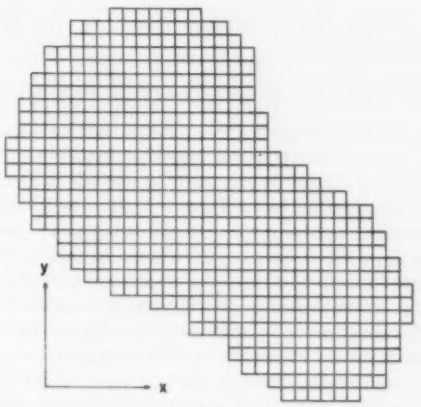

FIG. 1. Two-dimensional view of body of arbitrary shape portioned into small cubical blocks. The figure is not drawn to scale; the block size is relatively much too large.

the crowdions possess a preferred orientation with their long axes along [011]. In this case we may cut out the cubical blocks with (01$\bar{1}$), (011), and (100) faces, since these planes will be planes of symmetry for the crowdion. Upon the introduction of the defects, each cubical block will dilate and may be assumed to change shape. The new shape, however, must retain the above planes as planes of symmetry. The dilatations normal to these planes will differ because of the anisotropic nature of the crowdion. By applying the previously used procedure we may reassemble the crystal and shall find that it is homogeneously dilated and that the block faces are the principal planes of the deformation. The crystal will have changed shape, however, since the principal strains will now be unequal. As another example we may consider a crystal containing crowdions of random orientation. If we divide the crowdions into groups of particular orientations and carry out the usual procedure it is readily found that the crystal is homogeneously dilated and that the principal strains are equal. This result only follows, of course, if the crowdions of different orientation are present in equal number and are finely intermixed.

The foregoing arguments have considerable generality, and may be directly applied to any crystal system where suitable planes of symmetry may be found for the block faces. Cubic, tetragonal, hexagonal, and orthorhombic systems, may, therefore, be considered in this way if the crystal has sufficiently symmetrical groups of atoms around the lattice points. The result of our argument in every case is that a crystal containing a fine random distribution of centers of dilatation will undergo a homogeneous deformation where the principal strains may or may not be equal, depending upon the symmetry and orientation of the centers of dilatation. As mentioned previously, these arguments and results also apply

[11] The various numerical magnitudes involved in a typical case are considered in the Appendix.
[12] L. Tewordt, Phys. Rev. **109**, 61 (1958).

to uniformly heated crystals which, of course, dilate homogeneously.[13]

III. CHANGES IN X-RAY LATTICE PARAMETER

It is most convenient to discuss lattice parameter x-ray measurements on an imperfect crystal containing static point defects or thermal vibration defects in terms of an average perfect reference lattice which may be constructed according to the following procedure. We begin with the perfect crystal shown in Fig. 1. The defect structure is then introduced in such a way that the number of substitutional sites remains constant; i.e., vacancies are made by removing atoms from the crystal and interstitials are made by adding atoms from an external source. In the case of solute atoms a host lattice atom is removed for each solute atom inserted. We have already shown that the crystal will dilate homogeneously upon the introduction of the defect structure. Let us imagine the introduction of defects by a two-step process as follows: In step one we dilate the initially perfect crystal homogeneously by applying surface forces in order to produce a dilatation which is just that which would have been produced by adding the defect structure; in step two we introduce the defect structure. In this step the surface forces relax to zero and the crystal does not change shape.

It is readily shown that the average perfect lattice which best describes the average atomic structure of the defect crystal is just the homogeneously strained perfect lattice which is present at the end of step one [hereafter designated by the vectors $\mathbf{a}_1',\mathbf{a}_2',\mathbf{a}_3'$)]. Consider again the crystal as made up of blocks, as in Fig. 1, where each block initially contains N atoms. During the introduction of the defects, the center of mass of each block will remain at the center of each block because of the symmetry of the situation and the fact that the defects are randomly distributed.[14] Taking an origin at the center of mass, we have at the end of step one

$$\sum_{i=1}^{N} m\mathbf{r}_i'=0, \tag{1}$$

where $\mathbf{r}_i'$ is the position vector in the $(\mathbf{a}_1',\mathbf{a}_2',\mathbf{a}_3')$ lattice. After adding the defect structure we have

$$\sum_{i=1}^{N} m(\mathbf{r}_i'+\mathbf{u}_i)+\sum_{j=1}^{\Delta N} m\mathbf{r}_j'=0, \tag{2}$$

where ΔN represents the number of atoms which may have been added in the defect structure and $\mathbf{u}_i$ is the displacement of atom i, which is present during the entire procedure, from its ideal position in the $(\mathbf{a}_1',\mathbf{a}_2',\mathbf{a}_3')$ lattice. Since the ΔN atoms are randomly distributed around the center of mass, $\sum_{j=1}^{\Delta N} m\mathbf{r}_j'=0$ and, therefore, by using Eqs. (1) and (2),

$$\sum_{i=1}^{N} \mathbf{u}_i=0. \tag{3}$$

The $(\mathbf{a}_1',\mathbf{a}_2',\mathbf{a}_3')$ lattice therefore best represents the average positions of the atoms in the strained crystal and is most convenient as a reference lattice for describing x-ray diffraction effects. A similar result is obtained if a net number of atoms is removed when the defect structure is introduced.

The reference lattice of the defect crystal, $(\mathbf{a}_1',\mathbf{a}_2',\mathbf{a}_3')$, is obtained from the lattice of the originally perfect crystal, $(\mathbf{a}_1',\mathbf{a}_2',\mathbf{a}_3')$, by the same homogeneous distortion undergone by the macroscopic crystal. If $[C_{ij}]$ is the homogeneous deformation matrix of any macroscopic vector in the macroscopic crystal, we then have

$$\begin{aligned}[C_{ij}]&=[L_{ij}],\\ \mathbf{a}'&=[L_{ij}]\mathbf{a},\end{aligned} \tag{4}$$

where $[L_{ij}]$ is the deformation of the reference lattice. As discussed elsewhere,[8-10] Eq. (4) will not hold for a crystal in which the total number of substitutional sites may vary.

We next consider the problem of obtaining precise measurements of $[L_{ij}]$ using x-ray methods at any temperature up to the crystal melting temperature. Cochran[15] has treated the x-ray scattering from such a crystal containing defects by using Fourier transform methods, and we shall use his results. By letting

$$T_{C+\Delta}(\mathbf{S})=T_C(\mathbf{S})+T_\Delta(\mathbf{S}), \tag{5}$$

Cochran shows that the scattered x-ray intensity (apart from constant factors) is given by

$$J=|T_M(\mathbf{S})|^2+|T_\Delta(\mathbf{S})|^2. \tag{6}$$

$T_{C+\Delta}$ is the transform of the crystal with defects, T_C is the transform of a perfect crystal based upon the reference lattice, and T_Δ is the transform of the defect structure. $\mathbf{S}$ is the usual reciprocal lattice vector. $T_M(\mathbf{S})$ is the transform of a crystal having the reference lattice where every unit cell has the average structure factor of $C+\Delta$. Equation (6) holds to within a distance of about L^{-1} of any reciprocal lattice point if the crystal dimensions are of size L. As Cochran has pointed out, $|T_M(\mathbf{S})|^2$ represents the Laue-Bragg intensity, $|T_\Delta(\mathbf{S})|^2$ represents the diffuse intensity and is determined by the nature of the electron distribution constituting the defect structure Δ. We emphasize that all of these results so far are quite general, and that no assumptions have been made regarding the magnitudes or types of strains present.

According to these results, the defect structure reduces the intensity of the Laue-Bragg maxima, since the

[13] I. Waller has calculated the thermal expansion of a crystal model with free surfaces and shown it to be homogeneous [Ann. Physik **83**, 153 (1927)].

[14] This is not strictly true, because of possible fluctuations. The blocks are large enough, however, so that any fluctuations should be small (see Appendix) and may be taken to be zero for present purposes.

[15] W. Cochran, Acta Cryst. **9**, 259 (1958).

average structure factor of $C+\Delta$ is lower than that of C. In addition, no broadening of the Laue-Bragg intensity term occurs. Changes in position of the Laue-Bragg maxima are completely determined by the deformation of the reciprocal reference lattice. If Eq. (4) gives the homogeneous deformation of the reference lattice, then it is readily established that a corresponding deformation of the reciprocal reference lattice (denoted by *) occurs which is also homogeneous and is given by

$$\mathbf{a}'^{*}=[L_{ij}']^{-1}\mathbf{a}^{*}. \tag{7}$$

It follows immediately from Eqs. (4) and (7) that the shift in position of each reciprocal lattice point (*hkl*) will correspond to a change in the (*hkl*) interplanar spacing of the reference lattice which is exactly equal to the change in macroscopic dimensions of the crystal in that direction.[16]

If the shift in the (*hkl*) reciprocal lattice vector could be determined without further complication from measurements of the position of the Laue-Bragg intensity, the measured x-ray and macroscopic dilatations would, of course, be identical. However, difficulties may arise because of the decrease in intensity of the Laue-Bragg intensity and the presence of the diffuse scattering intensity represented by the last term in Eq. (6). The two sources of defect diffuse scattering in the present case will be the atomic displacements due to the presence of point defects and to thermal vibration.

Additional possible contributions to experimental error which are not usually considered include the Compton scattering, which increases monotonically with Bragg angle, and the assymmetry in the Laue-Bragg maxima introduced by refraction at the sample surface. These effects require consideration in the most precise absolute determination of lattice parameters; measurements of relative expansion are little affected by them.

Theoretical and experimental results[17] indicate that the thermal diffuse scattering is concentrated in clouds which are closely centrosymmetric around the reciprocal lattice points. Calculations[18–23] of the diffuse scattering due to the displacements caused by a random distribution of fairly dilute point defects indicate similar results. Most of the treatments of the point defect diffuse scattering have been made using certain restrictive assumptions such as small displacements and linear superposition of effects due to individual point defects. However, it may be demonstrated on very general grounds that the effects will still be qualitatively the same in the absence of these restrictions as long as the defects are of approximately atomic size. Beeman *et al.*[24] have reviewed a method for treating any defect structure by expanding it in a series of plane Fourier waves. If $\mathbf{t}_p$ is the wave vector of the pth wave, it is readily shown that a diffracted intensity will originate from this wave which will appear at the point $\mathbf{S}=\mathbf{B}+\mathbf{t}_p$ in reciprocal space where $\mathbf{B}$ is a lattice vector. For a random distribution of defects, the sum of all points will constitute a centrosymmetric cloud around each lattice point. The intensity at each point, of course, depends upon the amplitude of the corresponding wave. Long wavelength Fourier waves contribute intensities near the lattice points while short wavelength components produce a more extended diffuse scattering.

We expect the strain field of typical point defects to have appreciable values over distances extending over a fair number of interatomic spacings but to be very small compared to the crystal dimensions. For example, in the isotropic elastic approximation[1] the strain falls off radially as r^{-3}. The wavelengths $1/|\mathbf{t}_p|$ synthesizing such a defect structure will tend to produce clouds of diffuse scattering fairly near the reciprocal lattice since the spacing between lattice points is approximately $1/|\mathbf{a}_i'|$. This result has been verified in the cases where detailed calculations have been made using assumed approximate models for the displacements.[20,22,23] We conclude that in the general case, the diffuse scattering due to a random distribution of point defects will occur in clouds around the lattice points which are closely centrosymmetric. The closely centrosymmetric behavior of the diffuse scattering in the near vicinity of the reciprocal lattice points means that there will be very little spurious shift of the experimentally determined peak of the Laue-Bragg reflection arising from this source.

Since the diffuse scattering from monatomic solids containing fairly dilute concentrations of point defects is relatively weak under usual conditions, and since the Laue-Bragg intensity does not broaden, we may conclude that precise determinations of lattice parameter in such crystals at various temperatures up to the melting point should be possible. The situation may be quite different in crystals containing a high concentration of defects. In such cases the Laue-Bragg intensity may become low enough and the diffuse intensity high enough so that it is no longer possible to measure the position of the Laue-Bragg maxima. We shall not consider the x-ray effects from such crystals any further. Polar crystals which exhibit a very marked diminution of the high-angle Laue-Bragg maxima at high temperatures may also offer a more difficult case.

[16] Again we emphasize that this holds only when the number of substitutional sites remains constant.
[17] R. W. James, *The Optical Principles of the Diffraction of X-Rays* (G. Bell and Sons, London, England, 1954).
[18] W. H. Zachariasen, *Theory of X-Ray Diffraction in Crystals* (John Wiley & Sons, Inc., New York, 1945).
[19] H. Ekstein, Phys. Rev. **68**, 120 (1945).
[20] K. Huang, Proc. Roy. Soc. (London) **A190**, 102 (1947).
[21] T. J. Matsubara, J. Phys. Soc. Japan **7**, 270 (1952).
[22] H. Kansaki, J. Phys. Chem. Solids **2**, 24; 107 (1957).
[23] W. Cochran and G. Kartha, Acta Cryst. **9**, 941; 944 (1958).
[24] W. W. Beeman, P. Kaesberg, J. W. Anderegg, and M. B. Webb, in *Handbuch der Physik*, edited by S. Flügge (Springer-Verlag, Berlin, 1957), Vol. 32, p. 402.

IV. COMPARISON OF EXPANSION MEASUREMENTS

A comparison between expansion measurements has been made for nuclear reactor-irradiated LiF.[7] Agreement between macroscopic expansion ($\Delta l/l$) and lattice expansion ($\Delta a/a$) during the early stages of radiation-induced expansion was found within 6%, indicating that the predominant result of irradiation was the production of defects which do not alter the number of substitutional atomic sites (presumably Frenkel defects).

Many measurements of thermal expansion of solids have been made by both x-ray and macroscopic techniques. Comparison is usually made between the thermal expansion coefficients. Agreement between results obtained by the two methods is generally only within several percent. Disagreements are common; they are usually ascribed either to differences in temperature measurement or to differences in composition of the specimens. A very few direct and detailed comparisons have been made on identical material under adequately controlled conditions. The classic study on the rhombohedral crystal calcite, important for x-ray spectrometry, gave agreement between $\Delta l/l$ and $\Delta a/a$ in the temperature interval 18 to 100°C within the experimental error of 0.8%.[25]

The most complete and accurate comparison study appears to be that of 99.999% pure silver made by the writers,[10] who made measurements on the same sample using a single temperature scale. Measurements of $\Delta l/l$ and $\Delta a/a$ were made with a precision of 9 ppm throughout the temperature interval 13 to 750°C. Forty-two measurements of $\Delta l/l$ and 55 measurements of $\Delta a/a$ were made. The total linear expansion in this interval is nearly 1.64×10^{-2}. The agreement between the two methods was therefore within 0.06%.

Measurements on silver at higher temperatures up to 956°C (within 4 deg of the melting point) showed that additional substitutional atomic sites were generated thermally, their energy of formation being very close to the value obtained from electrical resistivity studies on quenched wires[26] and near the value expected from results on the close-packed metals gold and aluminum.[10] At the maximum temperature (about six times the characteristic temperature Θ of silver), where the point defect concentration was greater than $10^{19}/\text{cm}^3$, the (422) Laue-Bragg maximum was not broadened and the precise determination of its position could easily be made, as argued in Sec. III.

V. CHANGES IN DENSITY

The macroscopic density ρ and x-ray reference lattice parameter a' are related by

$$\rho=M\bar{n}/(a')^3 \tag{8}$$

for a cubic material, where $\bar{n}$ is the average number of atoms per unit cell of the reference lattice and M is the atomic mass. It is common to define an ideal x-ray density

$$\rho_0=Mn_0/(a')^3, \tag{9}$$

which is the density that the crystal with measured reference lattice parameter a' would have if it were otherwise perfect and the ideal number of atoms per unit cell, n_0. By measuring ρ and a' it should be possible in principle to measure point defect concentrations, since

$$c_v-c_i=(n_0-\bar{n})/n_0=(\rho_0-\rho)/\rho_0, \tag{10}$$

where c_v and c_i are the atomic fractions of vacancies and interstitials, respectively. This relation holds since the number of substitutional sites per lattice point of the reference lattice is always constant. Deviations in the number of atoms per unit cell can only occur, therefore, if some of the sites are vacant or if interstitials are present. It is not necessary to include effects due to the lattice dilatation, as has been suggested elsewhere.[27] This density method has had some apparent success in detecting large concentrations of vacancies in certain alloys of particular atom to electron ratio.[4–6] Unfortunately, the method has had only limited general success since the required physical constants are not known with sufficient precision and the specimens used may often contain unknown macroscopic defects.

APPENDIX

Lattice vacancies in thermal equilibrium at elevated temperatures may be taken as an example of negative centers of dilatation. The minimum concentration n in monatomic metals that the most accurate recent measurements (footnotes 9 and 10) could detect directly was about $3\times10^{18}/\text{cm}^3$. Blocks 3×10^{-5} cm (or about 1000 atoms) on a side would then contain about 8×10^4 vacancies. These block dimensions are very small compared to any usual laboratory specimen, which would have dimensions of the order 10^{-2} to 10^0 cm. The surface bumpiness due to defects near the surface would have a maximum size of about $n^{-\frac{1}{3}}\simeq7\times10^{-7}$ cm or 2% of a block edge. If the defect distribution is random, then the blocks are uniform in defect content to better than about 0.4% $[8\times10^4\pm(8\times10^4)^{\frac{1}{2}}]$ at this minimum concentration.

The technique of direct density measurements is less sensitive by roughly an order of magnitude because of the possible macroscopic inhomogeneities and impurity content of actual crystals and because of the uncertainty in Avogadro's number and the absolute values of x-ray wavelengths. The stringency of the conditions on block size is therefore relaxed, easily allowing, for example, the consideration of finely intermixed defects of different types.

[25] J. B. Austin, H. Saini, J. Weigle, and R. H. H. Pierce, Phys. Rev. **57**, 931 (1940).

[26] M. Doyama and J. S. Koehler, Phys. Rev. **119**, 939 (1960).

[27] See work cited in footnote 24, pp. 415 to 418.

Angular Distribution and Polarization of the Radiation Emitted by Electrons Accelerated in a Synchrotron*

D. E. Bedo, D. H. Tomboulian, and J. A. Rigert
Cornell University, Ithaca, New York

(Received August 15, 1960)

The paper presents evaluations of the angular distribution of the synchrotron radiation for a high-energy accelerator. The investigation indicates that the peak power, at wavelengths in excess of a certain critical value, does not occur in the orbital plane but at some angle above or below this plane. Expressions are given for the intensity components of the radiation polarized at right angles to, and in the plane of the orbit, respectively. The radiation emitted by a monoenergetic electron is, in general, elliptically polarized, the ratio between the major and minor axes depending on the angle ψ between the direction of observation and the orbital plane. For $\psi=0$ the radiation is linearly polarized, and approaches circular polarization with increasing values of ψ.

I. INTRODUCTION

In an earlier paper[1] the spectral characteristics of the electromagnetic radiation emitted by high-energy, centripetally accelerated electrons was examined for its applicability as a source of x rays, particular consideration being given to the intensity available in the region of soft x rays (approximately 100 A). The results presented in that paper pertained to the average power radiated into all angles over full or part acceleration intervals. In the contemplated use of the synchrotron as a source, it is of further interest to examine the intensity distribution and the state of polarization as a function of the angle of observation relative to the orbital plane.

In what follows, we shall extend the calculations given in the previous paper[1] to include numerical results on the angular distribution of the radiation expected from electrons which have acquired energies of several Bev in a high-energy synchrotron such as the Cambridge Electron Accelerator under construction. The information presented shall deal only with the angular dependence of the intensity at a fixed energy, without considering the distributions integrated over an acceleration interval.

II. EXPRESSIONS FOR THE ANGULAR DISTRIBUTIONS

The instantaneous power emitted per unit angle at the angle ψ, and per unit angular frequency interval centered at the radiated angular frequency ω, is given by Schwinger.[2] This spectral quantity, denoted by $P(\psi,\omega,t)$, has the form

$$P(\psi,\omega,t)=\frac{3}{4\pi^2}\frac{e^2}{R}\left(\frac{\omega}{\omega_c}\right)^2\left(\frac{E}{m_0c^2}\right)^7\left[1+\left(\frac{E\psi}{m_0c^2}\right)^2\right]^2 \times\left[K_{\frac{1}{3}}^2(\xi)+\frac{(E\psi/m_0c^2)^2}{1+(E\psi/m_0c^2)^2}K_{\frac{1}{3}}^2(\xi)\right]. \quad (1)$$

In the right-hand member of Eq. (1), the angle ψ is the angle between the direction of emission and the orbital plane, E is the electron energy at the time t, and $K_{\frac{1}{3}}(\xi)$ and $K_{\frac{2}{3}}(\xi)$ represent modified Bessel functions of the second kind. The argument of the Bessel functions is defined by

$$\xi\equiv\frac{\omega}{2\omega_c}\left[1+\left(\frac{E\psi}{m_0c^2}\right)^2\right]^{\frac{3}{2}}=\frac{\lambda_c}{2\lambda}\left[1+\left(\frac{E\psi}{m_0c^2}\right)^2\right]^{\frac{3}{2}}, \quad (2)$$

where λ represents the wavelength of the emitted radiation and λ_c is given by

$$\lambda_c=\frac{4\pi R}{3}\left(\frac{m_0c^2}{E}\right)^3, \quad (3)$$

where R is the orbital radius.

The formula for $P(\psi,\omega,t)$ specified by relation (1) may also be written in terms of λ. Upon conversion, the instantaneous power radiated per unit angle relative to the orbital plane, per unit wavelength interval centered at the wavelength λ, is given by

$$P(\psi,\lambda,t)=\frac{3}{2\pi}\left(\frac{e^2c}{R}\right)\left(\frac{\lambda_c}{\lambda}\right)^2\left(\frac{E}{m_0c^2}\right)^2\frac{1}{\lambda^2}\left[1+\left(\frac{E\psi}{m_0c^2}\right)^2\right]^2 \times\left[K_{\frac{1}{3}}^2(\xi)+\frac{(E\psi/m_0c^2)^2}{1+(E\psi/m_0c^2)^2}K_{\frac{2}{3}}^2(\xi)\right]. \quad (4)$$

In order to estimate the vertical spread of the radiation from a single electron in a circular orbit, it is instructive to study the behavior of the angular distribution as a function of the angle ψ holding λ and E constant.

Such a dependence, denoted by $P(\psi)|_{\lambda,E}$, represents the instantaneous power per unit angle per angstrom radiated at the wavelength λ in a direction ψ measured relative to the orbital plane. Table I gives the values of $P(\psi)|_{\lambda,E}$ as a function of ψ. The family of curves found in Fig. 1 represents plots of $P(\psi)|_{\lambda,E}$ at four different wavelengths. For these curves, the energy E was taken as 6.0 Bev. The four wavelengths, respectively given by $\lambda=0.1086$ A, 1.086 A, 10.86 A, and 108.6 A, were chosen

* Research supported in part by the Office of Ordnance Research, U. S. Army.

[1] D. H. Tomboulian and D. E. Bedo, J. Appl. Phys. **29**, 804 (1958).

[2] J. Schwinger, Phys. Rev. **75**, 1912 (1949).

TABLE I. For a constant electron energy of 6.0 Bev, the numerical quantities listed under a given wavelength represent $P(\psi)|_{\lambda,E}$, the power at the angle ψ per unit angle and unit wavelength centered at the particular wavelength. $P(\psi)|_{\lambda,E}$ is expressed in erg-sec^{-1}-rad^{-1}-A^{-1}. The values of the angle ψ are given in milliradians.

ψ in milliradians	$\lambda=0.1086$ A	$\lambda=1.086$ A	$\lambda=10.86$ A	$\lambda=108.6$ A
0.0	5.86×10^{4}	2.11×10^{4}	6.60×10	1.45×10^{-1}
0.00852	5.40×10^{4}	2.10×10^{4}	6.61×10	1.45×10^{-1}
0.0170	4.22×10^{4}	2.09×10^{4}	6.64×10	1.45×10^{-1}
0.0255	2.76×10^{4}	2.07×10^{4}		1.46×10^{-1}
0.0341	1.48×10^{4}	2.03×10^{4}	6.76×10	1.46×10^{-1}
0.0426	6.37×10^{3}	1.96×10^{4}		
0.0511	2.14×10^{3}	1.85×10^{4}	6.93×10	1.48×10^{-1}
0.0596	5.46×10^{2}	1.71×10^{4}		
0.0681	1.03×10^{2}	1.54×10^{4}	7.13×10	1.49×10^{-1}
0.0767	1.38×10	1.34×10^{4}		
0.0852	1.28	1.12×10^{4}	7.30×10	1.52×10^{-1}
0.0937	7.95×10^{-2}	9.04×10^{3}		
0.102	3.21×10^{-3}	6.95×10^{3}	7.40×10	
0.111	8.06×10^{-5}	5.09×10^{3}		1.56×10^{-1}
0.119		3.53×10^{3}	7.38×10	
0.136		1.44×10^{3}	7.22×10	1.60×10^{-1}
0.153		4.53×10^{2}	6.88×10	
0.170		1.08×10^{2}	6.36×10	1.66×10^{-1}
0.187		1.89×10	5.70×10	
0.204		2.35	4.93×10	1.72×10^{-1}
0.222		2.03×10^{-1}	4.09×10	
0.238		1.18×10^{-2}	3.26×10	1.75×10^{-1}
0.255		4.46×10^{-4}	2.48×10	1.76×10^{-1}
0.281			1.51×10	1.76×10^{-1}
0.306			8.13	1.73×10^{-1}
0.340			2.92	1.67×10^{-1}
0.366			1.16	1.60×10^{-1}
0.391			3.93×10^{-1}	1.50×10^{-1}
0.425			7.29×10^{-2}	1.35×10^{-1}
0.451			1.68×10^{-2}	1.21×10^{-1}
0.477			3.25×10^{-3}	1.07×10^{-1}
0.511			2.68×10^{-4}	8.82×10^{-2}
0.536			3.24×10^{-5}	7.43×10^{-2}
0.596				4.54×10^{-2}
0.681				1.77×10^{-2}
0.766				5.06×10^{-3}
0.851				1.02×10^{-3}
0.936				1.40×10^{-4}
1.022				1.26×10^{-5}
1.107				7.17×10^{-7}

so as to sample the angular width at typical spectral positions over the most intense portion of the 6.0 Bev spectrum. For purposes of computation it was convenient to assign values to the parameter ξ and from Eq. (2) to determine the corresponding angle ψ. Values of the modified Bessel functions $K_{\frac{1}{3}}(\xi)$ and $K^{\frac{2}{3}}(\xi)$ were prepared by the use of tables of Bessel functions of fractional order.[3] The ordinates of Fig. 1 represent $P(\psi)|_{\lambda,E}$ in absolute units (erg-sec^{-1}-A^{-1}-rad^{-1}). The spread of the radiation as measured by the angle ψ in milliradians is symmetric about the orbital plane. Correspondingly, the angles shown in Fig. 1 may be taken as those which lie above the orbital plane.

Inspection of the curves shows that at a fixed energy E, the angular spread increases with increasing wavelength. This can be seen by comparing the widths of the individual curves at the particular values of ψ at which the spectral intensity has dropped to 1% of that at the peak.

If the calculations are repeated at a lower value of E, a somewhat narrower spread will be found at each of the wavelengths chosen above. Hence the curves in Fig. 1 portray the largest angular spread to be attained during an acceleration interval over which the electron energy reaches the maximum value of 6.0 Bev.

At the two longer wavelengths ($\lambda=10.86$ A and $\lambda=108.6$ A) the angular distribution shows a "double hump." (The descriptive term becomes meaningful when we consider the entire angular spread above and below the orbital plane. The curve plotted in Fig. 1 includes only the right-hand half corresponding to the angular spread above the orbital plane.) Thus, the peak power at the longer wavelengths does not occur in the orbital plane but at some angle ψ away from the orbital plane. To investigate the conditions under which $P(\psi)|_{\lambda,E}$ may possess stationary values other than the one at the origin, we examine the derivative of $P(\psi,\lambda,E)$. Equation (5) gives the condition under which $dP/d\psi$ vanishes:

$$K_{\frac{1}{3}}(\xi)-3\xi\left[1+\frac{(E\psi/m_0c^2)^2}{1+(E\psi/m_0c^2)^2}\right]K^{\frac{1}{3}}(\xi)=0. \qquad (5)$$

For a fixed λ and E (here taken as 6.0 Bev), the solution of Eq. (5) specifies the angle ψ at which the power radiated is a maximum. Figure 2 depicts the angle

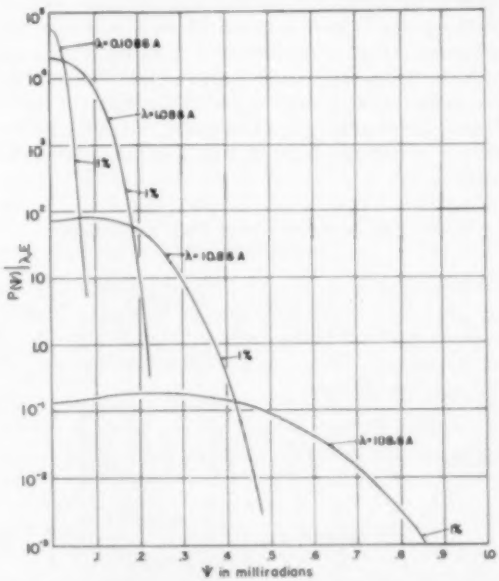

FIG. 1. Angular distributions at the four specified wavelengths at a fixed energy of 6.0 Bev. The ordinate $P(\psi)|_{\lambda,E}$ is expressed in erg-sec^{-1}-A^{-1}-rad^{-1}, and the abscissa ψ is in milliradians. The arrows indicate the angle at which the intensity has dropped to 1% of peak value.

[3] National Bureau of Standards, *Tables of Bessel Functions of Fractional Order* (Columbia University Press, New York, 1949), Vol. II.

corresponding to the peak of $P(\psi)$ for various values of λ. Examination of relation (5) leads to the observation that, for $E=6.0$ Bev, the maximum radiated power occurs at $\psi=0$, for values of $\lambda<1.39$ A.

It is also instructive to compare the angular distributions at a fixed wavelength for a series of electron energies. (See graphs in Fig. 3.) The values of $P(\psi)$ plotted here were again obtained from Eq. (4) by varying the energy parameter at the fixed wavelength of 108.6 A. In an accelerator, the electron energy varies over the acceleration cycle so that the observed angular distribution at a fixed wavelength reflects the effect of the variation of the electron energy. Actually, the observed distribution is obtainable by integrating the general expression found in Eq. (4) over the electron energy. The integrated results will differ from the monoenergetic distributions given in Fig. 1.

III. POLARIZATION OF THE RADIATION

Equation (4) may be regarded as the sum of the following two components:

$$P_2(\psi,\lambda,E)=C(\lambda,E)\left[1+\left(\frac{E\psi}{m_0c^2}\right)^2\right]^2 K_{\frac{1}{3}}^2(\xi) \qquad (6)$$

and

$$P_1(\psi,\lambda,E)=C(\lambda,E)\left[1+\left(\frac{E\psi}{m_0c^2}\right)^2\right]^2 \times\left[\frac{(E\psi/m_0c^2)^2}{1+(E\psi/m_0c^2)^2}\right]K_{\frac{1}{3}}^2(\xi), \qquad (7)$$

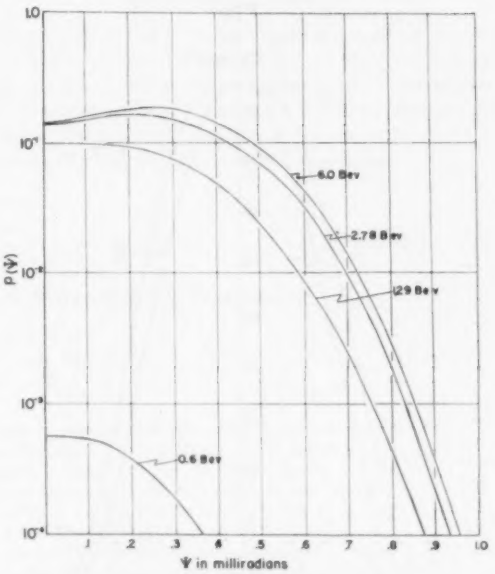

FIG. 3. Angular distributions at a fixed $\lambda=108.6$ A for several electron energies as indicated. Ordinates in erg-sec^{-1}-A^{-1}-rad^{-1}; the angle ψ is given in milliradians.

where

$$C(\lambda,E)\equiv\frac{3}{2\pi}\left(\frac{e^2c}{R}\right)\left(\frac{E}{m_0c^2}\right)^2\left(\frac{\lambda_c}{\lambda}\right)^2\frac{1}{\lambda^2}. \qquad (8)$$

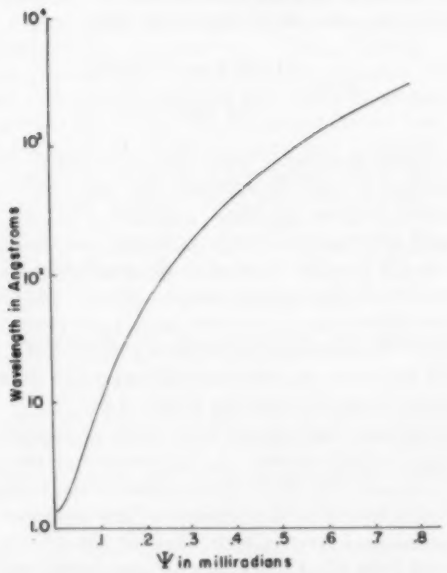

FIG. 2. At the longer wavelengths ($\lambda>1.39$ A in the present case) the peak power does not occur in the orbital plane but at some angle ψ. The curve above shows the angle corresponding to the peak value of $P(\psi)|_{\lambda,E}$ for values of λ plotted as ordinates.

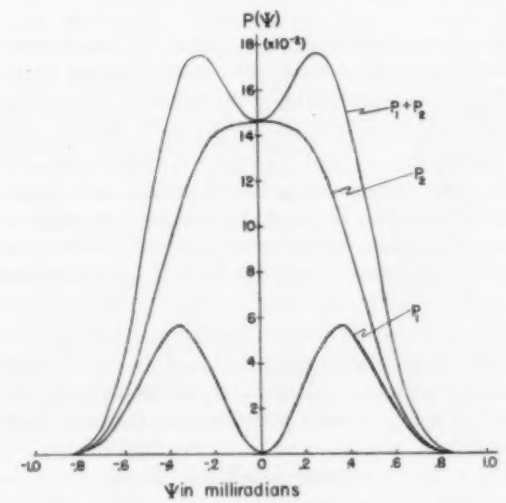

FIG. 4. The curves labeled as P_1 and P_2 represent, respectively, the intensity components polarized at right angles to, and in the orbital plane. Parameters: $E=6.0$ Bev; $R=26.36$ m; $\lambda=108.6$ A. The curve representing the sum of P_1 and P_2 is identical with the corresponding plot in Fig. 1, except that here $P(\psi)$, again in absolute units, is plotted on a linear scale. The peak power in P_1 and in the sum (P_1+P_2) is attained at values of ψ which are different from zero.

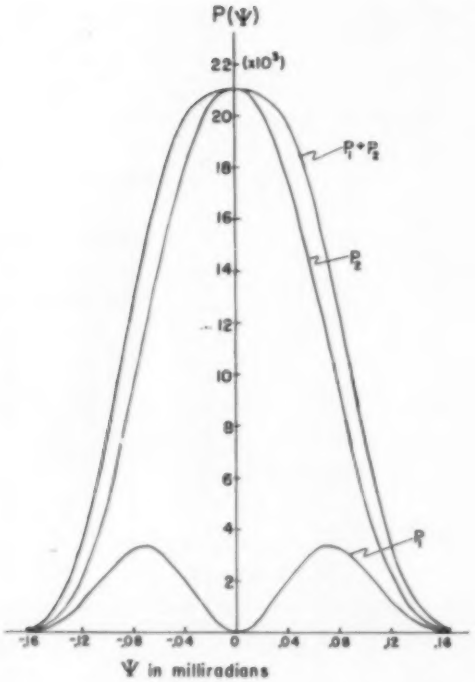

FIG. 5. Curves P_1 and P_2 represent, respectively, the intensity components polarized at right angles to, and in the orbital plane. Parameters: $E=6.0$ Bev, $R=26.26$ m, $\lambda=1.086$ A. Here P_1 shows the "double hump" character, but the sum (P_1+P_2) has its peak at $\psi=0$, since λ is less than the critical value. See discussion in text.

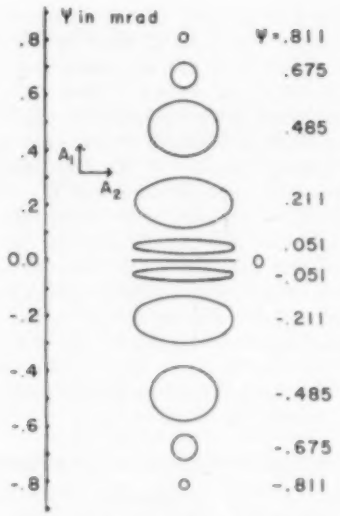

FIG. 6. The diagrams show the relative amplitudes and states of polarization at five different values of ψ above and below the orbital plane. A_1 and A_2 are the amplitudes of the radiation polarized, respectively, at right angles to, and in the plane of the orbit. Parameters: $E=6.0$ Bev, $R=26.26$ m, $\lambda=108.6$ A.

The above expressions for P_1 and P_2 may be identified with the results of Westfold,[4] who has deduced expressions for the polarization of the radiation from an electron gyrating ultrarelativistically in a magnetic field. Accordingly, P_1 and P_2 represent, respectively, the intensity components polarized parallel and perpendicular to the projection of the direction of the magnetic field in the plane normal to the direction of observation. In the synchrotron, the magnetic field is perpendicular to the orbital plane of the electron, and the two components P_1 and P_2 are very nearly the intensities of the radiation polarized, respectively, with the electric vector at right angles to, and parallel to, the orbital plane. The graphs in Figs. 4 and 5 represent plots of P_1 and P_2 and their sum, which is the same distribution shown in Fig. 1 for $\lambda=108.6$ A, except that in Fig. 4, the intensities are plotted on a linear scale. The particular wavelength $\lambda=108.6$ A chosen for the plots found in Fig. 4 is such as to give rise to maxima at values of ψ other than zero. In Fig. 5 only a single maximum appears (at $\psi=0$), since for this plot λ is chosen to be 1.086 A, a value less than the critical value of 1.39 A.

When $\psi=0$, $P_1=0$; hence, as illustrated by the intensity variations shown by Figs. 4 and 5, the radiation in the orbital plane ($\psi=0$) is linearly polarized, while at other angles the polarization is elliptic. From Eqs. (6) and (7), the ratio of the axes of the ellipse is

$$R(\psi)=\frac{[1+(E\psi/m_0c^2)^2]^{\frac{1}{2}}K_{\frac{1}{3}}(\xi)}{(E\psi/m_0c^2)K_{\frac{1}{3}}(\xi)}, \tag{9}$$

which ratio approaches unity with increasing ψ. As the intensities P_1 and P_2 approach the same value, the radiation becomes circularly polarized. From the numerical information already presented graphically in Fig. 4, it is possible to calculate the amplitudes A_1 and A_2 of the radiation polarized respectively at right angles to, and in the plane of, the orbit for certain values of the angle ψ. The results are portrayed in the graph of Fig. 6, which illustrates the relative amplitudes and states of polarization for five different values of ψ.

An attempt has recently been made by Joos[5] to investigate experimentally the polarization of the synchrotron radiation in the visible region of the spectrum. For both directions of polarization, Joos measured the variation in intensity with angle utilizing the light emitted from the Cornell synchrotron during the acceleration interval in which the electrons attained a

[4] K. C. Westfold, Astrophys. J. **130**, 241 (1959).

[5] P. Joos, Phys. Rev. Letters **4**, 558 (1960).

peak energy of 700 Mev. His results resemble somewhat the shapes portrayed in Fig. 4, but differ from them in several details. The phase relation between P_1 and P_2 was also checked approximately for large values of ψ, where it was possible to test the nearly circular nature of the polarization by converting it into linearly polarized light.

ACKNOWLEDGMENTS

A portion of this work was carried out while the first two authors served as consultants to Harvard University. Thanks are also due to Professor M. S. Livingston, the director of the Cambridge Electron Accelerator project, for his initial and continued interest in investigations dealing with the synchrotron radiation.

JOURNAL OF APPLIED PHYSICS VOLUME 31, NUMBER 12 DECEMBER, 1960

High-Temperature Discharges in Ferroelectric Ceramics*

JOHN W. NORTHRIP†
Sandia Corporation, Albuquerque, New Mexico
(Received July 7, 1960)

Ceramic disks of barium titanate and lead zirconate titanate, when heated above 100°C, exhibit current discharges which cannot be attributed to the ferroelectric polarization of the material. These discharges are largest in the temperature interval 300°–600°C and depend primarily on the electrode material and its method of application. Discharges of several millicoulombs at voltages up to one-half volt have been obtained from a ceramic disk one-half inch in diameter and 30 mils thick having a silver electrode and an indium counterelectrode. Although thermoelectric, pyroelectric, and electret effects are observed in these samples, these phenomena contribute only a very small portion of the total discharge. At constant temperature near 350°C the discharge decays with time as the sum of two exponentials, falling to half-maximum in periods of the order of one-half hour. At higher temperatures the decay rate increases, while temperature cycling produces a voltage cycling superimposed on the decay. These findings support an explanation of the effect in terms of solid state chemical activity between the metallic electrodes and the titanate lattice.

I. INTRODUCTION

CERTAIN ferroelectric titanates, when heated above 100°C, exhibit current discharges which cannot be attributed to the ferroelectric polarization of the material. Early work on this effect by Berlincourt[1] indicated that it was caused by space charges arising within the material during polarization. Blood, Levine, and Roberts[2] concluded that the effect was due to a migration of defects which resulted in a frozen-in polarization in excess of the normal polarization of the material. In a recent paper by Hurd, Simpson, and Tredgold[3] the discharges have been studied as a function of composition in barium titanate doped with other oxides. They suggested that the effect was due to an interaction between the oxygen vacancies in the ceramic and metal from the electrodes. The research reported here tends to support such an electrochemical model.

II. EXPERIMENTAL PROCEDURES AND RESULTS

A. Materials

A series of experiments was first carried out to determine what materials might exhibit this effect. Most of the previously mentioned studies had been carried out with either barium titanate or lead zirconate titanate ceramics. Therefore it had not been definitely determined whether the discharges were dependent on the ceramic properties, the ferroelectric properties, or the oxygen defect semiconductor properties of the material. It was found that single crystals of barium titanate exhibited the discharges, thus eliminating the ceramic state as a necessary factor in the effect. Positive results were also obtained with single crystals of titanium dioxide, a nonferroelectric material having the oxygen octahedral structure characteristic of the ferroelectric titanates. Both of these crystalline materials exhibited the high-temperature discharges immediately after being electroded although the effect was increased after the application of a strong electric field for a few minutes. These materials gave currents on the order of 0.2 to 0.3 $\mu a/cm^2$ which lasted for several minutes. Thus it is seen that these discharges must arise from the chemical or semiconductor nature of the material. The purpose of further study was then to determine what types of reactions might lead to these phenomena.

B. Electrodes

A second phase of the study dealt with the effect of electrodes on the high-temperature discharges from these materials. One-half-inch diameter disks of lead zirconate titanate ($PbZr_{0.56}Ti_{0.44}O_3$) were electroded with different metals and subjected to a dc field about 2 kv/cm. They were then heated at about 300°/hr

* Work performed under U. S. Atomic Energy Commission Contract.
† Present address: Physics Department, Oklahoma State University, Stillwater, Oklahoma.
[1] D. A. Berlincourt, Sandia Corporation Order No. WC-727 (March, 1956).
[2] H. L. Blood, S. Levine, and N. H. Roberts, J. Appl. Phys. **27**, 660 (1956).
[3] J. D. Hurd, A. W. Simpson, and R. H. Tredgold, Proc. Phys. Soc. (London) **73**, 448–454 (1959).

while the output current into a 100 kohm resistor was measured. The first group of samples tested had vacuum-plated gold electrodes on both surfaces. These produced currents becoming significant in the vicinity of 250°C, rising to a maximum of 0.2 μa at about 350°C, and then falling to zero at about 500°C. At the beginning of the main discharge, the samples sometimes exhibited minor charge flow which was of opposite sign to the main discharge. A second group of samples was electroded with a thin film of duPont Colloidal Silver Dispersion. These samples gave outputs in the same temperature range as the gold electroded samples but with maximum currents of the order of 1 μa. This indicates a total charge release of a few hundred μcoul/cm^2, an amount far greater than any known ferroelectric polarization or electret charge storage capability. If the sample was reheated after cooling this discharge was found to be greatly reduced. However, the effect could be regenerated either by subjecting the sample to an external field for a few minutes or by removing the old electrode and painting on a new one.

The third type of electrode used in this study was made by heating the sample slightly above the melting temperature of indium (about 150°C) and pressing liquid indium on the ceramic surface until wetting was obtained. These samples again gave currents of the order of 1–2 μa but the effect could be observed on several successive runs without any regenerative procedures. The obvious extension of these findings was to use one material for an electrode and a different material as a counterelectrode. This was done and currents in the range of 3–5 μa were consistently obtained (Fig. 1).

C. Poling

The effect of poling on these high-temperature discharges was studied using ceramic disks having silver electrodes. It was found that various poling procedures were capable of changing the discharge quantitatively but that each sample exhibited a qualitative pattern of discharge which was unchanged by poling procedures (Fig. 2). The temperature at which the discharge became noticeable, the temperature at which it reached a maximum, and the general discharge pattern were determined by the sample and its electrodes rather than by its previous electrical treatment.

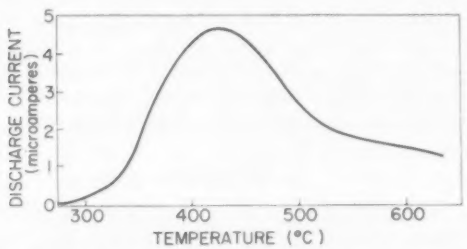

FIG. 1. Typical discharge current from a 0.5-in. diameter sample of lead zirconate titanate having a silver electrode and an indium counterelectrode. The rate of heating was 300°/hr. The area under the curve between 300°C and 600°C represents a total charge flow of 10 mcoul.

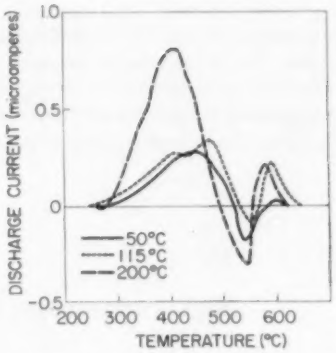

FIG. 2. Typical discharge patterns from a 0.5-in. diameter lead zirconate titanate disk having silver electrodes. The disk was poled at 20 kv/cm at the temperatures shown. Heating rate during discharge was 300°/hr.

D. Effect of Temperature

When samples having a silver electrode and an indium counterelectrode were held at a constant temperature above 300°C, a decay of the output was observed (Fig. 3). The output in this case gives very close fit to a curve representing the sum of two exponentials

$$I = Ae^{-t/\tau_1} + Be^{-t/\tau_2}.$$

In this expression A and B depend primarily on the particular sample, with the ratio A/B tending to increase as the temperature increases. The constants τ_1 and τ_2 are essentially independent of the sample. The constant τ_1 is temperature dependent, having a value about 2×10^3/sec at 350°C and 5×10^2/sec at 450°C. The constant τ_2 varied little in the temperature range studied, having a value near 1.6×10^1/sec. If the temperature was purposely cycled over a small range, a cycling of the voltage output was observed superimposed on the decay. Quantitatively this cycling was somewhat erratic but tended to be about 0.5 mv/deg during the highest outputs.

E. Effect of Circuit Load

While holding the sample at a constant high temperature the load resistance was varied to determine any charge limitations on the discharge phenomena. It was found that the current being drawn from the sample could be increased by a factor of 10 for short periods without noticeably affecting the subsequent behavior under the original load conditions. If we assume that the ceramic element can be represented by an open circuit emf plus an effective circuit resistance, it is a simple matter to calculate the values associated with these elements from the change of voltage occurring during a

step change of load resistance. The open circuit emf was not constant with time but showed the same form of decay observed in the load voltage. For very high resistances the load voltage was not affected by variation of the load, indicating that the mechanism should be represented as a voltage generator rather than a current generator. The effective sample resistance was found to depend on the temperature, being initially about 30 kohm at 350°C, 1500 ohms at 450°C, and 300 ohms at 550°C. A decrease in the effective resistance was also observed with time, reaching 30–40% of the original resistance over a period of 3 to 4 hrs.

III. DISCUSSION

High-temperature discharges such as those observed seem to be best explained by either a pyroelectric, a thermoelectric, or an electrochemical mechanism.

The existence of pyroelectricity presupposes a polarization of the material either as a polarization of the unit cell (ferroelectrics) or as a stored body charge (electrets). The magnitude of the observed discharges in the present study is two orders of magnitude larger than has been observed in either of these types of polarization.

Thermoelectric discharges occur when a body is heated in such a way as to maintain a temperature gradient across it. It is known that oxide materials such as rutile have thermoelectric coefficients of the order of one millivolt per degree. In the present study the maximum temperature gradient measured during heating was about ten centigrade degrees. The production of voltages of the order of 0.5 v by a single element indicates that thermoelectricity cannot be the dominant discharge mechanism.

The dependence of the discharge phenomenon on electrode material seems to substantiate the concept of voltages arising from electrochemical reaction. This conclusion is also supported by the finding that the discharge could be regenerated by either an externally applied field (a "charging" process) or by renewing the electrode. Examinations of the electrode interface have thus far failed to determine the exact chemical reactions responsible for the discharges. Hurd, *et al.*, have suggested that the reaction is one between the electrode metal and oxygen vacancies in the lattice. This is based on the observation that additions to the ceramic material which produce large vacancy concentrations also produce larger discharges.

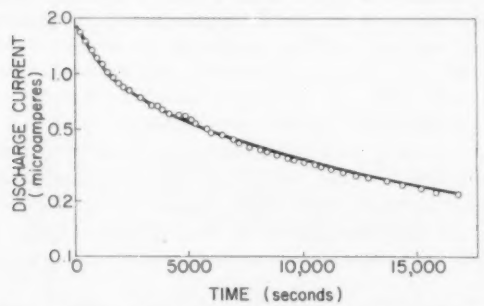

FIG. 3. Decay of discharge with time at 350°C for a 0.5-in. diameter lead zirconate titanate disk. The points represent experimental data while the curve represents the equation

$$I = 1.2e^{-t/\tau_1} + 0.6e^{-t/\tau_2} \qquad \tau_1 = 2\times10^3 \quad \tau_2 = 1.6\times10^4.$$

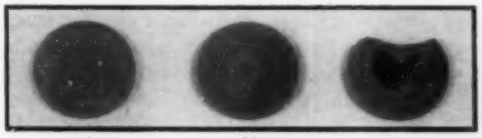

FIG. 4. Samples exhibiting darkening below electrodes. (a) Before heating; (b) after 15 minutes at 300°C; (c) after 1 hour at 400°C.

If one accepts the mechanism of a primary or secondary (storage) cell as the origin of the observed discharges, the problem then becomes one of explaining the observed decay phenomena. The simplest explanation lies in the assumption that the discharges are diffusion limited, becoming more so after the reaction has proceeded for long periods of time. This assumption is confirmed by examination of the samples after heating. The material under the electrodes was found to be much darker than the surrounding material (Fig. 4). At first glance it appeared that the electrode material had diffused into the ceramic to a depth of the order of 0.1 mm. However, chemical tests have failed to reveal the presence of the metal in the dark ceramic material and resistance measurements have indicated that the dark material actually has a resistivity more than an order of magnitude higher than that of its surroundings. This seems to indicate the formation of a depletion layer in the ceramic material near the electrode.

This model, however, is in direct contradiction to the results obtained from observation of the discharges with variation of load. From the model, one would expect outputs corresponding to a constant emf generator coupled with a slowly rising effective circuit resistance. Experiment has indicated a decrease with time in both the emf and the effective circuit resistance.

Another possible model, and one which better predicts the behavior of the emf, involves the concept of concentration cells. These could exist both at the ceramic-electrode interfaces and within the ceramic material. Recent studies[4] seem to indicate that wetting of a ceramic surface by indium is accomplished by the formation of an oxidized layer between the indium metal and the ceramic material. This would then provide the conditions necessary for a concentration cell at the interface with the oxygen vacancies acting as the carrier ions. Reaction with these carriers would then produce concentration gradients within the material,

[4] R. H. Plumlee, Sandia Corporation (unpublished).

giving rise to decay both by change of concentration at the interface and by production of a reverse emf across the material. This would explain the dependence of the decay on two exponentials rather than on a single kinetic mechanism. The observation of discharges when both electrodes were of the same material would have to be explained on the basis of unequal wetting characteristics causing different optimum temperatures for the production of voltage.

Another possibility for the production of these discharges follows from an analogy suggested by Green.[5] He reports the striking similarity between the electrons and holes in a semiconductor and ions in an electrolytic solution. Using this analogy we can imagine a model in which primary, secondary, or concentration cells are present and in which the carriers are electrons or holes rather than chemical species or vacancies. This analogy should be especially close in oxide semiconductors, which are characterized by high carrier concentrations and very low carrier mobility.

[5] M. Green, in *Modern Aspects of Electrochemistry, Number 2* (Academic Press, Inc., New York, 1959), p. 355.

IV. CONCLUSIONS

This study of high-temperature discharges in barium titanate and lead zirconate titanate supports a model involving a solid state chemical reaction between the electrodes and the base material. The effect is a maximum in the region 300° to 600°C and is primarily dependent on the electrode material.

ACKNOWLEDGMENTS

The author would like to thank Dr. Hans Jaffe and Don Berlincourt of Clevite Research Center for helpful discussions regarding ferroelectric materials and Dr. G. W. Anderson of Sandia Laboratory for suggesting the study.

JOURNAL OF APPLIED PHYSICS VOLUME 31, NUMBER 12 DECEMBER, 1960

Experimental Study of Arc Stability. I

J. D. Cobine and G. A. Farrall
General Electric Research Laboratory, Schenectady, New York

(Received June 16, 1960)

The stability of short arcs in gases and in metal vapors is closely related to the phenomena associated with the cathode spot. Use is made of improved techniques to study this phenomenon for a considerable range of electrode materials. The distribution of arc life for a given average current is shown to follow the survival law. These data demonstrate that a small percentage of arcs of a given current on very clean metal surfaces may have lifetimes that are extremely short or very long compared with the average life. The relation between the average life of an arc and its average current is shown generally to consist of two sharply defined sections each of the form $\ln t = A \ln I + B$. The distribution of lifetimes and the relation between average life and average current are shown for Hg, Cd, Zn, Cu_2Sb, Bi, Bi-Cu, Cu-In, Ag, Cu_2Sn, Al, Be, Cu, Cu-W-Th, Cu-MoC, Mo, and W. It is shown that high vapor pressure materials tend to produce more stable arcs than those having low vapor pressure.

INTRODUCTION

THE phenomenon of arc stability for cold metal electrodes has been considered for many years; but is still little understood. In 1900 Kaufman[1] proposed the criterion that the sum of the external circuit resistance and the dV/di of the arc volt-ampere characteristic at the operating point must be positive if a stable arc is to be obtained. About this time the concept of a minimum current for a stable arc was developed. This "minimum current" essentially represented an average value of the current at which the dV/di of the arc characteristic became infinite. Actually it was approximated in experiments by the limitations of voltages and resistance available. The values of the minimum current ranged from about 0.01 amp for carbon to about 1 amp for tungsten and are summarized by Holm.[2] As the applications of the electric arc expanded in industry, two opposite stability requirements developed. In circuit interrupters an unstable arc apparently was desired, while for arc-lamps, rectifiers, and welders great stability of the arc was essential.

In a study of arcs in inert gases Doan[3–5] and coworkers showed that arc cathodes were very unstable in the pure inert gases, argon, helium, neon, and that oxygen was necessary in the form of surface oxides if stable arcs were to be obtained. Later[6,7] it was noted

[1] W. Kaufman, Ann. Physik **2**, 158 (1900).

[2] R. Holm, *Electric Contacts* (Hugh Gebers Förlag, Uppsala, Sweden, 1946), p. 264.
[3] G. E. Doan and J. L. Myer, Phys. Rev. **40**, 36 (1932).
[4] G. E. Doan and A. M. Thorne, Phys. Rev. **46**, 49 (1934).
[5] G. E. Doan and W. C. Schulte, Phys. Rev. **47**, 783 (1935).
[6] C. G. Suits and J. P. Hocker, Phys. Rev. **53**, 670 (1938).
[7] J. D. Cobine, Phys. Rev. **53**, 911 (1938).

that oxides on the surface of metals were necessary for the glow-arc transition in the inert gases. The addition of the refractory oxides thoria ($\phi \doteq 2.7$ ev) and zirconia ($\phi \doteq 2.9$ ev) were shown[8] to produce exceedingly stable arcs of quite different nature in the inert gases. Brubaker[9] demonstrated that in hydrogen and in helium at pressures from 0.01–1000 mm Hg a low-current, metallic arc underwent of the order of 1000 interruptions per minute, while in oxygen at pressures exceeding 10 mm Hg the arc had zero interruptions, i.e., great stability.

Holm[10] states that in a good vacuum the minimum current is greatly increased from the values he tabulated for atmospheric arcs. He reports for these vacuum arcs minimum currents of 12 amp for outgased copper, of 40 amp for a single crystal of copper, and of 100 amp for tungsten. Denholm,[11] however, studying "vacuum" arcs between impure and probably gassy electrodes, found minimum currents (his mean "chopping" current) in the range 0.35–0.5 amp for steel, copper, and aluminum. These values are not unlike those found in air. The difference between these and the results of Holm may be attributed to the effects of gas on the surface.

The erratic branched tracks of cathode spots on mercury and other cold metals[12] have been interpreted by Kesaev,[13] using a somewhat idealized illustration, as evidence of arc instability due to "systematic" division and disintegration of the cathode spots. He was unable to identify the observed voltage variations with either the amplitude or the shape of the statistical fluctuations in the arc current. Thus it would seem that both emission phenomena and space-charge distribution may change independently. It is possible that the great differences inferred for the current density of the cathode spot on cold metals, ranging from the order of 10^5 amp/cm^2 reported by Cobine and Gallagher,[12] through the value of the order of 10^6 amp/cm^2 of Froome,[14] to values between 10^7 and 10^8 reported by Wroe,[15] may represent various stages experienced by a spot, or a complex of spots, as the cathode foot-point moves randomly over a cold metal surface. Thus instability might reasonably be expected to occur at random over an extended range of current. Indeed, this is exactly what was found for the mercury-pool arc by Copeland and Sparing.[16]

The study made by Copeland and Sparing shows a random distribution of arc lifetimes for a given current and that the average lifetime varies continuously with the current. This study showed that for a large number (N) of separate arcs, treated mathematically as starting simultaneously, the number of arcs ΔN that extinguished in a time interval ΔT was proportional to the number burning at the beginning of the time interval and to the length of the interval Δt. This yields a relation of the form $N = N_0 E^{-at}$ for any particular set of environmental conditions, as current, pressure, etc. Thus the lifetimes of the cathode spots of the mercury arc follow a typical survival law. There seems to be no particular evidence that would suggest that mercury is intrinsically different, as far as the cathode spot mechanism is concerned, from any other liquid or solid "cold" metal, i.e., that at temperatures too low for thermionic emission to account for any appreciable amount of the current.

It seemed to the present authors that a study, following the statistical methods of Copeland, of the vapor arcs drawn in good vacuum, between carefully outgassed and purified electrodes, might reveal considerable information on the nature of cathode spots on cold metals. With this in mind, the research now being reported was undertaken.

EXPERIMENTAL PROCEDURE

The experiments were conducted by manually separating current-carrying electrodes which were initially in contact and observing by means of a Tektronix type 545 cathode-ray oscilloscope the duration, or lifetime, of the arc that was drawn. It was decided that the determination of the lifetimes of 40 arcs would give reasonably representative results for a given set of experimental conditions. This number would be expected[17] to yield a relative mean error

$$\langle \Delta T^2/T^2 \rangle = 1/N = 1/40 = 0.025 \quad \text{or} \quad 2.5\%$$

and a probable relative error

$$0.6745(N)^{-\frac{1}{2}} = 10.3\%,$$

where T is the mean lifetime and N is the number of counts. To reduce the probable relative error to 5% would have required 160 arcs. It was not deemed practical to take a larger value of N because of the likelihood of excessive erosion which could seriously change the electrode surfaces, especially at the higher currents.

The arcs under study were drawn in sealed cylindrical glass envelopes of 3½ in. diameter and of approximately 1-liter volume. The electrodes were supported on ½-in.-diam metal rods passing through opposite ends of the envelope at metal bellows 2 in. in diam. The bellows were attached to the glass by 3-in. Fernico seals. The electrodes, except where specifically noted to the contrary, were ¾-in.-diam cylinders 1 in. in length. A movable metal shield, 3 in. in diam and 3½ in. long, prevented hot metallic vapor from striking the glass envelope during arcing. To each experimental assembly was attached an ionization gauge and a titanium getter tube for continual monitoring and control of the gas pressure.

[8] J. D. Cobine and C. J. Gallagher, Trans. Am. Inst. Elec. Engrs. **70**, 804 (1951).
[9] W. M. Brubaker, Phys. Rev. **83**, 979 (1951).
[10] See p. 270 of work cited in footnote 2.
[11] A. S. Denholm, Can. J. Phys. **36**, 476 (1958).
[12] J. D. Cobine and C. J. Gallagher, Phys. Rev. **74**, 1524 (1948).
[13] I. G. Kesaev, Soviet Phys.—Doklady **3**, No. 5, 967.
[14] K. D. Froome, Proc. Phys. Soc. (London) **60**, 424 (1948).
[15] H. Wroe, Nature **182**, 338 (1958).
[16] P. Copeland and W. H. Sparing, J. Appl. Phys. **16**, 302 (1945).
[17] P. L. Copeland, Am. J. Phys. **13**, 215 (1945).

All experimental arcing devices were processed by sealing to a mercury pump vacuum system with liquid nitrogen traps. The devices, where the melting points of the electrodes permitted, were baked for 4 hr at 450°C. Then metal parts such as the shield, electrodes, and supporting rods were heated by radio frequency for about 3 hr, or until no further gas was evolved, and then the switch was rebaked at 450°C. For metals with low melting temperatures the bakeout was obviously limited to a temperature slightly below the melting point, and high-voltage sparking while on the pump was substituted for the rf heating of the electrodes. This vacuum sparking of the electrode surfaces was continued with increasing voltage until the limit of the set (100 kv) was reached. As the sparking voltage increased, smaller and smaller bursts of gas were released at each breakdown. In all cases the residual gas pressure was below 2×10^{-6} mm Hg at the conclusion of processing.

It was evident, in view of the brief history presented in the introduction, that good vacuum technique would be necessary and that the gas content, especially oxygen, of the electrode materials used should be exceedingly low. The relatively low pressure of the test devices at the conclusion of processing indicates that the technique used was adequate. A group of high-purity gas-free metals was available in the Research Laboratory and was felt to be well suited to the requirements of this study. As a typical example of the high degree of freedom from gas of these metals it may be stated that a careful study of a sample of copper by Dr. Thomas A. Vanderslice of this Laboratory, with a mass spectrograph, revealed an ungettered gas content of 10^{-9} (i.e., 1 part per billion).

The evolution of gas upon arcing could be monitored by a transient ionization gauge. Most of the gas evolved was due to the arc cleaning of a small surface area, and at the higher currents by general heating of the electrodes and their supports. A monolayer of gas is formed in about 1 sec at a pressure of 10^{-6} mm Hg, and represents about 10^{15} atoms/cm^2. Thus it is not surprising that some change in pressure is noted upon arcing even at this pressure because a square centimeter scoured by rapidly moving arc spots could raise the pressure in the 1-liter volume switch to about 3×10^{-5} mm Hg. In general, the vacuum improves markedly with arcing due to the gettering action of fresh metal films deposited on surfaces adjacent to the arc, principally the metal shield.

The experimental devices were mounted in a mechanism such that the arcs could be drawn by operating a hand lever against a spring which normally held the electrodes open with a gap length of $\frac{7}{32}$ in. Power for all of the arcs studied was supplied by a 40 kw dc motor-generator set adjusted to 125 v. The arc current was varied by adjusting a series slide wire resistor. Since these resistors are somewhat inductive, circuit inductance will vary with the current being used.

In the initial stages of this work, arc lifetime was determined by connecting a coaxial line directly across the arcing electrodes and displaying the arc voltage on a Tektronix type 545 oscilloscope with a persistent phosphor screen. The oscilloscope was set to trigger upon

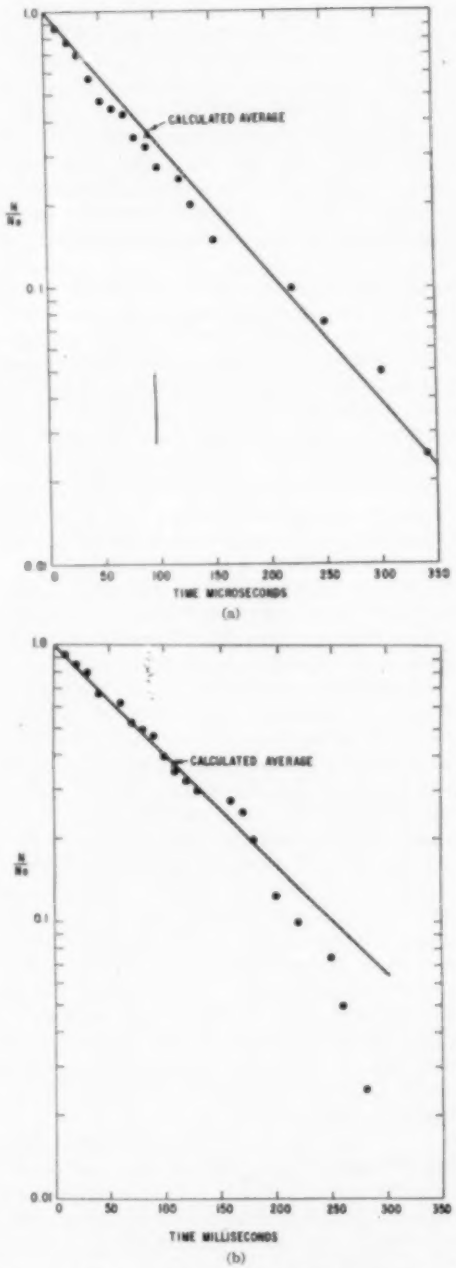

FIG. 1. Relative number of arcs lasting longer than time t. Copper electrodes $\frac{1}{4}$-in. diam, $\frac{7}{32}$-in. gap, 125 volts dc. (a) 3.42 amp (b) 38.5 amp.

the appearance of arc voltage so that arc lifetime could be read directly as that time for which the arc voltage was present. This method had two undesirable features: (1) the coaxial line connected across the electrodes resulted in an added capacitance in shunt with the arc, which was found to alter arc stability; (2) the arc noise voltage under certain conditions could cause rf breakdown at the input to the oscilloscope. Also, the abrupt cessation of current, sometimes called "chopping," that occurs at the end of the arc's life could induce excessive surge voltages in the measuring system. In view of this a photocell was used to observe duration of the light from the arc, but this method was useful only if the arc was in line of sight of the photocell. This was impractical at currents high enough to require the shield in position. Finally it was decided to use a pickup coil attached to the envelope of the arcing device to detect the radiated noise signal, characteristic of all the arcs studied. The output from a 5-turn coil 2 in. in diam was found ample in all cases. Since there is a signal from the coil only while the arc is burning, and since there is no direct connection to the arcing circuit, this latter method seemed ideal and was the one used for most of the data presented here. Excellent agreement in arc lifetime measurement was observed among the three methods discussed.

EXPERIMENTAL RESULTS

Typical experimental dc arc lifetime curves are shown in Figs. 1(a) and (b) for Cu contacts in vacuum for currents of 3.42 and 38.5 amp and a gap of $\frac{7}{32}$ in. The points represent the proportion of the 40 arcs drawn for this specific condition that had lifetimes equal to or greater than the indicated abscissa. The calculated average lifetime, indicated by $\times$ in Fig. 1, is the numerical average of the 40 values placed at the 0.368 ordinate. The number 0.368 is the value of N/N_0 which corresponds to the theoretical average of an exponential distribution. Early in this study it was found that reproducible results could be obtained only after considerable arcing at currents of from 10 to 20 amp. This conditioning effect is apparently the result of the "scouring" action of the arc spots, which move at random over the surface removing sorbed gases and producing a uniform surface "texture" as a result of erosion and condensation of metal vapor. The large amount of similar data accumulated for a wide range of currents and materials justifies the conclusion that the lifetimes of vapor arcs follow a characteristic survival law, comparable in form to those found by Copeland for mercury. Thus for a given current, both very long and very short lifetimes compared to the average value are to be expected. Stability of dc arcs is thus a purely random phenomenon.

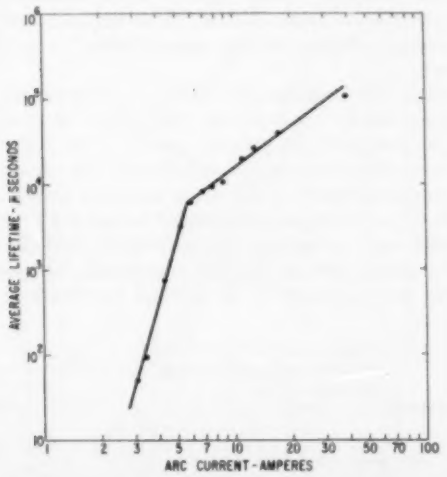

FIG. 2. Average arc lifetime for copper electrodes, 125 v dc.

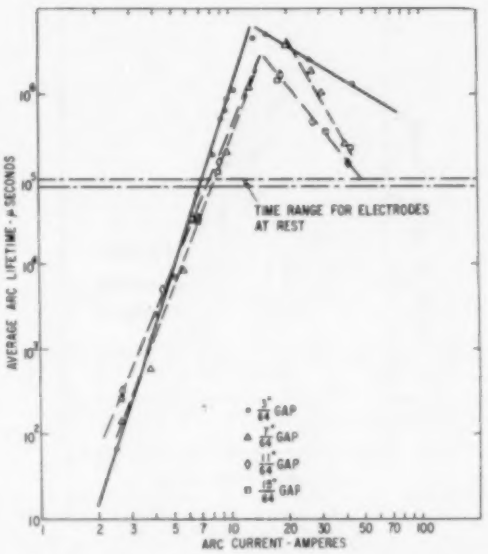

FIG. 3. Average arc lifetime for various gap lengths on molybdenum carbide contacts, 125 v dc.

The *average* lifetime t_a is shown in Fig. 2 as a function of the average current for the same material as Fig. 1. This average lifetime curve consists of two segments, each segment having the same statistical distribution of lifetimes. Figure 1(a) represents a typical distribution for the lower segment, while Fig. 1(b) is a typical distribution for the upper segment. Each segment, within its range, is of the form $\ln t_a = A \ln I + B$, where I is the average current and A and B are constants. It is evident that at a fairly definite value of current the average lifetime vs current function undergoes a distinct change. This will be seen later to be true for the other materials in our study.

In order to determine the possible effect of gap length for the short arc in vacuum the data of Fig. 3 were

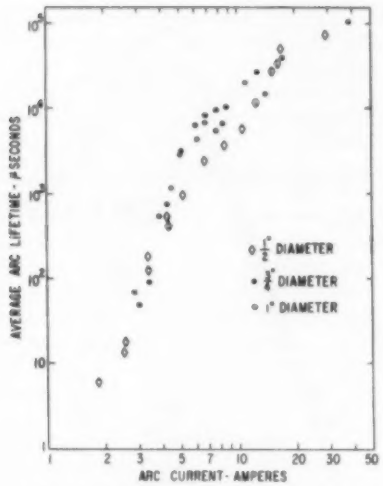

FIG. 4. Average arc lifetime for three different diameters of copper electrodes, 125 v dc.

taken, for four different gap lengths. The variation among the points for the different gaps is no more than could be attributed to changes in the surface due to prolonged arcing. The time for the contacts to be fully open was from $8\text{–}10\times10^4$ μsec, as indicated by the dotted lines of Fig. 3. Thus the short-time part of the data of this figure was taken for arcs with moving electrodes, while the longer life data were for arcs burning at constant gap length for most of their life. Since there is no difference in the two parts of the average life curve separated by the opening time lines, it could be inferred that gap length has little or no effect on the stability of the short vacuum arcs.

Other possible effects of geometry were also considered. The lifetimes of arcs on copper electrodes ½ in., ¾ in., and 1 in. in diam in three different arcing devices were measured with the results shown in Fig. 4. A systematic variation between the three sets of data is an apparent smoothing of the transition between the two segments for the small electrodes. Such other variations of lifetime with electrode diameter as do appear are not systematic and could be due entirely to variations in the cathode surfaces for each pair of electrodes. Further, the similarity of the results of these three different arcing devices at low currents seems reasonable verification of the reproducibility of arc lifetime measurement for a given material.

In order to establish the validity of the average lifetime curves as representative of the material under study, data were taken to determine the effects of capacitance in shunt with the arc, inductance in series with it and of varying an applied voltage. It was mentioned earlier that a capacitance across the arcing electrodes altered the measured average arc lifetime. The effects of the external circuit in modifying dc arc lifetime should be considered. Figure 5 is the diagram of the experimental circuit showing distributed inductance and capacitance of the line to the generator as lumped elements. The series resistances used to limit the current have inherent inductances. Thus the combination of L and R was different for each current. For currents less than 5 amps a slide wire resistor was used for which

$$L=\frac{0.67}{I}\ \text{mh} \tag{1}$$

where I = amp arc current. At currents equal to or greater than 5 amp a tapped power rheostat was substituted for the slide wire and the corresponding relation between arc current and inductance was

$$L=\frac{2.6}{I}\ \text{mh}. \tag{2}$$

It may be remarked here that the change in the current from 4 to 5 amp (and the change from slide wire to power rheostat) introduced an increase in inductance by a factor of 4 (0.17 to 0.7 mh). None of the data show significant variations in average lifetime of the arc in this current range that can be attributed to this change in inductance. A detailed inquiry as to the effect on arc lifetime of adding series inductance was not made. However, in the single instance in which we did examine this specifically, the addition of a much larger inductance, 3.14 mh, doubled the average arc lifetime on copper-bismuth contacts at a current of 2.64 amps.

The effect of shunt capacitance is shown in Fig. 6 for copper. It is evident from this figure that the shape of the low-current characteristic is unchanged by varying the shunt capacitance from zero (contact self-capacitance = 5 μμfd) to 1020 μμfd. There is, however, a marked lowering of this segment of the characteristic, resulting in a decrease of about two orders of magnitude of average lifetime for the range of shunt capacitance shown.

While the problem of stability was previously examined briefly to determine the effects of changing circuit constants, the primary goal of this research was to determine the relative stability of arcs on various electrode materials in the same electrical circuit. The wide variety of materials included in this work may be divided into two groups: (1) pure metals and (2) mixtures, alloys, and intermetallic compounds. The former group was examined in an attempt to obtain funda-

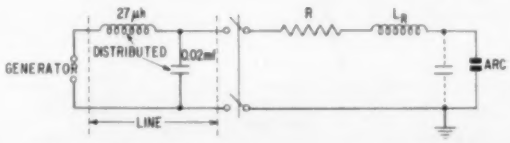

FIG. 5. Effective circuit for measurement of arc lifetime.

mental information on arc stability. The second group was of interest in establishing whether or not a stable (or unstable) electrode material could be combined with other metals to produce a material with high (or low) stability.

The results of this statistical study are shown in Fig. 7 for the pure metals and in Fig. 8 for the mixtures. Each of these curves represents from 10 to 20 data points distributed in the same way as is indicated in Fig. 2. Each data point represents the average of 40 individual arcs for the current in question, i.e., from 400 to 800 arcs determine a single curve. Most of the curves consist of two quite definite sections, only mercury, silver, tungsten, and copper-antimony having three. It may be that the lower segment represents arcs with a single stationary spot, while the upper segments represent arcs with multiple or moving spots. The data presented here are believed to be characteristic of the metals for which they are given, rather than simply a reflection of our particular geometry or method of processing the various electrode materials. In evidence of this, data were taken for tungsten in the experimental arc tube described above, and also with a Jennings RH4G vacuum switch which has tungsten contacts.[18,19] The latter had 1-in. diam electrodes and a gap of $\frac{1}{8}$ in. The internal shield and the total volume of the commercial switch were much smaller than for our experimental device. In spite of the differences in geometry and undoubted difference in processing, the stability data for the two switches were in good agreement, as shown in Fig. 9. However, there was a difference in the location of the break in the curve, as the figure shows.

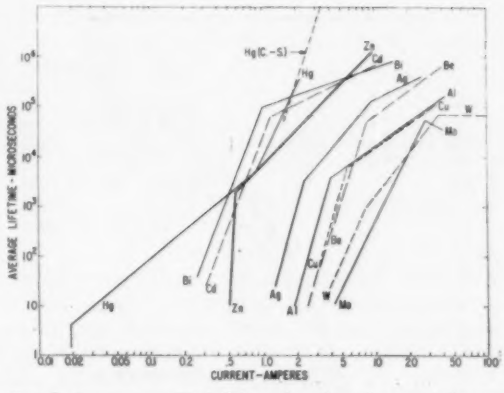

FIG. 7. Average arc lifetime as a function of current for pure electrode materials, 125 v dc. Hg(C.-S.) data by Copeland and Sparing.

Copeland's arc lifetime data for mercury were taken for currents such that the lifetimes were much longer than the range considered in Figs. 7 and 8. Data were therefore taken for mercury at lower currents in order to provide a comparison with the other metals studied.

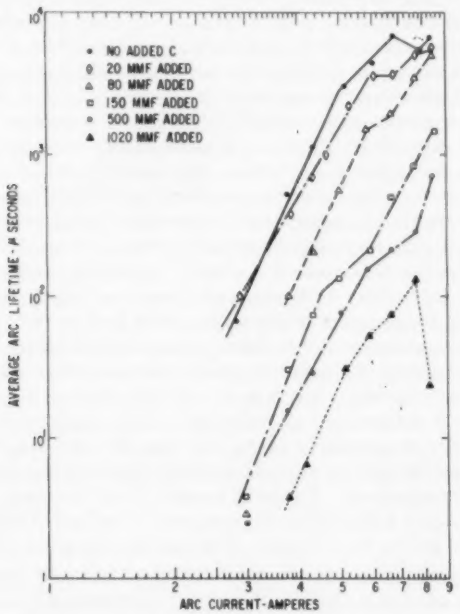

FIG. 6. Effect of capacitance on average arc lifetime on copper contacts, 125 v dc.

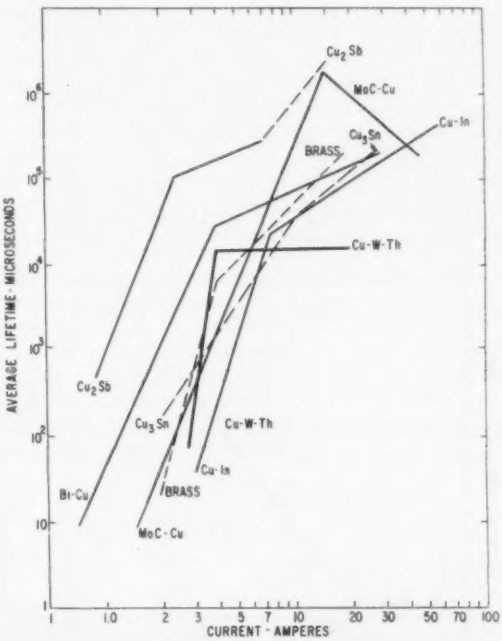

FIG. 8. Average arc lifetime as a function of current for various composite electrode materials, 125 v dc.

[18] H. C. Ross, Tele-Tech & Electronic Inds. **15**, 58 (1956).
[19] J. E. Jennings, A. C. Schwager, and H. C. Ross, Trans. Am. Inst. Elec. Engrs. **III 75**, 462 (1956).

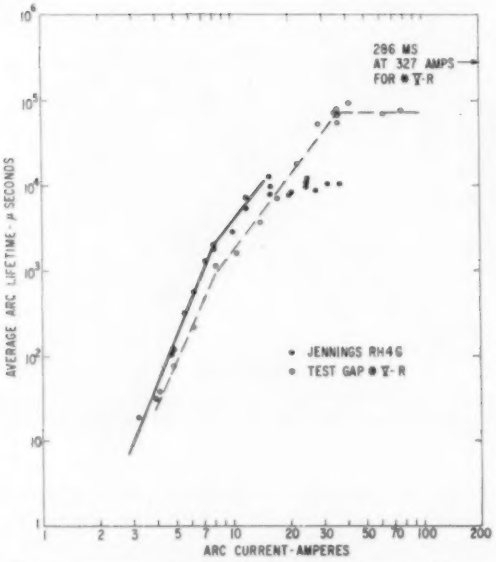

FIG. 9. Average arc lifetime as a function of current for two different sets of tungsten contacts, 125 v dc.

This was made possible by means of a mercury pool tube built for this purpose by Dr. G. H. Reiling of this Laboratory. This glass tube had an over-all height of 5 in. and diameter of $1\frac{1}{2}$ in. A molybdenum anode $\frac{3}{4}$ in. in diam was mounted on a metal bellows so that it could be brought into contact with the mercury cathode to start the arcs. A portion of the results of the investigations on this tube is shown by the solid line marked Hg in Fig. 7. These data represent the average arc lifetime on mercury at a tube temperature of 23.5°C. Data from Copeland and Sparing for mercury are shown by the indicated dotted curve. Although there are wide differences in the geometry and starting method for the two studies, the high current portion of the present data is in satisfying agreement with the earlier research.

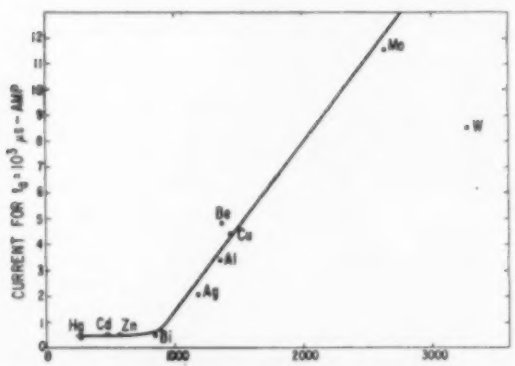

FIG. 10. Characteristic currents vs characteristic temperature for various electrode metals.

RELATION OF ARC LIFETIME AND VAPOR PRESSURE

The lifetime vs current curves of Fig. 7 represent the relative stabilities of the various metals when acting as cathodes for vacuum arcs. The characteristics appear from left to right in decreasing order of stability. If an *average* lifetime of 1 msec is considered, the values of current for which the various characteristics intersect this time ordinate will provide a convenient index for designating the relative stabilities of the metals.

An examination of the properties of the metals studied in this paper reveals that the most significant factor affecting the stability of vapor arcs is the vapor pressure of the cathode material. It has been shown[20] that at the foot-point of a stable arc the vapor pressure of the electrode metal, due to high-energy input to the surface, may be very high, even exceeding in density that corresponding to atmospheric pressure. This process is very important in the vacuum arc, since it is the only source of gas or vapor for maintaining a conducting path. The arc in vacuum contrasts considerably with atmospheric arcs in that most of the vaporization is from the cathode, the loss from the anode being relatively low, whereas in atmospheric arcs the erosion from the two electrodes is of the same order. It seems quite reasonable to assume that vapor-arc extinction would occur when the cathode-spot temperature became too low to produce some minimum density of vapor. This condition could be expected at a vapor density corresponding to a pressure of about 10^{-3} mm Hg, where the mean free path is about 5 cm, i.e., of the order of the tube dimensions. This is the pressure at which even hot cathode tubes become unstable. As seen in Fig. 7, this average time of 1 msec occurs in the lowest segment of the stability curves for each metal except mercury. In the discussion which follows, the temperature required to produce 1-μ vapor pressure[21] will be referred to as a "characteristic temperature." Likewise, the current corresponding to an experimental lifetime of 1 msec will be called the "characteristic current." A plot of the characteristic current as function of the characteristic temperature of the pure metals is shown in Fig. 10. This figure shows two rather definite groups of metals; Group I, consisting of Hg, Cd, Zn, and Bi, for which the characteristic current is very low, i.e., of the order of 0.5 amp, and is independent of characteristic temperature; and Group II, consisting of Ag, Cl, Cu, Be, and Mo, for which the current increases linearly with the characteristic temperature. Tungsten is entirely off the curve. It is evident from Fig. 7 that tungsten is also out of order with Mo on the sequence of decreasing vapor-pressure materials. This suggests a different mechanism for tungsten which is probably a thermionic type emitter in most cases. The fact that very high current densities have been indicated for tungsten[15] also suggests that Joule

[20] J. D. Cobine and E. E. Burger, J. Appl. Phys. **26**, 895 (1955).
[21] R. E. Honig, RCA Rev. **18**, 195 (1957).

heating is very important and phenomena similar to that occurring in exploding wires may be involved. If all the metals of Group II had roughly the same cathode-spot size, the linear increase in characteristic current with a characteristic temperature would be quite reasonable. This is because it would represent a linear power input, required by the increasing temperature that is necessary to produce the minimum operating pressure. Unfortunately, cathode-spot sizes as function of current are not sufficiently well established to make this more than a reasonable suggestion. A notable difference between the two groups of metals is the relatively high resistivities and low thermal conductivities of the metals of Group I. Both high thermal and electrical resistivities could be very important factors in determining the minimum current of these metals, since both can contribute strongly to heating below the active surface of the spot.

The composite materials used in this study were prepared in vacuum from the same gas-free metals referred to above. The designation of the materials and their composition are given in Table I. The stability curves for the composite materials, shown in Fig. 8, appear to follow substantially in the order dictated by the highest vapor-pressure constituent. The electrodes of Cu-In appear to be an exception in that the indium seems to have had little effect. Furthermore the relatively low ionization potential of the indium (5.76 ev) appears to have no effect on stability. It should be noted at this point that aluminum, which is more stable than copper, has an ionization potential of 5.98 ev compared to 7.72 for copper. The increased stability of aluminum relative to copper is thus attributed to the higher vapor pressure of aluminum and not to its low ionization potential. The Cu-W-Th is more stable than either copper or tungsten, showing the effect of the low work-function (3.38 ev) constituent, thorium, which is also a very low vapor pressure material. The effect of low work-function additives on arc stability has already been established for atmospheric arcs.[8] Except for Mo, W, and mixtures containing these two elements, all the upper segments of the lifetime curves have positive slopes.

It was not possible to reach a sufficiently high current to establish a perfectly stable arc in vacuum with any of the metals studied. It was felt that the heating and erosion that would occur at currents higher than those for which arc lifetime measurements were made would be excessive. These factors would prevent the taking of reliable statistical data in the present experimental device.

TABLE I. Composition of composite materials.[a]

Cu_2Sb	Stoichiometric
Bi-Cu	20% Bi 80% Cu
Cu_3Sn	Stoichiometric
Brass	20% Zn 80% Cu
Cu-MoC	Stoichiometric matrix of MoC impregnated with Cu
Cu-W-Th	Matrix of W+7% Th+2% Ta impregnated with Cu
Cu-In	90% Cu 10% In

[a] Weight proportions.

An important comparison can be made between the physical properties of copper and beryllium and their stability characteristics. Figure 8 shows that the lower segments of the stability curves of these two metals are very close together. The upper segments are practically parallel but that for beryllium is somewhat higher, i.e., has longer average lifetime, than that for copper. Table II lists what are believed to be the most pertinent physical properties of these two metals. It is evident that the only properties substantially the same for the two metals are the arc drops and the vapor pressures, which are indicated by the temperatures shown in the last two columns. Thus further weight is added to the concept that the principal factor affecting arc stability in vacuum is the vapor pressure of the cathode material. A study of the relation between arc drop, arc noise, and vapor pressure will be presented in some detail in Part II of this study.

ARC NOISE AND STABILITY

Observations on arc noise made during the lifetime measurements show that higher degrees of arc stability are accompanied by a smaller component of noise voltage. Three general observations suggest this conclusion. First, for any given material it was observed quite generally that the higher the arc current (higher stability) the smaller the amplitudes of noise voltage. Second, the noise component of arc voltage was found to be lower for the stable materials such as mercury, zinc, and cadmium than in the relatively unstable materials like tungsten and molybdenum. Finally, for all of the materials investigated the extinction of an arc was usually preceded by a noise voltage distinctly greater than the voltage observed while the arc was burning steadily. This higher noise voltage, for example, may appear for the last 5 to 20 μsec of an arc whose total lifetime was 100 μsec. This effect clearly is demonstrated in the following way. A Panoramic spectrum analyzer

TABLE II.

	At. wt.	Ionization potential (ev)	Work funct. (ev)	Resistivity (μ ohm-cm)	Heat cond. (cgs$\times 10^2$)	Sp. heat (cgs)	Heat of vaporiz. (ws/g.)	Average arc drop (volts)	Temp. for 1-μ °K	Boiling point °K
Be	9	9.28	3.92	10.1	333	0.397	34 300	18	1365	2750
Cu	63.54	7.68	4.61	1.69	927	0.092	6000	18	1415	2851

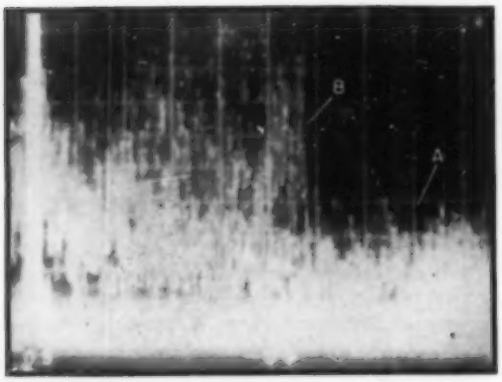

FIG. 11. The change in arc noise amplitude preceding arc extinction for beryllium contacts.

(Model SPA-3) was connected by means of a cathode-follower probe across the switch. The analyzer was set to sweep repetitively a 3-Mc bandwidth centered at 1.5 Mc, independent of whether or not an arc was burning. The arcing circuit was adjusted to deliver 20-amp current so that the expected arc lifetime was longer than the time required for the analyzer to sweep the 3-Mc spectrum. The noise was displayed on the cathode-ray tube of the analyzer. The result of this operation is shown in Fig. 11. The initiation of the arc can be seen as a slightly brighter noise pattern eight divisions from the left margin of the analyzer scale at *A*. The arc continued to burn while the analyzer completed its first sweep and scanned the spectrum again. On the third pass over the frequency band the arc extinguished at 5.8 divisions from the left side of the scale at *B*. The higher noise voltage occurring at arc extinction should be compared with the lower voltage measured at the same frequency on the previous sweep of the analyzer. The frequency being scanned at the moment of arc extinction was 1.74 Mc.

On the evidence available thus far, it appears that while high-amplitude noise is an indication of arc instability, such noise may be the necessary result of an arc being maintained under relatively unfavorable conditions such as insufficient metallic vapor density in the region of the cathode spot. If such a viewpoint is tenable, suppression of this noise by adding shunt capacitance, as noted previously, should deprive the arc of variational voltages that may help to keep it burning. The resultant shortening of arc lifetime by shunt capacitance would then agree with the results already presented in Fig. 6.

The increase in noise voltage prior to extinction suggests a fluctuating vapor density at the cathode spot with momentary deficiencies which cause increases in arc voltage. As the current tends to decrease, and di/dt increase, it is quite possible that for the cold metals a principle of minimum energy is more nearly satisfied by both vapor and ionization being supplied in bursts where the peak values considerably exceed the average requirements. The momentary oversupply of vapor reduces the rate of vapor evolution for a brief period. The initial vapor and ionization burst is depleted by diffusion and migration to such a low value that a new burst is required.

SUMMARY

In the range of circuit parameters investigated, metal vapor dc arc stability is a random phenomenon. Thus a probability of survival can be assigned to various metal-vapor arcs.

There is no precise value of current at which the arc is always interrupted. For all materials studied the average lifetime of dc arcs in the range of circuit parameters used is related to the average current by the equation $\ln\tau_a = A \ln I + B$.

The stability of the metal vapor dc arcs is relatively insensitive to gap length, electrode motion, electrode diameter, and geometry of the arcing chamber.

Shunt capacitance markedly decreases arc lifetime as it prevents, or reduces, voltage fluctuations necessary for providing additional vapor.

Metal vapor arc stability is largely dependent on the vapor pressure of the material used as cathode. Extinction probably occurs under energy conditions such that the vapor density at the surface is reduced to a value corresponding to a pressure of about 1 μHg.

The presence of a low work-function additive increases the stability of the metal vapor arc.

Note added in proof. Since submitting the manuscript of this paper the work of Kesaev[22] was noted. He shows for mercury vapor with various gaseous additives that the survival law holds for arc stability. There is substantial agreement between our data and his for the mean lifetimes for mercury at room temperature, and for the effects of the external circuit.

ACKNOWLEDGMENTS

Data for mercury have been made available through the cooperation of Dr. G. H. Reiling. The authors wish to express their thanks to Mr. R. H. Johnston for his assistance in taking experimental data. They also are grateful to Dr. A. H. Hull, Dr. J. A. Rich, and Dr. J. M. Lafferty for reading the manuscript and making helpful suggestions.

[22] I. G. Kesaev, Soviet Phys.—Tech. Phys. 4, 1351 (1960).

Atom Ejection Patterns in Single-Crystal Sputtering*

G. S. Anderson and G. K. Wehner
Mechanical Division of General Mills, Inc., Minneapolis, Minnesota
(Received April 20, 1960)

Experimental studies of the atom ejection patterns in single-crystal sputtering mostly by Hg^+ ions have been made. These patterns give evidence of the anisotropic spread of energy from a collision center, and support the concept of focusing collisions in nearest and next-nearest neighbor directions. In Ge the patterns were found to be strikingly similar to those from a bcc crystal. This could be explained by assuming that under ion bombardment so many interstitials are formed near the surface that the atom arrangement of the Ge crystal resembles that of a bcc lattice.

INTRODUCTION

THE discovery that atoms are sputtered from single crystals primarily in certain preferred crystallographic directions was made in 1955,[1-3] when tungsten single crystals were sputtered with low-energy mercury ions. It was observed that atoms were sputtered principally in nearest neighbor directions at very low-bombarding ion energy, and that next-nearest neighbor directions became important at higher energies. Since that time Koedam[4] and Yurasova[5] have made similar observations. Another interesting observation was made recently by Thompson.[6] He bombarded a gold foil, which had a strongly preferred orientation of grains, with protons which emerged from the foil with a mean energy of 0.3 Mev, and found that the Au atoms sputtered from the far side of the foil were preferentially ejected in the close packed directions. Thus he obtained a sputtered deposit pattern which is very similar to the one obtained at much lower bombarding energy from the front side of a (100) Au surface.

These atom ejection patterns are of interest in many respects. They seem to provide the key for a much better understanding of the sputtering process, and furnish strong evidence supporting a momentum transfer process in sputtering as opposed to an evaporation process. A dependence on crystallographic direction has never been observed when material is evaporated from a single crystal. Furthermore, these patterns provide a new tool for the experimental study of certain radiation damage problems, such as the anisotropic spread of energy from a collision center. Of much interest in this connection are the theoretical calculations of radiation damage events in an array of atoms, such as those made by a group under Vineyard.[7]

APPARATUS AND TECHNIQUES

The mercury ion bombardment studies were performed in a demountable mercury pool cathode tube as shown in Fig. 1. The single crystal target is a flat surface ~ 1 cm^2 in area which is parallel to a low-index crystallographic plane. It is immersed in the plasma of a low-pressure gas discharge. When a negative potential (with respect to the plasma potential) is applied to the target, the potential drop appears across the Langmuir sheath which covers the target. The energy of the bombarding ions is then determined by this potential drop. Since this energy is much larger than thermal ion energies, one has essentially normal ion incidence.

Sputtered products from the target were collected on glass plates mounted parallel to the target surface with a separation of about 3 cm. The disadvantage of this arrangement is that atoms ejected at large angles from the surface normal either cannot be collected or are deposited farther away from the target, which results in weaker deposits. The deposit pattern then does not give a true picture of the ejection pattern. The ideal

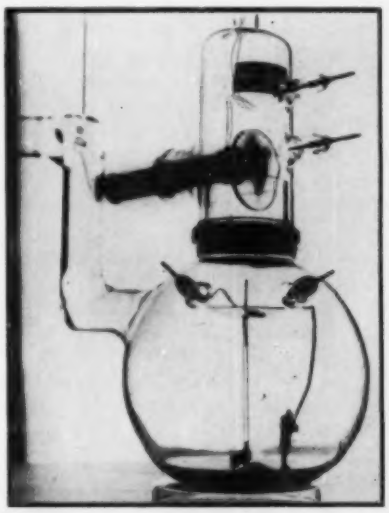

FIG. 1. Photograph of the demountable mercury pool cathode tube for ejection pattern studies.

* This work was supported in part by the U. S. Atomic Energy Commission.

[1] G. K. Wehner, J. Appl. Phys. **26**, 1056 (1955).
[2] G. K. Wehner, Phys. Rev. **102**, 690 (1956).
[3] G. K. Wehner, Appl. Sci. Research **B5**, 334 (1955).
[4] J. Koedam, Physica **25**, 742 (1959); **24**, 692 (1958).
[5] V. E. Yurasova, N. V. Pleshivtsev, and I. V. Orfanov, J. Exptl. Theoret. Phys. (U.S.S.R.) **37**, 966 (1959).
[6] M. W. Thompson, Phil. Mag. **4**, 139 (1959).
[7] A. Goland, M. Milgram, G. Vineyard, and J. Gibson, Bull. Am. Phys. Soc., Ser. II, **5**, 26 (1960).

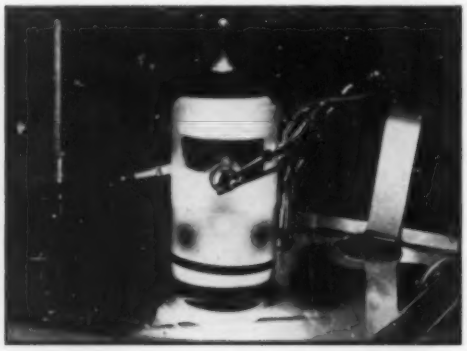

FIG. 2. Photograph of a ribbon deposit *in situ*.

arrangement for eliminating these difficulties would be a hemispherical glass collector with the target mounted at its center. Experiments with such spherical collectors, however, showed that other difficulties arise; for instance, the plasma becomes weaker due to an obstruction of the discharge, and the spherical deposits cannot be readily photographed. A compromise solution for these problems is to mount the target at the center of a glass ribbon which is bent into a semicircle (radius ~3 cm) against the inner wall of the tube. Figure 2 shows how the ejection pattern develops on the glass ribbon.

The collection of meaningful, reliable, and reproducible deposit patterns is to some degree an art which requires a delicate balance of many interrelated parameters. First, the mean free path of sputtered atoms must be larger than the tube dimensions, or the deposits will be diffuse and various errors will be introduced. In our Hg experiments, the lower part of the tube is immersed in an anti freeze solution kept near 0°C. The gas pressure is then of the order of 0.1 μ and the gas kinetic mean free path is of the order of 30 cm.

It was observed that clearer patterns result when the sputtering rate is high. Hence, with a low ion bombarding energy it is particularly important to increase the density of the bombarding ion current to the highest possible values (>5 ma/cm²) by increasing the plasma density in the target vicinity. This is achieved with a high anode current (3 amp), a control grid in the discharge,[8] and by the use of properly arranged external magnets. Magnetic fields, in fact, are one of the most efficient ways of increasing the local plasma density. Other methods, such as a funnel arrangement for guiding and concentrating the plasma to the target vicinity or operating the tube at higher anode voltage, have not been very successful. In order to assure a high sputtering rate in Hg, it is important to keep the target at an elevated temperature (>300°C) to prevent the formation of a Hg film at the target surface. At lower temperatures the dwelling time of Hg atoms at the target surface becomes so long that this interferes with the sputtering of target atoms, and the yields become substantially smaller.

In general, no major difficulties seem to arise with the sticking of the sputtered atoms at impact on the collector surface. This is in agreement with observations of Ditchburn,[9] who states that the presence of a plasma reduces nucleation difficulties. The presence of a plasma makes special precleaning of the collector surface in general unnecessary. Precoating the glass collector with thin uniform metal deposits for better nucleation conditions, or using conductive glass, brought no visible improvement. Resputtering of material from the collector surface may become a problem, particularly at very low arrival rates of atoms and at a high anode voltage (>40 ev). In this case, the primary or beam electrons cause the collector to assume a floating potential which is sufficiently negative to cause resputtering by ion bombardment. Thus, it seems to be important to operate the tube at a low anode voltage (<25 v). This helps, in addition, to keep the number of doubly ionized Hg atoms at low values (<0.3%). Resputtering is greatly enhanced when an inhomogeneous magnetic field causes the beam electrons to spiral into the collector. This causes a substantial negative charging of the collector, which may result in resputtering. Negative charging of the collector may also be caused by the γ electrons which are released from the target under the ion bombardment. These electrons are accelerated in the Langmuir sheath to the full bombarding energy in a direction normal to the target surface, and impinge on the collector opposite the target. Fortunately, γ coefficients for Hg in our energy range are rather small (<1%). Nevertheless, an outline of the crystal contours, marking the area on the collector where these additional fast electrons impinge, is occasionally noticed in the first stage of deposition.

The angle of incidence of the impinging ions is an

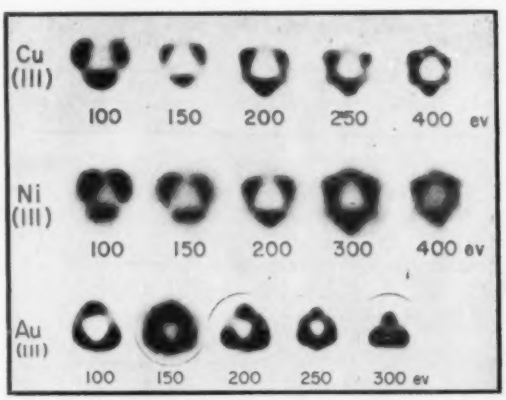

FIG. 3. Atom ejection patterns collected on flat disks for (111) surfaces of Cu, Ni, and Au.

[8] H. Fetz, Ann. Physik **37**, 1 (1940).

[9] R. W. Ditchburn, Proc. Roy. Soc. (London) **A141**, 169 (1933).

important parameter which must be controlled. If the target sides are electrically insulated and the Langmuir sheath is an appreciable fraction of the target radius, oblique incidence prevails near the target edges. Normal incidence was achieved by embedding the crystal in a graphite guard disk so that the flat graphite surface is flush with the target surface. The small amount of sputtered graphite does not interfere with the patterns. The single-crystal targets were carefully cut and ground to the proper orientation. The alignment of the surface, determined by back-reflection Laue patterns, was such that in no case was the surface normal more than two degrees from the desired crystallographic direction.

It is necessary to remove the distorted surface layer, which arises unavoidably from machining or mechanical polishing of the crystal, before a reliable deposit pattern can be obtained. This layer can be removed by electrolytic polishing before mounting the crystal in the tube. A simpler and quite sufficient method is to sputter the crystal for a certain time before the actual experiments are begun. Oxide layers are readily sputtered off in the very first stage of an experiment.

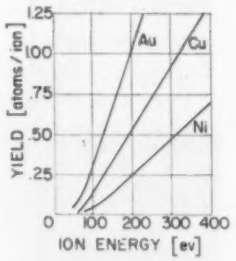

FIG. 4. Sputtering yield curves for Au, Cu, and Ni.

The definite advantage of the method described here is that the details of the patterns can be readily observed through the glass tube wall while they are being formed (as seen in Fig. 2) because the discharge plasma serves as a uniform light source. The relative sputtering rates in various directions can be more closely determined by comparing the density of the deposited material at various points on the ribbon. The ribbon can be scanned with a photometer while still in the discharge or after it has been removed from the tube. Of particular interest in these patterns are the angles between the main ejection directions and the normal to the target surface. These angles can be most conveniently determined while the ribbon is still in the discharge. For this purpose, a circular scale of 20-cm radius and graduated in degrees is mounted surrounding the tube in the plane of the collector, with the crystal surface at its center. The position where the normal to the crystal surface intersects the scale is determined by reflecting a light beam from the crystal surface. By visually aligning a deposit spot with the target surface, one can directly read the ejection angle on the scale with an accuracy which is limited by the sharpness of the spot.

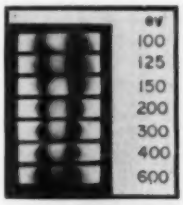

FIG. 5. Deposit patterns in the $(1\bar{1}0)$ plane from the Ni (111) surface.

EXPERIMENTAL RESULTS

Included in this section is a description of the patterns which were obtained on flat glass plate collectors. Although these are not of particularly good quality, since they were collected in the early stages of this work, they give a better survey of the appearance of the whole pattern than do the ribbons. All detailed studies performed so far have been essentially confined to normally incident Hg^+ ion bombardment. At the end of this section is a short discussion of preliminary results obtained with other gas ions.

To investigate the difference between single crystals of different materials but with the same crystal structure and orientation, (111) single crystal surfaces of Cu, Ni, and Au were studied at bombarding energies ranging from 100 to 400 ev. These patterns are shown in Fig. 3. At 100 ev bombarding energy, one obtains the three kidney-shaped spots corresponding roughly to the ⟨110⟩ directions. In Ni the spots seem to be somewhat more diffuse than in Cu or Au. The three spots are connected by weak bands which at higher energy begin to follow {111} planes, and develop into three additional spots (exceptionally pronounced in Cu at 400 ev) which are arranged symmetrically with respect to the original ⟨110⟩ spots. The kidney-shaped spots contract with higher energy to a more circular shape. A comparison of the patterns for Cu, Ni, and Au shows that very similar patterns arise at equal sputtering yields, which for these three metals are indicated in Fig. 4. The three additional spots which appear at high sputtering yields seem to be the same distance from the center of the pattern as the original three spots, and seem to disappear at higher target temperatures and at higher yields (Fig. 3: Au, 300 ev; for Cu and Ni at higher energies than shown in the picture). The additional spots appear at lower yields when the angle of incidence is changed from normal to oblique. Figure 5 shows the Ni pattern from the (111) surface collected on a glass ribbon in the $(1\bar{1}0)$ plane for the energy range 100—600 ev. Here one notices, in addition, that

FIG. 6. Atom ejection patterns collected on flat disks for a Ni (100) surface.

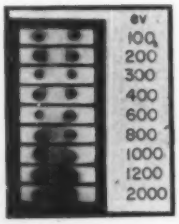

FIG. 7. Deposit patterns in the (010) plane from the Ni (100) surface.

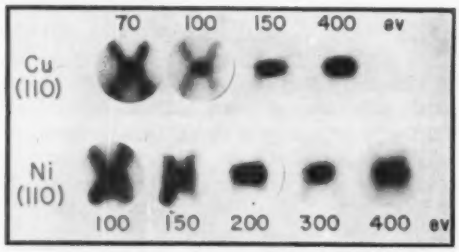

FIG. 8. Atom ejection patterns collected on flat disks for Cu and Ni (110) surfaces.

the spots have a tendency to converge somewhat at higher bombarding energy.

Figure 6 shows Ni (100) patterns obtained at energies ranging from 110 to 400 ev. The oval-shaped ⟨110⟩ spots, with their long axes pointing to the center of the pattern, are connected by weak bands roughly corresponding with {111} planes. The only major difference at higher energy is the appearance of a weak center spot which corresponds to the next-nearest neighbor direction. Figure 7 shows ribbon deposits from the same plane in the energy range 100 to 2000 ev. The weak center spot appears again at higher energy and the two ⟨110⟩ spots are somewhat farther apart at low energy. The pattern is obviously retained even at fairly high ion energy!

Figure 8 shows twofold symmetrical patterns from the (110) planes of Cu and Ni for energies up to 400 ev.

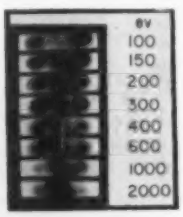

FIG. 9. Deposit patterns in the $(1\bar{1}1)$ plane from the Ni (110) surface.

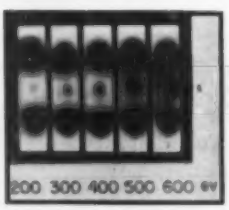

FIG. 10. Deposit patterns in the (011) plane from the Fe (100) surface.

The long axes of the four oval-shaped ⟨110⟩ spots (not including the center spot) do not point to the center of the pattern, and are connected by characteristic bands. The center spot is oval, with the long axis parallel to the $[1\bar{1}0]$ direction in the surface. The most pronounced feature at higher energy is that the center spot becomes increasingly dominant. Figure 9 shows the ribbon pattern in the $(1\bar{1}1)$ plane for the same surface of Ni for energies from 100 to 2000 ev. The center spot tends to disappear at very low energy and again the spots come somewhat closer together at higher energy.

Figure 10 shows ribbon patterns from the bcc Fe (100) surface for energies ranging from 200—600 ev. Here the nearest neighbor directions are the ⟨111⟩ directions, so the patterns are different in appearance from those of fcc crystals. The ribbon patterns from a Fe (110) surface are shown in Fig. 11 for deposits in the (001) plane and in Fig. 12 for deposits in the $(1\bar{1}0)$

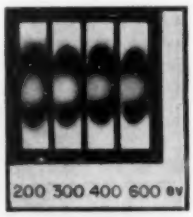

FIG. 11. Deposit patterns in the (001) plane from the Fe (110) surface.

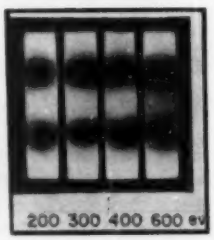

FIG. 12. Deposit patterns in the $(1\bar{1}0)$ plane from the Fe (110) surface.

plane for ion bombarding energies between 200 and 600 ev. The ejection angle is not very dependent on the bombarding ion energy. A pattern collected from the (110) surface with a ribbon in the $(1\bar{1}2)$ plane (Fig. 13) shows that two additional weak spots appear very obliquely to the target surface corresponding to the nearest neighbor directions in the target surface. Figure 14 shows the deposit patterns from the Fe (111) surface. The center spot becomes more pronounced with increasing energy. The round spot, corresponding roughly to a ⟨111⟩ direction 70° from the normal, decreases in intensity with increasing energy. The round spot on the other side of the normal corresponds roughly to a ⟨100⟩ next-nearest neighbor direction (55° from the normal). A pronounced band appears between the latter spot and the center.

More detailed studies were performed with Ge because its open diamond structure gives additional characteristics which are not present in the close-packed metals. Patterns from the Ge (100) surface in the (011)

plane for bombarding ions of energies ranging from 200—500 ev are shown in Fig. 15. Between 200 and 300 ev a center spot appears; at 500 ev the center spot is roughly of the same intensity as each of the other two spots; at 800 ev the center spot is roughly three times as intense as each of the other two spots. (This is not shown in the picture.) Above 300 ev, the spots are connected by bands. The ejection angle, relative to the surface normal, for the outer spots asymptotically approaches $45\pm2°$ for increasing bombarding ion energy, as Fig. 16 shows. This differs somewhat from the nearest neighbor ⟨111⟩ directions, which make an angle of 54.75° with the surface normal. At lower bombarding energy the angle increases beyond 54.75°.

FIG. 13. Deposit pattern in the $(1\bar{1}2)$ plane from the Fe (110) surface.

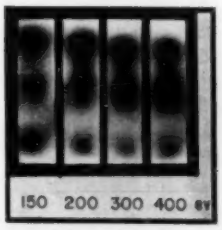

FIG. 14. Deposit patterns in the $(1\bar{1}0)$ plane from the Fe (111) surface.

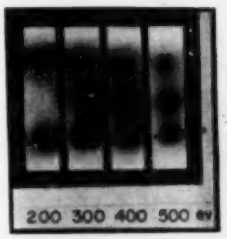

FIG. 15. Deposit patterns from the Ge (100) surface in the (011) plane.

The Ge (110) surface has, of course, twofold symmetry and hence requires examination in at least two planes. Figure 17 shows patterns obtained in the $(1\bar{1}0)$ plane for bombarding ion energies ranging from 200—800 ev. Two spots appear which are connected by a heavy band at higher energy, but no defined center spot appears. The ejection angle (with respect to the surface normal) as a function of bombarding energy is shown in Fig. 18. At high ion energies this angle asymptotically approaches $33\pm2°$. This is approximately the angle a nearest neighbor direction, ⟨111⟩, makes with

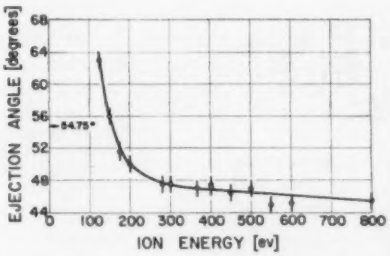

FIG. 16. Ejection angle vs ion energy for outer spots in Fig. 15.

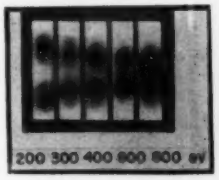

FIG. 17. Deposit patterns from Ge (110) surface in the $(1\bar{1}0)$ plane.

the surface normal (35.2°). This ejection angle is very sensitive to the angle of incidence as shown by the following experiment: One side of the target was protected by a graphite guard ring which insured normal ion incidence, while the other half was insulated with quartz, causing considerable oblique incidence as indicated in Fig. 19. The ejection angle at normal incidence, β, [shown in Fig. 19(b)] was 33°, while for oblique incidence the ejection angle α was only 23°. The deposit at A, which was due mainly to oblique incidence, was many times stronger than the deposit at B. This indicates that the sputtering rate for these energies ($\sim$600 ev) is substantially higher for oblique ion incidence than for normal incidence. A result which cannot be seen in the photograph of Fig. 17, but is often visible under conditions which are not yet quite clear, is that a second pair of rather diffuse spots appears at lower ion energy at an angle of about 64° from the normal. The position of these spots seems rather insensitive to the bombarding energy. These additional spots, whenever they appear, can be detected in the $(1\bar{1}0)$, $(\bar{1}11)$, and $(1\bar{1}1)$ planes for a (110) Ge target surface.

Deposit patterns from the Ge (110) surface in the (001) plane are shown in Fig. 20 for bombarding ion

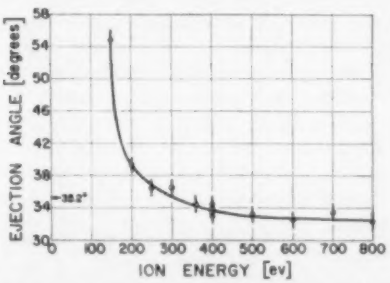

FIG. 18. Ejection angle vs ion energy for pattern in Fig. 17.

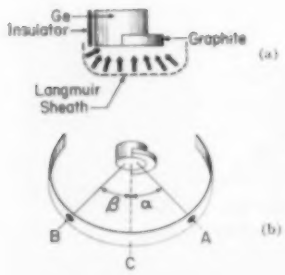

FIG. 19. Arrangement for determining the effect of angle of incidence.

FIG. 20. Deposit patterns from the Ge (110) surface in the (001) plane.

energies up to 800 ev. The crosswise band in the center of the pattern is the band connecting the spots in the $(1\bar{1}0)$ plane (Fig. 17). Figure 20 indicates that the spots come closer together at higher ion energy. Later experiments with more carefully controlled ion incidence, however, showed that the angle is actually rather insensitive to the bombarding ion energy. The spots appear to diverge at lower energies because of the additional spots in the $(\bar{1}11)$ and $(11\bar{1})$ planes. This detail cannot be seen readily in these pictures. Figure 21 shows that the average angle of the spots with respect to the surface normal is $39\pm2°$.

Figure 22 shows patterns obtained from the (111) Ge surface in the $(1\bar{1}0)$ plane. The center $[\bar{1}11]$ spot appears above 150 ev and increases in intensity with increasing bombarding energy. One well-separated round spot appears $59\pm2°$ from the surface normal (roughly corresponding to the $[11\bar{1}]$ direction). Its position is fairly independent of energy, as Fig. 23 shows, but it decreases in intensity relative to the center spot with increasing ion energy. The other spot, on the opposite side of the surface normal, was $47\pm2°$ from the surface normal (roughly corresponding to the [001] direction). Its position again is fairly independent of ion energy, but it is stronger than the 59° spot and is connected with the center spot by a heavy band. The angle of incidence seems to have minor influence on these patterns, as some experiments made without a guard ring indicate.

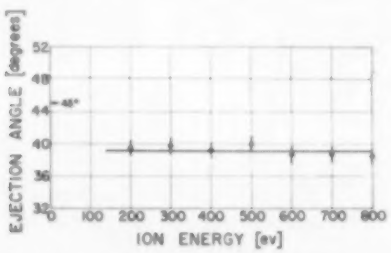

FIG. 21. Ejection angle vs ion energy for pattern in Fig. 20.

Some preliminary results have been obtained in bombardment studies with other gases including argon, neon, and helium. In general, one can say that the patterns have at comparable yields a close similarity with those collected under Hg^+ ion bombardment. This even holds for such a light gas as helium. A more detailed discussion of results in other gases will be postponed until more experimental results have been collected.

DISCUSSION OF RESULTS

Most of the existing theories of sputtering do not predict the observed dependence on crystallographic direction of the sputtering from single crystals. In fact, the only attempt to explain atom ejection patterns was made by Henschke.[10,11] In sputtering, a directional reversal of momentum is necessary to eject an atom from the surface. Henschke assumes that the ion is reflected from a lower surface atom and subsequently, on its return path, ejects a surface atom. An experimental fact is that a material like Be with atomic weight 9 is sputtered quite readily by Hg^+ ions with atomic weight 200. To account for sputtering in such cases where the bullet has a much higher mass than the target atom, Henschke refers to "target atoms acting like a solid wall," or, in other words, a much higher effective mass causing the impinging ion to be reflected. If this were true, then one should, of course, also expect reflection of "neutralized"

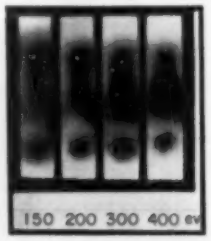

FIG. 22. Deposit patterns from the Ge (111) surface in the (110) plane.

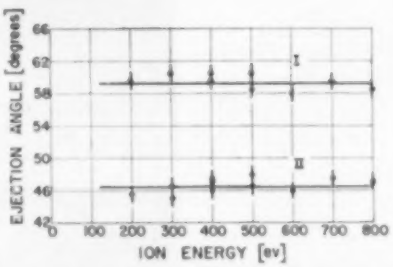

FIG. 23. Ejection angle vs ion energy for patterns in Fig. 22.

[10] E. B. Henschke, J. Appl. Phys. **28**, 411 (1957).
[11] E. B. Henschke, Phys. Rev. **106**, 737 (1957).

ions from the outermost atom layer, and consequently expect accommodation coefficients for ions on metal surfaces to be less than unity. It has been established, at least for Hg^+ ions, that this is not the case.[12] Hg^+ ions are fully accommodated, i.e., they come completely into thermal equilibrium with the target surface and are not reflected with a kinetic energy sufficient to separate atoms from the surface. The crucial condition which determines whether one must treat the impacts as consecutive two-particle collisions or as a collective simultaneous collision with an assembly is obviously whether the collision time proper is longer or shorter than the time necessary to bring the other neighboring atoms into play. In a hard sphere model, with the core diameters considerably smaller than the distance between atoms in the lattice, one can treat the impacts as consecutive two-particle collisions. Langberg[13] has shown that, even for the much softer Morse potential interaction between atoms, one need consider only two-body collisions in our energy range. The binding energy of atoms, which is weak in comparison with the kinetic energy which may be transferred, cannot change this picture. Of course this concept of sputtering by reflected ions may well be an acceptable mechanism for the case in which the mass of the incident ion is much less than the mass of a target atom.

A large "effective mass" resulting from "piled up" atoms would, indeed, not only preclude the possibility of focusing collisions, but also radically change many of the accepted concepts in radiation damage theory. Furthermore, Thompson[6] observed that atoms were sputtered in close packed directions from the far side of a single-crystal Au foil when bombarded with high energy protons on the front side. This experiment certainly does not support the "solid wall" effect.

There is, of course, no difficulty in accounting for the momentum reversal in a model of consecutive two-particle collisions as soon as more than two particles become involved.

The most valuable assistance in these problems comes from the field of radiation damage. Keywell[14] and Harrison[15] introduced radiation damage concepts in sputtering considerations without, however, taking crystal structure and anisotropies into account. Accordingly, a sputtered atom is the result of a radiation damage event in the surface vicinity, and sputtering becomes closely linked to displacement and replacement energies in a crystal lattice.

It has been shown by Silsbee[16] that momentum will be focused into straight close-neighbor rows of hard spheres so long as the ratio of sphere diameter to sphere spacing is not too small. Hence, the process becomes highly anisotropic and energy can be transferred over a considerable distance along close packed crystallographic directions (Leibfried[17]). Recently, Vineyard and others[7] calculated that focusing is also possible, although with less efficiency, in directions which are not close-packed directions if neighboring atoms are taken into consideration.

Before discussing the experimental results in detail, let us summarize the most important observations for normal Hg^+ ion incidence in metals. The situation in Ge will be discussed separately.

1. Atoms are preferably ejected in close-packed directions. This is true independent of the degree of surface roughness or of the surface configuration. It does not matter, for instance, if the crystal has the form of a sphere or if one sputters from a plane surface.

2. At higher ion energy, additional ejection directions appear which are next-nearest neighbor directions. In a less closely packed metal like bcc Fe, these directions appear at lower ion energy than in the fcc metals. Spots corresponding to these directions tend to be more diffuse than those corresponding to the close-neighbor directions.

3. At very low ion energy only those directions appear which require the least directional change of momentum, i.e., those which are very oblique to the surface. At higher ion energy more material is ejected in those (either nearest neighbor or next-nearest neighbor) directions which are closer to the surface normal.

4. The deposit spots have characteristic shapes, especially at low ion energy (for instance, the kidney-shaped spots from a {111} fcc surface). These spots become rounder and better defined at higher energy.

5. Certain spots are often connected by characteristic bands.

6. Comparing different metals of the same crystal structure, like Cu, Ni, and Au, reveals a close similarity of pattern appearances at the same sputtering yield (which requires, of course, different ion energies).

7. Patterns from a fcc {111} surface sometimes show additional spots forming a sixfold symmetrical pattern.

8. The spots have, in general, a tendency to deviate somewhat at low ion energy from the close-neighbor directions in a direction away from the surface normal.

9. The few observations in other gases so far seem to indicate that different rare gas ions, including He, give patterns similar to those obtained in Hg.

These observations lead to the following conclusions: The ejection of atoms in close-neighbor directions can be considered to be direct experimental evidence of the fact that energy is transferred most efficiently along closely packed rows of atoms (Silsbee focusing collisions). Less efficient, but nevertheless clearly visible at higher ion energy (in particular in the less closely packed bcc lattice), are the focusing collisions in next-nearest neighbor directions. This was predicted and discussed by Vineyard[7] and by Thompson.[18] It requires

[12] G. K. Wehner, J. Appl. Phys. **31**, 1392 (1960).
[13] E. Langberg, Phys. Rev. **111**, 91 (1958).
[14] F. Keywell, Phys. Rev. **97**, 1611 (1955).
[15] D. Harrison, Jr., Phys. Rev. **102**, 1473 (1956); **105**, 1202 (1957).
[16] R. H. Silsbee, J. Appl. Phys. **28**, 1246 (1957).
[17] G. Leibfried, J. Appl. Phys. **31**, 117 (1960).
[18] M. W. Thompson, Nucleonics **18**, 135 (1960).

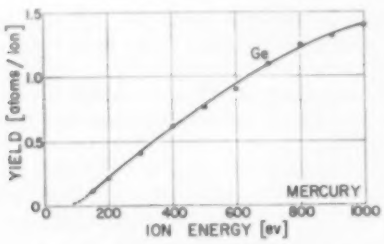

FIG. 24. Sputtering yield for Ge in Hg.

less energy to push an atom on a {100} surface in a direction normal to the surface through the barrier of four surrounding atoms in the bcc lattice than it does in the fcc lattice, because the barrier atoms are less closely spaced in the bcc system. At very low ion energy only the most favorable collisions lead to a sputtered atom. Favorable processes are those which require the least number of atom collisions for achieving a momentum reversal by more than 90°. In this case sputtering is strictly a surface phenomenon, with probably only the two or three outer layers involved, and with collisions in which not more than a few atoms participate. The least directional change of momentum under these circumstances naturally becomes the most favorable possibility for a successful removal of an atom from the surface. With the small number of collisions involved, focusing plays no major part, and the characteristic shape of certain spots, their connecting bands, and the small deviations of the spots from the close-neighbor directions, can be explained by considering the details of the collision possibilities. In this general picture it is not surprising that those spots which correspond to the next-nearest neighbor directions tend to be more diffuse. At higher ion energy the depth of action and the number of atoms which become involved in collisions leading to sputtered atoms increases. In fact, one must assume that the (neutralized) ion penetrates below the surface and that the center of activity has shifted deeper within. From this center, the shortest path to the surface along a direction in which focusing occurs has the highest probability of leading to a sputtering event. Consequently, all those nearest neighbor or next-nearest neighbor directions which are closer to the surface normal become the preferred ones for sputtering. Atoms of different target materials have different electronic structures; thus it takes different energies to make them behave alike or to cause equal sputtering yields and similar ejection patterns.

The sixfold symmetrical pattern which appears at higher ion energy from a {111} fcc surface was unexpected. Such a pattern can arise only from a hcp base plane surface, or from a fcc target with crystallites which have their {111} planes in the surface but are oriented to each other in twin positions. We are inclined to believe that, under higher ion energy bombardment, the surface layers become disoriented in such a way that many surface atoms appear in twin positions. There are indications that this "damage" can be annealed out at higher target temperature fast enough so that a subsequent ion finds again an undistorted single crystal (111) fcc surface. It is of interest to note that the (100) or (110) patterns show no indications of such "damage," a fact which is not surprising inasmuch as these surfaces do not offer alternate atomic positions, as do the closely packed (111) planes.

DISCUSSION OF GERMANIUM RESULTS

The much greater variety of observations for Ge requires a more detailed discussion. Ge, with the more open diamond structure, contains no straight close packed rows of atoms, as a consequence of covalent bonding. It should be emphasized that in the whole range of bombarding ion energies studied here, the average sputtering yield, as shown in Fig. 24, stays below 1.5 atoms per ion. Thus, only the more favorable impacts lead to a sputtered atom. At high bombarding energies, sputtering may be anticipated to proceed preferably in ⟨111⟩ directions. It appears not impossible that some focusing may be accomplished in the same way as in fcc or bcc next-nearest neighbor directions by the "lens effect" of the six neighbors surrounding a ⟨111⟩ direction. However, the details in the ejection patterns lead us to believe that under bombardment so many interstitials, either Ge or Hg, are formed, that the atom arrangement near the surface of the Ge crystal more closely resembles a bcc lattice. Such an explanation would at least remove the difficulty in accounting for the observed focusing, and explain the striking similarity between the bcc and Ge patterns.

1. (100) Target Surface; Collector in the (011) Plane

Here we notice that the ejection angle of the two symmetrical spots (corresponding roughly to the ⟨111⟩ directions in bcc Fe) decreases substantially with increasing ion energy and asymptotically approaches an angle of 45° at higher energy. The ⟨111⟩ nearest neighbor directions, however, make an angle of 54.75° with the surface normal. The strong increase of the ejection angle with decreasing ion energy is possibly a result of the bonding of the ejected surface atom to its other nearest neighbor, which causes the ejected atom to be pulled toward the surface. This would naturally become more pronounced for lower ejection energy. At high energy the bonding energy becomes small with respect to the energy of the ejected atom, and this effect disappears.

The center spot, which appears very pronouncedly at energies above 300 to 400 ev, was unexpected. Such a center spot appeared, as discussed above, for an Fe {100} surface, corresponding to a next-nearest neighbor direction. For the undistorted Ge structure, however, neighbors in this direction would be a full lattice con-

stant apart (roughly 2.3 times nearest neighbor distance), and so it is unlikely that such a well pronounced spot could arise. Furthermore, no focusing process seems likely. We are more inclined to believe that many atoms in and near the surface are pushed under the bombardment into interstitial positions such that (as in the bcc system) fairly close neighbors arise in the direction normal to the target surface. The center spot appears only at higher ion energy because the action must come from deeper inside, and more atomic collisions are necessary to accomplish the full 180° momentum reversal. The connecting bands are probably a result of the same collisions, because they appear together with the center spot, and it is likely in this case that this longer distance collision causes scattering in the directions observed.

2. (111) Target Surfaces

One spot appears fairly independent of ion energy at an angle of 59° from the surface normal, and is to be compared with a ⟨111⟩ direction which makes an angle of 70.5° with the surface normal. This spot is the most pronounced at low ion energy because it requires the least directional change of momentum. The atom is probably ejected rather energetically in this direction. Thus, the binding energies are probably so small, compared with ejection energies, that the ejection direction remains fairly insensitive to the ion energy.

The center spot, corresponding to the nearest neighbor [111] direction, appears only at higher energy when the action comes from deeper inside. At very high energy this direction represents the shortest path from a collision center to the surface, and the corresponding spot then becomes the most pronounced one.

The other spot appearing on the opposite side of the surface normal at 47° again requires interstitials for its explanation. These interstitials, which make the surface layers appear bcc, would provide the necessary next-nearest neighbor direction (at 55° from the normal) to account for this spot. The 8° deviation of this spot in the direction of the surface normal is probably due to the ejection atom's having received its impact from somewhat more underneath than would correspond to a ⟨100⟩ direction. As in the case of Fe, a heavy band arises in connection with a next-nearest neighbor collision when the impact comes from further underneath.

3. (110) Surface

a. ($1\bar{1}0$) Plane

The main spots approach an angle of 33° at higher ion energy. This angle agrees fairly well with the angle of 35° which a nearest neighbor ⟨111⟩ direction makes with the target surface. At low ion energy this angle increases substantially, possibly again caused by the bonding to the neighboring atoms.

b. (001) Plane

The explanation of the two elongated spots appearing 39° from the surface normal again requires the concept of interstitial atoms. These provide the next-nearest neighbor directions, just as in a bcc lattice, 45° from the normal. The spots are more diffuse and elongated because the collisions are not in nearest neighbor directions and the ejected atoms may receive an impact from more underneath.

c. Additional Spots

Some very peculiar pairs of spots appear at low ion energy at ~64° from the surface normal in the ($1\bar{1}0$), ($\bar{1}11$), and ($1\bar{1}1$) planes. Such spots can neither be explained with an ideal Ge structure nor with the interstitials, as discussed above. We propose another explanation as follows: On a (110) surface, one can see groups of three dangling bonds directed upward and toward each other as a result of the tetrahedral bonding. The surface atom could be bound to those three atoms in a position slightly above the plane of these atoms. Here, then, will be six new directions of fairly close neighbors which would correspond to the six 64° spots appearing in the pattern.

FUTURE OUTLOOK

The general picture presented above seemed to us to be the most consistent and most likely. There are many details, however, which remain unanswered. Why are certain ejection angles in Ge so sensitive to ion energy or the angle of incidence? What is the nature of the interstitials (Hg or Ge) which we have found necessary to assume for Ge?[19] It will be necessary to devise better controlled experiments for studying the influence of target temperature. Studies should be extended to other crystal systems like hcp. In this case, it will be of interest to see if, at higher energy, those spots which correspond to the nearest neighbor directions in the base plane come out much stronger than those corresponding to the zigzag rows out of the base plane.

ACKNOWLEDGMENTS

The skillful help of Roger Moseson in the experiments, crystal preparation, and photography, and of Emil Benz and Arthur Haut in the glass work and tube construction is gratefully acknowledged.

[19] *Note added in proof.* Later experiments with rare gas sputtering have shown that such interstitials are not Hg.

Letters to the Editor

Damage in UO_2 Films and Particles During Reactor Irradiation

T. K. Bierlein and B. Mastel*
General Electric Company, Hanford Atomic Products Operation, Richland, Washington
(Received August 19, 1960)

TRANSMISSION electron microscopy of thin UO_2 films irradiated to low exposures has disclosed the presence of fission fragment trajectories.[1,2] With increased exposure, the accumulated damage is sufficient to cause marked changes in the originally homogeneous thin films.

Approximately 100 A-thick films were prepared by vacuum evaporation of weighed chips of either reactor grade uranium or sintered UO_2 onto a carbon substrate, which in turn was supported on a standard electron microscope grid. Capsules containing the fims were irradiated in a special test position of a Hanford reactor at a maximum ambient temperature of 60°C. After irradiation, the specimens were examined directly by transmission electron microscopy and diffraction.

Microstructural changes in thin films of evaporated UO_2 irradiated in an air environment are illustrated in Fig. 1. Exposures in the range of 1 to 2×10^{16}nvt show typical fission fragment paths. After an exposure of 3.9×10^{17}nvt, fission fragment trajectories are still discernible, but localized regions of the film have become opaque to the electron beam. Small areas of the carbon substrate are completely free of UO_2, as is made evident by the high electron density in the transmitted beam. At higher exposures, 1.6×10^{18}nvt, the opaque regions become larger in size. Shadowing of the film shows these opaque regions to be flocculent outgrowths. At the highest exposure, 4.4×10^{19} nvt, the UO_2 has aggregated into isolated outgrowths on the carbon, with little material remaining in intimate contact with the substrate. The changes in the originally homogeneous film suggest either a surface migration of atoms or a chemical reaction with the air environment during reactor irradiation. Electron diffraction studies of these films show changes in line intensities and slight changes in interplanar spacing as a function of the irradiation. After an exposure of 3×10^{18}nvt, no sharp diffraction pattern was obtained. After a higher exposure to 4.4×10^{19}nvt, a sharp diffraction pattern was again obtained. The diffraction changes may be explained on the basis of destruction of crystallinity during irradiation to a critical exposure, after which additional exposure restores crystallinity. An alternate explanation, of course, is the possibility that the physical form of the UO_2 is not suitable for diffraction.

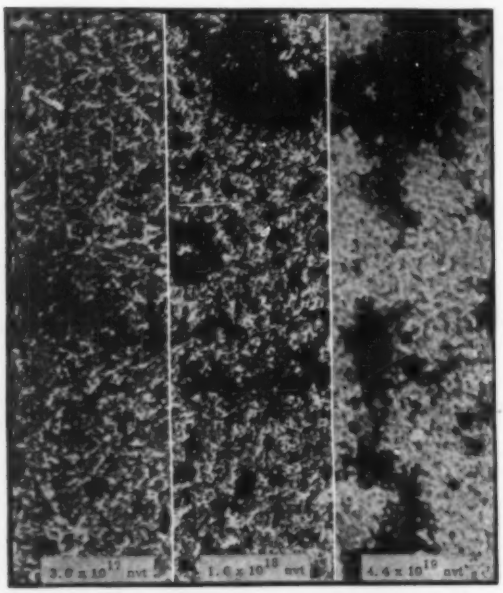

FIG. 1. Microstructural changes in thin films of evaporated UO_2 irradiated in an air environment. 25 000 X.

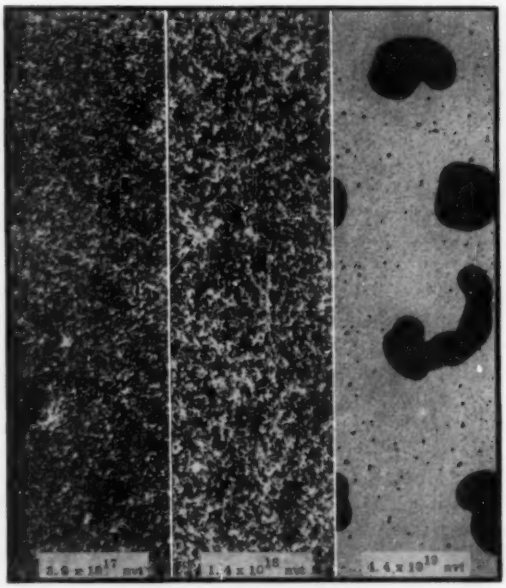

FIG. 2. Microstructural changes in thin films of evaporated UO_2 irradiated in vacuum. 25 000 X.

Similar films irradiated in evacuated capsules to low level exposures show fission fragment paths identical to those observed in films irradiated in capsules containing air. At an exposure of 3×10^{17}nvt (Fig. 2), the fission fragment paths are discernible and no gross transport of UO_2 has occurred. Growth of the crystallites begins at an exposure of approximately 1.4×10^{18}nvt, with small areas of the substrate being free of UO_2. Mass transport of UO_2 over the substrate is less than was the case in an air environment. After an exposure to 4.4×10^{19}nvt, the UO_2 is present as isolated dense filaments which also emanate from the supporting carbon substrate, but small dense particles on the substrate still exist. Electron diffraction patterns of films irradiated in vacuum are normal until the highest exposure of 4.4×10^{19}nvt is reached; then only broad diffuse lines appear.

Since the irradiated 100 A-thick films have a large surface to volume ratio and relatively poor bulk heat transfer properties, surface temperatures in the vicinity of a fission fragment may be quite high. Irradiation experiments were, therefore, conducted on particles of UO_2 one to two microns in diameter dispersed in a thin film of aluminum. Irradiations in evacuated capsules produced no change in the dispersed particles up to an exposure of 5×10^{17}nvt. After higher exposures (up to 4.4×10^{19}nvt) the particles became smooth and rounded; no evidence of UO_2 condensation on the aluminum film by either electron microscopy or diffraction was obtained. Irradiation in air-filled capsules, however, did give rise to UO_2 condensation on the aluminum film after exposures to 5×10^{17}nvt, as shown by microscopy and diffraction.

After higher exposures, 4.4×10^{19}nvt, the original particles disappeared and flocculent crystals, similar to those which form during equivalent air irradiations of 100 A-thick UO_2 films, appeared on the aluminum.

A comparison of the behavior of UO_2 films and particles irradiated in air and vacuum environments shows that (1) UO_2 is more stable during irradiation in vacuum than in air, and (2) UO_2 which has migrated and condensed takes on the form of dense, relatively smooth particles when irradiated in vacuum, whereas in air the condensed particles are flocculent aggregates. The relative importance of such parameters as thermal conductivity, vapor pressure, chemical reactivity, plastic deformation, density, and volume of material on the damage sustained by reactor fuel material must be established by critical irradiation and post-irradiation experiments. Since the damage sustained by UO_2 particles and films is due primarily to repeated fission events occurring in a given small volume of material, it is essential that the consequences of energy dissipation associated with a single fission event be understood. Investigation of individual fission events, such as those reported by Noggle and Stiegler, will contribute greatly to the understanding of radiation damage.

* Work performed under contract between the U. S. Atomic Energy Commission and General Electric Company.

[1] T. S. Noggle and J. O. Stiegler, J. Appl. Phys. **31**, 2197 (1960).

[2] T. K. Bierlein and B. Mastel, Hanford Atomic Prods. Operation Rept. HW-61656, printed by U. S. Atomic Energy Comm. (September 9, 1959).

Fission Fragment Damage in Nonfissionable Thin Films

T. K. Bierlein and B. Mastel*
General Electric Company, Hanford Atomic Products Operation, Richland, Washington

(Received August 19, 1960)

THIS communication describes a technique for observing and characterizing fission fragment damage in thin films of nonfissionable material. It has been established[1,2] that electron microscopy can disclose fission fragment tracks in thin films of irradiated UO_2; such tracks manifest themselves as spots or lines of high electron transmission in the image. Since the contrast arises from differences in electron scattering power in the film, the paths are assumed to be regions from which UO_2 has been removed.

Multilayered films containing regions free of UO_2 yield additional information on the interaction of fission fragments with material. A thin film of the material to be studied is evaporated or sputtered onto a carbon substrate supported by a conventional microscope grid. A double film of this type is then sprayed with a dilute aqueous suspension of polystyrene latex spheres, and the film is then coated with UO_2 by shadow casting at an angle of 15°. This technique yields discrete regions behind the polystyrene spheres which contain no fissionable UO_2. Multilayered films prepared in this manner have been irradiated with thermal neutrons and examined in the electron microscope.

Figure 1 shows the appearance of a multilayered film of UO_2-Pt-C and UO_2-ZrO_2-C after an exposure of 2×10^{18}nvt, thermal. A fission fragment originates in the UO_2 near the shadow region, the region containing no UO_2, and then travels through the shadow region. It is quite evident that the electron scattering power of the composite film along the fission fragment path has changed. Close examination of the fission fragment path in the platinum thin film discloses discrete perforations along the path length. These perforations may result from vaporization of material at localized points. Shadowing such films shows the topography of the track to be a perforated ridge. This suggests that deformation, as well as vaporization, has occurred along the path of the fission fragment. The fission fragment damage in thin films of zirconium dioxide is characterized by a more regular path of high electron transmission. The path is uniform in width throughout its length, in contrast to the wide perforations present along the paths found in platinum. Shadowing the zirconium dioxide film, however, discloses nodular imperfections superimposed on the track. The topography of the exposed, free surface of the film is identical to that obtained by first dissolving the UO_2 originally present, and then shadowing the original UO_2 material interface.

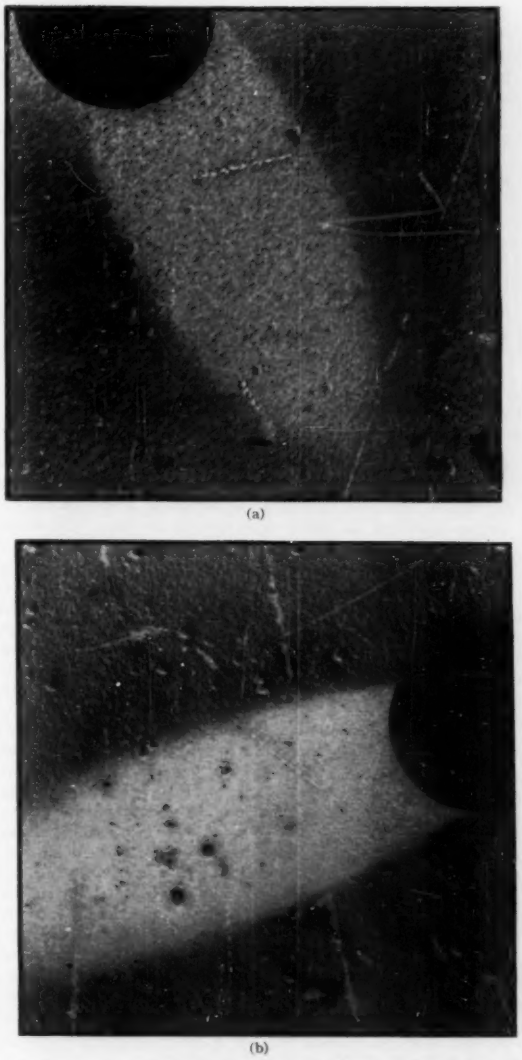

(a)

(b)

FIG. 1. Fission fragment tracks in multilayered films containing regions in which UO_2 is absent. Transmission electron micrographs, 25 000 X. (a) UO_2-Pt-C multilayered film. (b) UO_2-ZrO_2-C multilayered film.

The observed differences in behavior must be due to differences in chemical reactivity, thermal conductivity, plastic deformation, density, and the thickness of the constituent layers in the multilayered films. The importance of these factors on the registration of fission fragment damage in films and foils as revealed by transmission electron microscopy is being investigated. Fission fragment tracks have been observed in evaporated multilayered films of carbon, aluminum, silicon dioxide, and germanium. It is hoped

that the study of the fission fragment tracks themselves, the surface topography in regions free of fissionable material, as well as the surface topography of the UO_2 material interface, will provide fundamental information on the nature and extent of radiation damage in various materials.

* Work performed under contract between the U. S. Atomic Energy Commission and General Electric Company.

[1] T. S. Noggle and J. O. Stiegler, J. Appl. Phys. **31**, 2197 (1960).

[2] T. K. Bierlein and B. Mastel, Hanford Atomic Prods. Operation Rept. HW-61656, printed by U. S. Atomic Energy Comm. (September 9, 1959).

Noise Figure and Gain of Parametric Converters

H. HEFFNER
Electrical Engineering Department, Stanford University, Stanford, California
AND
G. WADE
Spencer Laboratory, Raytheon Company, Burlington, Massachusetts

(Received August 4, 1960)

SEVERAL people have called attention to an error in one of the thermal noise terms of our noise figure equation for a parametric frequency converter.[1] In particular, Professor van der Ziel has published the correct expression for this term.[2] One of our purposes here is to correct the remaining terms of the equation. These terms are due to noise current emanating from the variable element and to noise fluctuations in the value of the variable element. A second purpose is to point out the applicability of the noise, gain, and bandwidth analyses cited in footnote 1 to the nonregenerative converter, even though the model analyzed was a regenerative converter. A third incidental purpose is to note two typographical errors in the noise figure equation of the reference in footnote 1 for the regenerative parametric amplifier.

In footnote 1, the noise figure equation for the frequency converter was derived from inspection of that for the amplifier. The derivation assumed that both noise and signal powers in the input and idler tanks always convert from one tank to the other in the same way. Hence, corresponding noise figure terms were taken to be the same in the converter as in the amplifier (with the exception of a slight modification in one of the terms to exclude noise generated in the load). This assumption is incorrect. For any given flow of current, the corresponding voltages generated across the two tanks are related to each other in a way that depends on whether the given current is at the input or the idler frequency. The incorrect assumption led to an error (by an amount involving the factor G_{T1}/G) in several of the terms of the converter noise figure equation. The correct expression is readily derived by the procedure in Appendix II of the work cited in footnote 1, giving the noise figure for the amplifier. Using the symbols of footnote 1, we can write the correct expression as follows:

$$F_{\text{conv}}=1+\frac{G_1}{G_g}+\left(\frac{G_{C2}}{G_{T2}}\right)\frac{G_{T1}{}^2}{G_gG}\frac{\omega_1}{\omega_2}+\frac{1}{4KTBG_g}\left[\langle i_s{}^2\rangle+\langle i_4{}^2\rangle\frac{G_{T1}{}^2}{G_{T2}G}\frac{\omega_1}{\omega_2}\right]$$
$$+\frac{S_i}{N_i}\frac{\text{conv gain}}{4}\frac{\omega_1}{\omega_2}\frac{G_{T2}}{G_g}\left[\frac{(G_{T1}{}^2+G^2)}{G_{L2}G}\langle\rho^2\rangle+\frac{G_{T2}\omega_1}{G_{L2}\omega_2}\langle\sigma^2\rangle\right.$$
$$\left.+\frac{G_{T1}{}^2}{G_{T2}G_{L2}}\frac{\omega_2}{\omega_1}\langle\alpha^2\rangle+\frac{(G_{T1}-G)^2}{G_{L2}G}\langle\beta^2\rangle\right]. \quad (1)$$

The first three terms represent the thermal noise contributions which, for many forms of the converter, are the most important terms. The next two terms are the result of mean-square noise currents $\langle i_s{}^2\rangle$ and $\langle i_4{}^2\rangle$ introduced by the variable element at frequencies ω_1 and ω_2, respectively. The remaining terms represent signal-dependent noise caused by mean-square fractional fluctuations in the value of the variable element $\langle\rho^2\rangle$, $\langle\sigma^2\rangle$, $\langle\alpha^2\rangle$, and $\langle\beta^2\rangle$ at frequencies ω_3, $2\omega_1$, $2\omega_2$, and $\omega_2-\omega_1$, respectively.

The second purpose of this letter is to point out the applicability of the noise, gain, and bandwidth analyses in the work cited in footnote 1 to the nonregenerative upconverter. The model actually analyzed is a regenerative converter in which the pump frequency equals the sum of the idler and signal frequencies ($\omega_2=\omega_3+\omega_1$). For the nonregenerative or upper-sideband upconverter, the pump frequency equals the difference between the idler and signal frequencies ($\omega_2=\omega_3-\omega_1$). The noise, gain, and bandwidth expressions for the nonregenerative converter can be obtained from the corresponding expressions for the regenerative converter (as given in footnote 1) simply by replacing ω_1 with $-\omega_1$. For example, consider the conversion gain at resonance. For the regenerative converter we have[1]:

$$\text{resonance conversion gain}=G_{T2}\,\omega_1/(G_{T1}-G)^2, \quad (2)$$

where

$$G=\frac{\omega_1\omega_2C_x{}^2}{4G_{T2}}.$$

The substitution of $-\omega_1$ for ω_1 has the effect of changing the former effective negative conductance, $-G$, into a positive conductance. However, the sign of the gain expression remains positive because the numerator involves the product of G and the frequency ratio. In essence, the only effect of replacing ω_1 by $-\omega_1$ in the gain expression is to change the denominator from the square of the difference between two positive numbers to the square of the sum of two positive numbers. As seen in Eq. (1), the noise figure is changed only in the last term.

Our third purpose is to correct two typographical errors in the noise figure equation of the work cited in footnote 1 for the amplifier. Both of the errors occur in the signal-dependent terms. The correct noise figure equation is

$$F=1+\frac{G_1}{G_g}+\frac{G}{G_g}\frac{\omega_1}{\omega_2}+\frac{1}{4KTBG_g}\left[\langle i_s{}^2\rangle+\langle i_4{}^2\rangle\frac{G}{G_{T2}}\frac{\omega_1}{\omega_2}\right]$$
$$+\frac{S_i}{N_i}\frac{\text{gain}}{4}\frac{G}{G_g}\left[\frac{G}{G_L}2\langle\rho^2\rangle+\frac{G_{T2}}{G_L}\frac{\omega_1}{\omega_2}\langle\sigma^2\rangle+\frac{G}{G_{T2}}\frac{G}{G_L}\frac{\omega_2}{\omega_1}\langle\alpha^2\rangle\right]. \quad (3)$$

[1] H. Heffner and G. Wade, J. Appl. Phys. **29**, 1321 (1958).

[2] A. van der Ziel, J. Appl. Phys. **30**, 1449 (1959).

Ferromagnetic-Antiferromagnetic Interaction in Fe-FeS

J. H. GREINER, I. M. CROLL, AND M. SULICH
International Business Machines Corporation, Federal Systems Division, Owego, New York

(Received July 11, 1960; and in final form August 19, 1960)

EXCHANGE anisotropy effects[1] unidirectional properties, and a nonvanishing rotational hysteresis at high fields have been observed for compacts of fine sulfide coated iron particles. A $\sin\theta$ variation of the torque and a nonvanishing value of the rotational hysteresis for applied magnetic fields greater than $2K/I_s$ were found for samples cooled in a magnetic field from the Néel temperature of FeS (613°K). Samples cooled in a demagnetized state displayed no measurable change of torque with angle.

Torque curves were measured at 300° and 77°K. The measuring field was varied from 1000 to 6000 oe on samples cooled in 8000 oe

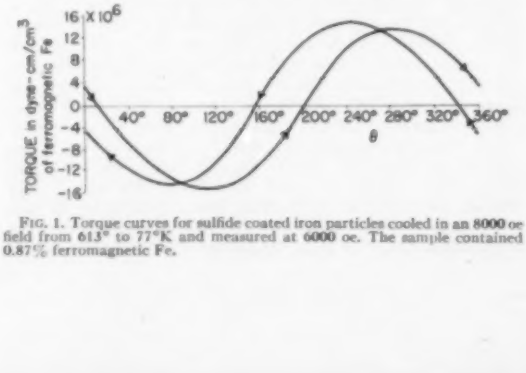

FIG. 1. Torque curves for sulfide coated iron particles cooled in an 8000 oe field from 613° to 77°K and measured at 6000 oe. The sample contained 0.87% ferromagnetic Fe.

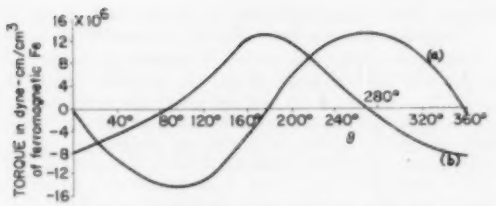

FIG. 2. (a) The average torque curve of Fig. 1 for both directions of rotation; (b) the difference in the torque curves of Fig. 1; counter clockwise minus clockwise, which gives a rotational hysteresis of 3.9×10^6 ergs/cm³ of Fe/cycle.

fields. The average torque increased with decreasing temperature and with increasing field. The maximum average torque at 1000 oe, for a decrease in the cooling temperature of 300° to 77°K, increased from 5.5×10^5 to 9.8×10^5 d-cm/cm³ of ferromagnetic Fe for a sample containing 4.5% ferromagnetic Fe. At 77°K, for an increase of measuring field of 1000 to 6000 oe, the maximum average torque increased from 1.2×10^6 to 7.3×10^6 d-cm/cm³ of ferromagnetic Fe for a sample containing 2.9% ferromagnetic Fe. Exchange anisotropy effects were also present when samples were measured in fields greater than the cooling field, e.g., when cooled in a 1000 oe field, a sample containing 2.9% ferromagnetic Fe with no magnetic history had a $\sin\theta$ dependence of torque, $T_{max}=2.9\times10^6$ d-cm/cm³ of ferromagnetic Fe for a measuring field of 6000 oe at 77°K.

Sixty-cycle *B-H* loops measurements at 300°K and 1000 oe showed asymmetric loops with up to 15% shift of the coercive force. Torque curves for a sample containing 0.87% ferromagnetic Fe measured at 77°K and 6000 oe are shown in Figs. 1 and 2.

Fine sulfide coated particles of iron, formed both by electrodeposition into mercury and by reduction precipitated iron formate, exhibited exchange anisotropy effects. The sulfide coating was applied by reacting the fine iron particles with H_2S between 420° and 620°K. The increase in weight was monitored by a quartz spring balance in the reaction tube. The uptake of sulfur gave an iron-rich composition. The amount of ferromagnetic material was determined by a Faraday balance and reported as percent Fe.

[1] W. H. Meiklejohn and C. P. Bean, Phys. Rev. **105**, 904 (1957).

Effect of Aging Time After Cleavage on the Plasticity of MgO Single Crystals

CARL A. STEARNS
Lewis Research Center, National Aeronautics and Space Administration, Cleveland, Ohio

(Received August 11, 1960)

A NUMBER of investigators have reported that they observed no change in the ductility of magnesium oxide single crystals with time after cleavage.[1,2] However, recent observations made at the Lewis Research Center definitely confirm the time effect on ductility previously reported for MgO.[3,4] The purpose of this note is to present these observations and to point out some factors that might explain the disparity among observers.

MgO single crystals were tested in bending under four-point loading. The tests were run at a constant deflection rate of 0.01 in/min in a bending apparatus described previously.[5] All bend specimens were cleaved by hand from random size pieces of a single melt of 99.999% pure MgO purchased from Semi-Elements, Inc. Some specimens were tested immediately after cleavage (i.e., the freshly cleaved tension and compression faces were at most 30 sec old when the test was started), while others were allowed to age for various times in air.

Results representative of about 25 such tests are presented in Fig. 1. The four curves shown in the figure actually demonstrate

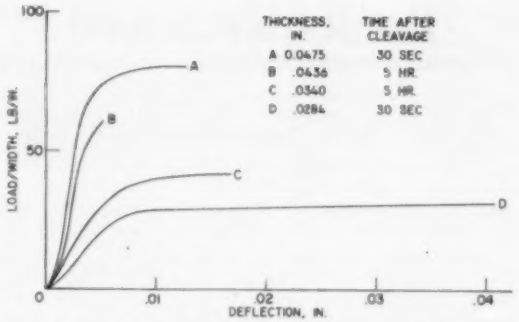

FIG. 1. Load deflection curves for as-cleaved magnesium oxide single crystals, showing time and size effects on ductility.

two phenomena: (1) a size effect on ductility, and (2) a time effect on ductility. A comparison of curves A with D, and B with C reveals that in either time range the thinner specimen is the more ductile. Likewise, comparing curves A to B and D to C shows that in either thickness range, the specimens tested within 30 sec after cleavage are considerably more ductile than the specimens tested 5 hr after cleavage. Tests run at intermediate times (not shown on the graph) lead one to conclude that the greatest change in ductility occurs within 30 sec after cleavage. Very little change, if any, is noted between 1 min and 5 hr.

One can now explain the discrepancy noted among observers concerning the time effect. First, for this effect to be seen, some tests must be performed immediately after cleaving. Second, the comparison of ductility must be made on specimens of comparable thickness, or else the size effect can mask the effect being studied.

It has been reported that protection of a freshly cleaved specimen of MgO from air does not inhibit the rate of loss of ductility with time after cleavage.[4] It should be pointed out that MgO is probably more reactive with the constituents of the air than NaCl, and since the MgO was cleaved in air before being stored in a protective material, an explanation of the time effect based on the reaction of surface layers is still quite plausible. An alternate explanation is suggested by recent dislocation etch pit studies on NaCl.[6] These studies have revealed that dislocations produced during cleavage move for some time after the cleavage force has been removed. This fact could be taken to indicate that the observed time effect is really a manifestation of an annealing process involving the fresh dislocations produced by cleavage.

The size effect observed in MgO crystals can also be explained in terms of dislocations produced during cleavage. In thin specimens the fresh dislocation loops extend well into the bulk and often completely through the specimen. These dislocations contribute to plastic deformation at low stresses and also act as nucleation sites for multiplication. When fresh dislocations do not extend appreciably into the bulk of the crystal as in thick specimens, there is a relatively thick band through the middle of the crystal that is void of centers from which plastic deformation can emanate. This explanation may also hold for the size effect observed in NaCl.[6] Attempts to examine the size effect for NaCl in detail, however, have been unsuccessful because some bending always occurs in the process of cleaving reasonably thin specimens of suitable length (about 40 mm) for bend testing.

The author is indebted to Dr. Robert A. Lad for many valuable discussions.

[1] P. J. Anderson and F. J. P. Clarke, "Some factors affecting the ductility of MgO," Atomic Energy Research Establishment Rept. No. R-2869 (1959).
[2] D. S. Thompson and J. P. Roberts, J. Appl. Phys. **31**, 433 (1960).
[3] R. A. Lad, C. A. Stearns, and M. G. DelDuca, Acta Met. **6**, 610 (1958).
[4] A. E. Gorum, E. R. Parker, and J. A. Pask, J. Am. Ceram. Soc. **41**, 161 (1958).
[5] C. A. Stearns, A. P. Pack, and R. A. Lad, "Factors affecting the plasticity of sodium chloride, lithium fluoride, and magnesium oxide single crystals," NASA Tech. Note D-75 (1959).
[6] C. A. Stearns (unpublished data).

Books Reviewed

Prompt, noncritical reviews appear in this column. Critical reviews of many of the books described here will appear in Physics Today, The Review of Scientific Instruments, *or* American Journal of Physics.

Non-Crystalline Solids. V. D. FRECHETTE, EDITOR. Pp. 530. John Wiley & Sons, Inc., New York, 1960. Price $15.00.

These papers represent the proceedings of a conference which brought together leading investigators from several fields interested in determining the domain of the term "non-crystalline solids," the structure of such solids, the methods capable of disclosing their structure—and the basis for finding, explaining, and deriving their properties.

The conference papers, and the remarks compiled, attest to the current extensive progress in the definition and description of amorphous structures. This treatise creates a common ground for dealing with phenomena and fundamentals of conventionally separated materials such as glass, evaporated films, and plastics. It also brings insight into the definite specificity of chemically different glasses (e.g., sulfur vs silica glass).

Physics of the Upper Atmosphere. J. A. RATCLIFFE, EDITOR. Pp. 563. Academic Press, Inc., New York, 1960. Price $14.50.

This book is concerned with that part of the atmosphere above a height of about 60 km. The experimental techniques employed, and the theories involved, in this field of investigation are varied and cover a wide range of subjects. The book has therefore been written by a team of workers, each of whom has contributed a chapter, in the form of a monograph, on his own specialty. Workers in one branch of the subject will find a detailed authoritative account, well supported by references, in the chapters with which they are most closely concerned. The other chapters will provide the background of allied knowledge.

Electromagnetic Energy Transmission and Radiation. RICHARD B. ADLER, LAN JEN CHU, AND ROBERT M. FANO. Pp. 612. John Wiley & Sons, Inc., New York, 1960. Price $14.50.

This book treats electromagnetic waves and oscillations in one-, two-, and three-space dimensions, using time-domain, complex-frequency-domain, and energy points of view.

To ensure a proper balance of emphasis between physical considerations and analytical technique, the authors avoid the more formal procedures of boundary-value problem solution by employing a method of field synthesis. This approach involves the study of elementary solutions in empty space, in enough detail to make clear in advance the kinds of boundary conditions simple combinations of them will require.

The significance of the various solutions is further illustrated by the simplest analytical models suggestive of practical devices.

Theory of Inertial Guidance. CONNIE L. MCCLURE. Pp. 302. Prentice-Hall, Inc., Englewood Cliffs, New Jersey, 1960. Price $12.00.

This book opens with a review of Cartesian transformations, vector quantities, kinematic fundamentals, and rigid body dynamics. It then concentrates attention on the salient features in classical gyrodynamics and the preliminary theory of stabilized platforms.

Nuclear Photo-Disintegration. J. S. LEVINGER. Pp. 141. Oxford University Press, New York, 1960. Price $2.00.

This book contains discussions of methods of calculation for atomic and nuclear photoeffects; the deuteron photoeffect; sum-rule calculations for nuclear photo-disintegration; systematics of radiative transitions between discrete states; shell model and collective model calculations of the cross section for nuclear photo-disintegration; and statistical model, direct interaction model, and quasi-deuteron model calculations of the products of nuclear photo-disintegration.

Photoconductivity of Solids. RICHARD H. BUBE. Pp. 433. John Wiley & Sons, Inc., New York, 1960. Price $14.75.

The book provides a unified physical description and interpretation of photoconductivity phenomena, drawing examples from many different kinds of materials. In addition, the correlation between photoconductivity and other related phenomena in insulators and semiconductors is given.

Other sections of this book examine the current theoretical understanding of the mechanisms of photoconductivity, together with a detailed exposition of particular phenomena which illustrate the variety of characteristics available. An extensive bibliography and a summary of most of the photoconducting materials which have been investigated is included.

Graphite and Its Crystal Compounds. A. R. UBBELOHDE AND F. A. LEWIS. Pp. 204. Oxford University Press, New York, 1960. Price $5.60.

This book presents a survey of studies on both the physical properties and the chemistry of graphite. The text aims to describe relationships of graphite with its crystal compounds, with diamond, and other carbons that are structurally more complex and chemically less pure. Access to more specialized treatments is provided by ample bibliography references to recent published literature.

X-ray Absorption and Emission in Analytical Chemistry. H. A. LIEBHAFSKY, H. G. PFEIFFER, E. H. WINSLOW AND P. D. ZEMANY. Pp. 357. John Wiley & Sons, Inc., New York, 1960. Price $13.50.

This has been written specifically for the analytical chemist who wants to understand and use the modern methods of x-ray spectrochemical analysis, employing x-ray absorption or x-ray emission. The authors describe the history and underlying theory, the reliability of x-ray emission methods, a variety of applications, and all the necessary equipment and techniques.

Hydromagnetic Channel Flows. LAWSON P. HARRIS. Pp. 88. The Technology Press and John Wiley & Sons, Inc., New York, 1960. Price $2.75.

This book presents analyses for three flows of viscous, incompressible, electrically conducting fluids in high-aspect-ratio rectangular channels subjected to transverse magnetic fields. The situations considered in this book are turbulent flow in the presence of a dc magnetic field and both laminar and turbulent flows in induction-driven flows.

The methods used are analogous to the "semiempirical" techniques of fluid mechanics in that their success depends on the combined use of the basic hydromagnetic equations, a dimensional analysis, and the results of experiment. Principal results of this study include a scheme for correlating experimental friction-factor data and methods for computing mean-velocity profiles, mean magnetic-field distortion, current distributions, and turbulent-shear distributions in the dc

turbulent flow. Curves are included that give velocity profiles, current distributions, and turbulent-shear distributions for a wide range of operating conditions. Methods are presented for relating the structure and operation of the induction-driven flows to the corresponding dc flows.

Viscoelasticity Phenomenological Aspects. J. T. BERGEN, EDITOR. Pp. 144. Academic Press, Inc., New York, 1960.

A symposium on phenomenological aspects of viscoelasticity was held on April 28 and 29, 1958, at the Research and Development Center of the Armstrong Cork Company, Lancaster, Pennsylvania. The seven papers presented at that time constitute the seven chapters of this book. As a book, therefore, it should not be looked upon as a text, or as a comprehensive work in the sense of a treatise, but as a collection of contributions which present the views of a number of authors in the field of viscoelasticity. Each of the seven authors deals with a different aspect of the field, but the central theme is adhered to throughout.

Cosmic Radio Waves. I. S. SHKLOVSKY. Pp. 413. Harvard University Press, Cambridge, Massachusetts, 1960. Price $12.50.

Cosmic Radio Waves presents the first comprehensive treatment of the radio emission from objects located far beyond the solar system. It is here that radio astronomy has achieved its most fundamental results, significantly enriching our understanding of the nature of primary cosmic rays and interstellar matter, the dynamics of our stellar system and cosmology. Dr. Shklovsky focuses attention upon the major problems in urgent need of further study, whether he is dealing with monochromatic radiation or with emission nebulae and their role in the spiral structure, with the gaseous halo of our galaxy, or with the interstellar gas in the galactic nucleus.

Diffraction Gratings as Measuring Scales. JOHN GUILD. Pp. 206. Oxford University Press, New York, 1960. Price $5.60.

During the last few years there have been very rapid developments, both in the techniques and the industrial and other applications, of the Moiré fringe method of fine measurement.

This book has been written to assist engineers and scientists who are interested in the practical application of the Moiré fringe method to exceptionally fine measurement and to the automatic control of machines working to extremely fine limits.

While the book is intended to be self-contained in that sufficient theoretical explanation is included to enable the applications to be understood, there will probably be many readers who will wish to obtain a fuller understanding of the fundamental theory.

Properties and Structure of Polymers. ARTHUR V. TOBOLSKY. Pp. 331. John Wiley & Sons, Inc., New York, 1960. Price $14.50.

In this volume, Arthur Tobolsky, Professor of Chemistry, Princeton University, discusses selected topics on the properties and behavior of polymers. A division of six chapters on elasticity and viscosity, aspects of polymer physics, mathematical treatment of linear viscoelasticity, viscoelastic behavior of polymers, chemical stress relaxation, and polymerization equilibria plus a number of appendices allows the student or research worker to attain a fairly comprehensive background in the field. The approach is in terms of molecular architecture and dynamics with the intention of providing a detailed treatise while at the same time avoiding the usual intricate mathematics often found in such a study.

Digital and Sampled-Data Control Systems. McGraw-Hill Electrical and Electronic Engineering Series. JULIUS T. TOU. Pp. 587. McGraw-Hill Book Company, Inc., New York, 1959. Price $15.00.

This volume is largely the outgrowth of a set of lecture notes, first prepared in 1956, for a two-semester course offered by the author to graduate students at the Moore School of the University of Pennsylvania. An adequate preparation in an introductory course on feedback control systems and sound knowledge of Laplace transforms and complex variable theory is assumed. Emphasis is placed on the development of basic theory. Many numerical examples are worked out in the text to clarify the development of the theory and to illustrate the discussion of the various methods. Approximately 70 problems of various types and complexity are included in Appendix 3. Appendix 2 contains a list of numbered references which covers the contributions of many workers in the field. Appendix 1 presents a fairly extensive table of z transforms and modified z transforms.

High-Energy Electron Scattering Tables. ROBERT HERMAN AND ROBERT HOFSTADTER. Pp. 273. Stanford University Press, Stanford, California, 1960. Price $8.50.

This volume, a preliminary handbook on the subject of electron scattering and nuclear structure, is designed especially for theoreticians and experimental investigators interested in carrying out and analyzing experiments in high-energy electron physics. The volume consists of 192 pages of tables, plus extensive introductory material.

Advances in Space Science. Vol. 2. FREDERICK I. ORDWAY, III, EDITOR. Pp. 436. Academic Press, Inc., New York, 1960. Price $13.00.

Five major areas are covered in the six chapters that comprise Volume 2 of Advances in Space Science: space physics, tracking, materials, electrical propulsion systems, and altitude control. While these subjects are obviously critical to the orderly development of space science and technology, they have not heretofore received comprehensive treatment in the permanent literature.

Books Received

Dynamics of Climate. RICHARD L. PFEFFER, EDITOR. Pp.136. Pergamon Press, New York, 1960. Price $6.50.

Electronics for Spectroscopists. C. G. CANNON, EDITOR. Pp. 327. Interscience Publishers, Inc., New York, 1960. Price $9.50.

Announcement

The Division of Electron Physics of the American Physical Society

The Division will hold its 1960 West Coast Meeting at the University of California, Berkeley, from December 29 to 31.

Invited speakers include Edward Gerjuoy, reviewing problems on atomic scattering; Homer Hagstrum, speaking on his work on secondary emission from ion bombardment, and Kenneth Clark, speaking on late afterglow spectroscopy.

Author Index to Volume 31

References with (L) are to Letters to the Editor; (E) to Errata

Abeles, B., G. D. Cody, and D. S. Beers. Apparatus for the measurement of thermal diffusivity of solids at high temperatures—1585

Acrivos, A., M. J. Shah, and E. E. Petersen. On the flow of a non-Newtonian liquid on a rotating disk—963

Adams, Edmond (see Hubbard, William M.)—368S

Adamsky, R. F. Preferred orientation and ordering in evaporated films of Fe, Ni, and Fe-Ni—289S

Addamiano, Arrigo and Manuel Aven. Some properties of zinc sulfide crystals grown from the melt—36

Adler, Robert and Glen Wade. Beam refrigeration by means of large magnetic fields—1201

Agarwal, Paul D. and D. C. Graham. Effect of eddy currents on domain wall configurations, wall motion, and loss for a domain model of cube-on-edge material—249S

—— **and L. Rabins.** Rigorous solution of eddy current losses in rectangular bar for single plane domain wall model—246S

Alger, R. S. (see Jordan, R. D.)—747

Allen, F. G., T. M. Buch, and J. T. Law. p layers on vacuum heated silicon—979

Allen, R. B., H. Bernstein, and A. D. Kurtz. Effect of oxide layers on the diffusion of phosphorus into silicon—334

Allen, Robert D., Louis F. Glasier, Jr., and Paul L. Jordan. Spectral emissivity, total emissivity, and thermal conductivity of molybdenum, tantalum, and tungsten above 2300°K—1382

Alley, R. E., Jr. and V. E. Legg. Effects of hydrostatic pressure on the properties of magnetic materials—239S

Allison, F. E. and J. Thomas Schriempf. Explosively loaded metallic cylinders. II—846

—— **and R. W. Watson.** Explosively loaded metallic cylinders. I—842

Alperin, H. A. Neutron diffraction investigation of the magnetic structure of nickel oxide—354S

Amelinckx, S., G. Strumane, and W. W. Webb. Dislocations in silicon carbide—1359

—— **and P. Delavignette.** Electron optical study of basal dislocations in graphite—2126

—— (see Delavignette, P.)—1691(L)

Anderson, Elmer E. and J. Richard Cunningham, Jr. High-permeability garnets—1687(L)

—— (see Cunningham, J. Richard, Jr.)—45S

—— (see McDuffie, G. E.)—47S

Anderson, Franklin R. and V. F. Holland. Ion-bombardment etching of synthetic fibers—1516

Anderson, G. S. and G. K. Wehner. Atom ejection patterns in single-crystal sputtering—2305

Anderson, J. M. Ultimate and secondary electron energies in the negative glow of a cold-cathode discharge in helium—511

—— **and L. A. Harris.** Negative glow plasma as a cathode for electron tubes—1463

Andrä, W., Z. Málek, W. Schüppel, and O. Stemme. "Spontaneous magnetic anisotropy" in polycrystalline thin films—442(L)

Andrews, C. L. Analog study of large-signal high-frequency diodes—1431

Andrews, R. D. (see Rudd, J. F.)—818

Antell, G. R. Chlorine and iodine as impurities in InAs and GaP—1686(L)

Arajs, Sigurds and D. S. Miller. Magnetic behavior of polycrystalline neodymium, holmium, and erbium from 300 to 1500°K—325S

—— **and D. S. Miller.** Paramagnetic susceptibilities of Fe and Fe-Si alloys—986

—— **and D. S. Miller.** Spontaneous magnetization of some gadolinium alloys—213(L)

Arbogast, C. L. (see Smith, J. F.)—99

Armstrong, R. W., J. W. Faust, Jr., and W. A. Tiller. Structural study of the compound $AgSbTe_2$—1954

Arnold, George W. (see Compton, W. Dale)—621

Arnott, R. J. (see Goodenough, J. B.)—342S

Arrott, Anthony (see Freeman, Michael W.)—404S

Ashkin, A. and L. D. White. Partition noise in electron beams at microwave frequencies—1351

Asimow, Robert. Precision lattice parameter measurements of cold-worked metals—410

Atwater, H. A. Microwave measurement of semiconductor carrier lifetimes—938(L)

Auer, P. L. Potential distributions in a low-pressure thermionic converter—2096

—— **and H. Hurwitz.** Positive column formation in ion sources employing surface ionization—1007

Aukerman, L. W. and R. K. Willardson. High-temperature Hall coefficient in GaAs—939(L)

Auld, B. A. Finite amplitude electromagnetic waves in gyromagnetic media—106S

—— Walker modes in large ferrite samples—1642

Avakian, P. and A. Smakula. Growth of cesium chloride crystals from solution and melt—1720

Aven, Manuel (see Addamiano, Arrigo)—36

Bachmann, L., W. H. Orr, T. N. Rhodin, and B. M. Siegel. Determination of surface structure using ultrahigh vacuum replication—1458

Backus, John and Norman E. Huston. Ion energies in a cold cathode discharge in a magnetic field—400

Bacon, Roger. Growth, structure, and properties of graphite whiskers—283

Baer, G., D. Ganz, and H. Thomas. Secondary recrystallization in vacuum annealed silicon iron—235S

Bagley, E. B. Hooke's law in shear and polymer melt fracture—1126(L)

—— **and A. M. Birks.** Flow of polyethylene into a capillary—556

Bailey, H. R. and B. K. Larkin. Remarks on "Some criteria for the *in situ* combustion of crude oil"—1123(L)

Bailey, John M. and Allan T. Gwathmey. Dislocation arrays in depth and recrystallization produced by surface deformation of single crystals of copper at high temperature—215(L)

Bailey, P. C. Absorption and reflectivity measurements on some rare earth iron garnets and α-Fe_2O_3—39S

Baker, G. S. (see Gabrysh, A. F.)—1785

Ballard, S. S. (see McCarthy, Kathryn A.)—1410

Balluffi, R. W. and R. O. Simmons. Changes in macroscopic shape, lattice parameter, and density in crystals due to point defects—2284

Barakat, Richard and Robert Barakat. Optical studies of the diffraction of water waves by circular and thin elliptic cylinders—474

Barakat, Robert (see Barakat, Richard)—474

Barbour, J. P. (see Dyke, W. P.)—790

Barker, R. C. and R. M. Brownell. DC measurements on tape-wound cores—243S

Barnes, Bentley T. Intensities of λ1850 and λ2537 in low-pressure mercury vapor lamps with rare gas present—852

Barr, L. W. and J. A. Morrison. Formation of cavities on dislocations in crystals of NaCl and KCl—617(L)
Bartell, L. S. Effect of specimen delocalization in electron diffraction studies of gas molecules—252
Bartholomew, C. Y. and A. R. LaPadula. Penetration depth investigation of gas cleanup with radioactive tracers—445(L)
Bartram, Ralph and Larry Spruch. Bounds on the elements of the equivalent network for scattering in waveguides. II. Application to dielectric obstacles—913
—— (see Spruch, Larry)—905
Batdorf, R. L., A. G. Chynoweth, G. C. Dacey, and P. W. Foy. Uniform silicon *p-n* junctions. I. Broad area breakdown—1153
——, **G. C. Dacey, R. L. Wallace, and D. J. Walsh.** Esaki diode in InSb—613(L)
Bate, G. and K. N. R. Taylor. Production and properties of thin layers of indium antimonide—991
Bate, R. T. (see Simon, R.)—2160
Bauer, Charles L. and Robert B. Gordon. Dislocation damping effects in rock salt—945
Bean, C. P. and I. S. Jacobs. Magnetization of a dilute suspension of a multidomain ferromagnetic—1228
Beck, Paul A. (see Rajan, N. S.)—731
Becker, J. H. Several new methods to measure the thermal diffusivity of semiconductors—612(L)
Bedo, D. E., D. H. Tomboulian, and J. A. Rigert. Angular distribution and polarization of the radiation emitted by electrons accelerated in a synchrotron—2289
Beers, D. S. (see Abeles, B.)—1585
Bell, James F. Propagation of large amplitude waves in annealed aluminum—277
—— Study of initial conditions in constant velocity impact—2188
Belov, K. P. and A. V. Pedko. Magnetostriction of gadolinium iron garnets—55S
——, **G. I. Katayev, and R. Z. Levitin.** Internal friction anomaly in ferromagnetics and antiferromagnetics near the Curie point—153S
Belser, Richard B. Alloying behavior of thin bimetal films, simultaneously or successively deposited—562
Bennett, A. I. (see Longini, R. L.)—1204
Bennett, Glenn E. Harmonic generation in a ferrimagnetic disk—97S
Bennion, David R. New multi-aperture magnetic logic element—129S
Berghammer, J. and S. Bloom. On the nonconservation of noise parameters in multivelocity beams—454
Berghezan, A. (see Fourdeux, A.)—918
Bergmann, Saul M. Submillimeter wave maser—275
Berman, R., E. L. Foster, B. Schneidmesser, and S. M. A. Tirmizi. Effects of irradiation on the thermal conductivity of synthetic sapphire—2156
Bernstein, H. (see Allen, R. B.)—334
Berry, Chester R. and Charles M. Combs. Antiferromagnetic $FeVO_3$—1130(L)
Bertolone, N. P. (see Webb, W. W.)—207
Besser, P. J. (see Muckenhirn, William O.)—304S
Beyer, R. T. (see Proud, J. M.)—543
Bickford, L. R., Jr. Intrinsic and anneal-induced anisotropy in cobalt-substituted *W*-type hexagonal oxides—259S
Bienvenue, L. L. (see Sosin, A.)—249
Bierlein, T. K. and B. Mastel. Damage in UO_3 films and particles during reactor irradiation—2314(L)
—— **and B. Mastel.** Fission fragment damage in nonfissionable thin films—2315(L)
Biorci, G., A. Ferro, and G. Montalenti. Effect of neutron bombardment on the magnetic properties of very high permeability iron—2046
——, **A. Ferro, and G. Montalenti.** Magnetic viscosity due to solute atoms pairs. I. Theory of the effect—2121
Bird, J. F. (see McClure, F. T.)—884
Birks, A. M. (see Bagley, E. B.)—556
Birks, L. S. Technique for calculating x-ray intensities in the electron probe microanalyzer—1297(L)
—— (see Sweeney, W. E.)—1061
Bjorklund, R. F. (see Pao, Yoh-Han)—1925
Blair, R. R. (see Easley, J. W.)—1772
Blakemore, J. S. and K. C. Nomura. Influence of transverse modes on photoconductive decay in filaments—753
——, **J. W. Schultz, and K. C. Nomura.** Some effects occurring in dislocated tellurium—2226
Blodgett, K. B. and T. A. Vanderslice. Mechanism of inert gas cleanup in a gaseous discharge—1017
Bloom, S. (see Berghammer, J.)—454
Bockemuehl, R. R. Field-effect modulation of photoconductance in a quasi-intrinsic semiconductor—2255
—— **and W. E. Sargeant.** Practical hysteresigraph—180S
Boerdijk, A. H. Diagrams representing states of operation of a general thermocouple—1141
Bohlmann, M. A. (see Kronenberg, K. J.)—82S
Bolef, D. I. and M. Menes. Elastic constants of single crystal aluminum antimonide—1426
—— **and M. Menes.** Measurement of elastic constants of RbBr, RbI, CsBr, and CsI by an ultrasonic cw resonance technique—1010
Boley, Forrest I. Scattering of radiation by a plasma—1692(L)
Bolling, G. F. and W. A. Tiller. Growth from the melt. I. Influence of surface intersections in pure metals—1345
—— **and W. A. Tiller.** Growth from the melt. Part II. Cellular interface morphology—2040
Bonfiglioli, G., A. Ferro, and A. Mojoni. Origin of the "first-order structure" of CP4-etched Ge surfaces—684
Borg, S. F. Three-dimensional wedge impact on a compressible fluid—438(L)
Boswell, F. W. C. (see Fourie, J. T.)—1136(L)
Boudart, M. (see Koros, R. M.)—1129(L)
Bovenkerk, H. P. (see Strong, H. M.)—39
Boyd, E. L. (see Pugh, E. W.)—293S
Bozorth, R. M. and D. D. Davis. Magnetic properties of ferromagnetic superconductors—321S
Brace, W. F. (see Dulaney, E. N.)—2233
Bradley, Arthur. Determination of dose rates from beta transmission currents—1826(L)
—— (see Gross, B.)—1035
Bradley, E. M. and M. Prutton. Magnetization reversal in uniaxial films near to the preferred direction—285S
Brady, L. E. (see Hamilton, J. F.)—609(L)
Bragg, Robert H., Irene Corvin, and John W. Buttrey. Small angle scattering investigation of Ludox mixtures—1183
Bragiński, Aleksander. Properties of manganese ferrites prepared at various oxygen pressures—339S
Brannen, E., H. Froelich, and T. W. W. Stewart. Generation of millimeter waves by the electron beam of a microtron—1829(L)
Bratina, W. J., U. M. Martius, and D. Mills. Magnetic contribution to the ultrasonic attenuation in annealed and deformed steel (SAE 1020)—241S
Brenden, B. B. and H. W. Newkirk. Method for determining the thermal conductivity of incandescent solids—737(L)
Brophy, J. E. (see Kostyshyn, B.)—772
Brophy, James J. and Robert J. Robinson. Current noise due to ohmic contacts on cadmium sulfide—1343
Broudy, R. M. and J. W. McClure. Statistics of the occupation of dislocation acceptors (one-dimensional interaction statistics)—1511

Brown, D. L. (see Weisz, R. S.)—269S
Brown, E. and G. H. Goedecke. Effect of atomic interaction potential on defect production in metals—932
Brown, Frederick C. (see Hanson, Roland C.)—210(L)
Brown, N. (see Marcinkowski, M. J.)—1303(L)
Brown, W. F., Jr., J. P. Hanton, and A. H. Morrish. Initial-permeability spectra of microscopic iron-oxide particles—214S
Brownell, R. M. (see Barker, R. C.)—243S
Brownlow, J. M., W. L. Shevel, Jr., and O. A. Gutwin. Ferrite films—new logic and storage devices—121S
Brueckner, Keith A. (see Klein, M. M.)—1437
Bube, Richard H. Mechanism of photoconductivity in microcrystalline powders—2239
—— Photoelectronic analysis of high-resistivity crystals: (a) GaAs, (b) Sb_2S_3—315
—— Saturation of photocurrent with light intensity—1301(L)
—— (see Williams, R.)—968
Buch, T. M. (see Allen, F. G.)—979
Buehler, E. and M. Tanenbaum. Method for the detection of flaws in yttrium iron garnet crystals—388
Buffler, C. R. Effects of surface irregularities on single crystal resonance parameters—222S
Bugnolo, Dimitri S. Transport equation for the spectral density of a multiple-scattered electromagnetic field—1176
Bullough, R., R. C. Newman, J. Wakefield, and J. B. Willis. Precipitation in silicon crystals containing aluminum—707
Bunch, M. D. (see Powell, Robert L.)—504
Bundy, F. P. (see Strong, H. M.)—39

Cable, J. W. (see Wilkinson, M. K.)—358S
Caird, R. S. (see Fowler, C. M.)—588
Callen, Earl R. Anisotropic magnetization—149S
Campbell, A. W. (see Davis, W. C.)—1225
Cardona, M. and W. Ruppel. Oscillations in germanium with an applied pulsed electric field—1826(L)
Carr, P. H. and S. Foner. Magnetic transitions in Ti_2O_3 and V_2O_3—344S
Carr, W. J., Jr. Explanation for the low-temperature behavior of the anisotropy of iron—69
Carson, John W. and Robert L. White. Paramagnetic resonance of Yb in aluminum and gallium garnets—53S
Carter, J. R., Jr., and R. A. Swalin. On the kinetics and mechanism of the precipitation of lithium from germanium—1191
Carter, R. E. (see Meiklejohn, W. H.)—164S
Caspari, M. E., S. Frankel, and M. A. Gilleo. Hyperfine interactions in magnetic materials by γ-γ angular correlation measurements—320S
Cassedy, E. S. and J. Fainberg. Total electromagnetic cross sections of imperfectly conducting cylinders—739(L)
Cassity, C. R. Stress waves in solids—1377
Castle, J. G. (see Wagner, P. E.)—1498(L)
Castro, P. S. and W. W. Happ. Performance of a thermoelectric converter under constant heat flux operation—1314
Catlin, Avery and Walter P. Walker. Mechanical properties of thin single-crystal gold film—2135
Cave, E. F. and L. V. Holroyd. Thermal expansion coefficients of bismuth—1357
Chace, William G. and Morton A. Levine. Classification of wire explosions—1298(L)
Chalmers, Bruce (see Wagner, Richard S.)—578
Champlin, Keith S. Hall field relaxation in semiconductors at high frequency—1770
Chang, H. (see Shevel, W. L., Jr.)—125S
Chang, K. K. N. Theory of a negative-resistance transmission line amplifier with distributed noise generators—871
Chang, Roger. Creep of Al_2O_3 single crystals—484
Charbonnier, F. M. (see Dyke, W. P.)—790
Chasanov, M. G. Heating in liquid helium resulting from neutron and gamma bombardment by a fission source—733(L)
Chen, C. L. (see Leiby, C. C., Jr.)—268
Cheng, C. H. (see Schroder, K.)—2154
Chester, P. F. (see Wagner, J. E.)—1498(L)
Chikazumi, Soshin. Roll magnetic anisotropy of iron-aluminum crystals—158S
Child, H. R. (see Wilkinson, M. K.)—358S
Chipman, D. R. Temperature dependence of the Debye temperatures of aluminum, lead, and beta brass by an x-ray method—2012
—— **and Arthur Paskin.** Comments on "determination of atomic scattering factors"—1130(L)
Chow, S. T. (see Hsiao, C. C.)—1869
Christenson, E. L. (see Domenicali, C. A.)—1730
Christy, Robert W. Formation of thin polymer films by electron bombardment—1680
Chu, E. L. On the concept of fictitious surface charges of an electron beam—381
Chynoweth, A. G. Uniform silicon p-n junctions. II. Ionization rates for electrons—1161
—— (see Batdorf, R. L.)—1153
Cleek, G. W. (see Spinner, S.)—1407
Cleland, J. W. (see Curtis, O. L., Jr.)—423
Clogston, A. M. Interaction of magnetic crystals with radiation in the range 10^4–10^6 cm^{-1}—198S
Closser, W. H. Drift mobility in neutron irradiated n-type germanium—1693(L)
Coale, Franklin S. High-speed ferrite rotating half-wave plate—170S
Cobine, J. D. and G. A. Farrall. An experimental study of arc stability. I—2296
Cody, G. D. (see Abeles, B.)—1585
Cohen, M. S., E. E. Huber, Jr., G. P. Weiss, and D. O. Smith. Investigations into the origin of anisotropy in oblique-incidence films—291S
—— (see Smith, D. O.)—295S, 1755
Coleman, Paul D. and Charles Enderby. Megavolt electronics Cerenkov coupler for the production of millimeter and submillimeter waves—1695(L)
—— (see Steier, William H.)—99S
Combs, Charles M. (see Berry, Chester R.)—1130(L)
Compton, W. Dale and George W. Arnold. Lattice displacements by fast electrons—621
Coomes, E. A. (see Gifford, F. E.)—235
Cooperman, Philip. Reply to the letters of Szasz, and Bailey and Larkin—1124(L)
Cormia, R. L. (see Turnbull, D.)—674
Cotter, L. (see Meister, R.)—854
Cowan, Monroe (see Gordy, Walter)—941(L)
Crapo, W. A. Time decrease of initial permeability in $Mn_xFe_{3-x}O_{4-\gamma}$—267S
Crawford, J. H. and F. W. Young, Jr. Mechanism for the production of F centers in NaCl by irradiation with gamma rays—1688(L)
Crocker, A. J. (see Richards, J. L.)—611(L)
Croft, William J. (see Greifer, Aaron P.)—85
Croll, I. M. (see Greiner, J. H.)—2316(L)
Cross, L. G. (see Makhov, G.)—936(L)
Culick, F. E. C. Comments on a ruptured soap film—1128(L)
Cunningham, J. Richard, Jr., and Elmer E. Anderson. Samarium substitutions in yttrium iron garnet—45S
—— (see Anderson, Elmer E.)—1687(L)
—— (see McDuffie, G. E.)—47S
Cunningham, R. L., P. Haymann, C. Lecomte, W. J. Moore, and J. J. Trillat. Etching of surfaces with 8-kev argon ions—839

Curtis, O. L., Jr., and J. W. Cleland. Monoenergetic neutron irradiation of germanium—423
Czyzak, S. J. (see Reynolds, D. C.)—94

Dacey, G. C. (see Batdorf, R. L.)—613(L), 1153
D'Amico, C. (see Hagstrum, H. D.)—715
Damon, R. W. and J. R. Eshbach. Magnetostatic modes of a ferromagnetic slab—104S
Danforth, W. E. and D. L. Goldwater. Density of a thorium monolayer for maximum thermionic emission—1715
Danielson, G. C. (see Wallace, D. C.)—168
Danno, Akibumi (see Yahagi, K.)—734(L)
Dash, W. C. Gold induced climb of dislocations in silicon—2275
—— Improvements on the pedestal method of growing silicon and germanium crystals—736(L)
Datz, Sheldon, R. E. Minturn, and E. H. Taylor. Thermal positive ion emission and the anomalous flicker effect—880
—— (see Minturn, Robert E.)—871
Davis, D. D. (see Bozorth, R. M.)—321S
Davis, D. H. Monte Carlo calculation of molecular flow rates through a cylindrical elbow and pipes of other shapes—1169
Davis, W. C. and A. W. Campbell. Ultra-high-speed photographs refuting "cohesion in plasma"—1225
Deckers, J. (see Koros, R. M.)—1129(L)
DeGrasse, R. W. and H. E. D. Scovil. Noise temperature measurement of a traveling-wave maser preamplifier—443(L)
Delavignette, P. and S. Amelinckx. Dislocation ribbons and stacking faults in graphite—1691(L)
—— (see Amelinckx S.)—2126
Della Torre, E. (see Woodward, J. G.)—56, 398S
dePackh, D. C. (see Godlove, T. F.)—2016
deVos, K. J. (see Koch, A. J. J.)—75S
Dexter, D. L. (see Rimmer, M. P.)—775
Diesel, T. J. (see Hollander, Lewis E.)—692
Dietrich, W. and W. E. Proebster. Millimicrosecond magnetization reversal in thin magnetic films—281S
Dillon, I. A. and R. M. Oman. Ion-bombardment etching of silicon and germanium—26
Dillon, J. F., Jr. Magnetostatic modes in disks and rods—1605
—— **and J. W. Nielsen.** Ferrimagnetic resonance in impurity doped yttrium iron garnet (YIG)—43S
Diorio, A. F. (see Posner, A. S.)—536
Dismant, John H. Reviving the classical theory of friction by a modern dislocation theory of deformation revision—221(L)
—— Reviving the classical theory of friction by a modern dislocation theory of deformation revision—942(E)
Dixon, P. A. (see Maradudin, A. A.)—329S
Domenicali, C. A. and E. L. Christenson. Effects of internal oxidation and heat treatment on the electrical resistivity of dilute CuMn, CuFe, and CuCo alloys—1730
Donahoe, F. J. and L. R. Testardi. Experimental test of the first Kelvin relation—1304(L)
Donovan, R. E. and A. A. Vuylsteke. On the possibility of maser action in nuclear quadrupole systems—614(L)
Dooley, J. A. (see Easley, J. W.)—1024
Dougal, Arwin A. (see Takeda, Susumu)—412
Dragsdorf, R. Dean. Elastic moduli of face-centered cubic cobalt—434(L)
Drickamer, H. G. (see Gregg, D. W.)—494
—— (see Wiederhorn, S.)—1666
Drougard, M. E. Detailed study of switching current in barium titanate—352
Dugan, Anthony F. Contribution of anode emission to space charge in thermionic power converters—1397
Dulaney, E. N. and W. F. Brace. Velocity behavior of a growing crack—2233
Dunlap, W. C. (see Ruth, Ralph P.)—995
Dunn, C. G. and C. J. McHargue. On a complex recrystallization texture in 3% silicon iron—1767
—— **and J. L. Walter.** Orientation density and its use in quantitative texture studies—827
Duwez, Pol, R. H. Willens, and W. Klement, Jr. Continuous series of metastable solid solutions in silver-copper alloys—1136(L)
——, **R. H. Willens, and W. Klement, Jr.** Metastable electron compound in Ag-Ge alloys—1137(L)
——, **R. H. Willens, and W. Klement, Jr.** Metastable solid solutions in the gallium antimonide-germanium pseudobinary system—1500(L)
Dyke, W. P., F. M. Charbonnier, R. W. Strayer, R. L. Floyd, J. P. Barbour, and J. K. Trolan. Electrical stability and life of the heated field emission cathode—790
—— (see Martin, E. E.)—782

Easley, J. W. and R. R. Blair. Fast neutron bombardment of germanium and silicon Esaki diodes—1772
—— **and J. A. Dooley.** On the neutron bombardment reduction of transistor current gain—1024
Eckstein, Yakov, A. W. Lawson, and Darrell H. Reneker. Elastic constants of bismuth—1534
Edmond, J. T. Heat treatment of gallium arsenide—1428
—— **and C. Hilsum.** Heat treatment effects in indium arsenide—1300(L)
Eggenberger, J. S. Influence of nearby conductors in thin film switching—287S
Eichbaum, Barlane R. Development of high-speed coincident current memory cores—117S
Einspruch, Norman G., E. J. Witterholt, and Rohn Truell. Scattering of a plane transverse wave by a spherical obstacle in an elastic medium—806
Elbaum, C. Dislocations in metal crystals grown from the melt—1413
Elliott, B. J., T. Schaug-Pettersen, and H. J. Shaw. Pulsed ferrimagnetic microwave generator—400S
Enderby, Charles (see Coleman, P. D.)—1695(L)
English, Albert C. Detection of growth striations in germanium crystals—1498(L)
Enz, U. (see Smit, J.)—137S
Eshbach, J. R. (see Damon, R. W.)—104S
Everhart, T. E. Simple theory concerning the reflection of electrons from solids—1483
Ewald, A. W. (see Wolfson, R. G.)—1973
Eyring, Henry (see Gabrysh, A. F.)—1785
—— (see Kim, Wan Kyue)—358

Fainberg, J. (see Cassedy, E. S.)—739(L)
Fan, George J. Y. Analysis of a practical perpendicular head for digital purposes—402S
Fang, P. H. and R. S. Roth. Ferroelectric and ferrimagnetic properties of $(Ba_{1-2x}R_{2x})(Nb_{1-x}Fe_{1+x})O_3$—278S
Farrall, G. A. (see Cobine, J. D.)—2296
Fatuzzo, Ennio. Bias in ferroelectric colemanite—1029
Faust, J. W., Jr., and A. Sagar. Effect of the polarity of the III–V intermetallic compounds on etching—331
—— (see Armstrong, R. W.)—1954
Ferro, A. (see Biorci, G.)—2046, 2121
—— (see Bonfiglioli, G.)—684
Fine, M. E. (see Wolfson, R. G.)—1973
Fisher, E. S. (see McSkimin, H. J.)—1627
Fisher, R. M. (see Marcinkowski, M. J.)—1303(L), 1687(L)

Flaschen, S. S., A. David Pearson, and I. L. Kalnins. Improvement of semiconductor surfaces by low melting glasses, possibly functioning as ion getters—431(L)
——, **A. David Pearson, and William R. Northover.** Low melting sulfide-halogen inorganic glasses—219(L)
Fletcher, P. C. (see Solt, I. H.)—100S
Fletcher, R. C. (see LeCraw, R. C.)—95S
Flippen, R. B. and S. A. Friedberg. Magnetic susceptibilities of single crystal $NiCl_2 \cdot 6H_2O$ and $CoCl_2 \cdot 6H_2O$ at low temperatures—338S
Flom, Donald G. Rolling friction of polymeric materials. I. Elastomers—306
Floyd, R. L. (see Dyke, W. P.)—790
Fochs, P. D. Improved method of growing CdS crystals from the vapor phase—1733
Folen, V. J. Influence of ionic order on the magnetocrystalline anisotropy and crystalline field parameters in lithium ferrite monocrystals—166S
—— (see Rado, G. T.)—62
—— (see Schnitzler, A. D.)—348S
Foner, S. and L. R. Momo. CW millimeter wave maser using Fe^{3+} in TiO_2—742(L)
—— (see Carr, P. H.)—344S
—— (see Momo, L. R.)—443(L)
Ford, N. C., Jr. Domain wall velocities in thin iron-nickel films—300S
Foster, E. L. (see Berman, R.)—2156
Foster, K. and J. J. Kramer. Effect of directional orientation on the magnetic properties of cube-oriented magnetic sheets—233S
—— (see Pavlovic, D.)—231S
Fotland, Richard A. Some electrical properties of amorphous selenium films—1558
Fourdeux, A., A. Berghezan, and W. W. Webb. Stacking faults in zinc—918
Fourie, J. T., F. Weinberg, and F. W. C. Boswell. Preparation of tin single crystals for transmission electron microscopy—1136(L)
—— **and H. G. F. Wilsdorf.** The production of dislocation loops by a combined climb and glide mechanism—2219
Fowler, C. A., Jr., E. M. Fryer and David Treves. Observation of domains in iron whiskers under high fields—2267
Fowler, C. M., W. B. Garn, and R. S. Caird. Production of very high magnetic fields by implosion—588
Fowles, G. R. Attenuation of the shock wave produced in a solid by a flying plate—655
Foy, J. E. and R. J. Parker. Permanent magnet leakage permeance evaluation based on polar radiation analogy—188S
Foy, P. W. (see Batdorf, R. L.)—1153
Frank, F. C. and M. B. Ives. Orientation-dependent dissolution of germanium—1996
Frank, R. C. and J. E. Thomas, Jr. Germanium crystals grown from hollow cylindrical seeds—1689(L)
Frankel, S. (see Caspari, M. E.)—320S
Frankl, D. R. Surface space-charge calculations for semiconductors—1752
Freeman, A. J. and R. E. Watson. Effect of crystalline fields on magnetic form factors—374S
Freeman, Michael W. (M.D.), Anthony Arrott, and John H. L. Watson. Magnetism in medicine—404S
Freitas, L. G. (see Mascarenhas, S.)—1684
Freudenthal, A. M. Prediction of fatigue life—2196
—— Thermal stress analysis and Grueneisen's relation—434(L)
Friedberg, S. A. (see Flippen, R. B.)—338(S)
Frisch, H. L. (see Morrison, J. A.)—1621
Froelich, H. (see Brannen, E.)—1829(L)
Fryer, E. M. (see Fowler, C. A., Jr.)—2267
Fuller, C. S. (see Whelan, J. M.)—1507(L)
Fuller, Harrison W. and Murray E. Hale. Determination of magnetization distribution in thin films using electron microscopy—238
—— **and Murray E. Hale.** Domains in thin magnetic films observed by electron microscopy—1699
—— **and Murray E. Hale.** Static and dynamic studies of magnetization distribution in thin films by electron microscopy—308S
—— (see Rubinstein, Harvey)—437(L)

Gabrysh, A. F., H. Eyring, M. E. Wadsworth, G. S. Baker, and T. Ree. Study of irradiation effects and the H^3+H^3 buildup in tantalum—1785
Gaines, George L., Jr. Backscattering of carbon-14 beta radiation—741(L)
Ganz, D. (see Baer, G.)—235S
Garn, W. B. (see Fowler, C. M.)—588
Garvin, H. L., W. B. Teutsch, and R. W. Pidd. Generation of alternating current in the cesium cell—1508(L)
Gatos, Harry C. and Mary C. Lavine. Dislocation etch pits on the {111} and {$\bar{1}\bar{1}\bar{1}$} surfaces on InSb—743(L)
——, **P. L. Moody, and M. C. Lavine.** Growth of InSb crystals in the (111) polar direction—212(L)
—— (see Moody, P. L.)—1696(L)
—— (see Warekois, E. P.)—1302(L)
Gazza, George E. (see Tarpinian, A.)—1657
Geil, P. H. (see Reneker, D. H.)—1916
Geiszler, T. D. and R. A. Henschke. Broadband reciprocal ferrite phase shifters—174S
Geller, S. Magnetic interactions and distribution of ions in the garnets—30S
Germer, L. H. and C. D. Hartman. Oxygen in nickel—2085
Gerritsen, H. J., S. E. Harrison, and H. R. Lewis. Chromium-doped titania as a maser material—1566
—— **and H. R. Lewis.** Operation of a chromium-doped titania maser—608(L)
Gerson, Robert. Dielectric properties of lead titanate zirconate ceramics at very low frequencies—1615
—— Variation in ferroelectric characteristics of lead zirconate titanate ceramics due to minor chemical modifications—188
Gibson, Edward F. (see Powell, Robert L.)—504, 1221
Gifford, F. E. and E. A. Coomes. Torsion induced recrystallization of molybdenum and tungsten filaments—235
Gilfrich, John V. (see Hubbard, William M.)—368S
Gilleo, M. A. (see Caspari, M. E.)—320S
Gilman, J. J. Terraces on etchpits—936(L)
—— Direct measurements of the surface energies of crystals—2208
—— **and W. G. Johnston.** Behavior of individual dislocations in strain-hardened LiF crystals—687
—— (see Johnston, W. G.)—632
Giordmaine, J. A. and T. C. Wang. Molecular beam formation by long parallel tubes—463
Giron, V. S. (see Néel, L.)—27S
Gjevre, J. A. (see Smith, J. F.)—645
Glasier, Louis F. (see Allen, R. D.)—1382
Godlove, T. F. and D. C. dePackh. Adiabatic collapse of a relativistic electron beam—2016
Goedecke, G. H. (see Brown, E.)—932
Goetzberger, A. Uniform avalanche effect in silicon three-layer diodes—2260
—— **and W. Shockley.** Metal precipitates in silicon p-n junctions—1821
Goldring, G., M. Schieber, and Z. Vager. On the incorporation of neodymium in mixed yttrium-neodymium-iron garnets—2057

Goldstein, Martin. Depolarized components of light scattered by glasses. II. Influence of nonannealable strains on the scattering—1697(E)
Goldwater, D. L. (see Danforth, W. E.)—1715
Goodenough, John B. Direct cation-cation interactions in primarily ionic solids—359S
——, **A. Wold, and R. J. Arnott.** Interpretation of the magnetic and crystallographic properties of several iron, nickel, and iron-nickel nitrides—342S
Gordon, E. I. Charged-particle orbits in varying magnetic fields—1187
Gordon, Robert B. (see Bauer, C. L.)—945
Gordy, Walter and Monroe Cowan. Proposed molecular amplifier and coherent generator for millimeter and submillimeter waves—941(L)
Gorton, H. C. (see Wieber, R. H.)—608(L)
Gossard, A. C. (see Portis, A. M.)—205S
Gosselin, C. M. (see Grosskreutz, J. C.)—1127(L)
Gossick, B. R. Correlation between certain extinction bands of solids and plasma resonance—650
—— Dipole mode of minority carrier diffusion with reference to point contact rectification—29
—— Optical absorption by free carriers in a semiconductor containing a dispersed colloidal phase—648
—— Transistor with base containing a dispersed colloidal phase—745(L)
Gottlieb, Peter. Double pump degenerate ferrite amplifier —172S
—— Nonlinear effects of crystalline anisotropy on ferromagnetic resonance—2059
Graham, C. D., Jr. Temperature dependence of anisotropy and saturation magnetization in iron and iron-silicon alloys —150S
Graham, D. C. (see Agarwal, P. D.)—249S
Graham, R. A. Depth of indentation on an impacting projectile—619(L)
Granath, J. A. Instrumentation applications of inverse-Wiedemann effect—178S
Gray, Glenn A. Single-velocity equivalents for multivelocity electron streams—370
Green, J. J. (see Schlömann, E.)—385S
Greenberg, J. Mayo. Scattering by nonspherical particles —82
Greenler, Robert G. and William S. Rothwell. Ductility of NaCl crystals—616(L)
Gregg, D. W. and H. G. Drickamer. Effect of pressure on phosphor decay—494
Greifer, Aaron P. and William J. Croft. Rectangular hysteresis loop ferrites with large Barkhausen steps—85
Greiner, J. H., I. M. Croll, and M. Sulich. Ferromagnetic-antiferromagnetic interaction in Fe-FeS—2316(L)
Griffiths, V. (see Saimoto, S.)—1693(L)
Gross, Bernhard, Arthur Bradley, and Arthur P. Pinkerton. Beta particle transmission currents in solid dielectrics —1035
Gross, K. A. (see Weaver, C. W.)—626
Grosskreutz, J. C. and C. M. Gosselin. Surface deformation of aluminum in fatigue—1127(L)
Grover, G. M. (see Ranken, W. A.)—2140
Gumnick, J. L. and D. W. Juenker. Field dependence of photoelectric emission from tantalum—102
Gutwin, O. A. (see Brownlow, J. M.)—121S
Gwathmey, Allan T. (see Bailey, John M.)—215(L)
—— (see Young, F. W., Jr.)—225
Gyorgy, E. M. Flux reversal in soft ferromagnetics—110S
—— **and F. B. Hagedorn.** Interaction between high-power microwave losses and magnetic flux reversal—1775
—— (see Hagedorn, F. B.)—398S
Haas, George A. and John T. Jensen, Jr. Thermionic properties of UC—1231
Hagedorn, F. B. and E. M. Gyorgy. Switching behavior of low-remanence ferrite—398S
—— (see Gyorgy, E. M.)—1775
Hagstrum, Homer D. Detection of metastable atoms and ions—897
—— **and C. D'Amico.** Production and demonstration of atomically clean metal surfaces—715
Hakeem, M. A. and Harry S. Robertson. Alkali vapor plasmas—2063(L)
Hale, Murray E. (see Fuller, Harrison W.)—238, 308S, 1699
—— (see Rubinstein, Harvey)—437(L)
Hall, R. C. Magnetic anisotropy and magnetostriction of ordered and disordered cobalt-iron alloys—157S
—— Single-crystal magnetic anisotropy and magnetostriction studies in iron-base alloys—1037
Hall, William J. (see Powell, Robert L.)—496
Ham, Joe S. Kinetic theory of thermal diffusion in dilute polymer solutions—1853
Hames, F. A. Ferromagnetic alloy phases near the compositions Ni_2MnIn, Ni_2MnGa, Co_2MnGa, Pd_2MnSb, and PdMnSb—370S
Hamilton, D. R. Interferometric determination of twist and polytype in silicon carbide whiskers—112
—— **and R. G. Seidensticker.** Propagation mechanism of germanium dendrites—1165
Hamilton, J. F. and L. E. Brady. Print-out process in photographic emulsion grains—609(L)
Haneman, D. Behavior of InSb surfaces during heat treatment—217(L)
Hanes, G. R. A multiple tube collimator for gas beams—2171
Hanson, Roland C. and Frederick C. Brown. Hall mobility of holes in AgBr—210(L)
Hanton, J. P. (see Brown, W. F.)—214S
Happ, W. W. (see Castro, P. S.)—1314
Harada, Roy (see McCaldin, J. O.)—2065(L)
Harden, James L. (see Powell, Robert L.)—1221
Harker, K. J. Determination of electrode shapes for axially symmetric electron guns—2165
Harris, A. B. (see Meyer, Horst)—49S
Harris, C. C. Alternative forms of some exponential and power functions for graphical representation—215(L)
—— Alternative forms of some exponential and power functions for graphical representation—942(E)
Harris, L. A. (see Anderson, J. M.)—1463
Harrison, Don E., Jr. (see Yonts, O. C.)—447, 1583
Harrison, S. E. (see Gerritsen, H. J.)—1566
Hart, Philip J. Effect of gas pressure and cone angle on the velocities of electrically excited shock waves—436(L)
Hart, R. W. (see McClure, F. T.)—884
Harte, K. J. Flux reversal by noncoherent rotation in magnetic films—283S
Hartman, C. D. (see Germer, L. H.)—2085
Haszko, S. E. (see Wolfe, R.)—1959
Haymann, P. (see Cunningham, R. L.)—839
Haynes, A. and C. C. Hsiao. Effect of temperature and reactor irradiation on the strength of biaxially oriented polyethylene terephthalate—1871
Heffner, H. and G. Wade. Noise figure and gain of parametric converters—2316(L)
Heidenreich, R. D. (see Nesbitt, E. A.)—228S
Heikes, Robert R. (see McGuire, Thomas R.)—276S
—— (see Sherman, B.)—1
Heimke, G. Temperature dependence of the saturation magnetization of ferrites with magnetoplumbite structure—271S

Helmer, J. C., F. B. Jacobus, and P. A. Sturrock. Focusing molecular beams of NH_3—458
Hendricks, C. D. (see Shelton, H.)—1243
Henry, Irvin G. Phase oscillations in high current synchrotrons—1338
Henry, Warren E. Strong field magnetization at low temperatures and approach to absolute saturation of thulium metal—323S
Henschke, R. A. (see Geiszler, T. D.)—174S
Herring, Conyers. Effect of random inhomogeneities on electrical and galvanomagnetic measurements—1939
—— State of *d* electrons in transition metals—3S
Hershberger, W. D. Absorption and reflection spectrum of a plasma—417
Heuer, A. (see Straley, R.)—126S
Hickmott, T. W. Interaction of atomic hydrogen with glass —128
Hill, R. M. and S. K. Ichiki. Microwave noise from low-pressure arcs—735(L)
Hilsum, C. (see Edmond, J. T.)—1300(L)
Hirai, Nishio (see Kim, Wan Kyue)—358
Hirsch, R. L. Effect of interelectrode spacing on cesium thermionic converter performance—2064(L)
Hoffman, L. C. (see Statton, W. O.)—404
Hoffman, R. W. (see Yelon, Arthur)—1672
Hokkeling, P. (see Koch, A. J. J.)—75S
Holden, F. C., J. B. Melehan, H. R. Ogden, and R. I. Jaffee. Formation and initial growth of single-asperity solid-state bonds—670
Holland, V. F. (see Anderson, F. R.)—1516
Hollander, Lewis E. and T. J. Diesel. Piezoresistive effect in *p*-type PbTe—692
Holmes, D. K. and G. Leibfried. Range of radiation induced primary knock-ons in the hard core approximation —1046
Holroyd, L. V. (see Cave, E. F.)—1357
Holt, D. B. Filled and empty dangling bonds in III-V compounds—2231
Holwech, Ivar. Recovery of internal friction in aluminum after plastic deformation—928
Hooper, E. T., Jr. (see Krall, A. D.)—178S
Hoskins, R. H. and R. C. Pastor. Charred dextrose as a paramagnetic resonance standard—1506(L)
Houston, B. B. and Marriner K. Norr. Dislocation etch pits on *p*-type lead telluride—615(L)
Hsiao, C. C. and S. T. Chow. Effect of reactor irradiation on the tensile strength of uniaxially oriented polyethylene terephthalate—1869
—— (see Haynes, A.)—1871
—— (see Robinson, A.)—1602
Hsu, Hwei-Piao. Aperture fields in the diffraction by a slit —1742
—— (see Plonsey, Robert)—445(E)
Hubbard, William M., Edmond Adams, and John V. Gilfrich. Magnetic moments of alloys of gadolinium with some of the transition elements—368S
Huber, E. E. (see Cohen, M. S.)—291S
—— (see Smith, D. O.)—295S
Hughes, F. L. (see Matarrese, L. M.)—2063(L)
Hung, John Wenchung. Transfer function and error probability of a digital magnetic tape recording system—396S
Hurwitz, H. (see Auer, P. L.)—1007
Huston, Norman E. (see Backus, John)—400
Huyett, M. J. (see Lundberg, J. L.)—1131(L)
Hyndman, D. and G. F. Origlio. NMR absorption in Teflon fibers—1849

Ichiki, S. K. (see Hill, R. M.)—735(L)
Iida, Shuichi. Role of cation vacancy in magnetic annealing of iron-cobalt ferrites—251S
Irving, B. A. Shapes of etch hillocks and pits and their correlation with measured etch rates—109
Itoh, T. and Musha, T. Monte Carlo calculations of the motions of electrons in helium—744(L)
Itzkan, I. Solutions of the equations of space charge flow for radial flow between concentric spherical electrodes—652
Ives, M. B. (see Frank, F. C.)—1996

Jacobs, I. S. High field magnetization study of ferrimagnetic arrangements in chromite spinels—263S
—— **and P. E. Lawrence.** Exchange anisotropy memory effect—1388
—— (see Bean, C. P.)—1228
Jacobus, F. B. (see Helmer, J. C.)—458
Jaffe, L. D. (see Martens, H. E.)—1122(L)
Jaffee, R. I. (see Holden, F. C.)—670
Janes, Sargent G. and H. Koritz. Numerical calculation of absolute bremsstrahlung intensity for a fully ionized dissociated hydrogenic gas—525
Jelley, J. V. Time discrimination in solid-state infrared quantum counters—1145
Jensen, John T., Jr. (see Haas, George A.)—1231
Jensen, R. V. (see Rosi, F. D.)—1105
Johnson, Curtis C. Theory of fast-wave parametric amplification—338
Johnston, W. G. and J. J. Gilman. Dislocation multiplication in lithium fluoride crystals—632
—— (see Gilman, J. J.)—687
Jones, R. V. (see Rodrigue, G. P.)—376S
Jordan, Paul L. (see Allen, Robert D.)—1382
Jordan, R. D. and R. S. Alger. Specific ionization measurements and energy requirements for *F*-center formation—747
Joseph, L. (see Tompkins, J. E.)—176S
Juenker, D. W. (see Gumnick, J. L.)—102
Juretschke, H. J. Electromagnetic theory of dc effects in ferromagnetic resonance—1401

Kalnins, I. L. (see Flaschen, S. S.)—431(L)
Kaminow, I. P. Volume dependence of ferrimagnetic resonance properties in $Ni_{1-x}Co_xFe_2O_4$—220S
Kanamori, Junjiro. Crystal distortion in magnetic compounds—14S
Kane, B. (see Straley, R.)—126S
Kaplan, T. A. Classical theory of spin configurations in the cubic spinel—364S
Karal, Frank C., Jr. (see Keller, J. B.)—1039
Katayev, G. I. (see Belov, K. P.)—153S
Katz, J. M. (see Seiden, P. E.)—1291
Keedy, D. A., J. Powers, and R. S. Stein. Theoretical calculation of the birefringence of polypropylene crystals —1911
Keh, A. S. Dislocation networks in a low-alloy steel—1501(L)
—— Dislocations in indented magnesium oxide crystals—1538
Keller, Joseph B. and Frank C. Karal, Jr. Surface wave excitation and propagation—1039
Kelley, Clinton M. (see Wiechec, Walter)—131S
Kelley, R. H. (see Kulp, B. A.)—1057
Kelly, Donald and Henry Margenau. High-frequency breakdown of air—1617
Kennedy, David P. Minority carrier current in a linearly graded drift field—218(L)
—— Minority carrier recombination in a cylindrical transistor base region—954
—— Spreading resistance in cylindrical semiconductor devices—1490
Kerr, John T. (see Todd, Johnson B.)—51

Kerwin, Larkin and Paul Marmet. Recent appearance potential measurements using an electrostatic electron selector—2071
Kilkson, Rein (see Toth, R. S.)—1117
Killeen, J. and B. A. Lippmann. Circuit dynamics of the pinch—1549
Kim, Wan Kyue, Nishio Hirai, Taikyue Ree, and Henry Eyring. Theory of non-Newtonian flow. III. Method for analyzing non-Newtonian flow curves—358
Kingery, W. D. Regelation, surface diffusion, and ice sintering—833
—— **and M. P. Lepie.** Solution-precipitation deformation under an applied stress—610(L)
Kino, G. S. Parametric amplifier theory for plasmas and electron beams—1449
Kirk, E. S. (see Smith, Mac J.)—1504(L)
Kirschbaum, Albert J. (see Sparks, Joseph T.)—356S
Kiseda, J. R. (see Seelbach, W. C.)—135S
Kittel, C. Microwave resonance in rare earth iron garnets —11S
Kleber, E. V. (see Vickery, R. C.)—366S
Klein, Milton M. and Keith A. Brueckner. Plasma propulsion by a rapidly varying magnetic field—1437
Kleinman, D. A. and A. L. Schawlow. Corbino disk—2176
Klement, W., Jr. (see Duwez, Pol)—1136(L), 1137(L), 1500(L)
Knechtli, R. C. and R. D. Weglein. Diode capacitors for parametric amplification—1134(L)
Koch, A. J. J., P. Hokkeling, M. G. v.d. Steeg, and K. J. deVos. New material for permanent magnets on a base of Mn and Al—75S
Koehler, W. C. (see Wilkinson, M. K.)—358S
Kohler, Dale. Promotion of cubic grain growth in 3% silicon iron by control of annealing atmosphere composition —408S
Kolbe, C. L. and D. L. Martin. Hot working of Alnico 5 alloys—84S
Kondorsky, E. I. and V. L. Sedov. Antiferromagnetism of iron in face-centered crystalline lattice and the causes of anomalies in Invar physical properties—331S
Kooi, C. F. (see Seiden, P. E.)—1291
Koritz, H. (see Janes, Sargent G.)—525
Koros, R. M., J. Deckers, and M. Boudart. More experiments on liquid films—1129(L)
Kostelec, Joze. Reciprocity law failure in ZnO and Se—441(L)
Kostyshyn, B., J. E. Brophy, I. Oi, and D. D. Roshon, Jr. External fields from domain walls of cobalt film—772
Kouvel, J. S. Exchange anisotropy in Cu-Mn and Ag-Mn alloys—142S
—— (see Pry, R. H.)—162S
Krall, A. D. and E. T. Hooper, Jr. Ferromagnetic powders in waveguides at elevated temperatures—178S
Kramer, J. J. (see Foster, K.)—233S
Kronenberg, K. J. Transmission electron diffraction of Alnico V—80S
—— **and M. A. Bohlmann.** Long-term magnetic stability of Alnico and barium ferrite magnets—82S
Kuczynski, G. C. Anomalous thermionic emission from UC and $(ZrC)_{0.8}(UC)_{0.2}$—1500(L)
Kuhlmann-Wilsdorf, Doris, and H. G. F. Wilsdorf. On the behavior of thermal vacancies in pure aluminum—516
Kulp, B. A. and R. H. Kelley. Displacement of the sulfur atom in CdS by electron bombardment—1057
Kurtz, A. D. and R. Yee. Diffusion of boron into silicon —303
—— (see Allen, R. B.)—334

LaBonte, A. E. (see Muckenhirn, William O.)—304S
Lad, R. A. (see Stearns, C. A.)—231
Ladell, J. (see Spielberg, N.)—1660
Lalevic, Bogoljub. Criteria for the choice of a superconducting bolometer—1234
Lambe, J. (see Makhov, G.)—936(L)
Landauer, Rolf. Parametric amplification along nonlinear transmission lines—479
Landel, Robert F. and Paul J. Stedry. Stress as a reduced variable: stress relaxation of SBR rubber at large strains —1885
LaPadula, A. R. (see Bartholomew, C. Y.)—445(L)
Larkin, B. K. (see Bailey, H. R.)—1123(L)
Larrabee, R. D. and M. C. Steele. Oscillistor—new type of semiconductor oscillator—1519
Lauriente, M. and G. E. Lynn. Characteristics of Supermendur at 500°C—237S
Lavine, Mary C. (see Gatos, Harry C.)—212(L), 743(L)
—— (see Moody, P. L.)—1696(L)
—— (see Warekois, E. P.)—1302(L)
Law, J. T. (see Allen, F. G.)—979
Lawrence, P. E. (see Jacobs, I. S.)—1388
—— (see Rodbell, D. S.)—275S
Lawson, A. W. (see Eckstein, Y.)—1534
Lecomte, C. (see Cunningham, R. L.)—839
Leder, Lewis B. and J. A. Suddeth. Characteristic energy losses of electrons in carbon—1422
LeCraw, R. C., R. C. Fletcher, and E. G. Spencer. Electron spin relaxation in ferromagnetic insulators—95S
Lee, C. A. and G. Kaminsky. Anomalous barrier capacitance in p-n junctions of InSb—1717
Lee, T. H. Energy distribution and cooling effect of electrons emitted from an arc cathode—924
Legg, V. E. (see Alley, R. E.)—239S
Leibfried, G. Defects in dislocations produced by focusing collisions in fcc lattices—117
—— (see Holmes, D. K.)—1046
Leiby, C. C., Jr., and C. L. Chen. Diffusion coefficients, solubilities, and permeabilities for He, Ne, H_2 in Vycor glass—268
Leliak, P. Manipulation of cesium—609(L)
Lepie, M. P. (see Kingery, W. D.)—610(L)
Levengood, W. C. and T. S. Vong. Spiral dislocations on glass fracture surfaces—1416
Levi, E. P. Permanent magnets obtained by drawing compacts of parallel iron wires—1469
Levi, Leo. Response of a loaded idealized piezoelectric plate to an electric signal—1237
Levine, H. S. and C. J. MacCallum. Grain boundary and lattice diffusion in polycrystalline bodies—595
Levine, Morton A. (see Chace, William G.)—1298(L)
Levitin, R. Z. (see Belov, K. P.)—153S
Lewis, H. R. (see Gerritsen, H. J.)—608(L), 1566
Lewis, H. W. and J. R. Reitz. Efficiency of the plasma thermocouple—723
Li, James C. M. and Charles D. Needham. Some elastic properties of a screw dislocation wall—1318
Lichtman, David. Use of the omegatron in the determination of parameters affecting limiting pressures in vacuum devices—1213
Lin, S. T. Magnetic behavior in the transition region of a hematite single crystal—273S
Lindemann, W. W. and R. K. Mueller. Grain-boundary photoresponse—1746
Lineweaver, Jack L. (see Todd, B. Johnson)—51
Lippmann, B. A. (see Killeen, J.)—1549
Litovitz, T. (see Meister, R.)—854
Little, Warren J. and Kathryn A. McCarthy. On the observation of macroscopic spirals on gallium arsenide surfaces—1298(L)
Livingston, J. D. Etch pits at dislocations in copper—1071
Logan, R. A. and A. J. Peters. Impurity effects upon mobility in silicon—122

Long, T. R. Electrodeposited memory elements for a nondestructive memory—123S
Longini, R. L., A. I. Bennett, and W. J. Smith. Growth of atomically flat surfaces on germanium dendrites—1204
Lotgering, F. K. (see Smit, J.)—137S
Lothe, Jens. Theory of dislocation climb in metals—1077
Lougher, E. H. (see Simon, R.)—2160
Low, J. R., Jr. (see Stein, Dale F.)—362
Luborsky, F. E. and T. O. Paine. Angular variation of the magnetic properties of elongated single-domain iron particles—66S
—— **and T. O. Paine.** Coercive force and remanence of 25 A to 2000 A diameter cobalt, iron, and iron-cobalt alloy—68S
—— (see Paine, T. O.)—78S
Lucovsky, Gerald. Photoeffects in nonuniformly irradiated p-n junctions—1088
Lundberg, J. L., M. B. Wilk, and M. J. Huyett. Solubilities and diffusivities of nitrogen in polyethylene—1131(L)
Lurio, A. and E. Stern. Dielectric behavior of single crystals of tri-glycine sulfate (TGS) from 1 kc to 2500 Mc—1125(L)
—— **and E. Stern.** Measurements of the dielectric constant of $BaTiO_3$ single crystals in the paraelectric region at X band—1805
Lynn, G. E. (see Lauriente, M.)—237S

MacCallum, C. J. (see Levine, H. S.)—595
Macrakis, Michael S. Theoretical and experimental study of the back-scattering cross section of an infinite ribbon—2261
Mader, Charles L. (see Zinn, John)—323
Maiman, T. H. Maser behavior: temperature and concentration effects—222(L)
Maissel, Leon. Thermal expansion of silicon—211(L)
Makhov, G., L. G. Cross, R. W. Terhune, and J. Lambe. Effect of nuclear polarization on the behavior of solid state masers—936(L)
Makolagwa, Stefan. Effect of potassium ions on the reaction and final properties of Mn-Zn ferrite—339S
Málek, Z. (see Andrä, W.)—442(L)
Mandelkern, L. (see Posner, A. S.)—536
Maradudin, A. A. and P. A. Dixon. Effect of impurities on the low-temperature spontaneous magnetization of cubic ferromagnetic crystals—329S
Marcinkowski, M. J. and R. M. Fisher. Direct observation of antiphase domain boundaries in the $AuCu_3$ superlattice—1687(L)
——, **R. M. Fisher, and N. Brown.** Direct observation of superdislocations in a superlattice—1303(L)
Margenau, Henry (see Kelly, D.)—1617
Marhoeffer, C. J. (see Meister, R.)—854
Marinace, John C. (see Ruth, Ralph P.)—995
Maringer, R. E. Effects of directional ordering on the damping of zone-melted iron—229S
Marmet, Paul (see Kerwin, Larkin)—2071
Marsh, S. P. (see McQueen, R. G.)—1253
Marshall, S. A. and A. R. Reinberg. Paramagnetic resonance absorption of nickel in sapphires—336S
Marshall, Walter (see Sparks, Joseph T.)—356S
Martens, H. E. and L. D. Jaffe. Tensile strength of pyrolytic graphite up to 2750°C—1122(L)
Martin, D. L. (see Kolbe, C. L.)—84S
Martin, Don S., Jr. (see Reade, Richard F.)—1965
Martin, E. E., J. K. Trolan, and W. P. Dyke. Stable, high density field emission cold cathode—782
Martin, Edward A. Experimental investigation of a high-energy density, high-pressure arc plasma—255
Martin, Stanley B. Simple radiant heating method for determining the thermal diffusivity of cellulosic materials—1101
Martius, U. M. (see Bratina, W. J.)—241S
Mascarenhas, S. and Freitas, L. G. Influence of crystallographic orientation on the charge formation during phase changes in solids—1684
Mason, Peter. Longitudinal wave propagation in stretched polymers—1706
Mastel, B. (see Bierlein, T. K.)—2314(L), 2315(L)
Masters, Joseph I. Instability of magnetic resonance in single crystal spheres of yttrium iron garnet—41S
Matarrese, L. M. and F. L. Hughes. Modification in technique for growing single crystals of ZnF_2:Mn—2063(L)
Matisoo, J. (see Pugh, E. W.)—293S
Matthias, Bernd. Relations between superconductors and ferromagnets—23S
Maurer, William C. and John S. Rinehart. Impact crater formation in rock—1247
Mayer, Ludwig. Nucleation experiments in thin magnetic MnBi films—384S
—— Observations on MnBi films during heat treatment—346
Mayfield, Earle B. and James W. Rogers. Cratering and shock wave phenomena in steel plates at high impact speeds—472
Mayfield, J. R. Microcalorimetric technique for the study of damping and hysteresis in ferromagnetic films—298S
McCaldin, J. O. Interaction between arsenic and aluminum in germanium—89
—— **and Roy Harada.** Influence of arsenic pressure on the doping of gallium arsenide with germanium—2065(L)
McCarthy, Kathryn A. and Stanley S. Ballard. Thermal conductivity of eight halide crystals in the temperature range 220°K to 390°K—1410
—— (see Little, Warren)—1298(L)
McClain, William C. (see Rinehart, John S.)—1809
McClure, F. T., R. W. Hart, and J. F. Bird. Acoustic resonance in solid propellant rockets—884
McClure, J. W. (see Broudy, R. M.)—1511
McDuffie, G. E., Jr., J. Richard Cunningham, Jr., and Elmer E. Anderson. Initial permeability characteristics of mixed yttrium-gadolinium iron garnets—47S
McGuire, Thomas R. and Robert R. Heikes. Magnetic properties of the $Li_xMn_{1-x}Se$ system—276S
McKay, R. W. and K. C. Smith. Effect of previous history on switching rate in ferrites—133S
McMahon, Robert E. (see Tancrell, Roger H.)—762
McQueen, R. G. and S. P. Marsh. Equation of state for nineteen metallic elements from shock-wave measurements to two megabars—1253
McSkimin, H. J. and E. S. Fisher. Temperature dependence of the adiabatic elastic moduli of single-crystal alpha uranium—1627
Mead, Warren (see Sparks, Joseph T.)—356S
Meckel, B. B., E. G. K. Schwarz, and R. A. Swalin. Microscopic study of neutron-irradiated germanium—1299(L)
Meiklejohn, W. H. and R. E. Carter. Exchange anisotropy in rock magnetism—164S
Meister, R., C. J. Marhoeffer, R. Sciamanda, L. Cotter, and T. Litovitz. Ultrasonic viscoelastic properties of associated liquids—854
Melehan, J. B. (see Holden, F. C.)—670
Mendel, E. and S. Weinig. Generation of dislocations by an electric field in MgO—738(L)
Mendelsohn, L. I. Rictometer system for calibrating transmitters of remote indicating compasses—183S
Menes, M. (see Bolef, D. I.)—1010, 1426
Meredith, Robert E. and Charles W. Tobias. Resistance to potential flow through a cubical array of spheres—1270
Merz, Kenneth M. X-ray study of ferromagnetic domains in cobalt zinc ferrite—147

Methfessel, S., S. Middelhoek, and H. Thomas. Domain walls in thin magnetic Ni-Fe films—302S
Meyer, Horst and A. B. Harris. Specific heat of some rare earth iron garnets and YIG at low temperatures—49S
—— (see Rodrigue, G. P.)—376S
Meyerhofer, D. (see Rosi, F. D.)—1105
Middelhoek, S. (see Methfessel, S.)—302S
Miksch, E. S. (see Pry, R. H.)—162S
Milano, U. (see Schlömann, E.)—385S
Miller, Arthur. Valence and distribution of manganese ions in ferrospinels—261S
Miller, D. S. (see Arajs, Sigurds)—213(L), 325S, 986
Miller, K. Dexter, Jr. Distribution of spray from impinging liquid jets—1132(L)
Miller, M. H. Comments on article by Cook—607
Miller, Robert C. and Albert Savage. Motion of 180° domain walls in metal electroded barium titanate crystals as a function of electric field and sample thickness—662
—— (see Savage, A.)—1546
Mills, D. (see Bratina, W. J.)—241S
Minturn, Robert E., Sheldon Datz, and Ellison H. Taylor. Thermal emission of alkali ion pulses from clean and oxygenated tungsten—871
—— (see Datz, Sheldon)—880
Mittlestadt, Verlyn R. (see Oskam, Hendrik J.)—940(L)
Miyake, Kiyoshi. Formation of cesium antimonide. I. Electrical resistivity of the film of cesium-antimony system—76
Mojoni, A. (see Bonfiglioli, G.)—684
Momo, L. R., R. A. Myers, and S. Foner. Pulsed field millimeter wave maser—443(L)
—— (see Foner, S.)—742(L)
Montalenti, G. (see Biorci, G.)—2046, 2121
Moody, P. L., H. C. Gatos, and M. C. Lavine. Growth of GaAs crystals in the ⟨111⟩ polar direction—1696(L)
—— (see Gatos, Harry C.)—212(L)
Moore, A. C. and A. S. Young. Some physical properties of thin magnetic films—279S
Moore, W. J. (see Cunningham, R. L.)—839
Morgan, J. V. (see Spencer, H. E.)—2024
Morgenthaler, Frederic R. Survey of ferromagnetic resonance in small ferrimagnetic ellipsoids—95S
—— (see Stiglitz, Martin P.)—37S
Morrish, A. H. (see Brown, W. F.)—214S
—— (see Watt, L. A. K.)—71S
Morrison, J. A. Noise propagation in drifting multivelocity electron beams—2066(L)
—— **and H. L. Frisch.** Bounds on the nonlinear diffusion controlled growth rate of spherical precipitates—1621
—— (see Barr, L. W.)—617(L)
Mortenson, K. E. Comments on "Diode capacitors for parametric amplification" by R. C. Knechtli and R. D. Weglein—1135(L)
—— Parametric diode figure of merit and optimization—1207
Moser, J. B. and D. H. Whitmore. Kinetics of sintering of sodium chloride in the presence of an inert gas—488
Muckenhirn, O. William, A. E. LaBonte, and P. J. Besser. Annular uniaxially magnetized domains in thin Ni-Fe films—304S
Mueller, D. K. (see Lindemann, W. W.)—1746
Musha, T. (see Itoh, T.)—744(L)
Myers, R. A. (see Momo, L. R.)—443(L)

Nanni, L. F. (see Slade, J. J., Jr.)—699
Nassau, K. and L. G. Van Uitert. Preparation of large calcium-tungstate crystals containing paramagnetic ions for maser applications—1508(L)
Nathans, Robert. Precise measurement of magnetic form factors—350S
—— (see Pickart, S. J.)—372S
Needham, Charles D. (see Li, James C. M.)—1318
Néel, L., R. Pauthenet, G. Rimet, and V. S. Giron. On the laws of magnetization of ferromagnetic single crystals and polycrystals. Application to uniaxial compounds—27S
Nelson, C. M. (see Weeks, R. A.)—1555
Nesbitt, E. A., R. D. Heidenreich, and A. J. Williams. Necessary factor for heat treatment of the permalloys in a magnetic field—228S
Neugebauer, C. A. Temperature dependence of the saturation magnetization of nickel films of thickness less than 100 A—152S
—— Tensile properties of thin, evaporated gold films—1096
Neurath, P. W. Simple recording torque magnetometer—184S
Nevitt, M. V. Magnetization of the compound TiFe—155
—— Magnetization of the compound TiFe—942(E)
Newkirk, H. W. (see Brenden, B. B.)—737(L)
Newman, R. C. (see Bullough, R.)—707
Niegisch, Walter D. and Paul R. Swan. Hollow pyramidal crystals of polyethylene and a mechanism of growth—1906
Nielsen, J. W. Improved method for the growth of yttrium-iron and yttrium-gallium garnets—51S
—— (see Dillon, J. F.)—43S
Nine, Harmon D. and Norman W. Schubring. Photographic verification of ultrasonic plane wave scattering by cylinders—1274
Noggle, T. S. and J. O. Stiegler. Electron microscope observations of fission fragment tracks in thin films of UO_2—2199
—— (see Stiegler, J. O.)—1827(L)
—— (see Young, F. W., Jr.)—604
Nolle, A. W. Effect of pressure on the dynamic shear behavior of polyisobutylene—1694(L)
Nomura, K. C. (see Blakemore, J. S.)—753, 2226
Normand, C. E. (see Yonts, O. C.)—447
Norr, Marriner K. (see Houston, B. B.)—615(L)
Northover, William R. (see Flaschen, S. S.)—219(L)
Northrip, John W. High temperature discharges in ferroelectric ceramics—2293
Novy, V. F. (see Vickery, R. C.)—366S

O'Connor, J. R. Peltier coefficient at a solid-liquid interface—1690(L)
Ogden, H. R. (see Holden, F. C.)—670
Oi, I. (see Kostyshyn, B.)—772
Okuda, Takayoshi and Kenzo Yamamoto. Asymmetrical triple probe method for determining energy distribution of electron in plasma—158
Olsen, Clayton E. Magnetic properties of uranium digermanide—340S
Olshaker, A. E. Experimental investigation in lead of the Whipple "meteor bumper"—2118
Oman, R. M. (see Dillon, I. A.)—26
Origlio, G. F. (see Hyndman, D.)—1849
Orr, W. H. (see Bachmann, L.)—1458
Osborn, John A. Preface—1S
Osborn, J. E. (see Robinson, A.)—1602
Oskam, Hendrik J. and Verlyn R. Mittlestadt. Influence of negative ions on ambipolar diffusion of electrons—940(L)
Overhauser, A. W. Mechanism of antiferromagnetism in dilute alloys—317S
Ozaki, H. T. (see Platzman, P. M.)—1597

Pack, A. E. (see Stearns, C. A.)—231
Paine, T. O. and F. E. Luborsky. "Interaction anisotropy" model of the structure of Alnico magnet alloys—78S
—— (see Luborsky, F. E.)—66S, 68S
Pankey, Titus, Jr. Anisotropy of the magnetic susceptibility of gallium—1802

Pao, Yoh-Han and R. F. Bjorklund. Wave functions and energy eigenvalues for the polytetrafluoroethylene chain—1925
Paré, V. K. (see Thompson, D. O.)—528
Parker, R. J. (see Foy, J. E.)—188S
Parratt, L. G. (see Wainfan, N.)—1331
Paskin, Arthur. Long-range magnetic interactions via conduction electrons—318S
—— (see Chipman, D. R.)—1130(L)
Pastor, R. C. (see Hoskins, R. H.)—1506(L)
Pauthenet, R. (see Néel, L.)—27S
Pavlovic, D. and K. Foster. Study of heat treatments for low coercive force 14 to 17% aluminum iron alloys—231S
Pease, M. C. Conservation laws of uniform linear homogeneous systems—1988
—— Time-dependent electron flow—70
Pearson, A. David (see Flaschen, S. S.)—219(L), 431(L)
Pearson, R. F. Magnetic anisotropy in ferrimagnetic crystals—160S
Pedko, A. V. (see Belov, K. P.)—55S
Peet, C. S. (see Wieber, R. H.)—608(L)
Pell, E. M. Effect of Li-B ion pairing on Li^+ ion drift in Si—1675
—— Ion drift in an n-p junction—291
Perlman, M. M. Decay of wax electrets—356
Peter, M., H. G. R. Venkates, and M. W. P. Strandberg. Molecular trajectories in electric fields and state selection in a beam of sodium chloride—693
Peterlin, Anton. Chain folding and free energy density in polymer crystals—1934
Peters, A. J. (see Logan, R. A.)—122
Petersen, E. E. (see Acrivos, A.)—963
Phelps, A. V. Propagation constants for electromagnetic waves in weakly ionized, dry air—1723
Philip, A. G. Davis. Effect of viscosity on the splash caused by a drop of water falling into a mixture of glycerol and water—727
Philippoff, W. Determination of the anisotropy of bond-polarizability of liquids using flow-birefringence measurements—1899
Phillips, Victor A. Polyhedral holes in evaporated AuCu films—697
Philp, Sanborn F. Negative hydrogen and deuterium ion beams—1592
Pickart, S. J. and R. Nathans. Magnetic-form factor of Fe_3Al—372S
Pidd, R. W. (see Garvin, H. L.)—1508(L)
Pietrokowsky, Paul and Frank G. Youngkin. Ordering in the intermediate phases TiFe, TiCo, and TiNi—1763
Pinkerton, Arthur P. (see Gross, B.)—1035
Platzman, P. M. and H. T. Ozaki. Scattering of electromagnetic waves from an infinitely long magnetized cylindrical plasma—1597
Plonsey, Robert and Hwei-Piao Hsu. Diffraction by a slit—445(E)
Pohm, A. V., A. A. Read, R. M. Stewart, Jr., and R. F. Schauer. Operation of magnetic film parametrons in the 100- to 500-Mc region—119S
Pomerantz, Martin A., Remas A. Shatas, and William C. Schieve. Secondary electron emission of MgO crystals bombarded by relativistic electrons—2036
Porbansky, E. M. (see Trumbore, F. A.)—2068(L)
Portis, A. M. and A. C. Gossard. Nuclear resonance in ferromagnetic cobalt—205S
Posner, A. S., L. Mandelkern, C. R. Worthington, and A. F. Diorio. Low angle x-ray diffraction of fibrous polyethylene—536
Powell, Robert L., M. D. Bunch, and Edward F. Gibson. Low-temperature transport properties of commercial metals and alloys. III. Gold-cobalt—504
——, **William J. Hall, and Hans M. Roder.** Low-temperature transport properties of commercial metals and alloys. II. Aluminums—496
——, **James L. Harden, and Edward F. Gibson.** Low-temperature transport properties of commercial metals and alloys. IV. Reactor grade Be, Mo, and W—1221
Powers, J. (see Keedy, D. A.)—1911
Price, P. J. Intervalley noise—949
Primak, William. Large temperature range annealing—1524
Proebster, W. E. (see Dietrich, W.)—281S
Proud, J. M., Jr., R. T. Beyer, and Paul Tamarkin. Reflection of sound from randomly rough surfaces—543
Prutton, M. (see Bradley, E. M.)—285S
Pry, R. H., J. S. Kouvel, and E. S. Miksch. Exchange anisotropy in the system $Mn_{(1-x)}Cr_xSb$—162S
Pugh, E. W., J. Matisoo, D. E. Speliotis, and E. L. Boyd. Magnetic anisotropy in evaporated iron films—293S

Rabins, L. (see Agarwal, Paul D.)—246S
Rado, G. T. and V. J. Folen. Determination of molecular field coefficients in ferrimagnets—62
Rado, G. T. (see Schnitzler, A. D.)—348S
Radus, R. J. Magnetic field measurement using ultrasonics—186S
Rajan, N. S., R. M. Waterstrat, and Paul A. Beck. Temperature-dependence of the electrical resistivity of bcc Cr-Fe alloys—731
Ranken, W. A., G. M. Grover, and E. W. Salmi. Experimental investigations of the cesium plasma cell—2140
Rappaport, Paul (see Wysocki, Joseph J.)—571
Rasor, N. S. Figure of merit for thermionic energy conversion—163
Read, A. A. (see Pohm, A. V.)—119S
Reade, Richard F. and Don S. Martin, Jr. Diffusion of Ag^+, Cl^-, and Cd^{++} in silver chloride single crystals—1965
Ree, Taikyue (see Gabrysh, A. F.)—1785
—— (see Kim, Wan Kyue)—358
Reed, T. B. Determination of streaming velocity and the flow of heat and mass in high-current arcs—2047
Reggia, F. (see Tompkins, J. E.)—176S
Reinberg, A. R. (see Marshall, S. A.)—336S
Reitz, J. R. (see Lewis, H. W.)—723
Remeika, J. P. $GaFeO_3$: A ferromagnetic-piezoelectric compound—263S
Reneker, D. H. and P. H. Geil. Morphology of polymer single crystals—1916
—— (see Eckstein, Y.)—1534
Reynolds, D. C. and S. J. Czyzak. Dislocations in two types of CdS crystals—94
Rhodes, Marion B. (see Stein, Richard S.)—1873
Rhodin, T. N. (see Bachmann, L.)—1458
Richards, J. L. Growth of gallium arsenide by horizontal zone melting—600
—— **and A. J. Crocker.** Etch pits in gallium arsenide—611(L)
Rigert, J. A. (see Bedo, D. E.)—2289
Rigrod, W. W. Power flow and stored energy in thin electron beams—1147
Rimet, G. (see Néel, L.)—27S
Rimmer, M. P. and D. L. Dexter. Optical constants of germanium in the region 0–10 ev—775
Rinehart, John S. and William C. McClain. Experimental determination of stresses generated by an electric detonator—1809
—— (see Maurer, William C.)—1247
Rittner, E. S. On the theory of the close-spaced impregnated cathode thermionic converter—1065
Roberts, J. P. (see Thompson, D. S.)—433(L)
Robertson, Harry S. (see Hakeem, M. A.)—2063(L)

Robinson, A., J. E. Osborn, and C. C. Hsiao. Effect of orientation on strength of a model solid—1602
Robinson, Mark T., A. L. Southern, and William R. Willis. Diffusion of deuterium in deuteron-irradiated copper—1474
Robinson, Robert J. (see Brophy, James J.)—1343
Rodbell, D. S. and P. E. Lawrence. Metamagnetic behavior of manganese arsenide—275S
Roder, Hans M. (see Powell, Robert L.)—496
Rodrigue, G. P., H. Meyer, and R. V. Jones. Resonance measurements in magnetic garnets—376S
Rogers, James W. (see Mayfield, Earle B.)—472
Roof, R. B., Jr. Reply to comments on "Determination of atomic scattering factors"—1131(L)
Rosa, Richard J. Experimental magnetohydrodynamic power generator—735(L)
Rose, A. Photovoltaic effect derived from the Carnot cycle —1640
Rose, D. J. Mobility of hydrogen and deuterium positive ions in their parent gases—632
Rosenberg, D. (see Wehner, G. K.)—177
Rosenburg, Leonard (see Spruch, Larry)—2104
Rosenblatt, Jorge. Three-dimensional space charge flow— 1371
Roshon, D. D., Jr. (see Kostyshyn, B.)—772
Rosi, F. D., D. Meyerhofer, and R. V. Jensen. Properties of *p*-type GaAs prepared by copper diffusion—1105
Rossol, F. C. Subsidiary resonance in the coincidence region in yttrium iron garnet—2273
Roth, R. S. (see Fang, P. H.)—278S
Roth, Walter L. Neutron and optical studies of domains in NiO—2000
—— **and Glen A. Slack.** Antiferromagnetic structure and domains in single crystal NiO—352S
Rothwell, William S. (see Greenler, Robert G.)—616(L)
Rubinstein, Harvey, Harrison W. Fuller, and Murray E. Hale. Observation of Néel walls in thin films—437(L)
—— **and Robert J. Spain.** Cross-tie walls in thin films— 306S
Rudd, J. F. and R. D. Andrews. Photoelastic properties of polystyrene in the glassy state. III. Styrene derivatives and copolymers—818
Ruppel, W. (see Cardona, M.)—1826(L)
Ruth, Ralph P., John C. Marinace, and W. C. Dunlap, Jr. Vapor-deposited single-crystal germanium—995

Sáenz, A. W. Spin waves in complex exchange-coupled lattices and neutron scattering—108S
Sagar, A. (see Faust, J. W., Jr.)—331
Sagnis, James C., Jr., Michael Teig, and Robert L. Ward. Effect of geometry on thick film toroids—190S
Saimoto, S., V. Griffiths, and E. Teghtsoonian. Growth kinks in copper whiskers—1693(L)
Salkovitz, E. I. (see Schindler, A. I.)—245S
Salmi, E. W. (see Ranken, W. A.)—2140
Sargeant, W. E. (see Bockemuehl, R. R.)—180S
Sato, Hiroshi. Analysis of magnetic interactions in alloys of platinum with iron group transition elements—326S
Savage, Albert and R. C. Miller. Temperature dependence of the velocity of sidewise 180° domain-wall motion in $BaTiO_3$—1546
—— (see Miller, Robert C.)—662
Savage, Howard. Effect of Cu precipitation on dislocation etch pits in Ge—1472
Schauer, R. F. (see Pohm, A. V.)—119S
Schaug-Petterson, Tor. Growing spin waves in ferrites in unstable equilibrium—382S
—— (see Elliott, B. J.)—400S
Schawlow, A. L. (see Kleinman, D. A.)—2176
Schenk, H. L. (see Young, F. J.)—194S
Schieber, M. (see Goldring, G.)—2057
Schieve, William C. (see Pomerantz, Martin A.)—2036
Schindler, A. I. and E. I. Salkovitz. Effect of applying a magnetic field during neutron irradiation on the magnetic properties of Fe-Ni alloys—245S
Schlömann, Ernst. Generation of phonons in high-power ferromagnetic resonance experiments—1647
——, **J. J. Green, and U. Milano.** Recent developments in ferromagnetic resonance at high power levels—385S
—— (see Zeender, R. J.)—1112
Schmitt, Hans J. and Dipak L. Sengupta. On the reflection of electromagnetic waves from a medium excited by acoustic waves—439(L)
Schneidmesser, B. (see Berman, R.)—2156
Schnitzler, A. D., V. J. Folen, and G. T. Rado. Ionic ordering effects in the ferromagnetic resonance of lithium ferrite monocrystals—348S
Schock, Alfred. Effect of magnetic fields on thermionic power generators—1978
Schoening, F. R. L. On the strength of glass in water vapor —1779
Schriempf, J. Thomas (see Allison, F. E.)—846
Schroder, K. and C. H. Cheng. Correlation of low temperature caloric and magnetic effects in TiFe—2154
Schubring, Norman W. (see Nine, Harmon D.)—1274
Schultz, J. M. and J. Washburn. Effect of thermal history on the dislocation substructure near the surfaces of a lithium fluoride crystal—1800
Schultz, J. W. (see Blakemore, J. S.)—2226
Schulz, G. J. Use of SF_6^- for calibration of the electron energy scale—1134(L)
Schüppel, W. (see Andrä, W.)—442(L)
Schwarz, E. G. K. (see Meckel, B. B.)—1299(L)
Sciamanda, R. (see Meister, R.)—854
Scott, R. E. New complex phase in the copper-gold system —2112
Scovil, H. E. D. (see DeGrasse, R. W.)—443(L)
Seavey, M. H., Jr. Galvanomagnetic effects in ferromagnetic resonance—216S
Sedov, V. L. (see Kondorsky, E. I.)—331S
Seebold, R. E. (see Sweeney, W. E.)—1061
Seed, T. J. Electron damage in mica—1300(L)
Seelbach, W. C. and J. R. Kiseda. Elastic switching properties of some square loop materials in toroidal structures —135S
Seiden, P. E., C. F. Kooi, and J. M. Katz. Microwave properties of nonstoichiometric polycrystalline yttrium iron garnet—1291
—— **and H. J. Shaw.** High-power effects in ferrimagnetic resonance—432(L)
—— **and H. J. Shaw.** Saturation effects in ferrimagnetic resonance—224S
Seidensticker, R. G. (see Hamilton, D. R.)—1165
Sengupta, Dipak L. (see Schmitt, Hans J.)—439(L)
Sexton, W. C. (see Vickery, R. C.)—366S
Shah, M. J. (see Acrivos, A.)—963
Shatas, Romas A. (see Pomerantz, Martin A.)—2036
Shaw, H. J. (see Elliott, B. J.)—400S
—— (see Seiden, P. E.)—224S, 432(L)
Shelton, H., C. D. Hendricks, and R. F. Wuerker. Electrostatic acceleration of microparticles to hypervelocities —1243
Sherman, B., R. R. Heikes, and R. W. Ure, Jr. Calculation of efficiency of thermoelectric devices—1
Shevel, W. L., Jr., and H. Chang. New approach to high-speed storage—low flux density materials—125S
—— (see Brownlow, J. M.)—121S
Shockley, W. (see Goetzberger, A.)—1821
Shtrikman, S. and D. Treves. Fine structure of Bloch walls —1304(L)

—— **and D. Treves.** Internal structure of Bloch walls—147S
—— **and D. Treves.** On the remanence of ferromagnetic powders—58S
—— **and D. Treves.** On the resolution of Brown's paradox—72S
Sidles, P. H. (see Wallace, D. C.)—168
Siegel, B. M. (see Bachmann, L.)—1458
Siegman, A. E. Waves on a filamentary electron beam in a transverse-field slow-wave circuit—17
Simmons, R. O. (see Balluffi, R. W.)—2284
Simon, R., R. T. Bate, and E. H. Lougher. Measurement of thermal conductivity by utilization of the Peltier effect. III. Correction for wire radiation emissivity—2160
Simon, R. E. and W. E. Spicer. Field induced photoemission and hot-electron emission from germanium—1505(L)
—— **and R. L. Sproull.** Electron microscope studies of colloids in KCl—2224
Singer, J. R. Blood flow measurements using dynamical paramagnetic relaxation times, and paramagnetic tracer techniques—406S
—— Flow rates using nuclear or electron paramagnetic resonance techniques with applications to biological and chemical processes—125
Singh, Sampooran. Penetration of rotating shaped charges—578
Slack, Glen A. Crystallography and domain walls in antiferromagnetic NiO crystals—1571
—— (see Roth, Walter L.)—352S
Slade, J. J., Jr., and L. F. Nanni. Analysis of composite x-ray diffraction profiles—699
Slager, Donald M. (see Wharton, Charles B.)—428
Slaten, Lynore E. Precipitation of dispersed fine-particle magnetite—74S
Slichter, W. P. Defects in polyethylene crystals—1865
Smakula, A. (see Avakian, P.)—1720
Smit, J., F. K. Lotgering, and U. Enz. Anisotropy properties of hexagonal ferrimagnetic oxides—137S
Smith, D. O., M. S. Cohen, and G. P. Weiss. Oblique-incidence anisotropy in evaporated permalloy films—1735
——, **E. E. Huber, Jr., M. S. Cohen, and G. P. Weiss.** Anisotropy and inversion in permalloy films—295S
—— (see Cohen, M. S.)—291S
Smith, J. F. and C. L. Arbogast. Elastic constants of single crystal beryllium—99
—— **and J. A. Gjevre.** Elastic constants of yttrium single crystals in the temperature range 4.2–400°K—645
Smith, K. C. (see McKay, R. W.)—133S
Smith, Mac J., E. S. Kirk, and C. W. Spencer. Device for measurement of the electrical properties of Bi_2Se_3 at elevated temperatures—1504(L)
Smith, Thor L. and Paul J. Stedry. Time and temperature dependence of the ultimate properties of an SBR rubber at constant elongations—1892
Smith, W. J. (see Longini, R. L.)—1204
Smythe, W. R. Charged sphere in cylinder—553
Snyder, D. D. Bulk densities of separated copper isotopes—440(L)
Soden, R. R. (see Van Uitert, L. G.)—226S, 328
Solomon, Raymond. Anomalous surface channels on silicon p-n junctions—1791
Solt, I. H. and P. C. Fletcher. Magnetic anisotropy from the magnetostatic modes—100S
Sonder, E. and L. C. Templeton. Gamma irradiation of silicon. I. Levels in n-type material containing oxygen—1279
Soohoo, R. F. Initial susceptibility spectra of permalloy films—218S
Sosin, A. and L. L. Bienvenue. Effect of electron irradiation and subsequent thermal treatment on Young's modulus of copper—249
Southern, A. L. (see Robinson, Mark T.)—1474
Spain, Robert J. (see Rubinstein, H.)—306S
Sparks, Joseph T., Warren Mead, Albert J. Kirschbaum, and Walter Marshall. Neutron diffraction investigation of the $Fe_{1-\delta}S$ system—356S
Speliotis, D. E. (see Pugh, E. W.)—293S
Spencer, C. W. (see Smith, Mac J.)—1504(L)
Spencer, E. G. (see LeCraw, R. C.)—95S
Spencer, H. E. Noise and signal response in lead sulfide photoconductive films—504
—— **and J. V. Morgan.** Hole mobility and crystal size in lead sulfide photoconductive films—2024
Spicer, W. E. Photoemission and related properties of the alkali antimonides—2077
—— (see Simon, R. E.)—1505(L)
Spielberg, N. and J. Ladell. Crystallographic aspects of extra reflections in x-ray spectrochemical analysis—1659
Spinner, S. and G. W. Cleek. Temperature dependence of Young's modulus of vitreous germania and silica—1407
Sproull, R. L. (see Simon, R.)—2224
Spruch, Larry and Ralph Bartram. Bounds on the elements of the equivalent network for scattering in waveguides. I. Theory—905
—— **and Leonard Rosenberg.** Bounds on low energy scattering parameters—2104
—— (see Bartram, Ralph)—913
Stadler, H. L. Localized field permanent magnet arrays—196S
Stanton, Henry E. On the yield and energy distribution of secondary positive ions from metal surfaces—678
Statton, W. O. and L. C. Hoffman. Structure in vitreous silicate fibers as shown by small-angle scattering of x-rays—404
Stearns, Carl A. Effect of aging time after cleavage on the plasticity of MgO single crystals—2317(L)
——, **A. E. Pack, and R. A. Lad.** Factors affecting the ductility and strength of NaCl single crystals tested in flexure—231
Stedry, Paul J. (see Landel, Robert F.)—1885
—— (see Smith, Thor L.)—1892
v.d. Steeg, M. G. (see Koch, A. J. J.)—75S
Steele, M. C. (see Larrabee, R. D.)—1519
Steier, William H. and Paul D. Coleman. Theory and application of dipolar ferrite modes—99S
Stein, Dale F. and J. R. Low, Jr. Mobility of edge dislocations in silicon-iron crystals—362
Stein, H. J. Transitory electrical properties of n-type germanium after a neutron pulse—1309
Stein, Richard S. and Marion B. Rhodes. Photographic light scattering by polyethylene films—1873
—— (see Keedy, D. A.)—1911
Stemme, O. (see Andrä, W.)—442(L)
Stern, E. (see Lurio, A.)—1125(L), 1805
Stewart, R. M., Jr. (see Pohm, A. V.)—119S
Stewart, T. W. W. (see Brannen, E.)—1829(L)
Stiegler, J. O. and T. S. Noggle. Direct replica technique for copper—1827(L)
—— (see Noggle, T. S.)—2199
Stiglitz, Martin P. and Frederic R. Morgenthaler. Resonance experiments with single crystal yttrium iron garnets in pulsed magnetic fields—37S
Strandberg, M. W. P. (see Peter, M.)—693
—— (see Venkates, H. G. R.)—396
Straley, R., A. Heuer, B. Kane, and G. Tkach. Miniature memory planes for extreme environmental conditions—126S
Strayer, R. W. (see Dyke, W. P.)—790

Street, R. Magnetic properties of manganese copper alloys—310S
Strong, H. M., F. P. Bundy, and H. P. Bovenkerk. Flat panel vacuum thermal insulation—39
Strumane, G. (see Amelinckx, S.)—1359
Stuetzer, Otmar M. Ion drag pumps—136
Sturrock, P. A. In what sense do slow waves carry negative energy?—2052
—— (see Helmer, J. C.)—458
Suddeth, J. A. (see Leder, Lewis B.)—1422
Suhl, H. "Foldover" effects caused by spin wave interactions in ferromagnetic resonance—935(L)
Sulich, M. (see Greiner, J. H.)—2316(L)
Swanekamp, F. W. (see Van Uitert, L. G.)—226S
Swalin, R. A. (see Carter, J. R.)—1191
—— (see Meckel, B. B.)—1299(L)
Sweeney, W. E., Jr., R. E. Seebold, and L. S. Birks. Electron probe measurements of evaporated metal films—1061
Szasz, S. E. Discussion of criteria for the *in situ* combustion of crude oil—1122(L)
Szaynok, Anna. Influence of irradiation with rays on the electrification of KCl crystals—451
—— Influence of x-rays on the electrification of NaCl crystals—211(L)

Tai, Chen To. Evanescent modes in a partially filled gyromagnetic rectangular wave guide—220(L)
Takahashi, Noboru. Electron microscopic study of thin films of the aluminum-copper eutectic prepared by a melting method—1287
Takeda, Susumu and Arwin A. Dougal. Microwave study of afterglow discharge in water vapor—412
Tamarkin, Paul (see Proud, J. M.)—543
Tancrell, Roger H. and Robert E. McMahon. Studies in partial switching of ferrite cores—762
Tanenbaum, M. (see Buehler, E.)—388
Tannenbaum, E. Film stripping technique for making thin silica windows—940(L)
Tarpinian, Aram and George E. Gazza. Etch pits in pyrolytic graphite—1657
Taylor, Ellison H. (see Datz, S.)—880
—— (see Minturn, Robert E.)—876
Taylor, K. N. R. (see Bate, G.)—991
Teghtsoonian, E. (see Saimoto, S.)—1693(L)
Teig, Michael (see Sagnis, James C.)—190S
Templeton, L. C. (see Sonder, E.)—1279
Terhune, R. W. (see Makhov, G.)—936(L)
Testardi, L. R. (see Donahoe, F. J.)—1304(L)
Teutsch, W. B. (see Garvin, H. L.)—1508(L)
Thomas, H. (see Baer, G.)—235S
—— (see Methfessel, S.)—302S
Thomas, J. E., Jr. (see Frank, R. C.)—1689(L)
Thompson, D. O. and V. K. Paré. Effect of fast neutron bombardment at various temperatures upon the Young's modulus and internal friction of copper—528
Thompson, D. S. and J. P. Roberts. Flow of magnesium oxide single crystals—433(L)
Thomson, Robb. Radiation limited dislocation motion in crystals—617(L)
Tiller, W. A. (see Armstrong, R. W.)—1954
—— (see Bolling, G. F.)—1345, 2040
Tirmizi, S. M. A. (see Berman, R.)—2156
Tkach, G. (see Straley, R.)—126S
Tobias, Charles W. (see Meredith, R. E.)—1270
Todd, B. Johnson, Jack L. Lineweaver, and John T. Kerr. Outgassing caused by electron bombardment of glass—51
Tomboulian, D. H. (see Bedo, D. E.)—2289
Tompkins, J. E., F. Reggia, and L. Joseph. Multimode propagation in gyromagnetic rods and its application to traveling-wave devices—176S
Toth, Robert S., Rein Kilkson, and Dan Trivich. Preparation of large area single-crystal cuprous oxide—1117
Trammell, G. T. Theory of the low-lying states of some rare earth compounds—362S
Treitel, Sven. Thermal attenuation of nonlinear stress waves—391
Treves, David (see Fowler, C. A., Jr.)—2267
—— (see Shtrikman, S.)—58S, 72S, 147S, 1304(L)
Trillat, J. J. (see Cunningham, R. L.)—839
Trivich, Dan (see Toth, R. S.)—1117
Trolan, J. K. (see Dyke, W. P.)—790
—— (see Martin, E. E.)—782
Truell, Rohn (see Einspruch, Norman G.)—806
Trumbore, F. A. and W. M. Porbansky. Solvent evaporation technique for the growth of arsenic-doped germanium single crystals for Esaki diodes—2068(L)
Turnbull, D. and R. L. Cormia. A dynamic hard sphere model—674

Ure, R. W., Jr. (see Sherman, B.)—1

Vager, Z. (see Goldring, G.)—2057
Vanderslice, T. A. (see Blodgett, K. B.)—1017
Van Uitert, L. G. and R. R. Soden. Single crystal tungstates for resonance and emission studies—328
——, **R. R. Soden, and F. W. Swanekamp.** Resonance line widths of sintered nickel ferrites having low porosities—226S
—— (see Nassau, K.)—1508(L)
Venables, John D. Cleavage whiskers—1503(L)
Venkates, H. G. R. and M. W. P. Strandberg. Operating characteristics of a molecular-beam maser—396
—— (see Peter, M.)—693
Vickery, R. C., W. C. Sexton, V. F. Novy, and E. V. Kleber. Magneto structural studies on gadolinium-iron alloys—366S
Vivian, W. E. Transport of noise at microwave frequencies through a space-charge-limited diode—957
Vong, T. S. (see Levengood, W. C.)—1416
Vuylsteke, A. A. (see Donovan, R. E.)—614(L)

Wade, Glen (see Adler, Robert)—1201
—— (see Heffner, H.)—2316(L)
Wadsworth, M. E. (see Gabrysh, A. F.)—1785
Wagner, P. E., J. G. Castle, Jr., and P. F. Chester. Inversions by fast passage in a multilevel spin system—1498(L)
Wagner, Richard S. and Bruce Chalmers. Grain boundaries in germanium—578
Wainfan, N. and L. G. Parratt. X-ray reflection studies of the anneal and oxidation of some thin solid films—1331
Wakefield, J. (see Bullough, R.)—707
Walker, Walter P. (see Catlin, Avery)—2135
Wallace, D. C., P. H. Sidles, and G. C. Danielson. Specific heat of high purity iron by a pulse heating method—168
Wallace, R. L. (see Batdorf, R. L.)—613(L)
Walsh, D. J. (see Batdorf, R. L.)—613(L)
Walter, J. L. (see Dunn, C. G.)—827
Wang, T. C. (see Giordmaine, J. A.)—463
Ward, Robert L. Experimental flux pattern determination in magnetic cores—192S
—— (see Sagnis, James C.)—190S
Warekois, E. P. Low-temperature x-ray diffraction studies on vanadium sesquioxide—346S

——, **M. C. Lavine, and H. C. Gatos.** Damaged layers and crystalline perfection in the {111} surfaces of *III–IV* intermetallic compounds—1302(L)
Warren, B. E. X-ray measurement of grain size—2237
Washburn, J. (see Schultz, J. M.)—1800
Waters, William E. Electron sheet beam focusing with tape ladder lines—1814
Waterstrat, R. M. (see Rajan, N. S.)—731
Watson, John H. L. (see Freeman, Michael W.)—404S
Watson, R. E. (see Freeman, A. J.)—374S
Watson, R. W. (see Allison, F. E.)—842
Watt, L. A. K. and A. H. Morrish. Comparison of the critical single-domain size for Fe_3O_4 and γ-Fe_2O_3—71S
Weaver, C. W. and K. A. Gross. X-ray examination of brittle fractures in extruded chromium—626
Webb, W. W. Dislocation structure and the formation and strength of sodium chloride whiskers—194
—— **and N. P. Bertolone.** Novel mechanism for mass transport during whisker growth—cesium chloride from aqueous films—207
—— (see Amelinckx, S.)—1359
—— (see Fourdeux, A.)—918
Weeks, R. A. and C. M. Nelson. Irradiation effects and short-range order in fused silica and quartz—1555
Weglein, R. D. (see Knechtli, R. C.)—1134(L)
Wehner, G. K. Forces on ion-bombarded electrodes in a low-pressure plasma—1392
—— **and D. Rosenberg.** Angular distribution of sputtered material—177
—— (see Anderson, G. S.)—2305
Weinberg, F. (see Fourie, J. T.)—1136(L)
Weinig, S. (see Mendel, E.)—738(L)
Weiss, G. P. (see Cohen, M. S.)—291S
—— (see Smith, D. O.)—295S, 1746
Weiss, Jerald A. Tetrahedral junction—168S
Weiss, M. T. Ferrimagnetic resonance at high power—103S
—— High power effects on ferrimagnetic resonance—778
Weisz, R. S. and D. L. Brown. Square loop properties of copper-manganese ferrites—269S
Wernick, J. H. (see Wolfe, R.)—1959
Wharton, Charles B. and Donald M. Slager. Microwave determination of plasma density profiles—428
Whelan, J. M. and C. S. Fuller. Precipitation of copper in gallium arsenide—1507(L)
White, John E. Cathode of an arc in xenon—1709
—— Probes at high pressure—1502(L)
White, L. D. (see Ashkin, A.)—1351
White, Robert L. Use of magnetostatic modes as a research tool—86S
—— (see Carson, John W.)—53S
Whitmore, D. H. Excitation processes in ceramics and anomalous increase in thermal conductivity at elevated temperatures—1109
—— (see Moser, J. B.)—488
Whitmore, Frank C. Experimental study of thermal diffusion in dilute solutions of high polymers—1858
Wieber, R. H., H. C. Gorton, and C. S. Peet. Diffusion of copper into AlSb—608(L)
Wiechec, Walter and Clinton M. Kelley. Fast switching by domain walls in ferrites—131S
Wieder, H. H. Model for switching and polarization reversal in colemanite—180
Wiederhorn, S. and Drickamer, H. G. Optical observations concerning the polymorphic transition in the potassium halides—1666
Wilchinsky, Zigmond W. Measurement of orientation in polypropylene film—1969
Wilk, M. B. (see Lundberg, J. L.)—1131(L)
Wilkinson, M. K., H. R. Child, J. W. Cable, E. O. Wollan, and W. C. Koehler. Neutron diffraction investigations of the magnetic ordering in rare earth nitrides—358S
Willardson, R. K. (see Aukerman, L. W.)—939(L)
Willens, R. H. (see Duwez, Pol)—1136(L), 1137(L), 1500(L)
Williams, A. J. (see Nesbitt, E. A.)—228S
Williams, Richard and Richard H. Bube. Photoemission in the photovoltaic effect in cadmium sulfide crystals—968
Willis, J. B. (see Bullough, R.)—707
Willis, William R. (see Robinson, Mark T.)—1474
Wilsdorf, H. G. F. (see Fourie, J. T.)—2219
—— (see Kuhlmann-Wildsdorf, Doris)—516
Winans, G. (see Zei, D.)—1137(E)
Witterholt, E. J. (see Einspruch, Norman G.)—806
Wojtowicz, Peter J. High-temperature susceptibility of ferrimagnetic spinels—265S
Wold, A. (see Goodenough, J. B.)—342S
Wolfe, R., J. H. Wernick, and S. E. Haszko. Anomalous Hall effect in $AgSbTe_2$—1959
Wolfson, R. G., M. E. Fine, and A. W. Ewald. Transformation studies of gray tin single crystals—1973
Wollan, E. O. (see Wilkinson, M. K.)—358S
Woodward, J. G. and E. Della Torre. Particle interaction in magnetic recording tapes—56
—— **and E. Della Torre.** Particle interaction in magnetic recording tapes—398S
Worthington, C. R. (see Posner, A. S.)—536
Wuerker, R. F. (see Shelton, H.)—1243
Wysocki, Joseph J. Thermal conversion in *n*-type GaAs—1686(L)
—— **and Paul Rappaport.** Effect of temperature on photovoltaic solar energy conversion—571

Yahagi, Kichinosuke and Akibumi Danno. Gamma-ray induced conductivity in polyethylene coaxial cable—734(L)
Yamaguchi, S. On the temperature of an object irradiated with electrons—1825(L)
Yamamoto, Kenzo (see Okuda, Takayoshi)—158
Yariv, Amnon. Spontaneous emission from an inverted spin system—740(L)
Yee, R. (see Kurtz, A. D.)—303
Yelon, Arthur and R. W. Hoffman. Production of single-crystal copper films at low temperatures—1672
Yonts, O. C. and Don E. Harrison, Jr. Surface cleaning by cathode sputtering—1583
——, **C. E. Normand, and Don E. Harrison, Jr.** High-energy sputtering—447
Young, A. S. (see Moore, A. C.)—279S
Young, F. J. and H. L. Schenk. Method for measuring iron losses in elliptically polarized magnetic fields—194S
Young, F. W., Jr., and A. T. Gwathmey. Development of facets, spirals, and etch pits on copper crystals by heating to high temperatures in high vacua—225
—— **and T. S. Noggle.** Evidence for dislocation reactions in copper—604
—— (see Crawford, J. H.)—1688(L)
Young, J. R. Evolution of gases and ions from different anodes under electron bombardment—921
Youngkin, Frank G. (see Pietrokowsky, Paul)—1763

Zeender, R. J. and E. Schlomann. Ferromagnetic resonance in polycrystalline ferrites using circularly polarized radiation—1112
Zei, D. and J. G. Winans. Motion of high-speed arc spots in magnetic fields—1137(E)
Zinn, John and Charles L. Mader. Thermal initiation of explosives—323
Zwick, S. A. Note on evaporation—1735

Subject Index to Volume 31

References with (L) are to Letters to the Editor; (E) to Errata

Acoustics

Acoustic resonance in solid propellant rockets. F. T. McClure, R. W. Hart, and J. F. Bird—884

Measurement of elastic constants of RbBr, RbI, CsBr, and CsI by an ultrasonic cw resonance technique. D. I. Bolef and M. Menes—1010

On the reflection of electromagnetic waves from a medium excited by acoustic waves. Hans J. Schmitt and Dipak L. Sengupta—439(L)

Photographic verification of ultrasonic plane wave scattering by cylinders. Harmon D. Nine and Norman W. Schubring—1274

Reflection of sound from randomly rough surfaces. J. M. Proud, Jr., R. T. Beyer, and Paul Tamarkin—543

Stress waves in solids. C. R. Cassity—1377

Ultrasonic viscoelastic properties of associated liquids. R. Meister, C. J. Marhoeffer, R. Sciamanda, L. Cotter, and T. Litovitz—854

Ballistics

Acoustic resonance in solid propellant rockets. F. T. McClure, R. W. Hart, and J. F. Bird—884

Attenuation of the shock wave produced in a solid by a flying plate. G. R. Fowles—655

Comments on article by Cook. M. H. Miller—607(L)

Cratering and shock wave phenomena in steel plates at high impact speeds. Earle B. Mayfield and James W. Rogers—472

Depth of indentation on an impacting projectile. R. A. Graham—619(L)

Equation of state for nineteen metallic elements from shock-wave measurements to two megabars. R. G. McQueen and S. P. Marsh—1253

Explosively loaded metallic cylinders. I. F. E. Allison and R. W. Watson—842

Explosively loaded metallic cylinders. II. F. E. Allison and J. Thomas Schriempf—846

Impact crater formation in rock. William C. Maurer and John S. Rinehart—1247

Penetration of rotating shaped charges. Sampooran Singh—578

Stress waves in solids. C. R. Cassity—1377

Study of initial conditions in constant velocity impact. James F. Bell—2188

Ultra-high-speed photographs refuting "cohesion in plasma." W. C. Davis and A. W. Campbell—1225

Combustion

Discussion of criteria for the *in situ* combustion of crude oil. S. E. Szasz—1122(L)

Experimental determination of stresses generated by an electric detonator. John S. Rinehart and William C. McClain—1809

Remarks on "Some criteria for the *in situ* combustion of crude oil." H. R. Bailey and B. K. Larkin—1123(L)

Reply to the letters of Szasz, and Bailey and Larkin. Philip Cooperman—1124(L)

Crystals and Crystal Growth

Antiferromagnetic structure and domains in single crystal NiO. Walter L. Roth and Glen A. Slack—352S

Cleavage whiskers. John D. Venables—1503(L)

Crystallography and domain walls in antiferromagnetic NiO crystals. Glen A. Slack—1571

Damaged layers and crystalline perfection in the {111} surfaces of *III–V* intermetallic compounds. E. P. Warekois, M. C. Lavine, and H. C. Gatos—1302(L)

Detection of growth striations in germanium crystals. Albert C. English—1498(L)

Dielectric behavior of single crystals of tri-glycine sulfate (TGS) from 1 kc to 2500 Mc. A. Lurio and E. Stern—1125(L)

Direct measurements of the surface energies of crystals. J. J. Gilman—2208

Dislocation arrays in depth and recrystallization produced by surface deformation of single crystals of copper at high temperature. John M. Bailey and Allan T. Gwathmey—215(L)

Dislocation structure and the formation and strength of sodium chloride whiskers. W. W. Webb—194

Dislocations in indented magnesium oxide crystals. A. S. Keh—1538

Dislocations in metal crystals grown from the melt. C. Elbaum—1413

Effect of orientation on strength of a model solid. A. Robinson, J. E. Osborn, and C. C. Hsiao—1602

Effects of surface irregularities on single crystal resonance parameters. C. R. Buffler—222S

Elastic constants of single-crystal aluminum antimonide. D. I. Bolef and M. Menes—1426

Factors affecting the ductility and strength of NaCl single crystals tested in flexure. C. A. Stearns, A. E. Pack, and R. A. Lad—231

Flow of magnesium oxide single crystals. D. S. Thompson and J. P. Roberts—433(L)

Formation of cavities on dislocations in crystals of NaCl and KCl. L. W. Barr and J. A. Morrison—617(L)

Growth from the melt. I. Influence of surface intersections in pure metals. G. F. Bolling and W. A. Tiller—1345

Growth from the melt. II. Cellular interface morphology. G. F. Bolling and W. A. Tiller—2040

Growth kinks in copper whiskers. S. Saimoto, V. Griffiths, and E. Teghtsoonian—1693(L)

Growth of cesium chloride crystals from solution and melt. P. Avakian and A. Smakula—1720

Growth of GaAs crystals in the (111) polar direction. P. L. Moody, H. C. Gatos, and M. C. Lavine—1696(L)

Growth of gallium arsenide by horizontal zone melting. J. L. Richards—600

Growth of InSb crystals in the (111) polar direction. H. C. Gatos, P. L. Moody, and M. C. Lavine—212(L)

Growth, structure, and properties of graphite whiskers. Roger Bacon—283

Improved method of growing CdS crystals from the vapor phase. P. D. Fochs—1733

Improvements on the pedestal method of growing silicon and germanium crystals. W. C. Dash—736(L)

Influence of crystallographic orientation on the charge formation during phase changes in solids. S. Mascarenhas and L. G. Freitas—1684

Instability of magnetic resonance in single-crystal spheres of yttrium iron garnet. Joseph I. Masters—41S

Interferometric determination of twist and polytype in silicon-carbide whiskers. D. R. Hamilton—112

Mobility of edge dislocations in silicon-iron crystals. Dale F. Stein and J. R. Low, Jr.—362

Modification in technique for growing single crystals of ZnF_2:Mn. L. M. Matarrese and F. L. Hughes—2063(L)

Novel mechanism for mass transport during whisker growth—cesium chloride from aqueous films. W. W. Webb and N. P. Bertoione—207

Crystals and Crystal Growth (*continued*)
On the laws of magnetization of ferromagnetic single crystals and polycrystals. Application to uniaxial compounds. L. Néel, R. Pauthenet, G. Rimet, and V. S. Giron—27S
Photoemission in the photovoltaic effect in cadmium sulfide crystals. Richard Williams and Richard H. Bube—968
Precipitation in silicon crystals containing aluminum. R. Bullough, R. C. Newman, J. Wakefield, and J. B. Willis—707
Preparation of large calcium-tungstate crystals containing paramagnetic ions for maser applications. K. Nassau and L. G. Van Uitert—1508(L)
Preparation of large area single-crystal cuprous oxide. Robert S. Toth, Rein Kilkson, and Dan Trivich—1117
Preparation of tin single crystals for transmission electron microscopy. J. T. Fourie, F. Weinberg, and F. W. C. Boswell—1136(L)
Production of single-crystal copper films at low temperatures. Arthur Yelon and R. W. Hoffman—1672
Resonance experiments with single crystal yttrium iron garnets in pulsed magnetic fields. Martin P. Stiglitz and Frederic R. Morgenthaler—37S
Single-crystal magnetic anisotropy and magnetostriction studies in iron-base alloys. R. C. Hall—1037
Single crystal tungstates for resonance and emission studies. L. G. Van Uitert and R. R. Soden—328
Solvent evaporation technique for the growth of arsenic-doped germanium single crystals for Esaki diodes. F. A. Trumbore and E. M. Porbansky—2068(L)
Some properties of zinc sulfide crystals grown from the melt. Arrigo Addamiano and Manuel Aven—36
Structure in vitreous silicate fibers as shown by small-angle scattering of x-rays. W. O. Statton and L. C. Hoffman—404
Temperature dependence of the adiabatic elastic moduli of single-crystal alpha uranium. H. J. McSkimin and E. S. Fisher—1627
Transformation stutlies of gray tin single crystals. R. G. Wolfson, M. E. Fine, and A. W. Ewald—1973
Vapor-deposited single-crystal germanium. Ralph P. Ruth, John C. Marinace and W. C. Dunlap, Jr.—995

Cryogenic Devices and Applications
Criteria for the choice of a superconducting bolometer. Bogoljub Lalevic—1234
Heating in liquid helium resulting from neutron and gamma bombardment by a fission source. M. G. Chasanov—733(L)
Low-temperature transport properties of commercial metals and alloys. H. Aluminums. Robert L. Powell, William J. Hall, and Hans M. Roder—496
Low-temperature transport properties of commercial metals and alloys. III. Gold-cobalt. Robert L. Powell, M. D. Bunch, and Edward F. Gibson—504
Low-temperature transport properties of commercial metals and alloys. IV. Reactor grade Be, Mo, and W. Robert L. Powell, James L. Harden, and Edward F. Gibson—1221
Monte Carlo calculations of the motions of electrons in helium. T. Itoh and T. Musha—744(L)
Production of single-crystal copper films at low temperatures. Arthur Yelon and R. W. Hoffman—1672
Strong field magnetization at low temperatures and approach to absolute saturation of thulium metal. Warren E. Henry—323S

Defects in Solids, Dislocations
Behavior of individual dislocations in strain-hardened LiF crystals. J. J. Gilman and W. G. Johnston—687
Changes in macroscopic shape, lattice parameter, and density in crystals due to point defects. R. W. Balluffi and R. O. Simmons—2284
Cleavage whiskers. John D. Venables—1503(L)
Crystal distortion in magnetic compounds. Junjiro Kanamori—14S
Damaged layers and crystalline perfection in the {111} surfaces of *III–V* intermetallic compounds. E. P. Warekois, M. C. Lavine, and H. C. Gatos—1302(L)
Defects in dislocations produced by focusing collisions in fcc lattices. G. Leibfried—117
Detection of growth striations in germanium crystals. Albert C. English—1498(L)
Development of facets, spirals, and etch pits on copper crystals by heating to high temperatures in high vacua. F. W. Young, Jr., and A. T. Gwathmey—225
Direct observation of superdislocations in a superlattice. M. J. Marcinkowski, R. M. Fisher, and N. Brown—1303(L)
Dislocation arrays in depth and recrystallization produced by surface deformation of single crystals of copper at high temperature. John M. Bailey and Allan T. Gwathmey—215(L)
Dislocation damping effects in rock salt. Charles L. Bauer and Robert B. Gordon—945
Dislocation etch pits on p-type lead telluride. B. B. Houston and Marriner K. Norr—615(L)
Dislocation etch pits on the {111} and {$\bar{1}\bar{1}\bar{1}$} surfaces of InSb. Harry C. Gatos and Mary C. Lavine—743(L)
Dislocation multiplication in lithium fluoride crystals. W. G. Johnston and J. J. Gilman—632
Dislocation networks in a low-alloy steel. A. S. Keh—1501(L)
Dislocation ribbons and stacking faults in graphite. P. Delavignette and S. Amelinckx—1691(L)
Dislocation structure and the formation and strength of sodium chloride whiskers. W. W. Webb—194
Dislocations in two types of CdS crystals. D. C. Reynolds and S. J. Czyzak—94
Dislocations in indented magnesium oxide crystals. A. S. Keh—1538
Dislocations in metal crystals grown from the melt. C. Elbaum—1413
Dislocations in silicon carbide. S. Amelinckx, G. Strumane, and W. W. Webb—1359
Dynamic hard sphere model. D. Turnbull and R. L. Cormia—674
Effect of atomic interaction potential on defect production in metals. E. Brown and G. H. Goedecke—932
Effect of Cu precipitation on dislocation etch pits in Ge. Howard Savage—1472
Effect of thermal history on the dislocation substructure near the surfaces of a lithium fluoride crystal. J. M. Schultz and J. Washburn—1800
Electron optical study of basal dislocations in graphite. S. Amelinckx and P. Delavignette—2126
Etch pits at dislocations in copper. J. D. Livingston—1071
Etch pits in gallium arsenide. J. L. Richards and A. J. Crocker—611(L)
Etch pits in pyrolytic graphite. Aram Tarpinian and George E. Gazza—1657
Evidence for dislocation reactions in copper. F. W. Young, Jr., and T. S. Noggle—604
Formation of cavities on dislocations in crystals of NaCl and KCl. L. W. Barr and J. A. Morrison—617(L)
Generation of dislocations by an electric field in MgO. E. Mendel and S. Weinig—738(L)
Gold induced climb of dislocations in silicon. W. C. Dash—2275

Grain boundaries in germanium. Richard S. Wagner and Bruce Chalmers—581
Grain boundary and lattice diffusion in polycrystalline bodies. H. S. Levine and C. J. MacCallum—595
Growth kinks in copper whiskers. S. Saimoto, V. Griffiths, and E. Teghtsoonian—1693(L)
Irradiation effects and short-range order in fused silica and quartz. R. A. Weeks and C. M. Nelson—1555
Mechanism for the production of F centers in NaCl by irradiation with gamma rays. J. H. Crawford, Jr., and F. W. Young, Jr.—1688(L)
Method for the detection of flaws in yttrium iron garnet crystals. E. Buehler and M. Tanenbaum—388
Mobility of edge dislocations in silicon-iron crystals. Dale F. Stein and J. R. Low, Jr.—362
On the behavior of thermal vacancies in pure aluminum. Doris Kuhlmann-Wilsdorf and H. G. F. Wilsdorf—516
On the observation of macroscopic spirals on gallium arsenide surfaces. Warren J. Little and Kathryn A. McCarthy—1298(L)
Origin of the "first-order structure" of CP4-etched Ge surfaces. G. Bonfiglioli, A. Ferro, and A. Mojoni—684
Oxygen in nickel. L. H. Germer and C. D. Hartman—2085
Polyhedral holes in evaporated AuCu films. Victor A. Phillips—697
Precipitation in silicon crystals containing aluminum. R. Bullough, R. C. Newman, J. Wakefield, and J. B. Willis—707
Radiation limited dislocation motion in crystals. Robb Thomson—617(L)
Production of dislocation loops by a combined climb and glide mechanism. J. T. Fourie and H. G. F. Wilsdorf—2219
Reviving the classical theory of friction by a modern dislocation theory of deformation revision. John H. Dismant—221(L)
Shapes of etch hillocks and pits and their correlation with measured etch rates. B. A. Irving—109
Some effects occurring in dislocated tellurium. J. S. Blakemore, J. W. Schultz, and K. C. Nomura—2226
Some elastic properties of a screw dislocation wall. James C. M. Li and Charles D. Needham—1318
Specific ionization measurements and energy requirements for F-center formation. R. D. Jordan and R. S. Alger—747
Spiral dislocations on glass fracture surfaces. W. C. Levengood and T. S. Vong—1416
Stacking faults in zinc. A. Fourdeux, A. Berghezan, and W. W. Webb—918
Statistics of the occupation of dislocation acceptors (one-dimensional interaction statistics). R. M. Broudy and J. W. McClure—1511
Terraces on etchpits. J. J. Gilman—936(L)
Theory of dislocation climb in metals. Jens Lothe—1077

Dielectrics

Beta particle transmission currents in solid dielectrics. Bernhard Gross, Arthur Bradley, and Arthur P. Pinkerton—1035
Bounds on the elements of the equivalent network for scattering in waveguides. II. Application to dielectric obstacles. Ralph Bartram and Larry Spruch—913
Decay of wax electrets. M. M. Perlman—356
Detailed study of switching current in barium titanate. M. E. Drougard—352
Dielectric behavior of single crystals of tri-glycine sulfate (TGS) from 1 kc to 2500 Mc. A. Lurio and E. Stern—1125(L)
Dielectric properties of lead titanate zirconate ceramics at very low frequencies. Robert Gerson—1615
Generation of dislocations by an electric field in MgO. E. Mendel and S. Weinig—738(L)
Influence of irradiation with β rays on the electrification of KCl crystals. Anna Szaynok—451
Influence of x-rays on the electrification of NaCl crystals. Anna Szaynok—211(L)
Measurements of the dielectric constant of $BaTiO_3$ single crystals in the paraelectric region at X band. A. Lurio and E. Stern—1805
Motion of 180° domain walls in metal electroded barium titanate crystals as a function of electric field and sample thickness. Robert C. Miller and Albert Savage—662
Response of a loaded idealized piezoelectric plate to an electric signal. Leo Levi—1237
Temperature dependence of the velocity of sidewise 180° domain-wall motion in $BaTiO_3$. A. Savage and R. C. Miller—1546

Diffusion

Bounds on the nonlinear diffusion controlled growth rate of spherical precipitates. J. A. Morrison and H. L. Frisch—1621
Diffusion coefficients, solubilities, and permeabilities for He, Ne, H_2, and N_2 in Vycor glass. C. C. Leiby, Jr., and C. L. Chen—268
Diffusion of Ag^+, Cl^-, and Cd^{++} in silver chloride single crystals. Richard F. Reade and Don S. Martin, Jr.—1965
Diffusion of boron into silicon. A. D. Kurtz and R. Yee—303
Diffusion of copper into AlSb. R. H. Wieber, H. C. Gorton, and C. S. Peet—608(L)
Diffusion of deuterium in deuteron-irradiated copper. Mark T. Robinson, A. L. Southern, and William R. Willis—1474
Effect of oxide layers on the diffusion of phosphorus into silicon. R. B. Allen, H. Bernstein, and A. D. Kurtz—334
Kinetics of sintering of sodium chloride in the presence of an inert gas. J. B. Moser and D. H. Whitmore—488
Regelation, surface diffusion, and ice sintering. W. D. Kingery—833
Solubilities and diffusivities of nitrogen in polyethylene. J. L. Lundberg, M. B. Wilk, and M. J. Huyett—1131(L)

Elasticity and Anelasticity

Effect of orientation on strength of a model solid. A. Robinson, J. E. Osborn, and C. C. Hsiao—1602
Elastic constants of bismuth. Yakov Eckstein, A. W. Lawson, and Darrell H. Reneker—1534
Elastic constants of single crystal aluminum antimonide. D. I. Bolef and M. Menes—1426
Elastic constants of single crystal beryllium. J. F. Smith and C. L. Arbogast—99
Elastic constants of yttrium single crystals in the temperature range 4.2–400°K. J. F. Smith and J. A. Gjevre—645
Elastic moduli of face-centered cubic cobalt. R. Dean Dragsdorf—434(L)
Measurement of elastic constants of RbBr, RbI, CsBr, and CsI by an ultrasonic cw resonance technique. D. I. Bolef and M. Menes—1010
Propagation of large amplitude waves in annealed aluminum. James F. Bell—277
Recovery of internal friction in aluminum after plastic deformation. Ivar Holwech—928
Scattering of a plane transverse wave by a spherical obstacle in an elastic medium. Norman G. Einspruch, E. J. Witterholt, and Rohn Truell—806
Some elastic properties of a screw dislocation wall. James C. M. Li and Charles D. Needham—1318

Elasticity and Anelasticity *(continued)*
Stress waves in solids. C. R. Cassity—1377
Temperature dependence of the adiabatic elastic moduli of single-crystal alpha uranium. H. J. McSkimin and E. S. Fisher—1627
Temperature dependence of Young's modulus of vitreous germania and silica. S. Spinner and G. W. Cleek—1407
Tensile strength of pyrolytic graphite up to 2750°C. H. E. Martens and L. D. Jaffe—1122(L)
Thermal attenuation of nonlinear stress waves. Sven Treitel—391

Electrical Circuits and Networks
Bounds on the elements of the equivalent network for scattering in waveguides. I. Theory. Larry Spruch and Ralph Bartram—905
Bounds on the elements of the equivalent network for scattering in waveguides. II. Application to dielectric obstacles. Ralph Bartram and Larry Spruch—913
Circuit dynamics of the pinch. J. Killeen and B. A. Lippmann—1549
Comments on "Diode capacitors for parametric amplification" by R. C. Knechtli and R. D. Weglein. K. E. Mortenson—1135(L)
Diode capacitors for parametric amplification. R. C. Knechtli and R. D. Weglein—1134(L)
Proposed molecular amplifier and coherent generator for millimeter and submillimeter waves. Walter Gordy and Monroe Cowan—941(L)
Response of a loaded idealized piezoelectric plate to an electric signal. Leo Levi—1237
Theory of a negative-resistance transmission line amplifier with distributed noise generators. K. K. N. Chang—871

Electrical Conductivity
Charged sphere in cylinder. W. R. Smythe—553
dc measurements on tape-wound cores. R. C. Barker and R. M. Brownell—243S
Detailed study of switching current in barium titanate. M. E. Drougard—352
Effects of internal oxidation and heat treatment on the electrical resistivity of dilute CuMn, CuFe, and CuCo alloys. C. A. Domenicali and E. L. Christenson—1730
Effect of random inhomogeneities on electrical and galvanomagnetic measurements. Conyers Herring—1939
Electromagnetic theory of dc effects in ferromagnetic resonance. H. J. Juretschke—1401
Gamma-ray induced conductivity in polyethylene coaxial cable. Kichinosuke Yahagi and Akibumi Danno—734(L)
Generation of alternating current in the cesium cell. H. L. Garvin, W. B. Teutsch, and R. W. Pidd—1508(L)
Hall mobility of holes in AgBr. Roland C. Hanson and Frederick C. Brown—210(L)
Influence of crystallographic orientation on the charge formation during phase changes in solids. S. Mascarenhas and L. G. Freitas—1684
In what sense do slow waves carry negative energy? P. A. Sturrock—2052
Low-temperature transport properties of commercial metals and alloys. II. Aluminums. Robert L. Powell, William J. Hall, and Hans M. Roder—496
Low-temperature transport properties of commercial metals and alloys. III. Gold-cobalt. Robert L. Powell, M. D. Bunch, and Edward F. Gibson—504
Low-temperature transport properties of commercial metals and alloys. IV. Reactor grade Be, Mo, and W. Robert L. Powell, James L. Harden, and Edward F. Gibson—1221
Monte Carlo calculations of the motions of electrons in helium. T. Itoh and T. Musha—744(L)
Relations between superconductors and ferromagnets. Bernd Matthias—23S
Solutions of the equations of space charge flow for radial flow between concentric spherical electrodes. I. Itzkan—652
Some electrical properties of amorphous selenium films. Richard A. Fotland—1558
Spreading resistance in cylindrical semiconductor devices. David P. Kennedy—1490
Temperature-dependence of the electrical resistivity of bcc Cr-Fe alloys. N. S. Rajan, R. M. Waterstrat, and Paul A. Beck—731
Uniform silicon p-n junctions. I. Broad area breakdown. R. L. Batdorf, A. G. Chynoweth, G. C. Dacey, and P. W. Foy—1153

Electromagnetic Waves and Fields
Beam refrigeration by means of large magnetic fields. Robert Adler and Glen Wade—1201
Charged-particle orbits in varying magnetic fields. E. I. Gordon—1187
Diffraction by a slit. Robert Plonsey and Hwei-Piao Hsu—445(E)
Electromagnetic theory of dc effects in ferromagnetic resonance. H. J. Juretschke—1401
Electrostatic acceleration of microparticles to hypervelocities. H. Shelton, C. D. Hendricks, and R. F. Wuerker—1243
Evanescent modes in a partially filled gyromagnetic rectangular wave guide. Chen To Tai—220(L)
Finite amplitude electromagnetic waves in gyromagnetic media. B. A. Auld—106S
Megavolt electronics Cerenkov coupler for the production of millimeter and submillimeter waves. Paul D. Coleman and Charles Enderby—1695(L)
Microwave measurement of semiconductor carrier lifetimes. H. A. Atwater—938(L)
Microwave noise from low-pressure arcs. R. M. Hill and S. K. Ichiki—735(L)
Microwave properties of nonstoichiometric polycrystalline yttrium iron garnet. P. E. Seiden, C. F. Kooi, and J. M. Katz—1291
Propagation constants for electromagnetic waves in weakly ionized, dry air. A. V. Phelps—1723

Electron and Ion Emission
Anomalous thermionic emssion from UC and $(ZrC)_{s.s.}$-$(UC)_{s.s.}$ G. C. Kuczynski—1500(L)
Contribution of anode emission to space charge in thermionic power converters. Anthony F. Dugan—1397
Density of a thorium monolayer for maximum thermionic emission. W. E. Danforth and D. L. Goldwater—1715
Detection of metastable atoms and ions. Homer D. Hagstrum—897
Electrical stability and life of the heated field emission cathode. W. P. Dyke, F. M. Charbonnier, R. W. Strayer, R. L. Floyd, J. P. Barbour, and J. K. Trolan—790
Energy distribution and cooling effect of electrons emitted from an arc cathode. T. H. Lee—924
Field dependence of photoelectric emission from tantalum. J. L. Gumnick and D. W. Juenker—102
Field induced photoemission and hot-electron emission from germanium. R. E. Simon and W. E. Spicer—1505(L)
Formation of cesium antimonide. I. Electrical resistivity of the film of cesium-antimony system. Kiyoshi Miyake—76
Influence of negative ions on ambipolar diffusion of electrons. Hendrik J. Oskam and Verlyn R. Mittlestadt—940(L)
Negative hydrogen and deuterium ion beams. Sanborn F. Philp—1592

On the yield and energy distribution of secondary positive ions from metal surfaces. Henry E. Stanton—678
Photoemission and related properties of the alkali antimonides. W. E. Spicer—2077
Positive column formation in ion sources employing surface ionization. P. L. Auer and H. Hurwitz, Jr.—1007
Secondary electron emission of MgO crystals bombarded by relativistic electrons. Martin A. Pomerantz, Romas A. Shatas, and William C. Schieve—2036
Simple theory concerning the reflection of electrons from solids. T. E. Everhart—1483
Single crystal tungstates for resonance and emission studies. L. G. Van Uitert and R. R. Soden—328
Spontaneous emission from an inverted spin system. Amnon Yariv—740(L)
Stable, high density field emission cold cathode. E. E. Martin, J. K. Trolan, and W. P. Dyke—782
Thermal emission of alkali ion pulses from clean and oxygenated tungsten. Robert E. Minturn, Sheldon Datz, and Ellison H. Taylor—876
Thermal positive ion emission and the anomalous flicker effect. S. Datz, R. E. Minturn, and E. H. Taylor—880
Thermionic properties of UC. George A. Haas and John T. Jensen, Jr.—1231
Ultimate and secondary electron energies in the negative glow of a cold-cathode discharge in helium. J. M. Anderson—511

Electron and Ion Optics

Molecular trajectories in electric fields and state selection in a beam of sodium chloride. M. Peter, H. G. R. Venkates, and M. W. P. Strandberg—693
On the reflection of electromagnetic waves from a medium excited by acoustic waves. Hans J. Schmitt and Dipak L. Sengupta—439(L)
Proposed molecular amplifier and coherent generator for millimeter and submillimeter waves. Walter Gordy and Monroe Cowan—941(L)
Scattering of electromagnetic waves from the infinitely long magnetized cylindrical plasma. P. M. Platzman and H. T. Ozaki—1597
Strong field magnetization at low temperatures and approach to absolute saturation of thulium metal. Warren E. Henry—323S
Surface wave excitation and propagation. Joseph B. Keller and Frank C. Karal, Jr.—1039
Total electromagnetic cross sections of imperfectly conducting cylinders. E. S. Cassedy and J. Fainberg—739(L)
Transport equation for the spectral density of a multiple-scattered electromagnetic field. Dimitri S. Bugnolo—1176
Transport of noise at microwave frequencies through a space-charge-limited diode. W. E. Vivian—957

Electron Beams

Adiabatic collapse of a relativistic electron beam. T. F. Godlove and D. C. dePackh—2016
Angular distribution and polarization of the radiation emitted by electrons accelerated in a synchrotron. D. E. Bedo, D. H. Tomboulian, and J. A. Rigert—2289
Beam refrigeration by means of large magnetic fields. Robert Adler and Glen Wade—1201
Conservation laws of an interacting electron beam. Marshall C. Pease—2028
Determination of electrode shapes for axially symmetric electron guns. K. J. Harker—2165
Electron probe measurements of evaporated metal films. W. E. Sweeney, Jr., R. E. Seebold, and L. S. Birks—1061
Electron sheet beam focusing with tape ladder lines. William E. Waters—1814
Evolution of gases and ions from different anodes under electron bombardment. J. R. Young—921
Focusing molecular beams of NH_3. J. C. Helmer, F. B. Jacobus, and P. A. Sturrock—458
Generation of millimeter waves by the electron beam of a microtron. E. Brannen, H. Froelich, and T. W. W. Stewart—1829(L)
Molecular beam formation by long parallel tubes. J. A. Giordmaine and T. C. Wang—463
Noise propagation in drifting multivelocity electron beams. J. A. Morrison—2066(L)
Noise temperature measurement on a traveling wave maser preamplifier. R. W. DeGrasse and H. E. D. Scovil—443(L)
On the concept of fictitious surface charges of an electron beam. E. L. Chu—381
On the nonconservation of noise parameters in multivelocity beams. J. Berghammer and S. Bloom—454
Parametric amplifier theory for plasmas and electron beams. G. S. Kino—1449
Partition noise in electron beams at microwave frequencies. A. Ashkin and L. D. White—1351
Power flow and stored energy in thin electron beams. W. W. Rigrod—1147
Simple theory concerning the reflection of electrons from solids. T. E. Everhart—1483
Single-velocity equivalents for multivelocity electron streams. Glenn A. Gray—370
Technique for calculating x-ray intensities in the electron probe microanalyzer. L. S. Birks—1297(L)
Theory of fast-wave parametric amplification. Curtis C. Johnson—338
Time-dependent electron flow. M. C. Pease—70
Waves on a filamentary electron beam in a transverse-field slow-wave circuit. A. E. Siegman—17

Electron Diffraction

Effect of specimen delocalization in electron diffraction studies of gas molecules. L. S. Bartell—252

Electron Microscopy

Determination of magnetization distribution in thin films using electron microscopy. Harrison W. Fuller and Murray E. Hale—238
Direct replica technique for copper. J. O. Stiegler and T. S. Noggle—1827(L)
Electron microscope observations of fission fragment tracks in thin films of UO_2. T. S. Noggle and J. O. Stiegler—2199
Electron microscope studies of colloids in KCl. R. E. Simon and R. L. Sproull—2224
Electron microscopic study of thin films of the aluminum-copper eutectic prepared by a melting method. Noboru Takahashi—1287
Microscopic study of neutron-irradiated germanium. B. B. Meckel, E. G. K. Schwarz, and R. A. Swalin—1299(L)
Preparation of tin single crystals for transmission electron microscopy. J. T. Fourie, F. Weinberg, and F. W. C. Boswell—1136(L)
Proceedings of the Electron Microscope Society of America—1831

Electron Tubes

Electrical stability and life of the heated field emission cathode. W. P. Dyke, F. M. Charbonnier, R. W. Strayer, R. L. Floyd, J. P. Barbour, and J. K. Trolan—790
Negative glow plasma as a cathode for electron tubes. J. M. Anderson and L. A. Harris—1463
Transport of noise at microwave frequencies through a space-charge-limited diode. W. E. Vivian—957

Energy Conversion

Calculation of efficiency of thermoelectric devices. B. Sherman, R. R. Heikes, and R. W. Ure, Jr.—1

Energy Conversion (*continued*)
Contribution of anode emission to space charge in thermionic power converters. Anthony F. Dugan—1397
Diagrams representing states of operation of a general thermocouple. A. H. Boerdijk—1141
Effect of interelectrode spacing on cesium thermionic converter performance. R. L. Hirsch—2064(L)
Effect of magnetic fields on thermionic power generators. Alfred Schock—1978
Effect of temperature on photovoltaic solar energy conversion. Joseph J. Wysocki and Paul Rappaport—571
Efficiency of the plasma thermocouple. H. W. Lewis and J. R. Reitz—723
Experimental magnetohydrodynamic power generator. Richard J. Rosa—735(L)
Figure of merit for thermionic energy conversion. N. S. Rasor—163
Generation of alternating current in the cesium cell. H. L. Garvin, W. B. Teutsch, and R. W. Pidd—1508(L)
On the theory of the close-spaced impregnated cathode thermionic converter. E. S. Rittner—1065
Peltier coefficient at a solid-solid interface. J. R. O'Connor—1690(L)
Performance of a thermoelectric converter under constant heat flux operation. P. S. Castro and W. W. Happ—1314
Potential distributions in a low-pressure thermionic converter. P. L. Auer—2096
Thermionic properties of UC. George A. Haas and John T. Jensen, Jr.—1231

Explosives and Explosions
Classification of wire explosions. William G. Chace and Morton A. Levine—1298(L)
Thermal initiation of explosives. John Zinn and Charles L. Mader—323

Ferroelectricity
Bias in ferroelectric colemanite. Ennio Fatuzzo—1029
Dielectric properties of lead titanate zirconate ceramics at very low frequencies. Robert Gerson—1615
High-temperature discharges in ferroelectric ceramics. John W. Northrip—2293
Model for switching and polarization reversal in colemanite. H. H. Wieder—180
Motion of 180° domain walls in metal electroded barium titanate crystals as a function of electric field and sample thickness. Robert C. Miller and Albert Savage—662
Temperature dependence of the velocity of sidewise 180° domain-wall motion in $BaTiO_3$. A. Savage and R. C. Miller—1546
Variation in ferroelectric characteristics of lead zirconate titanate ceramics due to minor chemical modifications. Robert Gerson—188

Ferromagnetic Materials and Ferrites
Absorption, reflectivity, and Faraday rotation measurements on some rare-earth iron garnets and on α-Fe_2O_3. P. C. Bailey—39S
Analysis of a practical perpendicular head for digital purposes. George J. Y. Fan—402S
Analysis of magnetic interactions in alloys of platinum with iron group transition elements. Hiroshi Sato—326S
Angular variation of the magnetic properties of elongated single domain iron particles. F. E. Luborsky and T. O. Paine—66S
Anisotropy and inversion in permalloy films. D. O. Smith, E. E. Huber, Jr., M. S. Cohen, and G. P. Weiss—295S
Anisotropy properties of hexagonal ferrimagnetic oxides. J. Smit, F. K. Lotgering, and U. Enz—137S
Annular uniaxially magnetized domains in thin Ni-Fe films. O. William Muckenhirn, A. E. LeBonte, and P. J. Besser—304S
Antiferromagnetic $FeVO_3$. Chester R. Berry and Charles M. Combs—1130(L)
Antiferromagnetic structure and domains in single crystal NiO. Walter L. Roth and Glen A. Slack—352S
Antiferromagnetism of iron in face-centered crystalline lattice and the causes of anomalies in Invar physical properties. E. I. Kondorsky and V. L. Sedov—331S
Blood flow measurements using dynamical paramagnetic relaxation times, and paramagnetic tracer techniques. J. R. Singer—406S
Broadband reciprocal ferrite phase shifters. T. D. Geiszler and R. A. Henschke—174S
Characteristics of Supermendur at 500°C. M. Lauriente and G. E. Lynn—237S
Coercive force and remanence of 25 A to 2000 A diameter cobalt, iron, and iron-cobalt alloy. F. E. Luborsky and T. O. Paine—68S
Comparison of the critical single-domain size for Fe_3O_4 and γFe_2O_3. L. A. K. Watt and A. H. Morrish—71S
Cross-tie walls in thin films. Harvey Rubinstein and Robert J. Spain—306S
Crystallography and domain walls in antiferromagnetic NiO crystals. Glen A. Slack—1571
Direct-current measurements on tape-wound cores. R. C. Barker and R. M. Brownell—243S
Determination of molecular field coefficients in ferrimagnets. G. T. Rado and V. J. Folen—62
Direct cation-cation interactions in primarily ionic solids. John B. Goodenough—359S
Domain wall velocities in thin iron-nickel films. N. C. Ford, Jr.—300S
Domain walls in thin magnetic Ni-Fe films. S. Methfessel, S. Middlehoek, and H. Thomas—302S
Double pump degenerate ferrite amplifier. Peter Gottlieb—172S
Effect of applying a magnetic field during neutron irradiation on the magnetic properties of Fe-Ni alloys. A. I. Schindler and E. I. Salkovitz—245S
Effects of directional ordering on the damping of zone-melted iron. R. E. Maringer—229S
Effect of directional orientation on the magnetic properties of cube oriented magnetic sheets. K. Foster and J. J. Kramer—233S
Effect of eddy currents on domain wall configurations, wall motion and loss for a domain model of cube-on-edge material. P. D. Agarwal and D. G. Graham—249S
Effect of impurities on the low-temperature spontaneous magnetization of cubic ferromagnetic crystals. A. A. Maradudin and P. A. Dixon—329S
Effect of potassium ions on the reaction and final properties of Mn-Zn ferrite. Stefan Makolagwa—339S
Effect of previous history on switching rate in ferrites. R. W. McKay and K. C. Smith—133S
Elastic constants of yttrium single crystals in the temperature range 4.2–400°K. J. F. Smith and J. A. Gjevre—645
Electrodeposited memory elements for a nondestructive memory. T. R. Long—123S
Electron spin relaxation in ferromagnetic insulators. R. C. LeCraw, R. C. Fletcher, and E. G. Spencer—95S
Evanescent modes in a partially filled gyromagnetic rectangular wave guide. Chen To Tai—220(L)
Exchange anisotropy in rock magnetism. W. H. Meiklejohn and R. E. Carter—164S
Exchange anisotropy in the system $Mn_{1.7}Cr_xSb$. R. H. Pry, J. S. Kouvel, and E. S. Miksch—162S
Explanation for the low-temperature behavior of the anisotropy of iron. W. J. Carr, Jr.—69

Fast switching by domain walls in ferrites. Walter Wiechec and Clinton M. Kelley—131S
Ferrimagnetic resonance at high power. M. T. Weiss—103S
Ferrimagnetic resonance in impurity doped yttrium iron garnet (YIG). J. F. Dillon, Jr., and J. W. Nielsen—43S
Ferrite films—new logic and storage devices. J. M. Brownlow, W. L. Shevel, Jr., and O. A. Gutwin—121S
Ferroelectric and ferrimagnetic properties of $(Ba_{6-2x}R_{2x})(Nb_{9-x}Fe_{1+x})O_{30}$. P. H. Fang and R. S. Roth—278S
Ferromagnetic alloy phases near the compositions Ni_2MnIn, Ni_2MnGa, Co_2MnGa, Pd_2MnSb, and PdMnSb. F. A. Hames—370S
Ferromagnetic-antiferromagnetic interaction in Fe-FeS. J. H. Greiner, I. M. Croll, and M. Sulich—231S
Ferromagnetic powders in waveguides at elevated temperatures. A. D. Krall and E. T. Hooper, Jr.—178S
Ferromagnetic resonance in polycrystalline ferrites using circularly polarized radiation. R. J. Zeender and E. Schlomann—111S
Flux reversal in soft ferromagnetics. E. M. Gyorgy—110S
"Foldover" effects caused by spin wave interactions in ferromagnetic resonance. H. Suhl—935(L)
$GaFeO_3$: Ferromagnetic-piezoelectric compound. J. P. Remeika—263S
Growing spin waves in ferrites in unstable equilibrium. Tor Schaug-Petersen—382S
Harmonic generation in a ferrimagnetic disk. Glenn E. Bennett—98S
High field magnetization study of ferrimagnetic arrangements in chromite spinels. I. S. Jacobs—263S
High-permeability garnets. Elmer E. Anderson and J. Richard Cunningham, Jr.—1687(L)
High power effects in ferrimagnetic resonance. P. E. Seiden and H. J. Shaw—432(L)
High power effects on ferrimagnetic resonance. M. T. Weiss—778
High-speed ferrite rotating half-wave plate. Franklin S. Coale—170S
High-temperature susceptibility of ferrimagnetic spinels. Peter J. Wojtowicz—265S
Hot working of Alnico V alloys. C. L. Kolbe and D. L. Martin—84S
Hyperfine interactions in magnetic materials by γ-γ angular correlation measurements. M. E. Caspari, S. Frankel, and M. A. Gilleo—320S
Improved method for the growth of yttrium-iron and yttrium-gallium garnets. J. W. Neilsen—51S
Influence of ionic order on the magnetocrystalline anisotropy and crystalline field parameters in lithium ferrite monocrystals. V. J. Folen—166S
Initial permeability characteristics of mixetl yttrium-gadolinium iron garnets. G. E. McDuffie, Jr., J. Richard Cunningham, and Elmer E. Anderson—47S
Initial-permeability spectra of microscopic iron-oxide particles. W. F. Brown, Jr., J. F. Hanton, and A. M. Morrish—214S
Instability of magnetic resonance in single crystal spheres of yttrium iron garnet. Joseph I Masters—41S
"Interaction anisotropy" model of the structure of Alnico magnet alloys. T. O. Paine and F. E. Luborsky—78S
Interaction of magnetic crystals with radiation in the range 10^4–10^5 cm^{-1}. A. M. Clogston—198S
Interpretation of the magnetic and crystallographic properties of several iron, nickel, and iron-nickel nitrides. J. B. Goodenough, A. Wold, and R. J. Arnott—342S
Intrinsic and anneal-induced anisotropy in cobalt-substituted W-type hexagonal oxides. L. R. Bickford, Jr.—259S
Investigations into the origin of anisotropy in oblique-incidence films. M. S. Cohen, E. E. Huber, Jr., G. P. Weiss, and D. O. Smith—291S
Ionic ordering effects in the ferromagnetic resonance of lithium ferrite monocrystals. A. D. Schnitzler, V. J. Folen, and G. T. Rado—348S
Localized field permanent magnet arrays. H. L. Stadler—196S
Long-range magnetic interactions via conduction electrons. Arthur Paskin—318S
Long-term magnetic stability of Alnico and barium ferrite magnets. K. J. Kronenberg and M. A. Bohlmann—82S
Low-temperature x-ray diffraction studies on vanadium sesquioxide. E. P. Warekois—346S
Magnetic anisotropy and magnetostriction of ordered and disordered cobalt-iron alloys. R. C. Hall—157S
Magnetic anisotropy in evaporated iron films. E. W. Pugh, J. Matisoo, D. E. Speliotis, and E. L. Boyd—293S
Magnetic anisotropy in ferrimagnetic crystals. R. F. Pearson—160S
Magnetic behavior in the transition region of a hematite single crystal. S. T. Lin—273S
Magnetic behavior of polycrystalline neodymium, holmium, and erbium from 300 to 1500°K. Sigurds Arajs and D. S. Miller—325S
Magnetic contribution to the ultrasonic attenuation in annealed and deformed steel (SAE 1020). W. J. Bratina, U. M. Martius and D. Mills—241S
Magnetic field measurement using ultrasonics. R. J. Radus—186S
Magnetic form factor of Fe_3Al. S. J. Pickart and R. Nathans—372S
Magnetic interactions and distribution of ions in the garnets. S. Geller—30S
Magnetic moments of alloys of gadolinium with some of the transition elements. William M. Hubbard, Edmond Adams, and John V. Gilfrich—368S
Magnetic properties of ferromagnetic superconductors. R. M. Bozorth and D. D. Davis—321S
Magnetic properties of the $Li_xMn_{1-x}Se$ system. Thomas R. McGuire and Robert R. Heikes—276S
Magnetic properties of uranium digermanide. Clayton E. Olsen—340S
Magnetic transitions in Ti_2O_3 and V_2O_3. P. H. Carr and S. Foner—344S
Magnetization of a dilute suspension of a multidomain ferromagnetic. C. P. Bean and I. S. Jacobs—122S
Magnetization of the compound TiFe. M. V. Nevitt—155
Magnetostatic modes in disks and rods. J. F. Dillon, Jr.—160S
Magnetostatic modes of a ferromagnetic slab. R. W. Damon and J. R. Eshbach—104S
Magnetostriction of gadolinium iron garnets. K. P. Belov and A. V. Pedko—55S
Magneto structural studies on gadolinium-iron alloys. R. C. Vickery, W. C. Sexton, V. F. Novy, and E. V. Kleber—366S
Mechanism of antiferromagnetism in dilute alloys. A. W. Overhauser—317S
Metamagnetic behavior of manganese arsenide. D. S. Rodbell and P. E. Lawrence—275S
Method for the detection of flaws in yttrium iron garnet crystals. E. Buehler and M. Tanenbaum—38S
Microcalorimetric technique for the study of damping and hysteresis in ferromagnetic films. J. R. Mayfield—298S
Microwave properties of nonstoichiometric polycrystalline yttrium iron garnet. P. E. Seiden, C. F. Kooi, and J. M. Katz—129I
Microwave resonance in rare earth iron garnets. C. Kittel—11S

Ferromagnetic Materials and Ferrites *(continued)*
Neutron diffraction investigation of the $Fe_{1-x}S$ system. Joseph T. Sparks, Warren Mead, Albert J. Kirschbaum, and Walter Marshall—356S
Neutron diffraction investigation of the magnetic structure of nickel oxide. H. A. Alperin—354S
Neutron diffraction investigations of the magnetic ordering in rare earth nitrides. M. K. Wilkinson, H. R. Child, J. W. Cable, E. O. Wollan, and W. C. Koehler —358S
New material for permanent magnets on a base of Mn and Al. A. J. J. Koch, P. Hokkeling, M. G. v.d. Steeg, and K. J. deVos—75S
Nonlinear effects of crystalline anisotropy on ferromagnetic resonance. Peter Gottlieb—2059
Nuclear resonance in ferromagnetic cobalt. A. M. Portis and A. C. Gossard—205S
On internal friction anomaly in ferromagnetics and antiferromagnetics near the Curie point. K. P. Belov, G. I. Katayev, and R. Z. Levitin—153S
On the incorporation of neodymium in mixed yttrium-neodymium-iron garnets. G. Goldring, M. Schieber, and Z. Vager—2057
On the laws of magnetization of ferrimagnetic single crystals and polycrystals. Application to uniaxial compounds. L. Néel, R. Pauthenet, G. Rimet, and V. S. Giron—27S
On the remanence of ferromagnetic powders. S. Shtrikman and D. Treves—58S
Paramagnetic susceptibilities of Fe and Fe-Si alloys. Sigurds Arajs and D. S. Miller—986
Permanent magnet leadage permeance evaluation based on polar radiation analogy. J. E. Foy and R. J. Parker—188S
Permanent magnets obtained by drawing compacts of parallel iron wires. E. P. Levi—1469
Precipitation of dispersed fine-particle magnetite. Lynore E. Slaten—74S
Precise measurement of magnetic form factors. Robert Nathans—350S
Preferred orientation and ordering in evaporated films of Fe, Ni, and Fe-Ni. R. F. Adamsky—289S
Properties of manganese ferrites prepared at various oxygen pressures. Aleksander Bragiński—339S
Pulsed ferrimagnetic microwave generator. B. Elliot, T. Schaug-Peterson, and H. J. Shaw—400S
Recent developments in ferromagnetic resonance at high power levels. E. Schlömann, J. J. Green, and U. Milano —385S
Rectangular hysteresis loop ferrites with large Barkhausen steps. Aaron P. Greifer and William J. Croft—85
Relations between superconductors and ferromagnets. Bernd Matthias—23S
Resonance experiments with single crystal yttrium iron garnets in pulsed magnetic fields. Martin P. Stiglitz and Frederic R. Morgenthaler—37S
Resonance line widths of sintered nickel ferrites having low porosities. L. G. Van Uitert, R. R. Soden, and F. W. Swanekamp—226S
Resonance measurements in magnetic garnets. G. P. Rodrique, H. Meyer, and R. V. Jones—376S
Rigorous solution of eddy current losses in rectangular bar for single plane domain wall model. Paul D. Agarwal and L. Rabins—246S
Role of cation vacancy in magnetic annealing of iron-cobalt ferrites. Shuichi Iida—251S
Roll magnetic anisotropy of iron-aluminum crystals. Soshin Chikazumi—158S
Samarium substitutions in yttrium iron garnet. J. Richard Cunningham, Jr., and Elmer E. Anderson—45S
Saturation effects in ferrimagnetic resonance. P. E. Seiden and H. J. Shaw—224S
Secondary recrystallization in vacuum annealed silicon iron. G. Baer, D. Ganz, and H. Thomas—235S
Single-crystal magnetic anisotropy and magnetostriction studies in iron-base alloys. R. C. Hall—1037
Some physical properties of thin magnetic films. A. C. Moore and A. S. Young—279S
Specific heat of high purity iron by a pulse heating method. D. C. Wallace, P. H. Sidles, and G. C. Danielson—168
Specific heat of some rare earth iron garnets and YIG at low temperatures. Horst Meyer and A. B. Harris—49S
Spin waves in complex exchange-coupled lattices and neutron scattering. A. W. Saenz—108S
Spontaneous magnetizations of some gadolinium alloys. Sigurds Arajs and D. S. Miller—213(L)
Square loop properties of copper-manganese ferrites. R. S. Weisz and D. L. Brown—269S
State of *d* electrons in transition metals. Conyers Herring —3S
Static and dynamic studies of magnetization distribution in thin films by electron microscopy. Harrison W. Fuller and Murray E. Hale—308S
Studies in partial switching of ferrite cores. Roger H. Tancrell and Robert E. McMahon—762
Study of heat treatments for low coercive force 14-17 percent aluminum iron alloys. D. Pavlovic and K. Foster —231S
Survey of ferromagnetic resonance in small ferrimagnetic ellipsoids. Frederic R. Morgenthaler—95S
Switching behavior of low-remanence ferrite. F. B. Hagedorn and E. M. Gyorgy—398S
Temperature dependence of anisotropy and saturation magnetization in iron and iron-silicon alloys. C. D. Graham, Jr.—150S
Temperature dependence of the electrical resistivity of bcc Cr-Fe alloys. N. S. Rajan, R. M. Waterstrat, and Paul A. Beck—731
Temperature dependence of the saturation magnetization of ferrites with magnetoplumbite structure. G. Heimke —271S
Theory and application of dipolar ferrite modes. William H. Steier and Paul D. Coleman—99S
Time decrease in initial permeability in $Mn_xFe_{3-x}O_{4-y}$. W. A. Crapo—267S
Transmission electron diffraction of Alnico V. K. J. Kronenberg—80S
Valence and distribution of manganese ions in ferrospinels. Arthur Miller—261S
Volume dependence of ferrimagnetic resonance properties in $Ni_{1-x}Co_xFe_2O_4$. I. P. Kaminow—220S
Walker modes in large ferrite samples. B. A. Auld—1642
X-ray study of ferromagnetic domains in cobalt zinc ferrite. Kenneth M. Merz—147

Fluid Dynamics
Effect of gas pressure and cone angle on the velocities of electrically excited shock waves. Philip J. Hart—436(L)
Experimental magnetohydrodynamic power generator. Richard J. Rosa—735(L)
Monte Carlo calculation of molecular flow rates through a cylindrical elbow and pipes of other shapes. D. H. Davis—1169
On the flow of a non-Newtonian liquid on a rotating disk. A. Acrivos, M. J. Shah, and E. E. Petersen—963
Resistance to potential flow through a cubical array of spheres. Robert E. Meredith and Charles W. Tobias—1270
Three-dimensional wedge impact on a compressible fluid. S. F. Borg—438(L)

Fluid Flow, Low Speed
Effect of viscosity on the splash caused by a drop of water falling into a mixture of glycerol and water. A. G. Davis Philip—727
Flow of polyethylene into a capillary. E. B. Bagley and A. M. Birks—556
On the flow of a non-Newtonian liquid on a rotating disk. A. Acrivos, M. J. Shah, and E. E. Petersen—963
Theory of non-Newtonian flow. III. Method for analyzing non-Newtonian flow curves. Wan Kyue Kim, Nishio Hirai, Taikuye Ree, and Henry Eyring—358

Fracture
Effect of orientation on strength of a model solid. A. Robinson, J. E. Osborn, and C. C. Hsiao—1602
Hooke's law in shear and polymer melt fracture. E. B. Bagley—1126(L)
Spiral dislocations on glass fracture surfaces. W. C. Levengood and T. S. Voug—1416
X-ray examination of brittle fractures in extruded chromium. C. W. Weaver and K. A. Gross—626

Friction and Wear
Effect of fast neutron bombardment at various temperatures upon the Young's modulus and internal friction of copper. D. O. Thompson and V. K. Paré—528
Recovery of internal friction in aluminum after plastic deformation. Ivar Holwech—928
Reviving the classical theory of friction by a modern dislocation theory of deformation revision. John H. Dismant—221(L)
Reviving the classical theory of friction by a modern dislocation theory of deformation revision. John H. Dismant—942(E)
Rolling friction of polymeric materials. I. Elastomers. Donald G. Flom—306

Gaseous Electron Physics
Cathode of an arc in xenon. John E. White—1709
Detection of metastable atoms and ions. Homer D. Hagstrum—897
Energy distribution and cooling effect of electrons emitted from an arc cathode. T. H. Lee—924
Etching of surfaces with 8-kev argon ions. R. L. Cunningham, P. Hayman, C. Lecomte, W. J. Moore, and J. J. Trillat—839
Evolution of gases and ions from different anodes under electron bombardment. J. R. Young—921
Experimental study of arc stability. I. J. D. Cobine and G. A. Farrall—2296
Generation of alternating current in the cesium cell. H. L. Garvin, W. B. Teutsch, and R. W. Pidd—1508(L)
High-frequency breakdown of air. Donald Kelly and Henry Margenau—1617
Influence of negative ions on ambipolar diffusion of electrons. Hendrik J. Oskam and Verlyn R. Mittlestadt—940(L)
Intensities of λ1850 and λ2537 in low-pressure mercury vapor lamps with rare gas present. Bentley T. Barnes—852
Ion energies in a cold cathode discharge in a magnetic field. John Backus and Norman E. Huston—400
Mechanism of inert gas cleanup in a gaseous discharge. K. B. Blodgett and T. A. Vanderslice—1017
Microwave noise from low-pressure arcs. R. M. Hill and S. K. Ichiki—735(L)
Microwave study of afterglow discharge in water vapor. Susumu Takeda and Arwin A. Dougal—412
Mobility of hydrogen and deuterium positive ions in their parent gases. D. J. Rose—643
Motion of high-speed arc spots in magnetic fields. D. Zei and J. G. Winans—1137(E)
Negative hydrogen and deuterium ion beams. Sanborn F. Philp—1592
Numerical calculation of absolute bremsstrahlung intensity for a fully ionized dissociated hydrogenic gas. G. Sargent Janes and H. Koritz—525
Positive column formation in ion sources employing surface ionization. P. L. Auer and H. Hurwitz—1007
Probes at high pressure. John E. White—1502(L)
Surface cleaning by cathode sputtering. O. C. Yonts and Don E. Harrison, Jr.—1583
Three-dimensional space charge flow. Jorge Rosenblatt—1371
Ultimate and secondary electron energies in the negative glow of a cold-cathode discharge in helium. J. M. Anderson—511
Use of SF_6^- for calibration of the electron energy scale. G. J. Schulz—1134(L)

Liquids
Comments on a ruptured soap film. F. E. C. Culick—1128(L)
Distribution of spray from impinging liquid jets. K. Dexter Miller, Jr.—1132(L)
Dynamic hard sphere model. D. Turnbull and R. L. Cormia—674
More experiments on liquid films. R. M. Koros, J. Deckers, and M. Boudart—1129(L)
On the flow of a non-Newtonian liquid on a rotating disk. A. Acrivos, M. J. Shah, and E. E. Petersen—963
Ultrasonic viscoelastic properties of associated liquids. R. Meister, C. J. Marhoeffer, R. Sciamanda, L. Cotter, and T. Litovitz—854

Luminescence and Photoconductivity
Effect of pressure on phosphor decay. D. W. Gregg and H. G. Drickamer—494
Field induced photoemission and hot-electron emission from germanium. R. E. Simon and W. E. Spicer—1505(L)
Grain-boundary photoresponse. W. W. Lindemann and R. K. Mueller—1746
Hole mobility and crystal size in lead sulfide photoconductive films. H. E. Spencer and J. V. Morgan—2024
Influence of transverse modes on photoconductive decay in filaments. J. S. Blakemore and K. C. Nomura—753
Intensities of λ1850 and λ2537 in low-pressure mercury vapor lamps with rare gas present. Bentley T. Barnes—852
Mechanism of photoconductivity in microcrystalline powders. Richard H. Bube—2239
Noise and signal response in lead sulfide photoconductive films. H. E. Spencer—505
Photoeffects in nonuniformly irradiated *p-n* junctions. Gerald Lucovsky—1088
Photoelectronic analysis of high resistivity crystals: (a) GaAs, (b) Sb_2S_3. Richard H. Bube—315
Photoemission in the photovoltaic effect in cadmium sulfide crystals. Richard Williams and Richard H. Bube—968
Print-out process in photographic emulsion grains. J. F. Hamilton and L. E. Brady—609(L)
Saturation of photocurrent with light intensity. Richard H. Bube—1301(L)

Magnetic Resonance
Charged-particle orbits in varying magnetic fields. E. I. Gordon—1187
Classical theory of spin configurations in the cubic spinel. T. A. Kaplan—364S
Effects of surface irregularities on single crystal resonance parameters. C. R. Buffler—222S

Magnetic Resonance *(continued)*
Electromagnetic theory of dc effects in ferromagnetic resonance. H. J. Juretschke—1401
Electron spin relaxation in ferromagnetic insulators. R. C. LeCraw, R. C. Fletcher, and E. G. Spencer—95S
Ferrimagnetic resonance at high power. M. T. Weiss—103S
Ferrimagnetic resonance in impurity doped yttrium iron garnet (YIG). J. F. Dillon, Jr., and J. W. Nielsen—43S
Ferromagnetic resonance in polycrystalline ferrites using circularly polarized radiation. R. J. Zeender and E. Schlömann—1112
Flow rates using nuclear or electron paramagnetic resonance techniques with applications to biological and chemical processes. J. R. Singer—125
"Foldover" effects caused by spin wave interactions in ferromagnetic resonance. H. Suhl—935(L)
Galvanomagnetic effects in ferromagnetic resonance. M. H. Seavey, Jr.—216S
Generation of phonons in high-power ferromagnetic resonance experiments. Ernst Schlömann—1647
Growing spin waves in ferrites in unstable equilibrium. Tor Schaug-Petersen—382S
High-power effects in ferrimagnetic resonance. P. E. Seiden and H. J. Shaw—432(L)
High-power effects on ferrimagnetic resonance. M. T. Weiss—778
Hyperfine interactions in magnetic materials by γ-γ angular correlation measurements. M. E. Caspari, S. Frankel, and M. A. Gilleo—320S
Instability of magnetic resonance in single crystal spheres of yttrium iron garnet. Joseph I. Masters—41S
Inversions by fast passage in a multilevel spin system. P. E. Wagner, J. G. Castle, Jr., and P. F. Chester—1498(L)
Ionic ordering effects in the ferromagnetic resonance of lithium ferrite monocrystals. A. D. Schnitzler, V. J. Folen, and G. T. Rado—348S
Magnetic anisotropy from the magnetostatic modes. I. H. Solt, Jr., and P. C. Fletcher—100S
Magnetic susceptibilities of single crystal $NiCl_2 \cdot 6H_2O$ and $CoCl_2 \cdot 6H_2O$ at low temperatures. R. B. Flippen and S. A. Friedberg—338S
Magnetostatic modes in disks and rods. J. F. Dillon, Jr.—1605
Magnetostatic modes of a ferromagnetic slab. R. W. Damon and J. R. Eshbach—104S
Mechanism of antiferromagnetism in dilute alloys. A. W. Overhauser—317S
Microwave resonance in rare earth iron garnets. C. Kittel—11S
Paramagnetic resonance absorption of nickel in sapphires. S. A. Marshall and A. R. Reinberg—336S
Paramagnetic resonance of Yb in aluminum and gallium garnets. John W. Carson and Robert L. White—53S
Recent developments in ferromagnetic resonance at high power levels. E. Schlömann, J. J. Green, and U. Milano—385S
Resonance experiments with single crystal yttrium iron garnets in pulsed magnetic fields. Martin P. Stiglitz and Frederic R. Morgenthaler—37S
Resonance linewidths of sintered nickel ferrites having low porosities. L. G. Van Uitert, R. R. Soden, and F. W. Swanekamp—226S
Resonance measurements in magnetic garnets. G. P. Rodrigue, H. Meyer, and R. V. Jones—376S
Saturation effects in ferrimagnetic resonance. P. E. Seiden and H. J. Shaw—224S
Single crystal tungstates for resonance and emission studies. L. G. Van Uitert and R. R. Soden—328
Spin waves in complex exchange-coupled lattices and neutron scattering. A. W. Saenz—108S
Subsidiary resonance in the coincidence region in yttrium iron garnet. F. C. Rossol—2273
Survey of ferromagnetic resonance in small ferrimagnetic ellipsoids. Frederic R. Morgenthaler—95S
Theory of the low-lying states of some rare earth compounds. G. T. Trammell—362S
Use of magnetostatic modes as a research tool. Robert L. White—86S
Volume dependence of ferrimagnetic resonance properties. I. P. Kaminow—220S
Walker modes in large ferrite samples. B. A. Auld—1642

Magnetism, General
Analysis of magnetic interactions in alloys of platinum with iron group transition elements. Hiroshi Sato—326S
Angular variation of the magnetic properties of elongated single domain iron particles. F. E. Luborsky and T. O. Paine—66S
Anisotropic magnetization. Earl R. Callen—149S
Anisotropy and inversion in permalloy films. D. O. Smith, E. E. Huber, Jr., M. S. Cohen, and G. P. Weiss—295S
Anisotropy of the magnetic susceptibility of gallium. Titus Pankey, Jr.—1802
Anisotropy properties of hexagonal ferrimagnetic oxides. J. Smit, F. K. Lotgering, and U. Enz—137S
Annular uniaxially magnetized domains in thin Ni-Fe films. O. William Muckenhirn, A. E. LaBonte, and P. J. Besser—304S
Antiferromagnetism of iron in face-centered crystalline lattice and the causes of anomalies in Invar physical properties. E. I. Kondorsky and V. L. Sedov—331S
Beam refrigeration by means of large magnetic fields. Robert Adler and Glen Wade—1201
Charged-particle orbits in varying magnetic fields. E. I. Gordon—1187
Coercive force and remanence of 25 A to 2000 A diameter cobalt, iron, and iron-cobalt alloy. F. E. Luborsky and T. O. Paine—68S
Comparison of the critical single-domain size for Fe_3O_4 and γFe_2O_3. L. A. K. Watt and A. H. Morrish—71S
Corbino disk. D. A. Kleinman and A. L. Schawlow—2176
Correlation of low temperature caloric and magnetic effects in TiFe. K. Schroder and C. H. Cheng—2154
Cross-tie walls in thin films. Harvey Rubinstein and Robert J. Spain—306S
Crystal distortion in magnetic compounds. Junjiro Kanamori—14S
Crystallography and domain walls in antiferromagnetic NiO crystals. Glen A. Slack—1571
Determination of magnetization distribution in thin films using electron microscopy. Harrison W. Fuller and Murray E. Hale—238
Development of high-speed coincident current memory cores. Barlane R. Eichbaum—117S
Direct cation-cation interactions in primarily ionic solids. John B. Goodenough—359S
Domains in thin magnetic films observed by electron microscopy. Harrison W. Fuller and Murray E. Hale—1699
Domain wall velocities in thin iron-nickel films. N. C. Ford, Jr.—300S
Domain walls in thin magnetic Ni-Fe films. S. Methfessel, S. Middlehoek, and H. Thomas—302S
Double pump degenerate ferrite amplifier. Peter Gottlieb—172S
Effect of crystalline fields on magnetic form factors. A. J. Freeman and R. E. Watson—374S

Effect of directional orientation on the magnetic properties of cube oriented magnetic sheets. K. Foster and J. J. Kramer—233S
Effect of eddy currents on domain wall configurations, wall motion, and loss for a domain model of cube-on-edge material. P. D. Agarwal and D. G. Graham—249S
Effect of impurities on the low-temperature spontaneous magnetization of cubic ferromagnetic crystals. A. A. Maradudin and P. A. Dixon—329S
Effect of neutron bombardment on the magnetic properties of very high permeability iron. G. Biorci, A. Ferro, and G. Montalenti—2046
Effect of potassium ions on the reaction and final properties of Mn-Zn ferrite. Stefan Makolagwa—339S
Effects of directional ordering on the damping of zone-melted iron. R. E. Maringer—229S
Effects of hydrostatic pressure on the properties of magnetic materials. R. E. Alley, Jr., and V. E. Legg—239S
Elastic switching properties of some square loop materials in toroidal structures. W. C. Seelbach and J. R. Kiseda —135S
Electrodeposited memory elements for a nondestructive memory. T. R. Long—123S
Exchange anisotropy in Cu-Mn and Ag-Mn alloys. J. S. Kouvel—142S
Exchange anisotropy in rock magnetism. W. H. Meikle-john and R. E. Carter—164S
Exchange anisotropy in the system $Mn_{(1-x)}Cr_xSb$. R. H. Pry, J. S. Kouvel, and E. S. Miksch—162S
Exchange anisotropy memory effect. I. S. Jacobs and P. E. Lawrence—1388
Experimental flux pattern determination in magnetic cores. Robert L. Ward—192S
Explanation for the low-temperature behavior of the anisotropy of iron. W. J. Carr, Jr.—69
External fields from domain walls of cobalt film. B. Kostyshyn, J. E. Brophy, I. Oi, and D. D. Roshon, Jr.—772
Fast switching by domain walls in ferrites. Walter Wiechec and Clinton M. Kelley—131S
Fine structure of Bloch walls. S. Shtrikman and D. Treves—1304L
Finite amplitude electromagnetic waves in gyromagnetic media. B. A. Auld—106S
Flux reversal by noncoherent rotation in magnetic films. K. J. Harte—283S
Flux reversal in soft ferromagnetics. E. M. Gyorgy—110S
High field magnetization study of ferrimagnetic arrangements in chromite spinels. I. S. Jacobs—263S
High-temperature susceptibility of ferrimagnetic spinels. Peter J. Wojtowicz—265S
Hyperfine interactions in magnetic materials by γ-γ angular correlation measurements. M. E. Caspari, S. Frankel, and M. A. Gilleo—320S
Influence of ionic order on the magnetocrystalline anisotropy and crystalline field parameters in lithium ferrite monocrystals. V. J. Folen—166S
Influence of nearby conductors on thin film switching. J. S. Eggenberger—287S
Initial-permeability spectra of microscopic iron-oxide particles. W. F. Brown, Jr., J. F. Hanton, and A. M. Morrish—214S
Initial susceptibility spectra of permalloy films. R. F. Soohoo—218S
Instrumentation applications of inverse-Wiedemann effect. J. A. Granath—178S
"Interaction anisotropy" model of the structure of Alnico magnet alloys. T. O. Paine and F. E. Luborsky—78S
Interaction between high-power microwave losses and magnetic flux reversal. E. M. Gyorgy and F. B. Hagedorn —1775
Interaction of magnetic crystals with radiation in the range 10^4-10^5 cm^{-1}. A. M. Clogston—198S
Internal friction anomaly in ferromagnetics and antiferromagnetism near the Curie point. K. P. Belov, G. I. Katayev, and R. Z. Levitin—153S
Internal structure of Bloch walls. S. Shtrikman and D. Treves—147S
Interpretation of the magnetic and crystallographic properties of several iron, nickel, and iron-nickel nitrides. J. B. Goodenough, A. Wold, and R. J. Arnott—342S
Intrinsic and anneal-induced anisotropy in cobalt-substituted *W*-type hexagonal oxides. L. R. Bickford, Jr.—259S
Investigations into the origin of anisotropy in oblique-incidence films. M. S. Cohen, E. E. Huber, Jr., G. P. Weiss, and D. O. Smith—291S
Ionic ordering effects in the ferromagnetic resonance of lithium ferrite monocrystals. A. D. Schnitzler, V. J. Folen, and G. T. Rado—348S
Localized field permanent magnet arrays. H. L. Stadler—196S
Long-range magnetic interactions via conduction electrons. Arthur Paskin—318S
Long-term magnetic stability of Alnico and barium ferrite magnets. K. J. Kronenberg and M. A. Bohlmann—82S
Magnetic anisotropy from the magnetostatic modes. I. H. Solt, Jr., and P. C. Fletcher—100S
Magnetic anisotropy in evaporated iron films. E. W. Pugh, J. Matisoo, D. E. Speliotis, and E. L. Boyd—293S
Magnetic anisotropy in ferrimagnetic crystals. R. F. Pearson—160S
Magnetic-form factor of Fe_3Al. S. J. Pickart and R. Nathans—372S
Magnetic interactions and distribution of ions in the garnets. S. Geller—30S
Magnetic properties of ferromagnetic superconductors. R. M. Bozorth and D. D. Davis—321S
Magnetic properties of manganese copper alloys. R. Street —310S
Magnetic transitions in Ti_2O_3 and V_2O_3. P. H. Carr and S. Foner—344S
Magnetic viscosity due to solute atom pairs. I. Theory of the effect. G. Biorci, A. Ferro, and G. Montalenti—2121
Magnetism in medicine. Michael W. Freeman, M.D., Anthony Arrott, and John H. L. Watson—404S
Magnetization of a dilute suspension of a multidomain ferromagnetic. C. P. Bean and I. S. Jacobs—1228
Magnetization of the compound TiFe. M. V. Nevitt—155
Magnetization of the compound TiFe. M. V. Nevitt—942(E)
Magnetization reversal in uniaxial films near to the preferred direction. E. M. Bradley and M. Prutton—285S
Magneto structural studies on gadolinium-iron alloys. R. C. Vickery, W. C. Sexton, V. F. Novy, and E. V. Kleber—366S
Mechanism of antiferromagnetism in dilute alloys. A. W. Overhauser—317S
Method for measuring iron losses in elliptically polarized magnetic fields. F. J. Young and H. L. Schenk—194S
Microcalorimetric technique for the study of damping and hysteresis in ferromagnetic films. J. R. Mayfield—298S
Millimicrosecond magnetization reversal in thin magnetic films. D. W. Dietrich and W. E. Proebster—281S
Miniature memory planes for extreme environmental conditions. R. Straley, A. Heuer, B. Kane, and G. Tkach —126S
Mobility of edge dislocations in silicon-iron crystals. Dale F. Stein and J. R. Low—362

Magnetism, General (*continued*)
Multimode propagation in gyromagnetic rods and its application to traveling-wave devices. J. E. Tompkins, F. Reggia and L. Joseph—176S
Necessary factor for heat treatment of the permalloys in a magnetic field. E. A. Nesbitt, R. D. Heidenreich, and A. J. Williams—228S
Neutron and optical studies of domains in NiO. W. L. Roth—2000
Neutron diffraction investigation of the $Fe_{1-y}S$ system. Joseph T. Sparks, Warren Mead, Albert J. Kirschbaum, and Walter Marshall—356S
Neutron diffraction investigation of the magnetic structure of nickel oxide. H. A. Alperin—354S
Neutron diffraction investigations of the magnetic ordering in rare earth nitrides. M. K. Wilkinson, H. R. Child, J. W. Cable, E. O. Wollan, and W. C. Koehler—358S
New approach to high-speed storage—low flux density materials. W. L. Shevel, Jr., and H. Chang—125S
New material for permanent magnets on a base of Mn and Al. A. J. J. Koch, P. Hokkeling, M. G. v.d. Steeg, and K. J. deVos—75S
New multi-aperture magnetic logic element. David R. Bennion—129S
Nucleation experiments on thin magnetic MnBi films. Ludwig Mayer—384S
Observation of domains in iron whiskers under high fields. C. A. Fowler, Jr., E. M. Fryer, and David Treves—2267
Observation of Néel walls in thin films. Harvey Rubinstein, Harrison W. Fuller, and Murray E. Hale—437(L)
Observations on MnBi films during heat treatment. Ludwig Mayer—346
On the resolution of Brown's paradox. S. Shtrikman and D. Treves—72S
Operation of magnetic film parametrons in the 100- to 500-Mc region. A. V. Pohm, A. A. Read, R. M. Stewart, and R. F. Schauer—119S
Ordering in the intermediate phases TiFe, TiCo, and TiNi. Paul Pietrokowsky and Frank G. Youngkin—1763
Paramagnetic resonance absorption of nickel in sapphires. S. A. Marshall and A. R. Reinberg—336S
Paramagnetic resonance of Yb in aluminum and gallium garnets. John W. Carson and Robert L. White—53S
Paramagnetic susceptibilities of Fe and Fe-Si alloys. Sigurds Arajs and D. S. Miller—986
Particle interaction in magnetic recording tapes. J. G. Woodward and E. Della Torre—56
Permanent magnet leadage permeance evaluation based on polar radiation analogy. J. E. Foy and R. J. Parker—188S
Plasma propulsion by a rapidly varying magnetic field. Milton M. Klein and Keith A. Brueckner—1437
Practical hysteresigraph. R. R. Bockemuehl and W. E. Sargeant—180S
Precise measurement of magnetic form factors. Robert Nathans—350S
Preferred orientation and ordering in evaporated films of Fe, Ni, and Fe-Ni. R. F. Adamsky—289S
Preparation of large calcium-tungstate crystals containing paramagnetic ions for maser applications. K. Nassau and L. G. Van Uitert—1508(L)
Production of very high magnetic fields by implosion. C. M. Fowler, W. B. Garn, and R. S. Caird—588
Promotion of cubic grain growth in 3% silicon iron by control of annealing atmosphere composition. Dale Kohler—408S
Rictometer system for calibrating transmitters of remote indicating compasses. L. I. Mendelsohn—183S
Rigorous solution of eddy current losses in rectangular bar for single plane domain wall model. Paul D. Agarwal and L. Rabins—246S
Roll magnetic anisotropy of iron-aluminum crystals. Soshin Chikazumi—158S
Scattering of electromagnetic waves from the infinitely long magnetized cylindrical plasma. P. M. Platzman and H. T. Ozaki—1597
Simple recording torque magnetometer. P. W. Neurath—184S
Single-crystal magnetic anisotropy and magnetostriction studies in iron-base alloys. R. C. Hall—1037
Some physical properties of thin magnetic films. A. C. Moore and A. S. Young—279S
"Spontaneous magnetic anisotropy" in polycrystalline thin films. W. Andra, Z. Malek, W. Schuppel, and O. Stemme—422
Spontaneous magnetizations of some gadolinium alloys. Sigurds Arajs and D. S. Miller—213(L)
Square loop properties of copper-manganese ferrites. R. S. Weisz and D. L. Brown—269S
State of *d* electrons in transition metals. Conyers Herring—3S
Studies in partial switching of ferrite cores. Roger H. Tancrell and Robert E. McMahon—762
Switching behavior of low-remanence ferrite. F. B. Hagedorn and E. M. Gyorgy—398S
Temperature dependence of anisotropy and saturation magnetization in iron and iron-silicon alloys. C. D. Graham, Jr.—150S
Temperature dependence of the saturation magnetization of nickel films of thickness less than 100 A. C. A. Neugebauer—152S
Tetrahedral junction. Jerald A. Weiss—168S
Theory of the low-lying states of some rare earth compounds. G. T. Trammell—362S
Transfer function and error probability of a digital magnetic tape recording system. John Wenchung Hung—396S
Transmission electron diffraction of Alnico V. K. J. Kronenberg—80S
Use of magnetostatic modes as a research tool. Robert L. White—86S

Masers and Parametric Amplifiers
Charred dextrose as a paramagnetic resonance standard. R. H. Hoskins and R. C. Pastor—1506(L)
Chromium-doped titania as a maser material. H. J. Gerritsen, S. E. Harrison, and H. R. Lewis—1566
Comments on "Diode capacitors for parametric amplification" by R. C. Knechtli and R. D. Weglein. K. E. Mortenson—1135(L)
Cw millimeter wave maser using Fe^{3+} in TiO_2. S. Foner and L. R. Momo—742(L)
Diode capacitors for parametric amplification. R. C. Knechtli and R. D. Weglein—1134(L)
Effect of nuclear polarization on the behavior of solid state masers. G. Makhov, L. G. Cross, R. W. Terhune, and J. Lambe—936(L)
Focusing molecular beams of NH_3. J. C. Helmer, F. B. Jacobus, and P. A. Sturrock—458
High-power effects in ferrimagnetic resonance. P. E. Seiden and H. J. Shaw—432(L)
Inversions by fast passage in a multilevel spin system. P. E. Wagner, J. G. Castle, Jr., and P. F. Chester—1498(L)
Maser behavior: temperature and concentration effects. T. H. Maiman—222(L)
Megavolt electronics Cerenkov coupler for the production of millimeter and submillimeter waves. Paul D. Coleman and Charles Enderby—1695(L)

Microwave properties of nonstoichiometric polycrystalline yttrium iron garnet. P. E. Seiden, C. F. Kooi and J. M. Katz—1291
Noise figure and gain of parametric converters. H. Heffner and G. Wade—2316(L)
Noise temperature measurement on a traveling-wave maser preamplifier. R. W. DeGrasse and H. E. D. Scovil—443(L)
On the possibility of maser action in nuclear quadrupole systems. R. E. Donovan and A. A. Vuylsteke—614(L)
Operating characteristics of a molecular-beam maser. H. G. Venkates and M. W. P. Strandberg—396
Operation of a chromium doped titania maser. H. J. Gerritsen and H. R. Lewis—608(L)
Parametric amplification along nonlinear transmission lines. Rolf Landauer—479
Parametric amplifier theory for plasmas and electron beams. G. S. Kino—1449
Parametric diode figure of merit and optimization. K. E. Mortenson—1207
Preparation of large calcium-tungstate crystals containing paramagnetic ions for maser applications. K. Nassau and L. G. Van Uitert—1508(L)
Proposed molecular amplifier and coherent generator for millimeter and submillimeter waves. Walter Gordy and Monroe Cowan—941(L)
Pulsed field millimeter wave maser. L. R. Momo, R. A. Myers, and S. Foner—443(L)
Spontaneous emission from an inverted spin system. Amnon Yariv—740(L)
Submillimeter wave maser. Saul M. Bergmann—275
Theory of fast-wave parametric amplification. Curtis C. Johnson—338
Time discrimination in solid-state infrared quantum counters. J. V. Jelley—1145

Mass Spectrometry

Charged-particle orbits in varying magnetic fields. E. I. Gordon—1187
Use of the omegatron in the determination of parameters affecting limiting pressures in vacuum devices. David Lichtman—1213

Mathematics

Alternative forms of some exponential and power functions for graphical representation. C. C. Harris—215(L)
Alternative forms of some exponential and power functions for graphical representation. C. C. Harris—942(E)
Aperture fields in the diffraction by a slit. Hwei-Piao Hsu—1842
Bounds on low energy scattering parameters. Larry Spruch and Leonard Rosenberg—2104
Conservation laws of uniform linear homogeneous systems. M. C. Pease—1988
Diffraction by a slit. Robert Plonsey and Hwei-Piao Hsu—445(E)
Monte Carlo calculation of molecular flow rates through a cylindrical elbow and pipes of other shapes. D. H. Davis—1169
Monte Carlo calculations of the motions of electrons in helium. T. Itoh and T. Musha—744(L)
Optical studies of the diffraction of water waves by circular and thin elliptic cylinders. Richard Barakat and Robert Barakat—474
Phase oscillations in high current synchrotrons. Irvin G. Henry—1338
Resistance to potential flow through a cubical array of spheres. Robert E. Meredith and Charles W. Tobias—1270
Scattering by nonspherical particles. J. Mayo Greenberg—82
Scattering of a plane transverse wave by a spherical obstacle in an elastic medium. Norman G. Einspruch, E. J. Witterholt, and Rohn Truell—806
Scattering of electromagnetic waves from the infinitely long magnetized cylindrical plasma. P. M. Platzman and H. T. Ozaki—1597
Surface wave excitation and propagation. Joseph B. Keller and Frank C. Karal, Jr.—1039
Three-dimensional space charge flow. Jorge Rosenblatt—1371

Metallurgy, General

Alloying behavior of thin bimetal films, simultaneously or successively deposited. Richard B. Belser—562
Behavior of individual dislocations in strain-hardened LiF crystals. J. J. Gilman and W. G. Johnston—687
Bounds on the nonlinear diffusion controlled growth rate of spherical precipitates. J. A. Morrison and H. L. Frisch—1621
Bulk densities of separated copper isotopes. D. D. Snyder—440(L)
Cleavage whiskers. John D. Venables—1503(L)
Creep of Al_2O_3 single crystals. Roger Chang—484
Direct observation of antiphase domain boundaries in the $AuCu_3$ superlattice. M. J. Marcinkowski and R. M. Fisher—1686(L)
Dislocation etch pits on p-type lead telluride. B. B. Houston and Marriner K. Norr—615(L)
Dislocation etch pits on the {111} and {$\bar{1}\bar{1}\bar{1}$} surfaces of InSb. Harry C. Gatos and Mary C. Lavine—743(L)
Dislocation multiplication in lithium fluoride crystals. W. G. Johnston and J. J. Gilman—632
Dislocation ribbons and stacking faults in graphite. P. Delavignette and S. Amelinckx—1691(L)
Dislocations in indented magnesium oxide crystals. A. S. Keh—1538
Ductility of NaCl crystals. Robert G. Greenler and William S. Rothwell—616(L)
Elastic constants of bismuth. Yakov Eckstein, A. W. Lawson, and Darrell H. Reneker—1534
Elastic constants of single-crystal aluminum antimonide. D. I. Bolef and M. Menes—1426
Electron microscopic study of thin films of the aluminum-copper eutectic prepared by a melting method. Noboru Takahashi—1287
Etch pits in gallium arsenide. J. L. Richards and A. J. Crocker—611(L)
Etch pits in pyrolytic graphite. Aram Tarpinian and George E. Gazza—1657
Evidence for dislocation reactions in copper. F. W. Young, Jr., and T. S. Noggle—604
Factors affecting the ductility and strength of NaCl single crystals tested in flexure. C. A. Stearns, A. E. Pack, and R. A. Lad—231
Flow of magnesium oxide single crystals. D. S. Thompson and J. P. Roberts—433(L)
Formation and initial growth of single-asperity solid-state bonds. F. C. Holden, J. B. Melehan, H. R. Ogden, and R. I. Jaffee—670
Generation of dislocations by an electric field in MgO. E. Mendel and S. Weinig—738(L)
Grain boundaries in germanium. Richard S. Wagner and Bruce Chalmers—581
Grain boundary and lattice diffusion in polycrystalline bodies. H. S. Levine and C. J. MacCallum—595
Growth from the melt. I. Influence of surface intersections in pure metals. G. F. Bolling and W. A. Tiller—1345
Growth of GaAs crystals in the (111) polar direction. P. L. Moody, H. C. Gatos, and M. C. Lavine—1696(L)
Heat treatment effects in indium arsenide. J. T. Edmond and C. Hilsum—1300(L)

Metallurgy, General *(continued)*
Heat treatment of gallium arsenide. J. T. Edmond—1428
Hot working of Alnico 5 alloys. C. L. Kolbe and D. L. Martin—84S
Improvements on the pedestal method of growing silicon and germanium crystals. W. C. Dash—736(L)
Irradiation effects and short-range order in fused silica and quartz. R. A. Weeks and C. M. Nelson—1555
Kinetics of sintering of sodium chloride in the presence of an inert gas. J. B. Moser and D. H. Whitmore—488
Low-temperature transport properties of commercial metals and alloys. II. Aluminums. Robert L. Powell, William J. Hall, and Hans M. Roder—496
Low-temperature transport properties of commercial metals and alloys. III. Gold-cobalt. Robert L. Powell, M. D. Bunch, and Edward F. Gibson—504
Low-temperature transport properties of commercial metals and alloys. IV. Reactor grade Be, Mo, and W. Robert L. Powell, James L. Harden, and Edward F. Gibson—1221
Manipulation of cesium. P. Leliak—609(L)
Metastable electron compound in Ag-Ge alloys. Pol Duwez, R. H. Willens, and W. Klement, Jr.—1137(L)
Metastable solid solutions in the gallium-antimonide-germanium pseudobinary system. Pol Duwez, R. H. Willens, and W. Klement, Jr.—1500(L)
On the behavior of thermal vacancies in pure aluminum. Doris Kuhlmann-Wilsdorf and H. G. F. Wilsdorf—516
On the kinetics and mechanism of the precipitation of lithium from germanium. J. R. Carter, Jr., and R. A. Swalin—1191
Ordering in the intermediate phases TiFe, TiCo, and TiNi. Paul Pietrokowsky and Frank G. Youngkin—1763
Orientation density and its use in quantitative texture studies. C. G. Dunn and J. L. Walter—827
Oxygen in nickel. L. H. Germer and C. D. Hartman—2085
Precipitation in silicon crystals containing aluminum. R. Bullough, R. C. Newman, J. Wakefield, and J. B. Willis—707
Precipitation of copper in gallium arsenide. J. M. Whelan and C. S. Fuller—1507(L)
Precision lattice parameter measurements of cold-worked metals. Robert Asimow—410
Prediction of fatigue life. A. M. Freudenthal—2196
Preparation of large area single-crystal cuprous oxide. Robert S. Toth, Rein Kilkson, and Dan Trivich—1117
Production and demonstration of atomically clean metal surfaces. H. D. Hagstrum and C. D'Amico—715
Propagation mechanism of germanium dendrites. D. R. Hamilton and R. G. Seidensticker—1165
Propagation of large amplitude waves in annealed aluminum. James F. Bell—277
Range of radiation induced primary knock-ons in the hard core approximation. D. K. Holmes and G. Leibfried—1046
Recovery of internal friction in aluminum after plastic deformation. Ivar Holwech—928
Regelation, surface diffusion, and ice sintering. W. D. Kingery—833
Solution-precipitation deformation under an applied stress. W. D. Kingery and M. P. Lepie—610(L)
Surface deformation of aluminum in fatigue. J. C. Grosskreutz and C. M. Gosselin—1127(L)
Tensile properties of thin, evaporated gold films. C. A. Neugebauer—1096
Tensile strength of pyrolytic graphite up to 2750°C. H. E. Martens and L. D. Jaffe—1122(L)
Torsion induced recrystallization of molybdenum and tungsten filaments. F. E. Gifford and E. A. Coomes—235
Velocity behavior of a growing crack. E. N. Dulaney and W. F. Brace—2233
X-ray examination of brittle fractures in extruded chromium. C. W. Weaver and K. A. Gross—626
X-ray reflection studies of the anneal and oxidation of some thin solid films. N. Wainfan and L. G. Parratt—1331

Noise
Current noise due to ohmic contacts on cadmium sulfide. James J. Brophy and Robert J. Robinson—1343
Intervalley noise. P. J. Price—949
Microwave noise from low-pressure arcs. R. M. Hill and S. K. Ichiki—735(L)
Noise and signal response in lead sulfide photoconductive films. H. E. Spencer—505
Noise temperature measurement on a traveling-wave maser preamplifier. R. W. DeGrasse and H. E. D. Scovil—443(L)
On the nonconservation of noise parameters in multivelocity beams. J. Berghammer and S. Bloom—454
Partition noise in electron beams at microwave frequencies. A. Ashkin and L. D. White—1351
Theory of a negative-resistance transmission line amplifier with distributed noise generators. K. K. N. Chang—871
Transport of noise at microwave frequencies through a space-charge-limited diode. W. E. Vivian—957

Nuclear Physics
Backscattering of carbon-14 beta radiation. George L. Gaines, Jr.—741(L)
Bounds on low energy scattering parameters. Larry Spruch and Leonard Rosenberg—2104
Effect of fast neutron bombardment at various temperatures upon the Young's modulus and internal friction of copper. D. O. Thompson and V. K. Paré—528
Effect of nuclear polarization on the behavior of solid state masers. G. Makhov, L. G. Cross, R. W. Terhune, and J. Lambe—936(L)
Magnetic viscosity due to solute atom pairs. I. Theory of the effect. G. Biorci, A. Ferro, and G. Montalenti—2121
Nuclear resonance in ferromagnetic cobalt. A. M. Portis and A. C. Gossard—205S
Theoretical and experimental study of the back-scattering cross section of an infinite ribbon. Michael S. Macrakis—2261

Optical Properties
Correlation between certain extinction bands of solids and plasma resonance. B. R. Gossick—650
Depolarized components of light scattered by glasses. II. Influence of nonannealable strains on the scattering. Martin Goldstein—1697(E)
Optical absorption by free carriers in a semiconductor containing a dispersed colloidal phase. B. R. Gossick—648
Optical constants of germanium in the region 0–10 ev. M. P. Rimmer and D. L. Dexter—775
Optical observations concerning the polymorphic transition in the potassium halides. S. Wiederhorn and H. G. Drickamer—1666
Optical studies of the diffraction of water waves by circular and thin elliptic cylinders. Richard Barakat and Robert Barakat—474
Print-out process in photographic emulsion grains. J. F. Hamilton and L. E. Brady—609(L)

Small angle scattering investigation of Ludox mixtures. Robert H. Bragg, Irene Corvin, and John W. Buttrey —1183

Phase Transformations

Broadband reciprocal ferrite phase shifters. T. D. Geiszler and R. A. Henschke—1745

Influence of crystallographic orientation on the charge formation during phase changes in solids. S. Mascarenhas and L. G. Freitas—1684

New complex phase in the copper-gold system. R. E. Scott—2112

Ordering in the intermediate phases TiFe, TiCo, and TiNi. Paul Pietrokowsky and Frank G. Youngkin—1763

Plasma Physics

Absorption and reflection spectrum of a plasma. W. D. Hershberger—417

Alkali vapor plasmas. M. A. Hakeem and Harry S. Robertson—2063(L)

Asymmetrical triple probe method for determining energy distribution of electron in plasma. Takayoshi Okuda and Kenzo Yamamoto—158

Circuit dynamics of the pinch. J. Killeen and B. A. Lippmann—1549

Comments on article by Cook. M. H. Miller—607(L)

Correlation between certain extinction bands of solids and plasma resonance. B. R. Gossick—650

Determination of streaming velocity and the flow of heat and mass in high-current arcs. T. B. Reed—2047

Effect of gas pressure and cone angle on the velocities of electrically excited shock waves. Philip J. Hart—436(L)

Efficiency of the plasma thermocouple. H. W. Lewis and J. R. Reitz—723

Experimental investigation of a high-energy density, high-pressure arc plasma. Edward A. Martin—255

Experimental investigations of the cesium plasma cell. W. A. Ranken, G. M. Grover, and E. W. Salmi—2140

Forces on ion-bombarded electrodes in a low pressure plasma. G. K. Wehner—1392

Microwave determination of plasma density profiles. Charles B. Wharton and Donald M. Slager—428

Negative glow plasma as a cathode for electron tubes. J. M. Anderson and L. A. Harris—1463

Numerical calculation of absolute bremsstrahlung intensity for a fully ionized dissociated hydrogenic gas. G. Sargent Janes and H. Koritz—525

Parametric amplifier theory for plasmas and electron beams. G. S. Kino—1449

Plasma propulsion by a rapidly varying magnetic field. Milton M. Klein and Keith A. Brueckner—1437

Production of very high magnetic fields by implosion. C. M. Fowler, W. B. Garn, and R. S. Caird—588

Scattering of electromagnetic waves from an infinitely long magnetized cylindrical plasma. P. M. Platzman and H. T. Ozaki—1597

Scattering of radiation by a plasma. Forrest I. Boley—1692(L)

Surface deformation of aluminum in fatigue. J. C. Grosskreutz and C. M. Gosselin—1127(L)

Ultra-high-speed photographs refuting "cohesion in plasma." W. C. Davis and A. W. Campbell—1225

Plastic Deformation

Creep of Al_2O_3 single crystals. Roger Chang—484

Dislocation arrays in depth and recrystallization produced by surface deformation of single crystals of copper at high temperature. John M. Bailey and Allan T. Gwathmey—215(L)

Dislocation structure and the formation and strength of sodium chloride whiskers. W. W. Webb—194

Dislocations in indented magnesium oxide crystals. A. S. Keh—1538

Ductility of NaCl crystals. Robert G. Greenler and William S. Rothwell—616(L)

Effect of aging time after cleavage on the plasticity of MgO single crystals. Carl A. Stearns—2317(L)

Factors affecting the ductility and strength of NaCl single crystals tested in flexure. C. A. Stearns, A. E. Pack, and R. A. Lad—231

Flow of magnesium oxide single crystals. D. S. Thompson and J. P. Roberts—433(L)

On the strength of glass in water vapor. F. R. L. Schoening—1779

Radiation limited dislocation motion in crystals. Robb Thomson—617(L)

Recovery of internal friction in aluminum after plastic deformation. Ivar Holwech—928

Regelation, surface diffusion, and ice sintering. W. D. Kingery—833

Reviving the classical theory of friction by a modern dislocation theory of deformation revision. John H. Dismant—221(L)

Reviving the classical theory of friction by a modern dislocation theory of deformation revision. John H. Dismant—942(E)

Solution-precipitation deformation under an applied stress. W. D. Kingery and M. P. Lepie—610(L)

Tensile strength of pyrolytic graphite up to 2750°C. H. E. Martens and L. D. Jaffe—1122(L)

Polymers

Chain folding and free energy density in polymer crystals. Anton Peterlin—1934

Defects in polyethylene crystals. W. P. Slichter—1865

Determination of the anisotropy of bond-polarizability of liquids using flow-birefringence measurements. W. Philippoff—1899

Effect of orientation on strength of a model solid. A. Robinson, J. E. Osborn, and C. C. Hsiao—1602

Effect of pressure on the dynamic shear behavior of polyisobutylene. A. W. Nolle—1694(L)

Effect of reactor irradiation on the tensile strength of uniaxially oriented polyethylene terephthalate. C. C. Hsiao and S. T. Chow—1869

Effect of temperature and reactor irradiation on the strength of biaxially oriented polyethylene terephthalate. A. Haynes and C. C. Hsiao—1871

Experimental study of thermal diffusion in dilute solutions of high polymers. Frank C. Whitmore—1858

Flow of polyethylene into a capillary. E. B. Bagley and A. M. Birks—556

Formation of thin polymer films by electron bombardment. Robert W. Christy—1680

Gamma-ray induced conductivity in polyethylene coaxial cable. Kichinosuke Yahagi and Akibumi Danno—734(L)

Hollow pyramidal crystals of polyethylene and a mechanism of growth. Walter D. Niegisch and Paul R. Swan —1906

Hooke's law in shear and polymer melt fracture. E. B. Bagley—1126(L)

Kinetic theory of thermal diffusion in dilute polymer solutions. Joe S. Ham—1853

Lattice displacements by fast electrons. W. Dale Compton and George W. Arnold—621

Longitudinal wave propagation in stretched polymers. Peter Mason—1706

Low angle x-ray diffraction of fibrous polyethylene. A. S. Posner, L. Mandelkern, C. R. Worthington, and A. F. Diorio—536

Measurement of orientation in polypropylene film. Zigmond W. Wilchinsky—1969

Polymers (*continued*)
Morphology of polymer single crystals. D. H. Reneker and P. H. Geil—1916
NMR absorption in teflon fibers. D. Hyndman and G. F. Origlio—1849
Photoelastic properties of polystyrene in the glassy state. III. Styrene derivatives and copolymers. J. F. Rudd and R. D. Andrews—818
Photographic light scattering by polyethylene films. Richard S. Stein and Marion B. Rhodes—1873
Rolling friction of polymeric materials. I. Elastomers. Donald G. Flom—306
Simple radiant heating method for determining the thermal diffusivity of cellulosic materials. Stanley B. Martin —1101
Solubilities and diffusivities of nitrogen in polyethylene. J. L. Lundberg, M. B. Wilk, and M. J. Huyett—1131(L)
Stress as a reduced variable: Stress relaxation of SBR rubber at large strains. Robert F. Landel and Paul J. Stedry—1885
Theoretical calculation of the birefringence of polypropylene crystals. D. A. Keedy, J. Powers, and R. S. Stein—1911
Time and temperature dependence of the ultimate properties of an SBR rubber at constant elongations. Thor L. Smith and Paul J. Stedry—1892
Wave functions and energy eigenvalues for the polytetrafluoroethylene chain. Yoh-Han Pao and R. F. Bjorklund—1925

Radiation Effects
Backscattering of carbon-14 beta radiation. George L. Gaines, Jr.—741(L)
Beta particle transmission currents in solid dielectrics. Bernhard Gross, Arthur Bradley, and Arthur P. Pinkerton—1035
Characteristic energy losses of electrons in carbon. Lewis B. Leder and J. A. Suddeth—1422
Defects in dislocations produced by focusing collisions in fcc lattices. G. Leibfried—117
Determination of dose rates from beta transmission currents. Arthur Bradley—1826(L)
Diffusion of deuterium in deuteron-irradiated copper. Mark T. Robinson, A. L. Southern, and William R. Willis—1474
Displacement of the sulfur atom in CdS by electron bombardment. B. A. Kulp and R. H. Kelley—1057
Drift mobility in neutron irradiated *n*-type germanium. W. H. Closser—1693(L)
Effect of applying a magnetic field during neutron irradiation on the magnetic properties of Fe-Ni alloys. A. I. Schindler and E. I. Salkovitz—245S
Effect of electron irradiation and subsequent thermal treatment on Young's modulus of copper. A. Sosin and L. L. Bienvenue—249
Effect of fast neutron bombardment at various temperatures upon the Young's modulus and internal friction of copper. D. O. Thompson and V. K. Paré—528
Effects of irradiation on the thermal conductivity of synthetic sapphire. R. Berman, E. L. Foster, B. Schneidmesser, and S. M. A. Tirmizi—2156
Electron damage in mica. T. J. Seed—1300(L)
Forces on ion-bombarded electrodes in a low pressure plasma. G. K. Wehner—1392
Formation of thin polymer films by electron bombardment. Robert W. Christy—1680
Gamma irradiation of silicon. I. Levels in *n*-type material containing oxygen. E. Sonder and L. C. Templeton—1279
Gamma-ray induced conductivity in polyethylene coaxial cable. Kichinosuke Yahagi and Akibumi Danno—734(L)
Heating in liquid helium resulting from neutron and gamma bombardment by a fission source. M. G. Chasanov—733(L)
High-energy sputtering. O. C. Yonts, C. E. Normand, and Don E. Harrison—447
Influence of irradiation with β rays on the electrification of KCl crystals. Anna Szaynok—451
Ion-bombardment etching of synthetic fibers. Franklin R. Anderson and V. F. Holland—1516
Irradiation effects and short-range order in fused silica and quartz. R. A. Weeks and C. M. Nelson—1555
Large temperature range annealing. William Primak—1524
Mechanism for the production of F centers in NaCl by irradiation with gamma rays. J. H. Crawford, Jr., and F. W. Young, Jr.—1688(L)
Microscopic study of neutron-irradiated germanium. B. B. Meckel, E. G. K. Schwarz, and R. A. Swalin—1299(L)
Monoenergetic neutron irradiation of germanium. O. L. Curtis, Jr., and J. W. Cleland—423
On the neutron bombardment reduction of transistor current gain. J. W. Easley and J. A. Dooley—1024
On the temperature of an object irradiated with electrons. S. Yamaguchi—1825(L)
Photoeffects in nonuniformly irradiated p-n junctions. Gerald Lucovsky—1088
Radiation limited dislocation motion in crystals. Robb Thomson—617(L)
Range of radiation induced primary knock-ons in the hard core approximation. D. K. Holmes and G. Leibfried—1046
Specific ionization measurements and energy requirements for F-center formation. R. D. Jordan and R. S. Alger —747
Study of irradiation effects and the H^2+H^2 buildup in tantalum. A. F. Gabrysh, H. Eyring, M. E. Wadsworth, G. S. Baker, and T. Ree—1785
Transitory electrical properties of *n*-type germanium after a neutron pulse. H. J. Stein—1309

Rheology
Effect of pressure on the dynamic shear behavior of polyisobutylene. A. W. Nolle—1694(L)
Hooke's law in shear and polymer melt fracture. E. B. Bagley—1126(L)
Ion-bombardment etching of synthetic fibers. Franklin R. Anderson and V. F. Holland—1516
Photoelastic properties of polystyrene in the glassy state. III. Styrene derivatives and copolymers. J. F. Rudd and R. D. Andrews—818

Semiconductor Devices
Analog study of large-signal high-frequency diodes. C. L. Andrews—1431
Anomalous barrier capacitance in p-n junctions of InSb. C. A. Lee and G. Kaminsky—1717
Comments on "Diode capacitors for parametric amplification" by R. C. Knechtli and R. D. Weglein. K. E. Mortenson—1135(L)
Diode capacitors for parametric amplification. R. C. Knechtli and R. D. Weglein—1134(L)
Dipole mode of minority carrier diffusion with reference to point contact rectification. B. R. Gossick—29
Effect of temperature on photovoltaic solar energy conversion. Joseph J. Wysocki and Paul Rappaport—571
Fast neutron bombardment of germanium and silicon Esaki diodes. J. W. Easley and R. R. Blair—1772
Improvement of semiconductor surfaces by low melting glasses, possibly functioning as ion getters. S. S. Flaschen, A. David Pearson, and I. L. Kalnins—431(L)

Influence of transverse modes on photoconductive decay in filaments. J. S. Blakemore and K. C. Nomura—753
Ion drift in an *n-p* junction. E. M. Pell—291
Metal precipitates in silicon *p-n* junctions. A Goetzberger and W. Shockley—1821
Microwave measurement of semiconductor carrier lifetimes. H. A. Atwater—938(L)
Minority carrier recombination in a cylindrical transistor base region. David P. Kennedy—954
On the neutron bombardment reduction of transistor current gain. J. W. Easley and J. A. Dooley—1024
Oscillistor—New type of semiconductor oscillator. R. D. Larrabee and M. C. Steele—1519
Parametric diode figure of merit and optimization. K. E. Mortenson—1207
Photoeffects in nonuniformly irradiated *p-n* junctions. Gerald Lucovsky—1088
Photoemission in the photovoltaic effect in cadmium sulfide crystals. Richard Williams and Richard H. Bube—968
Photovoltaic effect derived from the Carnot cycle. A. Rose—1640
Spreading resistance in cylindrical semiconductor devices. David P. Kennedy—1490
Transistor with base containing a dispersed colloidal phase. B. R. Gossick—745(L)
Uniform avalanche effect in silicon three-layer diodes. A. Goetzberger—2260
Uniform silicon *p-n* junctions. I. Broad area breakdown. R. L. Batdorf, A. G. Chynoweth, G. C. Dacey, and P. W. Foy—1153
Uniform silicon *p-n* junctions. II. Ionization rates for electrons. A. G. Chynoweth—1161

Semiconductors

Anomalous Hall effect in $AgSbTe_2$. R. Wolfe, J. H. Wernick, and S. E. Haszko—1959
Anomalous surface channels on silicon *p-n* junctions. Raymond Solomon—1791
Behavior of InSb surfaces during heat treatment. D. Haneman—217(L)
Chlorine and iodine as impurities in InAs and GaP. G. R. Antell—1686(L)
Current noise due to ohmic contacts on cadmium sulfide. James J. Brophy and Robert J. Robinson—1343
Damaged layers and crystalline perfection in the {111} surfaces of *III-V* intermetallic compounds. E. P. Warekois, M. C. Lavine, and H. C. Gatos—1302(L)
Detection of growth striations in germanium crystals. Albert C. English—1498(L)
Device for measurement of the electrical properties of Bi_2Se_3 at elevated temperatures. Mac J. Smith, E. S. Kirk, and C. W. Spencer—1504(L)
Diffusion of boron into silicon. A. D. Kurtz and R. Yee —303
Diffusion of copper into AlSb. R. H. Wieber, H. C. Gorton, and C. S. Peet—608(L)
Dipole mode of minority carrier diffusion with reference to point contact rectification. B. R. Gossick—29
Dislocation etch pits on *p*-type lead telluride. B. B. Houston and Marriner K. Norr—615(L)
Dislocation etch pits on the {111} and $\{\overline{1}\overline{1}\overline{1}\}$ surfaces of InSb. Harry C. Gatos and Mary C. Lavine—743(L)
Dislocations in silicon carbide. S. Amelinckx, G. Strumane, and W. W. Webb—1359
Dislocations in two types of CdS crystals. D. C. Reynolds and S. J. Czyzak—94
Displacement of the sulfur atom in CdS by electron bombardment. B. A. Kulp and R. H. Kelley—1057
Drift mobility in neutron irradiated *n*-type germanium. W. H. Closser—1693(L)
Effect of Cu precipitation on dislocation etch pits in Ge. Howard Savage—1472
Effect of Li-B ion pairing on Li^+ ion drift in Si. E. M. Pell—1675
Effect of oxide layers on the diffusion of phosphorus into silicon. R. B. Allen, H. Bernstein, and A. D. Kurtz—334
Effect of the polarity of the *III-V* intermetallic compounds on etching. J. W. Faust, Jr., and A. Sagar—331
Esaki diode in InSb. R. L. Batdorf, G. C. Dacey, R. L. Wallace, and D. J. Walsh—613(L)
Etch pits in gallium arsenide. J. L. Richards and A. J. Crocker—611(L)
Field effect modulation of photoconductance in a quasi-intrinsic semiconductor. R. R. Bockemuehl—2255
Field induced photoemission and hot-electron emission from germanium. R. E. Simon and W. E. Spicer—1505(L)
Filled and empty dangling bonds in *III-V* compounds. D. B. Holt—2231
Formation of cesium antimonide. I. Electrical resistivity of the film of cesium-antimony system. Kiyoshi Miyake —76
Gamma irradiation of silicon. I. Levels in *n*-type material containing oxygen. E. Sonder and L. C. Templeton—1279
Germanium crystals grown from hollow cylindrical seeds. R. C. Frank and J. E. Thomas, Jr.—1689(L)
Growth of atomically flat surfaces on germanium dendrites. R. L. Longini, A. I. Bennett, and W. J. Smith —1204
Growth of GaAs crystals in the ⟨111⟩ polar direction. P. L. Moody, H. C. Gatos, and M. C. Lavine—1696(L)
Growth of gallium arsenide by horizontal zone melting. J. L. Richards—600
Growth of InSb crystals in the ⟨111⟩ polar direction. H. C. Gatos, P. L. Moody, and M. C. Lavine—212(L)
Hall field relaxation in semiconductors at high frequency. Keith S. Champlin—1770
Heat treatment effects in indium arsenide. J. T. Edmond and C. Hilsum—1300(L)
Heat treatment of gallium arsenide. J. T. Edmond—1428
High-temperature Hall coefficient in GaAs. L. W. Aukerman and R. K. Willardson—939(L)
Impurity effects upon mobility in silicon. R. A. Logan and A. J. Peters—122
Influence of arsenic pressure on the doping of gallium arsenide with germanium. J. O. McCaldin and Roy Harada—2065(L)
Interaction between arsenic and aluminum in germanium. J. O. McCaldin—89
Intervalley noise. P. J. Price—949
Ion-bombardment etching of silicon and germanium. I. A. Dillon, Jr., and R. M. Coman—26
Ion drift in an *n-p* junction. E. M. Pell—291
Metastable solid solutions in the gallium antimonide-germanium pseudobinary system. Pol Duwez, R. H. Willens, and W. Klement, Jr.—1500(L)
Microscopic study of neutron-irradiated germanium. B. B. Meckel, E. G. K. Schwarz, and R. A. Swalin—1299(L)
Microwave measurement of semiconductor carrier lifetimes. H. A. Atwater—938(L)
Minority carrier current in a linearly graded drift field. David P. Kennedy—218(L)
Monoenergetic neutron irradiation of germanium. O. L. Curtis, Jr., and J. W. Cleland—423
On the kinetics and mechanism of the precipitation of lithium from germanium. J. R. Carter, Jr., and R. A. Swalin—1191
On the observation of macroscopic spirals on gallium arsenide surfaces. Warren J. Little and Kathryn A. McCarthy—1298(L)

Semiconductors (*continued*)
Optical absorption by free carriers in a semiconductor containing a dispersed colloidal phase. B. R. Gossick—648
Optical constants of germanium in the region 0–10 ev. M. P. Rimmer and D. L. Dexter—775
Orientation-dependent dissolution of germanium. F. C. Frank and M. B. Ives—1996
Origin of the "first-order structure" of CP4-etched Ge surfaces. G. Bonfiglioli, A. Ferro, and A. Mojoni—684
Oscillations in germanium with an applied pulsed electric field. M. Cardona and W. Ruppel—1826(L)
Photoelectronic analysis of high resistivity crystals: (a) GaAs, (b) Sb_2S_3. Richard H. Bube—315
Piezoresistive effect in *p*-type PbTe. Lewis E. Hollander and T. J. Diesel—692
p layers on vacuum heated silicon. F. G. Allen, T. M. Buch, and J. T. Law—979
Precipitation in silicon crystals containing aluminum. R. Bullough, R. C. Newman, J. Wakefield, and J. B. Willis—707
Precipitation of copper in gallium arsenide. J. M. Whelan and C. S. Fuller—1507(L)
Propagation mechanism of germanium dendrites. D. R. Hamilton and R. G. Seidensticker—1165
Properties of *p*-type GaAs prepared by copper diffusion. F. D. Rosi, D. Meyerhofer, and R. V. Jensen—1105
Reciprocity law failure in ZnO and Se. Joze Kostelec—441(L)
Several new methods to measure the thermal diffusivity of semiconductors. J. H. Becker—612(L)
Some electrical properties of amorphous selenium films. Richard A. Fotland—1558
Some properties of zinc sulfide crystals grown from the melt. Arrigo Addamiano and Manuel Aven—36
Statistics of the occupation of dislocation acceptors (one-dimensional interaction statistics). R. M. Broudy and J. W. McClure—1511
Structural study of the compound $AgSbTe_2$. R. W. Armstrong, J. W. Faust, Jr., and W. A. Tiller—1954
Surface space-charge calculations for semiconductors. D. R. Frankl—1752
Temperature dependence of Young's modulus of vitreous germania and silica. S. Spinner and G. W. Cleek—1407
Thermal conversion in *n*-type GaAs. Joseph J. Wysocki—1686(L)
Thermal expansion coefficients of bismuth. E. F. Cave and L. V. Holroyd—1357
Thermal expansion of silicon. Leon Maissel—211(L)
Transitory electrical properties of *n*-type germanium after a neutron pulse. H. J. Stein—1309
Uniform silicon *p-n* junctions. II. Ionization rates for electrons. A. G. Chynoweth—1161
Vapor-deposited single-crystal germanium. Ralph P. Ruth, John C. Marinace, and W. C. Dunlap, Jr.—995

Shock Waves
Attenuation of the shock wave produced in a solid by a flying plate. G. R. Fowles—655
Cratering and shock wave phenomena in steel plates at high impact speeds. Earle B. Mayfield and James W. Rogers—472
Effect of gas pressure and cone angle on the velocities of electrically excited shock waves. Philip J. Hart—436(L)
Equation of state for nineteen metallic elements from shock-wave measurements to two megabars. R. G. McQueen and S. P. Marsh—1253
Ultra-high-speed photographs refuting "cohesion in plasma." W. C. Davis and A. W. Campbell—1225

Space Charge
Contribution of anode emission to space charge in thermionic power converters. Anthony F. Dugan—1397
Influence of negative ions on ambipolar diffusion of electrons. Hendrik J. Oskam and Verlyn R. Mittlestadt—940(L)
Solutions of the equations of space charge flow for radial flow between concentric spherical electrodes. I. Itzkar—652
Three-dimensional space charge flow. Jorge Rosenblatt—1371
Transport of noise at microwave frequencies through a space-charge-limited diode. W. E. Vivian—957

Space Physics
Acoustic resonance in solid propellant rockets. F. T. McClure, R. W. Hart, and J. F. Bird—884
Experimental investigation in lead of the Whipple "meteor bumper." A. E. Olshaker—2118

Spectra and Spectroscopy
Crystallographic aspects of extra reflections in x-ray spectrochemical analysis. N. Spielberg and J. Ladell—1660
Spectral emissivity, total emissivity, and thermal conductivity of molybdenum, tantalum, and tungsten above 2300°K. Robert D. Allen, Louis F. Glasier, Jr., and Paul L. Jordan—1382
Transport equation for the spectral density of a multiple-scattered electromagnetic field. Dimitri S. Bugnolo—1176

Surface Properties
Angular distribution of sputtered material. G. K. Wehner and D. Rosenberg—177
Atom ejection patterns in single crystal sputtering. G. S. Anderson and G. K. Wehner—2305
Behavior of InSb surfaces during heat treatment. D. Haneman—217(L)
Cratering and shock wave phenomena in steel plates at high impact speeds. Earle B. Mayfield and James W. Rogers—472
Determination of surface structure using ultra-high vacuum replication. L. Bachmann, W. H. Orr, T. N. Rhodin, and B. M. Siegel—1458
Direct measurements of the surface energies of crystals. J. J. Gilman—2208
Effect of oxide layers on the diffusion of phosphorus into silicon. R. B. Allen, H. Bernstein, and A. D. Kurtz—334
Effect of the polarity of the *III-V* intermetallic compounds on etching. J. W. Faust, Jr., and A. Sagar—331
Etching of surfaces with 8-kev argon ions. R. L. Cunningham, P. Haymann, C. Lecomte, W. J. Moore, and J. J. Trillat—839
Growth from the melt. I. Influence of surface intersections in pure metal. G. F. Bolling and W. A. Tiller—1345
Growth of atomically flat surfaces on germanium dendrites. R. L. Longini, A. I. Bennett, and W. J. Smith—1204
High-energy sputtering. O. C. Yonts, C. E. Normand, and Don E. Harrison, Jr.—447
Ion-bombardment etching of silicon and germanium. I. A. Dillon, Jr., and R. M. Oman—26
Ion-bombardment etching of synthetic fibers. Franklin R. Anderson and V. F. Holland—1516
On a complex recrystallization texture in 3% silicon iron. C. G. Dunn and C. J. McHargue—1767
On the yield and energy distribution of secondary positive ions from metal surfaces. Henry E. Stanton—678
Origin of the "first-order structure" of CP4-etched Ge surfaces. G. Bonfiglioli, A. Ferro, and A. Mojoni—684
Positive column formation in ion sources employing surface ionization. P. L. Auer and H. Hurwitz—1007

Production and demonstration of atomically clean metal surfaces. H. D. Hagstrum and C. D'Amico—715
Reflection of sound from randomly rough surfaces. J. M. Proud, Jr., R. T. Beyer, and Paul Tamarkin—543
Shapes of etch hillocks and pits and their correlation with measured etch rates. B. A. Irving—109
Simple theory concerning the reflection of electrons from solids. T. E. Everhart—1483
Spiral dislocations on glass fracture surfaces. W. C. Levengood and T. S. Vong—1416
Surface cleaning by cathode sputtering. O. C. Yonts and Don E. Harrison, Jr.—1583
Surface deformation of aluminum in fatigue. J. C. Grosskreutz and C. M. Gosselin—1127(L)
Thermal emission of alkali ion pulses from clean and oxygenated tungsten. Robert E. Minturn, Sheldon Datz, and Ellison H. Taylor—876

Thermal Conductivity and Thermal Properties
Device for measurement of the electrical properties of Bi_2Se_3 at elevated temperatures. Mac J. Smith, E. S. Kirk, and C. W. Spencer—1504(L)
Excitation processes in ceramics and anomalous increase in thermal conductivity at elevated temperatures. D. H. Whitmore—1109
Generation of phonons in high-power ferromagnetic resonance experiments. Ernst Schlömann—1647
Heat treatment of gallium arsenide. J. T. Edmond—1428
High-temperature Hall coefficient in GaAs. L. W. Aukerman and R. K. Willardson—939(L)
Low-temperature transport properties of commercial metals and alloys. II. Aluminums. Robert L. Powell, William J. Hall, and Hans M. Roder—496
Low-temperature transport properties of commercial metals and alloys. III. Gold-cobalt. Robert L. Powell, M. D. Bunch, and Edward F. Gibson—504
Low-temperature transport properties of commercial metals and alloys. IV. Reactor grade Be, Mo, and W. Robert L. Powell, James L. Harden, and Edward F. Gibson—1221
Measurement of thermal conductivity by utilization of the Peltier effect. III. Correction for wire radiation and determination of specimen radiation emissivity. R. Simon, R. T. Bate, and E. H. Lougher—2160
Method for determining the thermal conductivity of incandescent solids. B. B. Brenden and H. W. Newkirk—737(L)
Necessary factor for heat treatment of the permalloys in a magnetic field. E. A. Nesbitt, R. D. Heidenreich, and A. J. Williams—228S
Performance of a thermoelectric converter under constant heat flux operation. P. S. Castro and W. W. Happ—1314
Several new methods to measure the thermal diffusivity of semiconductors. J. H. Becker—612(L)
Simple radiant heating method for determining the thermal diffusivity of cellulosic materials. Stanley B. Martin—1101
Specific heat of high purity iron by a pulse heating method. D. C. Wallace, P. H. Sidles, and G. C. Danielson—168
Spectral emissivity, total emissivity, and thermal conductivity of molybdenum, tantalum and tungsten above 2300°K. Robert D. Allen, Louis F. Glasier, Jr., and Paul L. Jordan—1382
Study of heat treatments for low coercive force 14-17% aluminum iron alloys. D. Pavlovic and K. Foster—231S
Temperature dependence of anisotropy and saturation magnetization in iron and iron-silicon alloys. C. D. Graham—150S
Temperature dependence of the saturation magnetization of nickel films of thickness less than 100 A. C. A. Neugebauer—152S
Thermal conductivity of eight halide crystals in the temperature range 220°K to 390°K. Kathryn A. McCarthy and Stanley S. Ballard—1410
Thermal expansion coefficients of bismuth. E. F. Cave and L. V. Holroyd—1357
Thermal expansion of silicon. Leon Maissel—211(L)
Thermal stress analysis and Grueneisen's relation. A. M. Freudenthal—434(L)

Thermodynamic Properties
Apparatus for the measurement of thermal diffusivity of solids at high temperatures. B. Abeles, G. D. Cody, and D. S. Beers—1585
Energy distribution and cooling effect of electrons emitted from an arc cathode. T. H. Lee—924
Equation of state for nineteen metallic elements from shock-wave measurements to two megabars. R. G. McQueen and S. P. Marsh—1253
Optical observations concerning the polymorphic transition in the potassium halides. S. Wiederhorn and H. G. Drickamer—1666
Photovoltaic effect derived from the Carnot cycle. A. Rose—1640
Temperature dependence of the velocity of sidewise 180° domain-wall motion in $BaTiO_3$. A. Savage and R. C. Miller—1546
Thermal conversion in *n*-type GaAs. Joseph J. Wysocki—1686(L)

Thermoelectricity
Calculation of efficiency of thermoelectric devices. B. Sherman, R. R. Heikes, and R. W. Ure, Jr.—1
Continuous series of metastable solid solutions in silver-copper alloys. Pol Duwez, R. H. Willens, and W. Klement, Jr.—1136(L)
Diagrams representing states of operation of a general thermocouple. A. H. Boerdijk—1141
Experimental test of the first Kelvin relation. F. J. Donahoe and L. R. Testardi—1304(L)
Peltier coefficient at a solid-liquid interface. J. R. O'Connor—1690(L)

Thin Films
Alloying behavior of thin bimetal films, simultaneously or successively deposited. Richard B. Belser—562
Anisotropy and inversion in permalloy films. D. O. Smith, E. E. Huber, Jr., M. S. Cohen, and G. P. Weiss—295S
Annular uniaxially magnetized domains in thin Ni-Fe films. O. William Muckenhirn, A. E. LeBonte, and P. J. Besser—304S
Comments on a ruptured soap film. F. E. C. Culick—1128(L)
Cross-tie walls in thin films. Harvey Rubinstein and Robert J. Spain—306S
Damage in UO_2 films and particles during reactor irradiation. T. K. Bierlein and B. Mastel—2314(L)
Determination of magnetization distribution in thin films using electron microscopy. Harrison W. Fuller and Murray E. Hale—238
Domain wall velocities in thin iron-nickel films. N. C. Ford, Jr.—300S
Domain walls in thin magnetic Ni-Fe films. S. Methfessel, S. Middlehoek, and H. Thomas—302S
Electron microscopic study of thin films of the aluminum-copper eutectic prepared by a melting method. Noboru Takahashi—1287
Electron probe measurements of evaporated metal films. W. E. Sweeney, Jr., R. E. Seebold, and L. S. Birks—1061
External fields from domain walls of cobalt film. B. Kostyshyn, J. E. Brophy, I. Oi, and D. D. Roshon, Jr.—772

Thin Films (*continued*)
Ferrite films—new logic and storage devices. J. M. Brownlow, W. L. Shevel, Jr., and O. A. Gutwin—121S
Film stripping technique for making thin silica windows. E. Tannenbaum—940(L)
Fission fragment damage in nonfissionable thin films. T. K. Bierlein and B. Mastel—2315(L)
Flux reversal by noncoherent rotation in magnetic films. K. J. Harte—283S
Formation of thin polymer films by electron bombardment. Robert W. Christy—1680
Influence of nearby conductors on thin film switching. J. S. Eggenberger—287S
Initial susceptibility spectra of permalloy films. R. F. Soohoo—218S
Investigations into the origin of anisotropy in oblique-incidence films. M. S. Cohen, E. E. Huber, Jr., G. P. Weiss, and D. W. Smith—291S
Magnetic anisotropy in evaporated iron films. E. W. Pugh, J. Matisoo, D. E. Speliotis, and E. L. Boyd—293S
Magnetization reversal in uniaxial films near to the preferred direction. E. M. Bradley and M. Prutton—285S
Mechanical properties of thin single-crystal gold film. Avery Catlin and Walter P. Walker—2135
Microcalorimetric technique for the study of damping and hysteresis in ferromagnetic films. J. R. Mayfield—298S
Millimicrosecond magnetization reversal in thin magnetic films. W. Dietrich and W. E. Proebster—281S
More experiments on liquid films. R. M. Koros, J. Deckers, and M. Boudart—1129(L)
Noise and signal response in lead sulfide photoconductive films. H. E. Spencer—505
Nucleation experiments on thin magnetic MnBi films. Ludwig Mayer—384S
Oblique-incidence anisotropy in evaporated permalloy films. D. O. Smith, M. S. Cohen, and G. P. Weiss—1755
Observation of Néel walls in thin films. Harvey Rubinstein, Harrison W. Fuller, and Murray E. Hale—437(L)
Observations on MnBi films during heat treatment. Ludwig Mayer—346
Operation of magnetic film parametrons in the 100 to 500 Mc region. A. V. Pohm, A. A. Read, R. M. Stewart, and R. F. Schauer—119S
Polyhedral holes in evaporated AuCu films. Victor A. Phillips—697
Preferred orientation and ordering in evaporated films of Fe. Ni, and Fe-Ni. R. F. Adamsky—289S
Production and properties of thin layers of indium antimonide. G. Bate and K. N. R. Taylor—991
Production of single-crystal copper films at low temperatures. Arthur Yelon and R. W. Hoffman—1672
Some electrical properties of amorphous selenium films. Richard A. Fotland—1558
Some physical properties of thin magnetic films. A. C. Moore and A. S. Young—279S
"Spontaneous magnetic anisotropy" in polycrystalline thin films. W. Andrä, Z. Málek, W. Schüppel, and O. Stemme—422(L)
Static and dynamic studies of magnetization distribution in thin films by electron microscopy. Harrison W. Fuller and Murray E. Hale—308S
Temperature dependence of the saturation magnetization of nickel films of thickness less than 100 A. C. A. Neugebauer—152S
Tensile properties of thin, evaporated gold films. C. A. Neugebauer—1096
Transfer function and error probability of a digital magnetic tape recording system. John Wenchung Hung—396S
X-ray reflection studies of the anneal and oxidation of some thin solid films. N. Wainfan and L. G. Parratt—1331

Vacuum Technique
Determination of surface structure using ultra-high vacuum replication. L. Bachmann, W. H. Orr, T. N. Rhodin, and B. M. Siegel—1458
Development of facets, spirals, and etch pits on copper crystals by heating to high temperatures in high vacua. F. W. Young, Jr., and A. T. Gwathmey—225
Diffusion coefficients, solubilities, and permeabilities for He, Ne, H_2, and N_2 in Vycor glass. C. C. Leiby, Jr., and C. L. Chen—268
Flat panel vacuum thermal insulation. H. M. Strong, F. P. Bundy, and H. P. Bovenkerk—39
Interaction of atomic hydrogen with glass. T. W. Hickmott—128
Outgassing caused by electron bombardment of glass. B. Johnson Todd, Jack L. Lineweaver, and John T. Kerr—51
Penetration depth investigation of gas cleanup with radioactive tracers. C. Y. Bartholomew and A. R. LaPadula—445(L)
Use of the omegatron in the determination of parameters affecting limiting pressures in vacuum devices. David Lichtman—1213

Viscosity and Viscoelasticity
Effect of viscosity on the splash caused by a drop of water falling into a mixture of glycerol and water. A. G. Davis Philip—727
Ultrasonic viscoelastic properties of associated liquids. R. Meister, C. J. Marhoeffer, R. Sciamanda, L. Cotter, and T. Litovitz—854

X-Rays and Neutron Diffraction
Analysis of composite x-ray diffraction profiles. J. J. Slade, Jr., and L. F. Nanni—699
Comments on "Determination of atomic scattering factors." D. R. Chipman and Arthur Paskin—1130(L)
Crystallographic aspects of extra reflections in x-ray spectrochemical analysis. N. Spielberg and J. Ladell—1660
Influence of x-rays on the electrification of NaCl crystals. Anna Szaynok—211(L)
Low angle x-ray diffraction of fibrous polyethylene. A. S. Posner, L. Mandelkern, C. R. Worthington, and A. F. Diorio—536
Low-temperature x-ray diffraction studies on vanadium sesquioxide. E. P. Warekois—346S
Precision lattice parameter measurements of cold-worked metals. Robert Asimov—410
Reply to comments on "determination of atomic scattering factors." R. B. Roof, Jr.—1131(L)
Structure in vitreous silicate fibers as shown by small-angle scattering of x-rays. W. O. Statton and L. C. Hoffman—404
Technique for calculating x-ray intensities in the electron probe microanalyzer. L. S. Birks—1297(L)
Temperature dependence of the Debye temperatures of aluminum, lead, and beta brass by an x-ray method. D. R. Chipman—2012
X-ray examination of brittle fractures in extruded chromium. C. W. Weaver and K. A. Gross—626
X-ray measurement of grain size. B. E. Warren—2237
X-ray reflection studies of the anneal and oxidation of some thin solid films. N. Wainfan and L. G. Parratt—1331
X-ray study of ferromagnetic domains in cobalt zinc ferrite. Kenneth M. Merz—147

Miscellaneous Materials and Techniques

Absorption, reflectivity, and Faraday rotation measurements on some rare-earth iron garnets and on α-Fe_2O_3. P. C. Bailey—39S

Analog study of large-signal high-frequency diodes. C. L. Andrews—1431

Analysis of a practical perpendicular head for digital purposes. George J. Y. Fan—402

Angular distribution of sputtered material. G. K. Wehner and D. Rosenberg—177

Apparatus for the measurement of the thermal diffusivity of solids at high temperatures. B. Abeles, G. D. Cody, and D. S. Beers—1585

Blood flow measurements using dynamical paramagnetic relaxation times, and paramagnetic tracer techniques. J. R. Singer—406S

Criteria for the choice of a superconducting bolometer. Bogoljub Lalevic—1234

Decay of wax electrets. M. M. Perlman—356

Depolarized components of light scattered by glasses. II. Influence of nonannealable strains on the scattering. Martin Goldstein—1697(E)

Detailed study of switching current in barium titanate. M. E. Drougard—352

Development of high-speed coincident current memory cores. Barlane R. Eichbaum—117S

Device for measurement of the electrical properties of Bi_2Se_3 at elevated temperatures. Mac J. Smith, E. S. Kirk, and C. W. Spencer—1504(L)

Dynamic hard sphere model. D. Turnbull and R. L. Cormia—674

Effect of geometry on thick film toroids. James C. Sagnis, Jr., Michael Teig, and Robert L. Ward—190S

Effect of previous history on switching rate in ferrites. R. W. McKay and K. C. Smith—133S

Effects of hydrostatic pressure on the properties of magnetic materials. R. E. Alley, Jr., and V. E. Legg—239S

Elastic switching properties of some square loop materials in toroidal structures. W. C. Seelbach and J. R. Kiseda—135S

Electrodeposited memory elements for a nondestructive memory. T. R. Long—123S

Electrostatic acceleration of microparticles to hypervelocities. H. Shelton, C. D. Hendricks, and R. F. Wuerker—1243

Etching of surfaces with 8-kev argon ions. R. L. Cunningham, P. Hayman, C. Lecomte, W. J. Moore, and J. J. Trillat—839

Exchange anisotropy memory effect. I. S. Jacobs and P. E. Lawrence—1388

Exchange anisotropy in rock magnetism. W. H. Meiklejohn and R. E. Carter—164S

Experimental flux pattern determination in magnetic cores. Robert L. Ward—192S

Fast switching by domain walls in ferrites. Walter Wiechec and Clinton M. Kelley—131S

Ferrite films—new logic and storage devices. J. M. Brownlow, W. L. Shevel, Jr., and O. A. Gutwin—121S

Ferromagnetic powders in waveguides at elevated temperatures. A. D. Krall and E. T. Hooper, Jr.—178S

Finite amplitude electromagnetic waves in gyromagnetic media. B. A. Auld—106S

Flat panel vacuum thermal insulation. H. M. Strong, F. P. Bundy, and H. P. Bovenkerk—39

Flow rates using nuclear or electron paramagnetic resonance techniques with applications to biological and chemical processes. J. R. Singer—125

Flux reversal by noncoherent rotation in magnetic films. K. J. Harte—283S

$GaFeO_3$: A ferromagnetic-piezoelectric compound. J. P. Remeika—263S

Generation of phonons in high-power ferromagnetic resonance experiments. Ernst Schlömann—1647

Germanium crystals grown from hollow cylindrical seeds. R. C. Frank and J. E. Thomas, Jr.—1689(L)

Harmonic generation in a ferrimagnetic disk. Glenn E. Bennett—98S

High-speed ferrite rotating half-wave plate. Franklin S. Coale—170S

Improved method for the growth of yttrium-iron and yttrium-gallium garnets. J. W. Nielsen—51S

Improvement of semiconductor surfaces by low melting glasses, possibly functioning as ion getters. S. S. Flaschen, A. David Pearson, and I. L. Kalnins—431(L)

Influence of nearby conductors on thin film switching. J. S. Eggenberger—287S

Instrumentation applications of inverse-Wiedemann effect. J. A. Granath—178S

Interaction of atomic hydrogen with glass. T. W. Hickmott—128

Investigations into the origin of anisotropy in oblique-incidence films. M. S. Cohen, E. E. Huber, Jr., G. P. Weiss, and D. O. Smith—291S

Ion drag pumps. Otmar M. Stuetzer—136

Long-term magnetic stability of Alnico and barium ferrite magnets. K. J. Kronenberg and M. A. Bohlmann—82S

Low melting sulfide-halogen inorganic glasses. S. S. Flaschen, A. David Pearson, and William R. Northover—219(L)

Magnetic anisotropy and magnetostriction of ordered and disordered cobalt-iron alloys. R. C. Hall—157S

Magnetic field measurement using ultrasonics. R. J. Radus—186S

Magnetism in medicine. Michael W. Freeman, M.D., Anthony Arrott, and John H. L. Watson—404S

Magnetization reversal in uniaxial films near to the preferred direction. E. M. Bradley and M. Prutton—285S

Manipulation of cesium. P. Leliak—609(L)

Method for determining the thermal conductivity of incandescent solids. B. B. Brenden and H. W. Newkirk—737(L)

Method for measuring iron losses in elliptically polarized magnetic fields. F. J. Young and H. L. Schenk—194S

Microcalorimetric technique for the study of damping and hysteresis in ferromagnetic films. J. R. Mayfield—298S

Millimicrosecond magnetization reversal in thin magnetic films. W. Dietrich and W. E. Proebster—281S

Miniature memory planes for extreme environmental conditions. R. Straley, A. Heuer, B. Kane, and G. Tkach—126S

Molecular beam formation by long parallel tubes. J. A. Giordmaine and T. C. Wang—463

Molecular trajectories in electric fields and state selection in a beam of sodium chloride. M. Peter, H. G. R. Venkates, and M. W. P. Strandberg—693

Multimode propagation in gyromagnetic rods and its application to traveling-wave devices. J. E. Tompkins, F. Reggia, and L. Joseph—176S

Multiple tube collimator for gas beams. G. R. Hanes—2171

New approach to high-speed storage—low-flux density materials. W. L. Shevel, Jr., and H. Chang—125S

New multi-aperture magnetic logic element. David R. Bennion—129S

Note on evaporation. S. A. Zwick—1735

Nucleation experiments on thin magnetic MnBi films. Ludwig Mayer—384S

Operation of magnetic film parametrons in the 100- to 500-Mc region. A. V. Pohm, A. A. Read, R. M. Stewart, and R. F. Schauer—119S

Miscellaneous Materials and Techniques (*continued*)
Orientation density and its use in quantitative texture studies. C. G. Dunn and J. L. Walter—827
Particle interaction in magnetic recording tapes. J. G. Woodward and E. Della Torre—56, 398S
Penetration depth investigation of gas cleanup with radioactive tracers. C. Y. Bartholomew and A. R. LaPadula —445(L)
Phase oscillations in high current synchrotrons. Irvin G. Henry—1338
Photoemission and related properties of the alkali antimonides. W. E. Spicer—2077
Photographic verification of ultrasonic plane wave scattering by cylinders. Harmon D. Nine and Norman W. Schubring—1274
p layers on vacuum heated silicon. F. G. Allen, T. M. Buch, and J. T. Law—979
Practical hysteresigraph. R. R. Bockemuehl and W. E. Sargeant—180S
Precipitation of dispsersed fine-particle magnetite. Lynore E. Slaten—74S
Precise measurement of magnetic form factors. Robert Nathans—350S
Preparation of tin single crystals for transmission electron microscopy. J. T. Fourie, F. Weinberg, and F. W. C. Boswell—1136(L)
Print-out process in photographic emulsion grains. J. F. Hamilton and L. E. Brady—609(L)
Production and properties of thin layers of indium antimonide. G. Bate and K. N. R. Taylor—991
Production of very high magnetic fields by implosion. C. M. Fowler, W. B. Garn, and R. S. Caird—588
Promotion of cubic grain growth in 3% silicon iron by control of annealing atmosphere composition. Dale Kohler—408S
Properties of manganese ferrites prepared at various oxygen pressures. Aleksander Bragiński—339S
Properties of p-type GaAs prepared by copper diffusion. F. D. Rosi, D. Meyerhofer, and R. V. Jensen—1105
Pulsed ferrimagnetic microwave generator. B. Elliot, T. Schaug-Peterson, and H. J. Shaw—400S
Recent appearance potential measurements using an electrostatic electron selector. Larkin Kerwin and Paul Marmet—2071
Rictometer system for calibrating transmitters of remote indicating compasses. L. I. Mendelsohn—183S
Roll magnetic anisotropy of iron-aluminum crystals. Soshin Chikazumi—158S
Scattering of radiation by a plasma. Forrest I. Boley—1692(L)
Secondary recrystallization in vacuum annealed silicon iron. G. Baer, D. Ganz, and H. Thomas—235S
Several new methods to measure the thermal diffusivity of semiconductors. J. H. Becker—612(L)
Simple radiant heating method for determining the thermal diffusivity of cellulosic materials. Stanley B. Martin—1101
Simple recording torque magnetometer. P. W. Neurath—184S
Small angle scattering investigation of Ludox mixtures. Robert H. Bragg, Irene Corvin, and John W. Buttrey —1183
Specific heat of some rare earth iron garnets and YIG at low temperatures. Horst Meyer and A. B. Harris—49S
Tetrahedral junction. Jerald A. Weiss—168S
Theory and application of dipolar ferrite modes. William H. Steier and Paul D. Coleman—99S
Time discrimination in solid-state infrared quantum counters. J. V. Jelley—1145
Transfer function and error probability of a digital magnetic tape recording system. John Wenchung Hung—396S
Use of SF_6^- for calibration of the electron energy scale. G. J. Schulz—1134(L)
Vapor-deposited single crystal germanium. Ralph P. Ruth, John C. Marinace, and W. C. Dunlap, Jr.—995

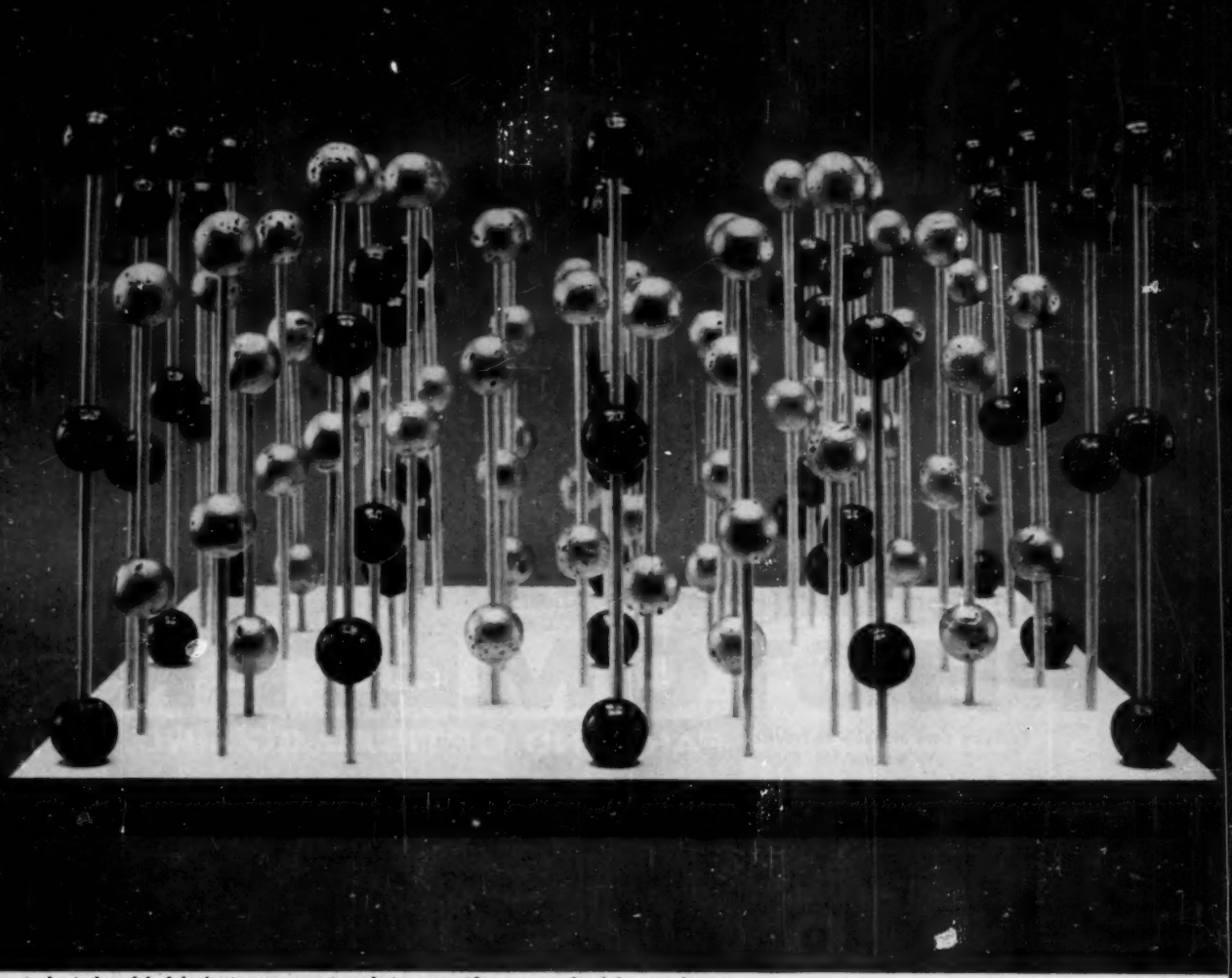

A physical model of the lattice structure in cadmium arsenide, an example of the complex compounds grown from the elements of the II-V groups of the periodic table.

Electron motion within a crystal lattice

Determination of the energy band structures of semiconductor crystals is necessary for complete understanding of the electron conduction processes in these crystals.

The energy band structure is the relationship between electron energy and momentum. While this relationship has been determined for some semiconductors, IBM scientists are now formulating energy band structures for an entirely new class of compounds consisting of elements from the II-V groups of the periodic table.

One of the experimental techniques they employ is based on a phenomenon known as *cyclotron resonance*. It occurs when electrons come under the influence of both a DC magnetic field and a radio-frequency electric field. The magnetic field causes the electrons to rotate in a helical path while the electric field induces oscillations. When the frequency of the electric field oscillation matches the frequency of the electron motion, the electrons absorb energy from the radio-frequency electric field. By measuring the strength of the magnetic field and the frequency of the electric field, the details of the energy band structure can be calculated.

Cyclotron resonance was first noticed by astrophysicists concerned with the propagation of radio waves through the ionosphere in the presence of the earth's magnetic field. In the laboratory, it can be observed in single crystals placed in a microwave cavity and immersed in a helium bath. The low-temperature environment reduces vibrations of the lattice, which tend to scatter the electrons and obscure the phenomenon.

By determining energy band structures for new compounds, these experiments are helping to broaden understanding of the basic properties of semiconductors. In addition, cyclotron resonance has proved valuable in the study of scattering mechanisms and the analysis of high-purity compounds.

IBM. RESEARCH

Investigate the many career opportunities available in exciting new fields at IBM.
International Business Machines Corporation, Dept. 579-Z, 590 Madison Avenue, New York 22, New York

NOW! 2 MODELS

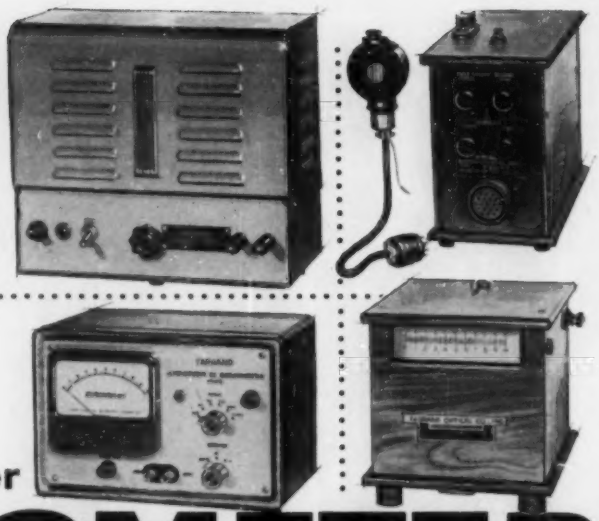

Provides a wide range of sensitivity, stability, and linear response particularly at extreme low-light levels. Choice of interchangeable photomultiplier tubes for optimum response in selected spectral regions. This compact, easy-to-operate instrument is now available in two models: battery power supply or transformer for line operation. Either model can be supplied with a galvanometer or with a highly sensitive microammeter.

Farrand Electron Multiplier PHOTOMETER

Technical data available on request
Specify Bulletin No. 804AP

FARRAND OPTICAL CO., INC.
BRONX BLVD. AND EAST 238th STREET • NEW YORK 70, N. Y.

NEWS from the NRC Vacuum MICRONICLE*

REDHEAD MAGNETRON GAUGE READS VACUUM TO BELOW 10^{-11} mm Hg

Direct measurement of pressure from 10^{-4} to less than 10^{-11} mm Hg is easy with the new Model 552 Redhead Magnetron Ultra-High Vacuum Gauge and Model 752 UHV Gauge Control.

Cold cathode operation keeps the Model 552 elements from vaporizing and eliminates the need for outgassing circuit. 8 lf-regulated emission simplifies operation and maintains high signal to background ratio on all ranges. High sensitivity of 4.5 amp/mm Hg (air) permits use of standard electrometer amplifier. Response is virtually linear and almost instantaneous.

Partially transistorized Model 752 has only four operating controls: two switches, range selector, and zero set. Connections are provided for 0-10 mv recorder. Short time constant permits observation of pressure fluctuations. Gauge, magnet, and control now in stock at $195, $50, and $850.

*Send for FREE periodical containing details on above plus other news about high vacuum.

NRC 16

NRC EQUIPMENT CORPORATION

A Subsidiary of National Research Corporation

Dept. P-12, 160 Charlemont Street, Newton 61, Mass.

In Translation . . .

Optika I Spektroskopiya
of the USSR Academy of Sciences

Published by the Optical Society of America as

Optics and Spectroscopy

Available as a unit with the
Journal of the Optical Society of America

Inquiries should be addressed to the American Institute of Physics, 335 East 45 Street, New York 17, New York.

Expanding electronics programs at

GOODYEAR AIRCRAFT

require the services of highly qualified men. Professional pride will be enhanced and mental stimulus provided by working on the team that is building some of the world's most advanced flight trainers, is developing the SUBROC antisubmarine weapon system, has vital parts in the BMEWS and Nike Zeus antimissile missile systems, and is leading the field in high resolution radar. GAC needs

COMPUTER SPECIALISTS

Math, physics, or EE degree required, MS or higher in most cases. Men who can analyze aircraft systems for simulation, develop analog and digital computer systems for simulation of aircraft behavior, generate input-output block diagrams and logic designs, study digital techniques for simulating multiple radar targets, and many other specialties.

SYSTEMS ENGINEERS
MATHEMATICIANS
PHYSICISTS

MS or PhD required for most openings, with three to ten years' experience in math and physics. Among openings are operations research, analysis of physical systems, model development, classical mechanics, noise and information theory, statistical analysis, nonlinear systems analysis, undersea warfare concepts and feasibility studies, scientific feasibility experiments, and industrial control systems.

The scientist will find ample laboratory facilities in which to develop his ideas. The company also offers outstanding fringe benefits in addition to salaries commensurate with the capabilities of the man.

Please send résumé to

Mr. C. G. Jones, Dept. 110

GOODYEAR AIRCRAFT

Akron 15, Ohio

Quartz monochromator features high speed, range from 1850Å to 3μ

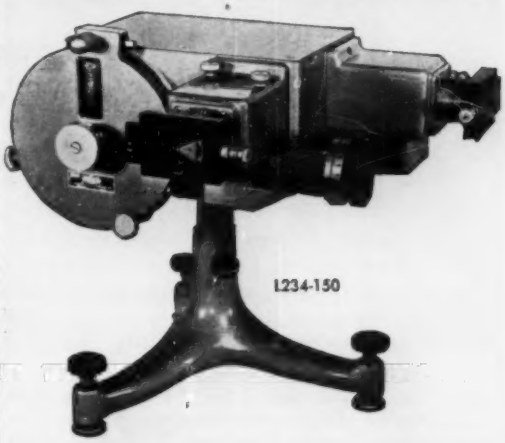

The Gaertner Quartz Monochromator gives you convenient reading with its large, flat wavelength dial. The Monochromator can be supplied with a camera attachment (L234-150A) which converts it to a high aperture spectrograph. This precision-made, quality instrument provides an exceptionally good monochromatic light source. Its high speed and wide range make it extremely useful in the study of absorption spectra, photosensitive materials, phosphorescence, energy distribution of light sources, and in many other applications.

Gaertner offers a diverse line of precision optical and measuring instruments to scientists in all fields. Our services include modifications of these instruments to meet unusual needs, complete design and manufacture of special instruments and optical systems, and manufacture of assemblies and instruments from customer sketches and drawings.

Write for information about optical or measuring instruments used in your field. For a detailed description of Gaertner Quartz Monochromators, request Bulletin 158-52.

Visit our exhibit at Physical Society—Physics Teachers' Meeting, February 1-4, Hotel New Yorker, New York City

Designed and manufactured in the U.S.A. by

Gaertner
SCIENTIFIC CORPORATION

1246 Wrightwood Ave., Chicago 14, Illinois • BU 1-5335

PLASMA ACCELERATION

The Fourth Lockheed Symposium on Magnetohydrodynamics

EDITED BY SIDNEY W. KASH

This fourth volume to grow out of Lockheed-sponsored symposia has for its theme the acceleration of plasma for propulsion for interplanetary travel. The papers present recent experimental and theoretical results concerning the principle means of accelerating ionized material for propulsion, including pulsed magnetic plasma accelerators and d-c electrostatic ion-electron accelerators. Detailed information is given on the problems involved and the obtainable thrust, specific impulse, and efficiency. $4.25

Order from your bookstore, please

STANFORD UNIVERSITY PRESS

AMF/R&D . . . seeks the

Literature Searcher

A new product idea is the sum of many parts . . . many isolated scientific facts which must be unlocked from the confines of mass data. The result of such investigation and winnowing can mean important breakthroughs in terms of time and method.

At American Machine and Foundry's modern Research and Development Laboratories in Springdale, Connecticut, a broad frontier of new concepts requires support in the physical science and engineering fields from an able literature searcher who can organize a technical information program.

You must have a degree in physics or engineering or its equivalent.

Send resume in complete confidence to Dick Parker

AMF

RESEARCH & DEVELOPMENT
DIVISION
AMERICAN MACHINE & FOUNDRY CO.
689 Hope Street, Springdale, Conn.

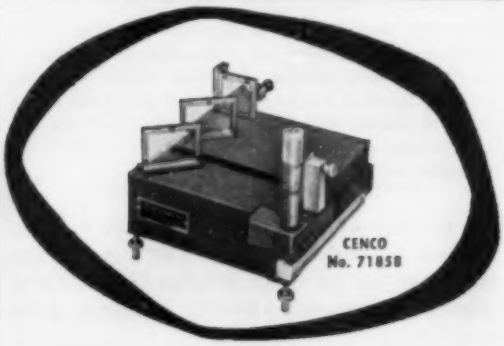

NOW! *a low cost Michelson*
INTERFEROMETER

This precision instrument is ingeniously designed to provide .2% accuracy at minimum cost. Directly calibrated in inches. Clear, well defined fringes are observable and measurable. Refractive properties of transparent materials can be easily studied. Sturdily constructed for classroom or laboratory research. Complete with monochromatic mercury light and illustrated experiment manual . . . only $209.95

cenco

CENTRAL SCIENTIFIC CO.
A Subsidiary of Cenco Instruments Corporation
1718-A Irving Park Road • Chicago 13, Illinois
Mountainside, N. J. Montreal Santa Clara
Somerville, Mass. Toronto Los Angeles
Birmingham, Ala. Ottawa Vancouver Houston
Cenco S.A., Breda, The Netherlands Tulsa

MODEL 55

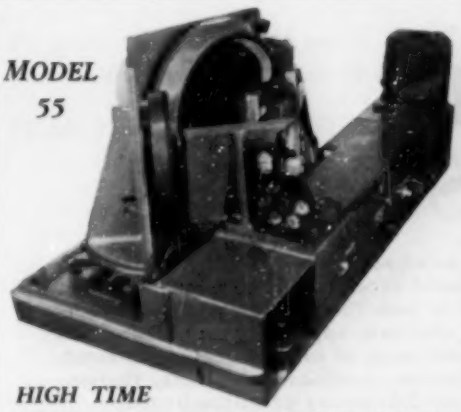

HIGH TIME RESOLUTION STREAK SPECTROGRAPH

A research instrument for investigation of transient luminous sources emitting radiations in the visible or ultraviolet spectrum. Provides a two dimensional time versus wavelength record on 35mm film. Spectral ranges 3050 to 4350 A° with 45 A°/mm dispersion, and 4200 to 6000 A° with 60 A°/mm dispersion. Relative aperture F/2.0. Resolvable time interval is 10^{-7} seconds.

Send for descriptive literature

Tropel, Inc., 52 West Ave., Fairport, N.Y.

CENCO® HYVAC GAS BALLAST PUMPS

For vacuum applications plant and laboratory. Eliminates use of oil separators, centrifuges, refrigerated traps. Wide range of capacities.

No. 91506-1 rated displacement, 70.0 liters per min....$284.25

cenco

CENTRAL SCIENTIFIC CO.
A Subsidiary of Cenco Instruments Corporation
1718-A Irving Park Road • Chicago 13, Illinois
Mountainside, N. J. Montreal Santa Clara
Somerville, Mass. Toronto Los Angeles
Birmingham, Ala. Ottawa Vancouver Houston
Cenco S.A., Breda, The Netherlands Tulsa

THE 1960's WILL BE A DECADE OF TIME COMPRESSION . . .

More people will travel further in a shorter time—men will move in geocentric orbits at 18,000 mph—space probes will shrink our celestial environment. To accomplish these things, the time between research and application engineering will shrink dramatically.

Convair believes that the full potential of Technology in the Sixties will be realized through ideas originating in the minds of creative scientists and engineers. To implement this conviction, Convair-Fort Worth is pursuing an active research program in the engineering and physical sciences.

A position on the staff of the newly formed Applied Research Section offers opportunity rarely found for physicists and engineers at the doctorate level. Research programs in the fields of astrophysics, relativity, gravitation, physics of materials, and geophysics are in the formative stages of planning and activation. Active and mature programs in electronics, space mechanics, and thermodynamics are underway.

If you can qualify, a position within this section will offer unlimited growth potential. For further information, forward your personal resume to Dr. E. L. Secrest, Chief of Applied Research, Convair-Fort Worth, P. O. Box 748 J, Fort Worth, Texas.

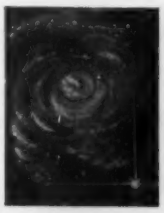

CONVAIR/FORT WORTH
CONVAIR DIVISION OF
GENERAL DYNAMICS

CHEMISTS
PHYSICISTS

Rapid and steady growth has created new openings in Melpar's Physical Sciences Laboratory for several experienced solid state chemists or physicists. Must be skilled in both theoretical and applied techniques, involving the selection, synthesis, application and testing of a wide variety of materials. Broad areas of interest include infrared, electroluminescence, semiconductors, nonlinear amplifiers, thermoelectricity, electro-chemistry, and fabrication of microcircuits.

Send complete resume to: **Professional Placement Manager**

MELPAR, INC.

A Subsidiary of Westinghouse Air Brake Co.

3343 Arlington Boulevard, Falls Church, Va.
In Historic Fairfax County. *(10 MILES FROM WASHINGTON, D.C.)*

Soviet Physics—SOLID STATE

Monthly. A cover to cover translation of the USSR Academy of Sciences journal, "Fizika Tverdogo Tela."

Soviet Physics—TECHNICAL PHYSICS

Monthly. A cover to cover translation of the USSR Academy of Sciences journal, "Zhurnal Tekhnicheskoi Fiziki."

Soviet Physics—CRYSTALLOGRAPHY

Bimonthly. A cover to cover translation of the USSR Academy of Sciences journal, "Kristallografiya."

Please address orders and inquiries to the publisher:

AMERICAN INSTITUTE OF PHYSICS
335 East 45th Street, New York 17, N. Y.

- **STUDENT SECTION NEWSLETTER**
- **SPEAKERS For STUDENT SECTIONS**
- **MOVIES and FILM STRIPS For STUDENT SECTIONS**
- **GRADUATE SCHOOL INFORMATION**
- **PLACEMENT INFORMATION**
- **PHYSICS TODAY**

The above is some of the information sent systematically to all American Institute of Physics Student Sections. There are now 2300 student members in over 100 sections.

A booklet describing in detail the procedure for establishing Student Sections and the benefits which student organizations derive from membership will be sent upon request. Address all inquiries to:

Mrs. Ethel E. Snider, National Secretary
Student Sections
American Institute of Physics
335 East 45th Street
New York 17, N. Y.

Be sure to examine these books from McGraw-Hill . . .

FIELD THEORY OF GUIDED WAVES

By Robert E. Collin, Case Institute of Technology. *McGraw-Hill Electrical and Electronic Engineering Series.* 591 pages, $16.50.

PRINCIPLES OF MECHANICS OF SOLIDS AND FLUIDS, Volume I

By Hsuan Yeh, University of Pennsylvania, and Joel I. Abrams, Yale University. *McGraw-Hill Series in Engineering Sciences.* 396 pages, $8.95.

WAVE PROPAGATION IN A RANDOM MEDIUM

By L. A. Chernov, U.S.S.R. Translated by Richard A. Silverman, New York University. 176 pages, $7.50.

TIME-HARMONIC ELECTROMAGNETIC FIELDS

By Roger V. Harrington, Syracuse University. Ready in January, 1961.

WAVE PROPAGATION IN A TURBULENT MEDIUM

By V. I. Tatarski, Academy of Sciences, U.S.S.R. Translated by Richard A. Silverman, New York University. Ready in January, 1961.

INTRODUCTION TO ATOMIC AND NUCLEAR PHYSICS

By Otto Oldenberg, Harvard University. Ready in January, 1961.

QUANTUM THEORY OF ATOMIC STRUCTURE, Volumes I and II

By John C. Slater, Massachusetts Institute of Technology. Volume I—502 pages, $11.00. Volume II—464 pages, $13.00.

Send for on-approval copies

McGraw-Hill Book Company, Inc.

330 West 42nd Street New York 36, N. Y.

Since final quality of your production of ferrites, electronic cores, and magnetic recording media depends on proper use of 3 specialized groups of magnetic materials . . . you'll find it mighty helpful to have all the latest, authoritative technical data describing the physical and chemical characteristics of each. This information is available to you just for the asking. Meanwhile, here are highlights of each product group.

PURE FERRIC OXIDES—For the production of ferrite bodies, we manufacture a complete range of high purity ferric oxide powders. These are available in both the spheroidal and acicular shapes, with average particle diameters from 0.2 to 0.8 microns. Impurities such as soluble salts, silica, alumina and calcium are at a minimum.

MAGNETIC IRON OXIDES—For magnetic recording—audio, video, instrumentation etc.—we produce a group of special magnetic oxides with a range of controlled magnetic properties. Both the black ferroso-ferric and brown gamma ferric oxides are available.

MAGNETIC IRON POWDERS—For the fabrication of magnetic cores in high-frequency, tele-communication, and other magnetic applications, we make a series of high purity iron powders.

If you have problems involving any of these materials, please let us go to work for you. We maintain fully equipped laboratories for the development of new and better inorganic materials. Write . . . stating your problem . . . to C. K. Williams & Co., Dept. 38, 640 N. 13th St., Easton, Penna.

WILLIAMS
COLORS & PIGMENTS

C. K. WILLIAMS & CO.

E. ST. LOUIS, ILL. • EASTON, PA. • EMERYVILLE, CAL.

a vacuum pump as compact as a . . .

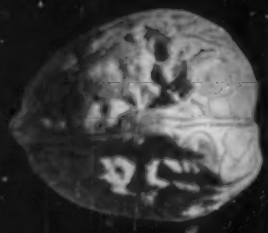

Yes, designed for compactness . . . and with no costly extras to buy. Saves up to 50% of your valuable floor space. But these are just a few of the revolutionary features of the new Stokes Series H Microvac pump.

Find out why Stokes offers you *more pumping performance per dollar*. Just write: Vacuum Equipment Division, F. J. STOKES CORPORATION, 5500 TABOR RD., PHILA. 20, PA.

STOKES

SEND TODAY
for your free
Vacuum Slide Calculator!

now from Librascope:

NARROW-BAND INTERFERENCE FILTERS

. . . with a new approach to side-band problems

Recent achievements at Librascope's Applied Research Center make it possible for you to now order high-precision, multilayer, narrow-band interference filters . . . custom-made to your specified wavelength, side-band requirement, and detector's spectral characteristics. Greater than 70% transmission and a half bandwidth of approximately 1% at specified peak wavelength. Delivery from stock: set of 8 filters uniformly distributed over visible spectrum . . . as well as mercury and sodium lines. Send your requirements for quotation today.

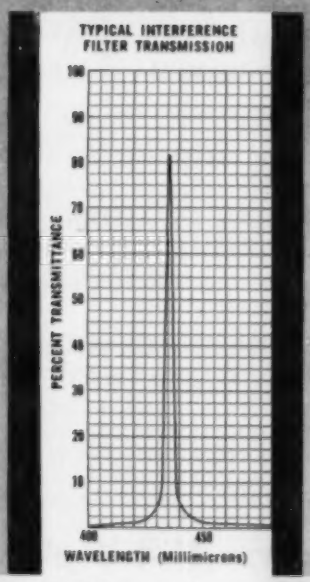

BURBANK BRANCH
LIBRASCOPE DIVISION
GENERAL PRECISION, INC.
100 East Tujunga • Burbank, Calif.

RESEARCH ENGINEERS & SCIENTISTS

Kollsman
Instrument Corporation

Announces
the Formation of a

NEW RESEARCH DIVISION

This division will undertake basic and applied research related to advanced tracking, computing, communications, control, instrumentation and display systems. The scope of these programs will include theoretical work in the basic sciences and experimental verification in the areas of:

SOLID STATE PHYSICS • SYSTEMS ANALYSIS
SPECTROSCOPY • DIGITAL TECHNIQUES
SYSTEMS SYNTHESIS • MICROMINIATURIZATION
GEOMETRICAL & PHYSICAL OPTICS
ELECTRO-CHEMICAL TECHNIQUES
CIRCUIT SYNTHESIS & IMPLEMENTATION
LIGHT GENERATION, MODULATION & DETECTION

The creation of this new research division provides qualified Engineers and Scientists an opportunity to join a recognized leader in automatic navigation and flight instrumentation . . . a dynamic organization in which "growth is based on technological superiority in our areas of interest."

To arrange a confidential interview, please forward a brief resume to Mr. John Whitton.

Kollsman
Instrument Corporation

80-08 45th AVE., ELMHURST 73, QUEENS, NEW YORK
A Subsidiary of Standard Kollsman Industries Inc.

TIFFEN OPTICAL FACILITIES FOR SCIENCE AND INDUSTRY

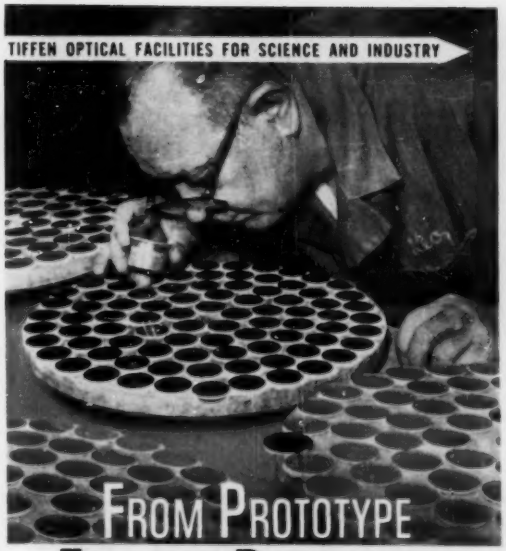

FROM PROTOTYPE THROUGH PRODUCTION

For over a decade, government agencies, industrial firms and photo studios have turned to TIFFEN for precision optical accessories. Now, TIFFEN offers their specialized knowledge, experience and expanded facilities to all industry employing optics in their product. TIFFEN's major facilities are partially described below:

BLANCHARDS . . . flat grinding to .00005". Diamond wheel shaping to .0001". ***EDGING*** . . . to less than .001", to 20" dia. Bevels and odd shapes ground. ***DRILLING*** . . . dia. 010" to 12", concentric to within .0005", on glass, ceramics, silicon, germanium, etc. ***GRINDING & POLISHING*** . . . 1mm. dia. to 24" dia., within 1/10 wavelength in flatness, under 2 seconds arc in parallel. Roof prisms to 2 seconds of arc accuracy. ***COATING*** . . . high vacuum deposition of all types of material, partial coatings for beam splitters and metallic neutral density filters. ***COLOR LABORATORY*** . . . includes Densichron, Beckman Du Spectrophotometer, Weston Foot Lambert Meter. ***FILTERS*** . . . laminated glass equal in environmental tests to solid glass, with superior color control, resolution to 100 lines per mm. ***MACHINING*** . . . multi-spindle automatic to 4", secondary machines to 10" capacity. ***TOOL ROOM*** . . . 23" swing lathes, grinders, millers. All tools and jigs manufactured internally.

Special problems? Write, call or visit: TIFFEN OPTICAL CO., 71 Jane St., Roslyn Hgts., L. I., N. Y.
West Coast Rep.: CRAIG CORP., 3410 So. La Cienega Blvd., Los Angeles 16, Cal.

TIFFEN DELIVERS THE GOODS!

INDEX TO ADVERTISERS

Name	*Page*
AEROSPACE CORPORATION	vi
AMERICAN MACHINE & FOUNDRY CO.	xxii
BECKMAN & WHITLEY, INC. .... Cover 2 Manufacturers of high-speed research cameras—both framing and sweeping-image type; specialized meteorological instruments; heat-flow transducers; and explosive-actuated mechanisms.	
BELL TELEPHONE LABORATORIES	v
CENTRAL SCIENTIFIC CO. .... xxii, xxiii Manufacturers of Cenco physical apparatus and instruments to meet all requirements of University, College and High School Physics Laboratories, Specializing in high vacuum pumps and development of instruments and apparatus for various sciences.	
CONVAIR/FORT WORTH DIV. OF GENERAL DYNAMICS	xxiii
DELCO RADIO DIV. OF GENERAL MOTORS	xvi
DOW CORNING CORPORATION ...	iii
FARRAND OPTICAL CO.	xx
GAERTNER SCIENTIFIC CORP.	xxi
Spectroscopes, spectrometers, spectrographs, spectrophotometers, heliostats, measuring microscopes, comparators, cathetometers, reading telescopes, interferometers, chronographs, dividing machines, etc.	
GENERAL RADIO CO. ..... Cover 3 Manufacturers of electronic measuring instruments; vacuum-tube voltmeters, amplifiers, and oscillators; wave analyzers, noise meters and analyzers, stroboscopes, laboratory standards of capacitance; inductance and frequency; impedance bridges, decade resistors and condensers, air condenser and variable inductors; rheostats, variacs, transformers; other laboratory accessories.	
GOODYEAR AIRCRAFT CORPORATION	xxi
HAMNER ELECTRONICS CO., INC. .	xiv
HARVEY-WELLS ELECTRONICS, INC.	ix
HUGHES AIRCRAFT CO.	xvii
IBM CORPORATION	xix
JET PROPULSION LABORATORY ..	x
JOHNS HOPKINS UNIVERSITY, THE APPLIED PHYSICS LAB. ...	xii
KEITHLEY INSTRUMENTS, INC. ..	iv
Vacuum tube electrometers, microammeters, kilovoltmeters, static detectors, meg-meg-ohm-meters, high gain dc amplifiers, dc vacuum tube voltmeters, high input impedance ac isolation amplifiers.	
KOLLSMAN INSTRUMENT CORP. .	xxvii
LOCKHEED MISSILES & SPACE DIV.	xiii
LOS ALAMOS SCIENTIFIC LAB. ...	vii
LIBRASCOPE DIV. OF GENERAL PRECISION, INC.	xxvi
McGRAW-HILL BOOK CO., INC. ...	xxv
MELPAR, INC.	xxiv
NRC EQUIPMENT CORP.	xx
Manufacturers of standard and special high vacuum compounds, equipment, and systems including mechanical booster, and diffusion pumps; gauges; valves; seals; connectors; melting and heat-treating furnaces; coaters; impregnators; gas in metal analyzers; driers and freeze driers; altitude chambers; and leak detectors.	
RAY PORTER ASSOCIATES, INC. ..	xxix
RAMO-WOOLDRIDGE LABS. .... Cover 4 Research, development, and manufacture in the field of electronic systems for commercial and military applications, and in the field of guided missiles.	

INDEX—*Continued*

Name	*Page*
STANFORD UNIVERSITY PRESS ..	xxii
STOKES CORP., F. J. ..... Mechanical and oil vapor pumps; vacuum valves, gauges and other components; vacuum furnaces, metalizers, processing systems and other special high vacuum equipment.	xxvi
SYLVANIA ELECTRONICS SYSTEM	
AMHERST LABORATORIES	xv
WALTHAM LABORATORIES	viii
TEKTRONIX, INC. ..... Manufacturers of Cathode-Ray Oscilloscopes, Auxiliary amplifiers, square-wave generators, vacuum-tube characteristic-curve tracers, L.C. Meters, constant-amplitude generators, operational accessories	xi
TIFFEN OPTICAL CO.	xxvii
TROPEL, INC.	xxiii
WELCH SCIENTIFIC CO., W. M. .... Manufacturers of high-vacuum pumps, both mechanical and diffusion; vacuum gauges; electrical measuring instruments; physics equipment; and other items for the physical and chemical laboratories.	xviii
WILLIAMS & CO., C. K.	xxv

GROUP LEADER

COLOR MEASUREMENT AND SPECIFICATION

Dynamic international chemical fiber producer needs graduate in chemistry, physics or related field with knowledge and experience in instrumental color measurement to supervise and expand color measurement and specification activities. Assignment involves instrumental color matching, development of instrumental color control, prediction of shade ranges based on historical color preference, and related activities. Write: Journal of Applied Physics, Box 1260, 335 East 45th St., New York 36, N. Y.

RESEARCH POSITIONS

DIRECTOR RADIATION SCIENCES (PhD) to—$30,000
Microwave, IR, Energy Conversion, Inc.

MANAGERS (3) (PhD) to—$25,000
Microwave, IR, Energy Conversion

SEMICONDUCTOR DEVICES $10,000 to $20,000
All fields—Chemists, Metallurgists, Physicists, (B.S., M.S., PhD)

All the above positions are outstanding opportunities with client companies of national reputation in their field. Applicants must have proven records of achievement.

All inquiries held in the strictest confidence

Ray Porter Associates, Inc.
3 Penn Center Plaza
Philadelphia 2, Pa.
LOcust 3-9119

Management Consultants serving industry in the field of executive search.

POSITIONS OPEN

THE UNIVERSITY OF LEEDS, ENGLAND
THE HOULDSWORTH SCHOOL OF APPLIED SCIENCE

Applications are invited from physicists and physical chemists for post-doctorate and pre-doctorate research appointments for interesting investigations of solid state diffusion and other physical properties of glasses and crystalline ionic solids, under the general supervision of Dr. J. P. Roberts. The pre-doctorate appointments offer the opportunity of study for the Ph.D. degree. Stipends up to £1,200 per annum will be paid. Applications (three copies) stating date of birth, education, qualifications and experience, together with the names of three referees, should be sent to the Registrar, The University, Leeds, 2 England (from whom further particulars may be obtained).

Soviet Physics | SOLID STATE

A translation, beginning with 1959 issues of "Fizika Tverdogo Tela" of the USSR Academy of Sciences. Offering results of theoretical and experimental investigations in the physics of semiconductors, dielectrics, and on applied physics associated with these problems. Also publishes papers on electronic processes taking place in the interior and on the surface of solids.

*Twelve issues, approx. 3,000 pages. $55 domestic, $59 foreign. Libraries * $25 domestic, $29 foreign. Single copies, $8.*

Soviet Physics | TECHNICAL PHYSICS

A translation, beginning with 1956 issues of "Zhurnal Tekhnicheskoi Fiziki" of the USSR Academy of Sciences. Contains work on plasma physics and magnetohydrodynamics, aerodynamics, ion and electron optics, and radio physics. Also publishes articles in mathematical physics, the physics of accelerators and molecular physics.

*Twelve issues, approx. 2,000 pages. $55 domestic, $59 foreign. Libraries * $25 domestic, $29 foreign. Single copies, $8.*

Soviet Physics | CRYSTALLOGRAPHY

A translation, beginning with 1957 issues of the journal "Kristallografiya" of USSR Academy of Sciences. Experimental and theoretical papers on crystal structure, lattice theory, diffraction studies, and other topics of interest to crystallographers, mineralogists, and metallurgists.

*Six issues, approx. 1,000 pages. $25 domestic, $27 foreign. Libraries * $10 domestic, $12 foreign. Single copies, $5.*

Orders and inquiries should be sent to:

American Institute of Physics

335 East 45 Street, New York 17, N.Y.

Subscription prices subject to annual variation depending on size of Russian originals.

UNIT OSCILLATORS

frequency ranges from 20c to 2000 Mc; 2700 Mc to 7425 Mc.

High Performance, Economical "Building Blocks" for the laboratory

- *High Output*
- *Good Stability*
- *Compact Size*
- *Convert to Sweep Oscillators with G-R Dial Drives*

20c to 500 Kc in 5 Ranges
Type 1210-C Unit R-C Oscillator
$180... ±3% accuracy — low-Z sine wave (80-mw/7v); high-Z sine wave (40-mw/45v); square wave (0-30 v p-p).

0.5 to 50 Mc in 2 Ranges
Type 1211-B Unit Oscillator...$295
±2% accuracy — 1500 mw (0.5 to 5 Mc), and 500 mw (5-50 Mc) into 50-ohm load.

50 to 250 Mc

Type 1215-B Unit Oscillator...$210
±1% accuracy — 100-mw minimum output into 50-ohm load; 200 mw over most of range.

65 to 500 Mc

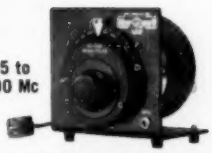

Type 1208-B Unit Oscillator...$230
±2% accuracy — 200-mw output into 50-ohms; 400 mw over most of range.

180 to 600 Mc

Type 1209-BL Unit Oscillator . . . $260 ±1% accuracy—300-mw output into 50-ohms; 400 mw over most of range.

250 to 920 Mc

Type 1209-B Unit Oscillator...$260
±1% accuracy — 200-mw output into 50-ohms; 300 mw over most of range.

900 to 2000 Mc

Type 1218-A Unit Oscillator...$465
±1% accuracy — 200-mw output into 50-ohms.

2700 to 7425 Mc
Depending on Klystron used
Type 1220-A Unit Klystron Oscillator...$235 (less Klystron) 40-mw output into 50-ohms.

1214 SERIES FIXED-FREQUENCY OSCILLATORS

Type No.	Frequency	Accuracy	Output	Price
1214-A	1000 c 400 c	±2%	200 mw/60 v	$75
1214-D	120 c	±2%	400 mw/60 v	$100
1214-E	1000 c 270 c	±2%	300 mw/28 v	$75
1214-M	1 Mc	±1%	300 mw/7 v	$75

(All 1214 Oscillators have built-in power supplies)

UNIT POWER SUPPLIES
for use with Unit Oscillators

Type 1201-B . . . $85
Regulated Power Supply
300 v dc, regulated to ±0.25%, 70 ma; 6.3 v ac at 4 a, unregulated

Type 1203-B . . . $45
Power Supply
6.3 v ac at 3 amp; 300 v dc at 50 ma.

Write For Complete Information

GENERAL RADIO COMPANY

WEST CONCORD, MASSACHUSETTS

The Best Instruments In Electronics

NEW YORK, WOrth 4-2722 NEW JERSEY, Ridgefield, WHitney 3-3140	CHICAGO Oak Park Village 8-9400	PHILADELPHIA Abington HAncock 4-7419	WASHINGTON, D.C. Silver Spring JUniper 5-1088	SAN FRANCISCO Los Altos WHitecliff 8-8233	LOS ANGELES Los Angeles HOllywood 9-6201	IN CANADA Toronto CHerry 6-2171

Progress in mechanizing some of the intellectual functions has been partial and uneven.

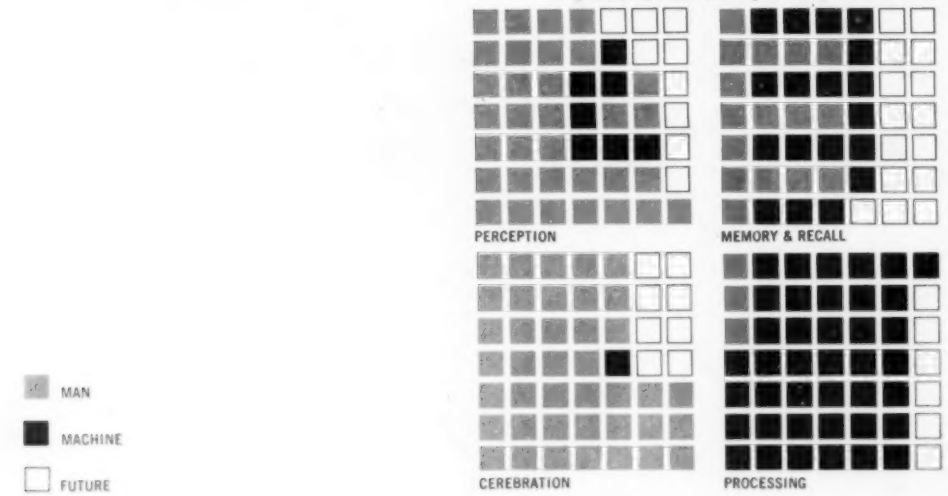

INTELLECTRONICS... Extending Man's Intellect By Electronics

Through the ages, from the invention of the wheel to the development of nuclear power plants, scientists and engineers have used matter and energy in various ways to extend man's physical powers. The needs of modern civilization now call for a greater emphasis on helping man do tasks that lie in the intellectual, rather than the physical, domain. Progress in mechanizing some of the intellectual functions has been partial and uneven, as the diagram above suggests. Our goal is to achieve a synthetic intelligence—part human and part mechanical—which combines the strongest features of both to produce a new order of intellectual power exceeding that of either men or machines operating separately.

At Ramo-Wooldridge's new Intellectronic Research Laboratory, fundamental research is being carried on in such fields as applied quantum mechanics, theoretical intellectronics and the physical phenomena associated with computer components and devices. The program includes exploration of the "room at the bottom," as exemplified by the non-equilibrium population of energy levels, the behavior of systems at temperatures near absolute zero, and other atomic and molecular properties as yet not fully exploited. Theoretical intellectronics involves the study of adaptive and self-teaching machines, and the investigation of methods for achieving a more efficient use of computers in the solution of physical problems. Still other lines of research are concerned with novel concepts of the function and organization of computers, such as the use of optical elements and the investigation of new methods of memory arrangements.

Physicists holding a Ph.D. degree or equivalent are invited to discuss their research interests in these areas with Dr. Burton D. Fried, Director, Intellectronic Research Laboratory, at the Annual Meeting of the American Physical Society in New York City. Inquiries may also be directed to Mr. Frank Nagel at

RAMO-WOOLDRIDGE

A DIVISION OF

THOMPSON RAMO WOOLDRIDGE INC.

8433 FALLBROOK AVENUE • CANOGA PARK, CALIFORNIA